TECHNISCHE UNIVERSITÄT MÜNCHEN

TUM School of Engineering and Design

Modeling and control of wind turbine systems with doubly-fed induction machines

Christian Johannes Georg Dirscherl, M.Sc.

Vollständiger Abdruck der von der TUM School of Engineering and Design der Technischen Universität München zur Erlangung des akademischen Grades eines

Doktors der Ingenieurwissenschaften

genehmigten Dissertation.

Vorsitzender:		Prof. Dr.-Ing. Hartmut Spliethoff
Prüfer der Dissertation:	1.	Prof. Dr.-Ing. Christoph M. Hackl
	2.	Prof. Dr. rer. nat. Thomas Hamacher

Die Dissertation wurde am 13.12.2021 bei der Technischen Universität München eingereicht und durch die TUM School of Engineering and Design am 17.08.2022 angenommen.

This document is typeset with LaTeX/TeX.

Danksagung

Ein Projekt im Umfang einer Promotion kann nur gelingen, wenn viele verschiedene Rädchen ineinander greifen. Motivation, Einsatz und Fleiß alleine reichen nicht aus. Es braucht auch das notwendige Glück, dass Dinge, die man selbst nicht beeinflussen kann, in die richtige Richtung laufen. Ich hatte dieses Glück und möchte mich im Folgenden bei allen Personen bedanken, ohne die meine Promotion auf diese Art und Weise nicht zustande gekommen wäre.
Ein ganz besonderer Dank gilt Prof. Dr.-Ing. Christoph M. Hackl für das Ermöglichen dieser Dissertation. Er betreute meine gesamte Promotion hervorragend, sicherte mir stets seine Unterstützung zu und hatte immer Zeit für Fragen und Diskussionen. Seine Herangehensweise, sowohl physikalische Zusammenhänge im Detail zu verstehen als auch diese mathematisch präzise niederzuschreiben, schätze ich sehr und war für mich äußerst lehrreich. Außerdem war es für mich sehr wertvoll, dass er für diese Arbeit einen gewissen Korridor vorgab, ich innerhalb dieses Korridors jedoch sämtliche Freiheiten hatte, eigene Ideen zu verwirklichen und selbständig zu arbeiten. Dafür bin ich sehr dankbar.
Bei Prof. Dr. Thomas Hamacher möchte ich mich ganz herzlich für die Übernahme des Zweitgutachtens und seine große Unterstützung als Direktor der MSE bedanken. Für die Übernahme des Prüfungsvorsitzes bedanke ich mich bei Prof. Dr.-Ing. Hartmut Spliethoff. Ein weiterer Dank gebührt meinem Mentor Dr. Sc. Vlaho Petrović, der mir mit seinen Erfahrungen und Ratschlägen sehr geholfen hat.
Ein ganz großer Dank gilt Korbinian Schechner. Es wird schwer, nochmals eine derart motivierende Büroatmosphäre zu erleben. Die endlosen Fachsimpeleien und unzähligen Whiteboard-Tüfteleien waren mir eine Freude. Auch die Beharrlichkeit, bei gegenseitigen Erklärungen so lange nachzuhaken, bis jedes kleinste Detail erklärt werden konnte, hat wesentlich zu dem tiefen Verständnis beigetragen, welches diese Arbeit erfordert. Meine Kollegen Hisham Eldeeb, Julian Kullick und Markus Landerer haben dazu ebenfalls einen erheblichen Beitrag geleistet. Dafür, und für die wunderbare gemeinsame Zeit, möchte ich mich bei ihnen herzlich bedanken.
Für die tolle Stimmung in unserer Forschungsgruppe danke ich auch den weiteren Mitgliedern, Mohamed Abdelrahem, Katharina Bär, Athina Birda, Simon Krüner, Cristian Ladisla und Zhenbin (James) Zhang.
Den MSE-Doktoranden, Mihael Čorić, Oliver Filonik, Akhila Jambagi, Michael Kramer, Jenny Lebert und Stephan Pröller möchte ich für die fachlichen Gespräche und insbesondere für die schöne Zeit abseits der Arbeit danken.
Während meiner Promotion betreute ich eine Vielzahl an Studienarbeiten. Für die gute Zusammenarbeit ein großes Dankeschön an meine Studenten, Martin Baumann, Andjelka Bujandric, Josef Fessler, Lucas S. De la Fuente Munita, Florian Hans, Weiqing Huang, Oliver Kalmbach, Johannes Kamhuber, Benedikt Kulot, Yi Lei, Max Lindner, Niklas Monzen, Michael Schreiber, Florian Wittl und Minghao Xu.
Der Prüfstand fand seinen Platz im Labor des Lehrstuhls für elektrische Antriebssysteme und Leistungselektronik. Vielen Dank an die Kollegen des Lehrstuhls, Prof. Dr.-Ing. Dr. h.c. Ralph Kennel, Hannes Börngen, Julien Cordier, Wolfgang Ebert, Alexander Florian, Heidi Jonas, Sascha Kühl, Peter Landsmann, Eyke Liegmann, Darshan Manoharan, Julia Menz, Dirk Paulus und Dietmar Schuster. Sowohl die fachlichen als auch die nicht-fachlichen Diskussionen bereiteten mir immer viel Freude.
Für die Hilfe beim Aufbau des Prüfstands möchte ich mich bei Oliver Kalmbach, Julian Kullick, Max Lindner, Korbinian Schechner und Dietmar Schuster bedanken. Ohne deren Hilfe wären meine Messungen nicht möglich gewesen.

Über zwei Jahre bezog unsere Forschungsgruppe Büros des Lehrstuhls für Windenergie. Wir wurden herzlich aufgenommen und fantastisch integriert. Dafür ein großes Dankeschön an die Kollegen des Lehrstuhls, Prof. Dr. Carlo L. Bottasso, Marta Bertelè, Pietro Bortolotti, Stefano Cacciola, Filippo Campagnolo, Mark Capellaro, Elli Matzner, Johannes Schreiber, Jesse Wang und Robin Weber. In diesem Zusammenhang auch ein Dank an Martina Thieme. Nach dieser Zeit siedelte unsere Forschungsgruppe in das neu errichtete Zentrum für Energie und Information über. Ich möchte allen Kollegen des ZEIs für die schöne Zeit danken.
Ein liebes Dankeschön geht auch an die Mitarbeiter der MSE-Verwaltung. Deren große Hilfsbereitschaft erleichterte mir sämtliche Bürokratie- und Organisationsbelange erheblich. Besonders Angela Brunnbauer, Christiane Hamacher, Sabine Kutscherauer und Monika Knürr gebührt mein Dank.
Bei Josef Ametsbichler und Korbinian Schechner bedanke ich mich herzlich für das Korrekturlesen dieser Arbeit.
Für die Finanzierung der Forschungsgruppe "Regelung von regenerativen Energiesystemen" möchte ich mich zudem beim (damaligen) Bayerischen Staatsministerium für Bildung und Kultus, Wissenschaft und Kunst bedanken.
Ein sehr großer Dank gilt auch meinen Eltern, die mich während meiner gesamten Ausbildungszeit wundervoll unterstützt haben. Die Sicherheit, mich voll und ganz auf mein Studium konzentrieren zu können, hat mir auf dem Weg zur Promotion sehr geholfen. Zu guter Letzt möchte ich mich bei meiner Frau und meiner Familie bedanken, die mich stets motivierten und auf die ich mich immer verlassen konnte.

Burgheim, November 2021 Christian Dirscherl

Contents

List of Figures

List of Tables

Nomenclature

The following list introduces the utilized nomenclature with descriptions:

$\mathbb{N}$, $\mathbb{R}$	natural and real numbers.
$\boldsymbol{x} := (x_1, \ldots, x_n)^\top \in \mathbb{R}^n$	column vector with $x_i \in \mathbb{R}$ for all $i \in \{1, \ldots, n\}$, $n \in \mathbb{N}$, where $^\top$ transposes the row vector $(x_1, \ldots, x_n)$.
$\|\boldsymbol{x}\| := \sqrt{\boldsymbol{x}^\top \boldsymbol{x}}$	Euclidean norm of $\boldsymbol{x} \in \mathbb{R}^n$, $n \in \mathbb{N}$.
$\boldsymbol{0}_n := (0, \ldots, 0)^\top \in \mathbb{R}^n$	zero vector, $n \in \mathbb{N}$.
$\boldsymbol{1}_n := (1, \ldots, 1)^\top \in \mathbb{R}^n$	unity vector, $n \in \mathbb{N}$.
$\boldsymbol{X} := \begin{bmatrix} x_{11} & \ldots & x_{1n} \\ \vdots & & \vdots \\ x_{m1} & \ldots & x_{mn} \end{bmatrix} \in \mathbb{R}^{m \times n}$	matrix with m rows and n columns, $m, n \in \mathbb{N}$, and coefficients $x_{pq} \in \mathbb{R}$ for $p \in \{1, \ldots, m\}$ and $q \in \{1, \ldots, n\}$.
$\boldsymbol{X}^{-1}$	inverse of $\boldsymbol{X} \in \mathbb{R}^{n \times n}$, $n \in \mathbb{N}$.
$\boldsymbol{X}^\top$	transpose of $\boldsymbol{X} \in \mathbb{R}^{m \times n}$, $m, n \in \mathbb{N}$.
$\boldsymbol{X} < 0$	negative definite matrix $\boldsymbol{X} \in \mathbb{R}^{n \times n}$, $n \in \mathbb{N}$.
$\det(\boldsymbol{X})$	determinant of $\boldsymbol{X} \in \mathbb{R}^{n \times n}$, $n \in \mathbb{N}$.
$\operatorname{rank}(\boldsymbol{X})$	rank of $\boldsymbol{X} \in \mathbb{R}^{m \times n}$, $m, n \in \mathbb{N}$.
$\operatorname{diag}(x_1, \ldots, x_n)^\top \in \mathbb{R}^{n \times n}$	diagonal matrix with entries $x_i \in \mathbb{R}$ for all $i \in \{1, \ldots, n\}$, $n \in \mathbb{N}$.
$\boldsymbol{I}_n := \operatorname{diag}(1, \ldots, 1)^\top \in \mathbb{R}^n$	identity matrix, $n \in \mathbb{N}$.
$\boldsymbol{O}_{m \times n} \in \mathbb{R}^{m \times n}$	zero matrix with m rows and n columns, $m, n \in \mathbb{N}$.
$\boldsymbol{1}_{m \times n} \in \mathbb{R}^{m \times n}$	unity matrix with m rows and n columns, $m, n \in \mathbb{N}$.
$\boldsymbol{x}$ (in X)^n	each element of the physical quantity $\boldsymbol{x}$ has unit X, $n \in \mathbb{N}$.
$\boldsymbol{x}^{xy} := (x^x, x^y)^\top$	quantity in the two-phase xy-reference frame.
$\boldsymbol{x}^{xyz} := (x^x, x^y, x^z)^\top$	quantity in the three-phase xyz-reference frame.
$\boldsymbol{x}^{x\text{-}y\text{-}z} := (x^x\text{–}x^y, x^y\text{–}x^z, x^z\text{–}x^x)^\top$	line-to-line quantity in the three-phase xyz-reference frame.
$\boldsymbol{X}^{xy} := \begin{bmatrix} X^{xx} & X^{xy} \\ X^{yx} & X^{yy} \end{bmatrix}$	matrix in the two-phase xy-reference frame.
$\boldsymbol{X}^{xyz} := \begin{bmatrix} X^{xx} & X^{xy} & X^{xz} \\ X^{yx} & X^{yy} & X^{yz} \\ X^{zx} & X^{zy} & X^{zz} \end{bmatrix}$	matrix in the three-phase xyz-reference frame.
$\boldsymbol{x}(t) \in \mathbb{R}^n$	value of $\boldsymbol{x}$ at $t \geq 0$, $n \in \mathbb{N}$.
$\boldsymbol{x}[k] := \boldsymbol{x}(kt_{\text{dis}}) \in \mathbb{R}^n$	sampled value of $\boldsymbol{x}$ at time instant $kt_{\text{dis}} \geq 0$ for $k \in \mathbb{N} \cup \{0\}$ and sampling time $t_{\text{dis}} > 0$, $n \in \mathbb{N}$.

Abstract

The thesis discusses modeling and control of wind turbine systems with doubly-fed induction machine (DFIM). A holistic model design yields the dynamic power flow, which allows for a detailed efficiency analysis. By means of a new DFIM model based on nonlinear flux maps and differential inductances, cross-couplings and saturation effects are considered. The flux and inductance maps are obtained by a specific experimental setup. An adaptive proportional-integral controller with disturbance and cross-coupling compensation regulates the rotor currents of the DFIM in an inner control loop. If an additional LC filter is implemented, an adaptive integral state-feedback controller with either filter current decoupling control or reference feed-forward compensation is proposed instead. In the outer cascade, a strategy for both machine torque and stator reactive power control is presented. The back-to-back converter with very small DC-link capacitor is connected to the grid via an LCL filter. The resonance frequency is damped actively and is close to the low sampling frequency of the real-time system, thus a controller design in discrete-time domain is required. A discrete integral state-feedback controller for the grid side currents is employed using the discrete linear-quadratic regulator theory. The gains of the proportional-integral controller for adjusting the DC-link voltage are determined by a detailed stability analysis based on the closed-loop dynamics of the overall grid side model. Experiments at the laboratory test-bench validate the very good control performances. Moreover, the simulation results match the experimental results with very high accuracy.

Kurzzusammenfassung

Die Arbeit befasst sich mit der Modellierung und Regelung von Windkraftanlagen mit doppelt gespeister Asynchronmaschine (DGAM). Ein ganzheitlicher Modellierungsansatz liefert den dynamischen Leistungsfluss, der eine detaillierte Effizienzanalyse ermöglicht. Mit Hilfe eines neuen DGAM-Modells, basierend auf nichtlinearen Flusskarten und differentiellen Induktivitäten, werden Kreuzkopplungen und Sättigungseffekte berücksichtigt. Ein spezieller Versuchsaufbau dient zur Gewinnung der Fluss- und Induktivitätskarten. Über einen adaptiven PI-Regler mit Kompensation der Kreuzkopplungs- und Störterme werden die Rotorströme der DGAM in einem inneren Regelkreis reguliert. Wird ein zusätzlicher LC-Filter installiert, empfiehlt sich stattdessen ein adaptiver Zustandsregler mit Integralanteil, der entweder eine Entkopplung der Filterströme oder eine Vorsteuerung der Referenzwerte beinhaltet. Außerdem wird ein Regelkonzept für das Maschinenmoment und die Statorblindleistung im äußeren Regelkreis vorgestellt. Der Back-To-Back-Konverter mit sehr kleinem Zwischenkreiskondensator ist über einen LCL-Filter ans Netz gekoppelt. Die Resonanzfrequenz wird aktiv bedämpft und liegt nahe an der Abtastfrequenz des Realzeitsystems, was eine zeitdiskrete Reglerauslegung erfordert. Für die Regelung der netzseitigen Ströme wird ein diskreter Zustandsregler mit Integralanteil eingesetzt. Bei dessen Auslegung wird auf die diskrete linear-quadratische Regelungstheorie zurückgegriffen. Die PI-Reglerparameter für die Zwischenkreisspannungsregelung werden über eine detaillierte Stabilitätsanalyse auf Basis der geschlossenen Regelkreisdynamik des netzseitigen Gesamtmodells bestimmt. Experimente am Laborprüfstand verifizieren die hochperformanten Regelungskonzepte. Zudem zeigt sich eine hohe Übereinstimmung zwischen den Simulations- und Messergebnissen.

Chapter 1

Introduction

Since the turn of the millennium, wind turbine systems have strongly increased their contribution to the electrical energy production in Germany. While in 2000, they only produced 9.5 TWh of electrical energy, more than 114 TWh were generated in 2018. In the same period, the installed capacity increased from 4.8 GW up to 59.6 GW. Hence, wind turbine systems contribute 17.5 % to the total electrical energy production in 2018. Only brown coal had a bigger share with 22 %. [1]
In Europe, 14.7 GW of new wind capacity was installed in 2020, which raised the total wind capacity to 220 GW. This means a share of 16 % of the annual electrical energy consumption in Europe. Scenarios in [2] regarding the amount of newly installed wind capacity in Europe forecast a further increase, e.g. about 25 GW in new onshore and offshore wind turbine systems are expected in 2025. [2]
The rising influence of wind power on the electrical energy production takes place not only in Europe but worldwide. In 2020, the global capacity of wind turbine systems reached 743 GW, which corresponds to a growth of 14 % compared to 650 GW of installed capacity in 2019 [3]. Therefore, wind turbine systems will exhibit an important impact on future power grids [4].

1.1 Motivation

Wind turbine systems with doubly-fed induction machine (DFIM) are the most widely used concept in Germany surpassed only by direct-drive wind turbine systems. In the period from 2000 to 2018, their annual share of newly installed wind turbine systems varies from about 20 %

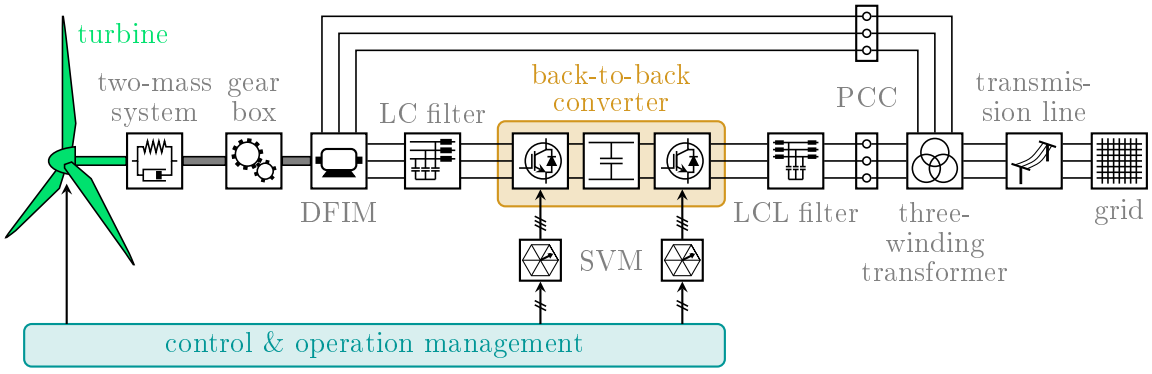

Figure 1.1: *Main components of wind turbine systems with doubly-fed induction machine (illustration is based on Fig. 1 in [5]).*

to almost 50 % [1].
Fig. 1.1 depicts the main components of wind turbine systems with DFIM. The turbine is coupled to the DFIM via a gear box that transmits slow turbine rotation to fast machine rotation. The damping and stiffness characteristics of the drive train are emulated by an additional two-mass system. In contrast to direct-drive wind turbine systems, here, the use of a gear box is necessary. The design of the DFIM does not allow for high pole pair numbers which would be essential to compensate for the different rotational speeds between turbine and DFIM without a gear box [6]. The DFIM is fed by two three-phase systems. Its stator is directly coupled to the three-winding transformer that feeds the generated power of the wind turbine system to the grid (via the transmission line). Due to the straight connection of the stator to the grid, the DFIM reacts sensitively to grid faults [7]. The rotor of the DFIM is connected to the three-phase system by slip rings that require high maintenance [8]. However, they allow to feed the rotor with an adjustable voltage so the DFIM is able to operate at variable speed (in a range of $\pm 30\,\%$ of its synchronous speed [9]). The back-to-back converter links the rotor to the three-winding transformer. Since the main amount of the power flows from the stator to the grid, only about 30 % of the generated power flows through the back-to-back converter [9, 10]. This makes it possible to reduce the size of the back-to-back converter and, consequently, to lower its costs. The (optional) LC filter between the rotor and the back-to-back converter smooths the voltage applied to the rotor so the stress on the machine is decreased. To filter the currents fed to the three-winding transformer, an additional LCL filter is used.
The control and the operation management ensure the desired operation of the wind turbine system. The operation management defines the control objectives and the control realizes these objectives (a) by adjusting the rotor blades and the nacelle of the turbine and (b) by applying pulsed switching signals to the back-to-back converter (including the space vector modulation (SVM) as modulation scheme).
One focus of this thesis is modeling of such wind turbine systems with DFIM. Accurate system models are essential for high-quality simulations. In [11] and [12], the necessity and benefits of model-based simulations are summarized. Often real systems do not exist to perform experiments and, hence, no gain in system knowledge can result from it. Also time efficiency and cost reasons can prevent operations with real components. In such cases, running simulations can be used to obtain relevant information. They allow for parameter variations—which mostly is not easy to accomplish in real systems—and thus extend the range of possible experiments. Moreover, all quantities can be measured with arbitrary sampling frequency and faulty test executions do not cause system damage. A crucial requirement for attaining valid knowledge by simulation is a precise and entire system model.
For that reason, this thesis presents a holistic model approach for wind turbine systems with DFIM. The performed simulations are compared to measurement data from experiments with real components to validate the correctness of the models. It will be shown that the results of the developed models show a very precise match with those of the real components. In addition, the thesis investigates the control of wind turbine systems with DFIM based on these models. The control needs to guarantee reliable and efficient operations of the wind turbine system, e.g. to achieve fast reference tracking, to compensate for disturbances or to minimize losses and thus costs. For this purpose, stable and high-performance controllers are designed. Experiments at the laboratory test-bench will verify the implemented control strategies.

1.2 State-of-the-art

To highlight the contributions of this thesis, it is necessary to discuss the state-of-the-art by summarizing previous research on the major focus of this thesis: the electrical system and its

control.[1] Therefore, Sec. 1.2.1 presents a literature review on the grid connection of electrical systems via power electronics[2] and Sec. 1.2.2 explains the state-of-the-art for modeling and control of doubly-fed induction machines.

1.2.1 Grid connection of electrical systems via power electronics

More and more electrical systems are coupled to the electrical grid via power electronics, e.g. photovoltaic systems, electric vehicles during the charging process or battery storage systems. This allows, inter alia, for independent control of active and reactive power exchanged with the grid [18]. For this purpose, grid-connected converters are used between a DC-link and the three-phase grid side. In case of wind turbine systems with DFIM, a back-to-back converter—which consists of two converters and a common DC-link (see Fig. 1.1)—connects the rotor of the DFIM to the grid side. Thereby, the power flow over the back-to-back converter is bi-directional depending on the operation. [19] shows that power flowing from the grid side into the back-to-back converter is a critical operation for system stability. Hence, the DC-link capacitor of the back-to-back converter, which stores energy and stabilizes the DC-link voltage, needs to be dimensioned carefully. For this reason, it is often oversized which results in several drawbacks. Large electrolyte capacitors are bulky and increase volume, weight and system costs. Moreover, a shorter lifetime due to their electrolyte reduces the reliability [20],[21]. Therefore, in this thesis, the back-to-back converter is equipped with a very small DC-link capacitance with regard to its power rating. Only few publications deal with a similarly small DC-link capacitance, e.g. [20],[22] and [23].

Due to the switching behavior of the converters' semiconductors, the grid side current is characterized by high order harmonics. Hence, to meet the total harmonic distortion limits of the grid code requirements, the use of a current filter is required. In this thesis, a high-performance LCL filter is installed, which exhibits better damping characteristics and system dynamics compared to conventional L-filters. This allows for smaller inductances and consequently for cost-efficiency and compact sizes [24]. In return, for preventing system instability, it is essential to damp its resonance frequency either actively or passively [25],[26]. To avoid additional losses—e.g. due to a damping resistor—an active damping by the implemented controller design is utilized, which guarantees highly efficient filtering. Besides, the resonance frequency of the used LCL filter is about one-third of the sampling frequency of the real-time system. This (high) ratio necessitates a system description in the discrete time domain for the controller design.[3]

In summary, the employed electrical system for the grid connection of the wind turbine system results in tough challenges for the control strategy: (i) a very small DC-link capacitance despite the bi-directional power flow, (ii) a high-performance LCL filter with (iii) active damping and (iv) a low sampling frequency close to the resonance frequency of the LCL filter. It requires a holistic approach for the grid side control that considers the challenges (i) to (iv) all at once. This has not been taken into account by previous research, e.g. each of the following studies rely on a rather large DC-link capacitance or do not consider the DC-link at all.

The grid side control of the wind turbine system is characterized by a cascaded structure, where the inner control-loop adjusts either the current flow or the power flow between DC-link and grid side. The objective of the outer control-loop is to guarantee a stable DC-link voltage.

[1] The mechanical system of the wind turbine systems with DFIM as in Fig. 1.1 is described by simplified models. For complex models and detailed knowledge on the mechanical system (and on the aerodynamics), further literature is needed (see e.g. [13–16]).

[2] Similarly, the literature review of Sec. 1.2.1 has already been published in [17].

[3] Conditions for a quasi-continuous controller design are given in [27], e.g. the ratio less than or equal to one-eighth between the dominant system frequency and the sampling frequency is considered sufficient. Obviously, the above ratio of one-third is much higher, therefore a quasi-continuous controller design is not feasible.

In [28], the grid side three-phase quantities are transformed to DC quantities with the help of Clarke's and Park's transformation together with a phase-locked loop. This allows for an inner power control by using two standard proportional-integral controllers in combination with a cross-coupling compensation. [29] picks up the same idea but employs current instead of power control. If only Clarke's transformation is applied to the grid side three-phase quantities, neither a phase-locked loop is necessary [30] nor cross-coupling terms exist [31],[32]. Instead, usually a frequency-locked loop is needed and the grid side quantities and their references are sinusoidal, thus requiring a quasi-proportional-resonant controller. Moreover, harmonics in the grid current must be suppressed by harmonic compensators [31],[32]. In [33], a voltage-oriented proportional-integral current controller with disturbance and cross-coupling compensation is extended by a virtual resistor based active damping, which uses the capacitor currents of the LCL filter to damp its resonance frequency and to stabilize the system. Therein, a classic proportional-integral controller is employed for DC-link voltage control. [34] presents a DC-link voltage droop controller for a single-phase converter with LCL filter. By a special sensing technique, the mean value of the DC-link voltage is calculated in such a way that the range of the controller bandwidth is enlarged. Nevertheless, the mean value estimation comes along with some time delay, which is counterproductive for a fast control performance. Further, [34] explains two power controller based on this droop control strategy. One optimized controller for power loss minimization and one adaptive controller considering the instantaneous DC-link current and the grid amplitude. In [35], an adaptive proportional-integral controller is proposed to regulate the DC-link voltage, where the controller gains are self-tuned depending on the operation point. On an experimental test-bench, the adaptive controller shows a better performance than a standard proportional-integral controller.[4] [36] presents a Lyapunov-based current control, where the control variable involves both inverter current and capacitor voltage of the LCL-filter. Besides a high robustness against parameter uncertainties and grid distortions, this control strategy guarantees global stability. [37] and [38] use simple cascaded proportional-integral controllers to regulate the DC-link voltage and the grid currents of the LCL-filter, but approximate the LCL-filter as conventional L-filter for the controller design. This is an over-simplification and—in respect of the reduced efficiency due to a passive damping method—not recommendable. In [39], a nonlinear sliding mode controller for the inner control-loop is combined with an proportional-integral controller for the outer DC-link voltage control. Also, other nonlinear controller designs can be found in literature. Applied methods are e.g. backstepping control [40],[41],[42] or input-output-linearization [43].

While the previous studies use continuous-time based controller designs, [44] presents a discrete-time model of an LCL-filtered converter. The discrete-time current control strategy combines a deadbeat controller with an optimal state-feedback pole assignment. By the proposed controller, an active damping of the resonance frequency is achieved and overcurrent protection is possible while preserving the pole locations. [45] proposes a current controller based on an internal model (IM), where the system is discretized by the step invariant method. The feedback gains are optimized by the linear matrix inequality approach so the IM-based current controller is stabilized. Using an additional state estimator allows for an active damping of the LCL filter's resonance frequency with a reduced number of sensors. [46] (time-continuous case) and [47] (discrete-continuous case) develop an observer-based state-space control for the converter side currents with complex-valued modeling and pole placement. In both studies, the model-based design enables an automatic tuning of the controller and the resonance frequency of the LCL filter is actively damped. The discrete-time approach in [47] yields a faster dynamic performance and a better resonance damping than the continuous-time approach in [46]. In [48] also, a discrete-time state-space controller is designed for the grid side currents of the LCL filter. The modeling

[4] This approach uses only a simple L-filter.

is carried out in the complex domain so this approach utilizes complex pole placement for the controller design. [49] and [50] employ a back-to-back converter with relatively large DC-link capacitance, where each of its two converter is connected to an electrical network via an LCL filter. In [49], a state-feedback controller regulates both output currents of the converter and DC-link voltage. Therefore, the controller design based on a unified converter and filter model, where the feedback gains are determined by a linear quadratic regulator. [50] proposes a power-based full-state feedback control for a back-to-back converter, where differential and common power concepts are investigated. The LCL filter and DC-link dynamics are aggregated in a power-based state-space model. A discrete linear quadratic regulator determines the feedback gains of the controller in such a way that both dc-link voltage regulation and active and reactive power control are achieved by a single controller. [51] focuses on current control of a converter with single phase LCL filter. Linear matrix inequality conditions are used for the design of the robust discrete linear quadratic controllers. Due to the assumption of a constant DC-link voltage, its control is not part of the study. [52] develops an approach for the current control of a three-phase LCL-filter, which uses a linear quadratic Gaussian servo controller technique. A discrete linear quadratic regulator current controller is combined with a Kalman filter. The grid currents and the DC-link voltage are measured, while the other states are estimated by the Kalman filter, which yields a better quality in noisy environments compared to a Luenberger observer. A proportional-integral controller regulates the DC-link voltage. Due to the large DC-link capacitance, an appropriate design of the controller gains is not necessary, why [52] provides neither tuning rules nor a stability analysis. A different technique to control the DC-link voltage is presented in [53]. Therein, a digital Takagi-Sugeno-Kang fuzzy controller is implemented, which uses both the actual control error of the DC-link voltage and its integral over time as controller inputs. Simulations show a promising performance of the fuzzy controller in terms of settling time and overshoots during transient conditions.

Several studies also use predictive control methods to control grid-connected converters via the LCL filter. A generalized predictive current controller is presented in [54]. It features low computational complexity and considers both harmonic distortion limits and robustness against filter component variations. A drawback is the employed damping resistor that causes efficiency losses. In [55], a model predictive control (MPC) technique is used for grid side current control. The control algorithm provides an analytical solution allowing for high prediction horizons. Moreover, an integral error feedback is introduced to assure steady-state accuracy for constant disturbances. Another MPC strategy for grid side current control is investigated in [56]. By means of a discrete-time system model, all switching states are checked and the one that minimizes a certain cost function is chosen. In addition, a duty ratio optimization technique is applied. According to simulation results, this model predictive current controller is able to obtain a good steady-state performance. [57] introduces two finite-control-set MPC algorithms for current control that eliminate low-order grid current harmonics and reduce sensitivity to grid voltage distortion. Experimental measurements verify, inter alia, that the proposed controllers provide low harmonic distortions of the grid current and a fast dynamic performance. In [58], the benefits of finite-control-set MPC and proportional-resonant control are merged by cascading both controllers. The outer proportional-resonant controller regulates the grid-side current and the inner MPC controller damps the resonance frequency of the LCL filter and is responsible for its capacitor voltage. This strategy avoids steady state errors, complex controller tunings and long prediction horizons. Instead, a dynamic control performance with a nicely damped resonance frequency is achieved. Finally, [59] presents a finite-control-set MPC strategy with a reduced number of sensors. By means of a virtual flux observer, which provides the grid voltage and grid-injected current reference, and an additional state observer for estimating the states of the LCL filter, only sensors for the grid-injected currents are needed. The proposed finite-

control-set MPC approach obtains a high quality grid-injected current under both balanced and unbalanced grid voltage conditions.

1.2.2 Doubly-fed induction machine and its control

Plenty of studies focus on modeling and especially on control of doubly-fed induction machines. By far the most of them use space vector models in a two-dimensional reference frame to describe the physical behavior of the DFIM. [60] and [61] employ a space vector model in a stator-fixed reference frame to achieve—for an encoderless operation—an estimation of machine angle and speed, respectively. More often, rotating reference frames in either flux or grid voltage orientation are used that allow for DFIM modeling by DC-quantities. E.g. [62–66] deal with DFIM models in stator flux orientation, while in [67] the reference frame is aligned with the space vector of the rotor flux. Since neither stator nor rotor flux can be measured directly, they must be obtained by flux estimation.

In this thesis, grid voltage orientation for the DFIM model is applied (as e.g. in [5, 68, 69]). A phase-locked loop detects, inter alia, the grid voltage angle to align the reference frame with the grid voltage. In contrast to the studies above, which all operate with constant machine parameters, the developed DFIM model also considers nonlinear characteristics by flux maps and differential inductances. This allows for taking e.g. cross-couplings and saturation effects into account.[5]

Another possible way to represent saturation effects is a nonlinear manipulation of the main inductance by the magnetic current, which is defined as the sum of stator and rotor current [75]. However, [75] points out that this method neglects the impact of the leakage fluxes on the saturation. This is why he proposes two additional nonlinear inductances for the stator and rotor circuit, respectively. While [75] was published in 1989, today's studies still use the idea to consider saturation effects by an appropriate adjustment of the main inductance. [71] performed experimental measurements to determine the relation between main inductance and magnetic current. In [76], a nonlinear factor depending on the magnetic current is multiplied with the constant value of the main inductance to obtain the saturated behavior. A drawback of modeling saturation effects by nonlinear manipulations is that it requires either complex parameter tunings or high measurement efforts to acquire appropriate look-up tables. To obtain the saturation characteristics of the DFIM by simulation, magnetic finite elements analysis can be applied as well, which warrants detailed knowledge of the DFIM's construction (see e.g. [77]). The same holds for magnetic equivalent circuits as in [78] and [79] as well as for the analytical field calculation of the DFIM presented in [80].

As already mentioned in Sec. 1.1, an optional LC filter can interconnect back-to-back converter and DFIM. Due to the switching behavior of the machine side converter, the converter outputs pulsed voltages that come along with high order harmonics. The LC filter reduces the harmonic distortion of the rotor currents and voltages [81] and the stress on the DFIM is decreased. Nevertheless, only few studies consider an additional LC filter in their system design, e.g. [69, 81–84]. [82] analysis different placements of LC filters in wind turbine applications with DFIM in order to eliminate shaft voltages. In [83], the LC filter is connected to different converter topologies for industrial medium-voltage drives. The objective is to compare the expense of power semiconductors and passive components of two-level, three-level neutral-point-clamped, three-level flying-capacitor, four-level flying-capacitor, and five-level series-connected H-bridge

[5] The developed DFIM model does not focus on iron losses, hence, those are neglected. Iron losses in stator and rotor occur due to hysteresis effects and eddy currents and can be integrated into the equivalent circuit diagram by a (nonlinear) ohmic resistance in parallel to the magnetizing inductance [70]. E.g. [71] and [72] use such an iron resistance. [73] and [74] also utilize this option, but for synchronous machines.

converters. An interesting investigation is performed in [84], where several LC filter configurations are examined. That is (a) a star connected LC filter with isolated neutral point, (b) a Δ-connected LC filter and (c) four star connected LC filters, where each of their neutral points exhibit at least one additional low-resistance connection to the DC-link of the converter.
[69] focus on the adjustment of the rotor current control of the DFIM that must be carried out due to the additional LC filter. Therein, a model predictive controller is proposed for a DFIM model with constant machine parameters. The electrical system, which includes an integral error feedback to achieve steady-state accuracy, is formulated as disturbed linear time-invariant multiple-input multiple-output system without constraints. This allows for both an analytical solution of the MPC problem and high prediction horizons.
This thesis has not only to consider the LC filter but also the nonlinear characteristics due to flux maps and differential inductances. For this purpose, a controller design based on adaptive integral state-feedback control in the discrete-time domain is developed. It includes either a filter current decoupling controller or a reference feed-forward compensation.
A standard way to control a DFIM without LC filter is to use a cascaded controller design, where the inner control-loop adjusts the rotor currents and the outer control-loop regulates, inter alia, the machine torque. In contrast to DFIM models with constant machine parameters, in this thesis, the gains of the proportional-integral controllers for the rotor currents need to be designed adaptively in order to take into account the operating point of the machine. Moreover, the nonlinear characteristics of the DFIM model necessitate enhanced feed-forward compensations to eliminate disturbance and cross-coupling effects.
In [85] and [86], the rotor current control is employed conventionally with constant gains of the proportional-integral controller and reduced feed-forward terms. [85] investigates a hybrid virtual impedance method to minimize low-order current harmonics, for which an extra compensation term is considered for the rotor current control. [86] addresses symmetrical faults in weak grids and uses grid voltage orientation, which is the most commonly applied reference frame for the control design besides stator flux orientation. [87] compares the two reference frames for the standard DFIM model with constant machine parameters. The analysis shows that—in opposition to the stator flux orientation—stability and damping of the system do not depend on the d-component of the rotor current for grid voltage orientation. As a consequence, a random amount of reactive power can be produced without endangering system stability.[6]
However, stator flux orientated controller designs are widespread, e.g. [89] and [90] propose proportional-integral controllers and feed-forward terms to control the rotor current. In [90], the implemented current control is further extended by two methods that estimate both machine angle and rotational speed. This allows for an encoderless controller design.
Several studies focus on control approaches without measuring machine angle and speed respectively. [91] presents a machine speed estimation based on a second-order generalized integrator that achieves accurate speed estimations even under distorted rotor current conditions. Integrating the machine speed yields the rotor position. This method can produce deviations due to small speed estimation errors and the unknown initial position. This is why an additional rotor position correction is employed to eliminate those deviations. In [92], two stator flux based model reference adaptive observers (SF-MRAO) are proposed for estimating the rotor speed and position in a stand-alone DFIM. The first approach uses notch filtering and obtains a similar estimation performance than a standard SF-MRAO method but with a reduced number of required voltage and current sensors. The second approach employs a linearized SF-MRAO which increases the estimation performance. Also, [93] does not implement a rotor position sensor but estimates the machine angle based on a backstepping technique and [94] combines a

[6] Obviously, system-related limits such as current or voltage maxima nevertheless restrict the possible reactive power that can be generated (see e.g. [88]).

rotor position observer for a stand-alone DFIM supplying nonlinear and unbalanced loads and a linear quadratic regulator that stabilizes the system states. Another approach is presented in [95]. Therein, the direct flux-vector control method is introduced. It is performed in the rotor reference frame and does not need machine speed nor position. Since the laboratory test-bench—used for this thesis—is equipped with an encoder, the control without rotor position sensor is not considered in this work.
Some studies integrate sliding mode controllers into their control strategy for the DFIM. In [96], a sub-synchronous resonance mitigation method, based on a nonlinear sliding mode controller, is introduced for series-compensated DFIM-based wind turbine systems. The rotor current references in stator flux orientation are determined by maximum power point tracking and stator reactive power regulation. [97] proposes an adaptive second-order sliding mode controller in order to deal with quickly varying disturbances. In [98], a discrete-time second-order sliding mode controller is implemented to adjust the optimum tip speed ratio of the turbine.
A controller design on the basis of input-to-state stability theory is presented in [99], where a certain control law outputs the rotor voltage references based on control Lyapunov functions. [99] determines the control Lyapunov functions via a systematic algorithm. In [100], an input-output-linearization of the DFIM—using the differential flatness theory—is invoked. Defining flat outputs obtain an equivalent DFIM description in the Brunovsky form for which a feedback controller is designed. Moreover, [100] combines this control strategy with a Kalman filtering approach to estimate additive input disturbances. A nonlinear damping control strategy to reduce sub-synchronous resonances in series-compensated DFIM-based wind farms is proposed in [101]. The control laws result from a partial feedback linearization technique that is applied to a partially linearized form of the DFIM system. In [102], a robust H_∞ control through the state-dependent Riccati equation method is introduced. To guarantee stabilizability and controllability, an input-to-state stability theory is applied to the DFIM. Further, the selection of both state-dependent coefficient matrices and weighting matrices is analyzed. The control objective in [102] is to reduce the impact of grid voltage dips on the system dynamics.
In general, since the stator of wind turbine systems with DFIM is directly coupled to the grid, the DFIM reacts sensitive to grid faults [103]. Accordingly, several studies examine control strategies to compensate for grid faults, e.g. some of them focus on the low-voltage ride through capability to ensure a stable operation (see e.g. [103–105]). In this thesis, such control strategies are not considered because only operations without grid faults are investigated.
Finally, [106] and [107] present two possible methods to control a DFIM that is connected to a current source inverter with DC-link inductor. Both studies introduce nonlinear control approaches for active and reactive power flow regulation.

1.3 Contributions

This section summarizes the contributions of this thesis and outlines its structure. Overall, the main contributions of the thesis are the following:

(i) to emulate DFIMs precisely, a nonlinear model based on nonlinear flux maps and differential inductances is developed. It considers magnetic cross-couplings as well as saturation effects (see Sec. 2.2.2.1).

(ii) a method is shown in order to obtain the nonlinear flux maps and differential inductances of the DFIM by measurements at the laboratory test-bench (see Sec. 2.2.2.2 and Sec. 2.2.2.4).

(iii) a holistic model of wind turbine systems with DFIM is derived, where both mechanical and electrical components of the wind turbine system are combined (see Sec. 2.3). Based on

this holistic model, the dynamic power flow of such a wind turbine system is investigated. This allows for a detailed efficiency analysis (see Sec. 2.4).

(iv) to ensure a high-performance grid side control, a discrete integral state-feedback controller of the grid side currents is developed (see Sec. 3.2.2).

(v) to realize a well tuned DC-link voltage proportional-integral controller, a detailed stability analysis based on the closed-loop dynamics of the overall grid side model is performed (see Sec. 3.2.3).

(vi) the nonlinear characteristics of the DFIM are considered by developing an adaptive rotor current proportional-integral controller with disturbance and cross-coupling compensation (see Sec. 3.3.2).

(vii) to comply with the tasks of using an additional LC-filter to couple the DFIM to the back-to-back converter, an adaptive integral state-feedback controller with either filter current decoupling control or reference feed-forward compensation is designed for the rotor currents in the discrete-time domain (see Sec. 3.3.3).

(viii) based on the nonlinear model of the DFIM, a method to control both machine torque and reactive power is shown (see Sec. 3.3.4).

(ix) experimental investigations at the test-bench are performed to validate the controller designs and to verify the matching of the developed models with their real components.

To explain the contributions (i) to (ix) comprehensibly, the thesis is structured as follows. Ch. 2 covers the mathematical models for all components of the wind turbine system as shown in Fig. 1.1 and describes their interactions. Moreover, these models will be merged into one holistic model of the whole wind turbine system. Its dynamic power flow is also discussed in Ch. 2. The control strategies and designs are presented in Ch. 3. Therein, additionally, the laboratory test-bench is explained and the experimental investigations (ix) are performed. Ch. 4 summarizes the thesis and provides an outlook.

Chapter 2

Modeling of wind turbine systems with doubly-fed induction machine

This chapter discusses the modeling of the wind turbine system and derives its dynamic power flow. Precise and detailed models are not only inevitable to understand the behavior of the wind turbine system, but also to obtain convincing simulation results. Moreover, the model-based designs of high-performance controllers necessitate accurate models as well. Sec. 2.1 covers the modeling of the mechanics of the wind turbine system. In Sec. 2.2, the electrical components of the wind turbine system are modeled. Sec. 2.3 combines the models of Sec. 2.1 and Sec. 2.2 to one holistic wind turbine system model. Its dynamic power flow is derived in Sec. 2.4. Moreover, section Sec. 2.4 introduces two steady-state operations, (i) the super-synchronous operation and (ii) the sub-synchronous operation.

2.1 Mechanical system

According to Fig. 1.1, the mechanical system of the wind turbine system is modeled by the following components:

(i) a turbine which extracts power from the wind,

(ii) a two-mass system to emulate the damping and stiffness characteristics of the drive train,

(iii) a gear box which transmits the slow turbine rotation to the fast machine rotation.

Since the dissertation focuses on the electrical system and its control, only simplified models of the mechanical components are presented. Fig. 2.1 depicts the front view of the turbine. It consists of three rotor blades with the rotor radius r_t (in m) which span the rotor area A_t (in m^2). The rotor blades rotate with the turbine rotational speed $\omega_t > 0$ (in $\frac{\mathrm{rad}}{\mathrm{s}}$) and exhibit the rotor tip velocity $r_t\omega_t$. The pitch angle β_t (in °) rotates each of the three rotor blades while the yaw angle γ_t rotates the entire nacelle. In the following it is assumed that

Assumption (A.2.1) *The yaw angle γ_t rotates the nacelle in such a way that the wind speed $v_w > 0$ (in $\frac{\mathrm{m}}{\mathrm{s}}$) enters the turbine area A_t perpendicularly.*

Then, the wind power p_w (in W), which hits the turbine area A_t (for details see e.g. [109]), is given by

$$p_w(t) = \frac{1}{2}\rho_w A_t v_w(t)^3 = \frac{1}{2}\rho_w \pi r_t^2 v_w(t)^3 \tag{2.1}$$

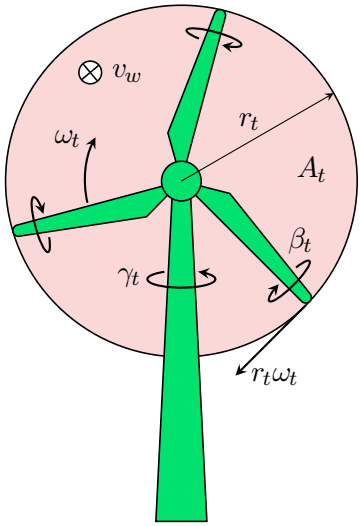

Figure 2.1: *Front view of a wind turbine (illustration is based on Fig. 6.9 in [108]).*

with air density ρ_w (in $\frac{\text{kg}}{\text{m}^3}$). The power coefficient c_p (in 1) characterizes the amount of wind power p_w extracted by the turbine and features the theoretical Betz limit $c_{p,\text{betz}} = \frac{16}{27}$ [110]. Exemplarily, Fig. 2.2 shows the power coefficient c_p of a 2 MW turbine, which is a function of the tip speed ratio λ_t (in 1) and the pitch angle β_t and has its maximum $c_{p,\text{opt}} \approx 0.44$ at the optimal pitch angle $\beta_{t,\text{opt}} = 0°$ and at the optimal tip speed ratio $\lambda_{t,\text{opt}} \approx 6.91$. Generally, the power coefficient c_p results in

$$c_t(t, \beta_t, \omega_t) := c_p\left(\beta_t, \tfrac{r_t\omega_t}{v_w(t)}\right) = c_p(\beta_t, \lambda_t) \leq c_{p,\text{betz}} = \frac{16}{27} \quad \text{with} \quad \lambda_t(t, \omega_t) := \frac{r_t\omega_t}{v_w(t)} \tag{2.2}$$

and—due to the time-varying wind speed $v_w(t)$—can be rewritten as turbine factor c_t (in 1). The turbine factor c_t depends on the time t (in s), on the pitch angle β_t and on the rotational speed ω_t of the turbine. Accordingly, the extracted amount of wind power p_w—the turbine power p_t (in W)—is given by

$$p_t(t, \beta_t, \omega_t) = c_t(t, \beta_t, \omega_t) p_w(t) \overset{(2.1)}{=} \frac{1}{2} c_t(t, \beta_t, \omega_t) \rho_w \pi r_t^2 v_w(t)^3 \,. \tag{2.3}$$

The turbine torque m_t (in Nm) results from the division of the turbine power p_t by the rotational

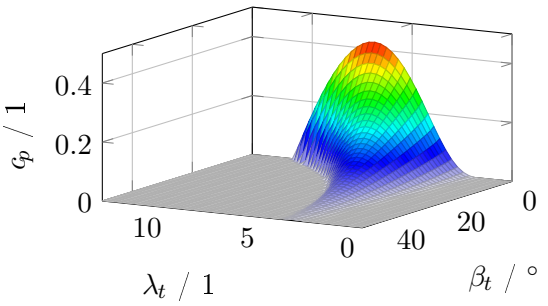

Figure 2.2: *Example of the power coefficient c_p as a function of the tip speed ratio λ_t and the pitch angle β_t (illustration is based on Fig. 24.9 in [111] with data from [112]).*

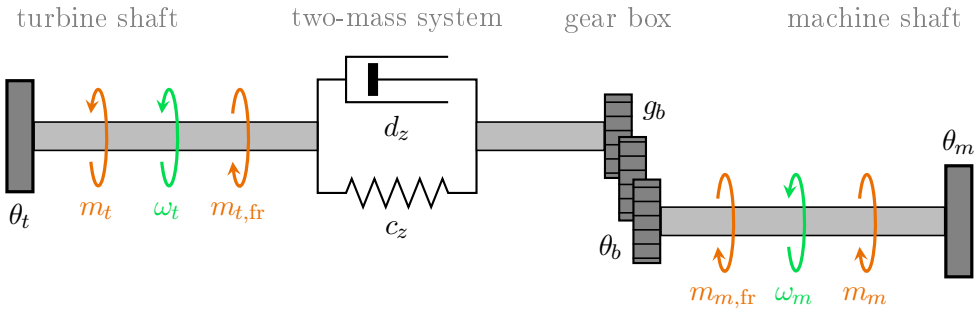

Figure 2.3: *Drive train of the wind turbine system with turbine shaft, two-mass system, gear box and machine shaft.*

speed $\omega_t > 0$, i.e.

$$m_t(t,\beta_t,\omega_t) = \frac{p_t(t,\beta_t,\omega_t)}{\omega_t} \overset{(2.3)}{=} \frac{c_t(t,\beta_t,\omega_t)\rho_w \pi r_t^2 v_w(t)^3}{2\omega_t}. \tag{2.4}$$

Fig. 2.3 depicts the structure of the turbine shaft, the two mass system, the gear box and the machine shaft. The turbine torque m_t acts on the turbine shaft which rotates with rotational speed ω_t. The turbine inertia (shaft included) is defined as θ_t (in kgm^2). Moreover, a friction torque $m_{t,\mathrm{fr}}$ (in Nm) acts against the turbine torque m_t. The two-mass system, which emulates the damping and stiffness characteristics of the mechanics, is characterized by the damping coefficient d_z (in $\frac{\mathrm{kg\,m}^2}{\mathrm{s}}$) and the stiffness coefficient c_z (in $\frac{\mathrm{kg\,m}^2}{\mathrm{s}^2}$). The gear box with inertia θ_b (in kgm^2) up-scales the slow rotation of the turbine side to the fast rotation of the machine side by the (constant) gear ratio g_b (in 1)[7]. The machine shaft rotates with rotational speed $\omega_m > 0$ (in $\frac{\mathrm{rad}}{\mathrm{s}}$) and—combined with the DFIM—has the machine inertia θ_m (in kgm^2). The machine torque m_m (in Nm) and an additional friction torque $m_{m,\mathrm{fr}}$ (in Nm) act both against the rotational direction.

In literature (see e.g. [113] and [114]), the models of the shaft dynamics, the two-mass system and the gear box are presented in detail. By combining these models to an overall model and by defining the angle difference $\phi_z := \phi_t - \frac{\phi_m}{g_b}$ (in rad) of the two-mass system as $\frac{\mathrm{d}}{\mathrm{d}t}\phi_z(t) = \omega_t(t) - \frac{\omega_m(t)}{g_b}$, the dynamics of the mechanical system are given by

$$\frac{\mathrm{d}}{\mathrm{d}t}\begin{pmatrix}\omega_t(t)\\ \phi_z(t)\\ \omega_m(t)\end{pmatrix} = \begin{bmatrix} -\frac{d_z}{\theta_t} & -\frac{c_z}{\theta_t} & \frac{d_z}{g_b\theta_t} \\ 1 & 0 & -\frac{1}{g_b} \\ \frac{d_z}{g_b(\theta_b+\theta_m)} & \frac{c_z}{g_b(\theta_b+\theta_m)} & -\frac{d_z}{g_b^2(\theta_b+\theta_m)} \end{bmatrix}\begin{pmatrix}\omega_t(t)\\ \phi_z(t)\\ \omega_m(t)\end{pmatrix} + \begin{pmatrix} \frac{m_t(t,\beta_t,\omega_t) - m_{t,\mathrm{fr}}(\omega_t)}{\theta_t} \\ 0 \\ -\frac{m_m(\boldsymbol{i}_s^{dq}, \boldsymbol{i}_r^{dq}) + m_{m,\mathrm{fr}}(\omega_m)}{\theta_b+\theta_m} \end{pmatrix} \tag{2.5}$$

with the initial values $\omega_{t,0} = \omega_t(0)$, $\phi_{z,0} = \phi_z(0)$ and $\omega_{m,0} = \omega_m(0)$ of the turbine rotational speed, the angle difference of the two-mass system and the machine rotational speed respectively.

Remark (R.2.1) *In this section, the wind speed and the rotational speeds of turbine and machine have been defined greater than zero, i.e.* $v_w > 0$, $\omega_t > 0$ *and* $\omega_m > 0$. *These are valid definitions because (i) a wind speed* $0 < v_{w,\min} \leq v_w$ *is necessary to achieve an economic operation of the wind turbine system [111] and (ii) the DFIM operates at a rotational speed* ω_m *between* $\pm 30\,\%$ *of its synchronous speed.*

[7] This is a very simplified model in which losses, backlash, etc. are neglected.

description	symbols & values with unit
machine parameters and quantities	
pole pair number of the machine	n_m (in 1)
electrical machine angle	$\phi_r(t) = n_m \phi_m(t)$ (in rad)
electrical machine rotational speed	$\omega_r(t) = n_m \omega_m(t)$ (in $\frac{\text{rad}}{\text{s}}$)
line-to-line, power and transformation matrices	
line-to-line matrices	$\boldsymbol{T}_{LTL}\,, \boldsymbol{T}_{ltl}\,, \boldsymbol{T}_{ltl}^{-1}$
power matrix	$\boldsymbol{T}_{\wp}$
Clarke transformation matrices	$\boldsymbol{T}_C\,, \boldsymbol{T}_C^{-1}\,, \boldsymbol{T}_c\,, \boldsymbol{T}_c^{-1}$
Park transformation matrices	$\boldsymbol{T}_P\,, \boldsymbol{T}_P^{-1}\,, \boldsymbol{T}_p\,, \boldsymbol{T}_p^{-1}$
90°-rotational matrices	$\boldsymbol{J}\,, \boldsymbol{J}^{-1}\,, \boldsymbol{J}'$
transformation quantities and reference frames	
transformation angle and rotational speed	ϕ_k (in rad) and ω_k (in $\frac{\text{rad}}{\text{s}}$)
electrical reference frames	$abc\,, uvw\,, s\,, \alpha\beta\,, r\,, \alpha_r\beta_r\,, k\,, dq$

Table 2.1: *Important parameters, quantities, matrices and reference frames to describe the electrical three-phase systems of the wind turbine system.*

2.2 Electrical system

This section discusses the modeling of the electrical components of the wind turbine system. In particular, as illustrated in Fig. 1.1, the electrical system consists of the following components:

(i) the doubly-fed induction machine (DFIM),

(ii) the machine side LC filter and the grid side LCL filter,

(iii) the back-to-back converter and

(iv) the grid connection via the three-winding transformer (and the transmission line).

Remark (R.2.2) *Note that in the appendix, mathematical preliminaries to model the electrical system are introduced (see Ch. A), which contain the space vector theory in Sec. A.1 and the line-to-line transformation in Sec. A.2. The mathematical preliminaries are expected to be known for the further thesis as well as all parameters, quantities, matrices and reference frames summarized in Tab. 2.1. If you are not familiar with the preliminaries and their nomenclature, please read Ch. A first.*

Each of the components (i) to (iv) is modeled both in three-phase reference frames and space vector reference frames. Sec. 2.2.1 discusses the grid connection of the wind turbine system via the three-winding transformer. In Sec. 2.2.2, a novel DFIM model is developed, which allows to consider nonlinear flux linkages and inductances. A comparison between this nonlinear model and the standard linear DFIM model (see e.g. [62–69]) is also given in Sec. 2.2.2. The LC filter between the DFIM and the back-to-back converter is introduced in Sec. 2.2.3. The back-to-back converter is discussed in Sec. 2.2.4 and, finally, Sec. 2.2.5 describes the LCL filter.

2.2.1 Grid

A common method to connect a single wind turbine system with DFIM to a higher voltage level, is to use a three-winding transformer which has a Δ-connection at the high voltage side and two

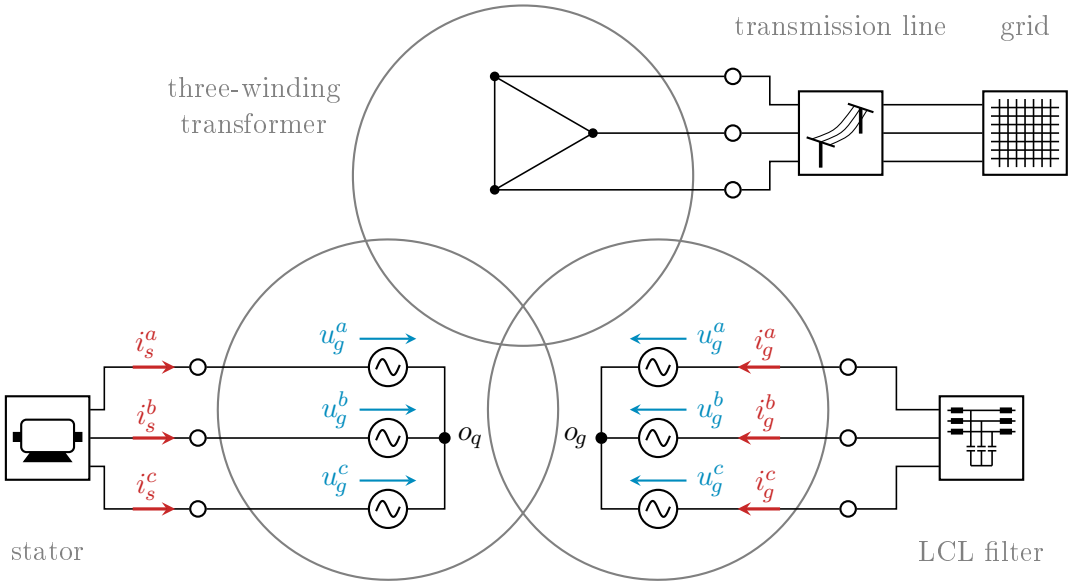

Figure 2.4: *Grid connection of the wind turbine system via the three-winding transformer and the transmission line.*

isolated star connections at the low voltage side (see Fig. 2.4) as in [115]. Hence, this leads to the following assumption:

Assumption (A.2.2) *The filter side and stator side winding of the three-winding transformer are modeled as symmetrical three-phase voltage $\boldsymbol{u}_g^{abc}$ (in V)^3 with isolated star connections o_g (filter side) and o_q (stator side).*

In accordance to (A.2.2), the grid voltage $\boldsymbol{u}_g^{abc}$ is given by

$$\boldsymbol{u}_g^{abc}(t) = \hat{u}_g(t) \begin{pmatrix} \cos\left(\phi_g(t)\right) \\ \cos\left(\phi_g(t) - \frac{2}{3}\pi\right) \\ \cos\left(\phi_g(t) - \frac{4}{3}\pi\right) \end{pmatrix} \quad \text{with} \quad \phi_g(t) = \int_0^t \underbrace{2\pi f_g(\tau)}_{=:\omega_g(\tau)} \mathrm{d}\tau + \underbrace{\phi_g(0)}_{=:\phi_{g,0}} \tag{2.6}$$

with grid voltage amplitude $\hat{u}_g$ (in V), grid rotational speed ω_g (in $\frac{\text{rad}}{\text{s}}$), grid frequency f_g (in Hz) and grid angle ϕ_g (in rad) with initial value $\phi_{g,0} = \phi_g(0)$.

Remark (R.2.3) *A faultless grid is characterized by a symmetrical three-phase voltage [111] such that (A.2.2) is a simplified but valid assumption. A more complex way to model the grid connection of the wind turbine system would consider the dynamics and losses of the three-winding transformer as well as the transmission line and the grid itself. Since here, the foci are on the modeling and control of one single wind turbine system, (A.2.2) is sufficient.*

With the help of the two trigonometric relations (see e.g. [116])

$$\left.\begin{aligned} &\cos\left(\phi_g(t) - \tfrac{2}{3}\right) - \cos\left(\phi_g(t) - \tfrac{4}{3}\pi\right) = -2\sin\left(\tfrac{\pi}{3}\right)\sin\left(\tfrac{2\phi_g(t)-2\pi}{2}\right) = \sqrt{3}\sin\left(\phi_g(t)\right) \\ &\cos\left(\phi_g(t)\right) + \cos\left(\phi_g(t) - \tfrac{2}{3}\pi\right) + \cos\left(\phi_g(t) - \tfrac{4}{3}\pi\right) = 0 \end{aligned}\right\} \quad \forall \phi_g \in \mathbb{R}\,,$$

applying Clarke's transformation matrix $\boldsymbol{T}_C$ to (2.6) yields the grid voltage $\boldsymbol{u}_g^s$ (in V)^3 in stator-

fixed s-reference frame:

$$\boldsymbol{u}_g^s(t) = \boldsymbol{T}_C \boldsymbol{u}_g^{abc}(t) \overset{(2.6)}{=} k_c \hat{u}_g(t) \begin{bmatrix} 1 & -\frac{1}{2} & -\frac{1}{2} \\ 0 & \frac{\sqrt{3}}{2} & -\frac{\sqrt{3}}{2} \\ \kappa_c & \kappa_c & \kappa_c \end{bmatrix} \begin{pmatrix} \cos(\phi_g(t)) \\ \cos\left(\phi_g(t) - \frac{2}{3}\pi\right) \\ \cos\left(\phi_g(t) - \frac{4}{3}\pi\right) \end{pmatrix} = \frac{3}{2} k_c \hat{u}_g(t) \begin{pmatrix} \cos(\phi_g(t)) \\ \sin(\phi_g(t)) \\ 0 \end{pmatrix} . \quad (2.7)$$

Accordingly—for a constant rotational speed ω_g and a constant voltage $\hat{u}_g$—the space vector $\boldsymbol{u}_g^s$ of the grid voltage rotates circularly in the $\alpha\beta$-plane, which is a general feature of symmetrical three phase systems. Due to (2.7) and the isolated star connections o_g and o_q (see (A.2.2)), the γ-components of both, the grid voltage u_g^γ and the currents i_g^γ and i_s^γ of grid and stator, respectively, are zero, i.e.

$$u_g^\gamma(t) = k_c \kappa_c (u_g^a(t) + u_g^b(t) + u_g^c(t)) = 0 \quad \text{and} \quad \begin{cases} i_g^\gamma(t) = k_c \kappa_c (i_g^a(t) + i_g^b(t) + i_g^c(t)) = 0 \\ i_s^\gamma(t) = k_c \kappa_c (i_s^a(t) + i_s^b(t) + i_s^c(t)) = 0 \,. \end{cases} \quad (2.8)$$

Considering (2.8) and the trigonometric function $\cos^2(\phi_g(t)) + \sin^2(\phi_g(t)) = 1$ for all $\phi_g \in \mathbb{R}$ (see e.g. [116]) and applying Park's transformation to (2.7) yields the grid voltage $\boldsymbol{u}_g^{dq}$ (in V)[2] (i) in an arbitrary dq-reference frame and (ii) in grid voltage orientation, i.e. $\phi_k(t) = \phi_g(t)$, which is given by

$$\begin{aligned} \boldsymbol{u}_g^{dq}(t) = \boldsymbol{T}_p^{-1}(\phi_k) \boldsymbol{u}_g^{\alpha\beta}(t) &\overset{(2.7)}{=} \frac{3}{2} k_c \hat{u}_g(t) \begin{bmatrix} \cos(\phi_k(t)) & \sin(\phi_k(t)) \\ -\sin(\phi_k(t)) & \cos(\phi_k(t)) \end{bmatrix} \begin{pmatrix} \cos(\phi_g(t)) \\ \sin(\phi_g(t)) \end{pmatrix} \\ &= \frac{3}{2} k_c \hat{u}_g(t) \begin{pmatrix} \cos(\phi_k(t))\cos(\phi_g(t)) + \sin(\phi_k(t))\sin(\phi_g(t)) \\ \cos(\phi_k(t))\sin(\phi_g(t)) - \sin(\phi_k(t))\cos(\phi_g(t)) \end{pmatrix} \overset{\phi_k(t)=\phi_g(t)}{=} \frac{3}{2} k_c \hat{u}_g(t) \begin{pmatrix} 1 \\ 0 \end{pmatrix} . \end{aligned} \quad (2.9)$$

Remark (R.2.4) *In accordance to* (2.9)*, a Park transformation—where the transformation angle ϕ_k rotates with the rotational speed ω_g—yields a constant grid voltage $\boldsymbol{u}_g^{dq}$ (for constant amplitude $\hat{u}_g$). In particular, if ϕ_k equals the grid angle ϕ_g, i.e. $\phi_k(t) = \phi_g(t)$, the q-component of the grid voltage is zero: $u_g^q(t) = 0$. On the contrary, a Park transformation—where the transformation angle ϕ_k does not rotate with the rotational speed ω_g—results in an oscillating grid voltage $\boldsymbol{u}_g^{dq}$.*

Remark (R.2.5) *Due to the strict requirements on the grid operators, for the faultless grid operation, it is valid to expect an (almost) constant grid rotational speed $\omega_g = 2\pi f_g$ and an (almost) constant voltage amplitude $\hat{u}_g$. In Europe, the grid frequency is $f_g = 50\,\text{Hz}$, whereas the voltage amplitude $\hat{u}_g$ depends on the voltage level of the grid.*

2.2.2 Doubly-fed induction machine (DFIM)

The DFIM converts the mechanical power—coming from the turbine—into (three-phase) electrical power. Compared to other machine topologies, the special characteristic of the DFIM is that both stator and rotor exhibit three-phase connections. While the stator is directly coupled to the grid via the three-winding transformer, the back-to-back converter feeds the rotor with a variable three-phase voltage (see Fig. 1.1). The use of wind turbine systems with DFIM yields several advantages and drawbacks [6–9]:

- advantages of wind turbine systems with DFIM:
  - a variable-speed operation with a range of about $\pm 30\,\%$ around its synchronous speed is possible;

  - only about 30 % of the mechanical power flows through the converter, which allows to reduce the rated power of the back-to-back converter;
  - the decoupled control of active and reactive power allows to contribute to the stability of the grid;

- drawbacks of wind turbine systems with DFIM:
  - a gear box is required, in contrast to direct-drive wind turbine systems;
  - the rotor uses high-maintenance slip rings;
  - since the stator is directly coupled to the grid via the three-winding transformer, the DFIM is sensitive towards grid faults.

The standard way to model a doubly-fed induction machine is the linear DFIM model (for details see Sec. 2.2.2.5), which is widespread in literature and can e.g. be found in [62–69]. It has been tried to emulate the DFIM at the test bench—which features nonlinear flux linkages and inductances—by this linear DFIM model. Moreover, the linear DFIM model has been used to design the rotor current PI controller of the DFIM on the basis of the magnitude optimum (for details see [117]) and to implement an additional disturbance compensation. In Sec. 2.2.2.6 the resulting disadvantages of the linear DFIM model concerning the modeling and the controller design are explained in detail. In the following the main drawbacks are listed:

(a) drawbacks of the modeling:
  - the wrong machine parameters cause stationary errors in the linear DFIM model since it cannot emulate the nonlinear flux linkages of the real machine; e.g. the deviation in the machine torque can exceed 25 %.
  - because of the constant and wrong inductances of the linear DFIM model, its dynamics differ strongly from the dynamics of the real machine.

(b) drawbacks of the controller design:
  - due to the wrong machine parameters, the design of the rotor current PI controller based on the magnitude optimum is too aggressive and can cause instability.
  - the bad tuning of the rotor current PI controller parameters results in a bad control performance.
  - the false disturbance compensation affects the rotor current control negatively.

These significant disadvantages of the linear DFIM model in respect of both, (a) modeling and (b) control, make it inevitable to develop a novel DFIM model which considers the nonlinear behavior of the DFIM at the test bench.
The proposed nonlinear model of the DFIM is based on nonlinear flux maps and differential inductances. Besides the good emulation of the DFIM behavior, the advantages of this method are: (i) the model is based on real physical properties and (ii) no knowledge about the interior of the DFIM (e.g. winding design, mechanical construction) is needed which often is not accessible, i.e. all necessary information can be extracted by measurements.
The section is structured as follows: Sec. 2.2.2.1 derives the nonlinear DFIM model (i) in the three-phase reference frames *abc* and *uvw*, (ii) in the stator-fixed and rotor-fixed reference frames s and r, respectively, and (iii) in the arbitrarily k-reference frame. Sec. 2.2.2.2 discusses, how the nonlinear flux maps can be measured at the test bench. In Sec. 2.2.2.3, three options to obtain the torque map of the DFIM are shown. Sec. 2.2.2.4 explains, how to measure the differential

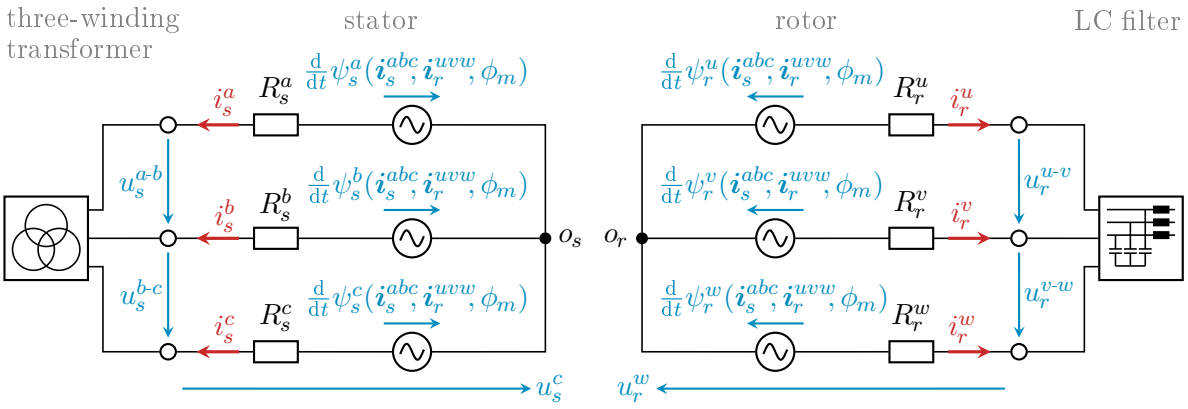

Figure 2.5: *Three-phase equivalent circuit of the doubly-fed induction machine.*

inductances in the laboratory. The nonlinear DFIM model is compared to the linear DFIM model, which is introduced in Sec. 2.2.2.5. The comparison of these DFIM models is shown in Sec. 2.2.2.6.

2.2.2.1 Nonlinear model

This section derives the nonlinear DFIM model—based on nonlinear flux linkages and differential inductances—in an arbitrary *dq*-reference frame. Starting point is the general three-phase equivalent circuit of a DFIM in Fig. 2.5 (cf. [118]).
Therein, the stator is connected to the three-winding transformer. It is fed by the line-to-line[8] stator voltage $\boldsymbol{u}_s^{a\text{-}b\text{-}c}$ (in V)^3. Since in wind turbine systems the DFIM operates in generator mode, the stator current $\boldsymbol{i}_s^{abc}$ (in A)^3 flows—through the stator resistances R_s^a, R_s^b and R_s^c (all in Ω)—out of the stator. Moreover, due to the nonlinear magnetic flux linkage $\boldsymbol{\psi}_s^{abc}$ (in Vs)^3, the voltage $\frac{\mathrm{d}}{\mathrm{d}t}\boldsymbol{\psi}_s^{abc}$ (in V)^3 is induced in the stator phases a, b and c which depend on the stator current $\boldsymbol{i}_s^{abc}$, on the rotor current $\boldsymbol{i}_r^{uvw}$ (in A)^3 and on the (mechanical) machine angle ϕ_m (in rad). The rotor of the DFIM is connected to the LC filter and features the same structure as the stator. It is fed by the line-to-line[9] rotor voltage $\boldsymbol{u}_r^{u\text{-}v\text{-}w}$ (in V)^3 and—through the rotor resistances R_r^u, R_r^v and R_r^w (all in Ω)—the rotor current $\boldsymbol{i}_r^{uvw}$ flows out of the rotor. Again, the nonlinear magnetic flux linkage $\boldsymbol{\psi}_r^{uvw}$ (in Vs)^3 induces the voltage $\frac{\mathrm{d}}{\mathrm{d}t}\boldsymbol{\psi}_r^{uvw}$ (in V)^3 in the rotor phases u, v and w.
For the further model derivation, the following assumptions are imposed:

Assumption (A.2.3) *The stator and rotor of the DFIM both have isolated star connections o_s and o_r (as the DFIM at the test bench). Accordingly the sums of the phase currents are zero, i.e. $i_s^a(t)+i_s^b(t)+i_s^c(t)=0$ and $i_r^u(t)+i_r^v(t)+i_r^w(t)=0$.*

Assumption (A.2.4) *Stator and rotor are designed symmetrically, i.e. each stator phase exhibits an identical winding number as well as each rotor phase. Moreover, the windings of the stator and rotor are sinusoidally distributed with a mechanical shift of $\frac{2}{3}$-times the pole pitch, which corresponds to an electrical shift of 120 °.*

Assumption (A.2.5) *Harmonics, hysteresis effects and eddy currents are neglected.*

[8]The phase voltage $\boldsymbol{u}_s^{abc}$ (in V)^3 is defined from its corresponding clamp to the star connection o_s.
[9]The phase voltage $\boldsymbol{u}_r^{uvw}$ (in V)^3 is defined from its corresponding clamp to the star connection o_r.

Assumption (A.2.6) *The resistance matrix of the stator* $\boldsymbol{R}_s^{abc} := \mathrm{diag}(R_s^a, R_s^b, R_s^c)$ *(in* Ω*)*$^{3\times3}$ *and the rotor* $\boldsymbol{R}_r^{uvw} := \mathrm{diag}(R_r^u, R_r^v, R_r^w)$ *(in* Ω*)*$^{3\times3}$ *as well as all differential inductances of the DFIM are not sensitive to temperature variations*[10]*.*

Nonlinear DFIM model in three-phase *abc-/uvw*-reference frame

Applying Kirchhoff's law to the equivalent circuit in Fig. 2.5 yields the three-phase voltage equations

$$\left.\begin{aligned} \boldsymbol{u}_s^{abc}(t) &= -\boldsymbol{R}_s^{abc}\boldsymbol{i}_s^{abc}(t) + \tfrac{\mathrm{d}}{\mathrm{d}t}\boldsymbol{\psi}_s^{abc}(\boldsymbol{i}_s^{abc}, \boldsymbol{i}_r^{uvw}, \phi_m) \\ \boldsymbol{u}_r^{uvw}(t) &= -\boldsymbol{R}_r^{uvw}\boldsymbol{i}_r^{uvw}(t) + \tfrac{\mathrm{d}}{\mathrm{d}t}\boldsymbol{\psi}_r^{uvw}(\boldsymbol{i}_s^{abc}, \boldsymbol{i}_r^{uvw}, \phi_m) \end{aligned}\right\} \tag{2.10}$$

with initial values $\boldsymbol{\psi}_{s,0}^{abc} = \boldsymbol{\psi}_s^{abc}(\boldsymbol{i}_{s,0}^{abc}, \boldsymbol{i}_{r,0}^{uvw}, \phi_{m,0})$ and $\boldsymbol{\psi}_{r,0}^{uvw} = \boldsymbol{\psi}_r^{uvw}(\boldsymbol{i}_{s,0}^{abc}, \boldsymbol{i}_{r,0}^{uvw}, \phi_{m,0})$ of the stator and rotor flux linkage. The initial values of the stator current, the rotor current and the machine angle are given by $\boldsymbol{i}_{s,0}^{abc} = \boldsymbol{i}_s^{abc}(0)$, $\boldsymbol{i}_{r,0}^{uvw} = \boldsymbol{i}_r^{uvw}(0)$ and $\phi_{m,0} = \phi_m(0)$. The time derivative of the stator flux linkage $\boldsymbol{\psi}_s^{abc}$ is given by[11]

$$\begin{aligned} &\frac{\mathrm{d}}{\mathrm{d}t}\boldsymbol{\psi}_s^{abc}(\boldsymbol{i}_s^{abc}, \boldsymbol{i}_r^{uvw}, \phi_m) \\ &= \underbrace{\frac{\partial \boldsymbol{\psi}_s^{abc}(\boldsymbol{i}_s^{abc}, \boldsymbol{i}_r^{uvw}, \phi_m)}{\partial \boldsymbol{i}_s^{abc}}}_{=:-\boldsymbol{L}_s^{abc}(\boldsymbol{i}_s^{abc}, \boldsymbol{i}_r^{uvw}, \phi_m)} \frac{\mathrm{d}}{\mathrm{d}t}\boldsymbol{i}_s^{abc}(t) + \underbrace{\frac{\partial \boldsymbol{\psi}_s^{abc}(\boldsymbol{i}_s^{abc}, \boldsymbol{i}_r^{uvw}, \phi_m)}{\partial \boldsymbol{i}_r^{uvw}}}_{=:-\boldsymbol{L}_{sr}^{abc}(\boldsymbol{i}_s^{abc}, \boldsymbol{i}_r^{uvw}, \phi_m)} \frac{\mathrm{d}}{\mathrm{d}t}\boldsymbol{i}_r^{uvw}(t) + \underbrace{\frac{\partial \boldsymbol{\psi}_s^{abc}(\boldsymbol{i}_s^{abc}, \boldsymbol{i}_r^{uvw}, \phi_m)}{\partial \phi_m}}_{=:\boldsymbol{\varphi}_{sm}^{abc}(\boldsymbol{i}_s^{abc}, \boldsymbol{i}_r^{uvw}, \phi_m)} \frac{\mathrm{d}}{\mathrm{d}t}\phi_m(t) \\ &= -\boldsymbol{L}_s^{abc}(\boldsymbol{i}_s^{abc}, \boldsymbol{i}_r^{uvw}, \phi_m)\frac{\mathrm{d}}{\mathrm{d}t}\boldsymbol{i}_s^{abc}(t) - \boldsymbol{L}_{sr}^{abc}(\boldsymbol{i}_s^{abc}, \boldsymbol{i}_r^{uvw}, \phi_m)\frac{\mathrm{d}}{\mathrm{d}t}\boldsymbol{i}_r^{uvw}(t) + \boldsymbol{\varphi}_{sm}^{abc}(\boldsymbol{i}_s^{abc}, \boldsymbol{i}_r^{uvw}, \phi_m)\omega_m(t)\,, \end{aligned} \tag{2.11}$$

with the three-phase differential inductance matrices of the stator $\boldsymbol{L}_s^{abc}$ and the coupling $\boldsymbol{L}_{sr}^{abc}$ (both in H)$^{3\times3}$, the vector $\boldsymbol{\varphi}_{sm}^{abc}$ (in $\frac{\mathrm{V\,s}}{\mathrm{rad}}$)^3 of the ϕ_m-derivative of the stator flux linkage $\boldsymbol{\psi}_s^{abc}$ and the (mechanical) rotational speed $\omega_m(t) = \frac{\mathrm{d}}{\mathrm{d}t}\phi_m(t)$ (in $\frac{\mathrm{rad}}{\mathrm{s}}$) of the machine. The time derivative of the rotor flux linkage $\boldsymbol{\psi}_r^{uvw}$ is calculated accordingly as follows

$$\begin{aligned} &\frac{\mathrm{d}}{\mathrm{d}t}\boldsymbol{\psi}_r^{uvw}(\boldsymbol{i}_s^{abc}, \boldsymbol{i}_r^{uvw}, \phi_m) \\ &= \underbrace{\frac{\partial \boldsymbol{\psi}_r^{uvw}(\boldsymbol{i}_s^{abc}, \boldsymbol{i}_r^{uvw}, \phi_m)}{\partial \boldsymbol{i}_s^{abc}}}_{=:-\boldsymbol{L}_{rs}^{uvw}(\boldsymbol{i}_s^{abc}, \boldsymbol{i}_r^{uvw}, \phi_m)} \frac{\mathrm{d}}{\mathrm{d}t}\boldsymbol{i}_s^{abc}(t) + \underbrace{\frac{\partial \boldsymbol{\psi}_r^{uvw}(\boldsymbol{i}_s^{abc}, \boldsymbol{i}_r^{uvw}, \phi_m)}{\partial \boldsymbol{i}_r^{uvw}}}_{=:-\boldsymbol{L}_r^{uvw}(\boldsymbol{i}_s^{abc}, \boldsymbol{i}_r^{uvw}, \phi_m)} \frac{\mathrm{d}}{\mathrm{d}t}\boldsymbol{i}_r^{uvw}(t) + \underbrace{\frac{\partial \boldsymbol{\psi}_r^{uvw}(\boldsymbol{i}_s^{abc}, \boldsymbol{i}_r^{uvw}, \phi_m)}{\partial \phi_m}}_{=:\boldsymbol{\varphi}_{rm}^{uvw}(\boldsymbol{i}_s^{abc}, \boldsymbol{i}_r^{uvw}, \phi_m)} \frac{\mathrm{d}}{\mathrm{d}t}\phi_m(t) \\ &= -\boldsymbol{L}_{rs}^{uvw}(\boldsymbol{i}_s^{abc}, \boldsymbol{i}_r^{uvw}, \phi_m)\frac{\mathrm{d}}{\mathrm{d}t}\boldsymbol{i}_s^{abc}(t) - \boldsymbol{L}_r^{uvw}(\boldsymbol{i}_s^{abc}, \boldsymbol{i}_r^{uvw}, \phi_m)\frac{\mathrm{d}}{\mathrm{d}t}\boldsymbol{i}_r^{uvw}(t) + \boldsymbol{\varphi}_{rm}^{uvw}(\boldsymbol{i}_s^{abc}, \boldsymbol{i}_r^{uvw}, \phi_m)\omega_m(t) \end{aligned} \tag{2.12}$$

with the three-phase differential inductance matrices of the rotor $\boldsymbol{L}_r^{uvw}$ and the coupling $\boldsymbol{L}_{rs}^{uvw}$ (both in H)$^{3\times3}$ and the vector $\boldsymbol{\varphi}_{rm}^{uvw}$ (in $\frac{\mathrm{V\,s}}{\mathrm{rad}}$)^3 of the ϕ_m-derivative of the rotor flux linkage $\boldsymbol{\psi}_r^{uvw}$.

Assumption (A.2.7) *Due to the magnetic interaction and (A.2.5), two phases* x *and* y *with* $x, y \in \{a, b, c, u, v, w\}$ *magnetically affect each other in the same way, i.e. for the differential inductances of the stator* $\boldsymbol{L}_s^{abc}$*, the rotor* $\boldsymbol{L}_r^{uvw}$ *and the couplings* $\boldsymbol{L}_{sr}^{abc}$ *and* $\boldsymbol{L}_{rs}^{uvw}$ *the following symmetry properties must hold:* $\boldsymbol{L}_s^{abc} = (\boldsymbol{L}_s^{abc})^\top$*,* $\boldsymbol{L}_r^{uvw} = (\boldsymbol{L}_r^{uvw})^\top$ *and* $\boldsymbol{L}_{sr}^{abc} = (\boldsymbol{L}_{rs}^{uvw})^\top$*.*

[10] Due to the good matching of the measurement and simulation results (see Sec. 2.2.2.6), (A.2.3)–(A.2.6) are reasonable (as well as (A.2.7)–(A.2.9) which are defined later in this section).

[11] The negative signs in (2.11) and (2.12) result from the defined current directions of the stator $\boldsymbol{i}_s^{abc}$ and rotor $\boldsymbol{i}_r^{uvw}$ current due to the operation in generator mode.

Nonlinear DFIM model in stator-/rotor-fixed reference frame

With the help of the Clarke transformation (and its inverse) the stator part of (2.10) is transformed into the stator-fixed s-reference frame as follows

$$\begin{aligned}\boldsymbol{u}_s^s(t) &= \boldsymbol{T}_C \boldsymbol{u}_s^{abc}(t) \overset{(2.10)}{=} -\boldsymbol{T}_C \boldsymbol{R}_s^{abc} \boldsymbol{i}_s^{abc}(t) + \boldsymbol{T}_C \frac{\mathrm{d}}{\mathrm{d}t} \boldsymbol{\psi}_s^{abc}(\boldsymbol{i}_s^{abc}, \boldsymbol{i}_r^{uvw}, \phi_m) \\ &= -\underbrace{\boldsymbol{T}_C \boldsymbol{R}_s^{abc} \boldsymbol{T}_C^{-1}}_{=:\boldsymbol{R}_s^s} \boldsymbol{i}_s^s(t) + \frac{\mathrm{d}}{\mathrm{d}t} \underbrace{\left(\boldsymbol{T}_C \boldsymbol{\psi}_s^{abc}(\boldsymbol{T}_C^{-1} \boldsymbol{i}_s^s, \boldsymbol{T}_C^{-1} \boldsymbol{i}_r^r, \phi_m)\right)}_{=:\boldsymbol{\psi}_s^s(\boldsymbol{i}_s^s, \boldsymbol{i}_r^r, \phi_m)} = -\boldsymbol{R}_s^s \boldsymbol{i}_s^s(t) + \frac{\mathrm{d}}{\mathrm{d}t} \boldsymbol{\psi}_s^s(\boldsymbol{i}_s^s, \boldsymbol{i}_r^r, \phi_m)\end{aligned} \tag{2.13}$$

with the stator voltage $\boldsymbol{u}_s^s$ (in V)^3, the stator current $\boldsymbol{i}_s^s$ (in A)^3, the stator resistance matrix $\boldsymbol{R}_s^s$ (in Ω)$^{3\times3}$, the stator flux linkage $\boldsymbol{\psi}_s^s$ (in Vs)^3 and the initial stator flux linkage $\boldsymbol{\psi}_{s,0}^s = \boldsymbol{\psi}_s^s(\boldsymbol{i}_{s,0}^s, \boldsymbol{i}_{r,0}^r, \phi_{m,0})$ (in Vs)^3, where the initial currents of the stator and the rotor are given by $\boldsymbol{i}_{s,0}^s = \boldsymbol{i}_s^s(0)$ and $\boldsymbol{i}_{r,0}^r = \boldsymbol{i}_r^r(0)$ respectively. Applying the Clarke transformation to the rotor part of (2.10) yields rotor voltage $\boldsymbol{u}_r^r$ (in V)^3 in the rotor-fixed r-reference frame:

$$\begin{aligned}\boldsymbol{u}_r^r(t) &= \boldsymbol{T}_C \boldsymbol{u}_r^{uvw}(t) \overset{(2.10)}{=} -\boldsymbol{T}_C \boldsymbol{R}_r^{uvw} \boldsymbol{i}_r^{uvw}(t) + \boldsymbol{T}_C \frac{\mathrm{d}}{\mathrm{d}t} \boldsymbol{\psi}_r^{uvw}(\boldsymbol{i}_s^{abc}, \boldsymbol{i}_r^{uvw}, \phi_m) \\ &= -\underbrace{\boldsymbol{T}_C \boldsymbol{R}_r^{uvw} \boldsymbol{T}_C^{-1}}_{=:\boldsymbol{R}_r^r} \boldsymbol{i}_r^r(t) + \frac{\mathrm{d}}{\mathrm{d}t} \underbrace{\left(\boldsymbol{T}_C \boldsymbol{\psi}_r^{uvw}(\boldsymbol{T}_C^{-1} \boldsymbol{i}_s^s, \boldsymbol{T}_C^{-1} \boldsymbol{i}_r^r, \phi_m)\right)}_{=:\boldsymbol{\psi}_r^r(\boldsymbol{i}_s^s, \boldsymbol{i}_r^r, \phi_m)} = -\boldsymbol{R}_r^r \boldsymbol{i}_r^r(t) + \frac{\mathrm{d}}{\mathrm{d}t} \boldsymbol{\psi}_r^r(\boldsymbol{i}_s^s, \boldsymbol{i}_r^r, \phi_m)\end{aligned} \tag{2.14}$$

with the rotor current $\boldsymbol{i}_r^r$ (in A)^3, the rotor resistance matrix $\boldsymbol{R}_r^r$ (in Ω)$^{3\times3}$, the rotor flux linkage $\boldsymbol{\psi}_r^r$ (in Vs)^3 and the initial rotor flux linkage $\boldsymbol{\psi}_{r,0}^r = \boldsymbol{\psi}_r^r(\boldsymbol{i}_{s,0}^s, \boldsymbol{i}_{r,0}^r, \phi_{m,0})$. The time derivative of the stator flux linkage $\boldsymbol{\psi}_s^s$ is given by

$$\begin{aligned}\frac{\mathrm{d}}{\mathrm{d}t} \boldsymbol{\psi}_s^s(\boldsymbol{i}_s^s, \boldsymbol{i}_r^r, \phi_m) &= \overbrace{\frac{\partial \boldsymbol{\psi}_s^s(\boldsymbol{i}_s^s, \boldsymbol{i}_r^r, \phi_m)}{\partial \boldsymbol{i}_s^s}}^{=:-\boldsymbol{L}_s^s(\boldsymbol{i}_s^s, \boldsymbol{i}_r^r, \phi_m)} \frac{\mathrm{d}}{\mathrm{d}t} \boldsymbol{i}_s^s(t) + \overbrace{\frac{\partial \boldsymbol{\psi}_s^s(\boldsymbol{i}_s^s, \boldsymbol{i}_r^r, \phi_m)}{\partial \boldsymbol{i}_r^r}}^{=:-\boldsymbol{L}_{sr}^s(\boldsymbol{i}_s^s, \boldsymbol{i}_r^r, \phi_m)} \frac{\mathrm{d}}{\mathrm{d}t} \boldsymbol{i}_r^r(t) + \overbrace{\frac{\partial \boldsymbol{\psi}_s^s(\boldsymbol{i}_s^s, \boldsymbol{i}_r^r, \phi_m)}{\partial \phi_m}}^{=:\boldsymbol{\varphi}_{sm}^s(\boldsymbol{i}_s^s, \boldsymbol{i}_r^r, \phi_m)} \frac{\mathrm{d}}{\mathrm{d}t} \phi_m(t) \\ &= -\boldsymbol{L}_s^s(\boldsymbol{i}_s^s, \boldsymbol{i}_r^r, \phi_m) \frac{\mathrm{d}}{\mathrm{d}t} \boldsymbol{i}_s^s(t) - \boldsymbol{L}_{sr}^s(\boldsymbol{i}_s^s, \boldsymbol{i}_r^r, \phi_m) \frac{\mathrm{d}}{\mathrm{d}t} \boldsymbol{i}_r^r(t) + \boldsymbol{\varphi}_{sm}^s(\boldsymbol{i}_s^s, \boldsymbol{i}_r^r, \phi_m) \omega_m(t)\end{aligned} \tag{2.15}$$

with the differential inductance matrices of the stator $\boldsymbol{L}_s^s$ and the coupling $\boldsymbol{L}_{sr}^s$ (both in H)$^{3\times3}$ and the vector $\boldsymbol{\varphi}_{sm}^s$ (in $\frac{\mathrm{Vs}}{\mathrm{rad}}$)^3 of the ϕ_m-derivative of the stator flux linkage $\boldsymbol{\psi}_s^s$. In accordance with (2.15) the time derivative of the rotor flux linkage $\boldsymbol{\psi}_r^r$ is calculated by

$$\begin{aligned}\frac{\mathrm{d}}{\mathrm{d}t} \boldsymbol{\psi}_r^r(\boldsymbol{i}_s^s, \boldsymbol{i}_r^r, \phi_m) &= \overbrace{\frac{\partial \boldsymbol{\psi}_r^r(\boldsymbol{i}_s^s, \boldsymbol{i}_r^r, \phi_m)}{\partial \boldsymbol{i}_s^s}}^{=:-\boldsymbol{L}_{rs}^r(\boldsymbol{i}_s^s, \boldsymbol{i}_r^r, \phi_m)} \frac{\mathrm{d}}{\mathrm{d}t} \boldsymbol{i}_s^s(t) + \overbrace{\frac{\partial \boldsymbol{\psi}_r^r(\boldsymbol{i}_s^s, \boldsymbol{i}_r^r, \phi_m)}{\partial \boldsymbol{i}_r^r}}^{=:-\boldsymbol{L}_r^r(\boldsymbol{i}_s^s, \boldsymbol{i}_r^r, \phi_m)} \frac{\mathrm{d}}{\mathrm{d}t} \boldsymbol{i}_r^r(t) + \overbrace{\frac{\partial \boldsymbol{\psi}_r^r(\boldsymbol{i}_s^s, \boldsymbol{i}_r^r, \phi_m)}{\partial \phi_m}}^{=:\boldsymbol{\varphi}_{rm}^r(\boldsymbol{i}_s^s, \boldsymbol{i}_r^r, \phi_m)} \frac{\mathrm{d}}{\mathrm{d}t} \phi_m(t) \\ &= -\boldsymbol{L}_{rs}^r(\boldsymbol{i}_s^s, \boldsymbol{i}_r^r, \phi_m) \frac{\mathrm{d}}{\mathrm{d}t} \boldsymbol{i}_s^s(t) - \boldsymbol{L}_r^r(\boldsymbol{i}_s^s, \boldsymbol{i}_r^r, \phi_m) \frac{\mathrm{d}}{\mathrm{d}t} \boldsymbol{i}_r^r(t) + \boldsymbol{\varphi}_{rm}^r(\boldsymbol{i}_s^s, \boldsymbol{i}_r^r, \phi_m) \omega_m(t)\end{aligned} \tag{2.16}$$

with the differential inductance matrices of the rotor $\boldsymbol{L}_r^r$ and the coupling $\boldsymbol{L}_{rs}^r$ (both in H)$^{3\times3}$ and the vector $\boldsymbol{\varphi}_{rm}^r$ (in $\frac{\mathrm{Vs}}{\mathrm{rad}}$)^3 of the ϕ_m-derivative of the rotor flux linkage $\boldsymbol{\psi}_r^r$.

Nonlinear DFIM model in arbitrary *k*-reference frame

Finally, the nonlinear DFIM model will be derived for an arbitrary k-reference frame. Therefore, the Park transformation (and its inverse) is used. The stator voltage $\boldsymbol{u}_s^k$ (in V)^3 is given by

$$\begin{aligned}\boldsymbol{u}_s^k(t) &= \boldsymbol{T}_P^{-1}(\phi_k)\boldsymbol{u}_s^s(t) \overset{(2.13)}{=} -\boldsymbol{T}_P^{-1}(\phi_k)\boldsymbol{R}_s^s\boldsymbol{i}_s^s(t) + \boldsymbol{T}_P^{-1}(\phi_k)\frac{\mathrm{d}}{\mathrm{d}t}\boldsymbol{\psi}_s^s(\boldsymbol{i}_s^s, \boldsymbol{i}_r^r, \phi_m)\\ &= -\underbrace{\boldsymbol{T}_P^{-1}(\phi_k)\boldsymbol{R}_s^s\boldsymbol{T}_P(\phi_k)}_{=:\boldsymbol{R}_s^k(\phi_k)}\boldsymbol{i}_s^k(t) + \boldsymbol{T}_P^{-1}(\phi_k)\frac{\mathrm{d}}{\mathrm{d}t}\underbrace{\left(\boldsymbol{\psi}_s^s(\boldsymbol{T}_P(\phi_k)\boldsymbol{i}_s^k, \boldsymbol{T}_P(\phi_k - n_m\phi_m)\boldsymbol{i}_r^k, \phi_m)\right)}_{=:\boldsymbol{T}_P(\phi_k)\boldsymbol{\psi}_s^k(\boldsymbol{i}_s^k, \boldsymbol{i}_r^k, \phi_m, \phi_k)}\\ &= -\boldsymbol{R}_s^k(\phi_k)\boldsymbol{i}_s^k(t) + \frac{\mathrm{d}}{\mathrm{d}t}\boldsymbol{\psi}_s^k(\boldsymbol{i}_s^k, \boldsymbol{i}_r^k, \phi_m, \phi_k) + \omega_k(t)\boldsymbol{J}'\boldsymbol{\psi}_s^k(\boldsymbol{i}_s^k, \boldsymbol{i}_r^k, \phi_m, \phi_k)\end{aligned} \tag{2.17}$$

with the stator current $\boldsymbol{i}_s^k$ (in A)^3, the stator resistance matrix $\boldsymbol{R}_s^k$ (in Ω)$^{3\times3}$, the stator flux linkage $\boldsymbol{\psi}_s^k$ (in Vs)^3 and the initial stator flux linkage $\boldsymbol{\psi}_{s,0}^k = \boldsymbol{\psi}_s^k(\boldsymbol{i}_{s,0}^k, \boldsymbol{i}_{r,0}^k, \phi_{m,0}, \phi_{k,0})$, where the initial values of the stator current, the rotor current and the transformation angle are given by $\boldsymbol{i}_{s,0}^k = \boldsymbol{i}_s^k(0)$, $\boldsymbol{i}_{r,0}^k = \boldsymbol{i}_r^k(0)$ and $\phi_{k,0} = \phi_k(0)$.

Applying the (inverse) Park transformation to the rotor part of (2.14) yields the rotor voltage $\boldsymbol{u}_r^k$ (in V)^3 as follows

$$\begin{aligned}&\boldsymbol{u}_r^k(t) = \boldsymbol{T}_P^{-1}(\phi_k - n_m\phi_m)\boldsymbol{u}_r^r(t) \overset{(2.14)}{=} -\boldsymbol{T}_P^{-1}(\phi_k - n_m\phi_m)\boldsymbol{R}_r^r\boldsymbol{i}_r^r(t) + \boldsymbol{T}_P^{-1}(\phi_k - n_m\phi_m)\frac{\mathrm{d}}{\mathrm{d}t}\boldsymbol{\psi}_r^r(\boldsymbol{i}_s^s, \boldsymbol{i}_r^r, \phi_m)\\ &= -\underbrace{\boldsymbol{T}_P^{-1}(\phi_k - n_m\phi_m)\boldsymbol{R}_r^r\boldsymbol{T}_P(\phi_k - n_m\phi_m)}_{=:\boldsymbol{R}_r^k(\phi_m, \phi_k)}\boldsymbol{i}_r^k(t)\\ &\qquad + \boldsymbol{T}_P^{-1}(\phi_k - n_m\phi_m)\frac{\mathrm{d}}{\mathrm{d}t}\overbrace{\left(\boldsymbol{\psi}_r^r(\boldsymbol{T}_P(\phi_k)\boldsymbol{i}_s^k, \boldsymbol{T}_P(\phi_k - n_m\phi_m)\boldsymbol{i}_r^k, \phi_m)\right)}^{=:\boldsymbol{T}_P(\phi_k - n_m\phi_m)\boldsymbol{\psi}_s^k(\boldsymbol{i}_s^k, \boldsymbol{i}_r^k, \phi_m, \phi_k)}\\ &= -\boldsymbol{R}_r^k(\phi_m, \phi_k)\boldsymbol{i}_r^k(t) + \frac{\mathrm{d}}{\mathrm{d}t}\boldsymbol{\psi}_r^k(\boldsymbol{i}_s^k, \boldsymbol{i}_r^k, \phi_m, \phi_k) + (\omega_k(t) - n_m\omega_m(t))\,\boldsymbol{J}'\boldsymbol{\psi}_r^k(\boldsymbol{i}_s^k, \boldsymbol{i}_r^k, \phi_m, \phi_k)\end{aligned} \tag{2.18}$$

with the rotor current $\boldsymbol{i}_r^k$ (in A)^3, the rotor resistance matrix $\boldsymbol{R}_r^k$ (in Ω)$^{3\times3}$, the rotor flux linkage $\boldsymbol{\psi}_r^k$ (in Vs)^3 and the initial rotor flux linkage $\boldsymbol{\psi}_{r,0}^k = \boldsymbol{\psi}_r^k(\boldsymbol{i}_{s,0}^k, \boldsymbol{i}_{r,0}^k, \phi_{m,0}, \phi_{k,0})$. The time derivative of the stator flux linkage $\boldsymbol{\psi}_s^k$ is calculated by

$$\begin{aligned}\frac{\mathrm{d}}{\mathrm{d}t}\boldsymbol{\psi}_s^k(\boldsymbol{i}_s^k, \boldsymbol{i}_r^k, \phi_m, \phi_k) &= \overbrace{\frac{\partial\boldsymbol{\psi}_s^k(\boldsymbol{i}_s^k, \boldsymbol{i}_r^k, \phi_m, \phi_k)}{\partial\boldsymbol{i}_s^k}}^{=:-\boldsymbol{L}_s^k(\boldsymbol{i}_s^k, \boldsymbol{i}_r^k, \phi_m, \phi_k)}\frac{\mathrm{d}}{\mathrm{d}t}\boldsymbol{i}_s^k(t) + \overbrace{\frac{\partial\boldsymbol{\psi}_s^k(\boldsymbol{i}_s^k, \boldsymbol{i}_r^k, \phi_m, \phi_k)}{\partial\boldsymbol{i}_r^k}}^{=:-\boldsymbol{L}_{sr}^k(\boldsymbol{i}_s^k, \boldsymbol{i}_r^k, \phi_m, \phi_k)}\frac{\mathrm{d}}{\mathrm{d}t}\boldsymbol{i}_r^k(t)\\ &\quad + \underbrace{\frac{\partial\boldsymbol{\psi}_s^k(\boldsymbol{i}_s^k, \boldsymbol{i}_r^k, \phi_m, \phi_k)}{\partial\phi_m}}_{=:\boldsymbol{\varphi}_{sm}^k(\boldsymbol{i}_s^k, \boldsymbol{i}_r^k, \phi_m, \phi_k)}\frac{\mathrm{d}}{\mathrm{d}t}\phi_m(t) + \underbrace{\frac{\partial\boldsymbol{\psi}_s^k(\boldsymbol{i}_s^k, \boldsymbol{i}_r^k, \phi_m, \phi_k)}{\partial\phi_k}}_{=:\boldsymbol{\varphi}_{sk}^k(\boldsymbol{i}_s^k, \boldsymbol{i}_r^k, \phi_m, \phi_k)}\frac{\mathrm{d}}{\mathrm{d}t}\phi_k(t)\\ &= -\boldsymbol{L}_s^k(\boldsymbol{i}_s^k, \boldsymbol{i}_r^k, \phi_m, \phi_k)\frac{\mathrm{d}}{\mathrm{d}t}\boldsymbol{i}_s^k(t) - \boldsymbol{L}_{sr}^k(\boldsymbol{i}_s^k, \boldsymbol{i}_r^k, \phi_m, \phi_k)\frac{\mathrm{d}}{\mathrm{d}t}\boldsymbol{i}_r^k(t)\\ &\quad + \boldsymbol{\varphi}_{sm}^k(\boldsymbol{i}_s^k, \boldsymbol{i}_r^k, \phi_m, \phi_k)\omega_m(t) + \boldsymbol{\varphi}_{sk}^k(\boldsymbol{i}_s^k, \boldsymbol{i}_r^k, \phi_m, \phi_k)\omega_k(t)\end{aligned} \tag{2.19}$$

with the differential inductance matrices of the stator $\boldsymbol{L}_s^k$ and the coupling $\boldsymbol{L}_{sr}^k$ (both in H)$^{3\times3}$ and the vectors $\boldsymbol{\varphi}_{sm}^k$ and $\boldsymbol{\varphi}_{sk}^k$ (both in $\frac{\mathrm{Vs}}{\mathrm{rad}}$)^3 of the ϕ_m- and ϕ_k-derivative of the stator flux linkage

$\boldsymbol{\psi}_s^k$. The time derivative of the rotor flux linkage $\boldsymbol{\psi}_r^k$ is obtained as follows

$$\begin{aligned}\frac{\mathrm{d}}{\mathrm{d}t}\boldsymbol{\psi}_r^k(\boldsymbol{i}_s^k,\boldsymbol{i}_r^k,\phi_m,\phi_k) &= \overbrace{\frac{\partial\boldsymbol{\psi}_r^k(\boldsymbol{i}_s^k,\boldsymbol{i}_r^k,\phi_m,\phi_k)}{\partial\boldsymbol{i}_s^k}}^{=:-\boldsymbol{L}_{rs}^k(\boldsymbol{i}_s^k,\boldsymbol{i}_r^k,\phi_m,\phi_k)}\frac{\mathrm{d}}{\mathrm{d}t}\boldsymbol{i}_s^k(t) + \overbrace{\frac{\partial\boldsymbol{\psi}_r^k(\boldsymbol{i}_s^k,\boldsymbol{i}_r^k,\phi_m,\phi_k)}{\partial\boldsymbol{i}_r^k}}^{=:-\boldsymbol{L}_r^k(\boldsymbol{i}_s^k,\boldsymbol{i}_r^k,\phi_m,\phi_k)}\frac{\mathrm{d}}{\mathrm{d}t}\boldsymbol{i}_r^k(t)\\ &\quad+\underbrace{\frac{\partial\boldsymbol{\psi}_r^k(\boldsymbol{i}_s^k,\boldsymbol{i}_r^k,\phi_m,\phi_k)}{\partial\phi_m}}_{=:\boldsymbol{\varphi}_{rm}^k(\boldsymbol{i}_s^k,\boldsymbol{i}_r^k,\phi_m,\phi_k)}\frac{\mathrm{d}}{\mathrm{d}t}\phi_m(t) + \underbrace{\frac{\partial\boldsymbol{\psi}_r^k(\boldsymbol{i}_s^k,\boldsymbol{i}_r^k,\phi_m,\phi_k)}{\partial\phi_k}}_{=:\boldsymbol{\varphi}_{rk}^k(\boldsymbol{i}_s^k,\boldsymbol{i}_r^k,\phi_m,\phi_k)}\frac{\mathrm{d}}{\mathrm{d}t}\phi_k(t)\\ &= -\boldsymbol{L}_{rs}^k(\boldsymbol{i}_s^k,\boldsymbol{i}_r^k,\phi_m,\phi_k)\frac{\mathrm{d}}{\mathrm{d}t}\boldsymbol{i}_s^k(t) - \boldsymbol{L}_r^k(\boldsymbol{i}_s^k,\boldsymbol{i}_r^k,\phi_m,\phi_k)\frac{\mathrm{d}}{\mathrm{d}t}\boldsymbol{i}_r^k(t)\\ &\quad+\boldsymbol{\varphi}_{rm}^k(\boldsymbol{i}_s^k,\boldsymbol{i}_r^k,\phi_m,\phi_k)\omega_m(t) + \boldsymbol{\varphi}_{rk}^k(\boldsymbol{i}_s^k,\boldsymbol{i}_r^k,\phi_m,\phi_k)\omega_k(t)\end{aligned} \tag{2.20}$$

with the differential inductance matrices of the rotor $\boldsymbol{L}_r^k$ and the coupling $\boldsymbol{L}_{rs}^k$ (both in H)$^{3\times3}$ and the vectors $\boldsymbol{\varphi}_{rm}^k$ and $\boldsymbol{\varphi}_{rk}^k$ (both in $\frac{\mathrm{V\,s}}{\mathrm{rad}}$)^3 of the ϕ_m- and ϕ_k-derivative of the rotor flux linkage $\boldsymbol{\psi}_r^k$.

Remark (R.2.6) *In* (2.11), (2.12), (2.15), (2.16), (2.19), *and* (2.20) *the differential inductances and the angle derivatives of the flux linkages are defined for different reference frames (abc, uvw, s, r and k). Besides their definitions, mathematical relations do exist, e.g. the differential inductance $\boldsymbol{L}_s^s$ of the stator can be obtained from its differential inductance $\boldsymbol{L}_s^{abc}$ in the abc-reference frame via $\boldsymbol{L}_s^s = \boldsymbol{T}_C\boldsymbol{L}_s^{abc}\boldsymbol{T}_C^{-1}$. Sec. B.2 investigates all these mathematical relations.*

For the further model derivation of the DFIM the following two assumption shall hold[12]:

Assumption (A.2.8) *The stator and rotor resistances are symmetrical, i.e. $R_s := R_s^a = R_s^b = R_s^c$ and $R_r := R_r^u = R_r^v = R_r^w$. Hence, the resistance matrices of stator and rotor simplify to $\boldsymbol{R}_s^k = R_s\boldsymbol{I}_3$ and $\boldsymbol{R}_r^k = R_r\boldsymbol{I}_3$, respectively.*

Assumption (A.2.9) *The stator flux linkage $\boldsymbol{\psi}_s^k$ and rotor flux linkage $\boldsymbol{\psi}_r^k$ are not functions of the machine angle ϕ_m and the transformation angle ϕ_k, i.e.*

$$\boldsymbol{\psi}_s^k(\boldsymbol{i}_s^k,\boldsymbol{i}_r^k) = \boldsymbol{\psi}_s^k(\boldsymbol{i}_s^k,\boldsymbol{i}_r^k,\phi_m,\phi_k) \quad \textit{and} \quad \boldsymbol{\psi}_r^k(\boldsymbol{i}_s^k,\boldsymbol{i}_r^k) = \boldsymbol{\psi}_r^k(\boldsymbol{i}_s^k,\boldsymbol{i}_r^k,\phi_m,\phi_k)\,.$$

Because of (A.2.9), the vectors $\boldsymbol{\varphi}_{rm}^k$ and $\boldsymbol{\varphi}_{rk}^k$ of the ϕ_m- and ϕ_k-derivatives of the stator $\boldsymbol{\psi}_s^k$ and rotor $\boldsymbol{\psi}_r^k$ flux linkage are zero, i.e. $\boldsymbol{\varphi}_{sm}^k = \boldsymbol{\varphi}_{sk}^k = \boldsymbol{\varphi}_{rm}^k = \boldsymbol{\varphi}_{rk}^k = \boldsymbol{0}_3$. Moreover, (A.2.3) causes the γ-components i_s^γ and i_r^γ of the stator and rotor current to be zero[13], i.e.

$$i_s^\gamma(t) = k_c\kappa_c(i_s^a(t) + i_s^b(t) + i_s^c(t)) = 0 \quad \text{and} \quad i_r^\gamma(t) = k_c\kappa_c(i_r^u(t) + i_r^v(t) + i_r^w(t)) = 0\,. \tag{2.21}$$

On the basis of (2.21) and (A.2.7), Sec. B.2 gives a mathematical explanation that the symmetrical properties of the differential inductances $\boldsymbol{L}_s^k$, $\boldsymbol{L}_r^k$, $\boldsymbol{L}_{sr}^k$ and $\boldsymbol{L}_{rs}^k$ of stator, rotor and coupling are given by

$$\left.\begin{aligned}&\boldsymbol{L}_s^k(\boldsymbol{i}_s^k,\boldsymbol{i}_r^k) = \boldsymbol{L}_s^k(\boldsymbol{i}_s^k,\boldsymbol{i}_r^k)^\top\ ,\ \boldsymbol{L}_r^k(\boldsymbol{i}_s^k,\boldsymbol{i}_r^k) = \boldsymbol{L}_r^k(\boldsymbol{i}_s^k,\boldsymbol{i}_r^k)^\top\\ \text{and}\quad&\boldsymbol{L}_m^k(\boldsymbol{i}_s^k,\boldsymbol{i}_r^k) := \boldsymbol{L}_{rs}^k(\boldsymbol{i}_s^k,\boldsymbol{i}_r^k) = \boldsymbol{L}_{sr}^k(\boldsymbol{i}_s^k,\boldsymbol{i}_r^k)^\top \ \Rightarrow\ \boldsymbol{L}_{sr}^k(\boldsymbol{i}_s^k,\boldsymbol{i}_r^k) = \boldsymbol{L}_m^k(\boldsymbol{i}_s^k,\boldsymbol{i}_r^k)^\top\end{aligned}\right\}, \tag{2.22}$$

[12] If (A.2.8) does not hold, i.e. $R_s^a \neq R_s^b \neq R_s^c$ and $R_r^u \neq R_r^v \neq R_r^w$, the stator resistance matrix $\boldsymbol{R}_s^k$ is a function of the transformation angle ϕ_k and the rotor resistance matrix $\boldsymbol{R}_r^k$ is a function of both transformation angle ϕ_k and machine angle ϕ_m. The analytical expressions of $\boldsymbol{R}_s^k$ and $\boldsymbol{R}_r^k$ are highlighted in Sec. B.1.

[13] Due to (2.8), the γ-components i_s^γ of the stator current has already been determined to zero.

with the overall differential coupling inductance $\boldsymbol{L}_m^k$ (in H)$^{3\times3}$ and where the third columns of the differential inductances $\boldsymbol{L}_s^k$, $\boldsymbol{L}_r^k$ and $\boldsymbol{L}_m^k$ of stator, rotor and coupling are zero, i.e. $\left(L_x^{d\gamma}(\boldsymbol{i}_s^k,\boldsymbol{i}_r^k), L_x^{q\gamma}(\boldsymbol{i}_s^k,\boldsymbol{i}_r^k), L_x^{\gamma\gamma}(\boldsymbol{i}_s^k,\boldsymbol{i}_r^k)\right)^\top = \boldsymbol{0}_3$ with $x \in \{s,r,m\}$.
Combining (A.2.8), (A.2.9) and (2.17), (2.18), (2.19), (2.20) and (2.22) results in[14]

$$\left.\begin{aligned}\begin{pmatrix}\boldsymbol{u}_s^k(t)\\ \boldsymbol{u}_r^k(t)\end{pmatrix} &= -\begin{bmatrix}R_s\boldsymbol{I}_3 & \boldsymbol{O}_{3\times3}\\ \boldsymbol{O}_{3\times3} & R_r\boldsymbol{I}_3\end{bmatrix}\begin{pmatrix}\boldsymbol{i}_s^k(t)\\ \boldsymbol{i}_r^k(t)\end{pmatrix} + \tfrac{\mathrm{d}}{\mathrm{d}t}\begin{pmatrix}\boldsymbol{\psi}_s^k(\boldsymbol{i}_s^k,\boldsymbol{i}_r^k)\\ \boldsymbol{\psi}_r^k(\boldsymbol{i}_s^k,\boldsymbol{i}_r^k)\end{pmatrix} + \begin{pmatrix}\omega_k(t)\boldsymbol{J}'\boldsymbol{\psi}_s^k(\boldsymbol{i}_s^k,\boldsymbol{i}_r^k)\\ (\omega_k(t)-\omega_r(t))\,\boldsymbol{J}'\boldsymbol{\psi}_r^k(\boldsymbol{i}_s^k,\boldsymbol{i}_r^k)\end{pmatrix}\\ \text{with}\quad \tfrac{\mathrm{d}}{\mathrm{d}t}\begin{pmatrix}\boldsymbol{\psi}_s^k(\boldsymbol{i}_s^k,\boldsymbol{i}_r^k)\\ \boldsymbol{\psi}_r^k(\boldsymbol{i}_s^k,\boldsymbol{i}_r^k)\end{pmatrix} &= -\begin{bmatrix}\boldsymbol{L}_s^k(\boldsymbol{i}_s^k,\boldsymbol{i}_r^k) & \boldsymbol{L}_m^k(\boldsymbol{i}_s^k,\boldsymbol{i}_r^k)^\top\\ \boldsymbol{L}_m^k(\boldsymbol{i}_s^k,\boldsymbol{i}_r^k) & \boldsymbol{L}_r^k(\boldsymbol{i}_s^k,\boldsymbol{i}_r^k)\end{bmatrix}\tfrac{\mathrm{d}}{\mathrm{d}t}\begin{pmatrix}\boldsymbol{i}_s^k(t)\\ \boldsymbol{i}_r^k(t)\end{pmatrix}\end{aligned}\right\} \tag{2.23}$$

where the time derivatives of the stator flux linkage $\boldsymbol{\psi}_s^k$ and the rotor flux linkage $\boldsymbol{\psi}_r^k$ in (2.23) can be rewritten as

$$\frac{\mathrm{d}}{\mathrm{d}t}\begin{pmatrix}\boldsymbol{\psi}_s^k(\boldsymbol{i}_s^{dq},\boldsymbol{i}_r^{dq})\\ \boldsymbol{\psi}_r^k(\boldsymbol{i}_s^{dq},\boldsymbol{i}_r^{dq})\end{pmatrix} = -\begin{bmatrix}\boldsymbol{L}_s^{dq}(\boldsymbol{i}_s^{dq},\boldsymbol{i}_r^{dq}) & \boldsymbol{0}_2 & \boldsymbol{L}_m^{dq}(\boldsymbol{i}_s^{dq},\boldsymbol{i}_r^{dq})^\top & \boldsymbol{0}_2\\ \boldsymbol{0}_2^\top & 0 & \boldsymbol{0}_2^\top & 0\\ \boldsymbol{L}_m^{dq}(\boldsymbol{i}_s^{dq},\boldsymbol{i}_r^{dq}) & \boldsymbol{0}_2 & \boldsymbol{L}_r^{dq}(\boldsymbol{i}_s^{dq},\boldsymbol{i}_r^{dq}) & \boldsymbol{0}_2\\ \boldsymbol{0}_2^\top & 0 & \boldsymbol{0}_2^\top & 0\end{bmatrix}\frac{\mathrm{d}}{\mathrm{d}t}\begin{pmatrix}\boldsymbol{i}_s^k(t)\\ \boldsymbol{i}_r^k(t)\end{pmatrix}. \tag{2.24}$$

Inserting (2.24) into system (2.23) yields the following: (i) the γ-components of the stator voltage u_s^γ and rotor voltage u_r^γ are zero, i.e.

$$u_s^\gamma(t) = k_c\kappa_c\big(u_s^a(t)+u_s^b(t)+u_s^c(t)\big) = 0 \quad\text{and}\quad u_r^\gamma(t) = k_c\kappa_c\big(u_r^u(t)+u_r^v(t)+u_r^w(t)\big) = 0 \tag{2.25}$$

and (ii) the current dynamics of the DFIM in an arbitrary dq-reference frame result in[15]

$$\begin{aligned}\frac{\mathrm{d}}{\mathrm{d}t}\begin{pmatrix}\boldsymbol{i}_s^{dq}(t)\\ \boldsymbol{i}_r^{dq}(t)\end{pmatrix} = &\begin{bmatrix}\boldsymbol{L}_s^{dq}(\boldsymbol{i}_s^{dq},\boldsymbol{i}_r^{dq}) & \boldsymbol{L}_m^{dq}(\boldsymbol{i}_s^{dq},\boldsymbol{i}_r^{dq})^\top\\ \boldsymbol{L}_m^{dq}(\boldsymbol{i}_s^{dq},\boldsymbol{i}_r^{dq}) & \boldsymbol{L}_r^{dq}(\boldsymbol{i}_s^{dq},\boldsymbol{i}_r^{dq})\end{bmatrix}^{-1}\\ &\left(-\begin{bmatrix}R_s\boldsymbol{I}_2 & \boldsymbol{O}_{2\times2}\\ \boldsymbol{O}_{2\times2} & R_r\boldsymbol{I}_2\end{bmatrix}\begin{pmatrix}\boldsymbol{i}_s^{dq}(t)\\ \boldsymbol{i}_r^{dq}(t)\end{pmatrix} - \begin{pmatrix}\boldsymbol{u}_s^{dq}(t)\\ \boldsymbol{u}_r^{dq}(t)\end{pmatrix} + \begin{pmatrix}\omega_k(t)\boldsymbol{J}\boldsymbol{\psi}_s^{dq}(\boldsymbol{i}_s^{dq},\boldsymbol{i}_r^{dq})\\ (\omega_k(t)-\omega_r(t))\,\boldsymbol{J}\boldsymbol{\psi}_r^{dq}(\boldsymbol{i}_s^{dq},\boldsymbol{i}_r^{dq})\end{pmatrix}\right).\end{aligned} \tag{2.26}$$

In Sec. 2.4.1 the power flow in the machine will be explained. Therein, the machine torque m_m is derived, which is given by

$$m_m(\boldsymbol{i}_s^{dq},\boldsymbol{i}_r^{dq}) = \frac{2}{3k_c^2}n_m\boldsymbol{i}_s^{dq}(t)^\top\boldsymbol{J}\boldsymbol{\psi}_s^{dq}(\boldsymbol{i}_s^{dq},\boldsymbol{i}_r^{dq}) = -\frac{2}{3k_c^2}n_m\boldsymbol{i}_r^{dq}(t)^\top\boldsymbol{J}\boldsymbol{\psi}_r^{dq}(\boldsymbol{i}_s^{dq},\boldsymbol{i}_r^{dq}). \tag{2.27}$$

2.2.2.2 Measurement of the flux maps in the laboratory

To be able to use the nonlinear DFIM model (2.26)–(2.27), the nonlinear flux linkages $\boldsymbol{\psi}_s^{dq}$ and $\boldsymbol{\psi}_r^{dq}$ of stator and rotor, respectively, as well as the differential inductances $\boldsymbol{L}_s^k$, $\boldsymbol{L}_r^k$ and $\boldsymbol{L}_m^k$ of stator, rotor and coupling need to be obtained by measurements in the laboratory. This section explains, how to measure the nonlinear flux linkages $\boldsymbol{\psi}_s^{dq}$ and $\boldsymbol{\psi}_r^{dq}$.
For this purpose, the DFIM must operate in stationary operation[16], i.e. all time derivatives in

[14] In the following, the electrical ω_r instead of the mechanical ω_m machine rotational speed will be used.

[15] Inverting the inductance matrix in (2.26) requires its full rank, i.e. $\det\begin{bmatrix}\boldsymbol{L}_s^{dq}(\boldsymbol{i}_s^{dq},\boldsymbol{i}_r^{dq}) & \boldsymbol{L}_m^{dq}(\boldsymbol{i}_s^{dq},\boldsymbol{i}_r^{dq})^\top\\ \boldsymbol{L}_m^{dq}(\boldsymbol{i}_s^{dq},\boldsymbol{i}_r^{dq}) & \boldsymbol{L}_r^{dq}(\boldsymbol{i}_s^{dq},\boldsymbol{i}_r^{dq})\end{bmatrix} \neq 0$.

[16] All quantities are marked with an additional * when they operate in the equilibrium of the stationary operation.

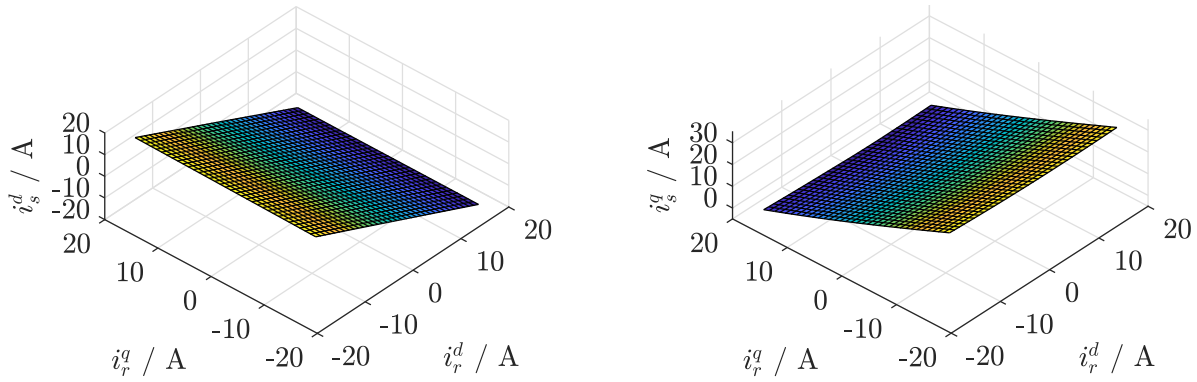

(a) *d-component* i_s^d *of the stator current.*

(b) *q-component* i_s^q *of the stator current.*

Figure 2.6: *Stator current* $\boldsymbol{i}_s^{dq}$ *over the rotor current* $\boldsymbol{i}_r^{dq}$ *(steady-state case***).*

(2.26) are zero: $\frac{\mathrm{d}}{\mathrm{d}t}(.)=0$. This leads to

$$\begin{pmatrix}\boldsymbol{u}_s^{dq\star}\\ \boldsymbol{u}_r^{dq\star}\end{pmatrix} \overset{(2.26)}{=} -\begin{bmatrix}R_s\boldsymbol{I}_2 & \boldsymbol{O}_{2\times2}\\ \boldsymbol{O}_{2\times2} & R_r\boldsymbol{I}_2\end{bmatrix}\begin{pmatrix}\boldsymbol{i}_s^{dq\star}\\ \boldsymbol{i}_r^{dq\star}\end{pmatrix} + \begin{pmatrix}\omega_k^\star \boldsymbol{J}\boldsymbol{\psi}_s^{dq}(\boldsymbol{i}_s^{dq\star},\boldsymbol{i}_r^{dq\star})\\ (\omega_k^\star-\omega_r^\star)\,\boldsymbol{J}\boldsymbol{\psi}_r^{dq}(\boldsymbol{i}_s^{dq\star},\boldsymbol{i}_r^{dq\star})\end{pmatrix}. \tag{2.28}$$

Moreover, the stator is directly connected to the grid. In Sec. 2.3.1, it is proven that this yields $\boldsymbol{u}_s^{dq}(t)=\boldsymbol{u}_g^{dq}(t)$. For the further derivation, the following assumption is imposed:

Assumption (A.2.10) *The dq-reference frame is grid voltage oriented, i.e.* $\phi_k(t)=\phi_g(t)$. *Moreover, the grid voltage has both a constant rotational speed* $\omega_g=2\pi f_g$ *and a constant amplitude* $\hat{u}_g$ *such that the grid voltage is given by* $\boldsymbol{u}_g^{dq} \overset{(2.9)}{=} \frac{3}{2}k_c\hat{u}_g(1\ 0)^\top$.

The stationary operation (2.28) in grid voltage orientation, where (A.2.10) pertains and the stator is fed by the grid voltage, i.e. $\boldsymbol{u}_s^{dq\star}=\boldsymbol{u}_g^{dq}$, simplifies to

$$\begin{pmatrix}\boldsymbol{u}_g^{dq}\\ \boldsymbol{u}_r^{dq\star}\end{pmatrix} \overset{(2.28)}{=} -\begin{bmatrix}R_s\boldsymbol{I}_2 & \boldsymbol{O}_{2\times2}\\ \boldsymbol{O}_{2\times2} & R_r\boldsymbol{I}_2\end{bmatrix}\begin{pmatrix}\boldsymbol{i}_s^{dq\star}\\ \boldsymbol{i}_r^{dq\star}\end{pmatrix} + \begin{pmatrix}\omega_g \boldsymbol{J}\boldsymbol{\psi}_s^{dq}(\boldsymbol{i}_s^{dq\star},\boldsymbol{i}_r^{dq\star})\\ (\omega_g-\omega_r^\star)\,\boldsymbol{J}\boldsymbol{\psi}_r^{dq}(\boldsymbol{i}_s^{dq\star},\boldsymbol{i}_r^{dq\star})\end{pmatrix}. \tag{2.29}$$

The stator part in (2.29), i.e. $\boldsymbol{u}_g^{dq}=-R_s\boldsymbol{i}_s^{dq\star}+\omega_g\boldsymbol{J}\boldsymbol{\psi}_s^{dq}(\boldsymbol{i}_s^{dq\star},\boldsymbol{i}_r^{dq\star})$, consists of four "unknown" quantities $\boldsymbol{i}_s^{dq\star}$ and $\boldsymbol{i}_r^{dq\star}$. For a fixed rotor current $\boldsymbol{i}_r^{dq\star}$, the stator flux linkage $\boldsymbol{\psi}_s^{dq}:\mathbb{R}^2\to\mathbb{R}^2,\ \boldsymbol{i}_s^{dq\star}\mapsto \boldsymbol{\psi}_s^{dq\star}(\boldsymbol{i}_s^{dq\star},\boldsymbol{i}_r^{dq\star}=\text{const.})$ is a bijective function. Consequently, combining this characteristic with the stator part of (2.29) yields a unique (implicit) relation between the stator current $\boldsymbol{i}_s^{dq\star}$ and the rotor current $\boldsymbol{i}_r^{dq\star}$ in steady state, such that $\boldsymbol{i}_s^{dq\star}=\boldsymbol{i}_s^{dq}(\boldsymbol{i}_r^{dq\star})$ pertains.
Hence, to determine both the stator flux linkage $\boldsymbol{\psi}_s^{dq\star}$ and the rotor flux linkage $\boldsymbol{\psi}_r^{dq\star}$ with

$$\left.\begin{aligned}\boldsymbol{\psi}_s^{dq\star} &:= \boldsymbol{\psi}_s^{dq}(i_s^{d\star},i_s^{q\star},i_r^{d\star},i_r^{q\star}) := \boldsymbol{\psi}_s^{dq}(\boldsymbol{i}_s^{dq\star},\boldsymbol{i}_r^{dq\star}) := \boldsymbol{\psi}_s^{dq}\big(\boldsymbol{i}_s^{dq}(\boldsymbol{i}_r^{dq\star}),\boldsymbol{i}_r^{dq\star}\big)\\ \boldsymbol{\psi}_r^{dq\star} &:= \boldsymbol{\psi}_r^{dq}(i_s^{d\star},i_s^{q\star},i_r^{d\star},i_r^{q\star}) := \boldsymbol{\psi}_r^{dq}(\boldsymbol{i}_s^{dq\star},\boldsymbol{i}_r^{dq\star}) := \boldsymbol{\psi}_r^{dq}\big(\boldsymbol{i}_s^{dq}(\boldsymbol{i}_r^{dq\star}),\boldsymbol{i}_r^{dq\star}\big)\end{aligned}\right\}, \tag{2.30}$$

only the rotor current $\boldsymbol{i}_r^{dq\star}$ is needed.
Fig. 2.6 shows the stator current $\boldsymbol{i}_s^{dq\star}$ as function of the rotor current $\boldsymbol{i}_r^{dq\star}$ of the DFIM at the test bench. The *d*-component $i_s^{d\star}$ of the stator current depends (almost) linearly on the *d*-component $i_r^{d\star}$ of the rotor current but with different sign. Moreover, the *q*-component $i_r^{q\star}$ of the rotor current hardly affects $i_s^{d\star}$ as well as the *d*-component $i_r^{d\star}$ of the rotor current hardly influences the *q*-component $i_s^{q\star}$ of the stator current. The *q*-component $i_s^{q\star}$ of the stator current depends (almost) linearly on the *q*-component $i_r^{q\star}$ but with different sign and an offset of about 14 A.

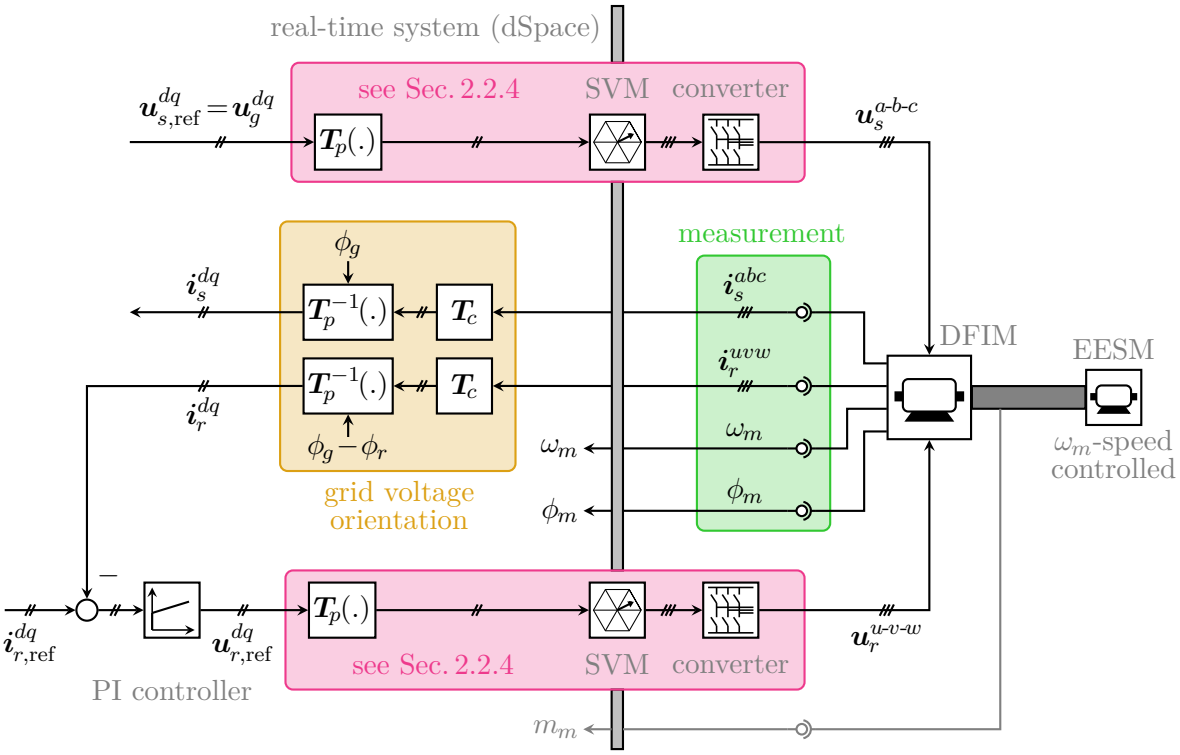

Figure 2.7: *Block diagram of the experimental setup to measure the flux maps.*

Fig. 2.7 depicts the implementation of the control and the laboratory setup to measure the flux maps of the stator flux linkage $\boldsymbol{\psi}_s^{dq\star}$ and rotor flux linkage $\boldsymbol{\psi}_r^{dq\star}$:

- **stator:** The stator of the DFIM is connected to a converter. With the help of the space vector modulation (SVM) and a specific Park transformation (— for details see Sec. 2.2.4) the reference $\boldsymbol{u}_{s,\mathrm{ref}}^{dq}$ (in V)[2] of the stator voltage is applied to the stator. By setting the reference stator voltage $\boldsymbol{u}_{s,\mathrm{ref}}^{dq}$ to the grid voltage, i.e. $\boldsymbol{u}_{s,\mathrm{ref}}^{dq} = \boldsymbol{u}_g^{dq}$, the converter substitutes the behavior of the grid/transformer[17] so that $\boldsymbol{u}_s^{dq\star} = \boldsymbol{u}_g^{dq}$ holds.

- **rotor:** The rotor of the DFIM is connected to a second converter. Again, SVM and Park transformation (— for details see Sec. 2.2.4) cause that the reference rotor voltage $\boldsymbol{u}_{r,\mathrm{ref}}^{dq}$ (in V)[2] is applied to the rotor such that $\boldsymbol{u}_r^{dq\star} = \boldsymbol{u}_{r,\mathrm{ref}}^{dq}$ holds. An outer rotor current PI controller[18] ensures steady-state tracking of the reference rotor current $\boldsymbol{i}_{r,\mathrm{ref}}^{dq}$ (in A)[2] so that $\boldsymbol{i}_r^{dq\star} = \boldsymbol{i}_{r,\mathrm{ref}}^{dq}$ pertains.

- **EESM:** An electrically excited synchronous machine (EESM) is used as prime mover. It is speed-controlled and yields an operation of constant rotational speed $\omega_r^\star = n_m \omega_m^\star$ for both machines.

- **measurements—:** Current sensors measure both the stator current $\boldsymbol{i}_s^{abc}$ and the rotor current $\boldsymbol{i}_r^{uvw}$. An additional encoder measures the machine rotational speed ω_m and the machine angle ϕ_m.

[17] The converter is used since it is important to measure the (differential) inductance maps (see Sec. 2.2.2.4).
[18] Since the DFIM model is not known yet, the control parameters must be tuned not too aggressive.

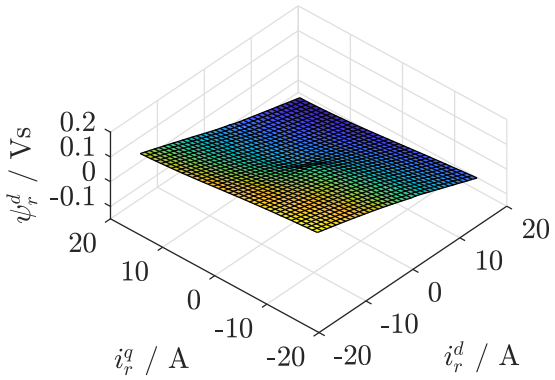

(a) *d-component* ψ_r^d *of the rotor flux.*

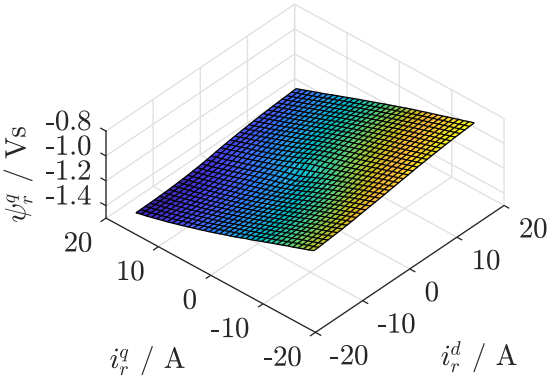

(b) *q-component* ψ_r^q *of the rotor flux.*

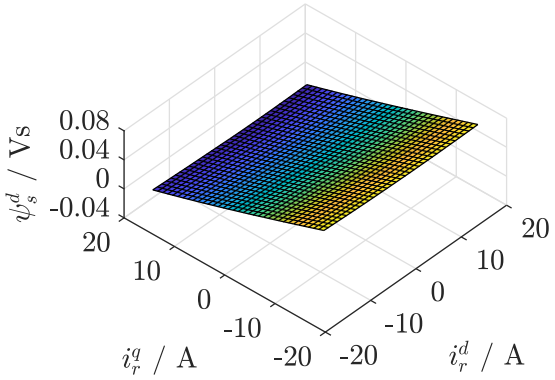

(c) *d-component* ψ_s^d *of the stator flux.*

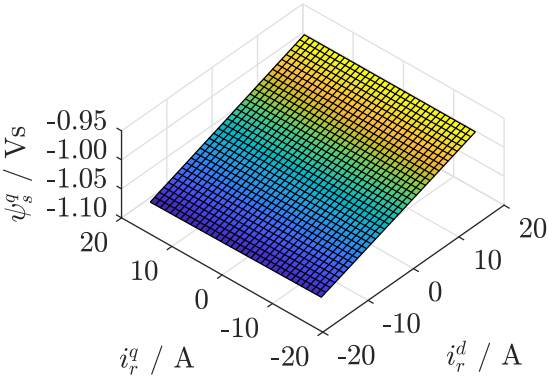

(d) *q-component* ψ_s^q *of the stator flux.*

Figure 2.8: *Rotor flux linkage* $\boldsymbol{\psi}_r^{dq}$ *and stator flux linkage* $\boldsymbol{\psi}_s^{dq}$ *over the rotor current* $\boldsymbol{i}_r^{dq}$ *(steady-state case***).*

- **grid voltage orientation—:** By means of Clarke's and (inverse) Park's transformation, the three-phase currents $\boldsymbol{i}_s^{abc}$ and $\boldsymbol{i}_r^{uvw}$ are transformed into the grid voltage oriented dq-reference frame. Since in the used laboratory setup there exists no *real* grid voltage, the real-time system (dSpace) must generate a *virtual* grid voltage $\boldsymbol{u}_g^{abc}$ as in (2.6) (considering (A.2.10)).

The setup is conducted for the following reference rotor current $\boldsymbol{i}_{r,\mathrm{ref}}^{dq}$:

$$\begin{aligned}&(i_{r,\mathrm{ref}}^d, i_{r,\mathrm{ref}}^q) \in \mathcal{D}\times\mathcal{Q} := \{-i_{r,\mathrm{lim}}^d, \dots, i_{r,\mathrm{lim}}^d\}\times\{-i_{r,\mathrm{lim}}^q, \dots, i_{r,\mathrm{lim}}^q\}\\ &= \{-ni_{r,\triangle}^d, -(n-1)i_{r,\triangle}^d, \dots, (n-1)i_{r,\triangle}^d, ni_{r,\triangle}^d\}\times\{-mi_{r,\triangle}^q, -(m-1)i_{r,\triangle}^q, \dots, (m-1)i_{r,\triangle}^q, mi_{r,\triangle}^q\}\end{aligned} \tag{2.31}$$

with $i_{r,\mathrm{lim}}^d = ni_{r,\triangle}^d$, $i_{r,\mathrm{lim}}^q = mi_{r,\triangle}^q$ and $n, m \in \mathbb{N}$ and where $i_{r,\triangle}^d$ and $i_{r,\triangle}^q$ (both in A) are the rotor current intervals in d- and q-direction. For each reference $(i_{r,\mathrm{ref}}^d, i_{r,\mathrm{ref}}^q) \in \mathcal{D}\times\mathcal{Q}$, the flux linkages of stator $\boldsymbol{\psi}_s^{dq\star}$ and rotor $\boldsymbol{\psi}_r^{dq\star}$ are calculated based on

$$\boldsymbol{\psi}_s^{dq\star} \overset{(2.29)}{=} \frac{1}{\omega_g}\boldsymbol{J}^{-1}\left(\boldsymbol{u}_g^{dq} + R_s\boldsymbol{i}_s^{dq\star}\right) \quad \text{and} \quad \boldsymbol{\psi}_r^{dq\star} \overset{(2.29)}{=} \frac{1}{\omega_g - \omega_r^\star}\boldsymbol{J}^{-1}\left(\boldsymbol{u}_{r,\mathrm{ref}}^{dq\star} + R_r\boldsymbol{i}_r^{dq\star}\right) \tag{2.32}$$

with $\boldsymbol{u}_{r,\mathrm{ref}}^{dq\star} = \boldsymbol{u}_{r,\mathrm{ref}}^{dq}(\boldsymbol{i}_s^{dq\star}, \boldsymbol{i}_r^{dq\star})$. Measurement errors can be decreased, if for each operation point the average values of a great number of measurement points are taken into account.
To obtain the flux linkages of stator $\boldsymbol{\psi}_s^{dq\star}$ and rotor $\boldsymbol{\psi}_r^{dq\star}$ over the whole domain $(i_{r,\mathrm{ref}}^d, i_{r,\mathrm{ref}}^q) \in$

description	symbols & values with unit
parameters of the flux maps	
reference limit of rotor current	$i^d_{r,\mathrm{lim}} = i^q_{r,\mathrm{lim}} = 17\,\mathrm{A}$
rotor current interval	$i^d_{r,\triangle} = i^q_{r,\triangle} = 1\,\mathrm{A}$
rotational speed of the machine	$\omega^\star_r = n_m \omega^\star_m = 240\,\frac{\mathrm{rad}}{\mathrm{s}}$
parameters of the inductance maps	
current interval	$i_\triangle = 0.5\,\mathrm{A}$
rotational speed of the machine	$\omega^\star_r = n_m \omega^\star_m = 240\,\frac{\mathrm{rad}}{\mathrm{s}}$

Table 2.2: *Parameters to measure the flux maps and the inductance maps.*

description	symbols & values with unit
parameters of the doubly-fed induction machine	
rated mechanical power	$p_{m,\mathrm{nom}} = 10\,\mathrm{kW}$
rated machine torque	$m_{m,\mathrm{nom}} = 55\,\mathrm{Nm}$
pole pair number	$n_m = 2$
stator resistance	$R_s = 0.72\,\Omega$
rotor resistance	$R_r = 0.55\,\Omega$
machine inertia	$\theta_m = 0.094\,\mathrm{kgm}^2$
rated stator current	$\hat{i}_{s,\mathrm{nom}} = 20.9\sqrt{2}\,\mathrm{A}$
rated rotor current	$\hat{i}_{r,\mathrm{nom}} = 17\sqrt{2}\,\mathrm{A}$
parameters of the grid	
voltage amplitude	$\hat{u}_g = 400\sqrt{\frac{2}{3}}\,\mathrm{V}$
frequency	$f_g = 50\,\mathrm{Hz}$
rotational speed	$\omega_g = 2\pi f_g \approx 314\,\frac{\mathrm{rad}}{\mathrm{s}}$

Table 2.3: *Parameters of the doubly-fed induction machine and the grid.*

$[-i^d_{r,\mathrm{lim}}, \ldots, i^d_{r,\mathrm{lim}}] \times [-i^q_{r,\mathrm{lim}}, \ldots, i^q_{r,\mathrm{lim}}]$, an interpolation between the operation points $(i^d_{r,\mathrm{ref}}, i^q_{r,\mathrm{ref}}) \in \mathcal{D}\times\mathcal{Q}$ is required. An additional smoothing can compensate for measurement inaccuracies, which finally leads to the desired flux maps.
Fig. 2.8 depicts the measured flux maps of the flux linkages of stator $\boldsymbol{\psi}^{dq\star}_s$ and rotor $\boldsymbol{\psi}^{dq\star}_r$. The parameters of the experiment are listed in Tab. 2.2. The data of both DFIM and grid at the test bench are summarized in Tab. 2.3.
The d-component $\psi^{d\star}_s$ of the stator flux linkage depends (almost) linearly on the q-component $i^{q\star}_r$ of the rotor current but with different sign. Moreover, the d-component $i^{d\star}_r$ of the rotor current hardly affects $\psi^{d\star}_s$ as well as the q-component $i^{q\star}_r$ of the rotor current hardly influences the q-component $\psi^{q\star}_s$ of the stator flux linkage. The q-component $\psi^{q\star}_s$ of the stator flux linkage depends (almost) linearly on the d-component $i^{d\star}_r$ of the rotor current and exhibits an offset of about $-1\,\mathrm{Vs}$. Both d-component $\psi^{d\star}_r$ and q-component $\psi^{q\star}_r$ of the rotor flux linkage depend on both components of the rotor current $\boldsymbol{i}^{dq\star}_r$. Like the q-component $\psi^{q\star}_s$ of the stator flux linkage, the q-component $\psi^{q\star}_r$ of the rotor flux linkage exhibits an offset of about $-1\,\mathrm{Vs}$.

2.2.2.3 Measurement of the torque map in the laboratory

Besides the flux maps as described in Sec. 2.2.2.2 it is important to know the torque map of the machine torque $m^\star_m := m_m(\boldsymbol{i}^{dq\star}_s, \boldsymbol{i}^{dq\star}_r)$. To obtain the torque map, there exist the following three

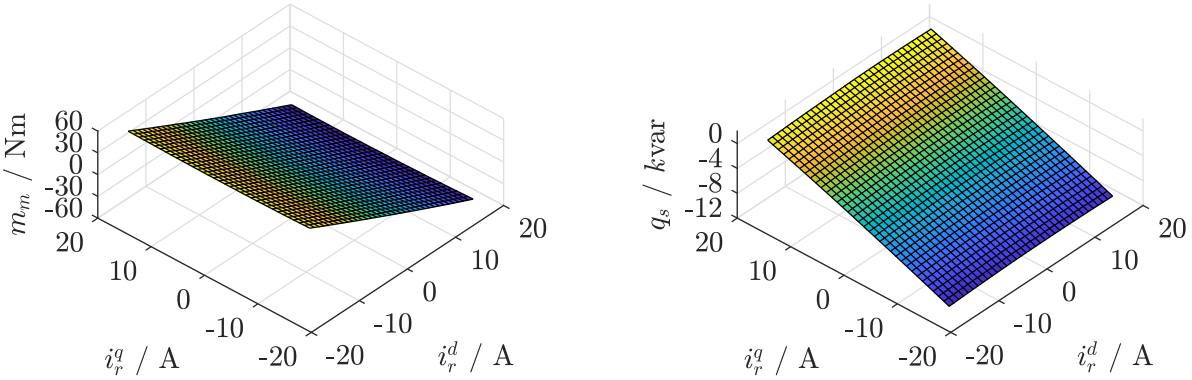

(a) *Machine torque m_m.* (b) *Reactive power q_s.*

Figure 2.9: *Machine torque m_m (left) and stator reactive power q_s (right) over the rotor current $\boldsymbol{i}_r^{dq}$ (steady-state case*).*

options:

(1) calculation via rotor current $\boldsymbol{i}_r^{dq\star}$ and flux linkage $\boldsymbol{\psi}_r^{dq\star}$: $m_m^\star \overset{(2.27)}{=} -\frac{2}{3k_c^2} n_m \boldsymbol{i}_r^{dq\top} \boldsymbol{J} \boldsymbol{\psi}_r^{dq\star}$,

(2) calculation via stator current $\boldsymbol{i}_s^{dq\star}$ and flux linkage $\boldsymbol{\psi}_s^{dq\star}$: $m_m^\star \overset{(2.27)}{=} \frac{2}{3k_c^2} n_m \boldsymbol{i}_s^{dq\top} \boldsymbol{J} \boldsymbol{\psi}_s^{dq\star}$,

(3) usage of an additional torque sensor (see Fig. 2.7) during the measurement of the flux maps (see Sec. 2.2.2.2).

Since torque sensors are expensive and thus—in contrary to the used test bench—rarely available, option (3) is not always possible. Fig. 2.9a shows the measured torque map, i.e. option (3), of the machine torque $m_m^\star$ as function of the rotor current $\boldsymbol{i}_r^{dq\star}$. The machine torque $m_m^\star$ depends (almost) linearly on the d-component $i_r^{d\star}$ of the rotor current but with different sign whereas the q-component $i_r^{q\star}$ of the rotor current hardly affects $m_m^\star$.
Fig. 2.10 depicts the percentage deviations between the calculated torques of options (1) and (2) and the measured torque of option (3), which are calculated via $\frac{|m_m^\star(1/2) - m_m^\star(3)|}{m_{m,\mathrm{nom}}}$ with the rated torque $m_{m,\mathrm{nom}}$ (in Nm). The rotor-based calculation of option (1) features a very precise matching with the measurement (see left of Fig. 2.10). The averaged deviation is 1.21 % and its maximal deviation is 3.45 %. Also the stator-based calculation of option (2) yields a very good result with an averaged deviation of 1.81 % and maximal deviation of 4.29 % (see right of Fig. 2.10). The deviations between the two calculated torques and the measured torque are due to inaccuracies in e.g. the measurement, the interpolation, the smoothing or the model assumptions. Compared to the divergence of the measured torque and the calculated torque of the linear model, where the averaged deviation is 11.33 % and the maximal deviation is 25.61 % (see Fig. 2.13), the nonlinear model yields significant improvements.

Remark (R.2.7) *For the control of the DFIM (see Ch. 3)—apart from the machine torque m_m—also the reactive power q_s of the stator is relevant. Hence, Fig. 2.9b depicts $q_s^\star$ as function of the rotor currents $\boldsymbol{i}_r^{dq\star}$. Since the reactive power q_s of the stator is given by (see e.g. [119], therein with $k_c = \frac{2}{3}$)*

$$q_s(t) = \frac{2}{3k_c^2} \boldsymbol{u}_s^{dq}(t)^\top \boldsymbol{J} \boldsymbol{i}_s^{dq}(t) \overset{(A.2.10)}{=} \frac{2}{3k_c^2} \left(\boldsymbol{u}_g^{dq}\right)^\top \boldsymbol{J} \boldsymbol{i}_s^{dq}(t) = -\frac{2}{3k_c^2} \hat{u}_g i_s^q(t) \;\Rightarrow\; q_s^\star = -\frac{2}{3k_c^2} \hat{u}_g i_s^{q\star}, \quad (2.33)$$

the stator reactive power $q_s^\star$ correlates with the scaled (by factor $-\frac{2}{3k_c^2}\hat{u}_g$) stator current $i_s^{q\star}$ and depends mainly on the q-component $i_r^{q\star}$ of the rotor current.

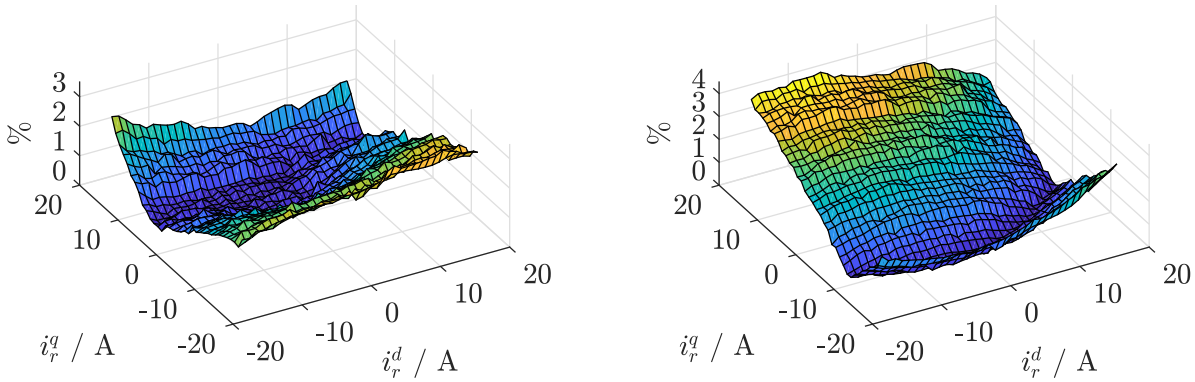

(a) *Rotor-based calculation: option (1).* (b) *Stator-based calculation: option (2).*

Figure 2.10: *Percentage deviation between the calculated and measured machine torque m_m of the nonlinear DFIM model over the rotor current $\boldsymbol{i}_r^{dq}$ (steady-state case*).*

2.2.2.4 Measurement of the differential inductance maps in the laboratory

With the help of the flux maps (see Sec. 2.2.2.2), its possible to describe the stationary behavior of the DFIM. To model the dynamics of the DFIM as well, it is important to know the inductances of the stator $\boldsymbol{L}_s^{dq}$, the rotor $\boldsymbol{L}_r^{dq}$ and the coupling $\boldsymbol{L}_m^{dq}$. This section will explain how to obtain these matrices. The explanation is given exemplary for the dq-element L_s^{dq} of the stator inductance $\boldsymbol{L}_s^{dq}$.

Due to (2.19), L_s^{dq} is defined as the directional derivative $L_s^{dq} := \frac{\partial \psi_s^d}{\partial i_s^q}$ and can be approximated by

$$L_s^{dq\star} := L_s^{dq}(\boldsymbol{i}_s^{dq\star}, \boldsymbol{i}_r^{dq\star}) = \frac{\partial \psi_s^d(\boldsymbol{i}_s^{dq\star}, \boldsymbol{i}_r^{dq\star})}{\partial i_s^{q\star}} \approx \frac{\psi_s^d(i_s^{d\star}, i_s^{q\star}+i_\triangle, i_r^{d\star}, i_r^{q\star}) - \psi_s^{d\star}}{\underbrace{i_s^{q\star} + i_\triangle - i_s^{q\star}}_{=i_\triangle}}. \tag{2.34}$$

Thus, it is necessary to be able to control all four currents i_s^d, i_s^q, i_r^d and i_r^q independently, since for the directional derivative only the q-component $i_s^{q\star}$ is changed by the current interval[19] $i_\triangle$ (in A), while the other three currents keep their constant operation points $i_s^{d\star}$, $i_r^{d\star}$ and $i_r^{q\star}$. This is not feasible for a constant stator voltage $\boldsymbol{u}_s^{dq\star} = \boldsymbol{u}_g^{dq}$, because the stator current $\boldsymbol{i}_s^{dq\star}$ then is a function of $\boldsymbol{i}_r^{dq\star}$. Consequently, to measure the differential inductance maps, the stator voltage $\boldsymbol{u}_s^{dq\star}$ needs to be changeable for what reason the stator of the DFIM needs to be connected to a converter.

Fig. 2.11 depicts the implementation of the control and the laboratory setup to measure the inductance maps for $\boldsymbol{L}_s^{dq}$, $\boldsymbol{L}_r^{dq}$ and $\boldsymbol{L}_m^{dq}$. It is identical to the setup for measuring the flux maps as in Fig. 2.7 (see Sec. 2.2.2.2) but with one significant deviation:

- **stator:** Instead of applying a constant grid voltage $\boldsymbol{u}_{s,\mathrm{ref}}^{dq} = \boldsymbol{u}_g^{dq}$ to the stator, the reference $\boldsymbol{u}_{s,\mathrm{ref}}^{dq}$ is variable. An outer stator current PI controller now ensures the tracking of the reference stator current $\boldsymbol{i}_{s,\mathrm{ref}}^{dq}$ (in A)[2], such that $\boldsymbol{i}_s^{dq} = \boldsymbol{i}_{s,\mathrm{ref}}^{dq}$ pertains.

In combination with the rotor current PI controller, which guarantees that $\boldsymbol{i}_r^{dq} = \boldsymbol{i}_{r,\mathrm{ref}}^{dq}$ holds, all four currents i_s^d, i_s^q, i_r^d and i_r^q can be controlled independently. Similar to (2.32), by controlling

[19] In theory, the smaller the current $i_\triangle$ the more precise is the approximation in (2.34). Nevertheless, $i_\triangle$ must not be chosen too small, since measurement inaccuracies affect the result especially for small $i_\triangle$.

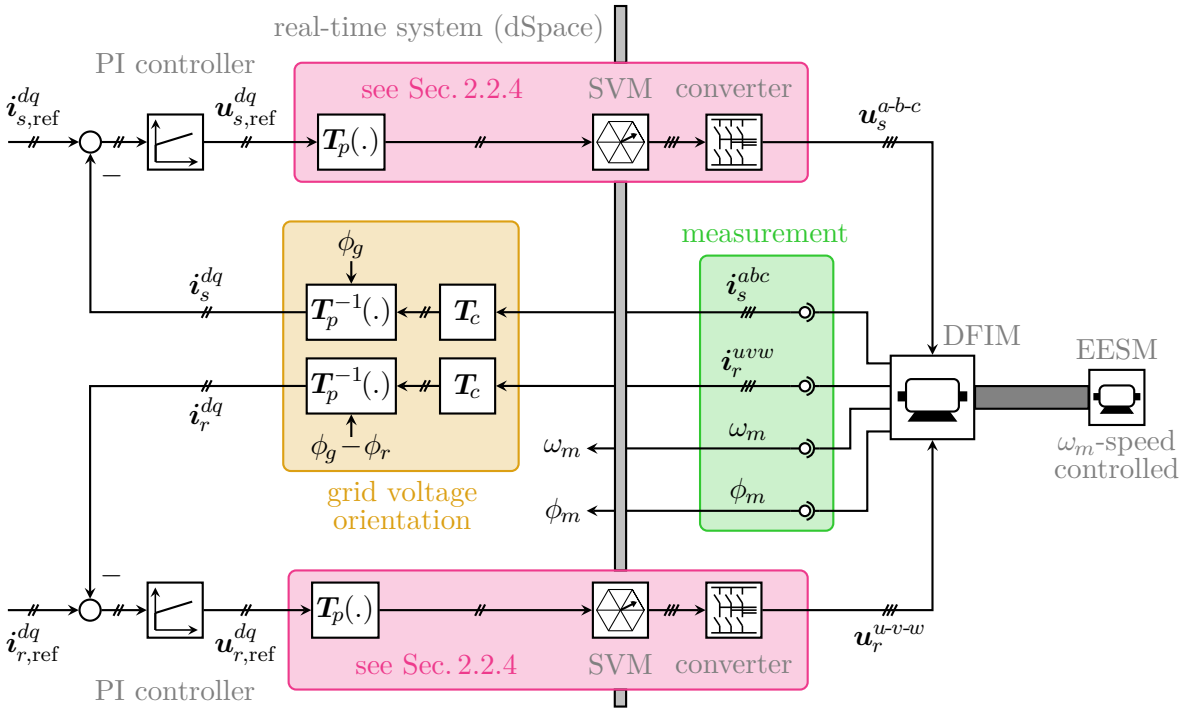

Figure 2.11: *Block diagram of the experimental setup to measure the inductance maps.*

the DFIM to the equilibrium $(i_s^{d\star},i_s^{q\star}+i_\triangle,i_r^{d\star},i_r^{q\star})$ the stator flux linkage $\boldsymbol{\psi}_s^{dq}$ and the rotor flux linkage $\boldsymbol{\psi}_r^{dq}$ can be calculated by

$$\left.\begin{aligned}\boldsymbol{\psi}_s^{dq}(i_s^{d\star},i_s^{q\star}+i_\triangle,i_r^{d\star},i_r^{q\star}) &= \tfrac{1}{\omega_g}\boldsymbol{J}^{-1}\left(\boldsymbol{u}_{s,\mathrm{ref}}^{dq}(i_s^{d\star},i_s^{q\star}+i_\triangle,i_r^{d\star},i_r^{q\star}) + R_s(\boldsymbol{i}_s^{dq\star}+(0\ i_\triangle)^\top)\right)\\ \boldsymbol{\psi}_r^{dq}(i_s^{d\star},i_s^{q\star}+i_\triangle,i_r^{d\star},i_r^{q\star}) &= \tfrac{1}{\omega_g-\omega_r^\star}\boldsymbol{J}^{-1}\left(\boldsymbol{u}_{r,\mathrm{ref}}^{dq}(i_s^{d\star},i_s^{q\star}+i_\triangle,i_r^{d\star},i_r^{q\star}) + R_r\boldsymbol{i}_r^{dq\star}\right)\end{aligned}\right\}. \tag{2.35}$$

Inserting the result of the stator flux $\boldsymbol{\psi}_s^{dq}(i_s^{d\star},i_s^{q\star}+i_\triangle,i_r^{d\star},i_r^{q\star})$ into (2.34) yields the dq-element $L_s^{dq\star}$ of the stator inductance $\boldsymbol{L}_s^{dq}(\boldsymbol{i}_s^{dq\star},\boldsymbol{i}_r^{dq\star})$. This method must be performed:

a) for all $(2n{+}1)(2m{+}1)$ operation points of Sec. 2.2.2.2 to obtain the inductance map of $L_s^{dq\star}$ (again, an additional interpolation and smoothing as for the flux maps is required),

b) for all four flux linkages ψ_s^d, ψ_s^q, ψ_r^d and ψ_r^q and

c) for each directional derivative, i.e. for all four currents i_s^d, i_s^q, i_r^d and i_r^q.

Finally, the symmetry properties of the differential inductances of the stator $\boldsymbol{L}_s^{dq}$, the rotor $\boldsymbol{L}_r^{dq}$ and the coupling $\boldsymbol{L}_m^{dq}$ as explained in (2.22) and (2.24) must be considered. This can easily be done by using the average values of the two corresponding elements. E.g. the dq-element $L_s^{dq\star}$ and qd-element $L_s^{qd\star}$ must be equal. Accordingly, both elements receive the value $\frac{L_s^{dq\star}+L_s^{qd\star}}{2}$ of the measured differential inductances.
Fig. 2.12 shows the (steady-state) inductance maps of the differential inductances of the stator $\boldsymbol{L}_s^{dq}$, the rotor $\boldsymbol{L}_r^{dq}$ and the coupling $\boldsymbol{L}_m^{dq}$. They feature the following essential properties:

- the shapes of the three dd-elements L_s^{dd}, L_r^{dd} and L_m^{dd} are very similar. The same pertains for the qq- and dq-elements as well as for the two qd-elements L_s^{qd} and L_r^{qd}. The shape of the qd-element L_m^{qd} of the coupling differs from the shapes of L_s^{qd} and L_r^{qd}.

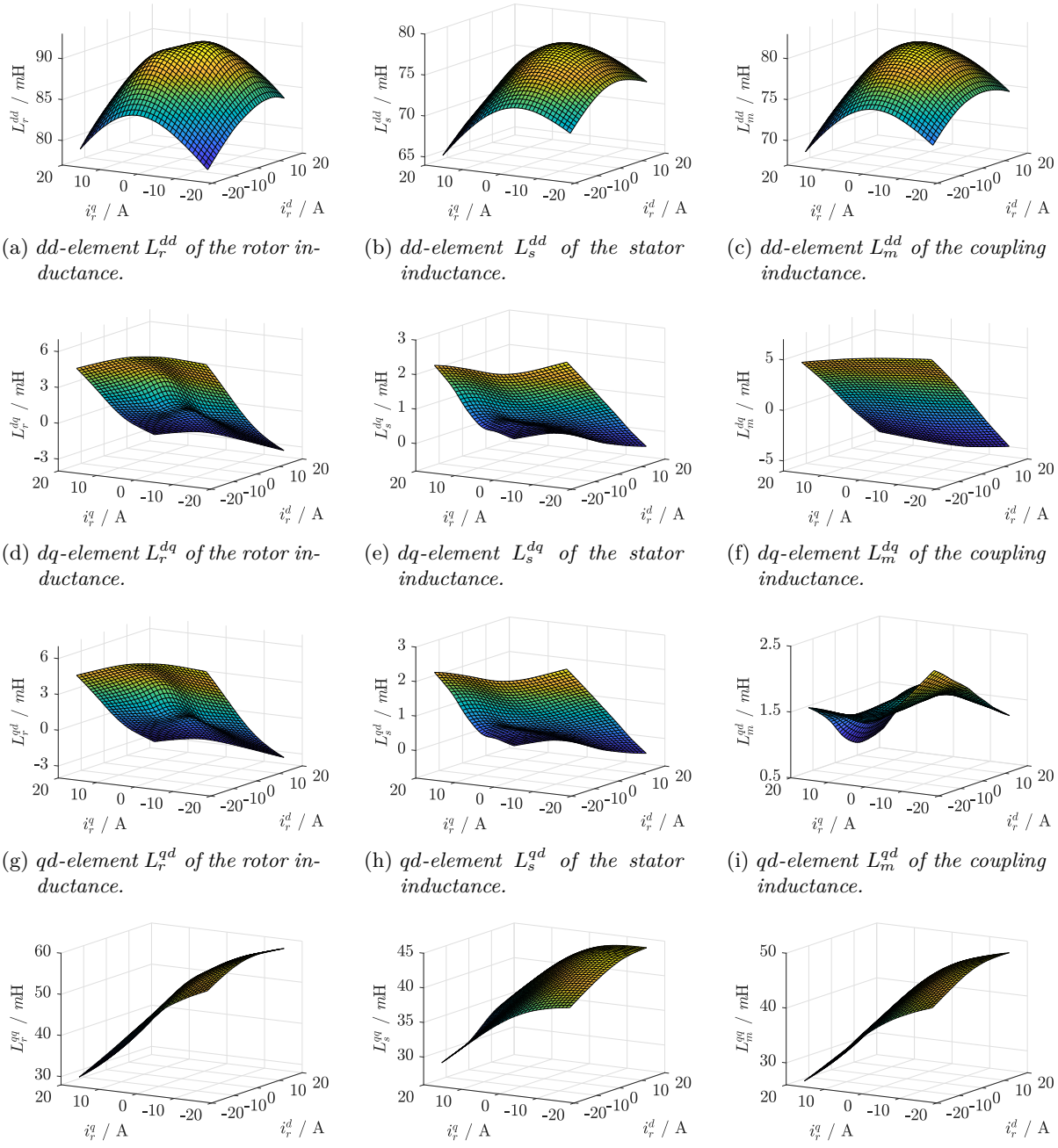

(a) *dd-element* L_r^{dd} *of the rotor inductance.*

(b) *dd-element* L_s^{dd} *of the stator inductance.*

(c) *dd-element* L_m^{dd} *of the coupling inductance.*

(d) *dq-element* L_r^{dq} *of the rotor inductance.*

(e) *dq-element* L_s^{dq} *of the stator inductance.*

(f) *dq-element* L_m^{dq} *of the coupling inductance.*

(g) *qd-element* L_r^{qd} *of the rotor inductance.*

(h) *qd-element* L_s^{qd} *of the stator inductance.*

(i) *qd-element* L_m^{qd} *of the coupling inductance.*

(j) *qq-element* L_r^{qq} *of the rotor inductance.*

(k) *qq-element* L_s^{qq} *of the stator inductance.*

(l) *qq-element* L_m^{qq} *of the coupling inductance.*

Figure 2.12: *Differential inductances of the rotor* $\boldsymbol{L}_r^{dq}$*, the stator* $\boldsymbol{L}_s^{dq}$ *and the coupling* $\boldsymbol{L}_m^{dq}$ *over the rotor current* $\boldsymbol{i}_r^{dq}$ *(steady-state case***).*

- the *dd*-elements L_s^{dd}, L_r^{dd} and L_m^{dd} are greater (partly by > 2) than their corresponding *qq*-elements L_s^{qq}, L_r^{qq} and L_m^{qq}.
- the *dq*- and *qd*-elements of $\boldsymbol{L}_s^{dq}$, $\boldsymbol{L}_r^{dq}$ and $\boldsymbol{L}_m^{dq}$ are small compared to the *dd*- and *qq*-elements but they are not zero (except for some particular operation points).
- all elements of $\boldsymbol{L}_s^{dq}$, $\boldsymbol{L}_r^{dq}$ and $\boldsymbol{L}_m^{dq}$ vary strongly depending on the operation point, e.g. the *qq*-element L_r^{qq} of the rotor inductance $\boldsymbol{L}_r^{dq}$ ranges from 30 mH up to 60 mH which expresses a variation of 100 %.

By integrating (i) the inductance maps of the differential inductances of the stator $\boldsymbol{L}_s^{dq}$, the rotor $\boldsymbol{L}_r^{dq}$ and the coupling $\boldsymbol{L}_m^{dq}$ and (ii) the flux maps of the flux linkages of the stator $\boldsymbol{\psi}_s^{dq}$ and the rotor $\boldsymbol{\psi}_r^{dq}$ (see Sec. 2.2.2.2) into the model (2.26)–(2.27), the nonlinear simulation model of the DFIM is ready-to-use. It is given by

$$\frac{\mathrm{d}}{\mathrm{d}t}\begin{pmatrix}\boldsymbol{i}_s^{dq}(t)\\ \boldsymbol{i}_r^{dq}(t)\end{pmatrix}=\begin{bmatrix}\boldsymbol{L}_s^{dq\star} & (\boldsymbol{L}_m^{dq\star})^\top\\ \boldsymbol{L}_m^{dq\star} & \boldsymbol{L}_r^{dq\star}\end{bmatrix}^{-1}\left(-\begin{bmatrix}R_s\boldsymbol{I}_2 & \boldsymbol{O}_{2\times2}\\ \boldsymbol{O}_{2\times2} & R_r\boldsymbol{I}_2\end{bmatrix}\begin{pmatrix}\boldsymbol{i}_s^{dq}(t)\\ \boldsymbol{i}_r^{dq}(t)\end{pmatrix}-\begin{pmatrix}\boldsymbol{u}_s^{dq}(t)\\ \boldsymbol{u}_r^{dq}(t)\end{pmatrix}+\begin{pmatrix}\omega_k(t)\boldsymbol{J}\boldsymbol{\psi}_s^{dq\star}\\ (\omega_k(t)-\omega_r(t))\,\boldsymbol{J}\boldsymbol{\psi}_r^{dq\star}\end{pmatrix}\right) \tag{2.36}$$

with the machine torque $m_m(\boldsymbol{i}_s^{dq}/\boldsymbol{i}_r^{dq})=\frac{2}{3k_c^2}n_m\boldsymbol{i}_s^{dq}(t)^\top\boldsymbol{J}\boldsymbol{\psi}_s^{dq\star}=-\frac{2}{3k_c^2}n_m\boldsymbol{i}_r^{dq}(t)^\top\boldsymbol{J}\boldsymbol{\psi}_r^{dq\star}$ and the initial currents $\boldsymbol{i}_{s,0}^{dq}=\boldsymbol{i}_s^{dq}(0)$ and $\boldsymbol{i}_{r,0}^{dq}=\boldsymbol{i}_r^{dq}(0)$.

Remark (R.2.8) *The nonlinear DFIM model requires the invertibility of the overall inductance matrix (see* (2.36)*). Thus, it is to check whether the overall inductance matrix has full rank, i.e. whether*

$$\det\begin{bmatrix}\boldsymbol{L}_s^{dq\star} & (\boldsymbol{L}_m^{dq\star})^\top\\ \boldsymbol{L}_m^{dq\star} & \boldsymbol{L}_r^{dq\star}\end{bmatrix}\neq 0 \tag{2.37}$$

holds for all possible operation points.

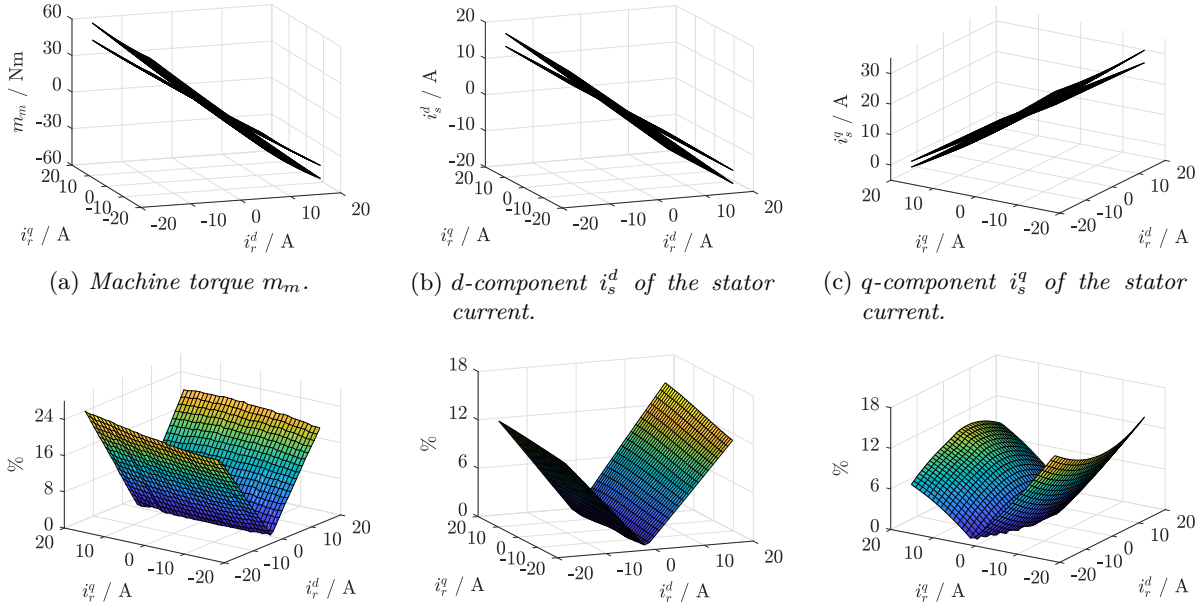

(a) *Machine torque m_m.*

(b) *d-component i_s^d of the stator current.*

(c) *q-component i_s^q of the stator current.*

(d) *Percentage error of the machine torque m_m as in* (2.39).

(e) *Percentage error of the d-component i_s^d of the stator current as in* (2.39).

(f) *Percentage error of the q-component i_s^q of the stator current as in* (2.39).

Figure 2.13: *Comparison of the DFIM (measurements) and the linear model: machine torque m_m and stator current $\boldsymbol{i}_s^{dq}$ over the rotor current $\boldsymbol{i}_r^{dq}$ (steady-state case*).*

description	symbols & values with unit
parameters of the linear DFIM model	
pole pair number	$n_m = 2$
stator resistance	$R_s = 0.72\,\Omega$
rotor resistance	$R_r = 0.55\,\Omega$
stator inductance	$L_s = 73.5\,\mathrm{mH}$
rotor inductance	$L_r = 86\,\mathrm{mH}$
coupling inductance	$L_m = 60\,\mathrm{mH}$

Table 2.4: *Parameters of the linear model of the doubly-fed induction machine.*

2.2.2.5 Linear model

The nonlinear DFIM model (2.36) will be compared to the standard linear DFIM model, which can e.g. be found in [62–69] and is given by

$$\left.\begin{aligned}
\boldsymbol{u}_s^{dq}(t) &= -R_s \boldsymbol{i}_s^{dq}(t) + \tfrac{\mathrm{d}}{\mathrm{d}t}\boldsymbol{\psi}_s^{dq}(t) + \omega_k(t)\boldsymbol{J}\boldsymbol{\psi}_s^{dq}(t) \quad , \ \boldsymbol{\psi}_{s,0}^{dq} = \boldsymbol{\psi}_s^{dq}(0) \\
\boldsymbol{u}_r^{dq}(t) &= -R_r \boldsymbol{i}_r^{dq}(t) + \tfrac{\mathrm{d}}{\mathrm{d}t}\boldsymbol{\psi}_r^{dq}(t) + (\omega_k(t) - \omega_r(t))\,\boldsymbol{J}\boldsymbol{\psi}_s^{dq}(t) \quad , \ \boldsymbol{\psi}_{r,0}^{dq} = \boldsymbol{\psi}_r^{dq}(0) \\
\boldsymbol{\psi}_s^{dq}(t) &= -L_s \boldsymbol{i}_s^{dq}(t) - L_m \boldsymbol{i}_r^{dq}(t) \quad , \quad \boldsymbol{\psi}_r^{dq}(t) = -L_r \boldsymbol{i}_r^{dq}(t) - L_m \boldsymbol{i}_s^{dq}(t) \quad \text{and} \\
m_m(t) &= \tfrac{2}{3k_c^2} n_m \boldsymbol{i}_s^{dq}(t)^\top \boldsymbol{J}\boldsymbol{\psi}_s^{dq}(t) = -\tfrac{2}{3k_c^2} n_m \boldsymbol{i}_r^{dq}(t)^\top \boldsymbol{J}\boldsymbol{\psi}_r^{dq}(t) = \tfrac{2}{3k_c^2} n_m L_m \boldsymbol{i}_r^{dq}(t)^\top \boldsymbol{J}\boldsymbol{i}_s^{dq}(t)
\end{aligned}\right\} \tag{2.38}$$

with the constant inductances of the stator L_s, the rotor L_r and the coupling L_m (all in H). In the laboratory, the three inductances L_s, L_r and L_m have been determined by measurements in idle and short circuit mode (which is a standard method but obviously do not represent the real operation). The parameters of the linear model are summarized in Tab. 2.4.

Clearly, the linear model of the DFIM does neither consider the nonlinear flux linkages of stator $\boldsymbol{\psi}_s^{dq}$ and rotor $\boldsymbol{\psi}_r^{dq}$ nor the features of the differential inductances (see Sec. 2.2.2.4) at all. Its simplification, to model the stator $\boldsymbol{L}_s^{dq}$, the rotor $\boldsymbol{L}_r^{dq}$ and the coupling $\boldsymbol{L}_m^{dq}$ inductance via the constant matrices $\boldsymbol{L}_s^{dq} = L_s\boldsymbol{I}_2$, $\boldsymbol{L}_r^{dq} = L_r\boldsymbol{I}_2$ and $\boldsymbol{L}_m^{dq} = L_m\boldsymbol{I}_2$ respectively, is insufficient to represent the dynamic behavior of the DFIM as will be shown in Sec. 2.2.2.6.

Moreover, the resulting linear flux linkages of stator $\boldsymbol{\psi}_s^{dq}$ and rotor $\boldsymbol{\psi}_r^{dq}$ result in large deviations in the stationary behavior. Fig. 2.13 compares the stationary operations of the real machine (measurements) and the linear DFIM model (2.38) (simulations). The upper row of Fig. 2.13 shows (a) the machine torque $m_m^\star$, (b) the d-component $i_s^{d\star}$ of the stator current and (c) the q-component $i_s^{q\star}$ of the stator current. In the lower row of Fig. 2.13, the corresponding percentage deviations are depicted in the sub-figures (d), (e) and (f). The percental deviations are defined as:

$$\frac{|m_m^\star(\mathrm{lin}) - m_m^\star(\mathrm{mea})|}{m_{m,\mathrm{nom}}} \quad \text{and} \quad \frac{|i_s^{d\star}(\mathrm{lin}) - i_s^{d\star}(\mathrm{mea})|}{\hat{i}_{s,\mathrm{nom}}} \quad \text{and} \quad \frac{|i_s^{q\star}(\mathrm{lin}) - i_s^{q\star}(\mathrm{mea})|}{\hat{i}_{s,\mathrm{nom}}}\,, \tag{2.39}$$

where the rated torque $m_{m,\mathrm{nom}}$ and the rated stator current $\hat{i}_{s,\mathrm{nom}}$ (in A) are listed in Tab. 2.3. The machine torque $m_m^\star$ features an averaged deviation of 11.33 % and the maximal deviation is 25.61 %. Also the stator current $\boldsymbol{i}_s^{dq\star}$ of the linear model deviates partially over 15 % from the measured ones. Clearly, these deviations are inappropriate to emulate the stationary operation of the DFIM.

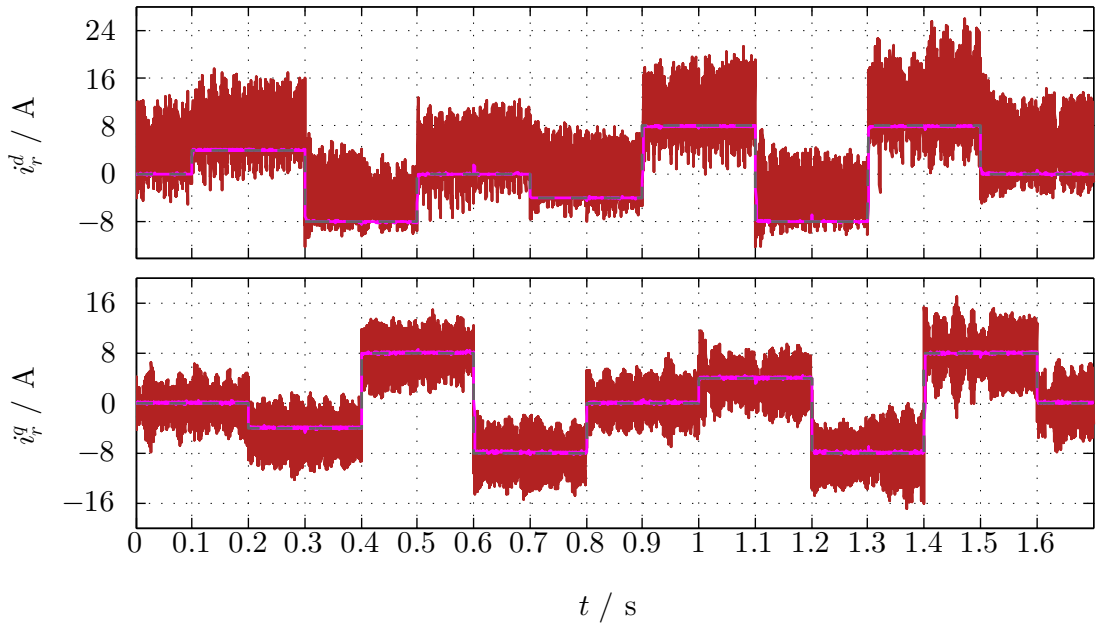

Figure 2.14: *Comparison of the real DFIM and the linear DFIM model:* — *real DFIM of the laboratory,* — *linear DFIM model as in* (2.38) *and* - - - *reference rotor current* $\boldsymbol{i}_{r,\mathrm{ref}}^{dq}$. *The controller design is based on the linear DFIM model with PI controller (magnitude optimum) and disturbance compensation.*

2.2.2.6 Comparison of linear and nonlinear model

Finally, this section compares — measurement results at the test bench with simulations using (i) the developed — nonlinear DFIM model (2.38) and the (ii) the common — linear DFIM model (2.36). The linear DFIM model has been used to design the rotor current PI controller of the DFIM on the basis of the magnitude optimum (for details see [117]) and to implement an additional disturbance compensation.

Fig. 2.14 shows the rotor current $\boldsymbol{i}_r^{dq}$ of the — measurements and the — linear DFIM model. The rotor current PI controller's task is to follow the - - - rotor current reference $\boldsymbol{i}_{r,\mathrm{ref}}^{dq}$. The simulation result of the linear DFIM model yields the following: (a) the rotor current $\boldsymbol{i}_r^{dq}$ shows a fast and accurate tracking of the rotor current reference $\boldsymbol{i}_{r,\mathrm{ref}}^{dq}$ and (b) changes in the orthogonal current component are well-compensated by the disturbance compensation. Hence, the designed rotor current PI controller features a good control performance for the linear DFIM model. In contrast, the measurements show an (almost) unstable behavior. E.g. at $t = 1.41\,\mathrm{s}$, the d-component i_r^d of the rotor current is $> 24\,\mathrm{A}$, i.e. over three-times greater than the corresponding rotor current reference $i_{r,\mathrm{ref}}^d = 8\,\mathrm{A}$. The same behavior for a rotor current reference $i_{r,\mathrm{ref}}^d = \hat{i}_{r,\mathrm{nom}}$, where $\hat{i}_{r,\mathrm{nom}}$ (in A) is the rated rotor current, would cause an immediate shutdown of the test-bench.

Consequently, the linear DFIM model cannot properly emulate the DFIM at the test bench. Even worse, to use the linear DFIM model for the rotor current PI controller design on the basis of the magnitude optimum can endanger stability of the rotor current control. For the following measurements and simulations, the parameters of the rotor current PI controller were reduced to yield a stable operation.

Fig. 2.15 depicts the rotor current $\boldsymbol{i}_r^{dq}$ and its corresponding - - - rotor current reference $\boldsymbol{i}_{r,\mathrm{ref}}^{dq}$ in the two upper subplots, the stator current $\boldsymbol{i}_s^{dq}$ in the two middle subplots and the machine torque m_m and the stator reactive power q_s in the last two subplots. Fig. 2.16 shows the same results

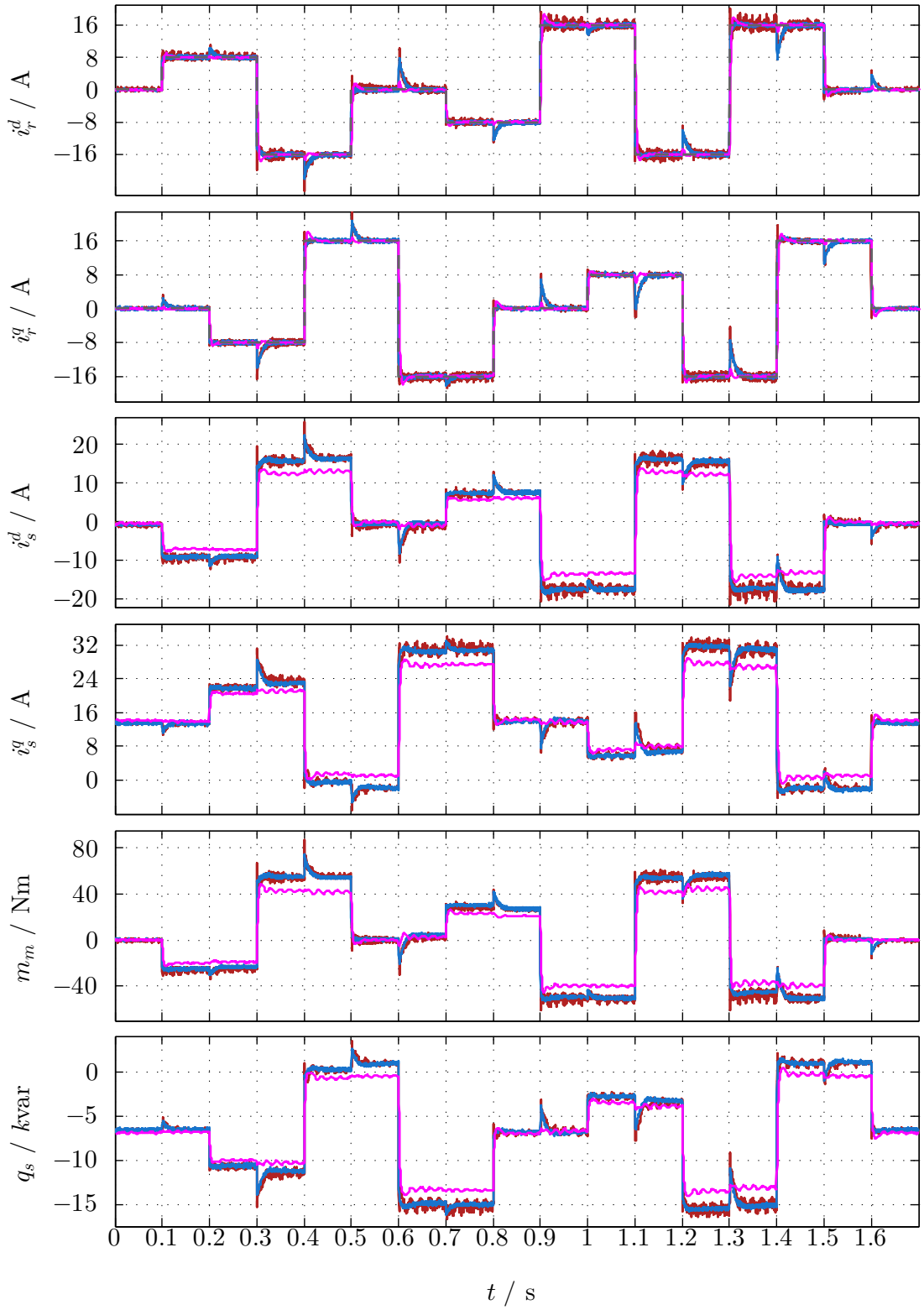

Figure 2.15: *Comparison of the real DFIM, the linear DFIM model and the nonlinear DFIM model:* — *real DFIM of the laboratory,* — *linear DFIM model as in* (2.38), — *nonlinear DFIM model as in* (2.36) *and* - - - *reference rotor current* $\boldsymbol{i}_{r,\mathrm{ref}}^{dq}$. *The controller design is based on the linear DFIM model with (conservative) PI controller and disturbance compensation.*

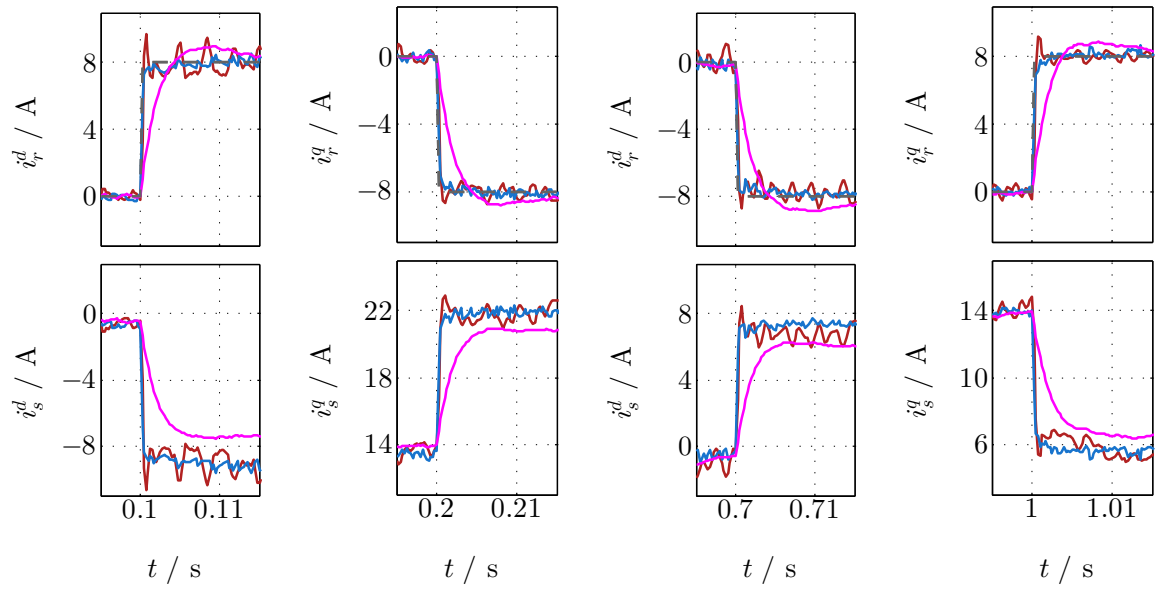

Figure 2.16: *Comparison of the real DFIM, the linear DFIM model and the nonlinear DFIM model – Zoom:* — *real DFIM of the laboratory,* — *linear DFIM model as in* (2.38), — *nonlinear DFIM model as in* (2.36) *and* - - - *reference rotor current* $\boldsymbol{i}_{r,\mathrm{ref}}^{dq}$. *The controller design is based on the linear DFIM model with (conservative) PI controller and disturbance compensation.*

for the rotor current $\boldsymbol{i}_r^{dq}$ and the stator current $\boldsymbol{i}_s^{dq}$, but presents zoomed versions at certain time steps to emphasize the dynamic behavior.
To compare the — measurements with the simulation results of the — nonlinear DFIM model and the — linear DFIM model, it is important to highlight the following attributes:

(a) the rotor current $\boldsymbol{i}_r^{dq}$ shows an accurate tracking of the rotor current reference $\boldsymbol{i}_{r,\mathrm{ref}}^{dq}$ for the measurements and for both DFIM models;

(b) for both, steady-state and dynamic behavior, the simulation results of the nonlinear DFIM model match (almost) exactly with the measurements;

(c) in contrast, steady-state and dynamic behavior of the simulation results of the linear DFIM model differ strongly from the measurement results;

(d) while again, changes in the orthogonal current component are well-compensated by the disturbance compensation for the linear DFIM model, for both the measurements and the nonlinear DFIM model, this (wrong) compensation yields a strong coupling between the orthogonal components.

Summarizing, the developed nonlinear DFIM model (2.36) based on nonlinear flux maps and differential inductances emulates the DFIM at the test-bench (almost) perfectly. In contrast, the common linear DFIM model (2.38) results in an unacceptable DFIM emulation. Moreover, the use of the linear DFIM model for the design of the rotor current controller might endanger stability of the rotor control system (see Fig. 2.14).

2.2.3 LC filter

This section presents the model of the LC filter which is connected between the rotor of the DFIM and the back-to-back converter (see Fig. 1.1 and Fig. 2.17). In Sec. 2.2.4, it will be shown

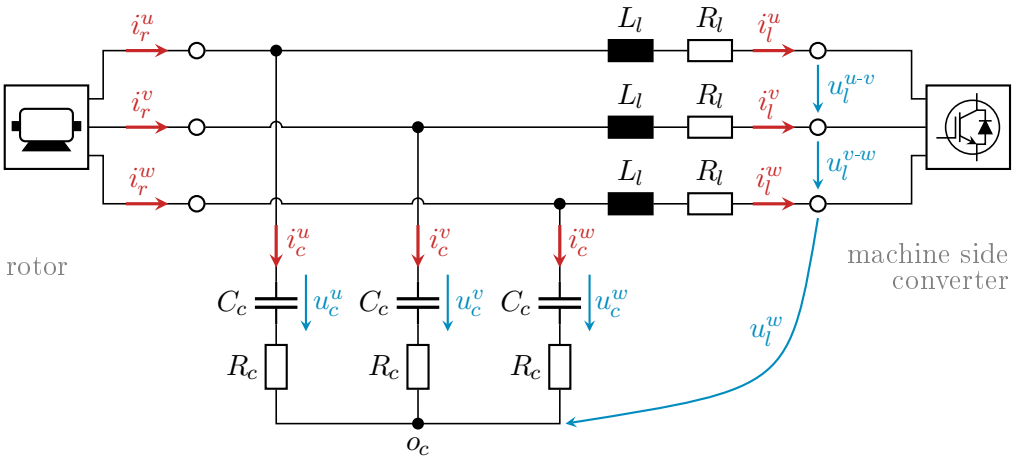

Figure 2.17: *Three-phase equivalent circuit of the LC filter.*

that the machine side converter will generate a pulsed output voltage. A direct feed of the rotor by this pulsed voltage (i) leads to high order harmonics and (ii) causes high stress on the machine. This can be avoided by using the LC filter, since it filters the pulsed output voltage of the machine side converter, such that the rotor is fed by an (almost) sinusoidal voltage. [81] Fig. 2.17 depicts the equivalent circuit of the LC filter (see e.g. [120], therein without resistances). The rotor current $\boldsymbol{i}_r^{uvw}$ flows into the LC filter and splits up into the two filter currents $\boldsymbol{i}_c^{uvw}$ and $\boldsymbol{i}_l^{uvw}$ (both in A)^3. Each phase u, v and w of the LC filter consists of the filter inductance L_l (in H) with series resistance R_l (in Ω) and the filter capacitance C_c (in F) with series resistance R_c (in Ω). At the filter capacitance C_c the voltage drop $\boldsymbol{u}_c^{uvw}$ (in V)^3 occurs. The machine side converter generates the line-to-line voltage $\boldsymbol{u}_l^{u\text{-}v\text{-}w}$ (in V)^3, where its equivalent phase voltage $\boldsymbol{u}_l^{uvw}$ (in V)^3 is defined from the corresponding clamp to the neutral point o_c. For the further procedure it is assumed that

Assumption (A.2.11) *The LC filter has got an isolated star connection o_c (see Fig. 2.17). Accordingly, the sum of the currents through the filter capacitance C_c is zero, i.e. $i_c^u(t)+i_c^v(t)+i_c^w(t)=0$.*

Then, applying Kirchhoff's law to the equivalent circuit in Fig. 2.17 yields the three-phase equations

$$\left.\begin{aligned} \boldsymbol{i}_c^{uvw}(t) &= \boldsymbol{i}_r^{uvw}(t) - \boldsymbol{i}_l^{uvw}(t) = C_c \tfrac{\mathrm{d}}{\mathrm{d}t}\boldsymbol{u}_c^{uvw}(t) \\ \boldsymbol{u}_l^{uvw}(t) &= -R_l \boldsymbol{i}_l^{uvw}(t) - L_l \tfrac{\mathrm{d}}{\mathrm{d}t}\boldsymbol{i}_l^{uvw}(t) + \boldsymbol{u}_c^{uvw}(t) + R_c\big(\boldsymbol{i}_r^{uvw}(t) - \boldsymbol{i}_l^{uvw}(t)\big) \end{aligned}\right\}. \tag{2.40}$$

By using Clarke's transformation, (2.40) is transformed to the rotor-fixed r-reference frame. The current equation of (2.40) is given by

$$\boldsymbol{i}_c^r(t) = \boldsymbol{T}_C \boldsymbol{i}_c^{uvw}(t) \overset{(2.40)}{=} \boldsymbol{T}_C\big(\boldsymbol{i}_r^{uvw}(t) - \boldsymbol{i}_l^{uvw}(t)\big) = \boldsymbol{T}_C C_c \frac{\mathrm{d}}{\mathrm{d}t}\boldsymbol{u}_c^{uvw}(t) = \boldsymbol{i}_r^r(t) - \boldsymbol{i}_l^r(t) = C_c \frac{\mathrm{d}}{\mathrm{d}t}\boldsymbol{u}_c^r(t) \tag{2.41}$$

with the filter currents $\boldsymbol{i}_c^r$ and $\boldsymbol{i}_l^r$ (both in A)^3, the rotor current $\boldsymbol{i}_r^r$ and the capacitance voltage $\boldsymbol{u}_c^r$ (in V)^3. The voltage equation results in

$$\begin{aligned} \boldsymbol{u}_l^r(t) = \boldsymbol{T}_C \boldsymbol{u}_l^{uvw}(t) &\overset{(2.40)}{=} -\boldsymbol{T}_C R_l \boldsymbol{i}_l^{uvw}(t) - \boldsymbol{T}_C L_l \frac{\mathrm{d}}{\mathrm{d}t}\boldsymbol{i}_l^{uvw}(t) + \boldsymbol{T}_C \boldsymbol{u}_c^{uvw}(t) + \boldsymbol{T}_C R_c\big(\boldsymbol{i}_r^{uvw}(t) - \boldsymbol{i}_l^{uvw}(t)\big) \\ &= -R_l \boldsymbol{i}_l^r(t) - L_l \frac{\mathrm{d}}{\mathrm{d}t}\boldsymbol{i}_l^r(t) + \boldsymbol{u}_c^r(t) + R_c\big(\boldsymbol{i}_r^r(t) - \boldsymbol{i}_l^r(t)\big) \end{aligned} \tag{2.42}$$

with filter voltage $\boldsymbol{u}_l^r$ (in V)[3]. Applying Park's transformation to (2.41) yields the current relation of the LC filter in an arbitrarily k-reference frame as follows:

$$\begin{aligned}\boldsymbol{i}_c^k(t) &= \boldsymbol{T}_P^{-1}(\phi_k-\phi_r)\boldsymbol{i}_c^r(t) \overset{(2.41)}{=} \boldsymbol{T}_P^{-1}(\phi_k-\phi_r)\big(\boldsymbol{i}_r^r(t)-\boldsymbol{i}_l^r(t)\big) = \boldsymbol{i}_r^k(t)-\boldsymbol{i}_l^k(t)\\ &= \boldsymbol{T}_P^{-1}(\phi_k-\phi_r)C_c\frac{\mathrm{d}}{\mathrm{d}t}\Big(\boldsymbol{T}_P(\phi_k-\phi_r)\boldsymbol{u}_c^k(t)\Big) = C_c\frac{\mathrm{d}}{\mathrm{d}t}\boldsymbol{u}_c^k(t)+(\omega_k(t)-\omega_r(t))\,C_c\boldsymbol{J}'\boldsymbol{u}_c^k(t)\,, \quad (2.43)\end{aligned}$$

where $\boldsymbol{i}_c^k$ and $\boldsymbol{i}_l^k$ (both in A)[3] are the filter currents, $\boldsymbol{i}_r^k$ is the rotor current and $\boldsymbol{u}_c^k$ (in V)[3] is the capacitance voltage in the k-reference frame. Accordingly, applying Park's transformation to (2.42) results in the following relation for the filter voltage $\boldsymbol{u}_l^k$ (in V)[3] in the k-reference frame:

$$\begin{aligned}\boldsymbol{u}_l^k(t) &= \boldsymbol{T}_P^{-1}(\phi_k-\phi_r)\boldsymbol{u}_l^r(t)\\ &\overset{(2.42)}{=} \boldsymbol{T}_P^{-1}(\phi_k-\phi_r)\left(-R_l\boldsymbol{i}_l^r(t)-L_l\frac{\mathrm{d}}{\mathrm{d}t}\Big(\boldsymbol{T}_P(\phi_k-\phi_r)\boldsymbol{i}_l^k(t)\Big)+\boldsymbol{u}_c^r(t)+R_c\big(\boldsymbol{i}_r^r(t)-\boldsymbol{i}_l^r(t)\big)\right)\\ &= -R_l\boldsymbol{i}_l^k(t)-L_l\frac{\mathrm{d}}{\mathrm{d}t}\boldsymbol{i}_l^k(t)-(\omega_k(t)-\omega_r(t))\,L_l\boldsymbol{J}'\boldsymbol{i}_l^k(t)+\boldsymbol{u}_c^k(t)+R_c\big(\boldsymbol{i}_r^k(t)-\boldsymbol{i}_l^k(t)\big)\,. \quad (2.44)\end{aligned}$$

Due to (A.2.11) and since the γ-component i_r^γ of the rotor current is zero (see (2.21)), i.e. $i_r^\gamma(t)=0$, for the γ-components i_c^γ and i_l^γ of the filter currents $\boldsymbol{i}_c^k$ and $\boldsymbol{i}_l^k$, the following must hold:

$$i_c^\gamma(t) = k_c\kappa_c\big(i_c^u(t)+i_c^v(t)+i_c^w(t)\big) = 0 \quad \Rightarrow \quad i_l^\gamma(t) = i_r^\gamma(t)-i_c^\gamma(t) = 0 \quad (2.45)$$

Inserting (2.45) into (2.43) and (2.44) yields

$$\frac{\mathrm{d}}{\mathrm{d}t}u_c^\gamma(t) = 0 \;\text{ and }\; u_l^\gamma(t) = u_c^\gamma(t) \quad \Leftrightarrow \quad u_l^\gamma(t) = u_c^\gamma(t) = \text{constant} \quad (2.46)$$

for the γ-components u_c^γ and u_l^γ of the capacitance voltage $\boldsymbol{u}_c^k$ and filter voltage $\boldsymbol{u}_l^k$, respectively. Consequently, all γ-components of the LC filter do not exhibit any dynamic behavior and can be neglected for the modeling of the filter dynamics. By considering (2.43) and (2.44), the filter dynamics in the dq-reference frame are given by

$$\begin{aligned}\frac{\mathrm{d}}{\mathrm{d}t}\begin{pmatrix}\boldsymbol{i}_l^{dq}(t)\\ \boldsymbol{u}_c^{dq}(t)\end{pmatrix} &= \begin{bmatrix}-\frac{R_l+R_c}{L_l}\boldsymbol{I}_2-(\omega_k(t)-\omega_r(t))\,\boldsymbol{J} & \frac{1}{L_l}\boldsymbol{I}_2\\ -\frac{1}{C_c}\boldsymbol{I}_2 & -(\omega_k(t)-\omega_r(t))\,\boldsymbol{J}\end{bmatrix}\begin{pmatrix}\boldsymbol{i}_l^{dq}(t)\\ \boldsymbol{u}_c^{dq}(t)\end{pmatrix}\\ &\quad+\begin{pmatrix}\frac{R_c}{L_l}\boldsymbol{I}_2\\ \frac{1}{C_c}\boldsymbol{I}_2\end{pmatrix}\boldsymbol{i}_r^{dq}(t)+\begin{pmatrix}-\frac{1}{L_l}\boldsymbol{I}_2\\ \boldsymbol{O}_{2\times2}\end{pmatrix}\boldsymbol{u}_l^{dq}(t) \quad (2.47)\end{aligned}$$

with the filter current $\boldsymbol{i}_l^{dq}$ (in A)[2] and its initial value $\boldsymbol{i}_{l,0}^{dq}=\boldsymbol{i}_l^{dq}(0)$, the capacitance voltage $\boldsymbol{u}_c^{dq}$ (in V)[2] and its initial value $\boldsymbol{u}_{c,0}^{dq}=\boldsymbol{u}_c^{dq}(0)$, the rotor current $\boldsymbol{i}_r^{dq}$ and the filter voltage $\boldsymbol{u}_l^{dq}$ (in V)[2].

2.2.4 Back-to-back converter

This section investigates the back-to-back converter and its related space vector modulation. The back-to-back converter is located between the LC filter of the DFIM's rotor and the LCL filter (see Fig. 1.1 and Fig. 2.18). The main goal of the back-to-back converter is to connect two three-phase systems with different (and variable) voltage amplitudes and frequencies. Here, the state-of-the-art and widely used [111] two-level back-to-back converter is employed, which consists of a common DC-link and two converters [121]. Each converter has six semi-conductors (for details see e.g. [122] or [123]), which will be driven by the output signal of the space vector modulation. For the modeling of the back-to-back converter, the following is assumed:

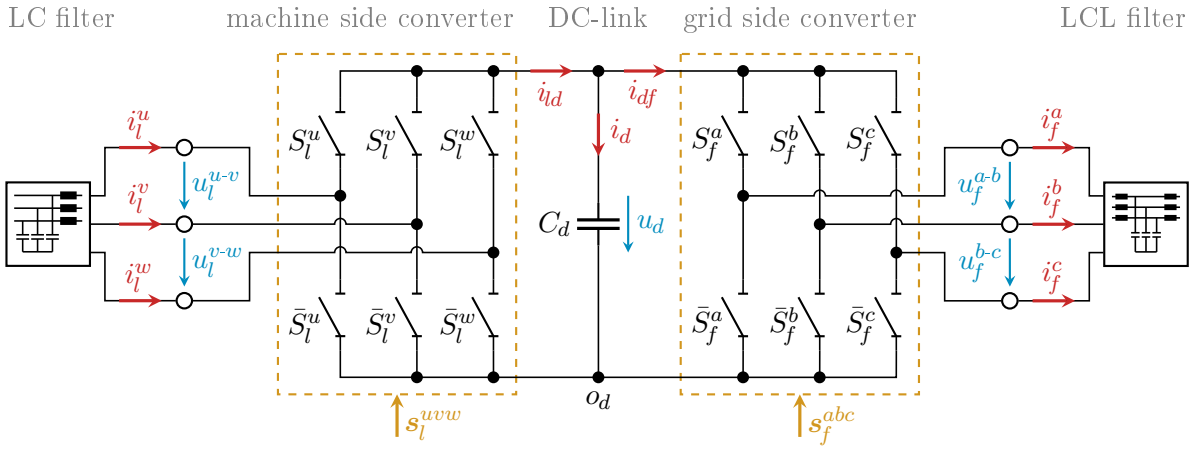

Figure 2.18: *Three-phase equivalent circuit of the back-to-back converter.*

Assumption (A.2.12) *The semi-conductors of the two converters are supposed to behave like ideal switches.*

Then, the back-to-back converter can be expressed by the equivalent circuit in Fig. 2.18. Its DC-link consists of the DC-link capacitance C_d (in F), where the DC-link voltage u_d (in V) drops and the DC-link current i_d (in A) flows in. While the current i_{ld} (in A) of the machine side converter feeds the DC-link, the current i_{df} (in A) of the grid side converter flows out of the DC-link. The neutral point of the DC-link is denoted by o_d. Due to (A.2.12), the machine side and the grid side converter together have the twelve (ideal) switches $S_l^u, \dots, \bar{S}_f^c$, two switches for each phase u, v, w, a, b, c. In each phase $j \in \{u, v, w\}$ and $i \in \{a, b, c\}$, either the upper switch is closed and the lower switch is open ($s_l^j = 1, s_f^i = 1$) or vice versa ($s_l^j = 0, s_f^i = 0$). Hence, the switching vectors $\boldsymbol{s}_l^{uvw}$ (in 1)^3 and $\boldsymbol{s}_f^{abc}$ (in 1)^3 of the machine side and grid side converter—which are generated by the corresponding space vector modulation—determine for each phase u, v, w, a, b, c, whether the upper or the lower switch is conducting. The machine side converter is linked to the LC filter of the rotor and generates the line-to-line voltage $\boldsymbol{u}_l^{u\text{-}v\text{-}w}$. Moreover, the filter current $\boldsymbol{i}_l^{uvw}$ flows into the machine side converter. Accordingly, the grid side converter is connected to the LCL filter and generates the line-to-line voltage $\boldsymbol{u}_f^{a\text{-}b\text{-}c}$ (in V)^3. The filter current $\boldsymbol{i}_f^{abc}$ (in V)^3 flows out of the grid side converter.
Applying Kirchhoff's law to the equivalent circuit in Fig. 2.18 yields the dynamics of the DC-link voltage

$$\frac{\mathrm{d}}{\mathrm{d}t} u_d(t) = \frac{1}{C_d} i_d(t) = \frac{1}{C_d} \left(i_{ld}(t) - i_{df}(t) \right) = \frac{1}{C_d} \left(\boldsymbol{s}_l^{uvw}(t)^\top \boldsymbol{i}_l^{uvw}(t) - \boldsymbol{s}_f^{abc}(t)^\top \boldsymbol{i}_f^{abc}(t) \right) \tag{2.48}$$

with initial value $u_{d,0} = u_d(0)$. By using the same relationships[20] as in (A.19) of Sec. A.1.4, the DC-link voltage dynamics of (2.48) can be transformed to the arbitrarily k-reference frame

$$\frac{\mathrm{d}}{\mathrm{d}t} u_d(t) = \frac{1}{C_d} \left(\boldsymbol{s}_l^r(t)^\top \boldsymbol{T}_\wp \boldsymbol{i}_l^r(t) - \boldsymbol{s}_f^s(t)^\top \boldsymbol{T}_\wp \boldsymbol{i}_f^s(t) \right) = \frac{1}{C_d} \left(\boldsymbol{s}_l^k(t)^\top \boldsymbol{T}_\wp \boldsymbol{i}_l^k(t) - \boldsymbol{s}_f^k(t)^\top \boldsymbol{T}_\wp \boldsymbol{i}_f^k(t) \right) \tag{2.49}$$

with the switching vectors $\boldsymbol{s}_l^r$, $\boldsymbol{s}_l^k$, $\boldsymbol{s}_f^s$ and $\boldsymbol{s}_f^k$ (all in 1)^3 of the machine side and the grid side converter, the LC filter currents $\boldsymbol{i}_l^r$ and $\boldsymbol{i}_l^k$ and the LCL filter currents $\boldsymbol{i}_f^s$ and $\boldsymbol{i}_f^k$ (both in A)^3.

[20] Replacing in (A.19): (i) the voltage $\boldsymbol{u}_x^{abc}$ by the switching vectors $\boldsymbol{s}_l^{uvw}$ and $\boldsymbol{s}_f^{abc}$ of the machine side and the grid side converter and (ii) the current $\boldsymbol{i}_x^{abc}$ by the filter currents $\boldsymbol{i}_l^{uvw}$ and $\boldsymbol{i}_f^{abc}$ yields (2.49).

Due to (2.45), the γ-component i_l^γ of the filter current $\boldsymbol{i}_l^k$ is zero, i.e. $i_l^\gamma(t)=0$. In Sec. 2.2.5, it will be shown, that also the γ-component i_f^γ of the filter current $\boldsymbol{i}_f^k$ is zero, i.e. $i_f^\gamma(t)=0$ (see (2.64)). Hence, the dynamics of the DC-link voltage u_d simplifies to

$$\frac{\mathrm{d}}{\mathrm{d}t}u_d(t)=\frac{2}{3k_c^2C_d}\left(\boldsymbol{s}_l^{dq}(t)^\top\boldsymbol{i}_l^{dq}(t)-\boldsymbol{s}_f^{dq}(t)^\top\boldsymbol{i}_f^{dq}(t)\right) \tag{2.50}$$

with the switching vectors $\boldsymbol{s}_l^{dq}$ and $\boldsymbol{s}_f^{dq}$ (both in 1)^2 of the machine side and the grid side converter and the filter currents $\boldsymbol{i}_l^{dq}$ and $\boldsymbol{i}_f^{dq}$ (both in A)^2.

With the help of the DC-link voltage u_d and the switching vectors $\boldsymbol{s}_l^{uvw}$ and $\boldsymbol{s}_f^{abc}$, the line-to-line voltages $\boldsymbol{u}_l^{u\text{-}v\text{-}w}$ and $\boldsymbol{u}_f^{a\text{-}b\text{-}c}$ can be calculated. Due to (i) Kirchhoff's law and (ii) Clarke's and Park's transformation, the following relations for $\boldsymbol{u}_l^{u\text{-}v\text{-}w}$ and $\boldsymbol{u}_f^{a\text{-}b\text{-}c}$ hold:

$$\left.\begin{aligned}\boldsymbol{u}_l^{u\text{-}v\text{-}w}(t)&=\boldsymbol{T}_{LTL}\boldsymbol{s}_l^{uvw}(t)u_d(t)=\boldsymbol{T}_{LTL}\boldsymbol{T}_C^{-1}\boldsymbol{s}_l^{r}(t)u_d(t)=\boldsymbol{T}_{LTL}\boldsymbol{T}_C^{-1}\boldsymbol{T}_P(\phi_k-\phi_r)\boldsymbol{s}_l^{k}(t)u_d(t)\\ \boldsymbol{u}_f^{a\text{-}b\text{-}c}(t)&=\boldsymbol{T}_{LTL}\boldsymbol{s}_f^{abc}(t)u_d(t)=\boldsymbol{T}_{LTL}\boldsymbol{T}_C^{-1}\boldsymbol{s}_f^{s}(t)u_d(t)=\boldsymbol{T}_{LTL}\boldsymbol{T}_C^{-1}\boldsymbol{T}_P(\phi_k)\boldsymbol{s}_f^{k}(t)u_d(t)\end{aligned}\right\}. \tag{2.51}$$

By using again Clarke's and Park's transformation, the line-to-line voltage $\boldsymbol{u}_l^{u\text{-}v\text{-}w}$ of (2.51) is transformed to the arbitrarily k-reference frame via

$$\begin{aligned}\boldsymbol{u}_l^k(t)&=\boldsymbol{T}_P^{-1}(\phi_k-\phi_r)\boldsymbol{T}_C\boldsymbol{u}_l^{uvw}(t)\qquad\overbrace{\qquad\qquad}^{=(\boldsymbol{0}_2^\top\ u_l^\gamma(t))^\top}\\ &\overset{(A.23)}{=}\boldsymbol{T}_P^{-1}(\phi_k-\phi_r)\boldsymbol{T}_C\boldsymbol{T}_{ltl}^{-1}\boldsymbol{u}_l^{u\text{-}v\text{-}w}(t)+\boldsymbol{T}_P^{-1}(\phi_k-\phi_r)\boldsymbol{T}_C\frac{1}{3k_c\kappa_c}\boldsymbol{1}_3u_l^\gamma(t)\\ &\overset{(2.51)}{=}\underbrace{\boldsymbol{T}_P^{-1}(\phi_k-\phi_r)\boldsymbol{T}_C\boldsymbol{T}_{ltl}^{-1}\boldsymbol{T}_{LTL}\boldsymbol{T}_C^{-1}\boldsymbol{T}_P(\phi_k-\phi_r)}_{=\mathrm{diag}(1,1,0)}\boldsymbol{s}_l^k(t)u_d(t)+\begin{pmatrix}\boldsymbol{0}_2\\ u_l^\gamma(t)\end{pmatrix}=\begin{pmatrix}\boldsymbol{s}_l^{dq}(t)u_d(t)\\ u_l^\gamma(t)\end{pmatrix}.\end{aligned} \tag{2.52}$$

Analogously, for the filter voltage $\boldsymbol{u}_f^k$ (in V)^3 in k-reference frame, the following holds:

$$\begin{aligned}\boldsymbol{u}_f^k(t)&=\boldsymbol{T}_P^{-1}(\phi_k)\boldsymbol{T}_C\boldsymbol{u}_f^{abc}(t)\overset{(A.23)}{=}\boldsymbol{T}_P^{-1}(\phi_k)\boldsymbol{T}_C\boldsymbol{T}_{ltl}^{-1}\boldsymbol{u}_f^{a\text{-}b\text{-}c}(t)+\boldsymbol{T}_P^{-1}(\phi_k)\boldsymbol{T}_C\frac{1}{3k_c\kappa_c}\boldsymbol{1}_3u_f^\gamma(t)\\ &\overset{(2.51)}{=}\underbrace{\boldsymbol{T}_P^{-1}(\phi_k)\boldsymbol{T}_C\boldsymbol{T}_{ltl}^{-1}\boldsymbol{T}_{LTL}\boldsymbol{T}_C^{-1}\boldsymbol{T}_P(\phi_k)}_{=\mathrm{diag}(1,1,0)}\boldsymbol{s}_f^k(t)u_d(t)+\begin{pmatrix}\boldsymbol{0}_2\\ u_f^\gamma(t)\end{pmatrix}=\begin{pmatrix}\boldsymbol{s}_f^{dq}(t)u_d(t)\\ u_f^\gamma(t)\end{pmatrix}.\end{aligned} \tag{2.53}$$

Note that in Sec. 2.2.5, the filter voltage $\boldsymbol{u}_f^{abc}$ (in V)^3 is defined in detail. Summarizing (2.52) and (2.53) yields the filter voltages $\boldsymbol{u}_l^{dq}$ and $\boldsymbol{u}_f^{dq}$ (in V)^2 in the arbitrarily dq-reference frame:

$$\boldsymbol{u}_l^{dq}(t)=\boldsymbol{s}_l^{dq}(t)u_d(t)\quad\text{and}\quad\boldsymbol{u}_f^{dq}(t)=\boldsymbol{s}_f^{dq}(t)u_d(t)\,. \tag{2.54}$$

Space vector modulation (SVM)

This subsection presents the space vector modulations for machine side and grid side converter (for details see e.g. [122]), which will generate the switching vectors $\boldsymbol{s}_l^{uvw}$ and $\boldsymbol{s}_f^{abc}$ based on the corresponding reference voltages $\breve{\boldsymbol{u}}_{l,\mathrm{ref}}^{\alpha_r\beta_r}$ and $\breve{\boldsymbol{u}}_{f,\mathrm{ref}}^{\alpha\beta}$ (both in V)^2. Since both space vector modulations work identically, first the one for the grid side converter will be explained and then, the results will be transferred to the space vector modulation for the machine side converter.

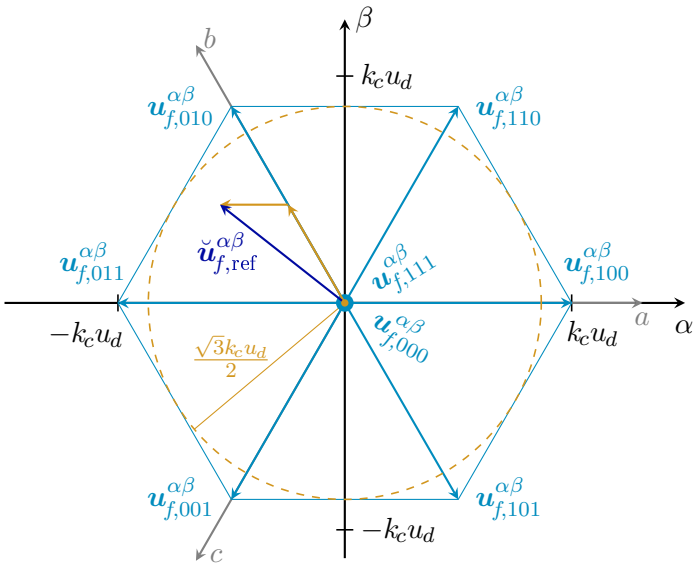

Figure 2.19: *Voltage hexagon of the grid side converter (illustration is based on Fig. 14.6 in [124]).*

In the stator-fixed $\alpha\beta$-reference frame—due to (2.54)—the filter voltage $\boldsymbol{u}_f^{\alpha\beta}$ (in V)^2 is given by

$$\boldsymbol{u}_f^{\alpha\beta}(t) = \boldsymbol{T}_p(\phi_k)\boldsymbol{u}_f^{dq}(t) \overset{(2.54)}{=} \boldsymbol{T}_p(\phi_k)\underbrace{\boldsymbol{T}_p^{-1}(\phi_k)\boldsymbol{T}_c\boldsymbol{s}_f^{abc}(t)}_{=\boldsymbol{s}_f^{dq}} u_d(t) = \boldsymbol{T}_c\boldsymbol{s}_f^{abc}(t)u_d(t)\,. \tag{2.55}$$

The switching vector $\boldsymbol{s}_f^{abc}$ can possess the following $2^3 = 8$ possible vectors: $\boldsymbol{s}_f^{abc}(t) = (x\,y\,z)^\top$ with $x, y, z \in \{0, 1\}$. Supposing a fixed DC-link voltage u_d, because of (2.55), the filter voltage $\boldsymbol{u}_f^{\alpha\beta}$ features a constant and discrete voltage $\boldsymbol{u}_{f,xyz}^{\alpha\beta}$ (in V)^3 for each of the eight switching vectors $\boldsymbol{s}_f^{abc}(t) = (x\,y\,z)^\top$. The eight voltages $\boldsymbol{u}_{f,xyz}^{\alpha\beta}$ are (a) summarized in Tab. 2.5 and (b) shown in Fig. 2.19 in the $\alpha\beta$-plane. The two zero vectors $\boldsymbol{s}_f^{abc}(t) = \boldsymbol{0}_3$ and $\boldsymbol{s}_f^{abc}(t) = \boldsymbol{1}_3$ yield the zero filter voltage $\boldsymbol{u}_f^{\alpha\beta} = \boldsymbol{0}_2$. The remaining six switching vectors $\boldsymbol{s}_f^{abc}$ span the regular voltage hexagon, where their corresponding filter voltages $\boldsymbol{u}_f^{\alpha\beta}$ feature the vector length: $\left\|\boldsymbol{u}_f^{\alpha\beta}\right\| = k_c u_d$. The voltage hexagon has got an incircle with radius $\frac{\sqrt{3}k_c u_d}{2}$.

$\boldsymbol{s}_f^{abc}$	$(0\ 0\ 0)^\top$	$(1\ 0\ 0)^\top$	$(1\ 1\ 0)^\top$	$(0\ 1\ 0)^\top$	$(0\ 1\ 1)^\top$	$(0\ 0\ 1)^\top$	$(1\ 0\ 1)^\top$	$(1\ 1\ 1)^\top$
u_f^α	0	$k_c u_d$	$\frac{k_c}{2} u_d$	$-\frac{k_c}{2} u_d$	$-k_c u_d$	$-\frac{k_c}{2} u_d$	$\frac{k_c}{2} u_d$	0
u_f^β	0	0	$\frac{\sqrt{3}k_c}{2} u_d$	$\frac{\sqrt{3}k_c}{2} u_d$	0	$-\frac{\sqrt{3}k_c}{2} u_d$	$-\frac{\sqrt{3}k_c}{2} u_d$	0
$\left\|\boldsymbol{u}_f^{\alpha\beta}\right\|$	0	$k_c u_d$	$k_c u_d$	$k_c u_d$	$k_c u_d$	$k_c u_d$	$k_c u_d$	0

Table 2.5: *Relationship between the switching vector $\boldsymbol{s}_f^{abc}$ and the filter voltage $\boldsymbol{u}_f^{\alpha\beta}$.*

Remark (R.2.9) *Since the filter voltage $\boldsymbol{u}_f^{\alpha\beta}$ can only possess the eight discrete voltages $\boldsymbol{u}_{f,xyz}^{\alpha\beta}$, a changing switching vector $\boldsymbol{s}_f^{abc}$ (over time) yields that the grid side converter feeds the LCL filter by a pulsed voltage.*

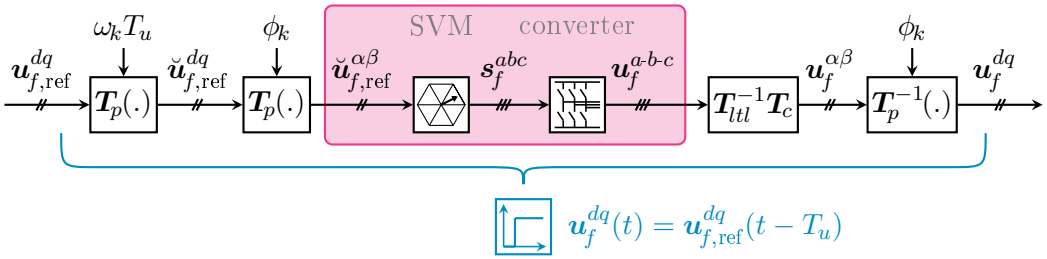

Figure 2.20: *Signal flow diagram for the generation of the reference filter voltage* $\boldsymbol{u}_{f,\mathrm{ref}}^{dq}$ *and its dead-time approximation in the arbitrarily dq-reference frame.*

Due to the discrete voltages $\boldsymbol{u}_{f,xyz}^{\alpha\beta}$, it is not possible for the grid side converter to generate the filter voltage reference $\breve{\boldsymbol{u}}_{f,\mathrm{ref}}^{\alpha\beta}$ directly. Instead, the space vector modulation is used, whose task is to create—for the switching vector $\boldsymbol{s}_f^{abc}$—a switching pattern over the time period T_{svm} (in s), such that the filter voltage reference $\breve{\boldsymbol{u}}_{f,\mathrm{ref}}^{\alpha\beta}$ (in V)^2 is generated by the grid side converter on average (see Fig. 2.19)[21].

Result (Res.2.1) *Summarizing, the space vector modulation in combination with* (2.55) *results in the pulsed filter voltage* $\boldsymbol{u}_f^{\alpha\beta}$*. Considering the certain dead-time* $T_u \propto T_{\mathrm{svm}} = \frac{1}{f_{\mathrm{svm}}} > 0$ *(in* s*), which is inversely proportional to the switching frequency* $f_{\mathrm{svm}} > 0$ *(in* Hz*) of the implemented space vector modulation (see [18]), the average value of the filter voltage* $\boldsymbol{u}_f^{\alpha\beta}$ *equals the filter voltage reference* $\breve{\boldsymbol{u}}_{f,\mathrm{ref}}^{\alpha\beta}$*.*

Remark (R.2.10) *The inside of the voltage hexagon in Fig. 2.19 marks all filter voltage references* $\breve{\boldsymbol{u}}_{f,\mathrm{ref}}^{\alpha\beta}$*, the grid side converter is able to generate on average. Obviously, to achieve a constant rotation of the filter voltage* $\boldsymbol{u}_f^{\alpha\beta}$ *in the* $\alpha\beta$*-plane, the length of the filter voltage reference* $\breve{\boldsymbol{u}}_{f,\mathrm{ref}}^{\alpha\beta}$ *must be limited to:* $\left\|\breve{\boldsymbol{u}}_{f,\mathrm{ref}}^{\alpha\beta}\right\| \leq \frac{\sqrt{3}k_c u_d}{2}$*.*

For the controller design, the switching behavior of the grid-converter and the resulting pulsed filter voltage $\boldsymbol{u}_f^{\alpha\beta}$ (see (R.2.9)) are not functional. Hence, the controller design will use the time-delayed average value of (Res.2.1) to approximate the switching behavior of the grid-converter, i.e. $\boldsymbol{u}_f^{\alpha\beta}(t) = \breve{\boldsymbol{u}}_{f,\mathrm{ref}}^{\alpha\beta}(t - T_u)$. Taking the integral representation of the transformation angel ϕ_k with the angle difference $\phi_{k,\triangle}$ (in rad) into account, i.e.

$$\phi_k(t) = \int_{t-T_u}^{t} \omega_k(\tau)\mathrm{d}\tau + \phi_k(t - T_u) =: \phi_{k,\triangle}(t) + \phi_k(t - T_u)\,, \tag{2.56}$$

the relation between the filter voltage $\boldsymbol{u}_f^{dq}$ and its reference $\breve{\boldsymbol{u}}_{f,\mathrm{ref}}^{dq}$ (in V)^2 in the arbitrarily dq-reference frame results in

$$\begin{aligned}\boldsymbol{u}_f^{dq}(t) &= \boldsymbol{T}_p^{-1}(\phi_k(t))\boldsymbol{u}_f^{\alpha\beta}(t) = \boldsymbol{T}_p^{-1}(\phi_k(t))\breve{\boldsymbol{u}}_{f,\mathrm{ref}}^{\alpha\beta}(t - T_u) = \underbrace{\boldsymbol{T}_p^{-1}(\phi_k(t))\boldsymbol{T}_p(\phi_k(t - T_u))}_{\overset{(2.56)}{=}\boldsymbol{T}_p^{-1}(\phi_{k,\triangle}(t))}\breve{\boldsymbol{u}}_{f,\mathrm{ref}}^{dq}(t - T_u) \\ &= \boldsymbol{T}_p^{-1}(\phi_{k,\triangle}(t))\breve{\boldsymbol{u}}_{f,\mathrm{ref}}^{dq}(t - T_u)\,.\end{aligned} \tag{2.57}$$

By estimating the angle difference $\phi_{k,\triangle}(t)$ via $\phi'_{k,\triangle}(t) := \omega_k(t - T_u)T_u$ (in rad), the rotation $\boldsymbol{T}_p^{-1}(\phi_{k,\triangle}(t))$ in (2.57) can be compensated by rotating the reference $\breve{\boldsymbol{u}}_{f,\mathrm{ref}}^{dq}(t\text{–}T_u)$ counter-clockwise

[21] Here, a more detailed explanation of the implementation of the space vector modulation is not given. In literature (see e.g. [122]), many different implementations are explained. The right choice depends on the goals of the space vector modulation, e.g. to achieve few harmonics or to avoid high switching losses.

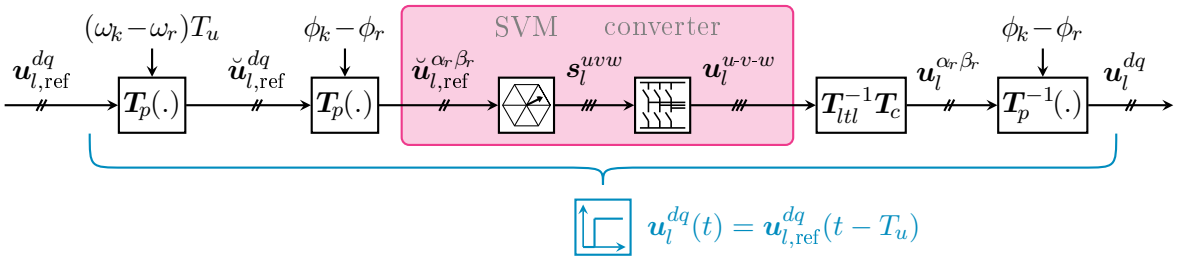

Figure 2.21: *Signal flow diagram for the generation of the reference filter voltage* $\boldsymbol{u}_{l,\mathrm{ref}}^{dq}$ *and its dead-time approximation in the arbitrarily dq-reference frame.*

via

$$\breve{\boldsymbol{u}}_{f,\mathrm{ref}}^{dq}(t-T_u)=\boldsymbol{T}_p(\phi'_{k,\triangle}(t))\boldsymbol{u}_{f,\mathrm{ref}}^{dq}(t-T_u) \tag{2.58}$$

with the rotated filter voltage reference $\boldsymbol{u}_{f,\mathrm{ref}}^{dq}$ (in V)^2. If the rotational speed ω_k is constant during the time interval $t\in[t-T_u,t]$, i.e. $\phi_{k,\triangle}(t)=\phi'_{k,\triangle}(t)$, applying (2.58) to (2.57) yields

$$\boldsymbol{u}_f^{dq}(t)=\boldsymbol{u}_{f,\mathrm{ref}}^{dq}(t-T_u)\,. \tag{2.59}$$

Fig. 2.20 depicts the block diagram of the grid side converter, which summarizes—besides the relevant transformations between different reference frames—the behaviors— of the space vector modulation and the grid side converter.

Remark (R.2.11) *The compensation of the rotation* $\boldsymbol{T}_p^{-1}(\phi_{k,\triangle}(t))$ *in* (2.57) *by* (2.58) *is a well-known method and can be found e.g. in [18]. In [46], this compensation is also presented for the complex vector theory.*

The structure of the grid side converter can be adapted one-to-one for the machine side converter. Fig. 2.21 shows the properties of the machine side converter in combination with the space vector modulation, which result in the generation of the pulsed filter voltage $\boldsymbol{u}_l^{\alpha_r\beta_r}$ (in V)^2. Considering the dead-time T_u, the average value of the filter voltage $\boldsymbol{u}_l^{\alpha_r\beta_r}$ equals the filter voltage reference $\breve{\boldsymbol{u}}_{l,\mathrm{ref}}^{\alpha_r\beta_r}$. The time-delay $\boldsymbol{u}_l^{\alpha_r\beta_r}(t)=\breve{\boldsymbol{u}}_{l,\mathrm{ref}}^{\alpha_r\beta_r}(t-T_u)$ between the filter voltage $\boldsymbol{u}_l^{\alpha_r\beta_r}$ and its reference $\breve{\boldsymbol{u}}_{l,\mathrm{ref}}^{\alpha_r\beta_r}$ in the $\alpha_r\beta_r$-reference frame results in an additional rotation between the filter voltage $\boldsymbol{u}_l^{dq}$ and its reference $\breve{\boldsymbol{u}}_{l,\mathrm{ref}}^{dq}$ (in V)^2 in the arbitrarily dq-reference frame, i.e. $\boldsymbol{u}_l^{dq}(t)=\boldsymbol{T}_p^{-1}(\phi_{kr,\triangle}(t))\breve{\boldsymbol{u}}_{l,\mathrm{ref}}^{dq}(t-T_u)$ with the angle difference $\phi_{kr,\triangle}$ (in rad). If the rotational speed $\omega_k(t)-\omega_r(t)$ is constant during the time interval $t\in[t-T_u,t]$, the counter-clockwise rotation $\breve{\boldsymbol{u}}_{l,\mathrm{ref}}^{dq}(t-T_u)=\boldsymbol{T}_p(\phi'_{kr,\triangle}(t))\boldsymbol{u}_{l,\mathrm{ref}}^{dq}(t-T_u)$ with estimated angle difference $\phi'_{kr,\triangle}(t):=(\omega_k(t-T_u)-\omega_r(t-T_u))T_u$ (in rad) yields

$$\boldsymbol{u}_l^{dq}(t)=\boldsymbol{u}_{l,\mathrm{ref}}^{dq}(t-T_u) \tag{2.60}$$

with the rotated filter voltage $\boldsymbol{u}_l^{dq}$ and its reference $\boldsymbol{u}_{l,\mathrm{ref}}^{dq}$ (in V)^2.

Remark (R.2.12) *For the controller design, grid-voltage orientation will be used for the arbitrarily dq-reference frame. Accordingly, the d-axis is aligned with the grid voltage* $\boldsymbol{u}_g^{dq}$ *and, because of (R.2.5), the transformation rotational speed* ω_k *equals the constant grid rotational speed* ω_g*, i.e.* $\omega_k=\omega_g=2\pi f_g$ *pertains. Moreover, the high inertias* θ_m *and* θ_b *of the DFIM and the gear box yield an (almost) constant electrical machine speed* ω_r *during the time interval* $t\in[t-T_u,t]$*. Thus, the approximations* (2.59) *and* (2.60) *are reasonable.*

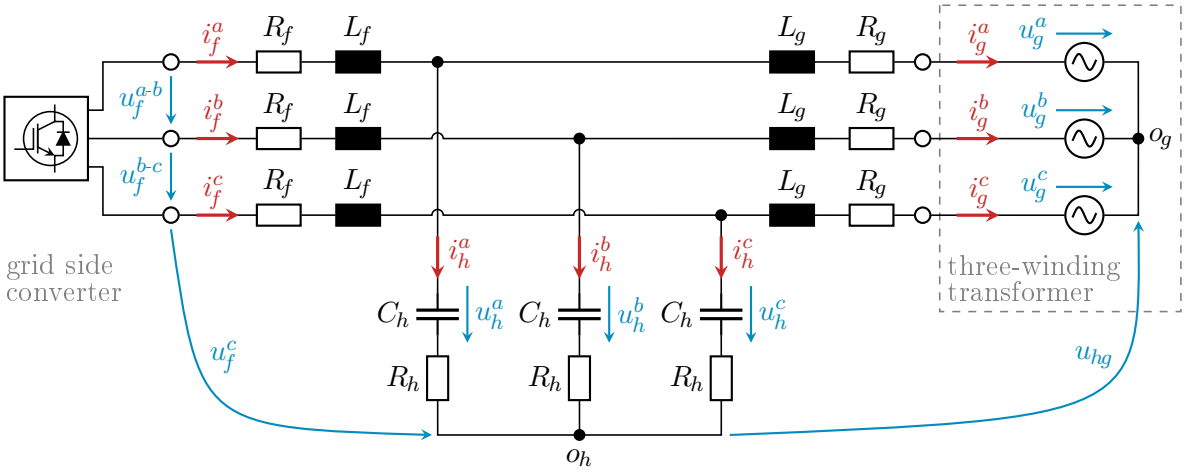

Figure 2.22: *Three-phase equivalent circuit of the LCL filter.*

2.2.5 LCL filter

This section presents the model of the LCL filter which connects the back-to-back converter to the three-winding transformer (see Fig. 1.1 and Fig. 2.22). Due to the switching behavior of the grid side converter (see Sec. 2.2.4), the LCL filter is fed by a pulsed voltage. Applying this pulsed voltage directly to the three-winding transformer causes huge harmonics in the grid current. This violates the ability to meet grid code requirements which become more and more important for a stable grid operation [18]. Consequently, a filter to damp these harmonics is inevitable. Compared to the conventional L-filter, the high-performance LCL filter features several advantages:

- the LCL filter is cost-efficient and exhibits a compact size, since smaller inductances are sufficient to achieve the same damping behavior [48],[121];
- an active damping of the resonance frequency of the LCL filter by an (intelligent) control allows for an LCL filter design without additional lossy components. This guarantees a highly efficient filtering [18];
- the LCL filter yields a better damping of the switching harmonics above the resonance frequency of the LCL filter [46].

Besides these advantages, the LCL filter is fraught with a severe drawback: its resonance frequency makes damping essential to assure a stable operation. This damping can be achieved (i) *passively* by using additional lossy components—e.g. a damping resistor—or (ii) *actively* by intelligent current control methods. [125]
Fig. 2.22 depicts the equivalent circuit of the LCL filter. Each phase a, b and c of the LCL filter consists of the filter inductances L_f and L_g (both in H) with series resistances R_f and R_g (both in Ω) respectively and the filter capacitance C_h (in F) with the voltage drop $\boldsymbol{u}_h^{abc}$ (in V)[3] and series resistance R_h (in Ω).

Remark (R.2.13) *Here, due to the active damping of the LCL filter's resonance frequency (see Sec. 3.2.2), the resistance R_h functions only as parasitic resistance of the filter capacitance C_h. Nevertheless, this model also considers a passively damped LCL filter with an additional damping resistor. Therefor, the resistance R_h represents both the parasitic resistance of the filter capacitance C_h and a possible damping resistor.*

The filter current $\boldsymbol{i}_f^{abc}$—coming from the grid side converter—splits up into the filter current $\boldsymbol{i}_h^{abc}$ (in A)^3, which flows through the filter capacitance C_h, and the grid current $\boldsymbol{i}_g^{abc}$ (in A)^3, which flows into the three-winding transformer with grid voltage $\boldsymbol{u}_g^{abc}$. The LCL filter is fed by the line-to-line voltage $\boldsymbol{u}_f^{a\text{-}b\text{-}c}$, where its equivalent phase voltage $\boldsymbol{u}_f^{abc}$ is defined from the corresponding clamp to the neutral point o_h. In the following, it is assumed that

Assumption (A.2.13) *The LCL filter has got an isolated star connection o_h (see Fig. 2.22). Accordingly, the sum of the currents through the filter capacitance C_h is zero, i.e. $i_h^a(t)+i_h^b(t)+i_h^c(t)=0$.*

Between the two isolated star connections o_h and o_g of LCL filter and three-winding transformer, the voltage u_{hg} (in V) occurs. Then, applying Kirchhoff's law to the equivalent circuit in Fig. 2.22 yields the LCL filter's three-phase model

$$\left.\begin{aligned}
\boldsymbol{i}_h^{abc}(t) &= \boldsymbol{i}_f^{abc}(t) - \boldsymbol{i}_g^{abc}(t) = C_h \tfrac{\mathrm{d}}{\mathrm{d}t}\boldsymbol{u}_h^{abc}(t) \\
\boldsymbol{u}_f^{abc}(t) &= R_f \boldsymbol{i}_f^{abc}(t) + L_l \tfrac{\mathrm{d}}{\mathrm{d}t}\boldsymbol{i}_f^{abc}(t) + \boldsymbol{u}_h^{abc}(t) + R_h\big(\boldsymbol{i}_f^{abc}(t) - \boldsymbol{i}_g^{abc}(t)\big) \\
\boldsymbol{u}_g^{abc}(t) &= -R_g \boldsymbol{i}_g^{abc}(t) - L_g \tfrac{\mathrm{d}}{\mathrm{d}t}\boldsymbol{i}_g^{abc}(t) + \boldsymbol{u}_h^{abc}(t) + R_h\big(\boldsymbol{i}_f^{abc}(t) - \boldsymbol{i}_g^{abc}(t)\big) + \mathbf{1}_3 u_{hg}(t)
\end{aligned}\right\}. \tag{2.61}$$

The use of Clarke's transformation converts (2.40) to the stator-fixed s-reference frame, i.e.

$$\left.\begin{aligned}
\boldsymbol{i}_h^s(t) &= \boldsymbol{T}_C \boldsymbol{i}_h^{abc}(t) = \boldsymbol{T}_C\big(\boldsymbol{i}_f^{abc}(t) - \boldsymbol{i}_g^{abc}(t)\big) = \boldsymbol{T}_C C_h \tfrac{\mathrm{d}}{\mathrm{d}t}\boldsymbol{u}_h^{abc}(t) = \boldsymbol{i}_f^s(t) - \boldsymbol{i}_g^s(t) = C_h \tfrac{\mathrm{d}}{\mathrm{d}t}\boldsymbol{u}_h^s(t) \\
\boldsymbol{u}_f^s(t) &= \boldsymbol{T}_C \boldsymbol{u}_f^{abc}(t) = \boldsymbol{T}_C\Big(R_f \boldsymbol{i}_f^{abc}(t) + L_f \tfrac{\mathrm{d}}{\mathrm{d}t}\boldsymbol{i}_f^{abc}(t) + \boldsymbol{u}_h^{abc}(t) + R_h\big(\boldsymbol{i}_f^{abc}(t) - \boldsymbol{i}_g^{abc}(t)\big)\Big) \\
&= R_f \boldsymbol{i}_f^s(t) + L_f \tfrac{\mathrm{d}}{\mathrm{d}t}\boldsymbol{i}_f^s(t) + \boldsymbol{u}_h^s(t) + R_h\big(\boldsymbol{i}_f^s(t) - \boldsymbol{i}_g^s(t)\big) \\
\boldsymbol{u}_g^s(t) &= \boldsymbol{T}_C \boldsymbol{u}_g^{abc}(t) = \boldsymbol{T}_C\Big(-R_g \boldsymbol{i}_g^{abc}(t) - L_g \tfrac{\mathrm{d}}{\mathrm{d}t}\boldsymbol{i}_g^{abc}(t) + \boldsymbol{u}_h^{abc}(t) + R_h\big(\boldsymbol{i}_f^{abc}(t) - \boldsymbol{i}_g^{abc}(t)\big) + \mathbf{1}_3 u_{hg}(t)\Big) \\
&= -R_g \boldsymbol{i}_g^s(t) - L_g \tfrac{\mathrm{d}}{\mathrm{d}t}\boldsymbol{i}_g^s(t) + \boldsymbol{u}_h^s(t) + R_h\big(\boldsymbol{i}_f^s(t) - \boldsymbol{i}_g^s(t)\big) + \begin{pmatrix}\mathbf{0}_2 \\ 3k_c\kappa_c u_{hg}(t)\end{pmatrix}
\end{aligned}\right\} \tag{2.62}$$

with the grid side currents $\boldsymbol{i}_f^s$, $\boldsymbol{i}_h^s$ and $\boldsymbol{i}_g^s$ (all in A)^3, the filter $\boldsymbol{u}_f^s$ and capacitance $\boldsymbol{u}_h^s$ voltage (both in V)^3 and the grid voltage $\boldsymbol{u}_g^s$. Correspondingly, applying Park's transformation to (2.62) results in the LCL filter model in the arbitrarily k-reference frame

$$\left.\begin{aligned}
\boldsymbol{i}_h^k(t) &= \boldsymbol{T}_P^{-1}(\phi_k)\boldsymbol{i}_h^s(t) = \boldsymbol{T}_P^{-1}(\phi_k)\big(\boldsymbol{i}_f^s(t) - \boldsymbol{i}_g^s(t)\big) = \boldsymbol{i}_f^k(t) - \boldsymbol{i}_g^k(t) \\
&= \boldsymbol{T}_P^{-1}(\phi_k) C_h \tfrac{\mathrm{d}}{\mathrm{d}t}\Big(\boldsymbol{T}_P(\phi_k)\boldsymbol{u}_h^k(t)\Big) = C_h \tfrac{\mathrm{d}}{\mathrm{d}t}\boldsymbol{u}_h^k(t) + \omega_k(t) C_h \boldsymbol{J}'\boldsymbol{u}_h^k(t) \\
\boldsymbol{u}_f^k(t) &= \boldsymbol{T}_P^{-1}(\phi_k)\boldsymbol{u}_f^s(t) = \boldsymbol{T}_P^{-1}(\phi_k)\Big(R_f \boldsymbol{i}_f^s(t) + L_f \tfrac{\mathrm{d}}{\mathrm{d}t}\Big(\boldsymbol{T}_P(\phi_k)\boldsymbol{i}_f^k(t)\Big) + \boldsymbol{u}_h^s(t) + R_h\big(\boldsymbol{i}_f^s(t) - \boldsymbol{i}_g^s(t)\big)\Big) \\
&= R_f \boldsymbol{i}_f^k(t) + L_f \tfrac{\mathrm{d}}{\mathrm{d}t}\boldsymbol{i}_f^k(t) + \omega_k(t) L_f \boldsymbol{J}'\boldsymbol{i}_f^k(t) + \boldsymbol{u}_h^k(t) + R_h\big(\boldsymbol{i}_f^k(t) - \boldsymbol{i}_g^k(t)\big) \\
\boldsymbol{u}_g^k(t) &= \boldsymbol{T}_P^{-1}(\phi_k)\boldsymbol{u}_g^s(t) \\
&= \boldsymbol{T}_P^{-1}(\phi_k)\left(-R_g \boldsymbol{i}_g^s(t) - L_g \tfrac{\mathrm{d}}{\mathrm{d}t}\Big(\boldsymbol{T}_P(\phi_k)\boldsymbol{i}_g^k(t)\Big) + \boldsymbol{u}_h^s(t) + R_h\big(\boldsymbol{i}_f^s(t) - \boldsymbol{i}_g^s(t)\big) + \left(\begin{pmatrix}\mathbf{0}_2 \\ 3k_c\kappa_c u_{hg}(t)\end{pmatrix}\right)\right) \\
&= -R_g \boldsymbol{i}_g^k(t) - L_g \tfrac{\mathrm{d}}{\mathrm{d}t}\boldsymbol{i}_g^k(t) - \omega_k(t) L_g \boldsymbol{J}'\boldsymbol{i}_g^k(t) + \boldsymbol{u}_h^k(t) + R_h\big(\boldsymbol{i}_f^k(t) - \boldsymbol{i}_g^k(t)\big) + \begin{pmatrix}\mathbf{0}_2 \\ 3k_c\kappa_c u_{hg}(t)\end{pmatrix}
\end{aligned}\right\} \tag{2.63}$$

with the grid side currents $\boldsymbol{i}_f^k$, $\boldsymbol{i}_h^k$ and $\boldsymbol{i}_g^k$ (all in A)^3 and the voltages $\boldsymbol{u}_f^k$, $\boldsymbol{u}_h^k$ and $\boldsymbol{u}_g^k$ (all in V)^3

of filter, capacitance and grid. Due to (A.2.13) and (2.8), the γ-components i_f^γ, i_h^γ and i_g^γ of the grid side currents $\boldsymbol{i}_f^k$, $\boldsymbol{i}_h^k$ and $\boldsymbol{i}_g^k$ are zero, since the following holds[22]:

$$\left.\begin{aligned} i_h^\gamma(t) &= k_c\kappa_c\left(i_h^a(t)+i_h^b(t)+i_h^c(t)\right)=0 \\ \text{and}\quad i_g^\gamma(t) &= k_c\kappa_c\left(i_g^a(t)+i_g^b(t)+i_g^c(t)\right)=0 \end{aligned}\right\} \quad\Leftrightarrow\quad i_f^\gamma(t)=i_h^\gamma(t)+i_g^\gamma(t)=0\,. \tag{2.64}$$

Applying (2.64) to (2.63) and considering $u_g^\gamma(t)=0$ (see (2.8)) gives the γ-components u_h^γ and u_f^γ of the capacitance voltage $\boldsymbol{u}_h^k$ and filter voltage $\boldsymbol{u}_f^k$ as follows

$$u_h^\gamma(t)=-3k_c\kappa_c u_{hg}(t)\ ,\ \frac{\mathrm{d}}{\mathrm{d}t}u_h^\gamma(t)=0 \text{ and } u_f^\gamma(t)=u_h^\gamma(t)\ \Leftrightarrow\ u_f^\gamma(t)=u_h^\gamma(t)=\text{constant}\,. \tag{2.65}$$

Consequently, all γ-components of the LCL filter do not contribute to its system dynamics. Thus, only the dq-components are considered in the model of the LCL filter dynamics. Merging (2.63), (2.64) and (2.65), the LCL filter dynamics are finally given by

$$\begin{aligned}\frac{\mathrm{d}}{\mathrm{d}t}\begin{pmatrix}\boldsymbol{i}_f^{dq}(t)\\ \boldsymbol{i}_g^{dq}(t)\\ \boldsymbol{u}_h^{dq}(t)\end{pmatrix} &= \begin{bmatrix}-\frac{R_f+R_h}{L_f}\boldsymbol{I}_2-\omega_k(t)\boldsymbol{J} & \frac{R_h}{L_f}\boldsymbol{I}_2 & -\frac{1}{L_f}\boldsymbol{I}_2\\ \frac{R_h}{L_g}\boldsymbol{I}_2 & -\frac{R_g+R_h}{L_g}\boldsymbol{I}_2-\omega_k(t)\boldsymbol{J} & \frac{1}{L_g}\boldsymbol{I}_2\\ \frac{1}{C_h}\boldsymbol{I}_2 & -\frac{1}{C_h}\boldsymbol{I}_2 & -\omega_k(t)\boldsymbol{J}\end{bmatrix}\begin{pmatrix}\boldsymbol{i}_f^{dq}(t)\\ \boldsymbol{i}_g^{dq}(t)\\ \boldsymbol{u}_h^{dq}(t)\end{pmatrix}\\ &\quad+\begin{bmatrix}\frac{1}{L_f}\boldsymbol{I}_2\\ \boldsymbol{O}_{2\times2}\\ \boldsymbol{O}_{2\times2}\end{bmatrix}\boldsymbol{u}_f^{dq}(t)+\begin{bmatrix}\boldsymbol{O}_{2\times2}\\ -\frac{1}{L_g}\boldsymbol{I}_2\\ \boldsymbol{O}_{2\times2}\end{bmatrix}\boldsymbol{u}_g^{dq}(t)\end{aligned} \tag{2.66}$$

with the filter current $\boldsymbol{i}_f^{dq}$ and its initial value $\boldsymbol{i}_{f,0}^{dq}=\boldsymbol{i}_f^{dq}(0)$, the grid current $\boldsymbol{i}_g^{dq}$ (in A)^2 and its initial value $\boldsymbol{i}_{g,0}^{dq}=\boldsymbol{i}_g^{dq}(0)$, the capacitance voltage $\boldsymbol{u}_h^{dq}$ (in V)^2 and its initial value $\boldsymbol{u}_{h,0}^{dq}=\boldsymbol{u}_h^{dq}(0)$, the filter voltage $\boldsymbol{u}_f^{dq}$ and the grid voltage $\boldsymbol{u}_g^{dq}$.

2.3 Holistic model of the wind turbine system

The previous sections of Ch. 2 presented the individual models of the mechanical components (see Sec. 2.1) and the electrical components (see Sec. 2.2) of the wind turbine system. This section will combine these models to one holistic model of the whole wind turbine system. Therefor, Sec. 2.3.1 discusses the voltage interfaces between the electrical components and calculates the voltage drops between the different neutral points. In Sec. 2.3.2, the holistic model of the wind turbine system will be presented, where the electrical three-phase systems are described in the dq-reference frame.

2.3.1 Relationships between the voltages of the electrical components

The stator of the DFIM is directly coupled to the three-winding transformer. By merging the equivalent circuit of the DFIM (see Fig. 2.5) with the one of the three-winding transformer (see Fig. 2.4), the grid voltages $\boldsymbol{u}_g^{abc}$ and $\boldsymbol{u}_g^k$ in abc- and k-reference frame are given by

$$\begin{aligned}&\boldsymbol{u}_g^{abc}(t)=\boldsymbol{u}_s^{abc}(t)+\boldsymbol{1}_3u_{sq}(t)\\ &\Rightarrow\ \boldsymbol{u}_g^k(t)=\boldsymbol{T}_P^{-1}(\phi_k)\boldsymbol{T}_C\boldsymbol{u}_g^{abc}(t)=\boldsymbol{T}_P^{-1}(\phi_k)\boldsymbol{T}_C\left(\boldsymbol{u}_s^{abc}(t)+\boldsymbol{1}_3u_{sq}(t)\right)=\boldsymbol{u}_s^k(t)+\begin{pmatrix}\boldsymbol{0}_2\\ 3k_c\kappa_cu_{sq}(t)\end{pmatrix}\,,\end{aligned} \tag{2.67}$$

[22] In (2.8) the γ-component i_g^γ of the grid current $\boldsymbol{i}_g^k$ has already been determined to zero.

where u_{sq} (in V) is the voltage between the neutral points o_s and o_q in Fig. 2.4. Since the γ-components of both the stator voltage $\boldsymbol{u}_s^k$ and grid voltage $\boldsymbol{u}_g^k$ are zero (see (2.25) and (2.8)), i.e. $u_s^\gamma(t)=u_g^\gamma(t)=0$, due to (2.67), the following holds $\boldsymbol{u}_s^{dq}(t)=\boldsymbol{u}_g^{dq}(t)$ and $u_{sq}(t)=0$.

The LC filter is connected to the rotor of the DFIM. In Fig. 2.17 and Fig. 2.5, the corresponding equivalent circuits are illustrated. Combining these equivalent circuits gives the rotor voltages $\boldsymbol{u}_r^{uvw}$ and $\boldsymbol{u}_r^k$ in uvw- and k-reference frame as follows

$$\begin{aligned}
&\boldsymbol{u}_r^{uvw}(t) = \boldsymbol{u}_c^{uvw}(t) + R_c(\boldsymbol{i}_r^{uvw}(t) - \boldsymbol{i}_l^{uvw}(t)) - \mathbf{1}_3 u_{rc}(t)\\
&\Rightarrow\ \boldsymbol{u}_r^k(t)=\boldsymbol{T}_P^{-1}(\phi_k-\phi_r)\boldsymbol{T}_C\boldsymbol{u}_r^{uvw}(t)=\boldsymbol{T}_P^{-1}(\phi_k-\phi_r)\boldsymbol{T}_C\big(\boldsymbol{u}_c^{uvw}(t)+R_c(\boldsymbol{i}_r^{uvw}(t)-\boldsymbol{i}_l^{uvw}(t))-\mathbf{1}_3 u_{rc}(t)\big)\\
&\qquad = \boldsymbol{u}_c^k(t) + R_c(\boldsymbol{i}_r^k(t) - \boldsymbol{i}_l^k(t)) - \begin{pmatrix}\mathbf{0}_2\\ 3k_c\kappa_c u_{rc}(t)\end{pmatrix}, \qquad (2.68)
\end{aligned}$$

where u_{rc} (in V) is the voltage between the neutral points o_r and o_c in Fig. 2.5 and Fig. 2.17, respectively. Due to (2.25) and (2.45), the γ-components of the rotor voltage $\boldsymbol{u}_r^k$, the rotor current $\boldsymbol{i}_r^k$ and the filter current $\boldsymbol{i}_l^k$ are zero, i.e. $u_r^\gamma(t)=0$ and $i_r^\gamma(t)=i_l^\gamma(t)=0$, such that (2.68) simplifies to

$$\boldsymbol{u}_r^{dq}(t) = \boldsymbol{u}_c^{dq}(t) + R_c(\boldsymbol{i}_r^{dq}(t) - \boldsymbol{i}_l^{dq}(t)) \quad \text{and} \quad u_{rc}(t) = \frac{1}{3k_c\kappa_c}u_c^\gamma(t) \overset{(2.46)}{=} \text{constant}\,. \qquad (2.69)$$

The machine side converter links the DC-link of the back-to-back converter to the LC filter. Merging their equivalent circuits as in Fig. 2.17 and Fig. 2.18, results in

$$\begin{aligned}
u_l^\gamma(t) &= \begin{pmatrix}0 & 0 & 1\end{pmatrix}\boldsymbol{T}_C\boldsymbol{u}_l^{uvw}(t) = \begin{pmatrix}0 & 0 & 1\end{pmatrix}\boldsymbol{T}_C\left(\boldsymbol{s}_l^{uvw}(t)u_d(t) - \mathbf{1}_3 u_{cd}(t)\right)\\
&= k_c\kappa_c\big(s_l^u(t)+s_l^v(t)+s_l^w(t)\big)u_d(t) - 3k_c\kappa_c u_{cd}(t) = k_c\kappa_c\mathbf{1}_3^\top\boldsymbol{s}_l^{uvw}(t)u_d(t) - 3k_c\kappa_c u_{cd}(t) \qquad (2.70)
\end{aligned}$$

with u_{cd} (in V) being the voltage between the neutral points o_c and o_d in Fig. 2.17 and Fig. 2.18. By recalling (2.46), in which the γ-components u_l^γ and u_c^γ of the filter voltage $\boldsymbol{u}_l^k$ and the capacitance voltage $\boldsymbol{u}_c^k$ are given by $u_l^\gamma(t)=u_c^\gamma(t)=\text{constant}$, it follows:

$$u_{cd}(t) \overset{(2.70)}{=} \frac{1}{3}\mathbf{1}_3^\top\boldsymbol{s}_l^{uvw}(t)u_d(t) - \frac{u_c^\gamma}{3k_c\kappa_c} \text{ and } u_{rd}(t)=u_{rc}(t)+u_{cd}(t) \overset{(2.69)}{=} \overbrace{\frac{1}{3}\mathbf{1}_3^\top\boldsymbol{s}_l^{uvw}(t)}^{\in\left\{0,\frac{1}{3},\frac{2}{3},1\right\}}u_d(t)\,. \qquad (2.71)$$

Hence, the voltage u_{rd} (in V) between the neutral points o_r and o_d can exhibit the four values ϵu_d with $\epsilon\in\{0,\frac{1}{3},\frac{2}{3},1\}$.

The grid side converter connects the LCL filter to the DC-link of the back-to-back converter. Combining their equivalent circuits of Fig. 2.22 and Fig. 2.18 yields the γ-component u_f^γ of the filter voltage $\boldsymbol{u}_f^k$ as

$$\begin{aligned}
u_f^\gamma(t) &= \begin{pmatrix}0 & 0 & 1\end{pmatrix}\boldsymbol{T}_C\boldsymbol{u}_f^{abc}(t) = \begin{pmatrix}0 & 0 & 1\end{pmatrix}\boldsymbol{T}_C\left(\boldsymbol{s}_f^{abc}(t)u_d(t) + \mathbf{1}_3 u_{dh}(t)\right)\\
&= k_c\kappa_c\big(s_f^a(t)+s_f^b(t)+s_f^c(t)\big)u_d(t) + 3k_c\kappa_c u_{dh}(t) = k_c\kappa_c\mathbf{1}_3^\top\boldsymbol{s}_f^{abc}(t)u_d(t) + 3k_c\kappa_c u_{dh}(t)\,, \qquad (2.72)
\end{aligned}$$

where u_{dh} (in V) is the voltage between the neutral points o_d and o_h in Fig. 2.18 and Fig. 2.22. In (2.65), the relation $u_{hg}(t)=-\frac{1}{3k_c\kappa_c}u_h^\gamma(t)$ between the voltage u_{hg} and the γ-component u_h^γ of the capacitance voltage $\boldsymbol{u}_h^k$ was derived. Moreover, (2.65) shows that $u_f^\gamma(t)=u_h^\gamma(t)=\text{constant}$

pertains. Thus, by taking (2.72) into account, the following holds

$$u_{dh}(t) = -\frac{1}{3}\mathbf{1}_3^\top \boldsymbol{s}_f^{abc}(t) u_d(t) + \frac{u_h^\gamma}{3k_c\kappa_c} \quad \text{and} \quad u_{dg}(t) = u_{dh}(t) + u_{hg}(t) = -\overbrace{\frac{1}{3}\mathbf{1}_3^\top \boldsymbol{s}_l^{uvw}(t)}^{\in\left\{0,\frac{1}{3},\frac{2}{3},1\right\}} u_d(t)\,. \quad (2.73)$$

In accordance to u_{rd}, the voltage u_{dg} (in V) between the neutral points o_d and o_g can exhibit the four values $-\epsilon u_d$ with $\epsilon \in \{0, \frac{1}{3}, \frac{2}{3}, 1\}$. Adding the two voltages u_{rd} and u_{dg}, because of (2.71) and (2.73), the voltage u_{rg} (in V) between the neutral points o_r and o_g is given by

$$u_{rg}(t) = u_{rd}(t) + u_{dg}(t) = \frac{1}{3}\mathbf{1}_3^\top \left(\boldsymbol{s}_l^{uvw}(t) - \boldsymbol{s}_f^{abc}(t)\right) u_d(t) = \nu(t) u_d(t)\ ,\ \nu(t) \in \left\{0, \pm\tfrac{1}{3}, \pm\tfrac{2}{3}, \pm 1\right\}\ . \quad (2.74)$$

2.3.2 Dynamics of the complete wind turbine system

This section merges the dynamics of mechanical and electrical components to obtain one holistic model of the whole wind turbine system. In particular, these dynamics consider

(i) the extraction of the wind power by the turbine in (2.4),

(ii) the dynamics in (2.5) of the two-mass system, the gear box and the shafts of the turbine and the machine,

(iii) the nonlinear DFIM model in (2.26),

(iv) the relation (2.27) of the nonlinear machine torque,

(v) the dynamics of the LC filter in (2.47),

(vi) the voltage model (2.54) of the machine side and the grid side converter,

(vii) the DC-link dynamics in (2.50),

(viii) the dynamics of the LCL filter in (2.66),

(ix) the correlation (2.67) between the stator voltage and the grid voltage and

(x) the voltage equation (2.69) for the rotor voltage.

Based on these equations, the state vector $\boldsymbol{x}_{\text{wts}}$, the input vector $\boldsymbol{u}_{\text{wts}}$ and the disturbance vector $\boldsymbol{d}_{\text{wts}}$ can be defined as follows[23]

$$\left.\begin{aligned} \boldsymbol{x}_{\text{wts}} &:= \left(\omega_t, \phi_z, \omega_m, \boldsymbol{i}_s^{dq}, \boldsymbol{i}_r^{dq}, \boldsymbol{i}_l^{dq}, \boldsymbol{u}_c^{dq}, u_d, \boldsymbol{i}_f^{dq}, \boldsymbol{i}_g^{dq}, \boldsymbol{u}_h^{dq}\right)^\top \in \mathbb{R}^{18}\,, \\ \boldsymbol{u}_{\text{wts}} &:= \left(\beta_t, \boldsymbol{s}_l^{dq}, \boldsymbol{s}_f^{dq}\right)^\top \in \mathbb{R}^5 \quad \text{and} \quad \boldsymbol{d}_{\text{wts}}(t) := \left(v_w(t), \boldsymbol{u}_g^{dq}(t)\right)^\top \in \mathbb{R}^3 \end{aligned}\right\}\,. \quad (2.75)$$

Then, the dynamics of the holistic model of the wind turbine system can be written as

$$\frac{\mathrm{d}}{\mathrm{d}t}\boldsymbol{x}_{\text{wts}}(t) = \boldsymbol{f}_{\text{wts}}(\boldsymbol{x}_{\text{wts}}, \boldsymbol{u}_{\text{wts}}, \boldsymbol{d}_{\text{wts}}(t))\ , \quad \boldsymbol{x}_{\text{wts}}(0) =: \boldsymbol{x}_{\text{wts},0} \quad (2.76)$$

[23] In (2.75), the denotation $\mathbb{R}^\iota$ with $\iota \in \{3, 5, 18\}$ does not contain any information about the units of $\boldsymbol{x}_{\text{wts}}$, $\boldsymbol{u}_{\text{wts}}$ and $\boldsymbol{d}_{\text{wts}}$ but only highlights their dimension. The units were introduced in the previous sections.

with the initial value $\boldsymbol{x}_{\mathrm{wts},0}$ and the nonlinear function $\boldsymbol{f}_{\mathrm{wts}}$. Considering all components as described above in (i)–(x), the nonlinear function $\boldsymbol{f}_{\mathrm{wts}}$ is given by

$$
\begin{aligned}
&\boldsymbol{f}_{\mathrm{wts}}(\boldsymbol{x}_{\mathrm{wts}}, \boldsymbol{u}_{\mathrm{wts}}, \boldsymbol{d}_{\mathrm{wts}}(t)) = \\
&\begin{pmatrix}
-\frac{d_z}{\theta_t}\omega_t - \frac{c_z}{\theta_t}\phi_z + \frac{d_z}{g_b\theta_t}\omega_m + \frac{\rho_w \pi r_t^2 c_t(t,\beta_t,\omega_t)}{2\theta_t\omega_t} v_w(t)^3 - \frac{m_{t,\mathrm{fr}}(\omega_t)}{\theta_t} \\
\omega_t - \frac{1}{g_b}\omega_m \\
\frac{d_z}{g_b(\theta_b+\theta_m)}\omega_t + \frac{c_z}{g_b(\theta_b+\theta_m)}\phi_z - \frac{d_z}{g_b^2(\theta_b+\theta_m)}\omega_m + \frac{2n_m}{3k_c^2(\theta_b+\theta_m)}\left(\boldsymbol{i}_r^{dq}\right)^\top \boldsymbol{J}\boldsymbol{\psi}_r^{dq}(\boldsymbol{i}_s^{dq},\boldsymbol{i}_r^{dq}) - \frac{m_{m,\mathrm{fr}}(\omega_m)}{\theta_b+\theta_m} \\
\begin{bmatrix} \boldsymbol{L}_s^{dq}(\boldsymbol{i}_s^{dq},\boldsymbol{i}_r^{dq}) & \boldsymbol{L}_m^{dq}(\boldsymbol{i}_s^{dq},\boldsymbol{i}_r^{dq})^\top \\ \boldsymbol{L}_m^{dq}(\boldsymbol{i}_s^{dq},\boldsymbol{i}_r^{dq}) & \boldsymbol{L}_r^{dq}(\boldsymbol{i}_s^{dq},\boldsymbol{i}_r^{dq}) \end{bmatrix}^{-1} \begin{pmatrix} -R_s\boldsymbol{i}_s^{dq} - \boldsymbol{u}_g^{dq}(t) + \omega_k \boldsymbol{J}\boldsymbol{\psi}_s^{dq}(\boldsymbol{i}_s^{dq},\boldsymbol{i}_r^{dq}) \\ R_c\boldsymbol{i}_l^{dq} - (R_r+R_c)\boldsymbol{i}_r^{dq} - \boldsymbol{u}_c^{dq} + (\omega_k - n_m\omega_m)\boldsymbol{J}\boldsymbol{\psi}_s^{dq}(\boldsymbol{i}_s^{dq},\boldsymbol{i}_r^{dq}) \end{pmatrix} \\
-\left(\frac{R_l+R_c}{L_l}\boldsymbol{I}_2 + (\omega_k - n_m\omega_m)\,\boldsymbol{J}\right)\boldsymbol{i}_l^{dq} + \frac{1}{L_l}\boldsymbol{u}_c^{dq} + \frac{R_c}{L_l}\boldsymbol{I}_2\boldsymbol{i}_r^{dq} - \frac{1}{L_l}\boldsymbol{s}_l^{dq}u_d \\
-\frac{1}{C_c}\boldsymbol{i}_l^{dq} - (\omega_k - n_m\omega_m)\,\boldsymbol{J}\boldsymbol{u}_c^{dq} + \frac{1}{C_c}\boldsymbol{i}_r^{dq} \\
\frac{2}{3k_c^2C_d}\left(\boldsymbol{s}_l^{dq}\right)^\top \boldsymbol{i}_l^{dq} - \frac{2}{3k_c^2C_d}\left(\boldsymbol{s}_f^{dq}\right)^\top \boldsymbol{i}_f^{dq} \\
-\left(\frac{R_f+R_h}{L_f}\boldsymbol{I}_2 + \omega_k\boldsymbol{J}\right)\boldsymbol{i}_f^{dq} + \frac{R_h}{L_f}\boldsymbol{i}_g^{dq} - \frac{1}{L_f}\boldsymbol{u}_h^{dq} + \frac{1}{L_f}\boldsymbol{s}_f^{dq}u_d \\
\frac{R_h}{L_g}\boldsymbol{i}_f^{dq} - \left(\frac{R_g+R_h}{L_g}\boldsymbol{I}_2 + \omega_k\boldsymbol{J}\right)\boldsymbol{i}_g^{dq} + \frac{1}{L_g}\boldsymbol{u}_h^{dq} - \frac{1}{L_g}\boldsymbol{u}_g^{dq}(t) \\
\frac{1}{C_h}\boldsymbol{i}_f^{dq} - \frac{1}{C_h}\boldsymbol{i}_g^{dq} - \omega_k\boldsymbol{J}\boldsymbol{u}_h^{dq}
\end{pmatrix}
\end{aligned}
\tag{2.77}
$$

and, eventually, in combination with (2.75) and (2.76), represents the holistic model of the whole wind turbine system.

2.4 Power flow

This section investigates the power flow based on the holistic model of the wind turbine system presented in Sec. 2.3.2. The exchanges of power with the intrinsic energy storages (e.g. charging/discharging of the DC-link capacitor, speed-up/-down of the turbine and machine shaft) are considered as well as the power losses (e.g. in the resistances). In [5], the dynamic power flow has already been published for a less complex model. The enhancements of the derived power flow in this section compared to the one in [5] are the following: (a) the two-mass system is considered, (b) the nonlinear DFIM model is used instead of the simple linear model, (c) the additional LC filter is integrated and (d) the more complicated LCL filter is utilized instead of a simple L-filter.
Fig. 2.23 depicts a typical wind speed profile, which varies over time[24]. This characteristic motivates the *dynamic* power flow, since it is essential for the modeling to take these fluctuations into account. As mentioned in [5], in general, the dynamic power flow causes the following benefits:

- it yields a deep understanding of the interacting components of the wind turbine system;
- the knowledge of the power losses makes a detailed efficiency analysis possible;
- the potentials of the intrinsic energy storages can be investigated precisely;

[24]For the provided wind data profile, the author would like to thank the contributing organizations of the FINO-Project: Bundesministerium für Umwelt, Naturschutz, Bau und Reaktorsicherheit (BMUB), Projektträger Jülich (PTJ)/Forschungszentrum Jülich GmbH, Bundesamt für Seeschifffahrt und Hydrographie (BSH) and DEWI GmbH.

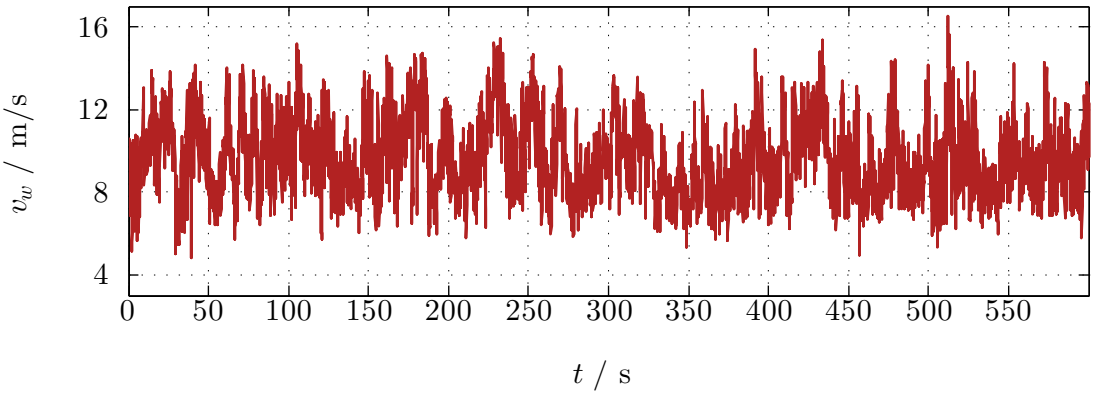

Figure 2.23: *Realistic wind speed profile.*

- the operation of the wind turbine system (e.g. control strategies) can be optimized regarding e.g. cost efficiency or loss reduction.

Therefor, Sec. 2.4.1 discusses the dynamic power flow in detail. To highlight important properties of the wind turbine system in stationary operation, in Sec. 2.4.2, this dynamic power flow is simplified to the stationary power flow.

2.4.1 Dynamic power flow

This section presents the dynamic power flow starting from the wind power p_w and ending in the power p_n (in W), which is fed to the grid.

Remark (R.2.14) *To simplify the readability of this section, the arguments of the upcoming power definitions are restricted to time t.*

The turbine extracts power from the wind, such that the wind power p_w splits up into the the turbine power

$$p_t(t) \overset{(2.1),(2.3)}{=} p_w(t) - \overbrace{(1 - c_t(t, \beta_t, \omega_t))\,\frac{1}{2}\rho_w \pi r_t^2 v_w(t)^3}^{=:p_{t,\mathrm{lo}}(t)} = p_w(t) - p_{t,\mathrm{lo}}(t) \tag{2.78}$$

and the power "loss" $p_{t,\mathrm{lo}}$ (in W) remaining in the wind[25]. To model the power flow through the further mechanical components, i.e. the two-mass system, the gear box and the shafts of the turbine and the machine, the dynamics in (2.5) are considered. A multiplication of the first row of (2.5) by $\theta_t\omega_t$ results in

$$\theta_t\omega_t(t)\frac{\mathrm{d}}{\mathrm{d}t}\omega_t(t) = -d_z\omega_t(t)^2 - c_z\phi_z(t)\omega_t(t) + \frac{d_z}{g_b}\omega_m(t)\omega_t(t) + m_t(t, \beta_t, \omega_t)\omega_t(t) - m_{t,\mathrm{fr}}(\omega_t)\omega_t(t) \tag{2.79}$$

and, accordingly, a multiplication of the third row of (2.5) by $(\theta_b + \theta_m)\,\omega_m$ yields

$$\begin{aligned}(\theta_b + \theta_m)\,\omega_m(t)\frac{\mathrm{d}}{\mathrm{d}t}\omega_m(t) = \frac{d_z}{g_b}\omega_t(t)\omega_m(t) + \frac{c_z}{g_b}\phi_z(t)\omega_m(t) - \frac{d_z}{g_b^2}\omega_m(t)^2 \\ - m_m(\boldsymbol{i}_s^{dq}, \boldsymbol{i}_r^{dq})\omega_m(t) - m_{m,\mathrm{fr}}(\omega_m)\omega_m(t)\,.\end{aligned} \tag{2.80}$$

[25] Clearly, the power $p_{t,\mathrm{lo}}$ can not be regarded as a "real" loss, since it is theoretically impossible for the turbine, to extract the entire power out of the wind.

Adding (2.79) and (2.80) gives

$$\begin{aligned}\theta_t\omega_t(t)\frac{\mathrm{d}}{\mathrm{d}t}\omega_t(t) + (\theta_b+\theta_m)\,\omega_m(t)\frac{\mathrm{d}}{\mathrm{d}t}\omega_m(t)\\ = -d_z\omega_t(t)^2 + 2\frac{d_z}{g_b}\omega_t(t)\omega_m(t) - \frac{d_z}{g_b^2}\omega_m(t)^2 - c_z\phi_z(t)\omega_t(t) + \frac{c_z}{g_b}\phi_z(t)\omega_m(t)\\ - m_m(\boldsymbol{i}_s^{dq},\boldsymbol{i}_r^{dq})\omega_m(t) - m_{m,\mathrm{fr}}(\omega_m)\omega_m(t) + m_t(t,\beta_t,\omega_t)\omega_t(t) - m_{t,\mathrm{fr}}(\omega_t)\omega_t(t)\,. \quad (2.81)\end{aligned}$$

By using (a) the binomial theorem (see e.g. [116]) and (b) the relation $\frac{\mathrm{d}}{\mathrm{d}t}\phi_z(t) = \omega_t(t) - \frac{\omega_m(t)}{g_b}$ (cf. Sec. 2.1), (2.81) simplifies to

$$\begin{aligned}\overbrace{m_m(\boldsymbol{i}_s^{dq},\boldsymbol{i}_r^{dq})\omega_m(t)}^{=:p_m(t)} = \overbrace{m_t(t,\beta_t,\omega_t)\omega_t(t)}^{=:p_t(t)} - \overbrace{m_{t,\mathrm{fr}}(\omega_t)\omega_t(t)}^{=:p_{t,\mathrm{fr}}(t)} - \overbrace{\theta_t\omega_t(t)\frac{\mathrm{d}}{\mathrm{d}t}\omega_t(t)}^{=:p_{\theta_t}(t)} - \overbrace{c_z\phi_z(t)\frac{\mathrm{d}}{\mathrm{d}t}\phi_z(t)}^{=:p_{c_z}(t)}\\ \underbrace{-d_z\left(\omega_t(t)-\frac{\omega_m(t)}{g_b}\right)^2}_{=:p_{d_z}(t)} \underbrace{-(\theta_b+\theta_m)\,\omega_m(t)\frac{\mathrm{d}}{\mathrm{d}t}\omega_m(t)}_{=:p_{\theta_m}(t)} \underbrace{-m_{m,\mathrm{fr}}(\omega_m)\omega_m(t)}_{=:p_{m,\mathrm{fr}}(t)}\,. \quad (2.82)\end{aligned}$$

Consequently, the mechanical machine power p_m (in W) is composed by the turbine power p_t minus (i) the power losses of the turbine friction $p_{t,\mathrm{fr}}$, the damping p_{d_z} and the machine friction $p_{m,\mathrm{fr}}$ (all in W) and (ii) the power exchanges with the turbine shaft p_{θ_t}, the two-mass stiffness p_{c_z} and the machine shaft p_{θ_m} (all in W). Summarizing (2.82), the dynamic power flow of the mechanical system leads to

$$p_m(t) = p_t(t) - p_{t,\mathrm{fr}}(t) - p_{\theta_t}(t) - p_{c_z}(t) - p_{d_z}(t) - p_{\theta_m}(t) - p_{m,\mathrm{fr}}(t)\,. \quad (2.83)$$

In the following, the dynamic power flow of the electrical system is derived. Starting with the DFIM, due to (A.20) and (2.26), the sum of the stator power p_s and the rotor power p_r (both in W) is given by

$$\begin{aligned}&p_s(t) + p_r(t)\\ &= \frac{2}{3k_c^2}\boldsymbol{i}_s^{dq}(t)^\top\boldsymbol{u}_s^{dq}(t) + \frac{2}{3k_c^2}\boldsymbol{i}_r^{dq}(t)^\top\boldsymbol{u}_r^{dq}(t)\\ &= \frac{2}{3k_c^2}\boldsymbol{i}_s^{dq}(t)^\top\left(-R_s\boldsymbol{i}_s^{dq}(t) - \boldsymbol{L}_s^{dq}(\boldsymbol{i}_s^{dq},\boldsymbol{i}_r^{dq})\frac{\mathrm{d}}{\mathrm{d}t}\boldsymbol{i}_s^{dq}(t) - \boldsymbol{L}_m^{dq}(\boldsymbol{i}_s^{dq},\boldsymbol{i}_r^{dq})^\top\frac{\mathrm{d}}{\mathrm{d}t}\boldsymbol{i}_r^{dq}(t) + \omega_k(t)\boldsymbol{J}\boldsymbol{\psi}_s^{dq}(\boldsymbol{i}_s^{dq},\boldsymbol{i}_r^{dq})\right)\\ &\quad + \frac{2}{3k_c^2}\boldsymbol{i}_r^{dq}(t)^\top\Big(-R_r\boldsymbol{i}_r^{dq}(t) - \boldsymbol{L}_r^{dq}(\boldsymbol{i}_s^{dq},\boldsymbol{i}_r^{dq})\frac{\mathrm{d}}{\mathrm{d}t}\boldsymbol{i}_r^{dq}(t) - \boldsymbol{L}_m^{dq}(\boldsymbol{i}_s^{dq},\boldsymbol{i}_r^{dq})\frac{\mathrm{d}}{\mathrm{d}t}\boldsymbol{i}_s^{dq}(t) + (\omega_k(t)-\omega_r(t))\boldsymbol{J}\boldsymbol{\psi}_r^{dq}(\boldsymbol{i}_s^{dq},\boldsymbol{i}_r^{dq})\Big)\\ &= \underbrace{\frac{2}{3k_c^2}\omega_k(t)\boldsymbol{i}_s^{dq}(t)^\top\boldsymbol{J}\boldsymbol{\psi}_s^{dq}(\boldsymbol{i}_s^{dq},\boldsymbol{i}_r^{dq}) + \frac{2}{3k_c^2}\left(\omega_k(t)-\omega_r(t)\right)\boldsymbol{i}_r^{dq}(t)^\top\boldsymbol{J}\boldsymbol{\psi}_r^{dq}(\boldsymbol{i}_s^{dq},\boldsymbol{i}_r^{dq})}_{=:p_m(t)} \underbrace{-\frac{2}{3k_c^2}R_s\left\|\boldsymbol{i}_s^{dq}(t)\right\|^2}_{=:p_{R_s}(t)}\\ &\quad \underbrace{-\frac{2}{3k_c^2}R_r\left\|\boldsymbol{i}_r^{dq}(t)\right\|^2}_{=:p_{R_r}(t)} \underbrace{-\frac{2}{3k_c^2}\boldsymbol{i}_s^{dq}(t)^\top\boldsymbol{L}_s^{dq}(\boldsymbol{i}_s^{dq},\boldsymbol{i}_r^{dq})\frac{\mathrm{d}}{\mathrm{d}t}\boldsymbol{i}_s^{dq}(t)}_{=:p_{L_s}(t)} \underbrace{-\frac{2}{3k_c^2}\boldsymbol{i}_r^{dq}(t)^\top\boldsymbol{L}_r^{dq}(\boldsymbol{i}_s^{dq},\boldsymbol{i}_r^{dq})\frac{\mathrm{d}}{\mathrm{d}t}\boldsymbol{i}_r^{dq}(t)}_{=:p_{L_r}(t)}\\ &\quad \underbrace{-\frac{2}{3k_c^2}\boldsymbol{i}_s^{dq}(t)^\top\boldsymbol{L}_m^{dq}(\boldsymbol{i}_s^{dq},\boldsymbol{i}_r^{dq})^\top\frac{\mathrm{d}}{\mathrm{d}t}\boldsymbol{i}_r^{dq}(t)}_{=:p_{L_{sr}}(t)} \underbrace{-\frac{2}{3k_c^2}\boldsymbol{i}_r^{dq}(t)^\top\boldsymbol{L}_m^{dq}(\boldsymbol{i}_s^{dq},\boldsymbol{i}_r^{dq})\frac{\mathrm{d}}{\mathrm{d}t}\boldsymbol{i}_s^{dq}(t)}_{=:p_{L_{rs}}(t)}\\ &= p_m(t) - p_{R_s}(t) - p_{R_r}(t) - p_{L_s}(t) - p_{L_r}(t) - p_{L_{sr}}(t) - p_{L_{rs}}(t)\,. \quad (2.84)\end{aligned}$$

Hence, the mechanical machine power p_m splits up into (i) the stator power p_s, (ii) the rotor power p_r, (iii) the losses p_{R_s} and p_{R_r} (both in W) in the stator resistance R_s and in the rotor

resistance R_r and (iv) the variations p_{L_s}, p_{L_r}, $p_{L_{sr}}$ and $p_{L_{rs}}$ (all in W) of the stored magnetic energy in the stator inductance $\boldsymbol{L}_s^{dq}$, the rotor inductance $\boldsymbol{L}_r^{dq}$ and the coupling inductance $\boldsymbol{L}_m^{dq}$, respectively. Since the stator is directly coupled to the three-winding transformer, the stator power p_s flows directly to the three-winding transformer.
In view of (2.82) and (2.84), the machine torque $m_m(\boldsymbol{i}_s^{dq}, \boldsymbol{i}_r^{dq})$ can be calculated, which is only a function of the stator current $\boldsymbol{i}_s^{dq}$ and the rotor current $\boldsymbol{i}_r^{dq}$. It is given by

$$\begin{aligned} m_m(\boldsymbol{i}_s^{dq}, \boldsymbol{i}_r^{dq}) &\overset{(2.82)}{=} \frac{p_m(\boldsymbol{i}_s^{dq}, \boldsymbol{i}_r^{dq}, \omega_m)}{\omega_m(t)} \\ &\overset{(2.84)}{=} -\frac{2n_m}{3k_c^2}\boldsymbol{i}_r^{dq}(t)^\top \boldsymbol{J}\boldsymbol{\psi}_r^{dq}(\boldsymbol{i}_s^{dq},\boldsymbol{i}_r^{dq}) + \frac{2}{3k_c^2}\frac{\omega_k(t)}{\omega_m(t)} \overbrace{\left(\boldsymbol{i}_s^{dq}(t)^\top \boldsymbol{J}\boldsymbol{\psi}_s^{dq}(\boldsymbol{i}_s^{dq},\boldsymbol{i}_r^{dq}) + \boldsymbol{i}_r^{dq}(t)^\top \boldsymbol{J}\boldsymbol{\psi}_r^{dq}(\boldsymbol{i}_s^{dq},\boldsymbol{i}_r^{dq})\right)}^{\overset{!}{=}0} \end{aligned} \tag{2.85}$$

and, since $m_m(\boldsymbol{i}_s^{dq}, \boldsymbol{i}_r^{dq})$ does not depend on the machine rotational speed $\omega_m > 0$, the highlighted bracket in (2.85) must be zero[26]. Consequently, the following must hold

$$\boldsymbol{i}_s^{dq}(t)^\top \boldsymbol{J}\boldsymbol{\psi}_s^{dq}(\boldsymbol{i}_s^{dq}, \boldsymbol{i}_r^{dq}) = -\boldsymbol{i}_r^{dq}(t)^\top \boldsymbol{J}\boldsymbol{\psi}_r^{dq}(\boldsymbol{i}_s^{dq}, \boldsymbol{i}_r^{dq}) \ . \tag{2.86}$$

By inserting (2.86) into (2.84), the machine power p_m and the machine torque m_m (cf. (2.27) in Sec. 2.2.2.1) result in

$$\begin{aligned} p_m(t) &= \omega_m(t) m_m(\boldsymbol{i}_s^{dq},\boldsymbol{i}_r^{dq}) = \omega_m(t)\frac{2}{3k_c^2} n_m \boldsymbol{i}_s^{dq}(t)^\top \boldsymbol{J}\boldsymbol{\psi}_s^{dq}(\boldsymbol{i}_s^{dq},\boldsymbol{i}_r^{dq}) = -\omega_m(t)\frac{2}{3k_c^2} n_m \boldsymbol{i}_r^{dq}(t)^\top \boldsymbol{J}\boldsymbol{\psi}_r^{dq}(\boldsymbol{i}_s^{dq},\boldsymbol{i}_r^{dq}) \\ \Leftrightarrow\ m_m(\boldsymbol{i}_s^{dq}, \boldsymbol{i}_r^{dq}) &= \frac{2}{3k_c^2} n_m \boldsymbol{i}_s^{dq}(t)^\top \boldsymbol{J}\boldsymbol{\psi}_s^{dq}(\boldsymbol{i}_s^{dq}, \boldsymbol{i}_r^{dq}) = -\frac{2}{3k_c^2} n_m \boldsymbol{i}_r^{dq}(t)^\top \boldsymbol{J}\boldsymbol{\psi}_r^{dq}(\boldsymbol{i}_s^{dq}, \boldsymbol{i}_r^{dq}) \, . \end{aligned} \tag{2.87}$$

Remark (R.2.15) *Due to (A.2.5), hysteresis effects and eddy currents are neglected in the nonlinear DFIM model. If (A.2.5) does not hold, the machine torque m_m can not be calculated as in* (2.87)*.*

The power balance in the LC filter is given as follows: Due to (2.43), (2.44), (2.69) and (A.20), the rotor power p_r can be calculated as

$$\begin{aligned} p_r(t) &\overset{(A.20)}{=} \frac{2}{3k_c^2}\boldsymbol{i}_r^{dq}(t)^\top \boldsymbol{u}_r^{dq}(t) \overset{(2.43),(2.69)}{=} \frac{2}{3k_c^2}\left(\boldsymbol{i}_l^{dq}(t) + \boldsymbol{i}_c^{dq}(t)\right)^\top \left(\boldsymbol{u}_c^{dq}(t) + R_c \boldsymbol{i}_c^{dq}(t)\right) \\ &= \frac{2}{3k_c^2}\boldsymbol{u}_c^{dq}(t)^\top \boldsymbol{i}_c^{dq}(t) + \frac{2}{3k_c^2}\boldsymbol{u}_c^{dq}(t)^\top \boldsymbol{i}_l^{dq}(t) + \frac{2}{3k_c^2} R_c \left\|\boldsymbol{i}_c^{dq}(t)\right\|^2 + \frac{2}{3k_c^2} R_c \boldsymbol{i}_c^{dq}(t)^\top \boldsymbol{i}_l^{dq}(t) \\ &\overset{(2.43),(2.44)}{=} \frac{2}{3k_c^2}\boldsymbol{u}_c^{dq}(t)^\top \left(C_c \frac{\mathrm{d}}{\mathrm{d}t}\boldsymbol{u}_c^{dq}(t) + (\omega_k(t) - \omega_r(t))\, C_c \boldsymbol{J}\boldsymbol{u}_c^{dq}(t)\right)^\top \\ &\quad + \frac{2}{3k_c^2}\left(-R_c \boldsymbol{i}_c^{dq}(t) + R_l \boldsymbol{i}_l^{dq}(t) + L_l \frac{\mathrm{d}}{\mathrm{d}t}\boldsymbol{i}_l^{dq}(t) + (\omega_k(t) - \omega_r(t))\, L_l \boldsymbol{J}\boldsymbol{i}_l^{dq}(t) + \boldsymbol{u}_l^{dq}(t)\right)^\top \boldsymbol{i}_l^{dq}(t) \\ &\quad + \frac{2}{3k_c^2} R_c \left\|\boldsymbol{i}_r^{dq}(t) - \boldsymbol{i}_l^{dq}(t)\right\|^2 + \frac{2}{3k_c^2} R_c \boldsymbol{i}_c^{dq}(t)^\top \boldsymbol{i}_l^{dq}(t) \\ &= \overbrace{\frac{2}{3k_c^2} C_c \boldsymbol{u}_c^{dq}(t)^\top \frac{\mathrm{d}}{\mathrm{d}t}\boldsymbol{u}_c^{dq}(t)}^{=:p_{C_c}(t)} + \overbrace{\frac{2}{3k_c^2} R_c \left\|\boldsymbol{i}_r^{dq}(t) - \boldsymbol{i}_l^{dq}(t)\right\|^2}^{=:p_{R_c}(t)} + \overbrace{\frac{2}{3k_c^2} R_l \left\|\boldsymbol{i}_l^{dq}(t)\right\|^2}^{=:p_{R_l}(t)} \\ &\quad + \underbrace{\frac{2}{3k_c^2} L_l \boldsymbol{i}_l^{dq}(t)^\top \frac{\mathrm{d}}{\mathrm{d}t}\boldsymbol{i}_l^{dq}(t)}_{=:p_{L_l}(t)} + \underbrace{\frac{2}{3k_c^2}\boldsymbol{u}_l^{dq}(t)^\top \boldsymbol{i}_l^{dq}(t)}_{=:p_l(t)} \, . \end{aligned} \tag{2.88}$$

[26] Otherwise, for a constant stator current $\boldsymbol{i}_s^{dq}$ and rotor current $\boldsymbol{i}_r^{dq}$, a variation of the machine rotational speed ω_m would cause a change of the machine torque $m_m(\boldsymbol{i}_s^{dq}, \boldsymbol{i}_r^{dq})$, which is a contradiction.

Hence, the rotor power p_r results from the addition of (i) the filter losses p_{R_c} and p_{R_l} (both in W) in the filter resistances R_c and R_l respectively, (ii) the powers p_{C_c} and p_{L_l} (both in W), which express the charging/discharging of the filter capacitance C_c and the filter inductance L_l and (iii) the power p_l (in W) flowing from the LC filter to the machine side converter. Summarizing (2.88), the power balance in the LC filter can be written as

$$p_l(t) = p_r(t) - p_{R_c}(t) - p_{R_l}(t) - p_{C_c}(t) - p_{L_l}(t)\,. \tag{2.89}$$

The power exchange p_{C_d} (in W) in the DC-link capacitance C_d is given by

$$p_{C_d}(t) = C_d u_d(t)\frac{\mathrm{d}}{\mathrm{d}t}u_d(t) \overset{(2.50)}{=} \frac{2}{3k_c^2}\boldsymbol{i}_l^{dq}(t)^\top \underbrace{\boldsymbol{s}_l^{dq}(t)u_d(t)}_{\overset{(2.54)}{=}\boldsymbol{u}_l^{dq}(t)} - \frac{2}{3k_c^2}\boldsymbol{i}_f^{dq}(t)^\top \underbrace{\boldsymbol{s}_f^{dq}(t)u_d(t)}_{\overset{(2.54)}{=}\boldsymbol{u}_f^{dq}(t)} \overset{(A.20)}{=} p_l(t) - p_f(t) \tag{2.90}$$

and thus, yields the power flow through the back-to-back converter. The power p_l coming from the LC filter splits up into the power exchange p_{C_d} in the DC-link capacitance C_d and the power p_f (in W) flowing from the grid side converter to the LCL filter. Since the DC-link is modeled by a the DC-link capacitance C_d and (A.2.12) is supposed to hold true, the back-to-back converter is lossless[27].

The power p_g (in W), which flows from the LCL filter to the three-winding transformer, results from the power balance of the LCL filter, which is given by

$$\begin{aligned}
p_g(t) &\overset{(A.20)}{=} \frac{2}{3k_c^2}\boldsymbol{u}_g^{dq}(t)^\top\boldsymbol{i}_g^{dq}(t)\\
&\overset{(2.63)}{=} \frac{2}{3k_c^2}\left(-R_g\boldsymbol{i}_g^{dq}(t) - L_g\frac{\mathrm{d}}{\mathrm{d}t}\boldsymbol{i}_g^{dq}(t) - \omega_k(t)L_g\boldsymbol{J}\boldsymbol{i}_g^{dq}(t) + \boldsymbol{u}_h^{dq}(t) + R_h\boldsymbol{i}_h^{dq}(t)\right)^\top\boldsymbol{i}_g^{dq}(t)\\
&\overset{(2.63)}{=} -\frac{2}{3k_c^2}R_g\left\|\boldsymbol{i}_g^{dq}(t)\right\|^2 - \frac{2}{3k_c^2}L_g\boldsymbol{i}_g^{dq}(t)^\top\frac{\mathrm{d}}{\mathrm{d}t}\boldsymbol{i}_g^{dq}(t) - \frac{2}{3k_c^2}R_h\left\|\boldsymbol{i}_h^{dq}(t)\right\|^2 - \frac{2}{3k_c^2}\boldsymbol{u}_h^{dq}(t)^\top\boldsymbol{i}_h^{dq}(t)\\
&\quad + \frac{2}{3k_c^2}R_h\boldsymbol{i}_h^{dq}(t)^\top\boldsymbol{i}_f^{dq}(t) + \frac{2}{3k_c^2}\boldsymbol{u}_h^{dq}(t)^\top\boldsymbol{i}_f^{dq}(t)\\
&\overset{(2.63)}{=} -\frac{2}{3k_c^2}R_g\left\|\boldsymbol{i}_g^{dq}(t)\right\|^2 - \frac{2}{3k_c^2}L_g\boldsymbol{i}_g^{dq}(t)^\top\frac{\mathrm{d}}{\mathrm{d}t}\boldsymbol{i}_g^{dq}(t) - \frac{2}{3k_c^2}R_h\left\|\boldsymbol{i}_f^{dq}(t) - \boldsymbol{i}_g^{dq}(t)\right\|^2\\
&\quad - \frac{2}{3k_c^2}\boldsymbol{u}_h^{dq}(t)^\top\left(C_h\frac{\mathrm{d}}{\mathrm{d}t}\boldsymbol{u}_h^{dq}(t) + \omega_k(t)C_h\boldsymbol{J}\boldsymbol{u}_h^{dq}(t)\right) + \frac{2}{3k_c^2}R_h\boldsymbol{i}_h^{dq}(t)^\top\boldsymbol{i}_f^{dq}(t)\\
&\quad + \frac{2}{3k_c^2}\left(-R_f\boldsymbol{i}_f^{dq}(t) - L_f\frac{\mathrm{d}}{\mathrm{d}t}\boldsymbol{i}_f^{dq}(t) - \omega_k(t)L_f\boldsymbol{J}\boldsymbol{i}_f^{dq}(t) + \boldsymbol{u}_f^{dq}(t) - R_h\boldsymbol{i}_h^{dq}(t)\right)^\top\boldsymbol{i}_f^{dq}(t)\\
&= \overbrace{\frac{2}{3k_c^2}\boldsymbol{u}_f^{dq}(t)^\top\boldsymbol{i}_f^{dq}(t)}^{=:p_f(t)} - \overbrace{\frac{2}{3k_c^2}R_f\left\|\boldsymbol{i}_f^{dq}(t)\right\|^2}^{=:p_{R_f}(t)} - \overbrace{\frac{2}{3k_c^2}R_h\left\|\boldsymbol{i}_f^{dq}(t) - \boldsymbol{i}_g^{dq}(t)\right\|^2}^{=:p_{R_h}(t)} - \overbrace{\frac{2}{3k_c^2}R_g\left\|\boldsymbol{i}_g^{dq}(t)\right\|^2}^{=:p_{R_g}(t)}\\
&\quad \underbrace{- \frac{2}{3k_c^2}L_f\boldsymbol{i}_f^{dq}(t)^\top\frac{\mathrm{d}}{\mathrm{d}t}\boldsymbol{i}_f^{dq}(t)}_{=:p_{L_f}(t)} \underbrace{- \frac{2}{3k_c^2}C_h\boldsymbol{u}_h^{dq}(t)^\top\frac{\mathrm{d}}{\mathrm{d}t}\boldsymbol{u}_h^{dq}(t)}_{=:p_{C_h}(t)} \underbrace{- \frac{2}{3k_c^2}L_g\boldsymbol{i}_g^{dq}(t)^\top\frac{\mathrm{d}}{\mathrm{d}t}\boldsymbol{i}_g^{dq}(t)}_{=:p_{L_g}(t)}\\
&= p_f(t) - p_{R_f}(t) - p_{L_f}(t) - p_{R_h}(t) - p_{C_h}(t) - p_{R_g}(t) - p_{L_g}(t)\,.
\end{aligned} \tag{2.91}$$

Accordingly, the power p_g is composed by the power p_f—flowing from the grid side converter

[27] A standard back-to-back converter reaches an efficiency factor of about 98 %. Thus, this simplified model is reasonable. A detailed analysis of switching and conduction losses is explained in [126].

into the LCL filter—minus (i) the filter losses p_{R_f}, p_{R_h} and p_{R_g} (all in W) in the filter resistances R_f, R_h and R_g, respectively and (ii) the variations p_{C_h}, p_{L_f} and p_{L_g} (all in W) of the stored energy in the filter capacitance C_h and in the filter inductances L_f and L_g respectively.

Finally, the sum p_n (in W) of the stator power p_s and the power p_g coming from the LCL filter, i.e.

$$p_n(t) = p_s(t) + p_g(t)\,, \tag{2.92}$$

flows through the point of common coupling into the three-winding transformer and feeds the power grid.

Fig. 2.24 summarizes the dynamic power flow ((2.78) to (2.92)). The wind turbine system consists of — thirteen energy storages, which feature a bi-directional power flow. The overall power exchange p_{sto} (in W) by the energy storages is given by

$$\begin{aligned} p_{\text{sto}}(t) = \; & \overbrace{p_{\theta_t}(t) + p_{c_z}(t) + p_{\theta_m}(t)}^{\text{mechanical storages}} + \overbrace{p_{C_c}(t) + p_{C_d}(t) + p_{C_h}(t)}^{\text{capacitive storages}} \\ & + \underbrace{p_{L_s}(t) + p_{L_r}(t) + p_{L_{sr}}(t) + p_{L_{rs}}(t) + p_{L_l}(t) + p_{L_f}(t) + p_{L_g}(t)}_{\text{inductive storages}}\,. \end{aligned} \tag{2.93}$$

Moreover, there occur mechanical and resistive losses in the — components of the modeled wind turbine system. The aggregated power loss p_{lo} (in W) is obtained by

$$\begin{aligned} p_{\text{lo}}(t) = \; & \overbrace{p_{t,\text{lo}}(t) + p_{t,\text{fr}}(t) + p_{d_z}(t) + p_{m,\text{fr}}(t)}^{\text{mechanical losses}} \\ & + \underbrace{p_{R_s}(t) + p_{R_r}(t) + p_{R_c}(t) + p_{R_l}(t) + p_{R_f}(t) + p_{R_h}(t) + p_{R_g}(t)}_{\text{resistive losses}}\,, \end{aligned} \tag{2.94}$$

such that—by considering (2.93) and (2.94)—eventually, (2.92) can be rewritten as

$$p_n(t) = p_w(t) - p_{\text{lo}}(t) - p_{\text{sto}}(t)\,. \tag{2.95}$$

Remark (R.2.16) *The derived dynamic power flow is based on the modeled wind turbine system in Ch. 2. Therein, model assumptions have been imposed (e.g. the ideal behavior of the converter's semi-conductors in (A.2.12)), so that several losses in the wind turbine system are not considered, such as: (a) losses in the gear box, (ii) iron losses in the DFIM or (iii) switching and conduction losses in the machine side and grid side converter.*

2.4.2 Stationary power flow

In this section, the dynamic power flow of Sec. 2.4 is simplified to the stationary power flow[28]. To achieve a stationary operation, all time-derivatives of the holistic model dynamics (2.76) of the wind turbine system must be zero, i.e.

$$\frac{\mathrm{d}}{\mathrm{d}t}\boldsymbol{x}^{\star}_{\text{wts}}(t) := \boldsymbol{f}_{\text{wts}}(\boldsymbol{x}^{\star}_{\text{wts}}, \boldsymbol{u}^{\star}_{\text{wts}}, \boldsymbol{d}^{\star}_{\text{wts}}) = \boldsymbol{0}_{18}\,, \tag{2.96}$$

[28] Again, as in Sec. 2.2.2, all quantities are marked with an additional * when they operate in the equilibrium of the steady-state operation.

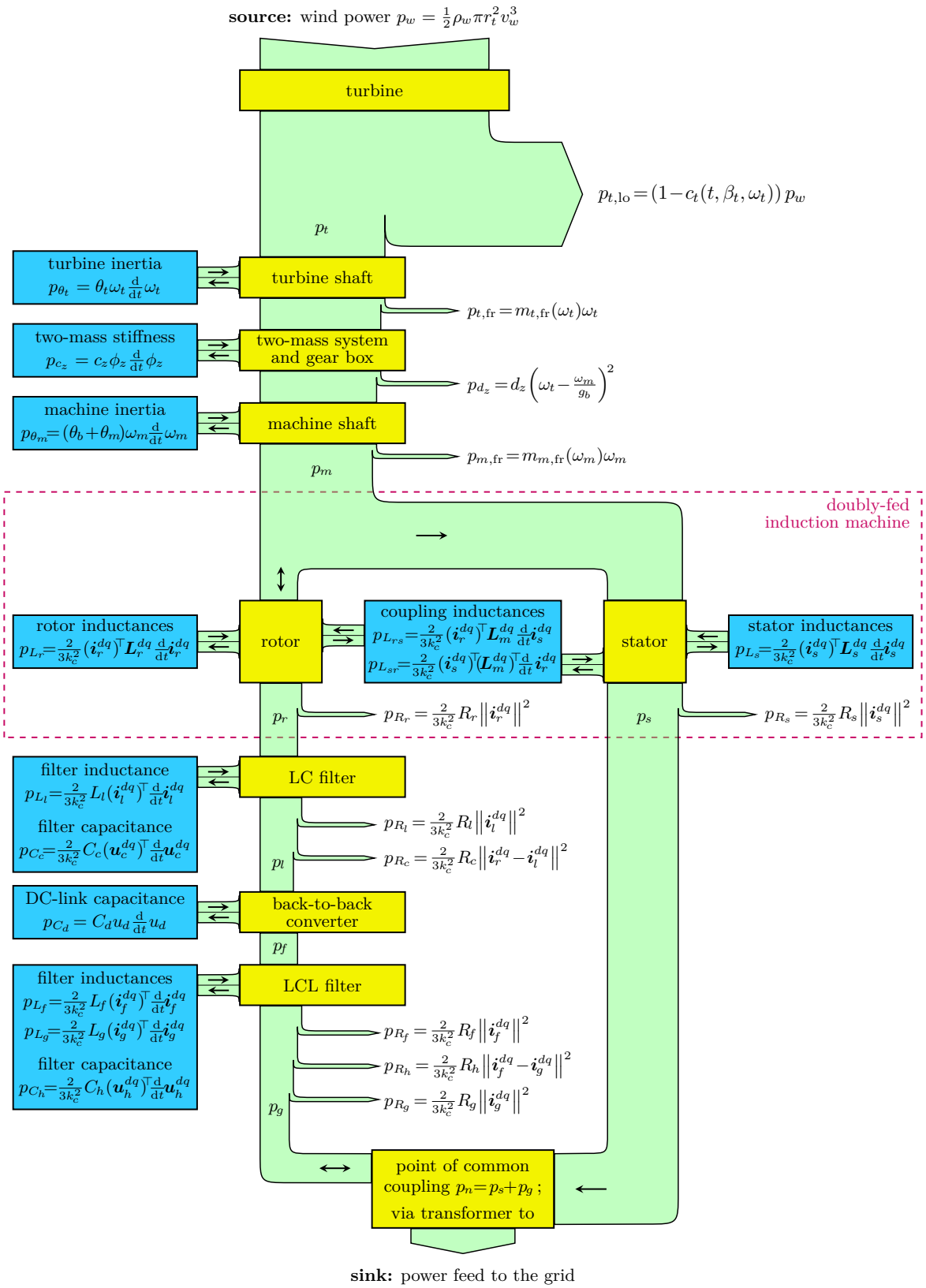

Figure 2.24: *Dynamic power flow within a wind turbine system with doubly-fed induction machine.*

where the state vector $\boldsymbol{x}_{\text{wts}}^{\star}$, the input vector $\boldsymbol{u}_{\text{wts}}^{\star}$ and the disturbance vector $\boldsymbol{d}_{\text{wts}}^{\star}$ are given by

$$\left.\begin{aligned}\boldsymbol{x}_{\text{wts}}^{\star} &:= \big(\omega_t^{\star}, \phi_z^{\star}, \omega_m^{\star}, (\boldsymbol{i}_s^{dq\star})^{\top}, (\boldsymbol{i}_r^{dq\star})^{\top}, (\boldsymbol{i}_l^{dq\star})^{\top}, (\boldsymbol{u}_c^{dq\star})^{\top}, u_d^{\star}, (\boldsymbol{i}_f^{dq\star})^{\top}, (\boldsymbol{i}_g^{dq\star})^{\top}, (\boldsymbol{u}_h^{dq\star})^{\top}\big)^{\top} \in \mathbb{R}^{18}\,,\\ \boldsymbol{u}_{\text{wts}}^{\star} &:= \big(\beta_t^{\star}, (\boldsymbol{s}_l^{dq\star})^{\top}, (\boldsymbol{s}_f^{dq\star})^{\top}\big)^{\top} \in \mathbb{R}^{5} \quad \text{and} \quad \boldsymbol{d}_{\text{wts}}^{\star} := \big(v_w^{\star}, (\boldsymbol{u}_g^{dq\star})^{\top}\big)^{\top} \in \mathbb{R}^{3}\end{aligned}\right\}\,. \tag{2.97}$$

Remark (R.2.17) *Clearly, due to the switching behavior of the machine side and grid side converter (see Sec. 2.2.4), a steady-state operation over time can only exist on average.*

In (R.2.4), it is explained that a transformation rotational speed $\omega_k \neq \omega_g$ yields an oscillating grid voltage $\boldsymbol{u}_g^{dq}$, which violates a stationary operation. Consequently, the following must hold:

Condition (C.2.1) *To accomplish a stationary operation, the transformation rotational speed $\omega_k^{\star}$ must equal the constant grid rotational speed $\omega_g^{\star}$, i.e. $\omega_k^{\star} = \omega_g^{\star}$.*

The steady-state dynamics (2.96) of the wind turbine system result in the stationary power flow, where all time-derivatives are zero. Hence, there exist no power exchanges with the energy storages in Fig. 2.24, i.e.

$$p_{\text{sto}}^{\star} = p_{\theta_t}^{\star} = p_{c_z}^{\star} = p_{\theta_m}^{\star} = p_{C_c}^{\star} = p_{C_d}^{\star} = p_{C_h}^{\star} = p_{L_s}^{\star} = p_{L_r}^{\star} = p_{L_{sr}}^{\star} = p_{L_{rs}}^{\star} = p_{L_l}^{\star} = p_{L_f}^{\star} = p_{L_g}^{\star} = 0\,. \tag{2.98}$$

Considering (2.94), (2.95) and (2.98)—and additionally taking (C.2.1) into account—yields the stationary power flow as follows

$$p_n^{\star} \overset{(2.95),(2.98)}{=} p_w^{\star} - p_{\text{lo}}^{\star} \overset{(2.94)}{=} p_w^{\star} - p_{t,\text{lo}}^{\star} - p_{t,\text{fr}}^{\star} - p_{d_z}^{\star} - p_{m,\text{fr}}^{\star} - p_{R_s}^{\star} - p_{R_r}^{\star} - p_{R_c}^{\star} - p_{R_l}^{\star} - p_{R_f}^{\star} - p_{R_h}^{\star} - p_{R_g}^{\star}\,. \tag{2.99}$$

Two important modes of the steady-state operation are (i) the *super-synchronous* operation and (ii) the *sub-synchronous* operation, which can be explained by means of the mechanical machine power $p_m^{\star}$. Since in wind turbine systems the machine constantly operates in generator mode, the machine torque $m_m^{\star}$ is positive[29], i.e. $m_m^{\star} > 0$. Accordingly, for the mechanical machine power $p_m^{\star}$, the following holds:

$$p_m^{\star} = \omega_m^{\star} m_m^{\star} \overset{(2.86),(2.87)}{=} \underbrace{\overbrace{\frac{\omega_g^{\star}}{n_m}}^{>0} \overbrace{\frac{2}{3k_c^2} n_m (\boldsymbol{i}_s^{dq\star})^{\top} \boldsymbol{J} \boldsymbol{\psi}_s^{dq\star}}^{=m_m^{\star}>0}}_{\text{power flow through the stator}} + \underbrace{\left(\omega_m^{\star} - \frac{\omega_g^{\star}}{n_m}\right) \overbrace{\frac{2}{3k_c^2} n_m (\boldsymbol{i}_r^{dq\star})^{\top} \boldsymbol{J}^{\top} \boldsymbol{\psi}_r^{dq\star}}^{=m_m^{\star}>0}}_{\text{power flow through the rotor}}\,. \tag{2.100}$$

Consequently, while the stator of the DFIM steadily feeds power to the three-winding transformer, the direction of the power flow over the rotor of the DFIM depends on the difference $\omega_m^{\star} - \frac{\omega_g^{\star}}{n_m}$. This leads to the two following operation modes[30]:

(i) **super-synchronous operation**, i.e. $\omega_m^{\star} > \frac{\omega_g^{\star}}{n_m}$: The power flows from the rotor into the three-winding transformer (power is injected to the three-winding transformer).

(ii) **sub-synchronous operation**, i.e. $\omega_m^{\star} < \frac{\omega_g^{\star}}{n_m}$: The power flows from the three-winding transformer into the rotor (power is drawn from the three-winding transformer).

[29] To be more accurate, the generator mode yields a positive mechanical machine power $p_m^{\star} > 0$, which—because of the definition of the machine rotational speed $\omega_m^{\star} > 0$—results in the positive machine torque $m_m^{\star} > 0$.

[30] In [127] the same definitions as here are presented, while [5] additionally considers copper losses in the definitions of super-synchronous and sub-synchronous operation mode.

Chapter 3

Control of wind turbine systems with doubly-fed induction machine

This chapter presents the control of the wind turbine system based on its holistic model (2.76). The main functions of the control are the following:

- to rapidly and accurately realize the tasks of the operation management,
- to guarantee a safe and stable operation of the wind turbine system,
- to ensure the targets of the grid code requirements.

Fig. 3.1 depicts the (simplified) overview of the control structure of the considered wind turbine system. The upper part shows the components of the wind turbine system:

- **mechanical components:** turbine, two-mass system, gear box,
- **electrical components:** DFIM, (optional) LC filter, back-to-back converter, LCL filter, point of common coupling, three-winding transformer, transmission line and grid.

Remark (R.3.1) *Only few publications (e.g. [69, 81–84]) consider the additional — LC filter, while the most publications couple the DFIM directly to the machine side converter. To cover both options with and without LC filter, control strategies for both cases are designed in this chapter.*

For the — measurements of the wind turbine system, here, the following assumption is imposed:

Assumption (A.3.1) *Except for the machine torque m_m[31], all relevant quantities are available for feedback. Tab. 3.1 summarizes these quantities.*

While the sensors send the measurement signals to the real-time system[32], the other way around, the space vector modulations apply the switching vectors $\boldsymbol{s}_l^{uvw}$ (or $\boldsymbol{s}_r^{uvw}$) and $\boldsymbol{s}_f^{abc}$ to the machine side and grid side converter, respectively. Moreover, the real-time system outputs a signal to adjust the pitch angle β_t.
The — operation management defines the control objectives and thus, generates the reference values for the control. In particular, these are the references of the machine rotational speed $\omega_{m,\text{ref}}$ (in $\frac{\text{rad}}{\text{s}}$), the stator reactive power $q_{s,\text{ref}}$ (in var), the DC-link voltage $u_{d,\text{ref}}$ (in V) and the q-component $i_{g,\text{ref}}^q$ (in A) of the grid current.

[31] As already mentioned in Sec. 2.2.2.3, a torque sensor is very expensive and thus, rarely implemented.
[32] Here, the well-known dSpace real-time system is used.

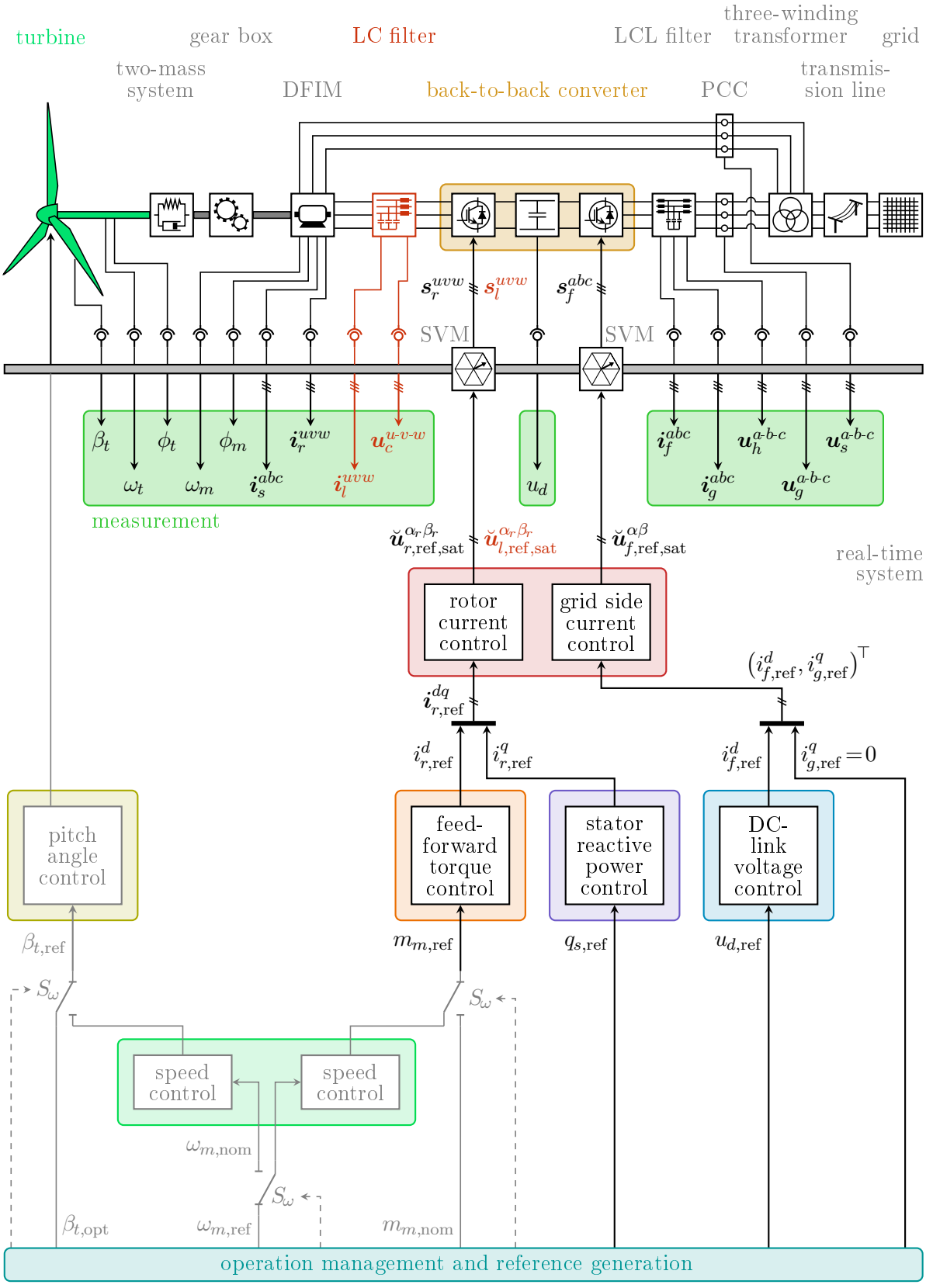

Figure 3.1: *Overview of a wind turbine system with doubly-fed induction machine and its control.*

description	symbols & values with unit
measured mechanical quantities	
pitch angle	β_t (in °)
turbine angle and rotational speed	ϕ_t (in rad) and ω_t (in $\frac{\text{rad}}{\text{s}}$)
machine angle and rotational speed	ϕ_m (in rad) and ω_m (in $\frac{\text{rad}}{\text{s}}$)
measured electrical machine side quantities	
stator current and line-to-line voltage	$\boldsymbol{i}_s^{abc}$ (in A)^3 and $\boldsymbol{u}_s^{a\text{-}b\text{-}c}$ (in V)^3
rotor current	$\boldsymbol{i}_r^{uvw}$ (in A)^3
filter current and line-to-line voltage	$\boldsymbol{i}_l^{uvw}$ (in A)^3 and $\boldsymbol{u}_c^{u\text{-}v\text{-}w}$ (in V)^3
DC-link measurement	
DC-link voltage	u_d (in V)
measured electrical grid side quantities	
filter current and line-to-line voltage	$\boldsymbol{i}_f^{abc}$ (in A)^3 and $\boldsymbol{u}_h^{a\text{-}b\text{-}c}$ (in V)^3
grid current and line-to-line voltage	$\boldsymbol{i}_g^{abc}$ (in A)^3 and $\boldsymbol{u}_g^{a\text{-}b\text{-}c}$ (in V)^3

Table 3.1: *Measured quantities in a wind turbine system with doubly-fed induction machine.*

The control itself splits up into two parts: (i) the control of the mechanical quantities and (ii) the control of the electrical quantities. The mechanical part consists of the — speed controller for the machine rotational speed ω_m and the — pitch controller for the pitch angle β_t. Depending on the operation regime (for details see [14, 128, 129]), the speed control is either accomplished via the machine torque m_m or via the pitch angle β_t. The two relevant operation regimes can be described as follows[33]:

(a) **maximum power point tracking:** The goal is to extract the maximum power from the wind, i.e. the turbine must work in the maximal power coefficient $c_{p,\text{opt}}$ (see Sec. 2.1 and Fig. 2.2). Due to (2.2), the pitch controller adjusts the pitch angle β_t to its optimal value, i.e. $\beta_{t,\text{ref}} = \beta_{t,\text{opt}}$ (both in °), and the speed controller yields the machine torque reference $m_{m,\text{ref}}$ (in Nm) in a way, so that $\omega_m = v_w \lambda_{t,\text{opt}}$ pertains[34].

(b) **rated operation:** This regime limits the machine power p_m to its rated power $p_{m,\text{nom}}$ (in W). Therefor, the speed controller adjusts (via the pitch controller) the machine rotational speed ω_m to its rated value $\omega_{m,\text{nom}}$ (in $\frac{\text{rad}}{\text{s}}$), i.e. $\omega_{m,\text{ref}} = \omega_{m,\text{nom}}$, and the torque controller receives the nominal machine torque $m_{m,\text{nom}}$ (in Nm) as reference, i.e. $m_{m,\text{ref}} = m_{m,\text{nom}}$.

The controller designs of the mechanical quantities herein do not differ from the ones in literature. Since many publications (e.g. [13],[14]) already explained those in detail, this work does not investigate the mechanical control part[35].
Instead, the focus is on the controller designs of the electrical quantities. Because of the developed nonlinear model of the DFIM, the commonly used control strategies for the machine side are not feasible anymore (cf. Sec. 2.2.2.6). Moreover, the special challenges on the grid side control, which are explained explicitly in Sec. 3.2, also require new control strategies for the grid side of the wind turbine system. Hence, novel controller designs must be originated both

[33] The transition between the two regimes is illustrated by the switch S_ω. Clearly, the real implementation of the transition is much more complicated and can e.g. be found in [14].

[34] Most often, the wind speed v_w is not measured and thus, v_w is not available for feedback. Therefor, the nonlinear speed controller as in [111] is commonly implemented to guarantee the relation $\omega_m = v_w \lambda_{t,\text{opt}}$.

[35] For this reason, Fig. 3.1 depicts the mechanical part of the control in gray.

for the machine side and for the grid side of the wind turbine system. For these new controller designs, the *dq*-reference frame will be *grid voltage oriented*. Because of (C.2.1), in this way, non-oscillating quantities can be achieved, which allows for using standard control methods (e.g. PI controllers). In accordance with Fig. 3.1, the controls of the electrical quantities and their respective tasks are the following:

- **feed-forward torque control——:** The torque controller needs to adjust the machine torque reference $m_{m,\mathrm{ref}}$. Depending on the operation regime, it must either comply with the reference trajectories of the speed control's output or cause the machine torque to keep its rated value $m_{m,\mathrm{nom}}$. Since the measurement of the machine torque m_m is not available, only a feed-forward control is possible.

- **stator reactive power control——:** To assure a stable grid operation, the wind turbine system needs to support the grid by supplying reactive power. The task of the stator reactive power control is to guarantee that the stator of the DFIM feeds the three-winding transformer with the reactive power $q_s = q_{s,\mathrm{ref}}$.

- **DC-link voltage control——:** The machine side and the grid side converter in combination with the corresponding space vector modulation generate the filter voltages $\boldsymbol{u}_l^{dq}$ (or $\boldsymbol{u}_r^{dq}$) and $\boldsymbol{u}_f^{dq}$, respectively. To ensure a proper generation of these voltages, the DC-link voltage must keep its (constant) reference value, i.e. $u_d = u_{d,\mathrm{ref}}$.

- **Rotor current control——:** The rotor current $\boldsymbol{i}_r^{dq}$ is used to realize the targets for the machine torque m_m (d-component) and for the stator reactive power q_s (q-component). Its controller outputs the reference filter voltage $\breve{\boldsymbol{u}}_{l,\mathrm{ref,sat}}^{\alpha_r\beta_r}$ (or $\breve{\boldsymbol{u}}_{r,\mathrm{ref,sat}}^{\alpha_r\beta_r}$) (both in V^2), which is applied to the machine side space vector modulation[36].

- **Grid side current control——:** This control needs (i) to adjust the reference $i_{f,\mathrm{ref}}^d$ (in A) of the filter current i_f^d, which is the control variable for DC-link voltage control[37] and (ii) to make sure that the q-component i_g^q of the grid current follows its reference $i_{g,\mathrm{ref}}^q = 0$ (in A). The output of the grid side current control is the filter voltage reference $\breve{\boldsymbol{u}}_{f,\mathrm{ref,sat}}^{\alpha\beta}$ (in V^2), which is applied to the grid side space vector modulation[38].

Remark (R.3.2) *The reactive power q_g (in* var*), which flows from the LCL filter into the three-winding transformer, is given by $q_g(t) = \frac{2}{3k_c^2}\boldsymbol{u}_g^{dq}(t)^\top \boldsymbol{J}\boldsymbol{i}_g^{dq}(t) = -\frac{2}{3k_c^2}\hat{u}_g(t)i_g^q(t)$ (see [123], therein with $k_c = \frac{2}{3}$). Consequently, the LCL filter does not feed any reactive power to the three-winding transformer, when the q-component i_g^q of the grid current is adjusted to zero, i.e. $i_g^q = 0 \Leftrightarrow q_g = 0$. This allows for an reduced size of the grid side converter, which saves costs regarding the purchase of the back-to-back converter. The drawback of controlling i_g^q to zero is, that this "degree of freedom" can not be used for different objectives; e.g. an injection of a non-zero reactive power q_g could ease the targets for the reactive power demand $q_{s,\mathrm{ref}}$ of the stator*[39]*. Then, an analysis of the power flow (see Sec. 2.4) might result in potentials to avoid resistive losses, which would lead to a less costly operation of the wind turbine system.*

[36] The filter voltage $\breve{\boldsymbol{u}}_{l,\mathrm{ref,sat}}^{\alpha_r\beta_r}$ equals the filter voltage $\breve{\boldsymbol{u}}_{l,\mathrm{ref}}^{\alpha_r\beta_r}$ in Fig. 2.21 (see Sec. 2.2.4), but with an additional saturation, which is defined in Sec. 3.3.2.1.

[37] To use the filter current i_f^d as control variable instead of the grid current i_g^d is motivated in Sec. 3.2.

[38] The filter voltage $\breve{\boldsymbol{u}}_{f,\mathrm{ref,sat}}^{\alpha\beta}$ equals the filter voltage $\breve{\boldsymbol{u}}_{f,\mathrm{ref}}^{\alpha\beta}$ in Fig. 2.20 (see Sec. 2.2.4), but with an additional saturation, which is defined in Sec. 3.2.2.2.

[39] The overall reactive power q_n (in var), which the wind turbine system injects via the three-winding transformer to the grid, is given by $q_n(t) = q_s(t) + q_g(t)$.

In the following sections, the new controller designs of the electrical quantities will be presented. First, Sec. 3.1 discusses the implemented phase-locked loop (PLL), which is necessary to transform the measurements of the electrical quantities (see Tab. 3.1) into the *grid voltage oriented* dq-reference frame. Sec. 3.2 presents the grid side control, where in Sec. 3.2.1 the implementation of the grid side at the laboratory test-bench is introduced. Sec. 3.2.2 describes the grid side current controller design. Based on this current controller, the DC-link voltage control is derived in Sec. 3.2.3. The machine side control is explained in Sec. 3.3 and consists of four parts: (a) the implementation of the machine side at the test-bench (Sec. 3.3.1), (b) the rotor current controller design without LC filter (Sec. 3.3.2) and (c) with LC filter (Sec. 3.3.3) and (d) the control of the machine torque and the stator reactive power, which is presented in Sec. 3.3.4.

3.1 Phase-locked loop (PLL)

The phase-locked loop (PLL) is utilized to extract (i) the grid angle ϕ_g, (ii) the grid rotational speed ω_g and (iii) the grid voltage $\boldsymbol{u}_g^{dq}$ from the measured line-to-line grid voltage $\boldsymbol{u}_g^{a\text{-}b\text{-}c}$. The PLL is a well-known method and there exist many different implementations (see e.g. [130],[131]). Here, the used PLL is taken from [111]. Its strategy is illustrated in Fig. 3.2.

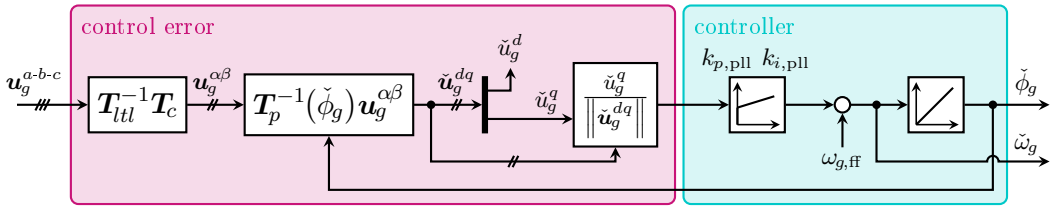

Figure 3.2: *Phase-locked loop (PLL) for the grid voltage oriented dq-reference frame (illustration is based on Fig. 24.15 in [111]).*

By means of the inverse line-to-line matrix $\boldsymbol{T}_{ltl}^{-1}$ and Clarke's transformation matrix $\boldsymbol{T}_c$, the measured line-to-line grid voltage $\boldsymbol{u}_g^{a\text{-}b\text{-}c}$ is transformed into the stator-fixed $\alpha\beta$-reference frame. Applying the inverse Park transformation matrix $\boldsymbol{T}_p^{-1}$—with the estimated grid angle $\check{\phi}_g$ (in rad) as its argument—to the grid voltage $\boldsymbol{u}_g^{\alpha\beta}$ yields the estimated grid voltage $\check{\boldsymbol{u}}_g^{dq}$ (in V)[2] in *grid voltage orientation*. Obviously, if the estimated grid angle $\check{\phi}_g$ equals the real grid angle ϕ_g, i.e. $\check{\phi}_g = \phi_g$, an ideal *grid voltage orientation* is achieved. To realize this goal, the PI controller in Fig. 3.2 adjusts the q-component $\check{u}_g^q$ of the estimated grid voltage to zero[40], i.e. $\check{u}_g^q = 0$. Hence, the — magenta box in Fig. 3.2 can be interpreted as control error $\phi_g - \check{\phi}_g$, whereas the — controller adjusts this error to zero. Due to the implemented integrator and the relationship $\frac{\mathrm{d}}{\mathrm{d}t}\check{\phi}_g(t) = \check{\omega}_g(t)$ with $\check{\phi}_{g,0} := \check{\phi}_g(0)$, the input of the integrator[41] matches with the estimated grid rotational speed $\check{\omega}_g$ (in $\frac{\mathrm{rad}}{\mathrm{s}}$).
More details to the PLL and how to determine its controller parameters can be found in [**?**]. For the following designs of the machine side and grid side control, the following should hold:

Assumption (A.3.2) *The PLL yields an ideal estimation of (i) the grid angle ϕ_g, (ii) the grid rotational speed ω_g and (iii) the grid voltage $\boldsymbol{u}_g^{dq}$. Moreover, (A.2.10) pertains.*

[40] To allow for a design of the PI controller's proportional gain $k_{p,\mathrm{pll}}$ (in $\frac{\mathrm{rad}}{\mathrm{s}}$) and integral gain $k_{i,\mathrm{pll}}$ (in $\frac{\mathrm{rad}}{\mathrm{s}^2}$), that is independent from the magnitude $\left\|\check{\boldsymbol{u}}_g^{dq}\right\|$ of the grid voltage vector, its q-component $\check{u}_g^q$ is normalized additionally.

[41] Since the grid rotational speed ω_g commonly features an almost constant value $\omega_{g,\mathrm{ff}}$ (in $\frac{\mathrm{rad}}{\mathrm{s}}$), this value can be feed-forwarded to improve the control performance.

3.2 Grid side control

This section presents the grid side control, which has two main objectives: (i) the tracking of the grid side current references $i_{f,\mathrm{ref}}^d$ and $i_{g,\mathrm{ref}}^q$ in an inner current control loop and (ii) to ensure a stable DC-link voltage control in an outer cascade. Simulations and measurements will verify both the correctness of the grid side model of the wind turbine system (2.76) and the excellent performance of the developed control strategies. Thereby, the wind turbine system in combination with its grid side implementation at the test-bench feature some characteristics, which make control strategies of previous publications (see Sec. 1.2.1) unfeasible to fulfill the two objectives (i) and (ii) above. The following characteristics necessitate the new designs of the grid side control:

- compared to common back-to-back converters, the one at the test bench possesses a tiny DC-link capacitance C_d relative to its power class (about ten-times smaller than standard values). Thus, power jumps at the DC-link result in significant voltage drops in the DC-link voltage u_d. This causes huge challenges for DC-link voltage control to guarantee a stable operation.
- the high resonance frequency f_{lcl} (in Hz) of the LCL filter[42] in relation to the small sampling frequency f_{dis} (in Hz) of the installed real-time system, where $\frac{f_{\mathrm{dis}}}{f_{\mathrm{lcl}}} \approx 3$ holds, makes a quasi-continuous controller design impossible. Instead, discretization strategies must be employed to allow for a discrete controller design.
- to obtain a loss-optimal operation of the grid side, no damping resistor is implemented to damp the LCL filter's resonance frequency f_{lcl}. Consequently, active damping of the resonance frequency f_{lcl} must be ensured by an intelligent control strategy.
- as already shown in Sec. 2.4.2, a wind turbine system with DFIM features a bi-directional power flow over the back-to-back converter depending on the machine rotational speed ω_m. In Sec. 3.2.3.2, it will be explained that injecting power from the machine side converter into the rotor is the critical case regarding the stability of the DC-link voltage control. Wind turbine systems without DFIM are not confronted by this critical case, since their machines always feed the DC-link.

These characteristics require a precise knowledge of the overall system—i.e. the interaction between the physical grid side components and their control—which must be incorporated into the control designs. Due to the tiny DC-link capacitance C_d, a very fast and aggressive DC-link voltage control is essential to ensure a robust DC-link control, since too big voltage drops in the DC-link voltage u_d endanger a stable operation. The quality of the DC-link voltage control also depends on the performance of the inner current control. Consequently, the synergy between these two controls is crucial, which necessitates a holistic control strategy for the grid side control. Among other things this motivates the use of the filter current i_f^d as control variable instead of the grid current i_g^d. Because the filter voltage u_f^d directly acts on the filter current i_f^d (see (2.66)), this allows for a very fast tracking of the corresponding reference current $i_{f,\mathrm{ref}}^d$.

3.2.1 Laboratory test-bench of the grid side

To verify the grid side part of the holistic wind turbine system model (2.76) via measurements, the relevant components were built-up at the test-bench as shown in Fig. 3.3.

[42] By neglecting the filter resistances R_f, R_g and R_h, the resonance frequency f_{lcl} of the LCL filter can be calculated by $f_{\mathrm{lcl}} = \frac{1}{2\pi}\sqrt{\frac{L_f + L_g}{L_f L_g C_h}}$ (see e.g. [46],[47])

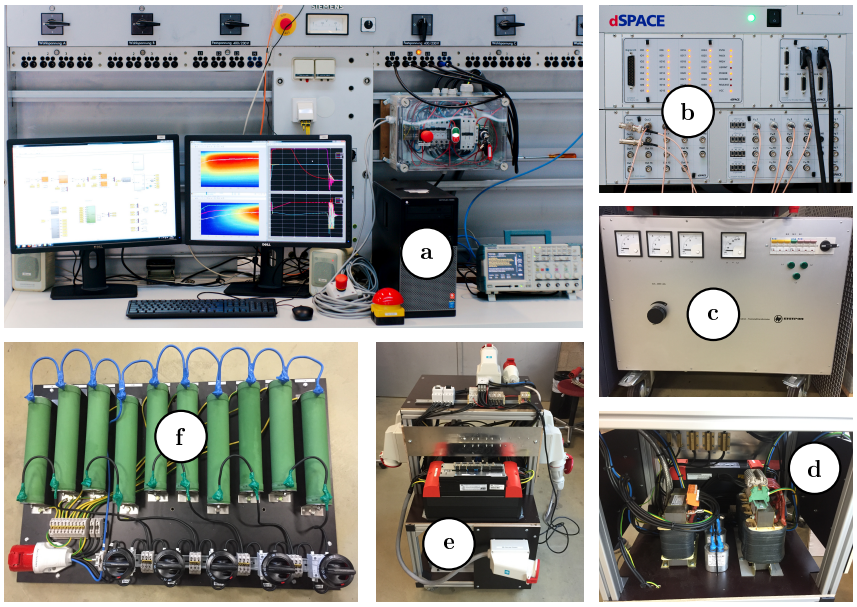

Figure 3.3: *Laboratory test-bench with (a) host computer, (b) dSpace real-time system, (c) two-winding transformer, (d) LCL filter, (e) grid side converter with DC-link and (f) resistance board.*

In particular these components are: (a) the host computer, (b) the dSpace real-time system, (c) the transformer[43], which couples the LCL filter to the grid, (d) the LCL filter, (e) the grid side converter with the DC-link and (f) the resistance board to emulate a resistive load.

Remark (R.3.3) *By means of the five switches of the resistance board (see Fig. 3.3), different resistances can be activated for the load of the DC-link. Thereby, the discrete resistance values are more challenging for the DC-link control than the ohmic-inductive behavior of the DFIM, since the switching yields instantaneous power jumps at the DC-link instead of continuous transients.*

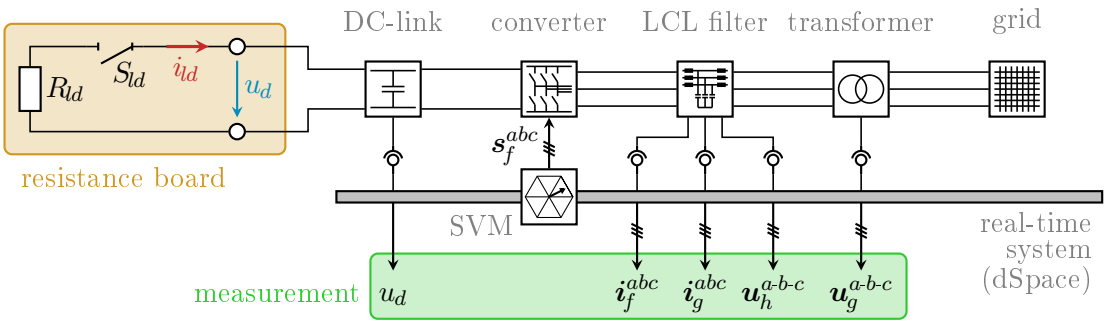

Figure 3.4: *Block diagram of the grid side experimental setup.*

Fig. 3.4 illustrates the interaction of the experimental setup and its physical components. The behavior of the — resistance board is expressed by the switch S_{ld} and the (varying) resistance R_{ld} (in Ω). According to Fig. 2.18, the current i_{ld} flows into the DC-link.

[43]Since the experimental setup does not require a third winding, instead of a three-winding transformer only a two-winding transformer is implemented at the laboratory test-bench.

description	symbols & values with unit
parameters of the dSpace real-time system	
sampling frequency	$f_{\text{dis}} = 4\,\text{kHz}$
sampling time	$t_{\text{dis}} = \frac{1}{f_{\text{dis}}} = 0.25\,\text{ms}$
parameters of the grid	
voltage amplitude	$\hat{u}_g = 400\sqrt{\frac{2}{3}}\,\text{V}$
frequency	$f_g = 50\,\text{Hz}$
rotational speed	$\omega_g = 2\pi f_g \approx 314\,\frac{\text{rad}}{\text{s}}$
parameters of the LCL filter	
resistances	$R_f = 0.1\,\Omega$ and $R_g = 0.2\,\Omega$
inductances	$L_f = 2.5\,\text{mH}$ and $L_g = 4.5\,\text{mH}$
capacitance	$C_h = 10\,\mu\text{F}$
damping resistance	$R_h = 0\,\Omega$ (no damping)
resonance frequency (resistances neglected)	$f_{\text{lcl}} = \frac{1}{2\pi}\sqrt{\frac{L_f+L_g}{L_f L_g C_h}} \approx 1.3\,\text{kHz}$
parameters of the converter and space vector modulation	
frequency of the space vector modulation	$f_{\text{svm}} = f_{\text{dis}} = 4\,\text{kHz}$
period of the space vector modulation	$T_{\text{svm}} = \frac{1}{f_{\text{svm}}} = 0.25\,\text{ms}$
sampling frequency of the space vector modulation	$f_{\text{dis,svm}} = 40\,\text{MHz}$ (see [132])
dead-time	$T_u = T_{\text{svm}} = 0.25\,\text{ms}$
parameters of the DC-link and resistance board	
capacitance	$C_d = 60\,\mu\text{F}$
resistance	$R_{ld} = \delta \cdot 0.5\,\text{k}\Omega\ ,\ \delta \in \{\frac{1}{4}, \frac{1}{3}, \frac{1}{2}, 1\}$
parameters of the simulation (Matlab/Simulink)	
solver (fixed step)	ode4
step time	$t_{\text{sim}} = 5\,\mu\text{s}$
Clarke transformation factors	$k_c = \frac{2}{3}$ and $\kappa_c = \sqrt{\frac{1}{2}}$

Table 3.2: *Parameters of Matlab/Simulink, the grid side and the dSpace real-time system.*

Voltage and current sensors — measure the following quantities[44]: the DC-link voltage u_d, the filter current $\boldsymbol{i}_f^{abc}$, the grid current $\boldsymbol{i}_g^{abc}$, the capacitance line-to-line voltage $\boldsymbol{u}_h^{a\text{-}b\text{-}c}$ and the grid line-to-line voltage $\boldsymbol{u}_g^{a\text{-}b\text{-}c}$. Consequently, the test-bench emulates perfectly the grid side of the modeled wind turbine system of Ch. 2 (cf. Fig. 3.1).
In Tab. 3.2, all relevant parameters of the experimental setup are summarized. For the purpose of comparability, clearly, the model simulations of the wind turbine system, which were implemented in Matlab/Simulink® from MathWorks®, use the same parameters. Additional simulation parameters are also listed in Tab. 3.2.

Remark (R.3.4) *A common LCL filter design yields filter inductances with $L_g < L_f$. Here, for the filter inductances it holds: $L_g = 4.5\,\text{mH} > 2.5\,\text{mH} = L_f$. The reason for that is not an odd LCL filter design but taking the inductive behavior of the transformer into account (via a series inductance regarding the filter inductance).*

[44] More precisely, the voltage sensors in the LCL filter measure the voltage $\boldsymbol{u}_h^{a\text{-}b\text{-}c} + R_h \boldsymbol{T}_{LTL}\left(\boldsymbol{i}_f^{abc} - \boldsymbol{i}_g^{abc}\right)$. For $R_h \neq 0$, the second term $R_h \boldsymbol{T}_{LTL}\left(\boldsymbol{i}_f^{abc} - \boldsymbol{i}_g^{abc}\right)$ must be subtracted to obtain the line-to-line voltage $\boldsymbol{u}_h^{a\text{-}b\text{-}c}$ as in Fig. 3.4.

3.2.2 Grid side current control with LCL filter

This section investigates the grid side current control. Its special challenges (see introduction of Sec. 3.2) require a fast and accurate tracking of the grid side current references $i_{f,\mathrm{ref}}^{d}$ and $i_{g,\mathrm{ref}}^{q}$. Therefor, an integral state-feedback controller—based on the discrete linear quadratic regulator (DLQR) theory—is designed. It is extended (i) by a reference voltage saturation (SAT), which takes the limited filter voltage $\boldsymbol{u}_f^{dq}$ into account and (ii) by an additional anti-wind up (AWU) to compensate for overshoots in the reference current tracking due to windup effects. The starting point are the LCL filter dynamics of (2.66), which are given by

$$\begin{aligned}\overbrace{\frac{\mathrm{d}}{\mathrm{d}t}\begin{pmatrix}\boldsymbol{i}_f^{dq}(t)\\ \boldsymbol{i}_g^{dq}(t)\\ \boldsymbol{u}_h^{dq}(t)\end{pmatrix}}^{=:\boldsymbol{x}_{\mathrm{lcl}}} &= \overbrace{\begin{bmatrix}-\frac{R_f+R_h}{L_f}\boldsymbol{I}_2-\omega_g\boldsymbol{J} & \frac{R_h}{L_f}\boldsymbol{I}_2 & -\frac{1}{L_f}\boldsymbol{I}_2\\ \frac{R_h}{L_g}\boldsymbol{I}_2 & -\frac{R_g+R_h}{L_g}\boldsymbol{I}_2-\omega_g\boldsymbol{J} & \frac{1}{L_g}\boldsymbol{I}_2\\ \frac{1}{C_h}\boldsymbol{I}_2 & -\frac{1}{C_h}\boldsymbol{I}_2 & -\omega_g\boldsymbol{J}\end{bmatrix}}^{=:\boldsymbol{A}_{\mathrm{lcl}}}\begin{pmatrix}\boldsymbol{i}_f^{dq}(t)\\ \boldsymbol{i}_g^{dq}(t)\\ \boldsymbol{u}_h^{dq}(t)\end{pmatrix}+\overbrace{\begin{bmatrix}\frac{1}{L_f}\boldsymbol{I}_2\\ \boldsymbol{O}_{2\times2}\\ \boldsymbol{O}_{2\times2}\end{bmatrix}}^{=:\boldsymbol{B}_{\mathrm{lcl}}}\boldsymbol{u}_f^{dq}(t)+\overbrace{\begin{bmatrix}\boldsymbol{O}_{2\times2}\\ -\frac{1}{L_g}\boldsymbol{I}_2\\ \boldsymbol{O}_{2\times2}\end{bmatrix}}^{=:\boldsymbol{E}_{\mathrm{lcl}}}\boldsymbol{u}_g^{dq}\\ &= \boldsymbol{A}_{\mathrm{lcl}}\boldsymbol{x}_{\mathrm{lcl}}(t)+\boldsymbol{B}_{\mathrm{lcl}}\boldsymbol{u}_f^{dq}(t)+\boldsymbol{E}_{\mathrm{lcl}}\boldsymbol{u}_g^{dq}\end{aligned} \tag{3.1}$$

with the state vector $\boldsymbol{x}_{\mathrm{lcl}}\in\mathbb{R}^6$, the system matrix $\boldsymbol{A}_{\mathrm{lcl}}\in\mathbb{R}^{6\times6}$, the input matrix $\boldsymbol{B}_{\mathrm{lcl}}\in\mathbb{R}^{6\times2}$ and the disturbance matrix $\boldsymbol{E}_{\mathrm{lcl}}\in\mathbb{R}^{6\times2}$. To achieve a steady-state accuracy of the grid side control, the LCL filter dynamics (3.1) are augmented by the dynamics of the integral state $\boldsymbol{x}_{i,\xi}^{dq}$ (in As), which are defined by

$$\frac{\mathrm{d}}{\mathrm{d}t}\boldsymbol{x}_{i,\xi}^{dq}(t)=\begin{pmatrix}i_{f,\mathrm{ref}}^{d}(t)-i_f^{d}(t)\\ i_{g,\mathrm{ref}}^{q}(t)-i_g^{q}(t)\end{pmatrix}=\begin{pmatrix}i_{f,\mathrm{ref}}^{d}(t)\\ i_{g,\mathrm{ref}}^{q}(t)\end{pmatrix}-\boldsymbol{C}_\xi\boldsymbol{x}_{\mathrm{lcl}}(t)\quad\text{with}\quad\boldsymbol{C}_\xi=\begin{bmatrix}1&0&0&0&0&0\\0&0&0&1&0&0\end{bmatrix}, \tag{3.2}$$

where $\boldsymbol{C}_\xi\in\mathbb{R}^{2\times6}$ is the output matrix and $\boldsymbol{x}_{i,\xi,0}^{dq}=\boldsymbol{x}_{i,\xi}^{dq}(0)$ is the initial value. For the further derivations, the following is imposed:

Assumption (A.3.3) *The dead time of the grid side converter (see* (2.59)*) is neglected, so that the filter voltage* $\boldsymbol{u}_f^{dq}$ *equals its reference, i.e.* $\boldsymbol{u}_f^{dq}(t)=\boldsymbol{u}_{f,\mathrm{ref}}^{dq}(t)$.

Then, by additionally considering (A.3.2), the augmented LCL filter dynamics result in

$$\begin{aligned}\overbrace{\frac{\mathrm{d}}{\mathrm{d}t}\begin{pmatrix}\boldsymbol{x}_{\mathrm{lcl}}(t)\\ \boldsymbol{x}_{i,\xi}^{dq}(t)\end{pmatrix}}^{=:\boldsymbol{x}_\xi(t)} &= \overbrace{\begin{bmatrix}\boldsymbol{A}_{\mathrm{lcl}} & \boldsymbol{O}_{6\times2}\\ -\boldsymbol{C}_\xi & \boldsymbol{O}_{2\times2}\end{bmatrix}}^{=:\boldsymbol{A}_\xi}\begin{pmatrix}\boldsymbol{x}_{\mathrm{lcl}}(t)\\ \boldsymbol{x}_{i,\xi}^{dq}(t)\end{pmatrix}+\overbrace{\begin{bmatrix}\boldsymbol{B}_{\mathrm{lcl}}\\ \boldsymbol{O}_{2\times2}\end{bmatrix}}^{=:\boldsymbol{B}_\xi}\boldsymbol{u}_{f,\mathrm{ref}}^{dq}(t)+\overbrace{\begin{bmatrix}\boldsymbol{E}_{\mathrm{lcl}} & \boldsymbol{O}_{6\times2}\\ \boldsymbol{O}_{2\times2} & \boldsymbol{I}_2\end{bmatrix}}^{=:\boldsymbol{E}_\xi}\underbrace{\begin{pmatrix}\boldsymbol{u}_g^{dq}\\ i_{f,\mathrm{ref}}^{d}(t)\\ i_{g,\mathrm{ref}}^{q}(t)\end{pmatrix}}_{=:\boldsymbol{d}_\xi(t)}\\ &= \boldsymbol{A}_\xi\boldsymbol{x}_\xi(t)+\boldsymbol{B}_\xi\boldsymbol{u}_{f,\mathrm{ref}}^{dq}(t)+\boldsymbol{E}_\xi\boldsymbol{d}_\xi(t)\ ,\ \boldsymbol{x}_\xi(0)=\boldsymbol{x}_{\xi,0}\end{aligned} \tag{3.3}$$

with the augmented state vector $\boldsymbol{x}_\xi\in\mathbb{R}^8$, the augmented disturbance vector $\boldsymbol{d}_\xi\in\mathbb{R}^4$, the augmented system matrix $\boldsymbol{A}_\xi\in\mathbb{R}^{8\times8}$, the augmented input matrix $\boldsymbol{B}_\xi\in\mathbb{R}^{8\times2}$ and the augmented disturbance matrix $\boldsymbol{E}_\xi\in\mathbb{R}^{8\times4}$.

In the already published paper [18], (3.3) is the basis for an integral state-feedback controller design by using the continuous linear quadratic regulator (LQR) theory[45]. Sec. 3.2.2.1 motivates that this controller design is not feasible for the implemented experimental setup due to the high resonance frequency f_{lcl} of the LCL filter with respect to the small sampling frequency f_{dis} of the dSpace real-time system. Instead, (3.3) first has to be discretized and then, based on the DLQR theory, the integral state-feedback controller can be designed. This is done in

[45] Therein, the filter current i_f^q is used as control variable instead of the grid current i_g^q, but the control strategy is the same.

Sec. 3.2.2.2. Simulation results in Sec. 3.2.2.3 verify the excellent control performance of the discrete controller.

Remark (R.3.5) *The experimental setup at the test-bench (see Fig. 3.4) requires a controlled DC-link voltage u_d to be able to control the grid side. Otherwise, the grid side converter in combination with the corresponding space vector modulation cannot generate the filter voltage reference $\boldsymbol{u}_{f,\mathrm{ref}}^{dq}$. Consequently, first only simulation results for the grid side current control are presented in Sec. 3.2.2.3 to validate its control performance. After the design of the DC-link voltage control (see Sec. 3.2.3), measurements of the overall grid side control will prove that the simulation results (almost) exactly match with the measurement results.*

3.2.2.1 Continuous integral state-feedback controller design

To allow for controlling the augmented LCL filter dynamics (3.3), they must be controllable. In Sec. C.1 it is derived that the following condition must be fulfilled:

Condition (C.3.1) *System* (3.3) *is controllable, if the controllability matrix $\boldsymbol{S}_\xi \in \mathbb{R}^{8\times 8}$ has full rank, i.e.* $\mathrm{rank}(\boldsymbol{S}_\xi) := \mathrm{rank}\left[\boldsymbol{B}_\xi \;\; \boldsymbol{A}_\xi\boldsymbol{B}_\xi \;\; \boldsymbol{A}_\xi^2\boldsymbol{B}_\xi \;\; \boldsymbol{A}_\xi^3\boldsymbol{B}_\xi\right] = 8$. *This is ensured, if and only if the following holds:*

$$L_g - R_g R_h C_h \neq 0 \quad \textit{and} \quad \frac{1}{\omega_g^2 C_h} \neq L_g - R_h C_h \left(R_g + R_h\right) . \tag{3.4}$$

If the damping resistor R_h is zero, i.e. $R_h = 0$, (C.3.1) simplifies to $\omega_g \neq \sqrt{L_g C_h}^{-1}$, such that ω_g must not be equivalent to the resonance frequency of the $L_g C_h$-circuit. Clearly, a functional LCL filter (like the implemented one at the test-bench) satisfies this condition. Hence, the control law of the integral state-feedback controller is given by

$$\boldsymbol{u}_{f,\mathrm{ref}}^{dq}(t) = -\left[\boldsymbol{K}_{x,\xi} \quad \boldsymbol{K}_{i,\xi}\right] \boldsymbol{x}_\xi(t) := -\boldsymbol{K}_\xi \boldsymbol{x}_\xi(t) \tag{3.5}$$

with the overall feedback matrix $\boldsymbol{K}_\xi \in \mathbb{R}^{2\times 8}$, which consists of the state-feedback matrix $\boldsymbol{K}_{x,\xi} \in \mathbb{R}^{2\times 6}$ and the integral-feedback matrix $\boldsymbol{K}_{i,\xi} \in \mathbb{R}^{2\times 2}$. Applying the control law (3.5) to the augmented LCL filter dynamics (3.3) yields the continuous-time closed-loop system of the grid side current controller:

$$\frac{\mathrm{d}}{\mathrm{d}t}\boldsymbol{x}_\xi(t) = \Big(\boldsymbol{A}_\xi - \boldsymbol{B}_\xi \boldsymbol{K}_\xi\Big)\boldsymbol{x}_\xi(t) + \boldsymbol{E}_\xi \boldsymbol{d}_\xi(t) \;,\; \boldsymbol{x}_\xi(0) = \boldsymbol{x}_{\xi,0} \,. \tag{3.6}$$

The overall feedback matrix $\boldsymbol{K}_\xi$ is determined by the LQR theory (for details see e.g. [133]). Therefore, the two weighting matrices $0 < \boldsymbol{Q}_\xi = \boldsymbol{Q}_\xi^\top \in \mathbb{R}^{8\times 8}$ and $0 < \boldsymbol{R}_\xi = \boldsymbol{R}_\xi^\top \in \mathbb{R}^{2\times 2}$ and the cost function J_ξ are invoked:

$$J_\xi\left(\boldsymbol{x}_\xi(t), \boldsymbol{u}_{f,\mathrm{ref}}^{dq}(t)\right) = \int_0^\infty \Big(\left(\boldsymbol{x}_\xi(t)\right)^\top \boldsymbol{Q}_\xi \boldsymbol{x}_\xi(t) + \left(\boldsymbol{u}_{f,\mathrm{ref}}^{dq}(t)\right)^\top \boldsymbol{R}_\xi \boldsymbol{u}_{f,\mathrm{ref}}^{dq}(t)\Big)\,\mathrm{d}t \,. \tag{3.7}$$

The minimization of the cost function J_ξ yields the optimal feedback matrix $\boldsymbol{K}_\xi = \boldsymbol{R}_\xi^{-1}\boldsymbol{B}_\xi^\top \boldsymbol{P}_\xi$, where $0 < \boldsymbol{P}_\xi = \boldsymbol{P}_\xi^\top \in \mathbb{R}^{8\times 8}$ solves the Riccati equation[46]

$$\boldsymbol{A}_\xi^\top \boldsymbol{P}_\xi + \boldsymbol{P}_\xi \boldsymbol{A}_\xi - \boldsymbol{P}_\xi \boldsymbol{B}_\xi \boldsymbol{R}_\xi^{-1} \boldsymbol{B}_\xi^\top \boldsymbol{P}_\xi + \boldsymbol{Q}_\xi = \boldsymbol{O}_{8\times 8} \,. \tag{3.8}$$

[46] In Matlab/Simulink, the command "LQR($\boldsymbol{A}_\xi, \boldsymbol{B}_\xi, \boldsymbol{Q}_\xi, \boldsymbol{R}_\xi, \boldsymbol{O}_{8\times 2}$)" solves the Riccati equation (3.8) and gives the optimal feedback matrix $\boldsymbol{K}_\xi$.

description	symbols & values with unit
maximum values of the grid side weighting matrices	
filter current	$i_{f,\max} = 30\,\mathrm{A}$
grid current	$i_{g,\max} = 30\,\mathrm{A}$
capacitance voltage	$u_{h,\max} = \hat{u}_g = 400\sqrt{\frac{2}{3}}\,\mathrm{V}$
integral state	$x_{i,\xi,\max} = 25\,\mathrm{mAs}$
filter voltage	$u_{f,\max} = \hat{u}_g = 400\sqrt{\frac{2}{3}}\,\mathrm{V}$
weighting factors of the grid side weighting matrices	
control error (standard case)	$\eta_{i,\xi} = 10$
weighting between states and input	$\eta_\xi = 0.5$

Table 3.3: *Design parameters for the integral state-feedback controller of the grid side currents.*

The two weighting matrices $\boldsymbol{Q}_\xi$ and $\boldsymbol{R}_\xi$ are defined on the basis of Bryson's rule (see [134]), but with one significant extension: Because the grid side current control must adjust the control error $(i^d_{f,\mathrm{ref}}\ i^q_{g,\mathrm{ref}})^\top - (i^d_f\ i^q_g)^\top$ to zero very quickly, the weighting factor $\eta_{i,\xi}$ (in 1) is introduced, which can prioritize this target. With that, the two weighting matrices $\boldsymbol{Q}_\xi$ and $\boldsymbol{R}_\xi$ result in

$$\boldsymbol{Q}_\xi = \eta_\xi \operatorname{diag}\left(\frac{1}{i^2_{f,\max}}\boldsymbol{I}_2\,,\ \frac{1}{i^2_{g,\max}}\boldsymbol{I}_2\,,\ \frac{1}{u^2_{h,\max}}\boldsymbol{I}_2\,,\ \frac{\eta_{i,\xi}}{x^2_{i,\xi,\max}}\boldsymbol{I}_2\right) \quad \text{and} \quad \boldsymbol{R}_\xi = \frac{1-\eta_\xi}{u^2_{f,\max}}\boldsymbol{I}_2\,, \tag{3.9}$$

where the maximally acceptable (a) filter current $i_{f,\max}$, (b) grid current $i_{g,\max}$, (c) capacitance voltage $u_{h,\max}$, (d) integral state $x_{i,\xi,\max}$ and (e) filter voltage $u_{f,\max}$ normalize the influences of their corresponding quantity onto the cost function J_ξ. Moreover, the factor $0<\eta_\xi<1$ weights the impact between the states $\boldsymbol{x}_\xi$ and the input $\boldsymbol{u}^{dq}_{f,\mathrm{ref}}$ onto the cost function J_ξ. Tab. 3.3 lists the maximally acceptable values (a)–(e) as well as the two weighting factors $\eta_{i,\xi}$ and η_ξ.

Fig. 3.5 presents the simulation result of the integral state-feedback control of the grid side currents, which is based on the continuous linear quadratic regulator (LQR) design (3.5) to (3.9). While the physical system (3.1) runs with step time $t_{\mathrm{sim}} = 5\,\mu\mathrm{s}$, the controller was sampled by the dSpace sampling frequency $f_{\mathrm{dis}} = 4\,\mathrm{kHz}$. The two plots depict (i) the —— simulated filter current i^d_f and grid current i^q_g and (ii) their corresponding - - - references $i^d_{f,\mathrm{ref}}$ and $i^q_{g,\mathrm{ref}}$, respectively. Obviously, the controller is unstable during the whole simulation and thus, the controller design (3.5) to (3.9) is not able to control the grid side currents. The reason—as already mentioned before—is the small ratio $\frac{f_{\mathrm{dis}}}{f_{\mathrm{lcl}}} \approx 3$ between the sampling frequency f_{dis} of the dSpace real-time system and the LCL filter's resonance frequency f_{lcl}. A quasi-continuous controller design is not feasible for the experimental setup at the test-bench.

3.2.2.2 Discrete integral state-feedback controller design

Instead of the quasi-continuous controller design of Sec. 3.2.2.1, the integral state-feedback controller for the grid side currents is designed based on the DLQR theory.[47] Therefor, the augmented LCL filter dynamics (3.3) are discretized via the step invariance method (see e.g. [135]) with the discretization time $t_{\mathrm{dis}} = \frac{1}{f_{\mathrm{dis}}}$ (in s). In combination with the taylor series (see [136]), the discrete system matrix $\boldsymbol{A}_{\xi,k} \in \mathbb{R}^{8\times 8}$ and the discrete input matrix $\boldsymbol{B}_{\xi,k} \in \mathbb{R}^{8\times 2}$ of the augmented

[47] Most parts of Sec. 3.2.2.2 and Sec. 3.2.2.3 have already been published in [17].

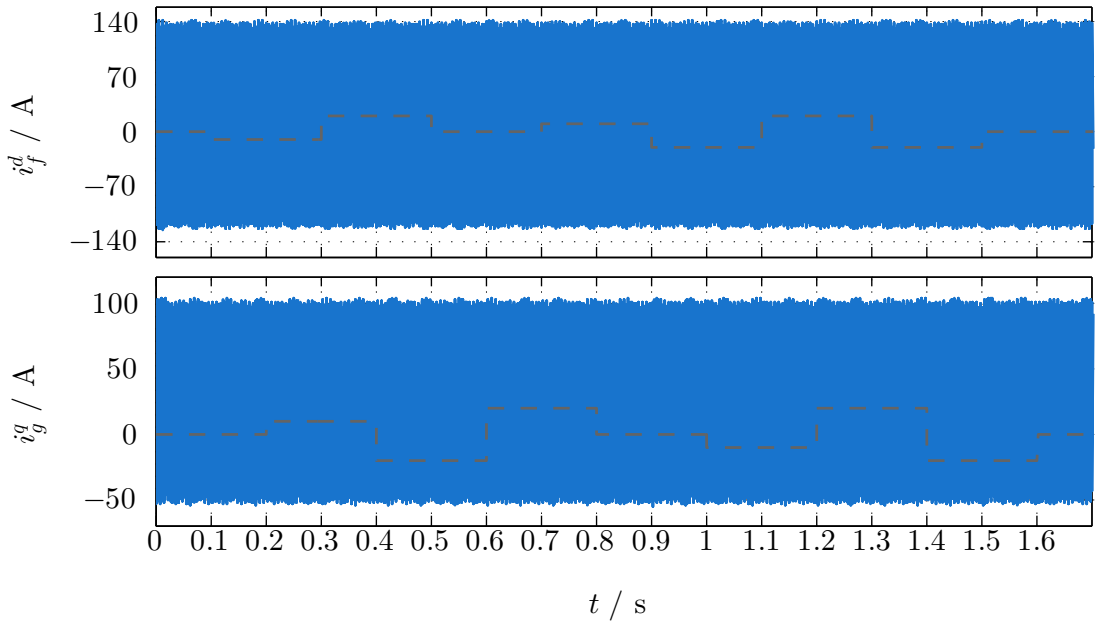

Figure 3.5: *Reference tracking of the grid side currents for a continuous integral state-feedback controller design:* — *simulated quantities and* - - - *reference currents* $i^d_{f,\mathrm{ref}}$ *and* $i^q_{g,\mathrm{ref}}$.

LCL filter dynamics are given by (see [136])[48]

$$\boldsymbol{A}_{\xi,k} = e^{\boldsymbol{A}_\xi t_{\mathrm{dis}}} = \boldsymbol{I}_8 + \boldsymbol{A}_\xi t_{\mathrm{dis}} \sum_{\nu=0}^{\infty} \boldsymbol{A}_\xi^\nu \frac{t_{\mathrm{dis}}^\nu}{(\nu+1)!} \quad \text{and} \quad \boldsymbol{B}_{\xi,k} = \boldsymbol{A}_\xi^{-1} \left(e^{\boldsymbol{A}_\xi t_{\mathrm{dis}}} - \boldsymbol{I}_8 \right) \boldsymbol{B}_\xi \,. \tag{3.10}$$

According to [135], a reasonable and sufficient approximation of the discrete system matrix $\boldsymbol{A}_{\xi,k}$ only considers the first nine terms of the sum in (3.10), i.e. the following discretization rule is used:

$$\boldsymbol{Z}_\xi = t_{\mathrm{dis}} \sum_{\nu=0}^{8} \boldsymbol{A}_\xi^\nu \frac{t_{\mathrm{dis}}^\nu}{(\nu+1)!} \quad \Rightarrow \quad \boldsymbol{A}_{\xi,k} = \boldsymbol{I}_8 + \boldsymbol{Z}_\xi \boldsymbol{A}_\xi \;,\; \boldsymbol{B}_{\xi,k} = \boldsymbol{Z}_\xi \boldsymbol{B}_\xi \;,\; \boldsymbol{E}_{\xi,k} = \boldsymbol{Z}_\xi \boldsymbol{E}_\xi \tag{3.11}$$

with the discretization matrix $\boldsymbol{Z}_\xi \in \mathbb{R}^{8\times 8}$. Consequently, the discrete form of the augmented LCL filter dynamics in (3.3) results in

$$\boldsymbol{x}_\xi[k+1] = \boldsymbol{A}_{\xi,k} \boldsymbol{x}_\xi[k] + \boldsymbol{B}_{\xi,k} \boldsymbol{u}^{dq}_{f,\mathrm{ref}}[k] + \boldsymbol{E}_{\xi,k} \boldsymbol{d}_\xi[k] \;,\; \boldsymbol{x}_\xi[0] = \boldsymbol{x}_{\xi,0} \,. \tag{3.12}$$

By defining the overall discrete feedback matrix $\boldsymbol{K}_{\xi,k} \in \mathbb{R}^{2\times 8}$, which splits up into the discrete state-feedback matrix $\boldsymbol{K}_{x,\xi,k} \in \mathbb{R}^{2\times 6}$ and the discrete integral-feedback matrix $\boldsymbol{K}_{i,\xi,k} \in \mathbb{R}^{2\times 2}$, the control law of the discrete integral state-feedback controller is given by

$$\boldsymbol{u}^{dq}_{f,\mathrm{ref}}[k] = -\begin{bmatrix} \boldsymbol{K}_{x,\xi,k} & \boldsymbol{K}_{i,\xi,k} \end{bmatrix} \boldsymbol{x}_\xi[k] := -\boldsymbol{K}_{\xi,k} \boldsymbol{x}_\xi[k] \,. \tag{3.13}$$

Applying the control law (3.13) to the system dynamics (3.12) yields the discrete-time closed-

[48] In [45] it is explained that the discrete disturbance matrix $\boldsymbol{E}_{\xi,k} \in \mathbb{R}^{8\times 2}$ of the augmented LCL filter dynamics can be calculated in the same way as the discrete input matrix $\boldsymbol{B}_{\xi,k}$, i.e. $\boldsymbol{E}_{\xi,k} = \boldsymbol{A}_\xi^{-1} \left(e^{\boldsymbol{A}_\xi t_{\mathrm{dis}}} - \boldsymbol{I}_8 \right) \boldsymbol{E}_\xi$.

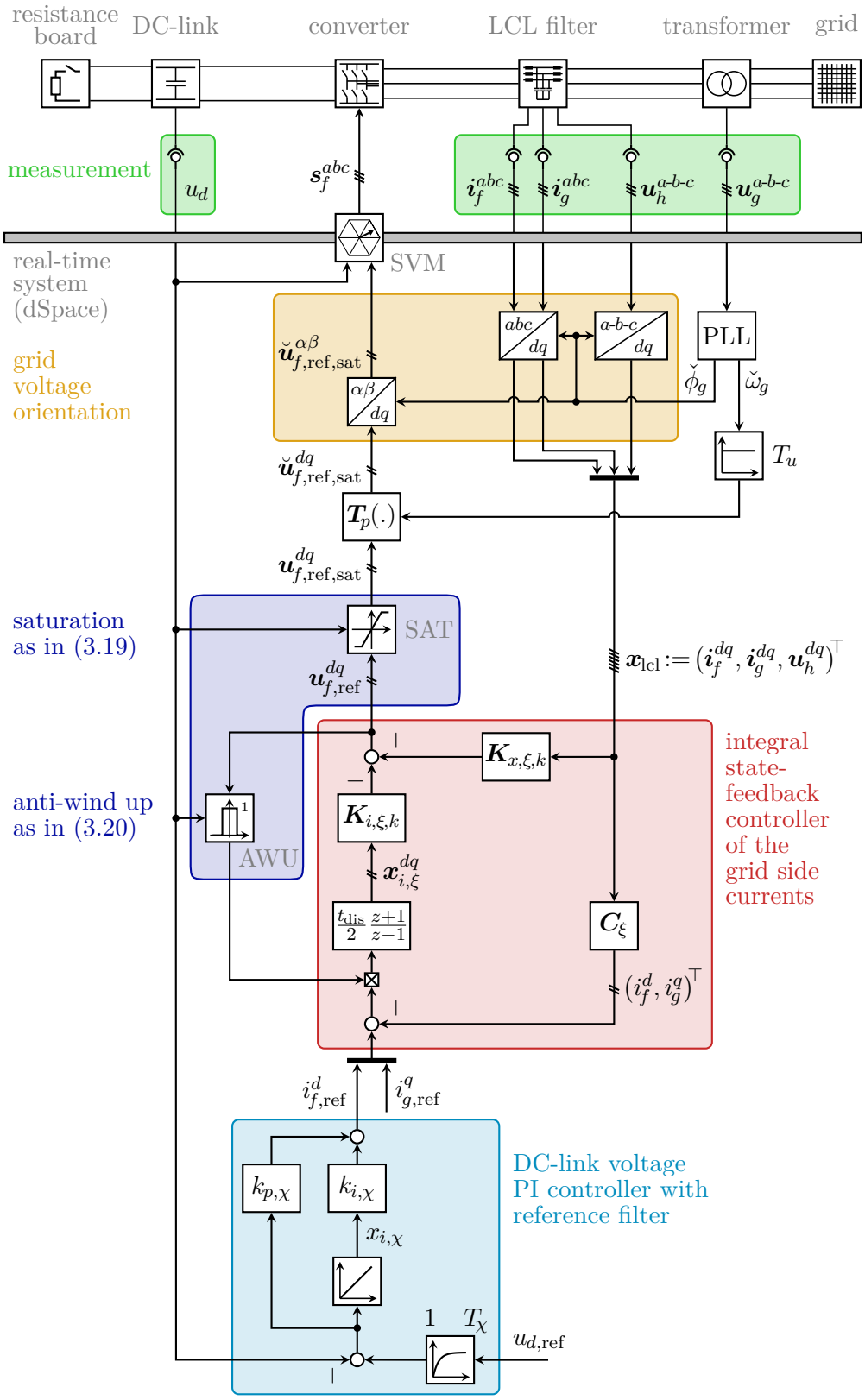

Figure 3.6: *Block diagram of the grid side experimental setup and its holistic control strategy.*

loop system of the grid side current controller

$$\boldsymbol{x}_{\xi}[k+1] = \Big(\boldsymbol{A}_{\xi,k} - \boldsymbol{B}_{\xi,k}\boldsymbol{K}_{\xi,k}\Big)\boldsymbol{x}_{\xi}[k] + \boldsymbol{E}_{\xi,k}\boldsymbol{d}_{\xi}[k]\ ,\ \boldsymbol{x}_{\xi}[0] = \boldsymbol{x}_{\xi,0}\,. \tag{3.14}$$

To determine the overall discrete feedback matrix $\boldsymbol{K}_{\xi,k}$, the DLQR theory is invoked (for details see e.g. [137]). By choosing the following cost function:

$$J_{\xi,k}(\boldsymbol{x}_{\xi}[k], \boldsymbol{u}^{dq}_{f,\mathrm{ref}}[k]) = \sum_{k=0}^{\infty}\Big(\big(\boldsymbol{x}_{\xi}[k]\big)^{\top}\boldsymbol{Q}_{\xi,k}\boldsymbol{x}_{\xi}[k] + \big(\boldsymbol{u}^{dq}_{f,\mathrm{ref}}[k]\big)^{\top}\boldsymbol{R}_{\xi,k}\boldsymbol{u}^{dq}_{f,\mathrm{ref}}[k]\Big) \tag{3.15}$$

with the weighting matrices $0 < \boldsymbol{Q}_{\xi,k} = \boldsymbol{Q}^{\top}_{\xi,k} \in \mathbb{R}^{8\times 8}$ and $0 < \boldsymbol{R}_{\xi,k} = \boldsymbol{R}^{\top}_{\xi,k} \in \mathbb{R}^{2\times 2}$, the minimization of the cost function $J_{\xi,k}$ results in the optimal feedback matrix

$$\boldsymbol{K}_{\xi,k} = \Big(\boldsymbol{R}_{\xi,k} + \big(\boldsymbol{B}_{\xi,k}\big)^{\top}\boldsymbol{P}_{\xi,k}\boldsymbol{B}_{\xi,k}\Big)^{-1}\big(\boldsymbol{B}_{\xi,k}\big)^{\top}\boldsymbol{P}_{\xi,k}\boldsymbol{A}_{\xi,k} \tag{3.16}$$

where $0 < \boldsymbol{P}_{\xi,k} = \big(\boldsymbol{P}_{\xi,k}\big)^{\top} \in \mathbb{R}^{8\times 8}$ solves the discrete-time algebraic Riccati equation[49]

$$\boldsymbol{P}_{\xi,k} - \big(\boldsymbol{A}_{\xi,k}\big)^{\top}\boldsymbol{P}_{\xi,k}\boldsymbol{A}_{\xi,k} + \big(\boldsymbol{A}_{\xi,k}\big)^{\top}\boldsymbol{P}_{\xi,k}\boldsymbol{B}_{\xi,k}\Big(\boldsymbol{R}_{\xi,k} + \big(\boldsymbol{B}_{\xi,k}\big)^{\top}\boldsymbol{P}_{\xi,k}\boldsymbol{B}_{\xi,k}\Big)^{-1}\big(\boldsymbol{B}_{\xi,k}\big)^{\top}\boldsymbol{P}_{\xi,k}\boldsymbol{A}_{\xi,k} - \boldsymbol{Q}_{\xi,k} = \boldsymbol{O}_{8\times 8}\,. \tag{3.17}$$

Again, as the weighting matrices $\boldsymbol{Q}_{\xi}$ and $\boldsymbol{R}_{\xi}$ for the continuous case (see (3.9)), the equivalent discrete weighting matrices $\boldsymbol{Q}_{\xi,k}$ and $\boldsymbol{R}_{\xi,k}$ are defined by

$$\boldsymbol{Q}_{\xi,k} = \eta_{\xi}\,\mathrm{diag}\left(\frac{1}{i^2_{f,\max}}\boldsymbol{I}_2\,,\ \frac{1}{i^2_{g,\max}}\boldsymbol{I}_2\,,\ \frac{1}{u^2_{h,\max}}\boldsymbol{I}_2\,,\ \frac{\eta_{i,\xi}}{x^2_{i,\xi,\max}}\boldsymbol{I}_2\right) \quad \text{and} \quad \boldsymbol{R}_{\xi,k} = \frac{1-\eta_{\xi}}{u^2_{f,\max}}\boldsymbol{I}_2\,. \tag{3.18}$$

Remark (R.3.6) *The DLQR theory* (3.15) *to* (3.18) *requires that the pair* $(\boldsymbol{A}_{\xi,k}, \boldsymbol{B}_{\xi,k})$ *is stabilizable. Due to the complexity of the discrete system matrix* $\boldsymbol{A}_{\xi,k}$ *(see* (3.11)*), an analytical expression for this condition as in (C.3.1) is not feasible.*

To enhance the control performance of the integral state-feedback controller for the grid side currents, it is extended (i) by a reference voltage saturation (SAT) and (ii) by an additional anti-wind up (AWU). The principles of both SAT and AWU are adopted from [138]. The reason for the two extensions is the limited filter voltage $\boldsymbol{u}^{dq}_{f}$. As already noted in (A.2.10), a rotation of the filter voltage $\boldsymbol{u}^{dq}_{f}$ with constant vector length $\left\|\boldsymbol{u}^{dq}_{f}\right\|$ in the $\alpha\beta$-plane is only possible for $\left\|\boldsymbol{u}^{dq}_{f}\right\| \leq \frac{\sqrt{3}k_c u_d}{2}$ (see Sec. 2.2.4). The saturation function $h_{i,\xi}$ takes this restriction into account and limits the reference filter voltage $\boldsymbol{u}^{dq}_{f,\mathrm{ref}}$ as follows:

$$\boldsymbol{u}^{dq}_{f,\mathrm{ref,sat}}[k] = h_{i,\xi}(\boldsymbol{u}^{dq}_{f,\mathrm{ref}}, u_d)\boldsymbol{u}^{dq}_{f,\mathrm{ref}}[k] \quad \text{with} \quad h_{i,\xi}(\boldsymbol{u}^{dq}_{f,\mathrm{ref}}, u_d) = \begin{cases} \frac{\sqrt{3}k_c u_d[k]}{2\left\|\boldsymbol{u}^{dq}_{f,\mathrm{ref}}[k]\right\|} & \text{, if } \left\|\boldsymbol{u}^{dq}_{f,\mathrm{ref}}[k]\right\| > \frac{\sqrt{3}k_c u_d[k]}{2} \\ 1 & \text{, if } \left\|\boldsymbol{u}^{dq}_{f,\mathrm{ref}}[k]\right\| \leq \frac{\sqrt{3}k_c u_d[k]}{2}\,. \end{cases} \tag{3.19}$$

Moreover, the simulation results in Sec. 3.2.2.3 will show, that integral windup effects may cause overshoots in the reference current tracking. To compensate for that, the (discrete) integration

[49] In Matlab/Simulink, the command "dlqr($\boldsymbol{A}_{\xi,k}, \boldsymbol{B}_{\xi,k}, \boldsymbol{Q}_{\xi,k}, \boldsymbol{R}_{\xi,k}, \boldsymbol{O}_{8\times 2}$)" solves the Riccati equation (3.17) and outputs the optimal feedback matrix $\boldsymbol{K}_{\xi,k}$.

of $\boldsymbol{x}_{i,\xi}^{dq}$ in (3.12) will be paused, if the following holds:

$$\left\|\boldsymbol{u}_{f,\mathrm{ref}}^{dq}[k]\right\| > \frac{\sqrt{3}k_c u_d[k]}{2} \quad \Longrightarrow \quad \boldsymbol{x}_{i,\xi}^{dq}[k+1] = \boldsymbol{x}_{i,\xi}^{dq}[k]\,. \tag{3.20}$$

Fig. 3.6 depicts the overall control strategy of the grid side current control and illustrates its interaction with the physical components at the test-bench. The — measurement quantities are fed to the dSpace real-time system. By means of the PLL and the transformations of Clarke and Park, the three-phase measurements are transformed into the — *grid voltage oriented dq*-reference frame, which yields the state vector $\boldsymbol{x}_{\mathrm{lcl}}$ of the LCL filter. The state vector $\boldsymbol{x}_{\mathrm{lcl}}$ and the references $i_{f,\mathrm{ref}}^{d}$ and $i_{g,\mathrm{ref}}^{q}$ of the grid side currents are applied to the implemented integral state-feedback controller with control law (3.13). In the case of of a reference filter voltage $\left\|\boldsymbol{u}_{f,\mathrm{ref}}^{dq}\right\| > \frac{\sqrt{3}k_c u_d}{2}$, (i) the — SAT limits the reference filter voltage to $\boldsymbol{u}_{f,\mathrm{ref,sat}}^{dq}$ (see (3.19)) and (ii) the — AWU pauses the integration of $\boldsymbol{x}_{i,\xi}^{dq}$ (see (3.20)). As described in Sec. 2.2.4 and illustrated in Fig. 2.20, the space vector modulation—in combination with Park's and Clarke's transformation—generates the switching vector $\boldsymbol{s}_f^{abc}$ based on the reference filter voltage $\boldsymbol{u}_{f,\mathrm{ref,sat}}^{dq}$. To close the loop, the switching vector $\boldsymbol{s}_f^{abc}$ is applied to the grid side converter.

Remark (R.3.7) *The grid side current control needs to be designed very aggressively. Hence, it is important for the integrator of $\boldsymbol{x}_{i,\xi}^{dq}$ to be as stable as possible. Therefor, the most stable standard discrete-time integrator of Matlab/Simulink is used (see Fig. 3.6). This integrator uses the integration method "trapezoidal" based on the bilinear transform (also known as Tustin's method, for details see [136]).*

3.2.2.3 Reference tracking of the grid side currents

This section analyzes the control performance of the discrete integral state-feedback controller for the grid side currents via simulation results. The following four experiments are investigated:

(ξ.1) the — implemented control strategy which is composed of: (a) the control law (3.13), where the overall feedback matrix $\boldsymbol{K}_{\xi,k}$ results from the DLQR theory (3.15) to (3.18), (b) the grid side parameters of Tab. 3.2 and the design parameters of Tab. 3.3 and (c) the additional SAT and AWU methods of (3.19) and (3.20) respectively.

(ξ.2) the impacts of SAT and AWU are shown. Therefor, one simulation uses only SAT but not AWU. Another simulation utilizes neither SAT nor AWU.

(ξ.3) the influences of the weighting factor $\eta_{i,\xi}$ are illustrated by carrying out a simulation with reduced weighting factor $\eta_{i,\xi} = 1 < 10$.

(ξ.4) at the test-bench, the measurements can only be saved with the sampling frequency f_{dis}. For the purpose of comparability, this sampling frequency f_{dis} is also chosen to save the simulation results. In this experiment, the sampling frequency is increased to $f_{\mathrm{sim}} = \frac{1}{t_{\mathrm{sim}}}$ (in Hz).

For all four Experiments (ξ.1)–(ξ.4), the simulation setup exhibits a fixed DC-link voltage $u_d = 750\,\mathrm{V}$. Fig. 3.7 presents the simulation results for — Experiment (ξ.1). The control objective is the tracking of the - - - references $i_{f,\mathrm{ref}}^{d}$ and $i_{g,\mathrm{ref}}^{q}$ of the grid side currents. The plots depict the LCL filter states from top to bottom: (a) the filter current $\boldsymbol{i}_f^{dq}$, (b) the grid current $\boldsymbol{i}_g^{dq}$ and (c) the capacitance voltage $\boldsymbol{u}_h^{dq}$. In the first and in the fourth plot, it can be seen, that the proposed control strategy of Experiment (ξ.1) yields an excellent control performance. The grid side

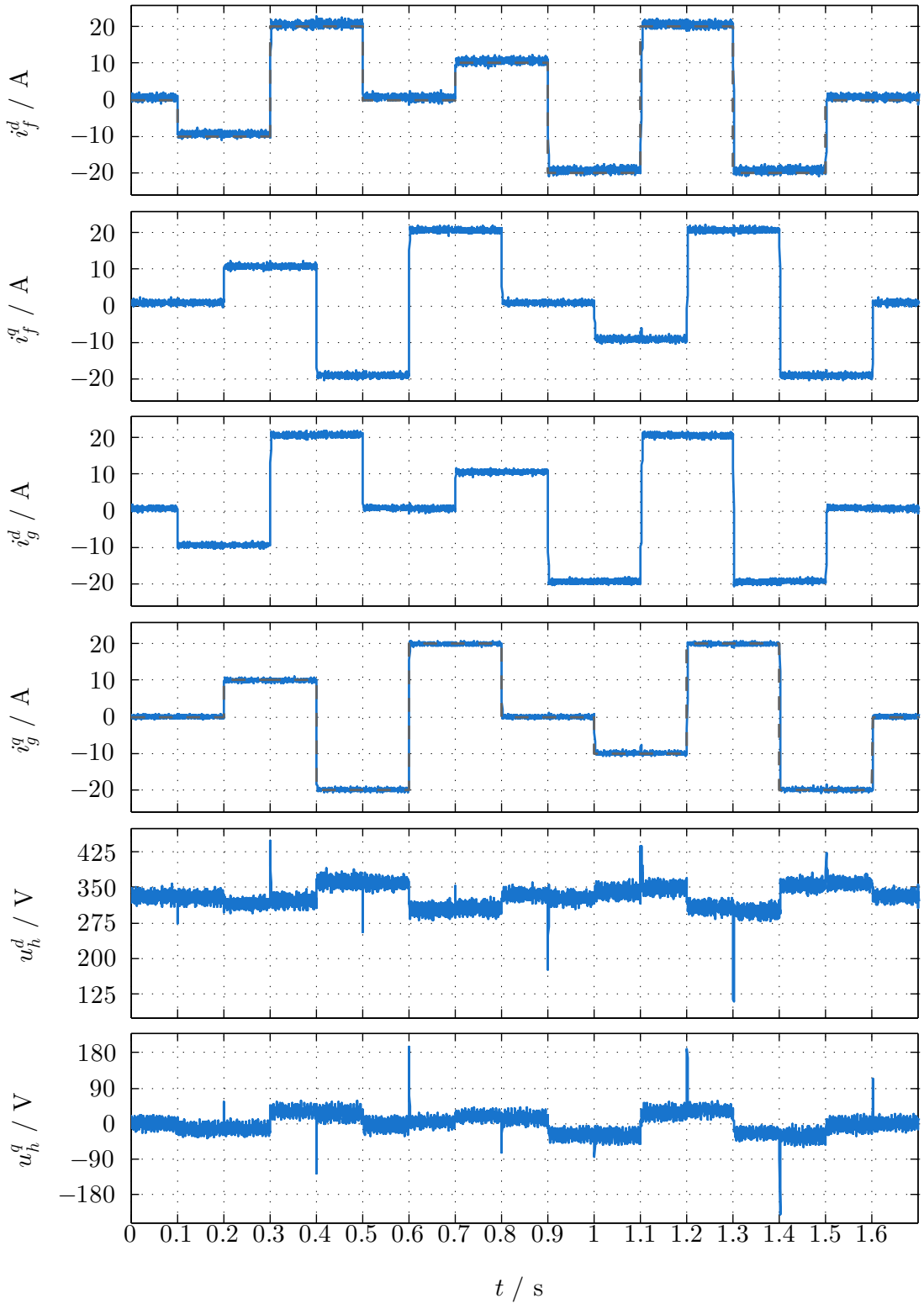

Figure 3.7: *Experiment (ξ.1):* — *simulated quantities and* - - - *reference currents* $i^d_{f,\mathrm{ref}}$ *and* $i^q_{g,\mathrm{ref}}$.

currents i_f^d and i_g^q track their corresponding references $i_{f,\mathrm{ref}}^d$ and $i_{g,\mathrm{ref}}^q$ very quickly and precisely. Moreover, the extension of the LCL filter dynamics by the integral state $\boldsymbol{x}_{i,\xi}^{dq}$ guarantees steady-state accuracy. Further on, Fig. 3.7 shows that reference jumps in the orthogonal component do not disturb the control of the grid side currents i_f^d and i_g^q. Only at $t=1.1\,\mathrm{s}$, a huge jump of 40 A in the reference current $i_{f,\mathrm{ref}}^d$ affects the grid current i_g^q (which is hardly noticeable). The capacitance voltages u_h^d and u_h^q feature high peaks in reaction to the reference jumps in the current component i_f^d and i_g^q, respectively.
In Fig. 3.8, the results for Experiment ($\xi.2$) are shown. The standard —— Experiment ($\xi.1$) is compared to the following two simulation setups: —— depicts the simulation results, where AWU is not in use and —— illustrates the impacts onto the grid side current control, if both SAT and AWU are deactivated[50]. The plots picture from top to bottom the following quantities: (a) the d-component i_f^d of the filter current, (b) the q-component i_g^q of the grid current, (c) the saturated reference voltage $\boldsymbol{u}_{f,\mathrm{ref,sat}}^{dq}$ and (d) its norm $\left\|\boldsymbol{u}_{f,\mathrm{ref,sat}}^{dq}\right\|$. The simulation results highlight the following characteristics:

- both SAT (in —— and ——) and AWU (in ——) only are active, when the reference filter current $i_{f,\mathrm{ref}}^d$ exhibits large positive jumps. Otherwise, the three simulations of ($\xi.2$) result in the same control behavior.
- if AWU is deactivated (in —— and ——), this leads to large overshoots in the filter current i_f^d in reaction to the positive jumps of its reference $i_{f,\mathrm{ref}}^d$. For these time instants (see e.g. at $t=1.1\,\mathrm{s}$), also the control performance of the grid current i_g^q is affected negatively.
- in the fifth plot of Fig. 3.8, SAT (in —— and ——) restricts the norm $\left\|\boldsymbol{u}_{f,\mathrm{ref,sat}}^{dq}\right\|$ of the saturated reference voltage to its - - - limit $\frac{\sqrt{3}k_c u_d}{2} \approx 433\,\mathrm{V}$. The deactivation of SAT (in ——) gives unrealistic references $\boldsymbol{u}_{f,\mathrm{ref,sat}}^{dq}$.

Hence, both SAT and AWU comply with their tasks and enhance the control performance significantly. Fig. 3.9 shows the same simulation results of Experiment ($\xi.2$) again (as in Fig. 3.8), but zooms in at the certain time instants $t=0.3\,\mathrm{s}$, $t=0.6\,\mathrm{s}$, $t=1.1\,\mathrm{s}$ and $t=1.3\,\mathrm{s}$. At $t=0.6\,\mathrm{s}$ and $t=1.3\,\mathrm{s}$, both SAT and AWU do not interfere and, hence, all three simulations match (almost) exactly. Moreover, the excellent control performance of the designed grid side current controller is highlighted, since reference jumps of 40 A are adjusted within 2 ms for the grid current i_g^q at $t=0.6\,\mathrm{s}$ and for the filter current i_f^d at $t=1.3\,\mathrm{s}$. The time instants $t=0.3\,\mathrm{s}$ and $t=1.1\,\mathrm{s}$ illustrate the positive impacts of SAT and AWU onto the control performance in detail, especially the 40 A reference jump in the filter current $i_{f,\mathrm{ref}}^d$ at $t=1.1\,\mathrm{s}$ shows their necessity. Therein, the standard —— Experiment ($\xi.1$) shows a very good tracking of the reference filter current $i_{f,\mathrm{ref}}^d$, where the 40 A reference jump is adjusted within $<5\,\mathrm{ms}$ without any overshoots. Also the control of the grid current i_g^q is not affected substantially and the saturated reference filter voltage $\boldsymbol{u}_{f,\mathrm{ref,sat}}^{dq}$ has realistic values. In contrast, the simulations of —— and —— exhibit overshoots of 15 A in the filter current i_f^d because of windup effects. These overshoots are not acceptable regarding (a) the high peak currents of 35 A and (b) the time delay in adjusting the reference filter current $i_{f,\mathrm{ref}}^d$. Moreover, the —— simulation without SAT causes a reference filter voltage $\boldsymbol{u}_{f,\mathrm{ref,sat}}^{dq}$, which is impossible to generate and strongly disturbs the control of the grid current i_g^q.
Fig. 3.10 and Fig. 3.11 show the results of Experiment ($\xi.3$). Therein, the standard —— Experiment ($\xi.1$) with weighting factor $\eta_{h,\xi}=10$ is compared to a simulation with —— reduced weighting factor $\eta_{h,\xi}=1$. Fig. 3.10 pictures the d-component i_f^d of the filter current, the q-component i_g^q of

[50] If SAT is deactivated (in ——), then the saturated reference voltage $\boldsymbol{u}_{f,\mathrm{ref,sat}}^{dq}$ equals the unsaturated one, i.e. $\boldsymbol{u}_{f,\mathrm{ref,sat}}^{dq}=\boldsymbol{u}_{f,\mathrm{ref}}^{dq}$.

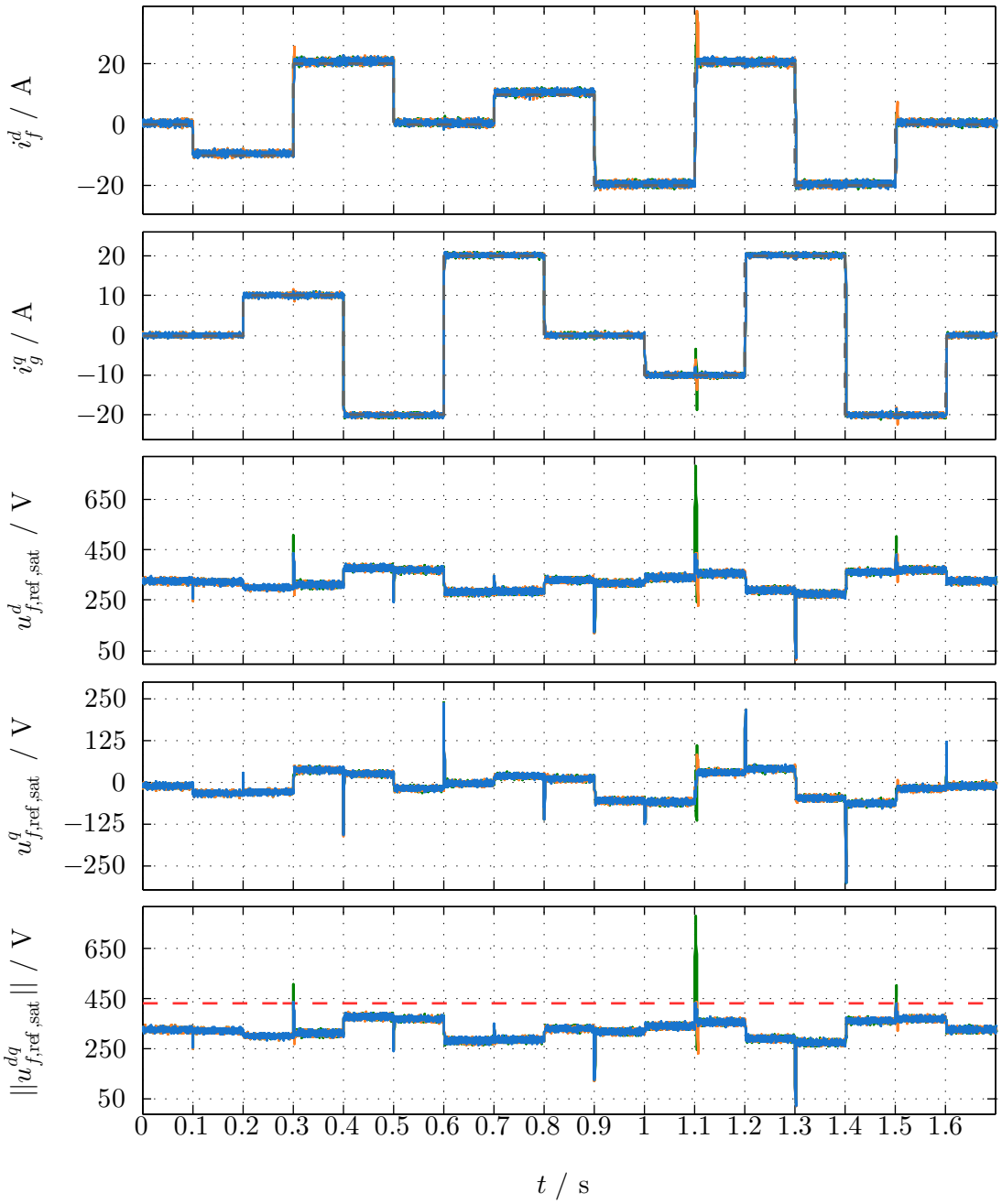

Figure 3.8: *Experiment (ξ.2):* — *simulated quantities with both SAT and AWU in use,* — *simulated quantities with only SAT in use,* — *simulated quantities with neither SAT nor AWU in use,* - - - *reference voltage limit* $\frac{\sqrt{3}k_c u_d}{2} \approx 433\,\mathrm{V}$ *and* - - - *reference currents* $i_{f,\mathrm{ref}}^d$ *and* $i_{g,\mathrm{ref}}^q$.

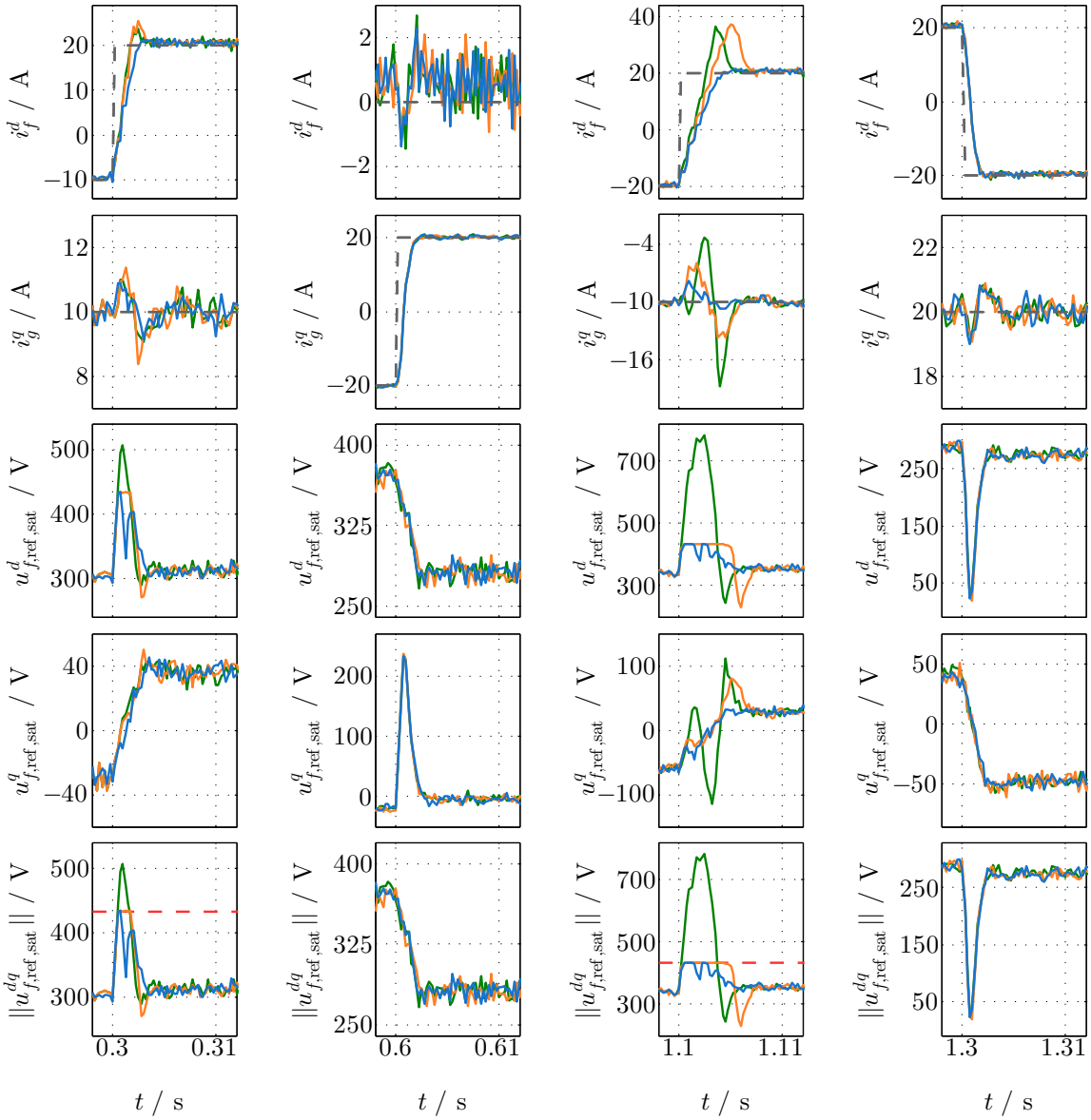

Figure 3.9: *Experiment (ξ.2) – Zoom:* — *simulated quantities with both SAT and AWU in use,* — *simulated quantities with only SAT in use,* — *simulated quantities with neither SAT nor AWU in use,* - - - *reference voltage limit* $\frac{\sqrt{3}k_c u_d}{2} \approx 433\,\mathrm{V}$ *and* - - - *reference currents* $i^d_{f,\mathrm{ref}}$ *and* $i^q_{g,\mathrm{ref}}$.

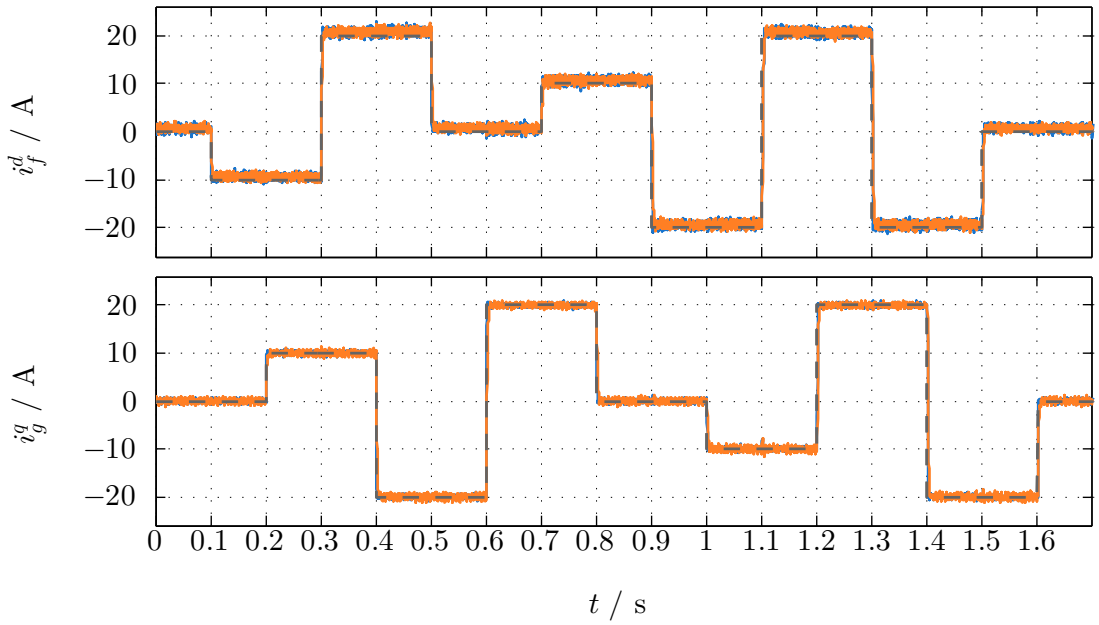

Figure 3.10: *Experiment (ξ.3):* — *simulated quantities with weighting factor* $\eta_{i,\xi} = 10$, — *simulated quantities with weighting factor* $\eta_{i,\xi} = 1$ *and* - - - *reference currents* $i_{f,\mathrm{ref}}^d$ *and* $i_{g,\mathrm{ref}}^q$.

the grid current and their corresponding - - - references $i_{f,\mathrm{ref}}^d$ and $i_{g,\mathrm{ref}}^q$. In both simulations, steady-state accuracy is achieved as well as a good tracking of the references $i_{f,\mathrm{ref}}^d$ and $i_{g,\mathrm{ref}}^q$. The difference of the two simulations is presented in Fig. 3.11, where zooms of the following time instants are shown: (a) $t = 0.3\,\mathrm{s}$ and $t = 0.9\,\mathrm{s}$ for the filter current i_f^d and (b) $t = 1.2\,\mathrm{s}$ and $t = 1.4\,\mathrm{s}$ for the grid current i_g^q. The control performance of the simulation with — standard weighting factor $\eta_{i,\xi} = 10$ is much faster than the one with — reduced weighting factor $\eta_{i,\xi} = 1$. Since the stability of the outer DC-link voltage controller requires a very fast grid side current controller to guarantee a stable operation, the prioritization of its control error $(i_{f,\mathrm{ref}}^d \; i_{g,\mathrm{ref}}^q)^\top - (i_f^d \; i_g^q)^\top$ in the weighting matrix $\boldsymbol{Q}_{\xi,k}$ via the weighting factor $\eta_{i,\xi}$ is crucial.
The fourth Experiment (ξ.4) is depicted in Fig. 3.12. In the previous plots of the Experiments (ξ.1)–(ξ.3), it seems that the noise of the filter current $\boldsymbol{i}_f^{dq}$ does not differ significantly from the one of the grid current $\boldsymbol{i}_g^{dq}$. This is a false conclusion. The reason is that the simulation results are stored with the sampling frequency f_{dis}. In Experiment (ξ.4), this sampling frequency is

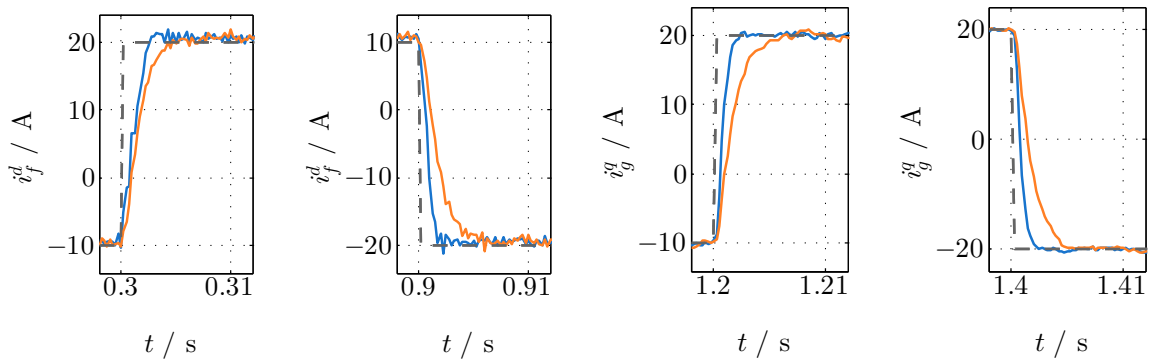

Figure 3.11: *Experiment (ξ.3) – Zoom:* — *simulated quantities with weighting factor* $\eta_{i,\xi} = 10$, — *simulated quantities with weighting factor* $\eta_{i,\xi} = 1$ *and* - - - *reference currents* $i_{f,\mathrm{ref}}^d$ *and* $i_{g,\mathrm{ref}}^q$.

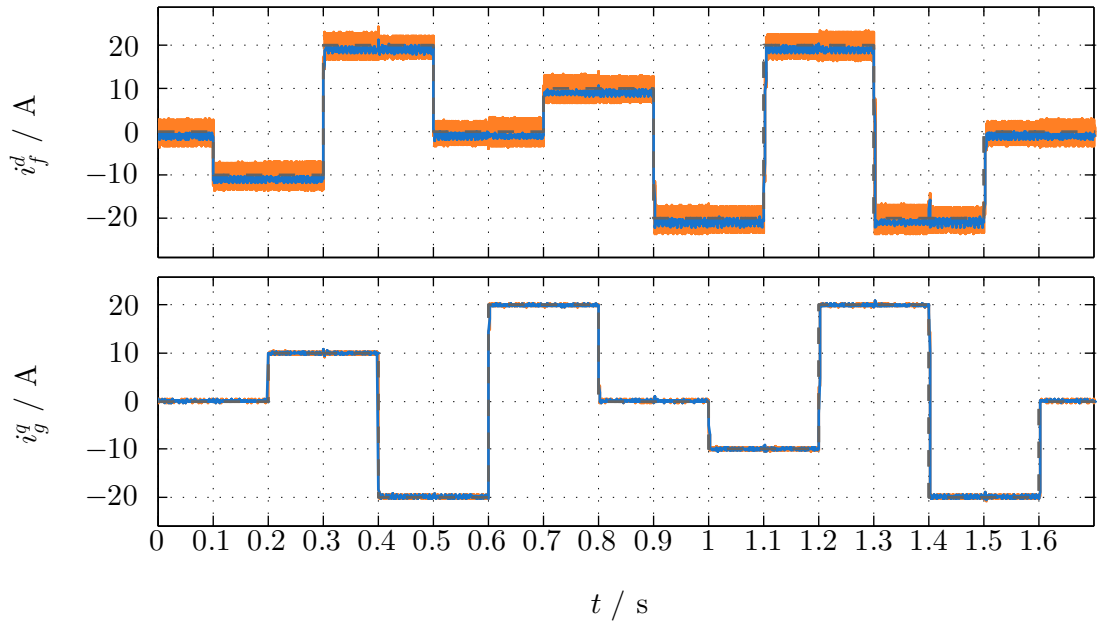

Figure 3.12: *Experiment (ξ.4):* — *simulated quantities are stored with sampling frequency* f_{dis}, — *simulated quantities are stored with increased sampling frequency* f_{sim} *and* - - - *reference currents* $i^d_{f,\text{ref}}$ *and* $i^q_{g,\text{ref}}$.

increased to f_{sim}. Again, Fig. 3.12 illustrates (a) the d-component i_f^d of the filter current, (b) the q-component i_g^q of the grid current and (c) their corresponding - - - references $i^d_{f,\text{ref}}$ and $i^q_{g,\text{ref}}$. The simulation results are stored (i) with the — sampling frequency f_{dis} and (ii) with the — sampling frequency f_{sim}. While the grid current i_g^q does not feature any differences between the two simulations, the noise of the filter current i_f^d is greater for the — sampling frequency f_{sim}. Consequently, to store the quantities of the simulation with the — sampling frequency f_{dis} does not yield the real behavior of the filter current $\boldsymbol{i}_f^{dq}$. Since the measurements at the test-bench can only be stored with the sampling frequency f_{dis}, for the purpose of comparability, further simulations continue using the sampling frequency f_{dis} to store their results.

3.2.3 DC-link voltage control with LCL filter

This section presents the DC-link voltage control strategy. The most parts have already been published in [17]. The small DC-link capacitance C_d requires a rather aggressive controller design to avoid critical voltage drops of the DC-link voltage u_d. This necessitates to know the overall grid side model precisely, which considers the physical behavior as well as its interaction with the grid side control. Therefor, the following steps are undertaken:

(i) the small signal dynamics of the physical system are derived in the discrete-time domain,

(ii) these dynamics are extended by the inner grid side current controller and the outer DC-link voltage controller (see Sec. 3.2.3.1), which yields the closed-loop dynamics of the overall grid side model and

(iii) a detailed stability analysis—based on the closed-loop dynamics—is performed. It is shown that the stability of the DC-link voltage control depends strongly on the operation point (see Sec. 3.2.3.2).

The DC-link voltage controller is designed as standard PI controller with additional reference filter to compensate for overshoots in the reference tracking of the DC-link voltage u_d. The proportional gain $k_{p,\chi}$ (in $\frac{\mathrm{A}}{\mathrm{V}}$) and integral gain $k_{i,\chi}$ (in $\frac{\mathrm{A}}{\mathrm{V\,s}}$) of the PI controller result from the stability analysis of the closed-loop system. To verify the controller design as well as the correctness of the grid side model, simulation and measurement results—considering reference tracking and disturbance rejection of the DC-link voltage control—are presented in Sec. 3.2.3.3 and Sec. 3.2.3.4, respectively.
In Sec. 2.4.1, the dynamics of the DC-link voltage u_d were derived as follows

$$\frac{\mathrm{d}}{\mathrm{d}t}u_d(t) \overset{(2.90)}{=} \frac{1}{C_d u_d(t)}\left(p_l(t) - \frac{2}{3k_c^2}\boldsymbol{i}_f^{dq}(t)^\top \boldsymbol{u}_f^{dq}(t)\right) =: h_d(u_d, \boldsymbol{i}_f^{dq}, \boldsymbol{u}_f^{dq}, p_l)\ ,\ u_d(0) = u_{d,0}\,, \quad (3.21)$$

and can be expressed by the nonlinear function h_d. Hence, the nonlinear dynamics of the DC-link voltage u_d depends on (a) the DC-link voltage u_d itself, (b) the filter current $\boldsymbol{i}_f^{dq}$, (c) the filter voltage $\boldsymbol{u}_f^{dq}$ and (d) the power p_l flowing from the machine side converter into the DC-link. Defining the small signals of (a)–(d) as follows[51]

$$\widetilde{u}_d := u_d - u_d^\star\ ,\ \widetilde{\boldsymbol{i}}_f^{dq} := \boldsymbol{i}_f^{dq} - \boldsymbol{i}_f^{dq\star}\ ,\ \widetilde{\boldsymbol{u}}_f^{dq} := \boldsymbol{u}_f^{dq} - \boldsymbol{u}_f^{dq\star} \quad \text{and} \quad \widetilde{p}_l := p_l - p_l^\star\,, \quad (3.22)$$

allows to linearize the DC-link voltage dynamics (3.21) around the equilibrium $\star = (u_d^\star, \boldsymbol{i}_f^{dq\star}, \boldsymbol{u}_f^{dq\star}, p_l^\star)$ at steady-state operation $\frac{\mathrm{d}}{\mathrm{d}t}u_d^\star(t) = h_d(\star) = 0$. Hence, for $\nu \in \{u_d, \boldsymbol{i}_f^{dq}, \boldsymbol{u}_f^{dq}, p_l\}$, applying the Taylor series expansion[52] to (3.21) results in the small signal dynamics of the DC-link voltage given by

$$\begin{aligned}\frac{\mathrm{d}}{\mathrm{d}t}\widetilde{u}_d(t) &= \frac{\mathrm{d}}{\mathrm{d}t}(u_d(t) - u_d^\star(t)) = \frac{\mathrm{d}}{\mathrm{d}t}u_d(t) - \frac{\mathrm{d}}{\mathrm{d}t}u_d^\star(t)\\ &= \underbrace{h_d(\star)}_{=\frac{\mathrm{d}}{\mathrm{d}t}u_d^\star(t)} + \sum_\nu \left.\frac{\partial h_d(u_d, \boldsymbol{i}_f^{dq}, \boldsymbol{u}_f^{dq}, p_l)}{\partial \nu}\right|_\star \widetilde{\nu}(t) + \delta_d(t) - \frac{\mathrm{d}}{\mathrm{d}t}u_d^\star(t)\\ &= -\frac{1}{u_d^\star}\underbrace{h_d(\star)}_{=0}\widetilde{u}_d(t) - \frac{2}{3k_c^2 C_d u_d^\star}\left((\boldsymbol{i}_f^{dq\star})^\top \widetilde{\boldsymbol{u}}_f^{dq}(t) + (\boldsymbol{u}_f^{dq\star})^\top \widetilde{\boldsymbol{i}}_f^{dq}(t)\right) + \frac{1}{C_d u_d^\star}\widetilde{p}_l(t) + \delta_d(t) \quad (3.23)\end{aligned}$$

with initial value $\widetilde{u}_d(0) = \widetilde{u}_{d,0}$. The term $\delta_d(t) := \delta_d(\widetilde{u}_d, \widetilde{\boldsymbol{i}}_f^{dq}, \widetilde{\boldsymbol{u}}_f^{dq}, \widetilde{p}_l, \star)$ (in $\frac{\mathrm{V}}{\mathrm{s}}$) characterizes the higher order terms of the Taylor series. In the following, it is imposed:

Assumption (A.3.4) *The higher order terms δ_d of the Taylor series are neglected, i.e. $\delta_d(t) = 0$.*

The dynamics of the LCL filter in (3.1) are a linear time-invariant system (LTI-system). Consequently, its small signal dynamics are identical to (2.66). The small signals $\widetilde{\ }$ and the stationary operation points * of the equilibrium $\frac{\mathrm{d}}{\mathrm{d}t}\boldsymbol{x}_{\mathrm{lcl}}^\star(t) = 0$ are defined by

$$\widetilde{\boldsymbol{x}}_{\mathrm{lcl}} := \boldsymbol{x}_{\mathrm{lcl}} - \boldsymbol{x}_{\mathrm{lcl}}^\star = \begin{pmatrix} \boldsymbol{i}_f^{dq} - \boldsymbol{i}_f^{dq\star} \\ \boldsymbol{i}_g^{dq} - \boldsymbol{i}_g^{dq\star} \\ \boldsymbol{u}_h^{dq} - \boldsymbol{u}_h^{dq\star} \end{pmatrix} =: \begin{pmatrix} \widetilde{\boldsymbol{i}}_f^{dq} \\ \widetilde{\boldsymbol{i}}_g^{dq} \\ \widetilde{\boldsymbol{u}}_h^{dq} \end{pmatrix} \quad \text{and} \quad \widetilde{\boldsymbol{u}}_g^{dq} := \boldsymbol{u}_g^{dq} - \boldsymbol{u}_g^{dq\star} \overset{(A.3.2)}{=} \boldsymbol{0}_2\,. \quad (3.24)$$

Thus, because of (A.3.4), combining the small signal dynamics (a) of the LCL filter (3.1) and

[51] Small signals are always denoted by an additional $\widetilde{\ }$ above their corresponding quantity.
[52] Details about the Taylor series expansion can e.g. be found in [139].

(b) of the DC-link voltage (3.23) results in the combined continuous-time dynamics

$$\frac{\mathrm{d}}{\mathrm{d}t}\overbrace{\begin{pmatrix}\widetilde{\boldsymbol{x}}_{\mathrm{lcl}}(t)\\ \widetilde{u}_d(t)\end{pmatrix}}^{=:\widetilde{\boldsymbol{x}}_d(t)} = \overbrace{\begin{bmatrix}\boldsymbol{A}_{\mathrm{lcl}} & \boldsymbol{0}_6\\ -\frac{2}{3k_c^2\overline{C}_d u_d^\star}\left(\boldsymbol{u}_f^{dq\star}\right)^\top & \boldsymbol{0}_5^\top\end{bmatrix}}^{=:\boldsymbol{A}_d^\star}\begin{pmatrix}\widetilde{\boldsymbol{x}}_{\mathrm{lcl}}(t)\\ \widetilde{u}_d(t)\end{pmatrix} + \overbrace{\begin{bmatrix}\boldsymbol{B}_{\mathrm{lcl}}\\ -\frac{2}{3k_c^2\overline{C}_d u_d^\star}\left(\boldsymbol{i}_f^{dq\star}\right)^\top\end{bmatrix}}^{=:\boldsymbol{B}_d^\star}\widetilde{\boldsymbol{u}}_f^{dq}(t) + \overbrace{\begin{pmatrix}\boldsymbol{0}_6\\ \frac{1}{\overline{C}_d u_d^\star}\end{pmatrix}}^{=:\boldsymbol{e}_d^\star}\widetilde{p}_l(t)$$

$$= \boldsymbol{A}_d^\star\widetilde{\boldsymbol{x}}_d(t) + \boldsymbol{B}_d^\star\widetilde{\boldsymbol{u}}_f^{dq}(t) + \boldsymbol{e}_d^\star\widetilde{p}_l(t)\ ,\ \widetilde{\boldsymbol{x}}_d(0) = \widetilde{\boldsymbol{x}}_{d,0} \tag{3.25}$$

with the state vector $\widetilde{\boldsymbol{x}}_d \in \mathbb{R}^7$. Obviously, the system matrix $\boldsymbol{A}_d^\star \in \mathbb{R}^{7\times 7}$, the input matrix $\boldsymbol{B}_d^\star \in \mathbb{R}^{7\times 2}$ and the disturbance vector $\boldsymbol{e}_d^\star \in \mathbb{R}^7$ depend on the operation point.
To obtain the discrete-time dynamics of (3.25) with discretization time t_{dis}, the same discretization method as in Sec. 3.2.2.2 is used. Accordingly, the discrete system matrix $\boldsymbol{A}_{d,k}^\star \in \mathbb{R}^{7\times 7}$, the discrete input matrix $\boldsymbol{B}_{d,k}^\star \in \mathbb{R}^{7\times 2}$ and the discrete disturbance vector $\boldsymbol{e}_{d,k}^\star \in \mathbb{R}^7$ are calculated by[53]

$$\boldsymbol{Z}_d^\star = t_{\mathrm{dis}}\sum_{\nu=0}^{8}\left(\boldsymbol{A}_d^\star\right)^\nu\frac{t_{\mathrm{dis}}^\nu}{(\nu+1)!} \quad\Rightarrow\quad \boldsymbol{A}_{d,k}^\star = \boldsymbol{I}_7 + \boldsymbol{Z}_d^\star\boldsymbol{A}_d^\star\ ,\ \boldsymbol{B}_{d,k}^\star = \boldsymbol{Z}_d^\star\boldsymbol{B}_d\ ,\ \boldsymbol{e}_{d,k}^\star = \boldsymbol{Z}_d^\star\boldsymbol{e}_d^\star\,, \tag{3.26}$$

where $\boldsymbol{Z}_d^\star \in \mathbb{R}^{7\times 7}$ represents the discretization matrix. Concluding, the discrete-time dynamics are given by

$$\widetilde{\boldsymbol{x}}_d[k+1] = \boldsymbol{A}_{d,k}^\star\widetilde{\boldsymbol{x}}_d[k] + \boldsymbol{B}_{d,k}^\star\widetilde{\boldsymbol{u}}_f^{dq}[k] + \boldsymbol{e}_{d,k}^\star\widetilde{p}_l[k]\ ,\ \widetilde{\boldsymbol{x}}_d[0] = \widetilde{\boldsymbol{x}}_{d,0}\,. \tag{3.27}$$

3.2.3.1 PI controller design and closed-loop dynamics

This section (i) introduces the DC-link voltage PI controller, (ii) extends the discrete dynamics of (3.27) by the inner grid side current controller and the outer DC-link voltage PI controller and (iii) derives the closed-loop system of the overall grid side model.
First, the discrete dynamics of (3.27) are augmented by the "trapezoidal" integrator for the integral state $\boldsymbol{x}_{i,\xi}^{dq}$ of the inner grid side current controller (for details see [136]). The discrete-time dynamics of the integral state $\boldsymbol{x}_{i,\xi}^{dq}$ with discretization time t_{dis} are given by

$$\begin{aligned}\boldsymbol{x}_{i,\xi}^{dq}[k+1] &= \boldsymbol{x}_{i,\xi}^{dq}[k] + \frac{t_{\mathrm{dis}}}{2}\left(\begin{pmatrix}i_{f,\mathrm{ref}}^d[k+1]\\ i_{g,\mathrm{ref}}^q[k+1]\end{pmatrix} - \boldsymbol{C}_\xi\boldsymbol{x}_{\mathrm{lcl}}[k+1] + \begin{pmatrix}i_{f,\mathrm{ref}}^d[k]\\ i_{g,\mathrm{ref}}^q[k]\end{pmatrix} - \boldsymbol{C}_\xi\boldsymbol{x}_{\mathrm{lcl}}[k]\right)\\ &\overset{(3.25)}{=} \boldsymbol{x}_{i,\xi}^{dq}[k] + \frac{t_{\mathrm{dis}}}{2}\begin{pmatrix}i_{f,\mathrm{ref}}^d[k+1] + i_{f,\mathrm{ref}}^d[k]\\ i_{g,\mathrm{ref}}^q[k+1] + i_{g,\mathrm{ref}}^q[k]\end{pmatrix} - \frac{t_{\mathrm{dis}}}{2}\underbrace{\begin{bmatrix}\boldsymbol{C}_\xi & \boldsymbol{0}_2\end{bmatrix}}_{=:\boldsymbol{C}_{d,k}}\left(\boldsymbol{x}_d[k+1] + \boldsymbol{x}_d[k]\right)\end{aligned} \tag{3.28}$$

with initial value $\boldsymbol{x}_{i,\xi}^{dq}[0] = \boldsymbol{x}_{i,\xi,0}^{dq}$ and output matrix $\boldsymbol{C}_{d,k} \in \mathbb{R}^{2\times 7}$. Note that the small signal dynamics of (3.28) are identical. Defining the following small signals $\widetilde{\ }$ and stationary operation points * of the equilibrium $\boldsymbol{x}_{i,\xi}^{dq}[k+1] = \boldsymbol{x}_{i,\xi}^{dq}[k]$ by

$$\widetilde{\boldsymbol{x}}_{i,\xi}^{dq} := \boldsymbol{x}_{i,\xi}^{dq} - \boldsymbol{x}_{i,\xi}^{dq\star}\ ,\ \widetilde{i}_{f,\mathrm{ref}}^d := i_{f,\mathrm{ref}}^d - i_{f,\mathrm{ref}}^{d\star}\ \text{ and }\ \widetilde{i}_{g,\mathrm{ref}}^q := i_{g,\mathrm{ref}}^q - i_{g,\mathrm{ref}}^{q\star}\,, \tag{3.29}$$

the extension of (3.27) by the dynamics (3.28) of the integral state $\boldsymbol{x}_{i,\xi}^{dq}$ results in the augmented

[53] Since (i) the last column of the system matrix $\boldsymbol{A}_d^\star$ is the zero vector $\boldsymbol{0}_7$ and (b) the first six rows of the disturbance vector $\boldsymbol{e}_d^\star$ are zero as well, the discrete disturbance vector $\boldsymbol{e}_{d,k}^\star$ equals the continuous one, i.e. $\boldsymbol{e}_{d,k}^\star = \boldsymbol{e}_d^\star$.

dynamics

$$\begin{aligned}\overbrace{\begin{pmatrix}\widetilde{\boldsymbol{x}}_d[k+1]\\ \widetilde{\boldsymbol{x}}_{i,\xi}^{dq}[k+1]\end{pmatrix}}^{=:\widetilde{\boldsymbol{x}}_\chi[k+1]} &= \overbrace{\begin{bmatrix}\boldsymbol{A}_{d,k}^\star & \boldsymbol{O}_{7\times2}\\ -\frac{t_\mathrm{dis}}{2}\boldsymbol{C}_{d,k}\left(\boldsymbol{A}_{d,k}^\star+\boldsymbol{I}_7\right) & \boldsymbol{I}_2\end{bmatrix}}^{=:\boldsymbol{A}_\chi^\star}\begin{pmatrix}\widetilde{\boldsymbol{x}}_d[k]\\ \widetilde{\boldsymbol{x}}_{i,\xi}^{dq}[k]\end{pmatrix} + \overbrace{\begin{bmatrix}\boldsymbol{B}_{d,k}^\star\\ -\frac{t_\mathrm{dis}}{2}\boldsymbol{C}_{d,k}\boldsymbol{B}_{d,k}^\star\end{bmatrix}}^{=:\boldsymbol{B}_\chi^\star}\widetilde{\boldsymbol{u}}_f^{dq}[k]\\ &\quad+\underbrace{\begin{bmatrix}\boldsymbol{e}_{d,k}^\star & \boldsymbol{O}_{8\times2}\\ -\frac{t_\mathrm{dis}}{2}\boldsymbol{C}_{d,k}\boldsymbol{e}_{d,k}^\star & \frac{t_\mathrm{dis}}{2}\boldsymbol{1}_2^\top\end{bmatrix}}_{=:\boldsymbol{E}_\chi^\star}\underbrace{\begin{pmatrix}\widetilde{p}_l[k]\\ \widetilde{i}_{g,\mathrm{ref}}^q[k]\\ \widetilde{i}_{g,\mathrm{ref}}^q[k+1]\end{pmatrix}}_{=:\widetilde{\boldsymbol{d}}_\chi[k,k+1]}+\underbrace{\begin{pmatrix}\boldsymbol{0}_7\\ \frac{t_\mathrm{dis}}{2}\\ 0\end{pmatrix}}_{=:\boldsymbol{b}_\chi}\left(\widetilde{i}_{f,\mathrm{ref}}^d[k]+\widetilde{i}_{f,\mathrm{ref}}^d[k+1]\right)\\ &= \boldsymbol{A}_\chi^\star\widetilde{\boldsymbol{x}}_\chi[k]+\boldsymbol{B}_\chi^\star\widetilde{\boldsymbol{u}}_f^{dq}[k]+\boldsymbol{E}_\chi^\star\widetilde{\boldsymbol{d}}_\chi[k,k+1]+\boldsymbol{b}_\chi\left(\widetilde{i}_{f,\mathrm{ref}}^d[k]+\widetilde{i}_{f,\mathrm{ref}}^d[k+1]\right)\end{aligned}\tag{3.30}$$

with the augmented state vector $\widetilde{\boldsymbol{x}}_\chi\in\mathbb{R}^9$ and its initial value $\widetilde{\boldsymbol{x}}_\chi[0]=\widetilde{\boldsymbol{x}}_{\chi,0}$, the input vector $\boldsymbol{b}_\chi\in\mathbb{R}^9$ and the disturbance vector $\widetilde{\boldsymbol{d}}_\chi\in\mathbb{R}^3$. The system matrix $\boldsymbol{A}_\chi^\star\in\mathbb{R}^{9\times9}$, the input matrix $\boldsymbol{B}_\chi^\star\in\mathbb{R}^{9\times2}$ and the disturbance matrix $\boldsymbol{E}_\chi^\star\in\mathbb{R}^{9\times3}$ depend on the operation point[54].
In the next steps, the augmented dynamics in (3.30) will be extended as follows:

- the control law (3.13) of the grid side current controller is considered,
- the control law of the DC-link voltage PI controller is introduced and applied to (3.30) and
- the integral state $x_{i,\chi}$ (in Vs) extends the augmented dynamics in (3.30).

Due to (A.3.3), the control law (3.13) for the integral state-feedback controller of the grid side currents can be rewritten as

$$\boldsymbol{u}_f^{dq}[k]\overset{(A.3.3)}{=}\boldsymbol{u}_{f,\mathrm{ref}}^{dq}[k]\overset{(3.13)}{=}-\begin{bmatrix}\boldsymbol{K}_{x,\xi,k} & \boldsymbol{0}_2 & \boldsymbol{K}_{i,\xi,k}\end{bmatrix}\boldsymbol{x}_\chi[k]=:-\boldsymbol{K}_\chi\boldsymbol{x}_\chi[k]\ \Leftrightarrow\ \widetilde{\boldsymbol{u}}_f^{dq}[k]=-\boldsymbol{K}_\chi\widetilde{\boldsymbol{x}}_\chi[k]\tag{3.31}$$

with the feedback matrix $\boldsymbol{K}_\chi\in\mathbb{R}^{2\times9}$. Fig. 3.6 depicts the implementation of the — DC-link voltage PI controller. By means of the proportional gain $k_{p,\chi}$ and the integral state $x_{i,\chi}$ in combination with the integral gain $k_{i,\chi}$, the control error $u_{d,\mathrm{ref}}-u_d$ is adjusted to zero[55] via the filter current reference $i_{f,\mathrm{ref}}^d$, which functions as control variable. The discrete-time dynamics of the integral state $x_{i,\chi}$ with discretization time t_dis are calculated by

$$\begin{aligned}x_{i,\chi}[k+1] &= x_{i,\chi}[k]+t_\mathrm{dis}\left(u_{d,\mathrm{ref}}[k]-u_d[k]\right)\\ &= x_{i,\chi}[k]+t_\mathrm{dis}\Big(u_{d,\mathrm{ref}}[k]-\overbrace{\begin{pmatrix}\boldsymbol{0}_6^\top & 1\end{pmatrix}}^{=:\boldsymbol{c}_\chi^\top}\boldsymbol{x}_d[k]\Big)\ ,\ x_{i,\chi,0}:=x_{i,\chi}[0]\end{aligned}\tag{3.32}$$

with the output vector $\boldsymbol{c}_\chi\in\mathbb{R}^7$. The small signal dynamics of (3.32) are identical. The following small signals $\widetilde{\ }$ and stationary operation points * of the equilibrium $x_{i,\chi}[k+1]=x_{i,\chi}[k]$ are defined: $\widetilde{u}_{d,\mathrm{ref}}:=u_{d,\mathrm{ref}}-u_{d,\mathrm{ref}}^\star$ and $\widetilde{x}_{i,\chi}:=x_{i,\chi}-x_{i,\chi}^\star$.
In view of Fig. 3.6, the control law of the — DC-link voltage PI controller is given by

$$i_{f,\mathrm{ref}}^d[k]=k_{i,\chi}x_{i,\chi}[k]+k_{p,\chi}\left(u_{d,\mathrm{ref}}[k]-u_d[k]\right)=k_{i,\chi}x_{i,\chi}[k]+k_{p,\chi}\left(u_{d,\mathrm{ref}}[k]-\boldsymbol{c}_\chi^\top\boldsymbol{x}_d[k]\right)\ .\tag{3.33}$$

[54] The zero entries in the output matrix $\boldsymbol{C}_{d,k}$ and in the disturbance vector $\boldsymbol{e}_d^\star=\boldsymbol{e}_{d,k}^\star$ yield $\boldsymbol{C}_{d,k}\boldsymbol{e}_{d,k}^\star=\boldsymbol{C}_{d,k}\boldsymbol{e}_d^\star=\boldsymbol{0}_2$.
[55] For the further calculations, because of (R.3.8), the implemented reference filter in Fig. 3.6 is neglected.

Due to (3.27) and (3.32), the reference filter current $i^d_{f,\mathrm{ref}}$ for the time-step $k{+}1$ is calculated by

$$\begin{aligned} i^d_{f,\mathrm{ref}}[k{+}1] &= k_{i,\chi} x_{i,\chi}[k{+}1] + k_{p,\chi}\left(u_{d,\mathrm{ref}}[k{+}1] - \boldsymbol{c}_\chi^\top \boldsymbol{x}_d[k{+}1]\right) \\ &= k_{i,\chi} x_{i,\chi}[k] + k_{i,\chi} t_{\mathrm{dis}} u_{d,\mathrm{ref}}[k] - k_{i,\chi} t_{\mathrm{dis}} \boldsymbol{c}_\chi^\top \boldsymbol{x}_d[k] \\ &\quad + k_{p,\chi} u_{d,\mathrm{ref}}[k{+}1] - k_{p,\chi} \boldsymbol{c}_\chi^\top \left(\boldsymbol{A}^\star_{d,k} \boldsymbol{x}_d[k] + \boldsymbol{B}^\star_{d,k} \boldsymbol{u}_f^{dq}[k] + \boldsymbol{e}^\star_{d,k} p_l[k]\right), \end{aligned} \tag{3.34}$$

such that the sum $\widetilde{i}^d_{f,\mathrm{ref}}[k]{+}\widetilde{i}^d_{f,\mathrm{ref}}[k{+}1]$ in (3.30)—because of (3.33) and (3.34)—results in

$$\begin{aligned} \widetilde{i}^d_{f,\mathrm{ref}}[k] + \widetilde{i}^d_{f,\mathrm{ref}}[k{+}1] &= 2k_{i,\chi}\widetilde{x}_{i,\chi}[k] + (k_{p,\chi} + k_{i,\chi} t_{\mathrm{dis}})\widetilde{u}_{d,\mathrm{ref}}[k] + k_{p,\chi}\widetilde{u}_{d,\mathrm{ref}}[k{+}1] - k_{p,\chi}\boldsymbol{c}_\chi^\top \boldsymbol{e}^\star_{d,k}\widetilde{p}_l[k] \\ &\quad + \underbrace{\left(k_{p,\chi}\boldsymbol{c}_\chi^\top \boldsymbol{B}^\star_{d,k}\boldsymbol{K}_\chi - \left(k_{p,\chi}\boldsymbol{c}_\chi^\top\left(\boldsymbol{I}_7 + \boldsymbol{A}^\star_{d,k}\right) + k_{i,\chi} t_{\mathrm{dis}}\boldsymbol{c}_\chi^\top \quad \boldsymbol{0}_2^\top\right)\right)}_{=:\left(\boldsymbol{a}^\star_\chi\right)^\top} \widetilde{\boldsymbol{x}}_\chi[k]\,. \end{aligned} \tag{3.35}$$

The vector $\boldsymbol{a}^\star_\chi \in \mathbb{R}^9$ depends on the operation point. Finally, (i) applying the control law (3.31) of the grid side current controller to (3.30) and (3.35), (ii) applying (3.35) to (3.30) and (iii) extending the dynamics of (3.30) by the dynamics (3.32) of the integral state of the DC-link voltage PI controller, yields the discrete-time closed-loop (small signal) dynamics of the grid side model

$$\begin{aligned} \begin{pmatrix} \widetilde{\boldsymbol{x}}_\chi[k{+}1] \\ \widetilde{x}_{i,\chi}[k{+}1] \end{pmatrix} &= \overbrace{\begin{bmatrix} \boldsymbol{A}^\star_\chi - \boldsymbol{B}^\star_\chi \boldsymbol{K}_\chi + \boldsymbol{b}_\chi\left(\boldsymbol{a}^\star_\chi\right)^\top & 2k_{i,\chi}\boldsymbol{b}_\chi \\ \begin{bmatrix} -t_{\mathrm{dis}}\boldsymbol{c}_\chi^\top & \boldsymbol{0}_2^\top \end{bmatrix} & 1 \end{bmatrix}}^{=:\boldsymbol{A}^\star_{\mathrm{cl}}} \begin{pmatrix} \widetilde{\boldsymbol{x}}_\chi[k] \\ \widetilde{x}_{i,\chi}[k] \end{pmatrix} \\ &\quad + \begin{bmatrix} (k_{p,\chi} + k_{i,\chi} t_{\mathrm{dis}})\boldsymbol{b}_\chi & k_{p,\chi}\boldsymbol{b}_\chi \\ t_{\mathrm{dis}} & 0 \end{bmatrix} \begin{pmatrix} \widetilde{u}_{d,\mathrm{ref}}[k] \\ \widetilde{u}_{d,\mathrm{ref}}[k{+}1] \end{pmatrix} + \begin{bmatrix} \boldsymbol{E}^\star_\chi - k_{p,\chi}\boldsymbol{b}_\chi \boldsymbol{c}_\chi^\top \boldsymbol{e}^\star_{d,k}\begin{pmatrix} 1 & 0 & 0 \end{pmatrix} \\ \boldsymbol{0}_3^\top \end{bmatrix} \widetilde{\boldsymbol{d}}_\chi[k, k{+}1]\,, \end{aligned} \tag{3.36}$$

where the closed-loop system matrix $\boldsymbol{A}^\star_{\mathrm{cl}} \in \mathbb{R}^{10\times 10}$ depends on the operation point. By means of the closed-loop system matrix $\boldsymbol{A}^\star_{\mathrm{cl}}$, the stability of the DC-link voltage PI controller can be analyzed locally. Before this will be done in Sec. 3.2.3.2, the two following aspects are important to keep in mind:

Remark (R.3.8) *Sec. 3.2.3.3 will show that—due to the very aggressive controller design—the tracking of the DC-link voltage reference $u_{d,\mathrm{ref}}$ causes overshoots in the DC-link voltage u_d. To avoid these overshoots, a first order lag system[56] with the time constant $T_\chi = 8t_{\mathrm{dis}}$ (in s) is used as reference filter (see Fig. 3.6). Usually, the DC-link voltage u_d is controlled to a constant value, such that the delaying reference filter does not deteriorate the control performance. Moreover, since the reference filter does not influence stability of the DC-link voltage control, for both (a) the previous derivation of the closed-loop system matrix $\boldsymbol{A}^\star_{cl}$ and (b) the stability analysis of the closed-loop system in Sec. 3.2.3.2, the reference filter is neglected.*

Remark (R.3.9) *The closed-loop system matrix $\boldsymbol{A}^\star_{cl}$ depends on the operation points of DC-link voltage $u^\star_d$, filter current $\boldsymbol{i}_f^{dq\star}$ and filter voltage $\boldsymbol{u}_f^{dq\star}$ (see (3.25)). Due to the constant grid*

[56] By considering the discretization time t_{dis}, a first-order lag system with time constant T_{fol} (in s) filters the input signal u_{fol} and gives the output signal x_{fol} as follows: $x_{\mathrm{fol}}[k{+}1] = \left(1 - \frac{t_{\mathrm{dis}}}{T_{\mathrm{fol}}}\right) x_{\mathrm{fol}}[k] + \frac{t_{\mathrm{dis}}}{T_{\mathrm{fol}}} u_{\mathrm{fol}}[k]$.

voltage $\boldsymbol{u}_g^{dq\star}=\boldsymbol{u}_g^{dq}$*, the LCL filter dynamics* (3.1) *in stationary operation are given by*

$$\frac{d}{dt}\boldsymbol{x}_{lcl}^{\star}=\boldsymbol{0}_6=\boldsymbol{A}_{lcl}\boldsymbol{x}_{lcl}^{\star}+\boldsymbol{B}_{lcl}\boldsymbol{u}_f^{dq\star}+\boldsymbol{E}_{lcl}\boldsymbol{u}_g^{dq}\,. \tag{3.37}$$

With the help of the "stationary" state vector $\boldsymbol{z}_{lcl}^{\star}\in\mathbb{R}^6$ *and system matrix* $\boldsymbol{N}_{lcl}\in\mathbb{R}^{6\times 6}$ *of the LCL filter,* (3.37) *can be rewritten. The "stationary" state vector* $\boldsymbol{z}_{lcl}^{\star}$ *and system matrix* $\boldsymbol{N}_{lcl}$ *are defined as follows:*

$$\boldsymbol{z}_{lcl}^{\star}:=\left(u_f^{d\star}\,i_f^{q\star}\,i_g^{d\star}\,u_f^{q\star}\,u_h^{d\star}\,u_h^{q\star}\right)^{\top}\quad\text{and}\quad\boldsymbol{N}_{lcl}:=\boldsymbol{A}_{lcl}\,\mathrm{diag}\left(0\,\boldsymbol{1}_2^{\top}\,0\,\boldsymbol{1}_2^{\top}\right)^{\top}+\boldsymbol{B}_{lcl}\begin{bmatrix}1 & \boldsymbol{0}_3^{\top} & \boldsymbol{0}_2^{\top}\\ \boldsymbol{0}_3^{\top} & 1 & \boldsymbol{0}_2^{\top}\end{bmatrix}\,. \tag{3.38}$$

Then, the "stationary" state vector $\boldsymbol{z}_{lcl}^{\star}$ *of the LCL filter can be calculated by means of the d-component* $i_f^{d\star}$ *of the filter current and the q-component* $i_g^{q\star}$ *of the grid current:*

$$\boldsymbol{z}_{lcl}^{\star}=-\boldsymbol{N}_{lcl}^{-1}\left(\boldsymbol{A}_{lcl}\begin{bmatrix}1 & \boldsymbol{0}_3^{\top} & \boldsymbol{0}_2^{\top}\\ \boldsymbol{0}_3^{\top} & 1 & \boldsymbol{0}_2^{\top}\end{bmatrix}^{\top}\begin{pmatrix}i_f^{d\star}\\ i_g^{q\star}\end{pmatrix}+\boldsymbol{E}_{lcl}\boldsymbol{u}_g^{dq}\right)\,. \tag{3.39}$$

Thus, to analyze the closed-loop system matrix $\boldsymbol{A}_{cl}^{\star}$ *regarding the stability of the DC-link voltage PI controller, it is sufficient only to consider the three operation points of: (i) the DC-link voltage* $u_d^{\star}$*, (ii) the d-component* $i_f^{d\star}$ *of the filter current and (iii) the q-component* $i_g^{q\star}$ *of the grid current. Obviously, the "stationary" system matrix* $\boldsymbol{N}_{lcl}$ *needs to have full rank to be invertible, i.e.* $\mathrm{rank}(\boldsymbol{N}_{lcl})=6$*. This is the case (for details see Sec. C.2), if and only if the following holds:*

$$\frac{1}{\omega_g^2 C_h}\neq L_g-R_hC_h\,(R_g+R_h)\quad\overset{R_h=0}{\Longrightarrow}\quad\omega_g\neq\frac{1}{\sqrt{L_gC_h}}\qquad\textit{(cf. (C.3.1))}\,. \tag{3.40}$$

A properly designed LCL filter always satisfies this condition.

3.2.3.2 Stability analysis of the DC-link voltage closed-loop system

This section analyzes the stability of the DC-link voltage PI controller based on the closed-loop system matrix $\boldsymbol{A}_{\mathrm{cl}}^{\star}$. The discrete dynamics (3.36) of the closed-loop system are stable, if and only if all ten eigenvalues $\lambda_{\mathrm{cl},\nu}^{\star}$ with $\nu\in\{1,\ldots,10\}$ of the closed-loop system matrix $\boldsymbol{A}_{\mathrm{cl}}^{\star}$ lie inside the unit circle of the complex plane[57], i.e. $|\lambda_{\mathrm{cl},\nu}^{\star}|<1$ [140]. This condition allows to obtain all pairs $(k_{p,\chi},k_{i,\chi})$ of the proportional gain $k_{p,\chi}$ and integral gain $k_{i,\chi}$, for which the closed-loop system matrix $\boldsymbol{A}_{\mathrm{cl}}^{\star}$ yields a stable operation. Clearly, since the closed-loop system matrix $\boldsymbol{A}_{\mathrm{cl}}^{\star}$ depends on the operation points of: (a) the d-component $i_f^{d\star}$ of the filter current, (b) the q-component $i_g^{q\star}$ of the grid current and (c) the DC-link voltage $u_d^{\star}$ (see (R.3.9)), these operation points strongly affect the region of stable pairs $(k_{p,\chi},k_{i,\chi})$.
Fig. 3.13 shows the regions of stable pairs $(k_{p,\chi},k_{i,\chi})$. Therein, the defined (x) standard case:

$$\text{—}\;\;i_f^{d\star}=0\,\mathrm{A}\;,\;\;i_g^{q\star}=0\,\mathrm{A}\;,\;\;u_d^{\star}=750\,\mathrm{V}\;,\;\;\eta_{i,\xi}=10\;,\;\;f_{\mathrm{dis}}=4\,\mathrm{kHz} \tag{3.41}$$

is compared to cases, where ceteris paribus the following is changed: (a) the d-component $i_f^{d\star}$ of the filter current, (b) the q-component $i_g^{q\star}$ of the grid current, (c) the DC-link voltage $u_d^{\star}$, (d) the weighting factor $\eta_{i,\xi}$ for the grid side current controller, (e) the sampling frequency $f_{\mathrm{dis}}=\frac{1}{t_{\mathrm{dis}}}$ of the dSpace real-time system (or discretization frequency) and (f) the dSpace real-time system allows (hypothetically) for a continuous operation. The stability analysis gives the following

[57] In Matlab/Simulink, this condition can be checked via the command: all(abs(eig($\boldsymbol{A}_{\mathrm{cl}}^{\star}$))<1).

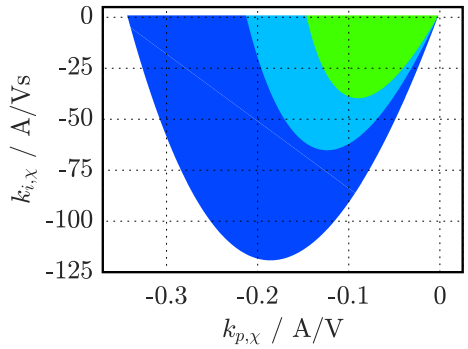

(a) *d-component* i_f^d *of the filter current:* $i_f^d = -\frac{5000\,\mathrm{W}}{\frac{3}{2}\sqrt{\frac{2}{3}}\,400\,\mathrm{V}} \approx -10.2\,\mathrm{A}$, $i_f^d = 0\,\mathrm{A}$ *and* $i_f^d = \frac{5000\,\mathrm{W}}{\frac{3}{2}\sqrt{\frac{2}{3}}\,400\,\mathrm{V}} \approx 10.2\,\mathrm{A}$.

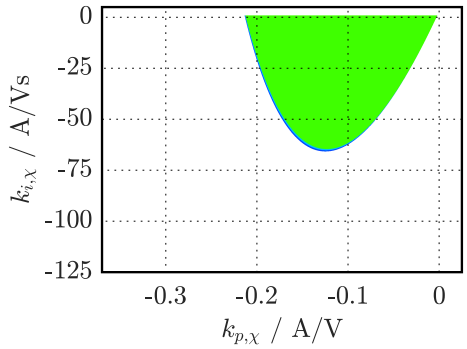

(b) *q-component* i_g^q *of the grid current:* $i_g^q = \frac{5000\,\mathrm{W}}{\frac{3}{2}\sqrt{\frac{2}{3}}\,400\,\mathrm{V}} \approx 10.2\,\mathrm{A}$, $i_g^q = 0\,\mathrm{A}$ *and* $i_g^q = -\frac{5000\,\mathrm{W}}{\frac{3}{2}\sqrt{\frac{2}{3}}\,400\,\mathrm{V}} \approx -10.2\,\mathrm{A}$.

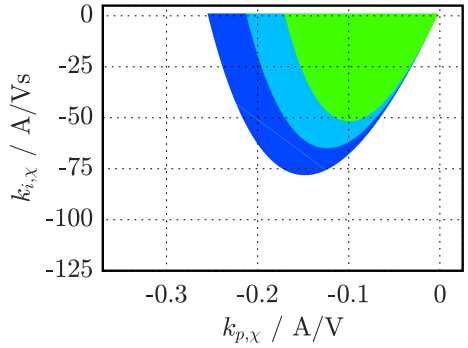

(c) *DC-link voltage* u_d: $u_d = 600\,\mathrm{V}$, $u_d = 750\,\mathrm{V}$ *and* $u_d = 900\,\mathrm{V}$.

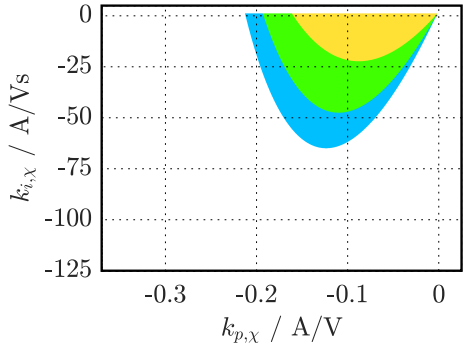

(d) *weighting factor* $\eta_{i,\xi}$ *of the grid side current controller:* $\eta_{i,\xi} = 1$, $\eta_{i,\xi} = 5$ *and* $\eta_{i,\xi} = 10$.

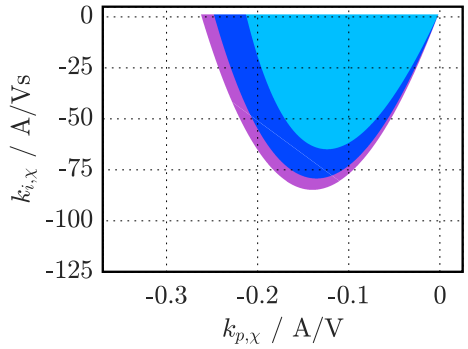

(e) *frequency* f_{dis} *of the discretization:* $f_{\mathrm{dis}} = 4\,\mathrm{kHz}$, $f_{\mathrm{dis}} = 8\,\mathrm{kHz}$ *and* $f_{\mathrm{dis}} = 12\,\mathrm{kHz}$.

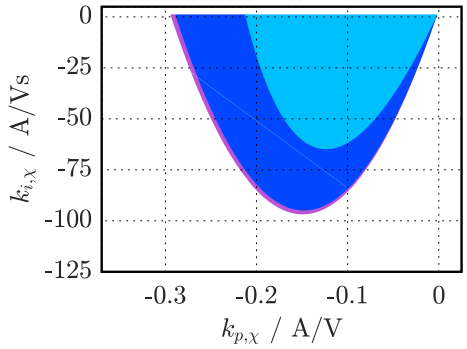

(f) *frequency* f_{dis} *of the discretization:* $f_{\mathrm{dis}} = 4\,\mathrm{kHz}$, $f_{\mathrm{dis}} = 80\,\mathrm{kHz}$ *and continuous operation of the dSpace real-time system.*

Figure 3.13: *Regions of stable pairs* $(k_{p,\chi}, k_{i,\chi})$ *for the DC-link voltage PI controller.*

results:

(x) **standard case**—: In the six plots of Fig. 3.13 the standard case (3.41) is depicted. The region of stable pairs $(k_{p,\chi}, k_{i,\chi})$ resembles a shifted parabola. Both the proportional gain $k_{p,\chi}$ and the integral gain $k_{i,\chi}$ must be negative, since a positive filter current $i_f^{d\star}$ discharges the DC-link. The range of feasible proportional gains $k_{p,\chi}$ is from $0\,\frac{\mathrm{A}}{\mathrm{V}}$ to about $-0.21\,\frac{\mathrm{A}}{\mathrm{V}}$ and the range of possible integral gains $k_{i,\chi}$ is from $0\,\frac{\mathrm{A}}{\mathrm{V\,s}}$ to about $-65\,\frac{\mathrm{A}}{\mathrm{V\,s}}$.

(a) **filter current** $i_f^{d\star}$: As depicted in Fig. 3.13a, the filter current $i_f^{d\star}$ has huge impact on the region of stable pairs $(k_{p,\chi}, k_{i,\chi})$. A — negative current $i_f^{d\star} \approx -10.2\,\mathrm{A}$ shrinks the region drastically, while a — positive current $i_f^{d\star} \approx 10.2\,\mathrm{A}$ enlarges this region. Consequently, injecting power to the three-winding transformer is uncritical regarding a stable operation. In contrast, a power flow from the three-winding transformer towards the DC-link endangers the stable operation. Since wind turbine systems with DFIM feature a bi-directional power flow through the back-to-back converter (depending on the machine rotational speed $\omega_m^\star$, see Sec. 2.4.2), it is important to consider both power flow directions.

(b) **grid current** $i_g^{q\star}$: The grid current $i_g^{q\star}$ hardly affects the region of stable pairs $(k_{p,\chi}, k_{i,\chi})$ (see Fig. 3.13b). It makes (almost) no difference, whether a negative $i_g^{q\star} \approx -10.2\,\mathrm{A}$ or a positive current $i_g^{q\star} \approx 10.2\,\mathrm{A}$ is flowing.

(c) **DC-link voltage** $u_d^\star$: Fig. 3.13c illustrates the impact of the DC-link voltage u_d onto the region of stable pairs $(k_{p,\chi}, k_{i,\chi})$. Due to (3.21), for the dynamics of the DC-link voltage u_d, it pertains: $\frac{\mathrm{d}}{\mathrm{d}t}u_d(t) \propto \frac{1}{u_d(t)}$. Hence, a — greater DC-link voltage $u_d^\star = 900\,\mathrm{V}$ enlarges the region of stable pairs $(k_{p,\chi}, k_{i,\chi})$, while it is reduced by a — smaller DC-link voltage $u_d^\star = 600\,\mathrm{V}$.

(d) **weighting factor** $\eta_{i,\xi}$: The results for the three different weighting factors — $\eta_{i,\xi} = 1$, — $\eta_{i,\xi} = 5$ and — $\eta_{i,\xi} = 10$ are shown in Fig. 3.13d. As expected, an aggressive controller design for the grid side currents yields a much larger region of stable pairs $(k_{p,\chi}, k_{i,\chi})$ than a conservative one.

(e) **sampling frequency** f_{dis}: If the dSpace real-time system is able to operate with a faster sampling frequency $f_{\mathrm{dis}} = \frac{1}{t_{\mathrm{dis}}}$, e.g. with — $f_{\mathrm{dis}} = 8\,\mathrm{kHz}$ or — $f_{\mathrm{dis}} = 12\,\mathrm{kHz}$, the region of stable pairs $(k_{p,\chi}, k_{i,\chi})$ can be extended (see Fig. 3.13e).

(f) **continuous operation**: Fig. 3.13f shows the result for a — continuous operation of the dSpace real-time system (not realizable), i.e. no discretization is necessary. Clearly, the region of stable pairs $(k_{p,\chi}, k_{i,\chi})$ is enlarged compared the — standard case. The result of the — continuous operation is similar to the one in —, where the sampling frequency f_{dis} has been increased to $f_{\mathrm{dis}} = 80\,\mathrm{kHz}$.

While the weighting factor $\eta_{i,\xi} = 10$ for the grid side current controller and the discretization frequency $f_{\mathrm{dis}} = 4\,\mathrm{kHz}$ are fixed, the operation points of (a) the d-component $i_f^{d\star}$ of the filter current, (b) the q-component $i_g^{q\star}$ of the grid current and (c) the DC-link voltage $u_d^\star$ vary during operation. Thus, the "worst-case" operation points must be chosen for the design of the proportional gain $k_{p,\chi}$ and the integral gain $k_{i,\chi}$, to guarantee stability for every operation. In view of Fig. 3.13, the worst-case is defined by

$$— \; i_f^{d\star} \approx -10.2\,\mathrm{A}\;,\; i_g^{q\star} \approx 10.2\,\mathrm{A}\;,\; u_d^\star = 600\,\mathrm{V}\;,\; \eta_{i,\xi} = 10\;,\; f_{\mathrm{dis}} = 4\,\mathrm{kHz}\,. \tag{3.42}$$

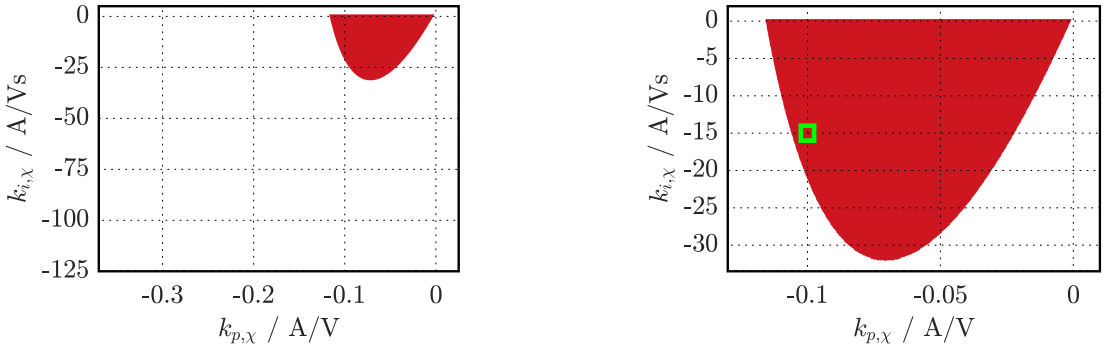

Figure 3.14: *Regions of stable pairs* $(k_{p,\chi}, k_{i,\chi})$ *for the worst-case operation, i.e.* — $i_f^d \approx -10.2\,\mathrm{A}$, $i_g^q \approx 10.2\,\mathrm{A}$, $u_d = 600\,\mathrm{V}$, $\eta_{i,\xi} = 10$ *and* $f_{\mathrm{dis}} = 4\,\mathrm{kHz}$. *The* — *box indicates the chosen proportional gain* $k_{p,\chi} = -0.1\,\frac{\mathrm{A}}{\mathrm{V}}$ *and integral gain* $k_{i,\chi} = -15\,\frac{\mathrm{A}}{\mathrm{Vs}}$ *for the DC-link voltage PI controller.*

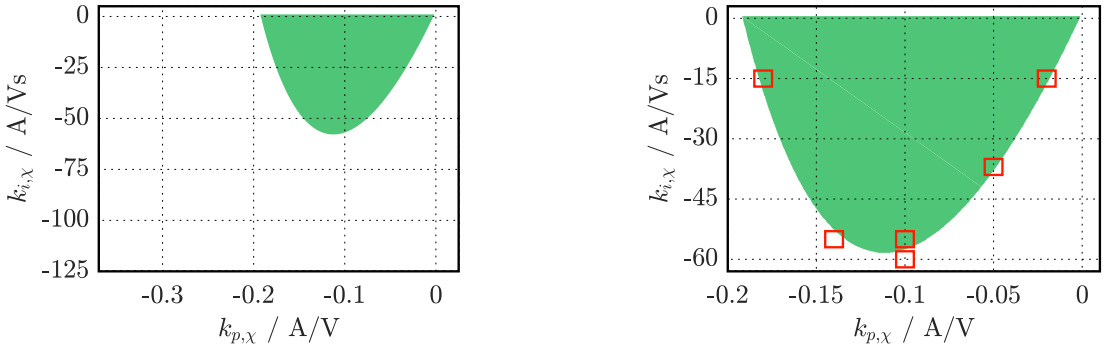

Figure 3.15: *Regions of stable pairs* $(k_{p,\chi}, k_{i,\chi})$ *for the critical operation of the test scenario, i.e.* — $i_f^d \approx -1\,\mathrm{A}$, $i_g^q \approx 10\,\mathrm{A}$, $u_d = 710\,\mathrm{V}$, $\eta_{i,\xi} = 10$ *and* $f_{\mathrm{dis}} = 4\,\mathrm{kHz}$. *The* — *boxes indicate the following pairs* $(k_{p,\chi}, k_{i,\chi})$ *from right to left: (i)* $k_{p,\chi} = -0.02\,\frac{\mathrm{A}}{\mathrm{V}}$, $k_{i,\chi} = -15\,\frac{\mathrm{A}}{\mathrm{Vs}}$; *(ii)* $k_{p,\chi} = -0.05\,\frac{\mathrm{A}}{\mathrm{V}}$, $k_{i,\chi} = -37\,\frac{\mathrm{A}}{\mathrm{Vs}}$; *(iii)* $k_{p,\chi} = -0.1\,\frac{\mathrm{A}}{\mathrm{V}}$, $k_{i,\chi} = -55\,\frac{\mathrm{A}}{\mathrm{Vs}}$ *and* $k_{i,\chi} = -60\,\frac{\mathrm{A}}{\mathrm{Vs}}$ *respectively; (iv)* $k_{p,\chi} = -0.14\,\frac{\mathrm{A}}{\mathrm{V}}$, $k_{i,\chi} = -55\,\frac{\mathrm{A}}{\mathrm{Vs}}$; *(v)* $k_{p,\chi} = -0.18\,\frac{\mathrm{A}}{\mathrm{V}}$, $k_{i,\chi} = -15\,\frac{\mathrm{A}}{\mathrm{Vs}}$.

The region of stable pairs $(k_{p,\chi}, k_{i,\chi})$ for the — worst-case operation is depicted in Fig. 3.14. The range of feasible proportional gains $k_{p,\chi}$ is from $0\,\frac{\mathrm{A}}{\mathrm{V}}$ to about $-0.12\,\frac{\mathrm{A}}{\mathrm{V}}$ and the one of possible integral gains $k_{i,\chi}$ is from $0\,\frac{\mathrm{A}}{\mathrm{Vs}}$ to about $-32\,\frac{\mathrm{A}}{\mathrm{Vs}}$. Compared to the region of stable pairs $(k_{p,\chi}, k_{i,\chi})$ for the — standard case, this region is drastically decreased.
In Fig. 3.14, the — box at $k_{p,\chi} = -0.1\,\frac{\mathrm{A}}{\mathrm{V}}$ and $k_{i,\chi} = -15\,\frac{\mathrm{A}}{\mathrm{Vs}}$ determines the chosen proportional gain $k_{p,\chi}$ and integral gain $k_{i,\chi}$, respectively. In Sec. 3.2.3.4 it will be shown that the proportional gain $k_{p,\chi}$ (mainly) is the one of the two PI controller gains $k_{p,\chi}$ and $k_{i,\chi}$, which is crucial to counteract critical voltage drops in the DC-link voltage u_d. Hence, the rather aggressive proportional gain $k_{p,\chi} = -0.1\,\frac{\mathrm{A}}{\mathrm{V}}$ is used.
To verify the correctness of the region of stable pairs $(k_{p,\chi}, k_{i,\chi})$, measurements at the test-bench were performed. Therefor, the following test scenario was used:
The DC-link is not supplied with any load, i.e. $p_l = 0$. Moreover, the objective is that the DC-link voltage u_d tracks its - - - reference $u_{d,\mathrm{ref}}$ as in Fig. 3.16, whose range is between 710 V and 790 V. The q-component i_g^q of grid side current can vary between $-10\,\mathrm{A}$ and $10\,\mathrm{A}$. In accordance to this test scenario, the most critical operation points are identified to be[58]:

$$\text{—}\quad i_f^{d\star} = -1\,\mathrm{A}\ ,\ i_g^{q\star} = 10\,\mathrm{A}\ ,\ u_d^{\star} = 710\,\mathrm{V}\ ,\ \eta_{i,\xi} = 10\ ,\ f_{\mathrm{dis}} = 4\,\mathrm{kHz}\,. \tag{3.43}$$

[58] Due to the strong oscillation of the DC-link voltage u_d in Fig. 3.16, an exact determination of the most critical operation points is not possible.

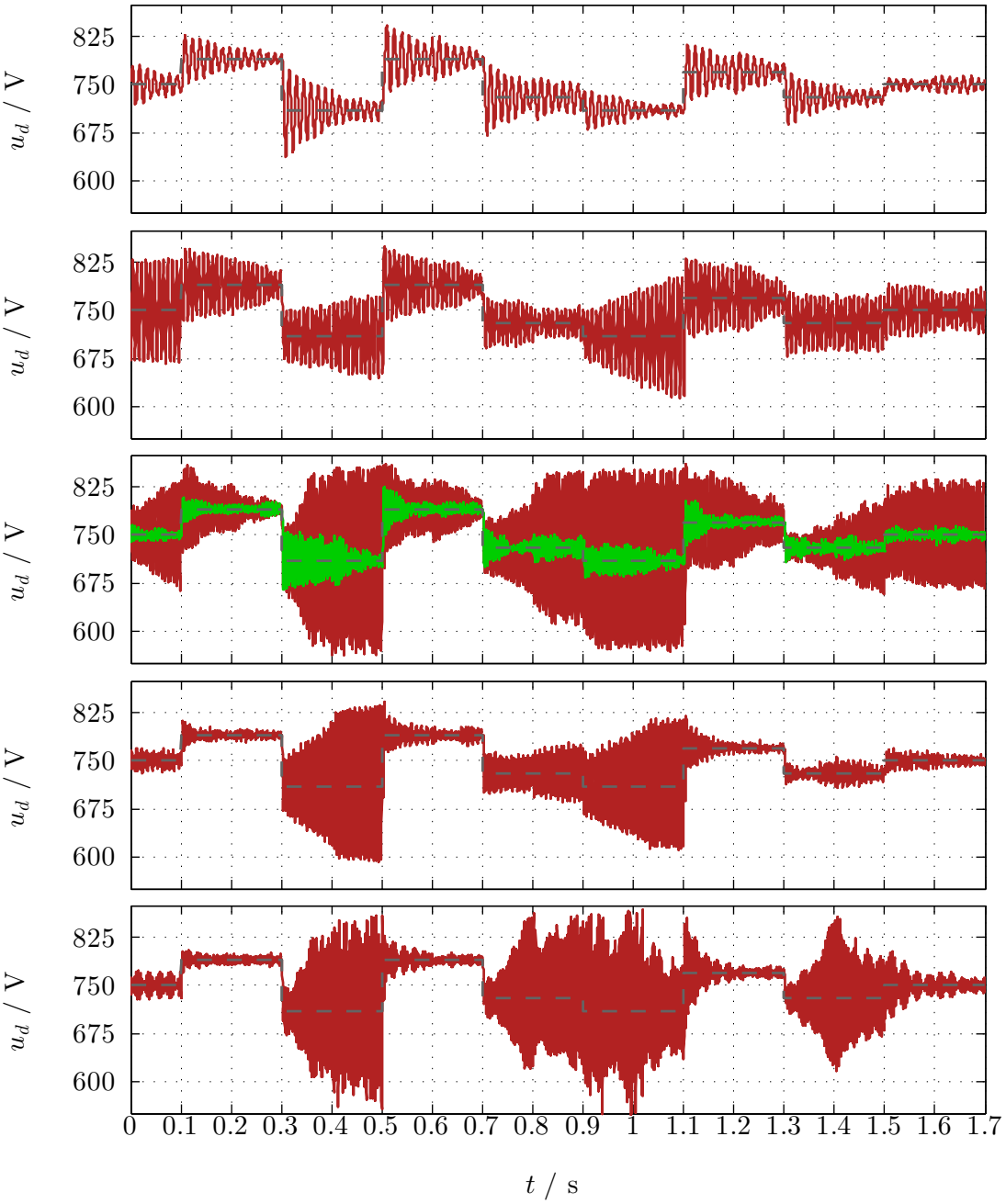

Figure 3.16: *Test scenario – Reference tracking of the DC-link voltage u_d with its - - - reference $u_{d,\mathrm{ref}}$:* — *measured DC-link voltage u_d with $k_{p,\chi} = -0.1\,\frac{\mathrm{A}}{\mathrm{V}}$, $k_{i,\chi} = -55\,\frac{\mathrm{A}}{\mathrm{V\,s}}$,* — *measured DC-link voltage u_d with the following pairs $(k_{p,\chi}, k_{i,\chi})$ (from top to bottom): (i) $k_{p,\chi} = -0.02\,\frac{\mathrm{A}}{\mathrm{V}}$, $k_{i,\chi} = -15\,\frac{\mathrm{A}}{\mathrm{V\,s}}$; (ii) $k_{p,\chi} = -0.05\,\frac{\mathrm{A}}{\mathrm{V}}$, $k_{i,\chi} = -37\,\frac{\mathrm{A}}{\mathrm{V\,s}}$; (iii) $k_{p,\chi} = -0.1\,\frac{\mathrm{A}}{\mathrm{V}}$, $k_{i,\chi} = -60\,\frac{\mathrm{A}}{\mathrm{V\,s}}$; (iv) $k_{p,\chi} = -0.14\,\frac{\mathrm{A}}{\mathrm{V}}$, $k_{i,\chi} = -55\,\frac{\mathrm{A}}{\mathrm{V\,s}}$; (v) $k_{p,\chi} = -0.18\,\frac{\mathrm{A}}{\mathrm{V}}$, $k_{i,\chi} = -15\,\frac{\mathrm{A}}{\mathrm{V\,s}}$.*

Fig. 3.15 depicts the region of stable pairs $(k_{p,\chi}, k_{i,\chi})$ for the — critical operation point. The test scenario was executed for the six pairs $(k_{p,\chi}, k_{i,\chi})$ of the PI controller gains, which (a) are illustrated by the — boxes in Fig. 3.15 and (b) are listed in Tab. 3.4.

	(i)	(ii)	(iii)	(iv)	(v)
$k_{p,\chi}$ (in $\frac{\mathrm{A}}{\mathrm{V}}$)	-0.02	-0.05	-0.1	-0.14	-0.18
$k_{i,\chi}$ (in $\frac{\mathrm{A}}{\mathrm{V\,s}}$)	-15	-37	-55 and -60	-55	-15

Table 3.4: *Pairs* $(k_{p,\chi}, k_{i,\chi})$ *to analyze the critical operation of the test scenario.*

Note that all these pairs $(k_{p,\chi}, k_{i,\chi})$ lie (almost) on the stability margin of the — critical operation point. Fig. 3.16 shows the corresponding measurement results. Each of the five plots illustrates the — DC-link voltage u_d and its - - - reference $u_{d,\mathrm{ref}}$ for the cases (i)–(v) (from top to bottom). The measurements match very well with the derived theory, because in each of the five subplots the DC-link voltage u_d tends to instability.
The third subplot of Fig. 3.16 highlights this result in particular. Therein, two measurement results of the DC-link voltage u_d are presented, one for — $k_{i,\chi} = -55\ \frac{\mathrm{A}}{\mathrm{V\,s}}$ and one for — $k_{i,\chi} = -60\ \frac{\mathrm{A}}{\mathrm{V\,s}}$ (in both cases the proportional gain is $k_{p,\chi} = -0.1\ \frac{\mathrm{A}}{\mathrm{V}}$). While an integral gain of — $k_{i,\chi} = -55\ \frac{\mathrm{A}}{\mathrm{V\,s}}$, which lies inside the stability region, yields a stable operation; an integral gain of — $k_{i,\chi} = -60\ \frac{\mathrm{A}}{\mathrm{V\,s}}$ causes instability, since this gain lies outside the stability region (cf. Fig. 3.15).

3.2.3.3 Reference tracking of the DC-link voltage

This section discusses reference tracking of the DC-link voltage u_d. Unless stated otherwise, the DC-link control uses the controller and filter parameters of Tab. 3.5. Fig. 3.6 summarizes the implementation of the holistic grid side control. The parameters of the experimental setup are listed in Tab. 3.2. Moreover, the DC-link is not supplied with any load, i.e. $p_l = 0$.
The objectives of this section are: (a) to validate the design of the DC-link voltage PI controller with reference filter and (b) to prove the excellent matching of the grid side model with the experimental setup at the test-bench. Therefor, the following experiments are conducted both in simulation and laboratory:

(χ.1) the final implementation of the control strategy (— measurement, — simulation), which is composed of (a) the discrete integral state-feedback controller of Sec. 3.2.2.2 with the design parameters of Tab. 3.3, (b) the DC-link voltage PI controller (3.32) and (3.33) and (c) its reference filter.

(χ.2) the necessity of the reference filter is explained. In this experiment, the reference filter is not in use (— measurement, — simulation).

(χ.3) again, the impact of the weighting factor $\eta_{i,\xi}$ onto the reference tracking of the grid current i_f^q is shown. The Experiment (χ.2) is repeated for the weighting factor $\eta_{i,\xi} = 1$ (— measurement, — simulation) and then compared to the outcomes of (χ.2). The experiment will demonstrate an almost perfect match of measurement and simulation results.

Fig. 3.17 presents the results of the Experiment (χ.1). The control objective is the tracking of the - - - references $u_{d,\mathrm{ref}}$ and $i_{g,\mathrm{ref}}^q$ of DC-link voltage u_d and q-component i_g^q of the grid current, respectively. The plots depict the following quantities from top to bottom: (a) the DC-link voltage u_d, (b) the filter current $\boldsymbol{i}_f^{dq}$, (c) the grid current $\boldsymbol{i}_g^{dq}$, (d) the capacitance voltage $\boldsymbol{u}_h^{dq}$ and (e) the reference filter voltage $\boldsymbol{u}_{f,\mathrm{ref}}^{dq}$. In the first and in the fifth plot, the excellent control performance of the proposed control strategy for Experiment (χ.1) can be seen. Both the DC-link voltage u_d and the grid current i_g^q track their corresponding references $u_{d,\mathrm{ref}}$ and $i_{g,\mathrm{ref}}^q$ very quickly and without any steady-state deviation. Moreover, the DC-link voltage control is hardly

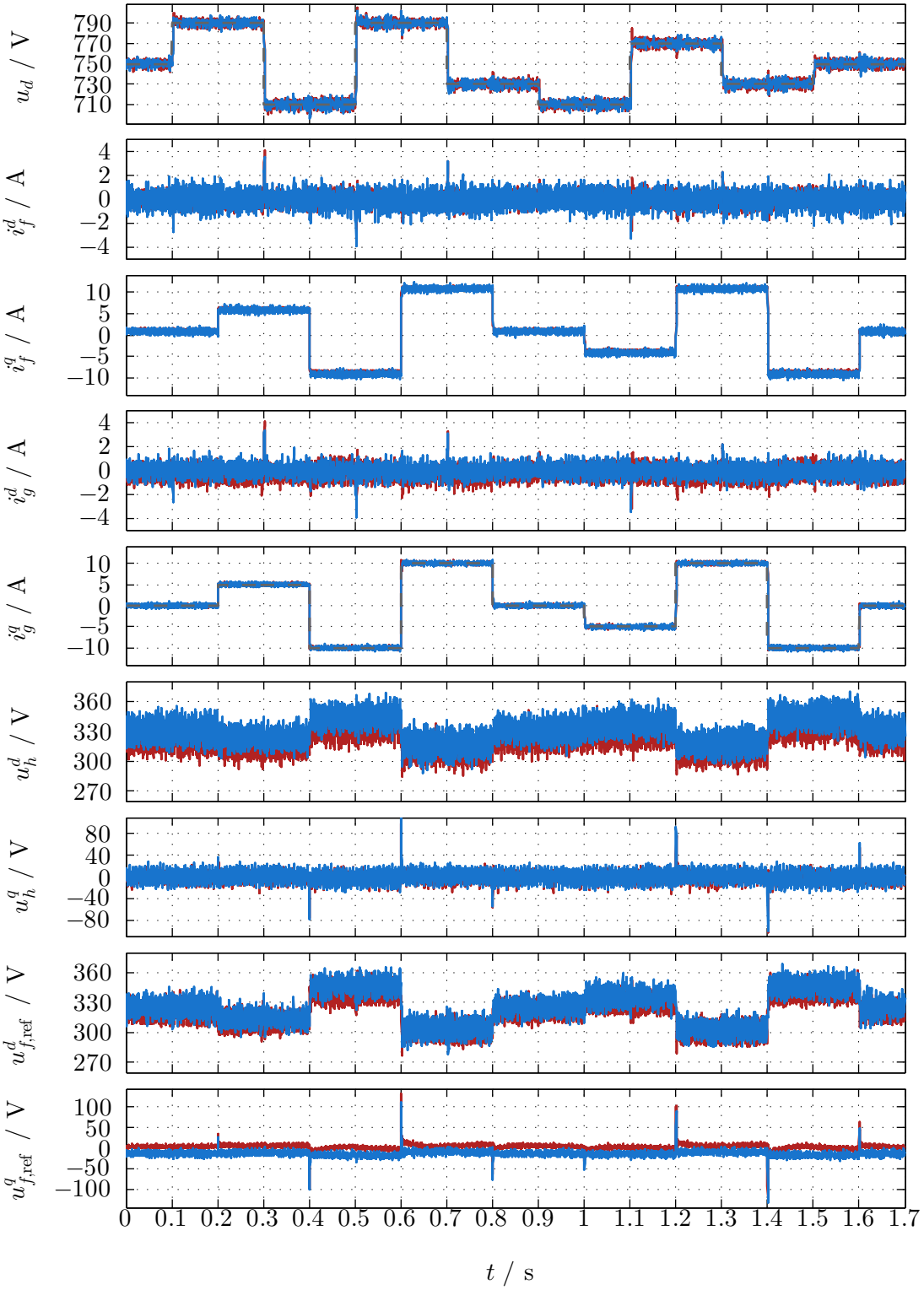

Figure 3.17: *Experiment (χ.1):* — *measured quantities,* — *simulated quantities and* - - - *references* $u_{\mathrm{d,ref}}$ *and* $i_{g,\mathrm{ref}}^q$ *of the DC-link voltage and the grid current respectively.*

description	symbols & values with unit
parameters of the PI controller	
proportional gain	$k_{p,\chi} = -0.1\,\frac{\mathrm{A}}{\mathrm{V}}$
integral gain	$k_{i,\chi} = -15\,\frac{\mathrm{A}}{\mathrm{V\,s}}$
parameter of the reference filter	
time constant	$T_\chi = 8t_{\mathrm{dis}} = 2\,\mathrm{ms}$

Table 3.5: *Parameters of the DC-link voltage control.*

disturbed by the current control of the grid current i_g^q and vice versa. Only at $t = 0.6\,\mathrm{s}$ and $t = 1.4\,\mathrm{s}$, reference jumps of 20 A in the reference grid current $i_{g,\mathrm{ref}}^q$ yield small interferences in the DC-link voltage u_d. Another outcome of Experiment (χ.1) is that the — measurement results are (almost) identical to the — simulation results[59]. Hence, the grid side model (as derived in Ch. 2) emulates the experimental setup at the test-bench perfectly. This can also be seen in Fig. 3.18. Therein, again the results of Experiment (χ.1) are plotted for the DC-link voltage u_d and the d-component i_f^d of the filter current, but zoomed in at the certain time instants $t = 0.1\,\mathrm{s}$, $t = 0.3\,\mathrm{s}$, $t = 0.5\,\mathrm{s}$ and $t = 0.7\,\mathrm{s}$. The plots illustrate that also the transients of the — measurements match the corresponding — simulation results. Further, the good performance of the DC-link voltage control is shown, since the DC-link voltage u_d is adjusted to its reference $u_{d,\mathrm{ref}}$ within 5 ms after reference jumps of 80 V.

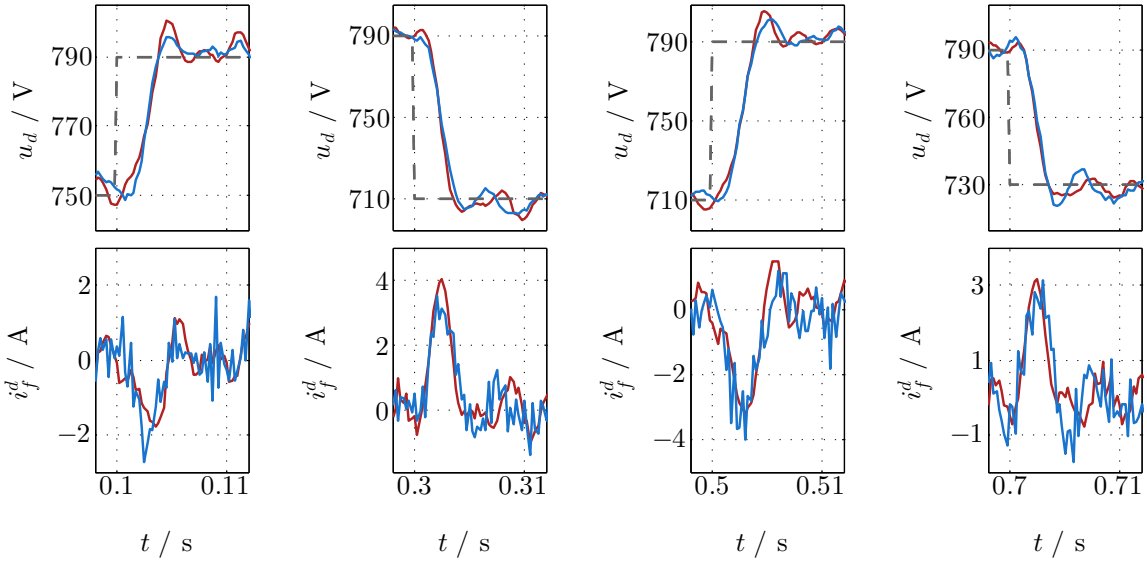

Figure 3.18: *Experiment (χ.1) – Zoom:* — *measured quantities,* — *simulated quantities and* - - - *references* $u_{d,\mathrm{ref}}$ *and* $i_{g,\mathrm{ref}}^q$ *of the DC-link voltage and the grid current respectively.*

Fig. 3.19 depicts the results of Experiment (χ.2) and highlights the necessity to filter the reference DC-link voltage $u_{d,\mathrm{ref}}$. The plots show the — measurements and the — simulation results of the DC-link voltage u_d, the d-component i_f^d of the filter current and the q-component i_g^q of the grid current. While the grid current i_g^q tracks its - - - reference $i_{g,\mathrm{ref}}^q$ equally as in Experiment (χ.1), the DC-link voltage u_d exhibits huge overshoots $> 40\,\mathrm{V}$ in reaction to jumps in its - - - reference $u_{d,\mathrm{ref}}$ (see e.g. at $t = 0.3\,\mathrm{s}$ or $t = 0.5\,\mathrm{s}$). This behavior is unacceptable and results from the

[59] Only the q-component $u_{f,\mathrm{ref}}^q$ of the reference filter voltage features small steady-state deviations.

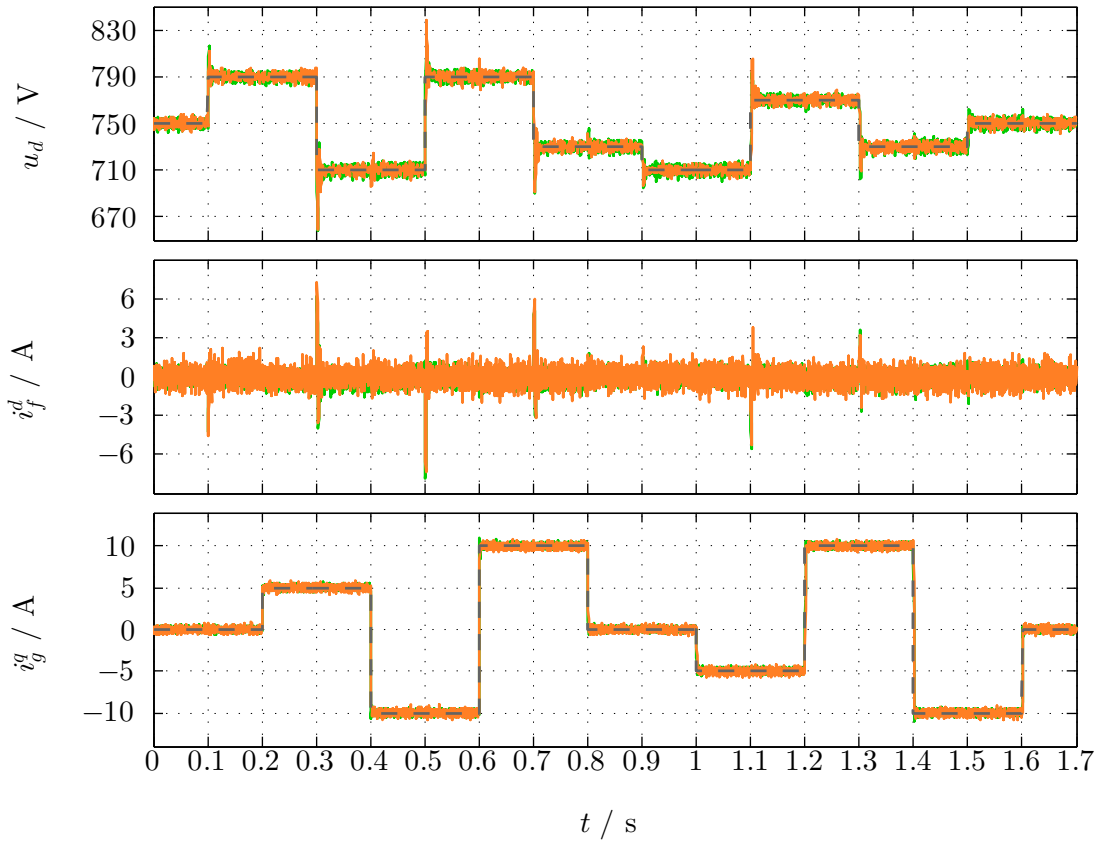

Figure 3.19: *Experiment (χ.2):* — *measured quantities,* — *simulated quantities and* - - - *references* $u_{d,\mathrm{ref}}$ *and* $i^q_{g,\mathrm{ref}}$ *of the DC-link voltage and the grid current respectively.*

very aggressive controller design (cf. Sec. 3.2.3.2). Due to the reference filter as in Fig. 3.6, the overshoots in the DC-link voltage u_d are avoided (as demonstrated by Experiment (χ.1), see Fig. 3.17).
Fig. 3.20 shows the results of Experiment (χ.2) for the q-component i_g^q of the grid current again (as in Fig. 3.19), but zooms in at certain time instants $t=0.4\,\mathrm{s}$, $t=0.6\,\mathrm{s}$, $t=1.2\,\mathrm{s}$ and $t=1.4\,\mathrm{s}$. Additionally, the results of Experiment (χ.3) are appended, i.e. the — measurements and the — simulation results for a reduced weighting factor $\eta_{i,\xi}=1$. As expected, the less aggressive weighting factor $\eta_{i,\xi}=1$ results in a slower control performance. For both Experiments (χ.2) and (χ.3), the transients of the measured grid current i_g^q are (almost) identical to the simulated ones. This proves—in combination with the other results of this section—that the simulation results of Sec. 3.2.2.3 are correct and are able to describe the behavior of the experimental setup almost perfectly.

3.2.3.4 Disturbance rejection of the DC-link voltage

Now, the disturbance rejection of the DC-link voltage regarding the power p_l of the machine side is discussed. To emulate the power p_l at the test bench, the resistance board as in Fig. 3.4 is used. The four resistance values $R_{ld}=\delta\cdot 0.5\,\mathrm{k\Omega}$ with $\delta\in\{\frac{1}{4},\frac{1}{3},\frac{1}{2},1\}$ operate as load of the DC-link.

Remark (R.3.10) *In (R.3.3), it was already explained that the resistive load is more challenging for the DC-link control than the ohmic-inductive behavior of the DFIM. Moreover, the resistance R_{ld} draws power from the DC-link, which has to be compensated for by the grid side. This causes a negative d-component of the filter current, i.e. $i_f^d<0$. Hence, this is the critical power direction*

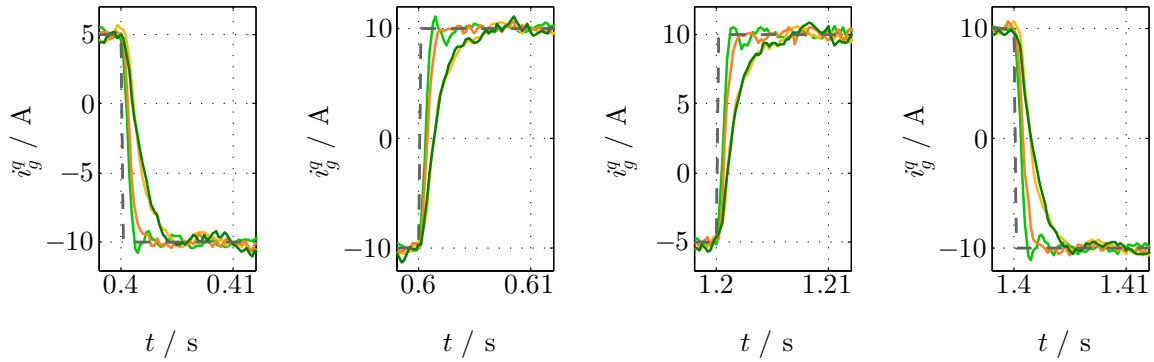

Figure 3.20: *Experiment (χ.3) – Zoom:* — *measured grid current* i_g^q *with weighting factor* $\eta_{i,\xi} = 10$, — *simulated grid current* i_g^q *with weighting factor* $\eta_{i,\xi} = 10$, — *measured grid current* i_g^q *with weighting factor* $\eta_{i,\xi} = 1$, — *simulated grid current* i_g^q *with weighting factor* $\eta_{i,\xi} = 1$ *and* - - - *reference* $i_{g,\mathrm{ref}}^q$ *of the grid current.*

for the DC-link control (see Fig. 3.13 and Sec. 3.2.3.2) and the resistance board is very suitable to investigate the disturbance rejection capability of the DC-link voltage control. Further, the resistance $\frac{1}{4} \cdot 0.5\,\mathrm{k\Omega} = 125\,\Omega$ *discharges the DC-link with its fixed voltage* $u_d = 750\,\mathrm{V}$ *by the power* $\frac{u_d^2}{R_{ld}} = 4.5\,\mathrm{kW}$. *This is equivalent to* 45 % *of the rated mechanical power* $p_{m,\mathrm{nom}} = 10\,\mathrm{kW}$ *of the DFIM (see Tab. 2.3). Commonly, only* 30 % *of the rated mechanical power* $p_{m,\mathrm{nom}}$ *flow through the back-to-back converter. Thus, the resistance board allows to draw more power from the DC-link than the DFIM of the laboratory test-bench.*

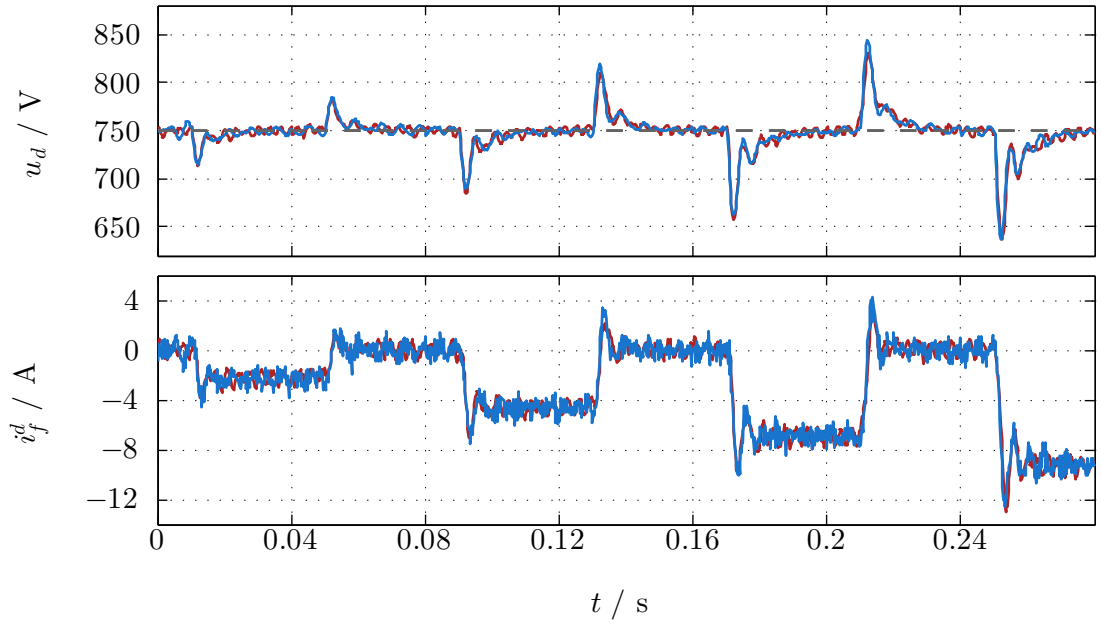

Figure 3.21: *Experiment (χ.4):* — *measured quantities,* — *simulated quantities and* - - - *reference* $u_{d,\mathrm{ref}}$ *of the DC-link voltage.*

The objectives of the DC-link voltage control in this section are: (i) to adjust the DC-link voltage to the fixed value $u_d = 750\,\mathrm{V}$ and (ii) to counteract disturbance due to load jumps induced by different resistances R_{ld}, such that the DC-link voltage u_d stays within the admissible range $u_d \in [600\,\mathrm{V}, 900\,\mathrm{V}]$. To be able to make valid evaluations of the DC-link voltage control performance, the following experiments are conducted:

(χ.4) the final implementation of the control strategy (— measurement, — simulation) as in Experiment (χ.1) is used. It is illustrated in Fig. 3.6.

(χ.5) the impact of the proportional gain $k_{p,\chi}$ is analyzed. Therefor, Experiment (χ.4) is repeated for the two proportional gains $k_{p,\chi} = -0.06\,\frac{\mathrm{A}}{\mathrm{V}}$ and $k_{p,\chi} = -0.14\,\frac{\mathrm{A}}{\mathrm{V}}$.

(χ.6) the choice of the integral gain $k_{i,\chi}$ of the DC-link voltage PI controller affects the disturbance rejection capability as well. Its influence is investigated by repeating Experiment (χ.4) for the integral gain $k_{i,\chi} = -1\,\frac{\mathrm{A}}{\mathrm{V\,s}}$.

(χ.7) to demonstrate the impact of the weighting factor $\eta_{i,\xi}$ of the grid side current controller, Experiment (χ.4) is repeated for the weighting factor $\eta_{i,\xi} = 1$.

Fig. 3.21 depicts the — measurement and — simulation results for Experiment (χ.4). In the upper plot, the DC-link voltage u_d and its constant reference $u_{d,\mathrm{ref}} = 750\,\mathrm{V}$ are shown. The lower plot illustrates the d-component i_f^d of the filter current. Within the 0.28 s duration of the experiment, the four resistance values $R_{ld} = \delta \cdot 0.5\,\mathrm{k\Omega}$ with $\delta \in \{\frac{1}{4}, \frac{1}{3}, \frac{1}{2}, 1\}$ are applied to the DC-link. This leads to power jumps of $\frac{u_d^2}{R_{ld}} = \frac{750^2\,\mathrm{V}^2}{\delta \cdot 0.5\,\mathrm{k\Omega}} = \frac{1}{\delta} \cdot 1.125\,\mathrm{kW} \leq 4.5\,\mathrm{kW}$ at $t = 0.01\,\mathrm{s}$, $t = 0.09\,\mathrm{s}$, $t = 0.17\,\mathrm{s}$ and $t = 0.25\,\mathrm{s}$, respectively. As a consequence, the DC-link voltage u_d drops by about $\frac{1}{\delta} \cdot 30\,\mathrm{V}$. Then, the DC-link voltage PI controller counteracts and adjusts the DC-link voltage u_d fast and accurately to its reference $u_{d,\mathrm{ref}} = 750\,\mathrm{V}$. Switching off the resistance R_{ld} at $t = 0.05\,\mathrm{s}$, $t = 0.13\,\mathrm{s}$ and $t = 0.21\,\mathrm{s}$ results in overshoots in the DC-link voltage u_d of about $\frac{1}{\delta} \cdot 30\,\mathrm{V}$. Then, the DC-link voltage PI controller stops these overshoots and again, controls the DC-link voltage u_d to its reference $u_{d,\mathrm{ref}} = 750\,\mathrm{V}$. Hence, the designed DC-link voltage PI controller yields a high-performance disturbance rejection capability, where even power jumps of $4.5\,\mathrm{kW} > 0.3 \cdot 10\,\mathrm{kW} = 0.3 \cdot p_{m,\mathrm{nom}}$ at the DC-link are nicely compensated so that the DC-link voltage stays within the admissible range $u_d \in [600\,\mathrm{V}, 900\,\mathrm{V}]$. Moreover, the — measurement and — simulation results exhibit (almost) the same performance. Both DC-link voltage u_d and filter current i_f^d match closely.

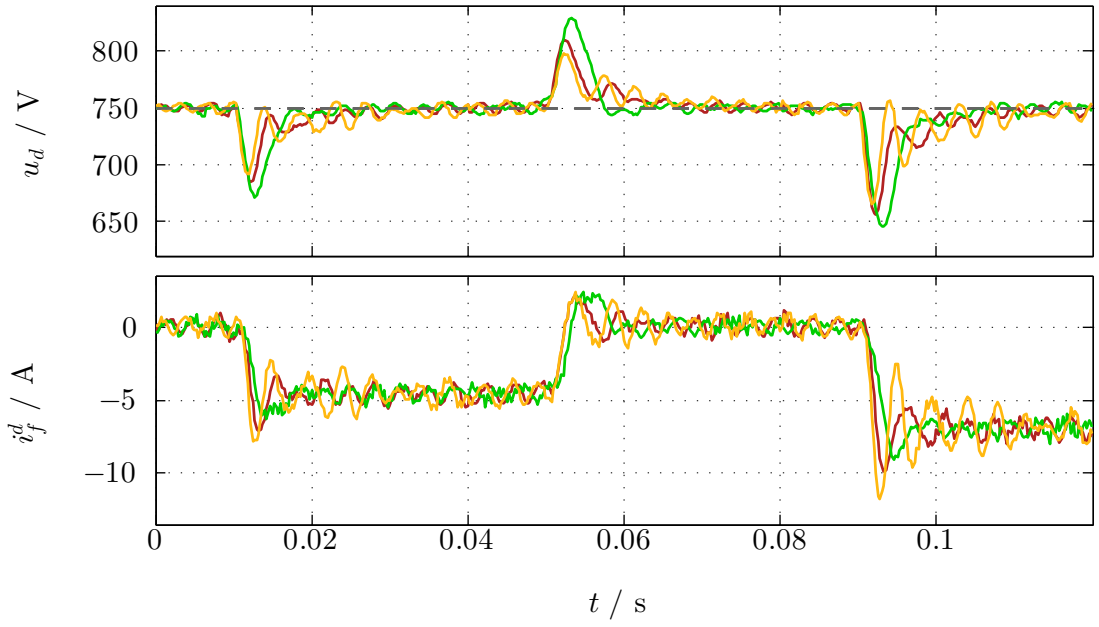

Figure 3.22: *Experiment (χ.5):* — *measured quantities with the proportional gain* $k_{p,\chi} = -0.1\,\frac{\mathrm{A}}{\mathrm{V}}$, — *measured quantities with the proportional gain* $k_{p,\chi} = -0.06\,\frac{\mathrm{A}}{\mathrm{V}}$, — *measured quantities with the proportional gain* $k_{p,\chi} = -0.14\,\frac{\mathrm{A}}{\mathrm{V}}$ *and - - - reference* $u_{d,\mathrm{ref}}$ *of the DC-link voltage.*

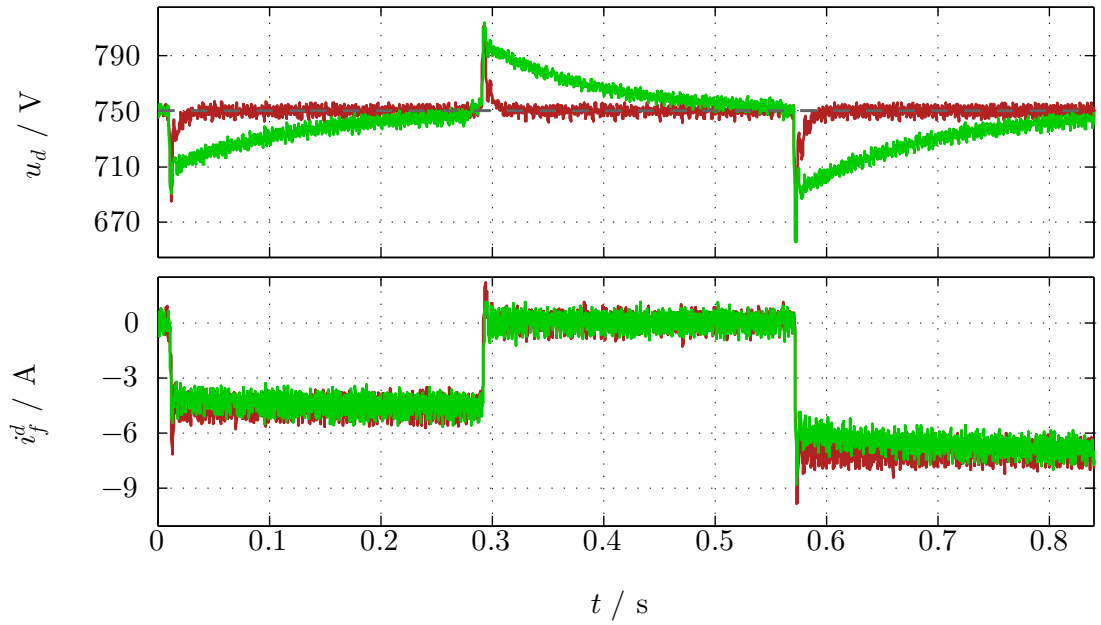

Figure 3.23: *Experiment (χ.6):* — *measured quantities with the integral gain* $k_{i,\chi} = -15\,\frac{\mathrm{A}}{\mathrm{V\,s}}$, — *measured quantities with the integral gain* $k_{i,\chi} = -1\,\frac{\mathrm{A}}{\mathrm{V\,s}}$ *and* - - - *reference* $u_{d,\mathrm{ref}}$ *of the DC-link voltage.*

Fig. 3.22 illustrates the results of Experiment (χ.5), i.e. the impact of the proportional gain $k_{p,\chi}$ on the disturbance rejection. Therefor, Experiment (χ.4) is conducted (i) for the — proportional gain $k_{p,\chi} = -0.06\,\frac{\mathrm{A}}{\mathrm{V}}$ and (ii) for the — proportional gain $k_{p,\chi} = -0.14\,\frac{\mathrm{A}}{\mathrm{V}}$. The two plots depict the measurement results of the DC-link voltage u_d and of the filter current i_f^d. As expected, the less-aggressive — proportional gain $k_{p,\chi} = -0.06\,\frac{\mathrm{A}}{\mathrm{V}}$ causes increased voltage drops and overshoots in the DC-link voltage u_d, whereas the — proportional gain $k_{p,\chi} = -0.14\,\frac{\mathrm{A}}{\mathrm{V}}$ reduces them. The drawback of the very aggressive — proportional gain $k_{p,\chi} = -0.14\,\frac{\mathrm{A}}{\mathrm{V}}$ are the strong oscillations both in the DC-link voltage u_d and in the d-component i_f^d of the filter current[60]. Thus, the proportional gain $k_{p,\chi}$ influences the disturbance rejection capability massively. The choice of the — proportional gain $k_{p,\chi} = -0.1\,\frac{\mathrm{A}}{\mathrm{V}}$ combines the three properties: (a) a stable operation, (b) a high-performance disturbance rejection and (c) minor oscillations.
In Fig. 3.23, measurement results of Experiment (χ.6) are presented, where the changed — integral gain $k_{i,\chi} = -1\,\frac{\mathrm{A}}{\mathrm{V\,s}}$ is used instead of the — integral gain $k_{i,\chi} = -15\,\frac{\mathrm{A}}{\mathrm{V\,s}}$ of Experiment (χ.4). Again, the two plots show the DC-link voltage u_d and the d-component i_f^d of the filter current. While the voltage drops and overshoots in the DC-link voltage u_d are (almost) equal for both cases, the less-aggressive — integral gain $k_{i,\chi} = -1\,\frac{\mathrm{A}}{\mathrm{V\,s}}$ requires much more time to adjust the DC-link voltage u_d to its reference $u_{d,\mathrm{ref}} = 750\,\mathrm{V}$. Consequently, the integral gain $k_{i,\chi}$ is not important to keep the DC-link voltage u_d within the admissible range $u_d \in [600\,\mathrm{V}, 900\,\mathrm{V}]$, but a clever choice allows for a fast adjustment of the DC-link voltage u_d.
Fig. 3.24 illustrates the measurement results of Experiment (χ.7), where the impact of the weighting factor $\eta_{i,\xi}$ of the grid side current controller on the DC-link voltage control is investigated. The two plots show the DC-link voltage u_d and the d-component i_f^d of the filter current (i) for the standard — weighting factor $\eta_{i,\xi} = 10$ of Experiment (χ.4) and (ii) for the decreased — weighting factor $\eta_{i,\xi} = 1$. Obviously, the weighting factor $\eta_{i,\xi}$ influences the disturbance rejection capability significantly. The reduced — weighting factor $\eta_{i,\xi} = 1$ yields bigger voltage drops and overshoots in the DC-link voltage u_d as well as strong oscillations in both the DC-link

[60] For more critical operation points, the proportional gain $k_{p,\chi} = -0.14\,\frac{\mathrm{A}}{\mathrm{V}}$ does not only yield strong oscillations but causes instability (see Fig. 3.14).

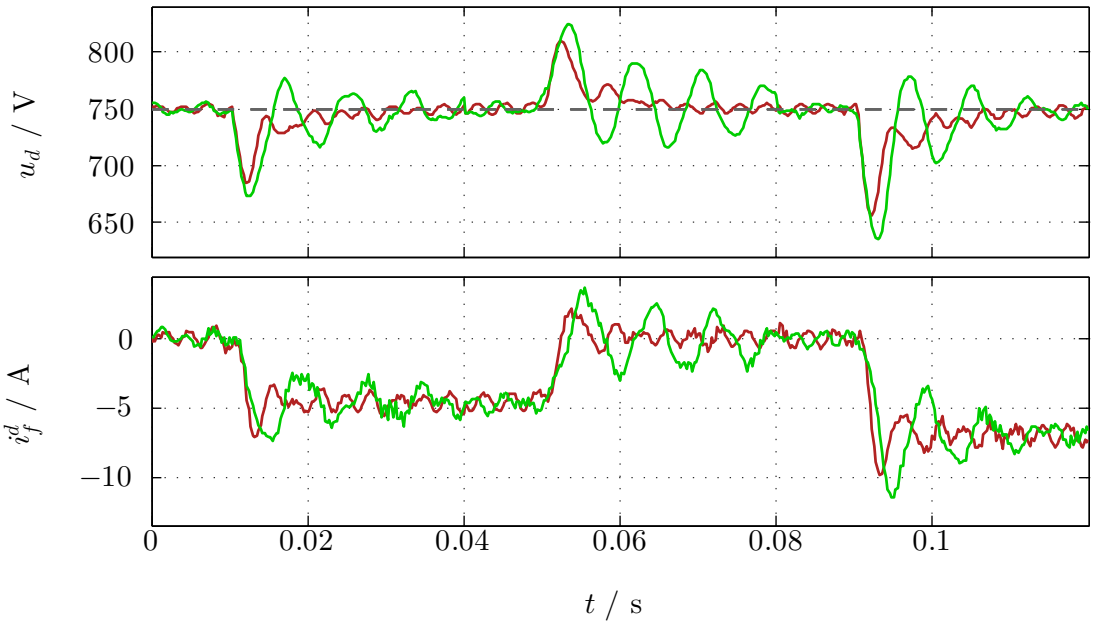

Figure 3.24: *Experiment (χ.7):* — *measured quantities with the weighting factor* $\eta_{i,\xi}=10$, — *measured quantities with the weighting factor* $\eta_{i,\xi}=1$ *and* - - - *reference* $u_{d,\mathrm{ref}}$ *of the DC-link voltage.*

voltage u_d and the filter current i_f^d. Hence, an aggressive choice of the weighting factor $\eta_{i,\xi}$ of the grid side current controller is inevitable to guarantee a high-performance disturbance rejection of the DC-link voltage control.

3.3 Machine side control

In this section, the machine side control is discussed, which has the two main objectives: (i) the tracking of the rotor current reference $\boldsymbol{i}_{r,\mathrm{ref}}^{dq}$ in an inner current control loop and (ii) to ensure a precise adjustment of the references of both the machine torque $m_{m,\mathrm{ref}}$ and the stator reactive power $q_{s,\mathrm{ref}}$ in an outer cascade. By means of simulations in Mabtlab/Simulink and measurements at the test-bench, the validity of the machine side model of the wind turbine system (2.76) will be shown as well as the very good performance of the developed control methods. The new control strategies are necessary, because they need to consider the characteristics of the developed nonlinear DFIM model (2.26). In particular, these characteristics are:

- both stator and rotor of the DFIM exhibit nonlinear flux linkages $\boldsymbol{\psi}_s^{dq}$ and $\boldsymbol{\psi}_r^{dq}$, respectively.
- the dynamics of the DFIM are determined by the differential inductances of the stator $\boldsymbol{L}_s^{dq}$, the rotor $\boldsymbol{L}_r^{dq}$ and the coupling $\boldsymbol{L}_m^{dq}$.
- the anti-diagonal elements of these differential inductances are *not* zero. This—in combination with the nonlinear flux linkages of the stator $\boldsymbol{\psi}_s^{dq}$ and the rotor $\boldsymbol{\psi}_r^{dq}$—results in magnetic cross-couplings between the d- and q-components.
- the interaction between the DFIM and the (optional) LC filter must be considered. Again, due to the small sampling frequency f_{dis}, a discretization strategy is used to allow for a discrete controller design.

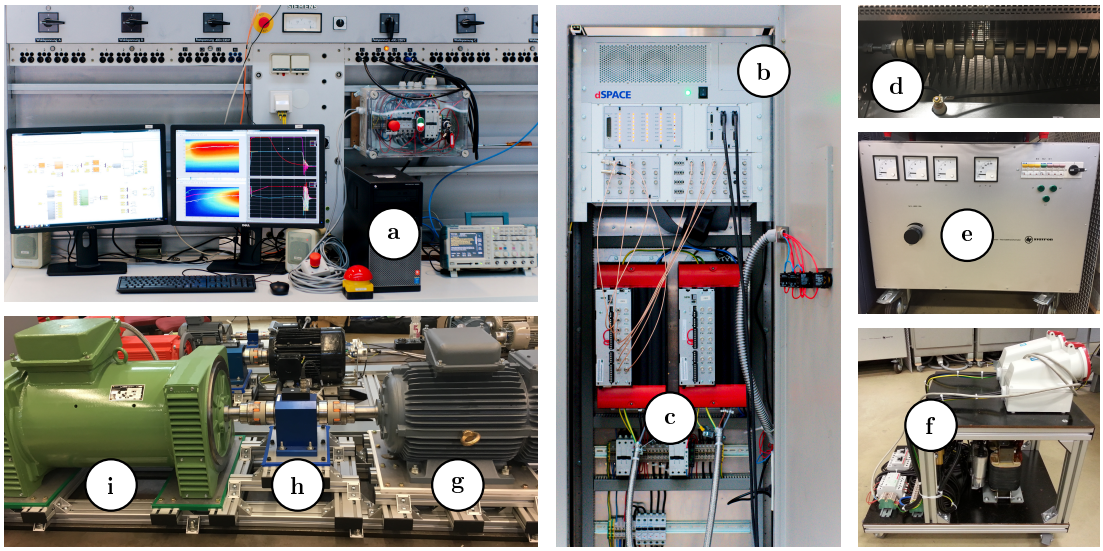

Figure 3.25: *Laboratory test-bench with (a) host computer, (b) dSpace real-time system, (c) machine side converter with DC-link, (d) chopper resistance, (e) two-winding transformer, (f) LC filter, (g) doubly-fed induction machine, (h) torque sensor and (i) electrically-excited synchronous machine.*

- in wind turbine systems, commonly no expensive torque sensor is installed. Hence, the nonlinear machine torque m_m must be adjusted via a feed-forward control method based on the nonlinear flux linkages of the stator $\boldsymbol{\psi}_s^{dq}$ and the rotor $\boldsymbol{\psi}_r^{dq}$.

The differential inductances of the stator $\boldsymbol{L}_s^{dq}$, the rotor $\boldsymbol{L}_r^{dq}$ and the coupling $\boldsymbol{L}_m^{dq}$ as well as the nonlinear flux linkages $\boldsymbol{\psi}_s^{dq}$ and $\boldsymbol{\psi}_r^{dq}$ of stator and rotor, respectively, depend on the operation point of the DFIM. Accordingly, the machine side control strategies must incorporate these dependencies, which necessitate adaptive controller designs with online adjustment. Therefor, the flux maps in Fig. 2.8 and the differential inductance maps in Fig. 2.12 are used.

3.3.1 Laboratory test-bench of the machine side

To verify the machine side part of the holistic wind turbine system model (2.76) via measurements, the relevant components were built-up at the test-bench as shown in Fig. 3.25.
In particular, these components are: (a) the host computer, (b) the dSpace real-time system, (c) the machine side converter with the DC-link and (d) the chopper resistance, (e) the two-winding transformer[61], which couples the stator to the grid, (f) the LC filter, (g) the DFIM, (h) the torque sensor to measure the machine torque m_m and (i) the EESM, which functions as variable-speed source or load.
Fig. 3.26 illustrates the interaction of the experimental setup and its physical components. Instead of the grid side of the wind turbine system and its control (see Sec. 3.2), the DC-link is fed by the diode rectifier, which is directly connected to the grid. Voltage and current sensors — measure the following quantities: the DC-link voltage u_d, the grid line-to-line voltage $\boldsymbol{u}_g^{a\text{-}b\text{-}c}$, the stator current $\boldsymbol{i}_s^{abc}$ and the rotor current $\boldsymbol{i}_r^{uvw}$. If the — LC filter is used, also the filter current $\boldsymbol{i}_l^{uvw}$ and the capacitance line-to-line voltage $\boldsymbol{u}_c^{u\text{-}v\text{-}w}$ are measured[62]. Additionally, the

[61] Since the experimental setup does not require a third winding, instead of a three-winding transformer only a two-winding transformer is implemented at the laboratory test-bench.

[62] More precisely, the voltage sensors in the LC filter measure the voltage $\boldsymbol{u}_c^{u\text{-}v\text{-}w} + R_c \boldsymbol{T}_{LTL} (\boldsymbol{i}_r^{uvw} - \boldsymbol{i}_l^{uvw})$. For

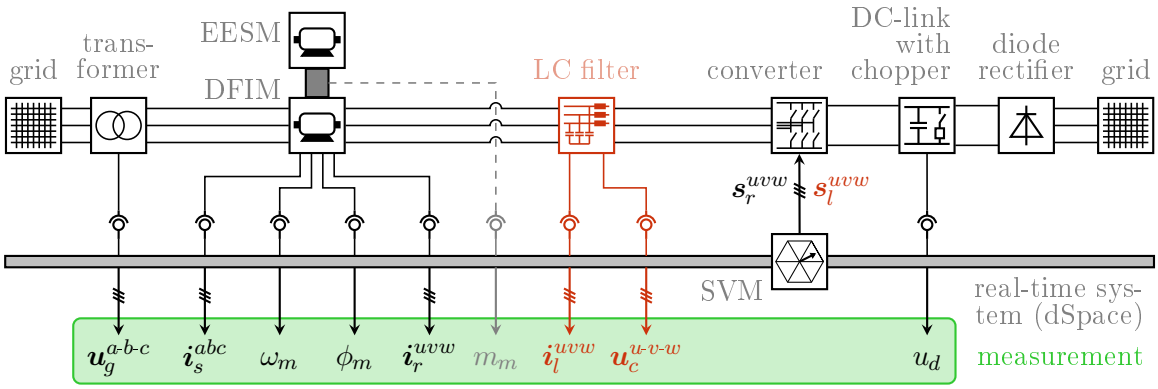

Figure 3.26: *Block diagram of the machine side experimental setup.*

DFIM is equipped with an encoder, which sends the machine rotational speed ω_m and the machine angle ϕ_m to the dSpace real-time system. The measured machine torque m_m is not used for the control, but it allows for evaluating the performance of the implemented feed-forward torque controller. Depending on the use of the — LC filter, the space vector modulation sends either the switching vector $\boldsymbol{s}_r^{uvw}$ or the switching vector $\boldsymbol{s}_l^{uvw}$ to the machine side converter. Tab. 3.6 lists all relevant parameters of the experimental setup[63]. For the purpose of comparability, the simulation model of the wind turbine system in Matlab/Simulink uses the same parameters. Additional simulation parameters are given in Tab. 3.2.

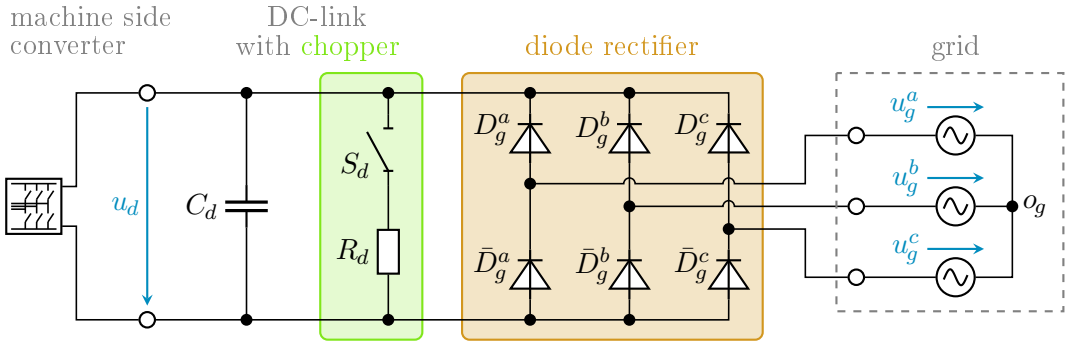

Figure 3.27: *Equivalent circuit of the diode rectifier and the principle of the DC-link with chopper.*

Fig. 3.27 shows the grid-connection of the DC-link via the — diode rectifier with its six diodes $D_g^a, \ldots, \bar{D}_g^c$. If the rotor of the DFIM draws power from the DC-link, then the diode rectifier supplies power to the DC-link and guarantees a minimal DC-link voltage $u_{d,\min}$. An important property of the diode rectifier is the unidirectional power flow from the grid to the DC-link. If the rotor of the DFIM injects power to the DC-link, its impossible to feed this power to the grid. This is the reason to use the — chopper resistance R_d (in Ω), which assures a maximal DC-link voltage $u_{d,\max}$. Its concept is expressed by the switch S_d, which closes when the DC-link voltage u_d exceeds its threshold $u_{d,\max}$. Then, the chopper resistance R_d dissipates the surplus power from the rotor[64].

$R_c \neq 0$, the second term $R_c \boldsymbol{T}_{LTL}\,(\boldsymbol{i}_r^{uvw} - \boldsymbol{i}_l^{uvw})$ must be subtracted to obtain the line-to-line voltage $\boldsymbol{u}_c^{u\text{-}v\text{-}w}$ as in Fig. 3.26.

[63] To allow for a sufficient voltage level of the DC-link voltage u_d, the diode rectifier is fed by a grid voltage amplitude $> \hat{u}_g$.

[64] This principle is a simplification to explain the function of the chopper resistance R_d. The real implementation is more complex.

description	symbols & values with unit
parameters of the dSpace real-time system	
sampling frequency	$f_{\text{dis}} = 4\,\text{kHz}$
sampling time	$t_{\text{dis}} = \frac{1}{f_{\text{dis}}} = 0.25\,\text{ms}$
parameters of the doubly-fed induction machine	
rated mechanical power	$p_{m,\text{nom}} = 10\,\text{kW}$
rated machine torque	$m_{m,\text{nom}} = 55\,\text{Nm}$
pole pair number	$n_m = 2$
stator resistance	$R_s = 0.72\,\Omega$
rotor resistance	$R_r = 0.55\,\Omega$
machine inertia	$\theta_m = 0.094\,\text{kgm}^2$
rated stator current	$\hat{i}_{s,\text{nom}} = 20.9\sqrt{2}\,\text{A}$
rated rotor current	$\hat{i}_{r,\text{nom}} = 17\sqrt{2}\,\text{A}$
parameters of the LC filter	
resistances	$R_l = 1\,\Omega$ and $R_c = 0\,\Omega$
inductance	$L_l = 4.5\,\text{mH}$
capacitance	$C_c = 30\,\mu\text{F}$
parameters of the stator side grid	
voltage amplitude	$\hat{u}_g = 400\sqrt{\frac{2}{3}}\,\text{V}$
frequency	$f_g = 50\,\text{Hz}$
rotational speed	$\omega_g = 2\pi f_g \approx 314\,\frac{\text{rad}}{\text{s}}$
parameters of the simulation (Matlab/Simulink)	
solver (fixed step)	ode4
step time	$t_{\text{sim}} = 5\,\mu\text{s}$
Clarke transformation factors	$k_c = \frac{2}{3}$ and $\kappa_c = \sqrt{\frac{1}{2}}$

Table 3.6: *Parameters of Matlab/Simulink, the machine side and the dSpace real-time system.*

The use of the — diode rectifier and the — chopper resistance R_d for the grid-connection of the DC-link imposes a drawback. It is illustrated in Fig. 3.28, where a typical measurement of the — DC-link voltage u_d is depicted. Since it is not controlled to a certain reference $u_{d,\text{ref}}$, the DC-link voltage u_d floats freely between its minimal and maximal value, i.e. $u_{d,\min} \leq u_d \leq u_{d,\max}$. In the following two cases, this leads to a strongly perturbed DC-link voltage u_d:

(i) the rotor feeds much power to the DC-link, e.g. within the time intervals $t \in [1\,\text{s}, \ldots, 1.1\,\text{s}]$ and $t \in [1.35\,\text{s}, \ldots, 1.5\,\text{s}]$. The chopper resistance R_d is active and it comes to a varying DC-link voltage u_d within a range of about 75 V.

(ii) the rotor consumes much power from the DC-link, e.g. within the time intervals $t \in [0.3\,\text{s}, \ldots, 0.5\,\text{s}]$ and $t \in [1.1\,\text{s}, \ldots, 1.3\,\text{s}]$. The diode rectifier supplies power to the DC-link, which results in a noisy DC-link voltage u_d within a range of about 75 V.

Due to the varying DC-link voltage u_d in the cases (i) and (ii), the machine side converter is disturbed in generating the reference voltage $\boldsymbol{u}_{l,\text{ref}}^{dq}$ (or $\boldsymbol{u}_{r,\text{ref}}^{dq}$). This leads to some oscillations in the machine side quantities. In the evaluation of the measurement results, this drawback of the experimental setup at the test-bench has to be considered.

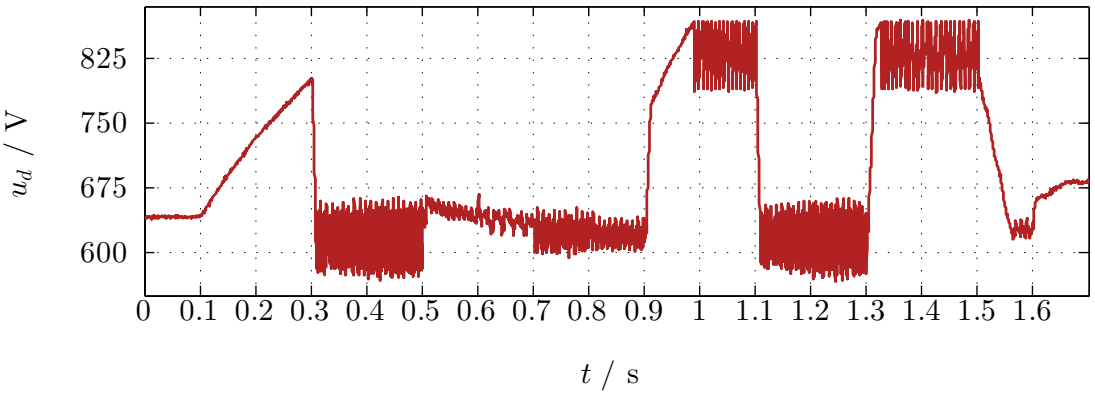

Figure 3.28: *Measurement of the DC-link voltage u_d: chopper resistance and diode rectifier operation.*

3.3.2 Rotor current control

This section discusses the rotor current control strategy, when the DFIM is directly coupled to the machine side converter (see the upper part of Fig. 3.29). The objective of the controller is to adjust the rotor current $\boldsymbol{i}_r^{dq}$ to its reference $\boldsymbol{i}_{r,\mathrm{ref}}^{dq}$ accurately. Therefor, an adaptive PI controller is designed, which allows to consider the system dependency on the operation point[65]. It is extended by (i) a disturbance compensation and (ii) a compensation of the cross-couplings, which occur because of the non-zero anti-diagonal elements of the differential inductances of the stator $\boldsymbol{L}_s^{dq}$, the rotor $\boldsymbol{L}_r^{dq}$ and the coupling $\boldsymbol{L}_m^{dq}$. Moreover, (iii) a reference voltage saturation (SAT), which takes the limited rotor voltage $\boldsymbol{u}_r^{dq}$ into account and (iv) an additional anti-wind up (AWU) to compensate for overshoots in the reference current tracking due to windup effects, are additionally implemented.

3.3.2.1 Adaptive PI controller design

The starting point of the controller design is the nonlinear DFIM dynamics (2.26), which are given by

$$\frac{\mathrm{d}}{\mathrm{d}t}\begin{pmatrix}\boldsymbol{i}_s^{dq}(t)\\ \boldsymbol{i}_r^{dq}(t)\end{pmatrix} = \boldsymbol{L}_{\mathrm{dfim}}^{dq}(\boldsymbol{i}_s^{dq},\boldsymbol{i}_r^{dq})^{-1}\begin{pmatrix}-\boldsymbol{u}_s^{dq}(t) - R_s\boldsymbol{i}_s^{dq}(t) + \omega_k(t)\boldsymbol{J}\boldsymbol{\psi}_s^{dq}(\boldsymbol{i}_s^{dq},\boldsymbol{i}_r^{dq})\\ -\boldsymbol{u}_r^{dq}(t) - R_r\boldsymbol{i}_r^{dq}(t) + (\omega_k(t)-\omega_r(t))\,\boldsymbol{J}\boldsymbol{\psi}_r^{dq}(\boldsymbol{i}_s^{dq},\boldsymbol{i}_r^{dq})\end{pmatrix} \tag{3.44}$$

and where the overall inductance matrix $\boldsymbol{L}_{\mathrm{dfim}}^{dq}$ (in H)$^{4\times4}$ of the DFIM is defined by

$$\boldsymbol{L}_{\mathrm{dfim}}^{dq}(\boldsymbol{i}_s^{dq},\boldsymbol{i}_r^{dq}) := \begin{bmatrix}\boldsymbol{L}_s^{dq}(\boldsymbol{i}_s^{dq},\boldsymbol{i}_r^{dq}) & \boldsymbol{L}_m^{dq}(\boldsymbol{i}_s^{dq},\boldsymbol{i}_r^{dq})^\top\\ \boldsymbol{L}_m^{dq}(\boldsymbol{i}_s^{dq},\boldsymbol{i}_r^{dq}) & \boldsymbol{L}_r^{dq}(\boldsymbol{i}_s^{dq},\boldsymbol{i}_r^{dq})\end{bmatrix}. \tag{3.45}$$

By rearranging the nonlinear DFIM dynamics (3.44), these dynamics can be written as

$$\left.\begin{aligned}\tfrac{\mathrm{d}}{\mathrm{d}t}\boldsymbol{i}_s^{dq}(t) &= \boldsymbol{L}_s^{dq}(\boldsymbol{i}_s^{dq},\boldsymbol{i}_r^{dq})^{-1}\Big(-\boldsymbol{u}_s^{dq}(t) - R_s\boldsymbol{i}_s^{dq}(t) - \boldsymbol{L}_m^{dq}(\boldsymbol{i}_s^{dq},\boldsymbol{i}_r^{dq})^\top\tfrac{\mathrm{d}}{\mathrm{d}t}\boldsymbol{i}_r^{dq}(t) + \omega_k(t)\boldsymbol{J}\boldsymbol{\psi}_s^{dq}(\boldsymbol{i}_s^{dq},\boldsymbol{i}_r^{dq})\Big)\\ \tfrac{\mathrm{d}}{\mathrm{d}t}\boldsymbol{i}_r^{dq}(t) &= \boldsymbol{L}_r^{dq}(\boldsymbol{i}_s^{dq},\boldsymbol{i}_r^{dq})^{-1}\Big(-\boldsymbol{u}_r^{dq}(t) - R_r\boldsymbol{i}_r^{dq}(t) - \boldsymbol{L}_m^{dq}(\boldsymbol{i}_s^{dq},\boldsymbol{i}_r^{dq})\tfrac{\mathrm{d}}{\mathrm{d}t}\boldsymbol{i}_s^{dq}(t) + (\omega_k(t)-\omega_r(t))\boldsymbol{J}\boldsymbol{\psi}_r^{dq}(\boldsymbol{i}_s^{dq},\boldsymbol{i}_r^{dq})\Big)\end{aligned}\right\} \tag{3.46}$$

with the initial values $\boldsymbol{i}_{s,0}^{dq} = \boldsymbol{i}_s^{dq}(0)$ and $\boldsymbol{i}_{r,0}^{dq} = \boldsymbol{i}_r^{dq}(0)$ of stator and rotor current, respectively.

[65] A similar control strategy can be found in [138], therein for reluctance synchronous machines.

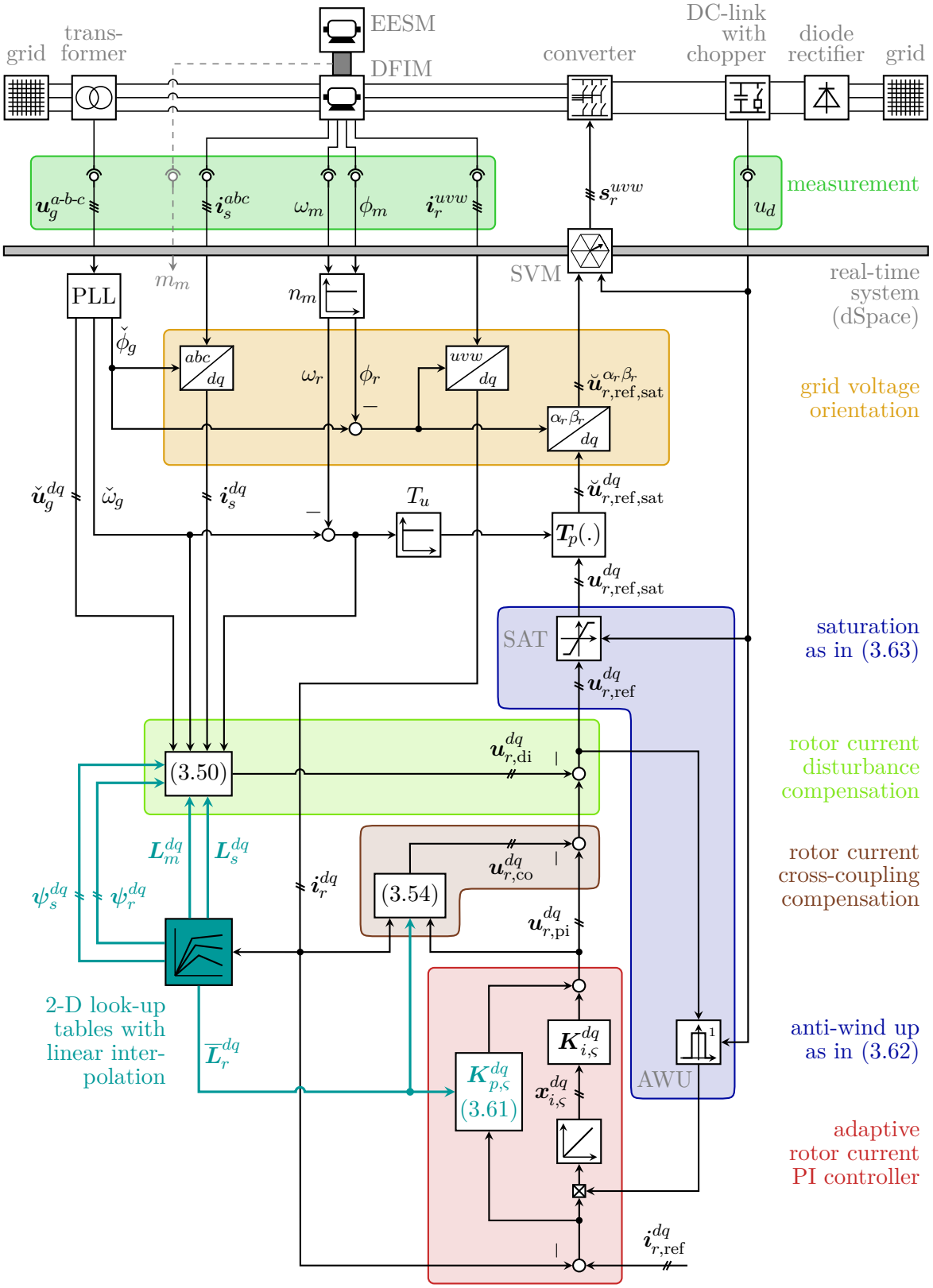

Figure 3.29: *Block diagram of the machine side experimental setup without LC filter and its control strategy for the rotor current.*

Definition (D.3.1) *The leakage coefficient matrices* $\boldsymbol{\Sigma}_s^{dq} \in \mathbb{R}^{2\times 2}$ *and* $\boldsymbol{\Sigma}_r^{dq} \in \mathbb{R}^{2\times 2}$ *of the stator and the rotor are defined by*

$$\left.\begin{aligned} \boldsymbol{\Sigma}_s^{dq}(\boldsymbol{i}_s^{dq},\boldsymbol{i}_r^{dq}) &:= \boldsymbol{I}_2 - \boldsymbol{L}_s^{dq}(\boldsymbol{i}_s^{dq},\boldsymbol{i}_r^{dq})^{-1}\boldsymbol{L}_m^{dq}(\boldsymbol{i}_s^{dq},\boldsymbol{i}_r^{dq})^{\top}\boldsymbol{L}_r^{dq}(\boldsymbol{i}_s^{dq},\boldsymbol{i}_r^{dq})^{-1}\boldsymbol{L}_m^{dq}(\boldsymbol{i}_s^{dq},\boldsymbol{i}_r^{dq}) \\ \text{and}\quad \boldsymbol{\Sigma}_r^{dq}(\boldsymbol{i}_s^{dq},\boldsymbol{i}_r^{dq}) &:= \boldsymbol{I}_2 - \boldsymbol{L}_r^{dq}(\boldsymbol{i}_s^{dq},\boldsymbol{i}_r^{dq})^{-1}\boldsymbol{L}_m^{dq}(\boldsymbol{i}_s^{dq},\boldsymbol{i}_r^{dq})\boldsymbol{L}_s^{dq}(\boldsymbol{i}_s^{dq},\boldsymbol{i}_r^{dq})^{-1}\boldsymbol{L}_m^{dq}(\boldsymbol{i}_s^{dq},\boldsymbol{i}_r^{dq})^{\top} \end{aligned}\right\}. \tag{3.47}$$

Applying these leakage coefficient matrices (3.47) to the nonlinear DFIM dynamics (3.46) yields

$$\left.\begin{aligned} \boldsymbol{L}_s^{dq}(\boldsymbol{i}_s^{dq},\boldsymbol{i}_r^{dq})\boldsymbol{\Sigma}_s^{dq}(\boldsymbol{i}_s^{dq},\boldsymbol{i}_r^{dq})\tfrac{\mathrm{d}}{\mathrm{d}t}\boldsymbol{i}_s^{dq}(t) &= -\boldsymbol{u}_s^{dq}(t) - R_s\boldsymbol{i}_s^{dq}(t) + \omega_k(t)\boldsymbol{J}\boldsymbol{\psi}_s^{dq}(\boldsymbol{i}_s^{dq},\boldsymbol{i}_r^{dq}) \\ &\quad -\boldsymbol{L}_m^{dq}(\boldsymbol{i}_s^{dq},\boldsymbol{i}_r^{dq})^{\top}\boldsymbol{L}_r^{dq}(\boldsymbol{i}_s^{dq},\boldsymbol{i}_r^{dq})^{-1}\Big(-\boldsymbol{u}_r^{dq}(t) - R_r\boldsymbol{i}_r^{dq}(t) + (\omega_k(t)-\omega_r(t))\,\boldsymbol{J}\boldsymbol{\psi}_r^{dq}(\boldsymbol{i}_s^{dq},\boldsymbol{i}_r^{dq})\Big) \\ \boldsymbol{L}_r^{dq}(\boldsymbol{i}_s^{dq},\boldsymbol{i}_r^{dq})\boldsymbol{\Sigma}_r^{dq}(\boldsymbol{i}_s^{dq},\boldsymbol{i}_r^{dq})\tfrac{\mathrm{d}}{\mathrm{d}t}\boldsymbol{i}_r^{dq}(t) &= -\boldsymbol{u}_r^{dq}(t) - R_r\boldsymbol{i}_r^{dq}(t) + (\omega_k(t)-\omega_r(t))\,\boldsymbol{J}\boldsymbol{\psi}_r^{dq}(\boldsymbol{i}_s^{dq},\boldsymbol{i}_r^{dq}) \\ &\quad -\boldsymbol{L}_m^{dq}(\boldsymbol{i}_s^{dq},\boldsymbol{i}_r^{dq})\boldsymbol{L}_s^{dq}(\boldsymbol{i}_s^{dq},\boldsymbol{i}_r^{dq})^{-1}\Big(-\boldsymbol{u}_s^{dq}(t) - R_s\boldsymbol{i}_s^{dq}(t) + \omega_k(t)\boldsymbol{J}\boldsymbol{\psi}_s^{dq}(\boldsymbol{i}_s^{dq},\boldsymbol{i}_r^{dq})\Big) \end{aligned}\right\}. \tag{3.48}$$

The following controller design bases on the nonlinear DFIM dynamics (3.48). The control law of the adaptive rotor current PI controller with control variable $\boldsymbol{u}_{r,\mathrm{ref}}^{dq}$ consists of three terms: (a) the voltage $\boldsymbol{u}_{r,\mathrm{pi}}^{dq}$ (in V)^2 of the PI controller, (b) the voltage $\boldsymbol{u}_{r,\mathrm{di}}^{dq}$ (in V)^2 of the disturbance compensation and (c) the voltage $\boldsymbol{u}_{r,\mathrm{co}}^{dq}$ (in V)^2 to compensate for the cross-couplings. The controller design supposes an *ideal* compensation of both disturbances and cross-couplings, which leads to:

Assumption (A.3.5) *The machine side converter generates the rotor voltage* $\boldsymbol{u}_r^{dq}$*. With respect to its reference* $\boldsymbol{u}_{r,\mathrm{ref}}^{dq}$*, this generation is subject to the dead time* T_u *(cf.* (2.60) *in Sec. 2.2.4), i.e.* $\boldsymbol{u}_r^{dq}(t) = \boldsymbol{u}_{r,\mathrm{ref}}^{dq}(t-T_u)$*. To consider this dead time* T_u *for the two compensations (b) and (c), the following ideal control law is assumed:*

$$\boldsymbol{u}_{r,\mathrm{ref}}^{dq}(t) = \boldsymbol{u}_{r,\mathrm{pi}}^{dq}(t) - \overline{\boldsymbol{u}}_{r,\mathrm{co}}^{dq}(t+T_u) - \boldsymbol{u}_{r,\mathrm{di}}^{dq}(t+T_u)\,, \tag{3.49}$$

where the voltage $\overline{\boldsymbol{u}}_{r,\mathrm{co}}^{dq}$ *(in* V*)*^{2} *characterizes the ideal compensation of the cross-couplings*[66]*.*

By means of (A.3.5) and the disturbance compensation, where the voltage $\boldsymbol{u}_{r,\mathrm{di}}^{dq}$ is given by

$$\begin{aligned} \boldsymbol{u}_{r,\mathrm{di}}^{dq}(t) = &-(\omega_k(t)-\omega_r(t))\,\boldsymbol{J}\boldsymbol{\psi}_r^{dq}(\boldsymbol{i}_s^{dq},\boldsymbol{i}_r^{dq}) \\ &+ \boldsymbol{L}_m^{dq}(\boldsymbol{i}_s^{dq},\boldsymbol{i}_r^{dq})\boldsymbol{L}_s^{dq}(\boldsymbol{i}_s^{dq},\boldsymbol{i}_r^{dq})^{-1}\left(-\boldsymbol{u}_s^{dq}(t) - R_s\boldsymbol{i}_s^{dq}(t) + \omega_k(t)\boldsymbol{J}\boldsymbol{\psi}_s^{dq}(\boldsymbol{i}_s^{dq},\boldsymbol{i}_r^{dq})\right), \end{aligned} \tag{3.50}$$

inserting the *ideal* control law (3.49) into (the rotor part of) the nonlinear DFIM dynamics (3.48) yields

$$\underbrace{\boldsymbol{L}_r^{dq}(\boldsymbol{i}_s^{dq},\boldsymbol{i}_r^{dq})\boldsymbol{\Sigma}_r^{dq}(\boldsymbol{i}_s^{dq},\boldsymbol{i}_r^{dq})}_{=:\overline{\boldsymbol{L}}_r^{dq}(\boldsymbol{i}_s^{dq},\boldsymbol{i}_r^{dq})}\frac{\mathrm{d}}{\mathrm{d}t}\boldsymbol{i}_r^{dq}(t) = -\boldsymbol{u}_{r,\mathrm{pi}}^{dq}(t-T_u) - R_r\boldsymbol{i}_r^{dq}(t) + \overline{\boldsymbol{u}}_{r,\mathrm{co}}^{dq}(t) \tag{3.51}$$

with the *new* rotor inductance $\overline{\boldsymbol{L}}_r^{dq}$ (in H)$^{2\times 2}$. A component-wise representation of (3.51) is given by

$$\left.\begin{aligned} \overline{L}_r^{dd}(\boldsymbol{i}_s^{dq},\boldsymbol{i}_r^{dq})\tfrac{\mathrm{d}}{\mathrm{d}t}i_r^d(t) &= -u_{r,\mathrm{pi}}^d(t-T_u) - R_r i_r^d(t) + \overline{u}_{r,\mathrm{co}}^d(t) - \overline{L}_r^{dq}(\boldsymbol{i}_s^{dq},\boldsymbol{i}_r^{dq})\tfrac{\mathrm{d}}{\mathrm{d}t}i_r^q(t) \\ \overline{L}_r^{qq}(\boldsymbol{i}_s^{dq},\boldsymbol{i}_r^{dq})\tfrac{\mathrm{d}}{\mathrm{d}t}i_r^q(t) &= -u_{r,\mathrm{pi}}^q(t-T_u) - R_r i_r^q(t) + \overline{u}_{r,\mathrm{co}}^q(t) - \overline{L}_r^{qd}(\boldsymbol{i}_s^{dq},\boldsymbol{i}_r^{dq})\tfrac{\mathrm{d}}{\mathrm{d}t}i_r^d(t) \end{aligned}\right\}. \tag{3.52}$$

[66] Note that both the *implemented* voltage $\boldsymbol{u}_{r,\mathrm{co}}^{dq}$ and the *ideal* voltage $\overline{\boldsymbol{u}}_{r,\mathrm{co}}^{dq}$ will be specified in (3.54) and (3.64).

By applying the first equation of (3.52) to the second one and vice versa, the component-wise rotor current dynamics are obtained

$$\left.\begin{aligned}\frac{\det\left(\overline{\boldsymbol{L}}_r^{dq}(\boldsymbol{i}_s^{dq},\boldsymbol{i}_r^{dq})\right)}{\overline{L}_r^{qq}(\boldsymbol{i}_s^{dq},\boldsymbol{i}_r^{dq})}\frac{\mathrm{d}}{\mathrm{d}t}i_r^d(t) &= -u_{r,\mathrm{pi}}^d(t-T_u)-R_r i_r^d(t)+\overline{u}_{r,\mathrm{co}}^d(t)+\frac{\overline{L}_r^{dq}(\boldsymbol{i}_s^{dq},\boldsymbol{i}_r^{dq})}{\overline{L}_r^{qq}(\boldsymbol{i}_s^{dq},\boldsymbol{i}_r^{dq})}\left(u_{r,\mathrm{pi}}^q(t-T_u)+R_r i_r^q(t)-\overline{u}_{r,\mathrm{co}}^q(t)\right)\\ \frac{\det\left(\overline{\boldsymbol{L}}_r^{dq}(\boldsymbol{i}_s^{dq},\boldsymbol{i}_r^{dq})\right)}{\overline{L}_r^{dd}(\boldsymbol{i}_s^{dq},\boldsymbol{i}_r^{dq})}\frac{\mathrm{d}}{\mathrm{d}t}i_r^q(t) &= -u_{r,\mathrm{pi}}^q(t-T_u)-R_r i_r^q(t)+\overline{u}_{r,\mathrm{co}}^q(t)+\frac{\overline{L}_r^{qd}(\boldsymbol{i}_s^{dq},\boldsymbol{i}_r^{dq})}{\overline{L}_r^{dd}(\boldsymbol{i}_s^{dq},\boldsymbol{i}_r^{dq})}\left(u_{r,\mathrm{pi}}^d(t-T_u)+R_r i_r^d(t)-\overline{u}_{r,\mathrm{co}}^d(t)\right)\end{aligned}\right\} \tag{3.53}$$

and, then, choosing the voltage $\overline{\boldsymbol{u}}_{r,\mathrm{co}}^{dq}$ of the cross-coupling compensation to be

$$\overline{\boldsymbol{u}}_{r,\mathrm{co}}^{dq}(t) = -\begin{pmatrix}\frac{\overline{L}_r^{dq}(\boldsymbol{i}_s^{dq},\boldsymbol{i}_r^{dq})}{\overline{L}_r^{qq}(\boldsymbol{i}_s^{dq},\boldsymbol{i}_r^{dq})}\left(u_{r,\mathrm{pi}}^q(t-T_u)+R_r i_r^q(t)\right)\\ \frac{\overline{L}_r^{qd}(\boldsymbol{i}_s^{dq},\boldsymbol{i}_r^{dq})}{\overline{L}_r^{dd}(\boldsymbol{i}_s^{dq},\boldsymbol{i}_r^{dq})}\left(u_{r,\mathrm{pi}}^d(t-T_u)+R_r i_r^d(t)\right)\end{pmatrix} \tag{3.54}$$

and applying (3.54) to (3.53) yields the decoupled rotor current dynamics as follows

$$\begin{bmatrix}\frac{\det\left(\overline{\boldsymbol{L}}_r^{dq}(\boldsymbol{i}_s^{dq},\boldsymbol{i}_r^{dq})\right)}{\overline{L}_r^{qq}(\boldsymbol{i}_s^{dq},\boldsymbol{i}_r^{dq})} & 0\\ 0 & \frac{\det\left(\overline{\boldsymbol{L}}_r^{dq}(\boldsymbol{i}_s^{dq},\boldsymbol{i}_r^{dq})\right)}{\overline{L}_r^{dd}(\boldsymbol{i}_s^{dq},\boldsymbol{i}_r^{dq})}\end{bmatrix}\frac{\mathrm{d}}{\mathrm{d}t}\boldsymbol{i}_r^{dq}(t) = -\underbrace{\left(1-\frac{\overline{L}_r^{dq}(\boldsymbol{i}_s^{dq},\boldsymbol{i}_r^{dq})\overline{L}_r^{qd}(\boldsymbol{i}_s^{dq},\boldsymbol{i}_r^{dq})}{\overline{L}_r^{dd}(\boldsymbol{i}_s^{dq},\boldsymbol{i}_r^{dq})\overline{L}_r^{qq}(\boldsymbol{i}_s^{dq},\boldsymbol{i}_r^{dq})}\right)}_{=\frac{\det\left(\overline{\boldsymbol{L}}_r^{dq}(\boldsymbol{i}_s^{dq},\boldsymbol{i}_r^{dq})\right)}{\overline{L}_r^{dd}(\boldsymbol{i}_s^{dq},\boldsymbol{i}_r^{dq})\overline{L}_r^{qq}(\boldsymbol{i}_s^{dq},\boldsymbol{i}_r^{dq})}}\left(\boldsymbol{u}_{r,\mathrm{pi}}^{dq}(t-T_u)+R_r\boldsymbol{i}_r^{dq}(t)\right). \tag{3.55}$$

By means of the definitions of the rotor time constants $T_r^d := \frac{\overline{L}_r^{dd}}{R_r}$ (in s) of the d-component and $T_r^q := \frac{\overline{L}_r^{qq}}{R_r}$ (in s) of the q-component, the decoupled rotor current dynamics (3.55) simplify to

$$\begin{bmatrix}T_r^d(\boldsymbol{i}_s^{dq},\boldsymbol{i}_r^{dq}) & 0\\ 0 & T_r^q(\boldsymbol{i}_s^{dq},\boldsymbol{i}_r^{dq})\end{bmatrix}\frac{\mathrm{d}}{\mathrm{d}t}\boldsymbol{i}_r^{dq}(t) := \begin{bmatrix}\frac{\overline{L}_r^{dd}(\boldsymbol{i}_s^{dq},\boldsymbol{i}_r^{dq})}{R_r} & 0\\ 0 & \frac{\overline{L}_r^{qq}(\boldsymbol{i}_s^{dq},\boldsymbol{i}_r^{dq})}{R_r}\end{bmatrix}\frac{\mathrm{d}}{\mathrm{d}t}\boldsymbol{i}_r^{dq}(t) = -\frac{1}{R_r}\boldsymbol{u}_{r,\mathrm{pi}}^{dq}(t-T_u)-\boldsymbol{i}_r^{dq}(t)\,. \tag{3.56}$$

Further, the time-delayed voltage $\boldsymbol{u}_{r,\mathrm{pi}}^{dq}(t-T_u)$ of the PI controller is replaced by the following approach:

Assumption (A.3.6) *The voltage $\boldsymbol{u}_{r,\mathrm{pi}}^{dq}(t-T_u) =: \overline{\boldsymbol{u}}_r^{dq}(t)$ is approximated by a first order lag system with gain 1 and time constant T_u, i.e. the following holds*

$$\frac{d}{dt}\overline{\boldsymbol{u}}_r^{dq}(t) = -\frac{1}{T_u}\overline{\boldsymbol{u}}_r^{dq}(t)+\frac{1}{T_u}\boldsymbol{u}_{r,\mathrm{pi}}^{dq}(t) \quad \textit{with} \quad \overline{\boldsymbol{u}}_{r,0}^{dq} = \overline{\boldsymbol{u}}_r^{dq}(0)\,. \tag{3.57}$$

The voltage $\overline{\boldsymbol{u}}_r^{dq}$ (in V)^2 functions as auxiliary variable and has no physical meaning.

(A.3.6) is a standard approximation for considering dead-times in control design and can be found e.g. in [111]. Applying (A.3.6) to the rotor current dynamics (3.56) yields

$$\left.\begin{aligned}&d\text{-component:} && \frac{\mathrm{d}}{\mathrm{d}t}\begin{pmatrix}i_r^d(t)\\ \overline{u}_r^d(t)\end{pmatrix} = \begin{bmatrix}-\frac{1}{T_r^d(\boldsymbol{i}_s^{dq},\boldsymbol{i}_r^{dq})} & -\frac{1}{R_r T_r^d(\boldsymbol{i}_s^{dq},\boldsymbol{i}_r^{dq})}\\ 0 & -\frac{1}{T_u}\end{bmatrix}\begin{pmatrix}i_r^d(t)\\ \overline{u}_r^d(t)\end{pmatrix}+\begin{pmatrix}0\\ \frac{1}{T_u}\end{pmatrix}u_{r,\mathrm{pi}}^d(t)\\ &q\text{-component:} && \frac{\mathrm{d}}{\mathrm{d}t}\begin{pmatrix}i_r^q(t)\\ \overline{u}_r^q(t)\end{pmatrix} = \begin{bmatrix}-\frac{1}{T_r^q(\boldsymbol{i}_s^{dq},\boldsymbol{i}_r^{dq})} & -\frac{1}{R_r T_r^q(\boldsymbol{i}_s^{dq},\boldsymbol{i}_r^{dq})}\\ 0 & -\frac{1}{T_u}\end{bmatrix}\begin{pmatrix}i_r^q(t)\\ \overline{u}_r^q(t)\end{pmatrix}+\begin{pmatrix}0\\ \frac{1}{T_u}\end{pmatrix}u_{r,\mathrm{pi}}^q(t)\end{aligned}\right\}. \tag{3.58}$$

The system dynamics in (3.58) are used to design the adaptive PI controller and represent a second-order lag system with gain $-\frac{1}{R_r}$, small time constant T_u and large time constants $T_r^d(\boldsymbol{i}_s^{dq},\boldsymbol{i}_r^{dq})$ and $T_r^q(\boldsymbol{i}_s^{dq},\boldsymbol{i}_r^{dq})$ for the d-component and q-component, respectively. The PI controller outputs the voltage

$$\boldsymbol{u}_{r,\mathrm{pi}}^{dq}(t) = \boldsymbol{K}_{p,\varsigma}^{dq}(\boldsymbol{i}_s^{dq},\boldsymbol{i}_r^{dq})(\boldsymbol{i}_{r,\mathrm{ref}}^{dq}(t) - \boldsymbol{i}_r^{dq}(t)) + \boldsymbol{K}_{i,\varsigma}^{dq}\boldsymbol{x}_{i,\varsigma}^{dq}(t) \tag{3.59}$$

with the integral state vector $\boldsymbol{x}_{i,\varsigma}^{dq}$ (in As)^2. The proportional gain matrix $\boldsymbol{K}_{p,\varsigma}^{dq}$ (in $\frac{\mathrm{V}}{\mathrm{A}}$)$^{2\times2}$ and the integral gain matrix $\boldsymbol{K}_{i,\varsigma}^{dq}$ (in $\frac{\mathrm{V}}{\mathrm{A\,s}}$)$^{2\times2}$ are defined by

$$\boldsymbol{K}_{p,\varsigma}^{dq}(\boldsymbol{i}_s^{dq},\boldsymbol{i}_r^{dq}) := \mathrm{diag}\big(k_{p,\varsigma}^d(\boldsymbol{i}_s^{dq},\boldsymbol{i}_r^{dq}), k_{p,\varsigma}^q(\boldsymbol{i}_s^{dq},\boldsymbol{i}_r^{dq})\big) \;\text{ and }\; \boldsymbol{K}_{i,\varsigma}^{dq} := \mathrm{diag}(k_{i,\varsigma}^d, k_{i,\varsigma}^q)\,. \tag{3.60}$$

The tuning of the proportional gains $k_{p,\varsigma}^d$ and $k_{p,\varsigma}^q$ and the integral gains $k_{i,\varsigma}^d$ and $k_{i,\varsigma}^q$ of the PI controller is based on the "magnitude optimum criterion" (see e.g. [117]), which results in

$$k_{p,\varsigma}^d(\boldsymbol{i}_s^{dq},\boldsymbol{i}_r^{dq}) = -\frac{\overline{L}_r^{dd}(\boldsymbol{i}_s^{dq},\boldsymbol{i}_r^{dq})}{2T_u}\;,\; k_{p,\varsigma}^q(\boldsymbol{i}_s^{dq},\boldsymbol{i}_r^{dq}) = -\frac{\overline{L}_r^{qq}(\boldsymbol{i}_s^{dq},\boldsymbol{i}_r^{dq})}{2T_u} \;\text{ and }\; k_{i,\varsigma}^d = k_{i,\varsigma}^q = -\frac{R_r}{2T_u}\,. \tag{3.61}$$

As already mentioned in the introduction of this section, the rotor current controller is equipped additionally with (a) an anti-wind up strategy (AWU) and (b) a reference voltage saturation (SAT). The anti-wind up function $a_{i,\varsigma}$ pauses the integration for the integral state $\boldsymbol{x}_{i,\varsigma}^{dq}$ if the reference rotor voltage $\boldsymbol{u}_{r,\mathrm{ref}}^{dq}$ exceeds its achievable range, i.e.

$$\frac{\mathrm{d}}{\mathrm{d}t}\boldsymbol{x}_{i,\varsigma}^{dq}(t) = a_{i,\varsigma}(\boldsymbol{u}_{r,\mathrm{ref}}^{dq}, u_d)(\boldsymbol{i}_{r,\mathrm{ref}}^{dq}(t) - \boldsymbol{i}_r^{dq}(t))\;,\; a_{i,\varsigma}(\boldsymbol{u}_{r,\mathrm{ref}}^{dq}, u_d) = \begin{cases} 0\;, \text{ if } \left\|\boldsymbol{u}_{r,\mathrm{ref}}^{dq}(t)\right\| > \frac{\sqrt{3}k_c u_d(t)}{2} \\ 1\;, \text{ if } \left\|\boldsymbol{u}_{r,\mathrm{ref}}^{dq}(t)\right\| \le \frac{\sqrt{3}k_c u_d(t)}{2} \end{cases} \tag{3.62}$$

with the initial value $\boldsymbol{x}_{i,\varsigma,0}^{dq} = \boldsymbol{x}_{i,\varsigma}^{dq}(0)$ of the integral state. The saturation function $h_{i,\varsigma}$ limits the reference rotor voltage $\boldsymbol{u}_{r,\mathrm{ref}}^{dq}$, which results in the saturated reference $\boldsymbol{u}_{r,\mathrm{ref,sat}}^{dq}$ (in V)^2 of the rotor voltage:

$$\boldsymbol{u}_{r,\mathrm{ref,sat}}^{dq}(t) = h_{i,\varsigma}(\boldsymbol{u}_{r,\mathrm{ref}}^{dq}, u_d)\boldsymbol{u}_{r,\mathrm{ref}}^{dq}(t) \;\text{ with }\; h_{i,\varsigma}(\boldsymbol{u}_{r,\mathrm{ref}}^{dq}, u_d) = \begin{cases} \frac{\sqrt{3}k_c u_d(t)}{2\left\|\boldsymbol{u}_{r,\mathrm{ref}}^{dq}(t)\right\|} & \text{, if } \left\|\boldsymbol{u}_{r,\mathrm{ref}}^{dq}(t)\right\| > \frac{\sqrt{3}k_c u_d(t)}{2} \\ 1 & \text{, if } \left\|\boldsymbol{u}_{r,\mathrm{ref}}^{dq}(t)\right\| \le \frac{\sqrt{3}k_c u_d(t)}{2}\,. \end{cases} \tag{3.63}$$

For the whole controller design, *ideal* compensations for both the disturbances and the cross-couplings have been supposed (see (A.3.5)). This necessitates the future voltage terms $\boldsymbol{u}_{r,\mathrm{di}}^{dq}(t+T_u)$ and $\overline{\boldsymbol{u}}_{r,\mathrm{co}}^{dq}(t+T_u)$, which are not known (not causal!). Hence, *static* compensations for the disturbances and the cross-couplings are used, so that the following control law is implemented:

$$\boldsymbol{u}_{r,\mathrm{ref}}^{dq}(t) = \boldsymbol{u}_{r,\mathrm{pi}}^{dq}(t) - \boldsymbol{u}_{r,\mathrm{co}}^{dq}(t) - \boldsymbol{u}_{r,\mathrm{di}}^{dq}(t) \;\text{ with }\; \boldsymbol{u}_{r,\mathrm{co}}^{dq}(t) := \begin{pmatrix} -\frac{\overline{L}_r^{dq}(\boldsymbol{i}_s^{dq},\boldsymbol{i}_r^{dq})}{\overline{L}_r^{qq}(\boldsymbol{i}_s^{dq},\boldsymbol{i}_r^{dq})}\left(u_{r,\mathrm{pi}}^q(t) + R_r i_r^q(t)\right) \\ -\frac{\overline{L}_r^{qd}(\boldsymbol{i}_s^{dq},\boldsymbol{i}_r^{dq})}{\overline{L}_r^{dd}(\boldsymbol{i}_s^{dq},\boldsymbol{i}_r^{dq})}\left(u_{r,\mathrm{pi}}^d(t) + R_r i_r^d(t)\right) \end{pmatrix}\,. \tag{3.64}$$

Remark (R.3.11) *The differential inductances of the stator $\boldsymbol{L}_s^{dq}$, the rotor $\boldsymbol{L}_r^{dq}$ and the coupling $\boldsymbol{L}_m^{dq}$ as well as the flux linkages $\boldsymbol{\psi}_s^{dq}$ and $\boldsymbol{\psi}_r^{dq}$ of stator and rotor are required to determine the proportional gain matrix $\boldsymbol{K}_{p,\varsigma}^{dq}$ and the compensation voltages $\boldsymbol{u}_{r,\mathrm{co}}^{dq}$ and $\boldsymbol{u}_{r,\mathrm{di}}^{dq}$ for the disturbances and cross-couplings. Therefor, the 2-D look-up tables (with linear interpolation) of Fig. 2.12 and Fig. 2.8 are used. Thus, the measured rotor current $\boldsymbol{i}_r^{dq}$ is sufficient to obtain the differential inductances $\boldsymbol{L}_s^{dq}$, $\boldsymbol{L}_r^{dq}$ and $\boldsymbol{L}_m^{dq}$ and the flux linkages $\boldsymbol{\psi}_s^{dq}$ and $\boldsymbol{\psi}_r^{dq}$.*

The implementation of the overall strategy of the adaptive rotor current PI controller is summarized in Fig. 3.29.

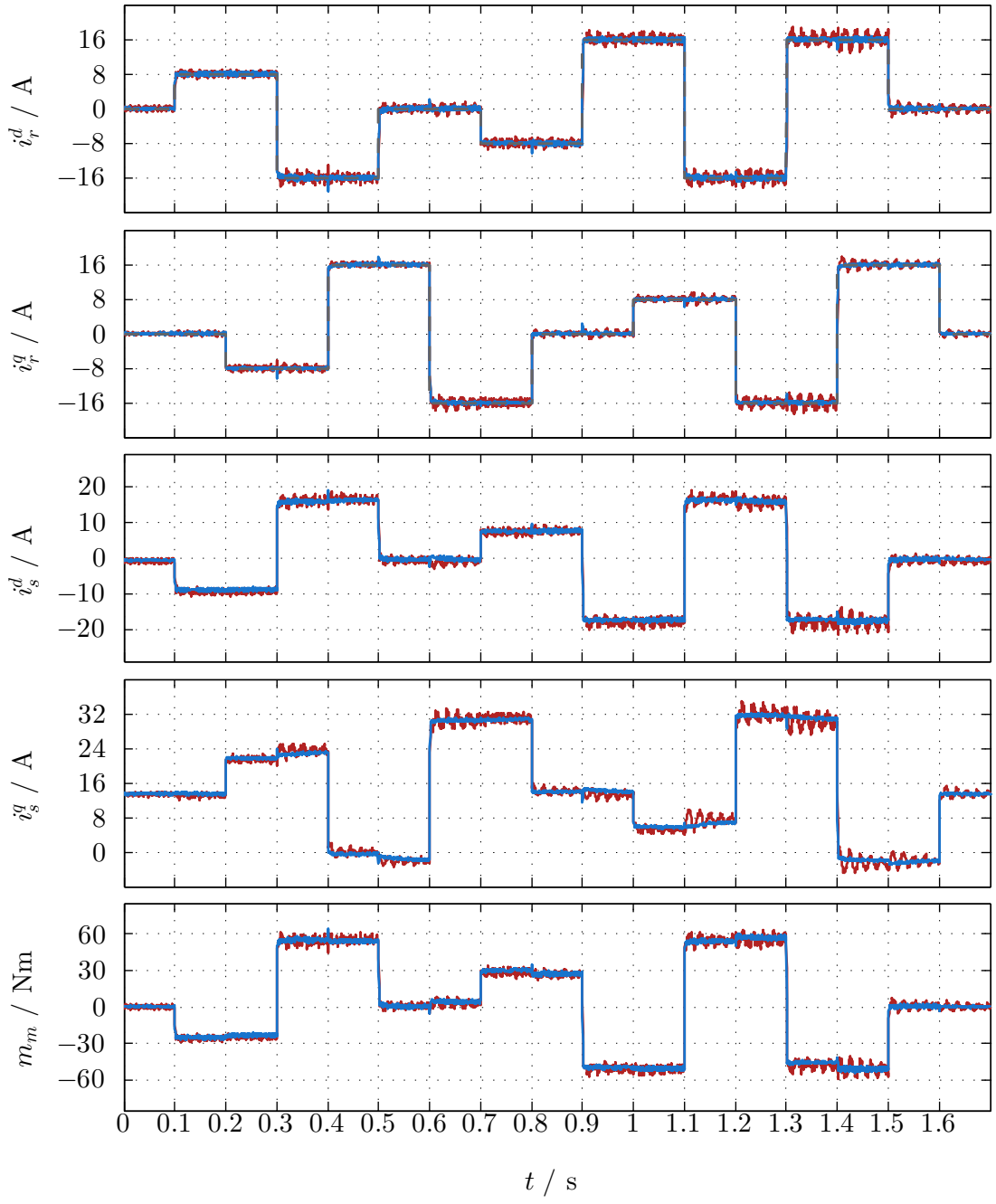

Figure 3.30: *Experiment (ς.1):* — *measured quantities,* — *simulated quantities and* - - - *reference* $\boldsymbol{i}_{r,\mathrm{ref}}^{dq}$ *of the rotor current.*

3.3.2.2 Reference tracking of the rotor currents

This section analyzes the reference tracking of the adaptive rotor current PI controller. Unless stated otherwise, the control law (3.64) is used and the parameters of the experimental setup are listed in Tab. 3.6. Fig. 3.29 depicts the experimental setup and the implemented current control. The objectives of this section are: (a) to validate the design of the adaptive rotor current PI

controller and (b) to verify the matching of the developed nonlinear DFIM model with the experimental setup at the test-bench. Therefor, the following experiments are conducted both in simulation and laboratory:

(ς.1) the implemented control strategy (— measurement, — simulation) which is composed of: (a) the adaptive PI controller (3.59) with its control parameters as in (3.61), (b) the disturbance compensation as in (3.50), (c) the cross-coupling compensation as in (3.64), (d) the anti-wind up strategy (3.62) and (e) the reference voltage saturation (3.63). The EESM is speed-controlled and adjusts the machine rotational speed ω_m to the constant value $120\,\frac{\text{rad}}{\text{s}} < \frac{\omega_g}{n_m}$ (sub-synchronous operation).

(ς.2) to investigate the impacts of the disturbance compensation and the cross-coupling compensation, Experiment (ς.1) is repeated but without the two compensations (b) and (c).

(ς.3) to demonstrate that the control strategy works well independently from the machine rotational speed ω_m, Experiment (ς.1) is conducted for the machine rotational speed $\omega_m = 170\,\frac{\text{rad}}{\text{s}} > \frac{\omega_g}{n_m}$ (super-synchronous operation).

Fig. 3.30 presents the results of Experiment (ς.1). The control objective is tracking of the - - - reference $\boldsymbol{i}_{r,\text{ref}}^{dq}$ of the rotor current. The plots depict the following quantities from top to bottom: (a) the rotor current $\boldsymbol{i}_r^{dq}$, (b) the stator current $\boldsymbol{i}_s^{dq}$ and (c) the machine torque m_m. The first two plots validate the good control performance of the implemented rotor current controller. The rotor current reference $\boldsymbol{i}_{r,\text{ref}}^{dq}$ is tracked quickly and precisely and reference jumps do hardly affect the control of the orthogonal component. Moreover, the — simulation results match very well with the — measurements. Their only differences—the small oscillations in the — measurements—result from the structure of the experimental setup as already explained in Sec. 3.3. In cases of big machine torques $|m_m|$, the DC-link operates either in *chopper resistance mode* or in *diode rectifier mode* as shown in Fig. 3.28. This disturbs the voltage generation of the machine side converter and causes oscillations, e.g. during the time intervals $t \in [1.2\,\text{s}, 1.3\,\text{s}]$ or $t \in [1.4\,\text{s}, 1.5\,\text{s}]$. By contrast, the *normal DC-link operation* in the time interval $t \in [0\,\text{s}, 0.3\,\text{s}]$ allows to generate the rotor voltage $\boldsymbol{u}_r^{dq}$ correctly without any oscillations.

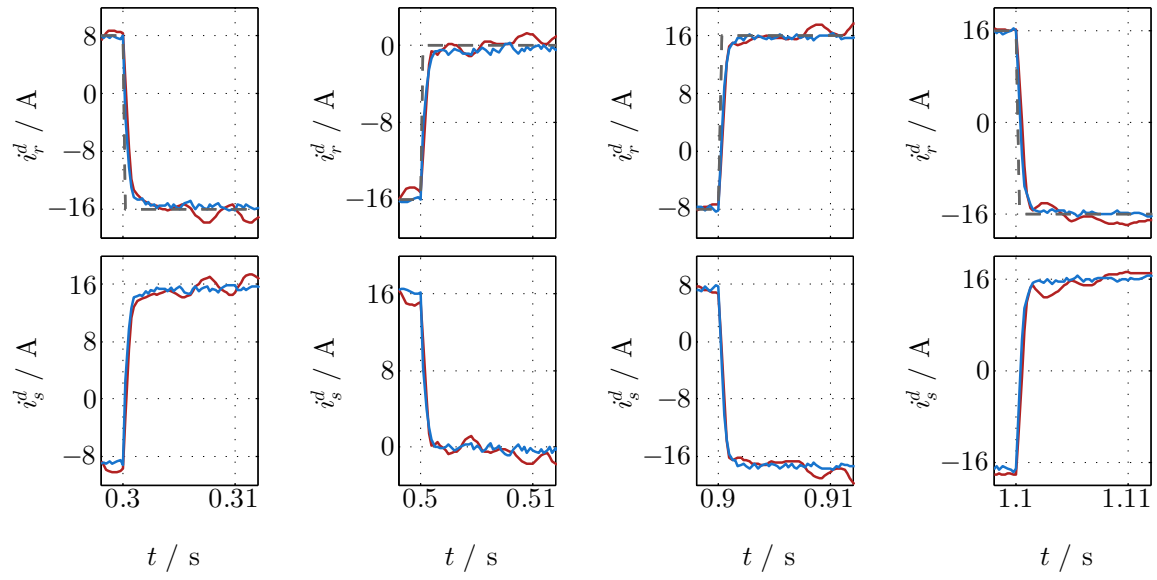

Figure 3.31: *Experiment (ς.1) – Zoom of the d-component:* — *measured quantities,* — *simulated quantities and* - - - *reference* $i_{r,\text{ref}}^d$ *of the rotor current.*

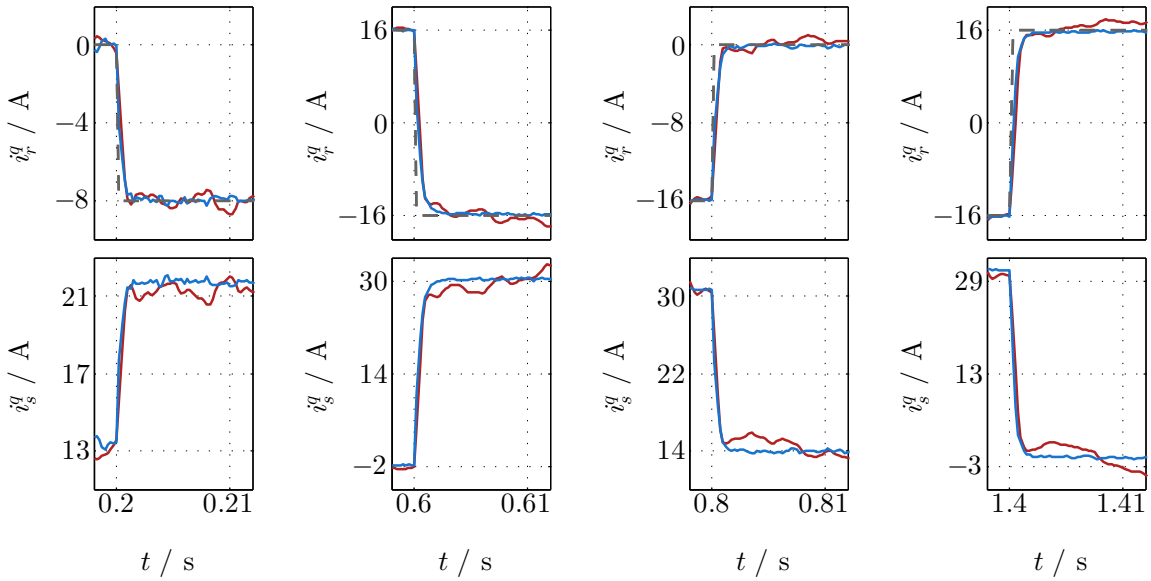

Figure 3.32: *Experiment (ς.1) – Zoom of the q-component:* — *measured quantities,* — *simulated quantities and* - - - *reference* $i^q_{r,\mathrm{ref}}$ *of the rotor current.*

Fig. 3.31 and Fig. 3.32 show zoomed results of Experiment (ς.1). Fig. 3.31 depicts the d-components i_r^d and i_s^d of the stator current and rotor current, respectively, while Fig. 3.32 illustrates the corresponding q-components i_r^q and i_s^q. In both figures, the dynamics of the — simulation results are (almost) identical to the ones of the — measurements, which verifies the strategy to model the DFIM dynamics by the differential inductances of the stator $\boldsymbol{L}_s^{dq}$, the rotor $\boldsymbol{L}_r^{dq}$ and the coupling $\boldsymbol{L}_m^{dq}$ as shown in Fig. 2.12. Moreover, the excellent control performance is highlighted. The rotor current $\boldsymbol{i}_r^{dq}$ is adjusted to its - - - reference $\boldsymbol{i}_{r,\mathrm{ref}}^{dq}$ within about 2 ms in reaction to reference jumps of up to 32 A. Further, the rotor current $\boldsymbol{i}_r^{dq}$ does not exhibit any overshoots.

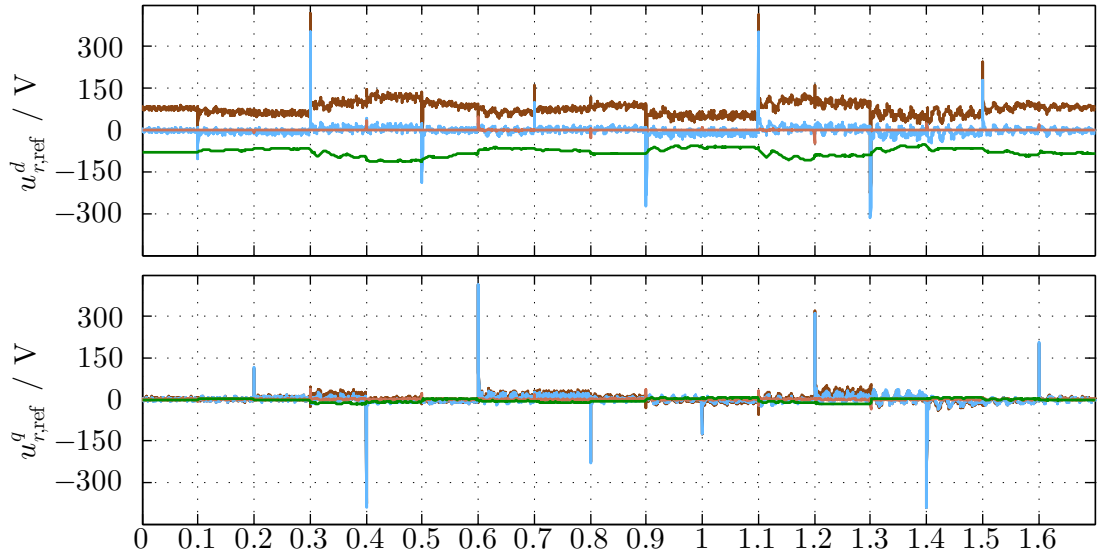

Figure 3.33: *Experiment (ς.1) – Control law:* — *measured reference* $\boldsymbol{u}^{dq}_{r,\mathrm{ref}}$ *of the rotor voltage, which consists of: (a) the* — *measured voltage* $\boldsymbol{u}^{dq}_{r,\mathrm{pi}}$ *of the PI controller, (b) the* — *measured voltage* $\boldsymbol{u}^{dq}_{r,\mathrm{di}}$ *of the disturbance compensation and (c) the* — *measured voltage* $\boldsymbol{u}^{dq}_{r,\mathrm{co}}$ *of the cross-coupling compensation.*

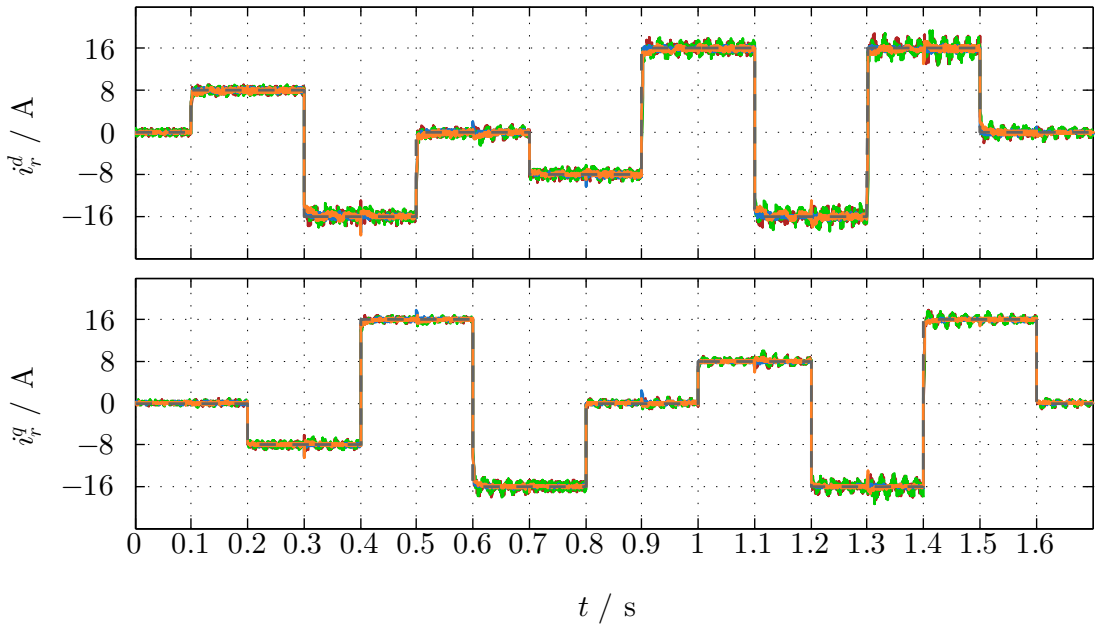

Figure 3.34: *Experiment (ς.2):* — *measured rotor current* $\boldsymbol{i}_r^{dq}$ *with disturbance compensation and cross-coupling compensation,* — *simulated rotor current* $\boldsymbol{i}_r^{dq}$ *with disturbance compensation and cross-coupling compensation,* — *measured rotor current* $\boldsymbol{i}_r^{dq}$ *without disturbance compensation and cross-coupling compensation,* — *simulated rotor current* $\boldsymbol{i}_r^{dq}$ *without disturbance compensation and cross-coupling compensation and* - - - *reference* $\boldsymbol{i}_{r,\mathrm{ref}}^{dq}$ *of the rotor current.*

Fig. 3.33 shows the — reference $\boldsymbol{u}_{r,\mathrm{ref}}^{dq}$ of the rotor voltage of Experiment (ς.1), which consists of: (a) the — voltage $\boldsymbol{u}_{r,\mathrm{pi}}^{dq}$ of the PI controller, (b) the — voltage $\boldsymbol{u}_{r,\mathrm{di}}^{dq}$ of the disturbance compensation and (c) the — voltage $\boldsymbol{u}_{r,\mathrm{co}}^{dq}$ of the cross-coupling compensation. The disturbance compensation voltage $\boldsymbol{u}_{r,\mathrm{di}}^{dq}$ mainly accounts for the steady-state part of the rotor voltage reference $\boldsymbol{u}_{r,\mathrm{ref}}^{dq}$, while the voltage $\boldsymbol{u}_{r,\mathrm{pi}}^{dq}$ of the PI controller causes huge reference peaks in reaction to jumps in the rotor current reference $\boldsymbol{i}_{r,\mathrm{ref}}^{dq}$, i.e. it is responsible for the transient behavior. The voltage $\boldsymbol{u}_{r,\mathrm{co}}^{dq}$ of the cross-coupling compensation is almost zero in the steady-state operation and features only small peaks in reaction to reference jumps in the orthogonal component of the rotor current $\boldsymbol{i}_r^{dq}$.

Fig. 3.34 shows the outcomes of Experiment (ς.2), where the impact of the disturbance compensation and the cross-coupling compensation is investigated. The results (— measurement, — simulation) of Experiment (ς.1) are compared to the ones of Experiment (ς.2), where both, disturbance compensation and cross-coupling compensation, are not used (— measurement, — simulation). The two plots depict the rotor current $\boldsymbol{i}_r^{dq}$ and its - - - reference $\boldsymbol{i}_{r,\mathrm{ref}}^{dq}$. Because (i) the integral state $\boldsymbol{x}_{i,\varsigma}^{dq}$ adopts the steady-state part of the rotor voltage reference $\boldsymbol{u}_{r,\mathrm{ref}}^{dq}$ from the disturbance compensation voltage $\boldsymbol{u}_{r,\mathrm{di}}^{dq}$ and (ii) the influence of the cross-coupling compensation voltage $\boldsymbol{u}_{r,\mathrm{co}}^{dq}$ onto the rotor voltage reference $\boldsymbol{u}_{r,\mathrm{ref}}^{dq}$ is very small, the results of the two experiments differ only slightly. Thus, the two compensations are helpful but not essential to obtain a good control performance.

Fig. 3.35 illustrates the results of Experiment (ς.3). Therein, Experiment (ς.1), which operates at the machine rotational speed $\omega_m = 120\,\frac{\mathrm{rad}}{\mathrm{s}} < \frac{\omega_g}{n_m}$, is repeated for the machine rotational speed $\omega_m = 170\,\frac{\mathrm{rad}}{\mathrm{s}} > \frac{\omega_g}{n_m}$. Again, the two plots depict the rotor current $\boldsymbol{i}_r^{dq}$ and its - - - reference $\boldsymbol{i}_{r,\mathrm{ref}}^{dq}$. The reference tracking (— measurement, — simulation) of Experiment (ς.3) features

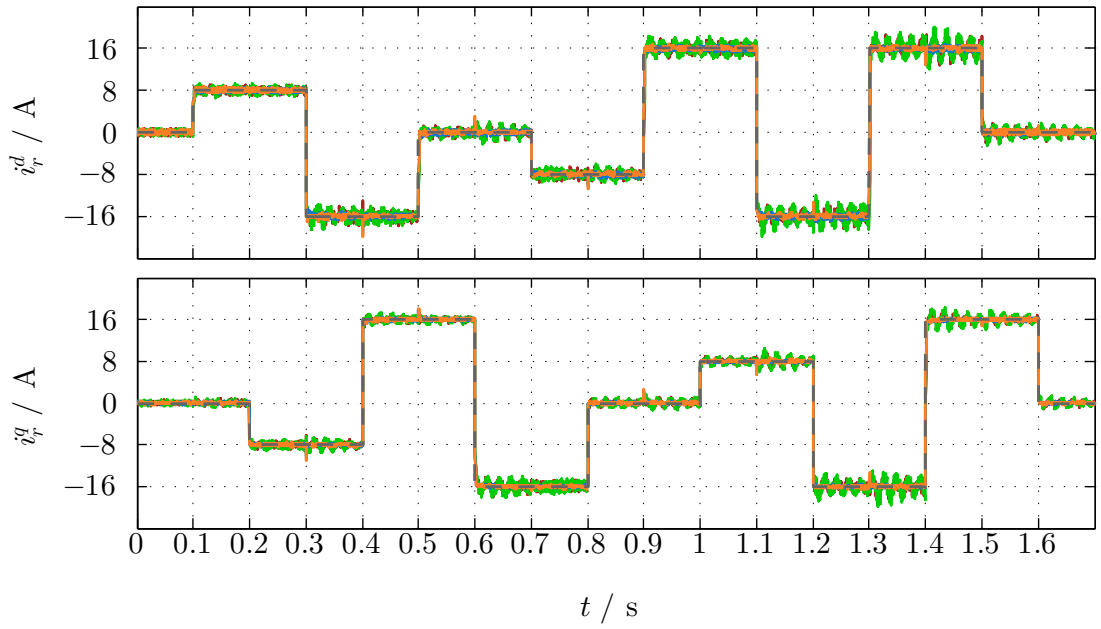

Figure 3.35: *Experiment (ς.3):* — *measured rotor current* $\boldsymbol{i}_r^{dq}$ *with machine rotational speed* $\omega_m = 120\,\frac{\text{rad}}{\text{s}}$, — *simulated rotor current* $\boldsymbol{i}_r^{dq}$ *with machine rotational speed* $\omega_m = 120\,\frac{\text{rad}}{\text{s}}$, — *measured rotor current* $\boldsymbol{i}_r^{dq}$ *with machine rotational speed* $\omega_m = 170\,\frac{\text{rad}}{\text{s}}$, — *simulated rotor current* $\boldsymbol{i}_r^{dq}$ *with machine rotational speed* $\omega_m = 170\,\frac{\text{rad}}{\text{s}}$ *and - - - reference* $\boldsymbol{i}_{r,\text{ref}}^{dq}$ *of the rotor current.*

(almost) the same performance as the one (— measurement, — simulation) of Experiment (ς.1). Accordingly, the very good quality of the designed rotor current control does not depend on the operation point of the machine rotational speed ω_m.

3.3.3 Rotor current control with LC filter

This section presents the rotor current control strategy, when the DFIM is coupled to the machine side converter via the additional LC filter (see the upper part of Fig. 3.36). The objective of the controller is to adjust the rotor current $\boldsymbol{i}_r^{dq}$ precisely to its reference $\boldsymbol{i}_{r,\text{ref}}^{dq}$. Therefor, two adaptive integral state-feedback controllers based on the DLQR theory are designed, which allow for taking the system dependency on the operation point into account. One uses an additional reference feed-forward compensation and the other one is equipped with a filter current decoupling controller. Moreover, both controllers are extended (i) by a reference voltage saturation (SAT), which considers the limited filter voltage $\boldsymbol{u}_l^{dq}$, and (ii) by an additional anti-wind up (AWU) to compensate for overshoots in the reference current tracking because of windup effects.

3.3.3.1 Linearizing the nonlinear model of the machine side

In the first step, the nonlinear dynamics will be linearized by means of the Taylor series expansion. By defining the state vector $\boldsymbol{x}_{\text{lcm}} \in \mathbb{R}^8$, the input vector $\boldsymbol{u}_{\text{lcm}} \in \mathbb{R}^2$ and the disturbance vector $\boldsymbol{d}_{\text{lcm}} \in \mathbb{R}^4$ as follows

$$\boldsymbol{x}_{\text{lcm}} := \left((\boldsymbol{i}_s^{dq})^\top, (\boldsymbol{i}_r^{dq})^\top, (\boldsymbol{i}_l^{dq})^\top, (\boldsymbol{u}_c^{dq})^\top\right)^\top \,,\; \boldsymbol{u}_{\text{lcm}} := \boldsymbol{u}_l^{dq} \quad \text{and} \quad \boldsymbol{d}_{\text{lcm}} := \left((\boldsymbol{u}_g^{dq})^\top, \omega_k, \omega_r\right)^\top \,, \tag{3.65}$$

in view of the holistic model (2.76) of the wind turbine system, the dynamics of the DFIM in

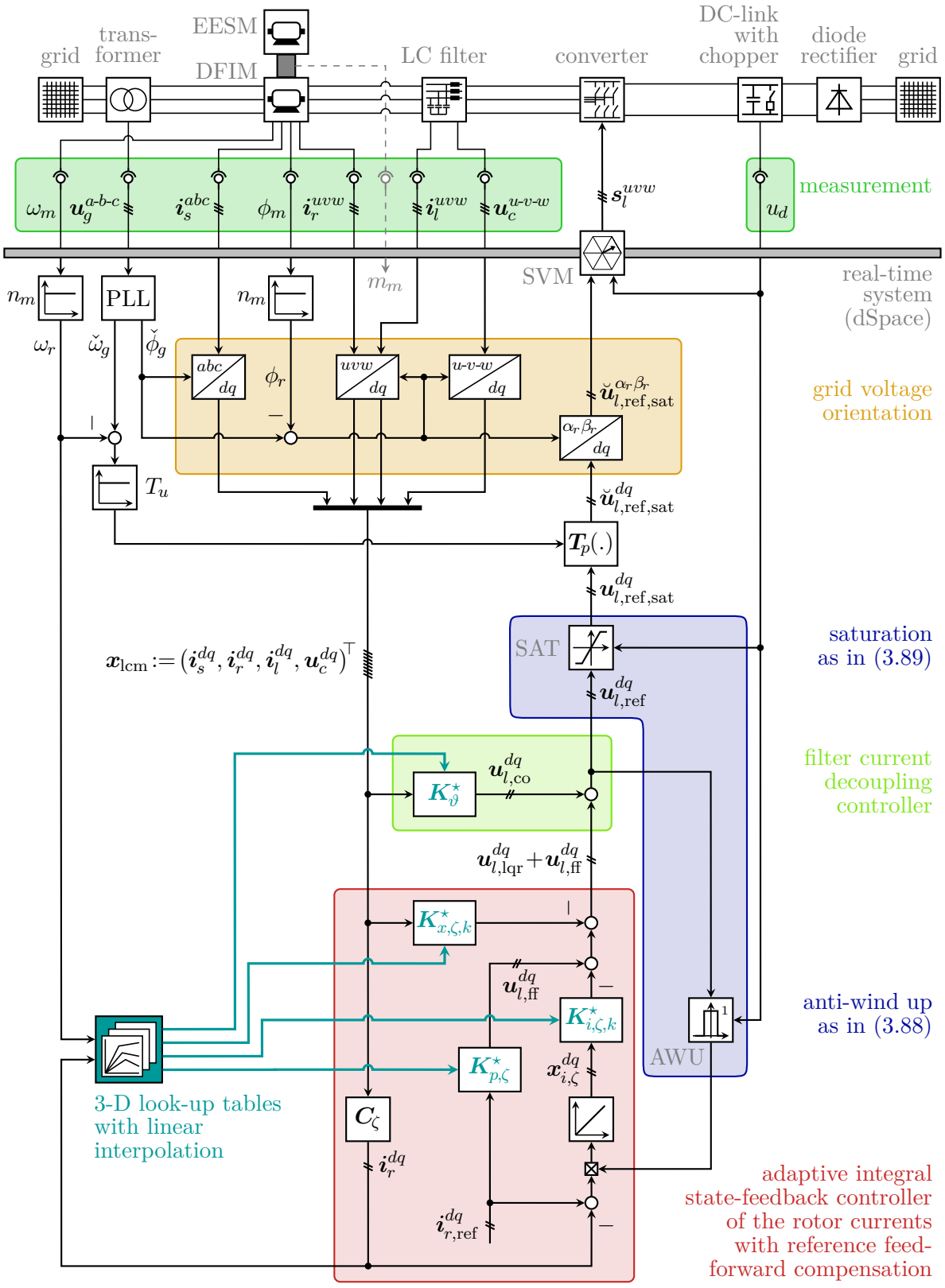

Figure 3.36: *Block diagram of the machine side experimental setup with LC filter and its control strategy for the rotor current.*

combination with the LC filter are given by

$$\begin{aligned}\frac{\mathrm{d}}{\mathrm{d}t}\boldsymbol{x}_{\mathrm{lcm}}(t) &:= \boldsymbol{f}_{\mathrm{lcm}}(\boldsymbol{x}_{\mathrm{lcm}},\boldsymbol{u}_{\mathrm{lcm}},\boldsymbol{d}_{\mathrm{lcm}}) \overset{(2.77),(3.45)}{=} \\ &\begin{pmatrix} \boldsymbol{L}_{\mathrm{dfim}}^{dq}(\boldsymbol{i}_s^{dq},\boldsymbol{i}_r^{dq})^{-1}\begin{pmatrix} -R_s\boldsymbol{i}_s^{dq}(t)-\boldsymbol{u}_g^{dq}(t)+\omega_k(t)\boldsymbol{J}\boldsymbol{\psi}_s^{dq}(\boldsymbol{i}_s^{dq},\boldsymbol{i}_r^{dq}) \\ R_c\boldsymbol{i}_l^{dq}(t)-(R_r+R_c)\boldsymbol{i}_r^{dq}(t)-\boldsymbol{u}_c^{dq}(t)+(\omega_k(t)-\omega_r(t))\boldsymbol{J}\boldsymbol{\psi}_s^{dq}(\boldsymbol{i}_s^{dq},\boldsymbol{i}_r^{dq}) \end{pmatrix} \\ -\left(\frac{R_l+R_c}{L_l}\boldsymbol{I}_2+(\omega_k(t)-\omega_r(t))\,\boldsymbol{J}\right)\boldsymbol{i}_l^{dq}(t)+\frac{1}{L_l}\boldsymbol{u}_c^{dq}(t)+\frac{R_c}{L_l}\boldsymbol{i}_r^{dq}(t)-\frac{1}{L_l}\boldsymbol{u}_l^{dq}(t) \\ -\frac{1}{C_c}\boldsymbol{i}_l^{dq}(t)-(\omega_k(t)-\omega_r(t))\,\boldsymbol{J}\boldsymbol{u}_c^{dq}(t)+\frac{1}{C_c}\boldsymbol{i}_r^{dq}(t) \end{pmatrix}\end{aligned} \tag{3.66}$$

with the initial value $\boldsymbol{x}_{\mathrm{lcm},0}=\boldsymbol{x}_{\mathrm{lcm}}(0)$ and the nonlinear function $\boldsymbol{f}_{\mathrm{lcm}}$. The small signals $\widetilde{\nu}_{\mathrm{lcm}}:=\nu_{\mathrm{lcm}}-\nu_{\mathrm{lcm}}^{\star}$ with $\nu\in\{\boldsymbol{x},\boldsymbol{u},\boldsymbol{d}\}$ of the state vector, the input vector and the disturbance vector respectively exhibit the following entries:

$$\left.\begin{aligned}&\widetilde{\boldsymbol{i}}_s^{dq}:=\boldsymbol{i}_s^{dq}-\boldsymbol{i}_s^{dq\star}\ ,\ \widetilde{\boldsymbol{i}}_r^{dq}:=\boldsymbol{i}_r^{dq}-\boldsymbol{i}_r^{dq\star}\ ,\ \widetilde{\boldsymbol{i}}_l^{dq}:=\boldsymbol{i}_l^{dq}-\boldsymbol{i}_l^{dq\star}\ ,\ \widetilde{\boldsymbol{u}}_c^{dq}:=\boldsymbol{u}_c^{dq}-\boldsymbol{u}_c^{dq\star}\\ &\widetilde{\boldsymbol{u}}_l^{dq}:=\boldsymbol{u}_l^{dq}-\boldsymbol{u}_l^{dq\star}\ ,\ \widetilde{\boldsymbol{u}}_g^{dq}:=\boldsymbol{u}_g^{dq}-\boldsymbol{u}_g^{dq\star}\ ,\ \widetilde{\omega}_k:=\omega_k-\omega_k^{\star}\ ,\ \widetilde{\omega}_r:=\omega_r-\omega_r^{\star}\end{aligned}\right\}. \tag{3.67}$$

Then, the small signal dynamics of the machine side results from linearizing its dynamics (3.66) around the equilibrium $\star=(\boldsymbol{i}_s^{dq\star},\boldsymbol{i}_r^{dq\star},\boldsymbol{i}_l^{dq\star},\boldsymbol{u}_c^{dq\star},\boldsymbol{u}_l^{dq\star},\boldsymbol{u}_g^{dq\star},\omega_k^{\star},\omega_r^{\star})$ of the stationary operation $\frac{\mathrm{d}}{\mathrm{d}t}\boldsymbol{x}_{\mathrm{lcm}}^{\star}(t)=\boldsymbol{f}_{\mathrm{lcm}}(\star)=\boldsymbol{0}_8$. Applying the Taylor series expansion to (3.66) yields

$$\begin{aligned}\frac{\mathrm{d}}{\mathrm{d}t}\widetilde{\boldsymbol{x}}_{\mathrm{lcm}}(t) &= \frac{\mathrm{d}}{\mathrm{d}t}\left(\boldsymbol{x}_{\mathrm{lcm}}(t)-\boldsymbol{x}_{\mathrm{lcm}}^{\star}(t)\right)=\frac{\mathrm{d}}{\mathrm{d}t}\boldsymbol{x}_{\mathrm{lcm}}(t)-\frac{\mathrm{d}}{\mathrm{d}t}\boldsymbol{x}_{\mathrm{lcm}}^{\star}(t)\\ &\overset{=\frac{\mathrm{d}}{\mathrm{d}t}\boldsymbol{x}_{\mathrm{lcm}}^{\star}}{=}\ \boldsymbol{f}_{\mathrm{lcm}}(\star)+\overbrace{\left.\frac{\partial\boldsymbol{f}_{\mathrm{lcm}}(\boldsymbol{x}_{\mathrm{lcm}},\boldsymbol{u}_{\mathrm{lcm}},\boldsymbol{d}_{\mathrm{lcm}})}{\partial\boldsymbol{x}_{\mathrm{lcm}}}\right|_{\star}}^{=:\boldsymbol{A}_{\mathrm{lcm}}^{\star}}\widetilde{\boldsymbol{x}}_{\mathrm{lcm}}(t)+\overbrace{\left.\frac{\partial\boldsymbol{f}_{\mathrm{lcm}}(\boldsymbol{x}_{\mathrm{lcm}},\boldsymbol{u}_{\mathrm{lcm}},\boldsymbol{d}_{\mathrm{lcm}})}{\partial\boldsymbol{u}_{\mathrm{lcm}}}\right|_{\star}}^{=:\boldsymbol{B}_{\mathrm{lcm}}}\widetilde{\boldsymbol{u}}_{\mathrm{lcm}}(t)\\ &\quad+\underbrace{\left.\frac{\partial\boldsymbol{f}_{\mathrm{lcm}}(\boldsymbol{x}_{\mathrm{lcm}},\boldsymbol{u}_{\mathrm{lcm}},\boldsymbol{d}_{\mathrm{lcm}})}{\partial\boldsymbol{d}_{\mathrm{lcm}}}\right|_{\star}}_{=:\boldsymbol{E}_{\mathrm{lcm}}^{\star}}\widetilde{\boldsymbol{d}}_{\mathrm{lcm}}(t)+\boldsymbol{\delta}_{\mathrm{lcm}}(t)-\frac{\mathrm{d}}{\mathrm{d}t}\boldsymbol{x}_{\mathrm{lcm}}^{\star}(t)\end{aligned} \tag{3.68}$$

with the initial value $\widetilde{\boldsymbol{x}}_{\mathrm{lcm},0}=\widetilde{\boldsymbol{x}}_{\mathrm{lcm}}(0)$, the system matrix $\boldsymbol{A}_{\mathrm{lcm}}^{\star}:=\boldsymbol{A}_{\mathrm{lcm}}(\boldsymbol{i}_s^{dq\star},\boldsymbol{i}_r^{dq\star},\omega_k^{\star},\omega_r^{\star})\in\mathbb{R}^{8\times8}$, the input matrix $\boldsymbol{B}_{\mathrm{lcm}}\in\mathbb{R}^{8\times2}$ and the disturbance matrix $\boldsymbol{E}_{\mathrm{lcm}}^{\star}:=\boldsymbol{E}_{\mathrm{lcm}}(\boldsymbol{i}_s^{dq\star},\boldsymbol{i}_r^{dq\star},\boldsymbol{i}_l^{dq\star},\boldsymbol{u}_c^{dq\star})\in\mathbb{R}^{8\times4}$. The term $\boldsymbol{\delta}_{\mathrm{lcm}}(t):=\boldsymbol{\delta}_{\mathrm{lcm}}(\widetilde{\boldsymbol{x}}_{\mathrm{lcm}},\widetilde{\boldsymbol{u}}_{\mathrm{lcm}},\widetilde{\boldsymbol{d}}_{\mathrm{lcm}},\star)\in\mathbb{R}^8$ characterizes the higher order terms of the Taylor series. In the following, it is supposed that

Assumption (A.3.7) *The higher order terms of the Taylor series are negligible, i.e.* $\boldsymbol{\delta}_{lcm}(t)=\boldsymbol{0}_8$.

Because of the *grid voltage oriented dq*-reference frame and (A.3.2), (a) the constant grid voltage $\boldsymbol{u}_g^{dq}$ and (b) the constant grid rotational speed ω_g lead to the small signals $\widetilde{\boldsymbol{u}}_g^{dq}=\boldsymbol{0}_2$ and $\widetilde{\omega}_k=\widetilde{\omega}_g:=\omega_g-\omega_g^{\star}=0$. Moreover, the following assumption is imposed:

Assumption (A.3.8) *The machine rotational speed* ω_r *changes much slower than the electrical quantities of the state vector* $\boldsymbol{x}_{lcm}$*. Hence, the machine rotational speed* ω_r *is assumed to be constant and its small signal results in* $\widetilde{\omega}_r(t)=0$*.*

By means of (A.3.2), (A.3.7) and (A.3.8), the nonlinear system (3.66) can be approximated by its small signal (linearized) dynamics

$$\frac{\mathrm{d}}{\mathrm{d}t}\widetilde{\boldsymbol{x}}_{\mathrm{lcm}}(t)=\boldsymbol{A}_{\mathrm{lcm}}^{\star}\widetilde{\boldsymbol{x}}_{\mathrm{lcm}}(t)+\boldsymbol{B}_{\mathrm{lcm}}\widetilde{\boldsymbol{u}}_{\mathrm{lcm}}(t)\ ,\ \widetilde{\boldsymbol{x}}_{\mathrm{lcm},0}:=\widetilde{\boldsymbol{x}}_{\mathrm{lcm}}(0)\,. \tag{3.69}$$

The system matrix $\boldsymbol{A}^{\star}_{\mathrm{lcm}}$ and the input matrix $\boldsymbol{B}_{\mathrm{lcm}}$ are obtained by using (3.66) and (3.68). Defining the steady-state inductance matrix $\boldsymbol{L}^{dq\star}_{\mathrm{dfim}}$ (in H)$^{4\times4}$ of the DFIM

$$\boldsymbol{L}^{dq\star}_{\mathrm{dfim}} := \boldsymbol{L}^{dq}_{\mathrm{dfim}}(\boldsymbol{i}^{dq\star}_s,\boldsymbol{i}^{dq\star}_r) \overset{(3.45)}{=} \begin{bmatrix} \boldsymbol{L}^{dq}_s(\boldsymbol{i}^{dq\star}_s,\boldsymbol{i}^{dq\star}_r) & \boldsymbol{L}^{dq}_m(\boldsymbol{i}^{dq\star}_s,\boldsymbol{i}^{dq\star}_r)^{\top} \\ \boldsymbol{L}^{dq}_m(\boldsymbol{i}^{dq\star}_s,\boldsymbol{i}^{dq\star}_r) & \boldsymbol{L}^{dq}_r(\boldsymbol{i}^{dq\star}_s,\boldsymbol{i}^{dq\star}_r) \end{bmatrix} := \begin{bmatrix} \boldsymbol{L}^{dq\star}_s & \left(\boldsymbol{L}^{dq\star}_m\right)^{\top} \\ \boldsymbol{L}^{dq\star}_m & \boldsymbol{L}^{dq\star}_r \end{bmatrix} \tag{3.70}$$

and considering the following relationship:

$$\begin{aligned} &\left(\frac{\partial \boldsymbol{L}^{dq}_{\mathrm{dfim}}(\boldsymbol{i}^{dq}_s,\boldsymbol{i}^{dq}_r)^{-1}}{\partial x} \begin{pmatrix} -R_s\boldsymbol{i}^{dq}_s(t) - \boldsymbol{u}^{dq}_g(t) + \omega_k(t)\boldsymbol{J}\boldsymbol{\psi}^{dq}_s(\boldsymbol{i}^{dq}_s,\boldsymbol{i}^{dq}_r) \\ R_c\boldsymbol{i}^{dq}_l(t) - (R_r+R_c)\boldsymbol{i}^{dq}_r(t) - \boldsymbol{u}^{dq}_c(t) + (\omega_k(t)-\omega_r(t))\boldsymbol{J}\boldsymbol{\psi}^{dq}_s(\boldsymbol{i}^{dq}_s,\boldsymbol{i}^{dq}_r) \end{pmatrix} \right)\Bigg|_{\star} \\ &\overset{(3.66)}{=} \frac{\partial \boldsymbol{L}^{dq}_{\mathrm{dfim}}(\boldsymbol{i}^{dq}_s,\boldsymbol{i}^{dq}_r)^{-1}}{\partial x}\Bigg|_{\star} \boldsymbol{L}^{dq\star}_{\mathrm{dfim}} \frac{\mathrm{d}}{\mathrm{d}t} \begin{pmatrix} \boldsymbol{i}^{dq\star}_s \\ \boldsymbol{i}^{dq\star}_r \end{pmatrix} = \boldsymbol{0}_4 \quad \text{for any } x \in \left\{ i^d_s, i^q_s, i^d_r, i^q_r \right\}, \end{aligned} \tag{3.71}$$

leads to the system matrix $\boldsymbol{A}^{\star}_{\mathrm{lcm}}$ and the input matrix $\boldsymbol{B}_{\mathrm{lcm}}$ as follows (cf. (3.66)):

$$\left.\begin{aligned} \boldsymbol{A}^{\star}_{\mathrm{lcm}} &= \begin{bmatrix} (\boldsymbol{L}^{dq\star}_{\mathrm{dfim}})^{-1} & \boldsymbol{O}_{4\times2} & \boldsymbol{O}_{4\times2} \\ \boldsymbol{O}_{2\times4} & \frac{1}{L_l}\boldsymbol{I}_2 & \boldsymbol{O}_{4\times2} \\ \boldsymbol{O}_{2\times4} & \boldsymbol{O}_{2\times2} & \frac{1}{C_c}\boldsymbol{I}_2 \end{bmatrix} \left(\begin{bmatrix} -R_s\boldsymbol{I}_2 & \boldsymbol{O}_{2\times2} & \boldsymbol{O}_{2\times2} & \boldsymbol{O}_{2\times2} \\ \boldsymbol{O}_{2\times2} & -(R_r+R_c)\,\boldsymbol{I}_2 & R_c\boldsymbol{I}_2 & -\boldsymbol{I}_2 \\ \boldsymbol{O}_{2\times2} & R_c\boldsymbol{I}_2 & -(R_l+R_c)\,\boldsymbol{I}_2 & \boldsymbol{I}_2 \\ \boldsymbol{O}_{2\times2} & \boldsymbol{I}_2 & -\boldsymbol{I}_2 & \boldsymbol{O}_{2\times2} \end{bmatrix} \right. \\ &\qquad \left. - \begin{bmatrix} \omega_g\boldsymbol{J}\boldsymbol{L}^{dq\star}_s & \omega_g\boldsymbol{J}(\boldsymbol{L}^{dq\star}_m)^{\top} & \boldsymbol{O}_{2\times2} & \boldsymbol{O}_{2\times2} \\ (\omega_g-\omega^{\star}_r)\,\boldsymbol{J}\boldsymbol{L}^{dq\star}_m & (\omega_g-\omega^{\star}_r)\,\boldsymbol{J}\boldsymbol{L}^{dq\star}_r & \boldsymbol{O}_{2\times2} & \boldsymbol{O}_{2\times2} \\ \boldsymbol{O}_{2\times2} & \boldsymbol{O}_{2\times2} & (\omega_g-\omega^{\star}_r)\,L_l\boldsymbol{J} & \boldsymbol{O}_{2\times2} \\ \boldsymbol{O}_{2\times2} & \boldsymbol{O}_{2\times2} & \boldsymbol{O}_{2\times2} & (\omega_g-\omega^{\star}_r)\,C_c\boldsymbol{J} \end{bmatrix} \right) \\ \boldsymbol{B}_{\mathrm{lcm}} &= -\tfrac{1}{L_l}\begin{bmatrix} \boldsymbol{O}_{2\times4} & \boldsymbol{I}_2 & \boldsymbol{O}_{2\times2} \end{bmatrix}^{\top} \end{aligned} \right\}. \tag{3.72}$$

Obviously, while the input matrix $\boldsymbol{B}_{\mathrm{lcm}}$ is a constant matrix, the system matrix $\boldsymbol{A}^{\star}_{\mathrm{lcm}}$ depends on the operation point; particularly, on (a) the stator current $\boldsymbol{i}^{dq\star}_s$, (b) the rotor current $\boldsymbol{i}^{dq\star}_r$ and (c) the machine rotational speed $\omega^{\star}_r$. The adaptive controller designs of Sec. 3.3.3.2 allow to consider this varying system matrix $\boldsymbol{A}^{\star}_{\mathrm{lcm}}$. Moreover, in Sec. 2.2.2.2, it has been explained that the stator current $\boldsymbol{i}^{dq\star}_s$ results from the rotor current $\boldsymbol{i}^{dq\star}_r$ in the steady-state operation, i.e. $\boldsymbol{i}^{dq\star}_s = \boldsymbol{i}^{dq}_s(\boldsymbol{i}^{dq\star}_r)$. Hence, the operation points (b) of the rotor current $\boldsymbol{i}^{dq\star}_r$ and (c) of the machine rotational speed $\omega^{\star}_r$ are sufficient to determine the system matrix $\boldsymbol{A}^{\star}_{\mathrm{lcm}}$.

3.3.3.2 Adaptive integral state-feedback controller design

The design of the adaptive integral state-feedback controller for the rotor current $\boldsymbol{i}^{dq}_r$ uses the following assumption:

Assumption (A.3.9) *The dead time of the machine side converter (see* (2.60)*) is neglected, so that the filter voltage* $\boldsymbol{u}^{dq}_l$ *equals its reference, i.e.* $\boldsymbol{u}^{dq}_{l,\mathrm{ref}}(t) = \boldsymbol{u}^{dq}_l(t)$.

As already mentioned in the introduction of Sec. 3.3.3, two different state-feedback control strategies will be explained. Depending on the decision variable $\vartheta_i \in \{0,1\}$, the adaptive integral state-feedback controller is extended by:

- for $\vartheta_i = 0$: an additional reference feed-forward compensation;
- for $\vartheta_i = 1$: a filter current decoupling controller.

Both variants can be written in one common control law for the reference filter voltage $\boldsymbol{u}_{l,\mathrm{ref}}^{dq}$. It is given by

$$\boldsymbol{u}_{l,\mathrm{ref}}^{dq}(t) = \boldsymbol{u}_{l,\mathrm{lqr}}^{dq}(t) + \boldsymbol{u}_{l,\mathrm{co}}^{dq}(t) + \boldsymbol{u}_{l,\mathrm{ff}}^{dq}(t) \tag{3.73}$$

with (a) the voltage $\boldsymbol{u}_{l,\mathrm{lqr}}^{dq}$ (in V)^2 of the state-feedback controller, (b) the voltage $\boldsymbol{u}_{l,\mathrm{co}}^{dq}$ (in V)^2 of the filter current decoupling controller and (c) the voltage $\boldsymbol{u}_{l,\mathrm{ff}}^{dq}$ (in V)^2 of the reference feed-forward compensation.
The idea of the filter current decoupling controller is to eliminate the entries in the fifth and the sixth row of the system matrix $\boldsymbol{A}_{\mathrm{lcm}}^{\star}$. Then, the dynamics of the filter current $\boldsymbol{i}_{l}^{dq}$ are completely decoupled. This is achieved by the decoupling matrix $\boldsymbol{K}_{\vartheta}^{\star} \in \mathbb{R}^{2\times 8}$ and the voltage $\boldsymbol{u}_{l,\mathrm{co}}^{dq}$ is given by

$$\boldsymbol{u}_{l,\mathrm{co}}^{dq}(t) = \boldsymbol{K}_{\vartheta}^{\star}\boldsymbol{x}_{\mathrm{lcm}}(t) \text{ with } \boldsymbol{K}_{\vartheta}^{\star} = \vartheta_i \begin{bmatrix} \boldsymbol{O}_{2\times 2} & R_c\boldsymbol{I}_2 & -(R_l+R_c)\,\boldsymbol{I}_2 - (\omega_g-\omega_r^{\star})\,L_l\boldsymbol{J} & \boldsymbol{I}_2 \end{bmatrix} . \tag{3.74}$$

If the decision variable ϑ_i is zero, i.e. $\vartheta_i = 0$, the filter current decoupling controller is disabled. Then, the reference feed-forward compensation with the feed-forward matrix $\boldsymbol{K}_{p,\zeta}^{\star} \in \mathbb{R}^{2\times 2}$ is active. The voltage $\boldsymbol{u}_{l,\mathrm{ff}}^{dq}$ (in V)^2 of the reference feed-forward compensation is given by

$$\boldsymbol{u}_{l,\mathrm{ff}}^{dq}(t) = \boldsymbol{K}_{p,\zeta}^{\star}\boldsymbol{i}_{r,\mathrm{ref}}^{dq}(t) \text{ with } \boldsymbol{K}_{p,\zeta}^{\star} = \begin{cases} -\left(\boldsymbol{C}_{\zeta}\left(\boldsymbol{A}_{\mathrm{lcm}}^{\star}\right)^{-1}\boldsymbol{B}_{\mathrm{lcm}}\right)^{-1} & \text{, if } \vartheta_i = 0 \\ \boldsymbol{O}_{2\times 2} & \text{, if } \vartheta_i = 1 \end{cases} , \tag{3.75}$$

where (a) the output matrix $\boldsymbol{C}_{\zeta} \in \mathbb{R}^{2\times 8}$ is given by $\boldsymbol{C}_{\zeta} = \begin{bmatrix} \boldsymbol{O}_{2\times 2} & \boldsymbol{I}_2 & \boldsymbol{O}_{2\times 4} \end{bmatrix}$ and (b) the feed-forward matrix $\boldsymbol{K}_{p,\zeta}^{\star} \in \mathbb{R}^{2\times 2}$ is designed as suggested in [141][67].
The control law (3.73) of the reference filter voltage $\boldsymbol{u}_{l,\mathrm{ref}}^{dq}$ will be inserted into the small signal dynamics (3.69) of the machine side. Therefor, the following small signals $\widetilde{\ }$ and stationary operation points * are defined:

$$\widetilde{\boldsymbol{u}}_{l,\mathrm{ref}}^{dq} := \boldsymbol{u}_{l,\mathrm{ref}}^{dq} - \boldsymbol{u}_{l,\mathrm{ref}}^{dq\star} ,\ \widetilde{\boldsymbol{u}}_{l,\mathrm{lqr}}^{dq} := \boldsymbol{u}_{l,\mathrm{lqr}}^{dq} - \boldsymbol{u}_{l,\mathrm{lqr}}^{dq\star} ,\ \widetilde{\boldsymbol{u}}_{l,\mathrm{co}}^{dq} := \boldsymbol{u}_{l,\mathrm{co}}^{dq} - \boldsymbol{u}_{l,\mathrm{co}}^{dq\star} \text{ and } \widetilde{\boldsymbol{u}}_{l,\mathrm{ff}}^{dq} := \boldsymbol{u}_{l,\mathrm{ff}}^{dq} - \boldsymbol{u}_{l,\mathrm{ff}}^{dq\star} . \tag{3.76}$$

Due to (A.3.9), inserting the small signal equations of (i) the control law (3.73) and (ii) the filter current decoupling controller (3.74) into the dynamics (3.69) of the machine side yields the *new* small signal dynamics

$$\frac{\mathrm{d}}{\mathrm{d}t}\widetilde{\boldsymbol{x}}_{\mathrm{lcm}}(t) = \boldsymbol{A}_{\vartheta}^{\star}\widetilde{\boldsymbol{x}}_{\mathrm{lcm}}(t) + \boldsymbol{B}_{\mathrm{lcm}}\left(\widetilde{\boldsymbol{u}}_{l,\mathrm{lqr}}^{dq}(t) + \widetilde{\boldsymbol{u}}_{l,\mathrm{ff}}^{dq}(t)\right) \quad \text{with} \quad \boldsymbol{A}_{\vartheta}^{\star} = \boldsymbol{A}_{\mathrm{lcm}}^{\star} + \boldsymbol{B}_{\mathrm{lcm}}\boldsymbol{K}_{\vartheta}^{\star} . \tag{3.77}$$

For the decision variable $\vartheta_i = 0$, the *new* system matrix $\boldsymbol{A}_{\vartheta}^{\star} \in \mathbb{R}^{8\times 8}$ is similar to the system matrix $\boldsymbol{A}_{\mathrm{lcm}}^{\star}$. The *new* dynamics (3.77) are augmented by the dynamics of the integral state $\boldsymbol{x}_{i,\zeta}^{dq}$ (in As)^2:

$$\frac{\mathrm{d}}{\mathrm{d}t}\boldsymbol{x}_{i,\zeta}^{dq}(t) = \boldsymbol{i}_{r,\mathrm{ref}}^{dq}(t) - \boldsymbol{i}_{r}^{dq}(t) = \boldsymbol{i}_{r,\mathrm{ref}}^{dq}(t) - \boldsymbol{C}_{\zeta}\boldsymbol{x}_{\mathrm{lcm}}(t) \ ,\ \boldsymbol{x}_{i,\zeta,0}^{dq} := \boldsymbol{x}_{i,\zeta}^{dq}(0) . \tag{3.78}$$

The dynamics of the integral state $\boldsymbol{x}_{i,\zeta}^{dq}$ in (3.78) are a linear time-invariant system (LTI-system), so that the corresponding small signal dynamics are identical. The following small signals $\widetilde{\ }$ and stationary operation points * of the equilibrium $\frac{\mathrm{d}}{\mathrm{d}t}\boldsymbol{x}_{i,\zeta}^{dq\star}(t) = \boldsymbol{0}_2$ are defined: $\widetilde{\boldsymbol{i}}_{r,\mathrm{ref}}^{dq} := \boldsymbol{i}_{r,\mathrm{ref}}^{dq} - \boldsymbol{i}_{r,\mathrm{ref}}^{dq\star}$

[67] The reference feed-forward compensation cannot be combined with the filter current decoupling controller, since the decision variable $\vartheta_i = 1$ results in a non-invertible system matrix $\boldsymbol{A}_{\vartheta}^{\star} = \boldsymbol{A}_{\mathrm{lcm}}^{\star} + \boldsymbol{B}_{\mathrm{lcm}}\boldsymbol{K}_{\vartheta}^{\star}$.

and $\widetilde{\boldsymbol{x}}_{i,\zeta}^{dq} := \boldsymbol{x}_{i,\zeta}^{dq} - \boldsymbol{x}_{i,\zeta}^{dq\star}$. Then, by applying the reference feed-forward compensation (3.75) to the *new* dynamics (3.77), the augmented small signal dynamics of the machine side result in

$$\underbrace{\frac{\mathrm{d}}{\mathrm{d}t}\begin{pmatrix}\widetilde{\boldsymbol{x}}_{\mathrm{lcm}}(t)\\ \widetilde{\boldsymbol{x}}_{i,\zeta}^{dq}(t)\end{pmatrix}}_{=:\dot{\widetilde{\boldsymbol{x}}}_{\zeta}(t)} = \underbrace{\begin{bmatrix}\boldsymbol{A}_{\vartheta}^{\star} & \boldsymbol{O}_{8\times2}\\ -\boldsymbol{C}_{\zeta} & \boldsymbol{O}_{2\times2}\end{bmatrix}}_{=:\boldsymbol{A}_{\zeta}^{\star}}\begin{pmatrix}\widetilde{\boldsymbol{x}}_{\mathrm{lcm}}(t)\\ \widetilde{\boldsymbol{x}}_{i,\zeta}^{dq}(t)\end{pmatrix} + \underbrace{\begin{bmatrix}\boldsymbol{B}_{\mathrm{lcm}}\\ \boldsymbol{O}_{2\times2}\end{bmatrix}}_{=:\boldsymbol{B}_{\zeta}}\widetilde{\boldsymbol{u}}_{l,\mathrm{lqr}}^{dq}(t) + \underbrace{\begin{bmatrix}\boldsymbol{B}_{\mathrm{lcm}}\boldsymbol{K}_{p,\zeta}^{\star}\\ \boldsymbol{I}_2\end{bmatrix}}_{=:\boldsymbol{E}_{\zeta}^{\star}}\widetilde{\boldsymbol{i}}_{r,\mathrm{ref}}^{dq}(t)\ ,\ \widetilde{\boldsymbol{x}}_{\zeta,0} := \widetilde{\boldsymbol{x}}_{\zeta}(0) \tag{3.79}$$

with the augmented state vector $\widetilde{\boldsymbol{x}}_{\zeta} \in \mathbb{R}^{10}$, the augmented system matrix $\boldsymbol{A}_{\zeta}^{\star} \in \mathbb{R}^{10\times10}$, the augmented input matrix $\boldsymbol{B}_{\zeta} \in \mathbb{R}^{10\times2}$ and the augmented disturbance matrix $\boldsymbol{E}_{\zeta}^{\star} \in \mathbb{R}^{10\times2}$.
The augmented small signal dynamics (3.79) of the machine side will be used to design the discrete state-feedback controller. First, they are discretized to take the small sampling frequency f_{dis} of the dSpace real-time system in relation to the resonance frequency of the machine side into account[68]. To obtain the discrete-time dynamics for (3.79) with discretization time t_{dis}, the same discretization method as in Sec. 3.2.2.2 is used. Accordingly, the discrete system matrix $\boldsymbol{A}_{\zeta,k}^{\star} \in \mathbb{R}^{10\times10}$, the discrete input matrix $\boldsymbol{B}_{\zeta,k}^{\star} \in \mathbb{R}^{10\times2}$ and the discrete disturbance vector $\boldsymbol{E}_{\zeta,k}^{\star} \in \mathbb{R}^{10\times2}$ are calculated by

$$\boldsymbol{Z}_{\zeta}^{\star} = t_{\mathrm{dis}}\sum_{\nu=0}^{8}\left(\boldsymbol{A}_{\zeta}^{\star}\right)^{\nu}\frac{t_{\mathrm{dis}}^{\nu}}{(\nu+1)!} \quad \Rightarrow \quad \boldsymbol{A}_{\zeta,k}^{\star} = \boldsymbol{I}_{10} + \boldsymbol{Z}_{\zeta}^{\star}\boldsymbol{A}_{\zeta}^{\star}\ ,\ \boldsymbol{B}_{\zeta,k}^{\star} = \boldsymbol{Z}_{\zeta}^{\star}\boldsymbol{B}_{\zeta}\ ,\ \boldsymbol{E}_{\zeta,k}^{\star} = \boldsymbol{Z}_{\zeta}^{\star}\boldsymbol{E}_{\zeta}^{\star}\,, \tag{3.80}$$

where $\boldsymbol{Z}_{\zeta}^{\star} \in \mathbb{R}^{10\times10}$ functions as discretization matrix. Hence, the discrete form of the augmented machine side dynamics (3.79) is given by

$$\widetilde{\boldsymbol{x}}_{\zeta}[k+1] = \boldsymbol{A}_{\zeta,k}^{\star}\widetilde{\boldsymbol{x}}_{\zeta}[k] + \boldsymbol{B}_{\zeta,k}^{\star}\widetilde{\boldsymbol{u}}_{l,\mathrm{lqr}}^{dq}[k] + \boldsymbol{E}_{\zeta,k}^{\star}\widetilde{\boldsymbol{i}}_{r,\mathrm{ref}}^{dq}[k]\ ,\ \widetilde{\boldsymbol{x}}_{\zeta}[0] = \widetilde{\boldsymbol{x}}_{\zeta,0}\,. \tag{3.81}$$

The overall feedback matrix $\boldsymbol{K}_{\zeta,k}^{\star} \in \mathbb{R}^{2\times10}$ splits up into the state-feedback matrix $\boldsymbol{K}_{x,\zeta,k}^{\star} \in \mathbb{R}^{2\times8}$ and the integral-feedback matrix $\boldsymbol{K}_{i,\zeta,k}^{\star} \in \mathbb{R}^{2\times2}$, so that the control law $\boldsymbol{u}_{l,\mathrm{lqr}}^{dq}$ of the discrete integral state-feedback controller results in

$$\boldsymbol{u}_{l,\mathrm{lqr}}^{dq}[k] = -\begin{bmatrix}\boldsymbol{K}_{x,\zeta,k}^{\star} & \boldsymbol{K}_{i,\zeta,k}^{\star}\end{bmatrix}\boldsymbol{x}_{\zeta}[k] := -\boldsymbol{K}_{\zeta,k}^{\star}\boldsymbol{x}_{\zeta}[k]\,. \tag{3.82}$$

Applying the control law (3.82) to the discrete machine side dynamics (3.81) yields the closed-loop system of the rotor current controller

$$\widetilde{\boldsymbol{x}}_{\zeta}[k+1] = \left(\boldsymbol{A}_{\zeta,k}^{\star} - \boldsymbol{B}_{\zeta,k}^{\star}\boldsymbol{K}_{\zeta,k}^{\star}\right)\widetilde{\boldsymbol{x}}_{\zeta}[k] + \boldsymbol{E}_{\zeta,k}^{\star}\widetilde{\boldsymbol{i}}_{r,\mathrm{ref}}^{dq}[k]\ ,\ \widetilde{\boldsymbol{x}}_{\zeta,0} := \widetilde{\boldsymbol{x}}_{\zeta}[0]\,. \tag{3.83}$$

To determine the feedback matrix $\boldsymbol{K}_{\zeta,k}^{\star}$, again the DLQR theory is invoked (for details see e.g. [137]). By choosing the following cost function:

$$J_{\zeta,k}\left(\widetilde{\boldsymbol{x}}_{\zeta}[k], \widetilde{\boldsymbol{u}}_{l,\mathrm{lqr}}^{dq}[k]\right) = \sum_{k=0}^{\infty}\left(\left(\widetilde{\boldsymbol{x}}_{\zeta}[k]\right)^{\top}\boldsymbol{Q}_{\zeta,k}\widetilde{\boldsymbol{x}}_{\zeta}[k] + \left(\widetilde{\boldsymbol{u}}_{l,\mathrm{lqr}}^{dq}[k]\right)^{\top}\boldsymbol{R}_{\zeta,k}\widetilde{\boldsymbol{u}}_{l,\mathrm{lqr}}^{dq}[k]\right) \tag{3.84}$$

with weighting matrices $0 < \boldsymbol{Q}_{\zeta,k} = \boldsymbol{Q}_{\zeta,k}^{\top} \in \mathbb{R}^{10\times10}$ and $0 < \boldsymbol{R}_{\zeta,k} = \boldsymbol{R}_{\zeta,k}^{\top} \in \mathbb{R}^{2\times2}$, the minimization of

[68] The DFIM features an inductive behavior so that in combination with the LC filter, the machine side exhibits a similar structure as the LCL filter of the grid side (but with different parameters). Due to the nonlinear magnetic characteristics of the DFIM, it is not feasible to determine an exact value for the resonance frequency on the machine side. Nevertheless, simulations have shown that a quasi-continuous design yields an unstable operation.

description	symbols & values with unit
maximum values of the machine side weighting matrices	
stator current	$i_{s,\max} = \hat{i}_{s,\mathrm{nom}} = 20.9\sqrt{2}\,\mathrm{A}$
rotor current	$i_{r,\max} = \hat{i}_{r,\mathrm{nom}} = 17\sqrt{2}\,\mathrm{A}$
capacitance voltage	$u_{c,\max} = \hat{u}_g = 400\sqrt{\frac{2}{3}}\,\mathrm{V}$
filter current	$i_{l,\max} = \hat{i}_{r,\mathrm{nom}} = 17\sqrt{2}\,\mathrm{A}$
integral state	$x_{i,\zeta,\max} = 30\,\mathrm{mAs}$
filter voltage	$u_{l,\max} = \hat{u}_g = 400\sqrt{\frac{2}{3}}\,\mathrm{V}$
weighting factor of the machine side weighting matrices	
weighting between states and input	$\eta_\zeta = 0.5$

Table 3.7: *Design parameters for the adaptive integral state-feedback controller of the rotor current.*

the cost function $J_{\zeta,k}$ results in the optimal feed-back matrix

$$\boldsymbol{K}^\star_{\zeta,k} = \left(\boldsymbol{R}_{\zeta,k} + \left(\boldsymbol{B}^\star_{\zeta,k}\right)^\top \boldsymbol{P}^\star_{\zeta,k} \boldsymbol{B}^\star_{\zeta,k}\right)^{-1} \left(\boldsymbol{B}^\star_{\zeta,k}\right)^\top \boldsymbol{P}^\star_{\zeta,k} \boldsymbol{A}^\star_{\zeta,k}\,, \tag{3.85}$$

where $0 < \boldsymbol{P}^\star_{\zeta,k} = \left(\boldsymbol{P}^\star_{\zeta,k}\right)^\top \in \mathbb{R}^{10\times 10}$ solves the discrete-time algebraic Riccati equation

$$\boldsymbol{P}^\star_{\zeta,k} - \left(\boldsymbol{A}^\star_{\zeta,k}\right)^\top \boldsymbol{P}^\star_{\zeta,k} \boldsymbol{A}^\star_{\zeta,k} + \left(\boldsymbol{A}^\star_{\zeta,k}\right)^\top \boldsymbol{P}^\star_{\zeta,k} \boldsymbol{B}^\star_{\zeta,k} \left(\boldsymbol{R}_{\zeta,k} + \left(\boldsymbol{B}^\star_{\zeta,k}\right)^\top \boldsymbol{P}^\star_{\zeta,k} \boldsymbol{B}^\star_{\zeta,k}\right)^{-1} \left(\boldsymbol{B}^\star_{\zeta,k}\right)^\top \boldsymbol{P}^\star_{\zeta,k} \boldsymbol{A}^\star_{\zeta,k} - \boldsymbol{Q}_{\zeta,k} = \boldsymbol{O}_{10\times 10}\,. \tag{3.86}$$

Again, the two weighting matrices $\boldsymbol{Q}_{\zeta,k}$ and $\boldsymbol{R}_{\zeta,k}$ are defined on the basis of Bryson's rule [134]. Thus, they are defined by

$$\boldsymbol{Q}_{\zeta,k} = \eta_\zeta\, \mathrm{diag}\left(\frac{1}{i^2_{s,\max}}\boldsymbol{I}_2\,,\, \frac{1}{i^2_{r,\max}}\boldsymbol{I}_2\,,\, \frac{1}{i^2_{l,\max}}\boldsymbol{I}_2\,,\, \frac{1}{u^2_{c,\max}}\boldsymbol{I}_2\,,\, \frac{1}{x^2_{i,\zeta,\max}}\boldsymbol{I}_2\right) \text{ and } \boldsymbol{R}_{\zeta,k} = \frac{1-\eta_\zeta}{u^2_{l,\max}}\boldsymbol{I}_2\,, \tag{3.87}$$

where the maximal acceptable (a) stator current $i_{s,\max}$, (b) rotor current $i_{r,\max}$, (c) filter current $i_{l,\max}$, (d) capacitance voltage $u_{c,\max}$, (e) integral state $x_{i,\zeta,\max}$ and (f) filter voltage $u_{l,\max}$ norm the influences of their corresponding quantity onto the cost function $J_{\zeta,k}$. Moreover, the factor $0 < \eta_\zeta < 1$ weights the impact between the states $\boldsymbol{x}_\zeta$ and the input $\boldsymbol{u}^{dq}_{l,\mathrm{ref}}$ onto the cost function $J_{\zeta,k}$. Tab. 3.7 lists the maximal acceptable values (a)–(f) as well as the weighting factor η_ζ.

Remark (R.3.12) *The DLQR theory* (3.84) *to* (3.86) *requires that the pair* $(\boldsymbol{A}^\star_{\zeta,k}, \boldsymbol{B}^\star_{\zeta,k})$ *is stabilizable. Due to the complexity of the discrete system matrix* $\boldsymbol{A}^\star_{\zeta,k}$ *(see* (3.80)*) and its dependance on the operation point, an analytical expression for this condition as in (C.3.1) is not feasible.*

To enhance the control performance of the adaptive integral state-feedback controller for the rotor current, it is extended (i) by a reference voltage saturation (SAT), which considers the limited filter voltage $\boldsymbol{u}^{dq}_l$ and (ii) by an additional anti-wind up (AWU) to compensate for overshoots in the reference current tracking. The concepts of SAT and AWU are identical to those presented in Sec. 3.3.3.2. While the (discrete) integration of $\boldsymbol{x}^{dq}_{i,\zeta}$ will be paused, if the following holds:

$$\left\|\boldsymbol{u}^{dq}_{l,\mathrm{ref}}[k]\right\| > \frac{\sqrt{3}k_c u_d[k]}{2} \quad \Longrightarrow \quad \boldsymbol{x}^{dq}_{i,\zeta}[k+1] = \boldsymbol{x}^{dq}_{i,\zeta}[k]\,, \tag{3.88}$$

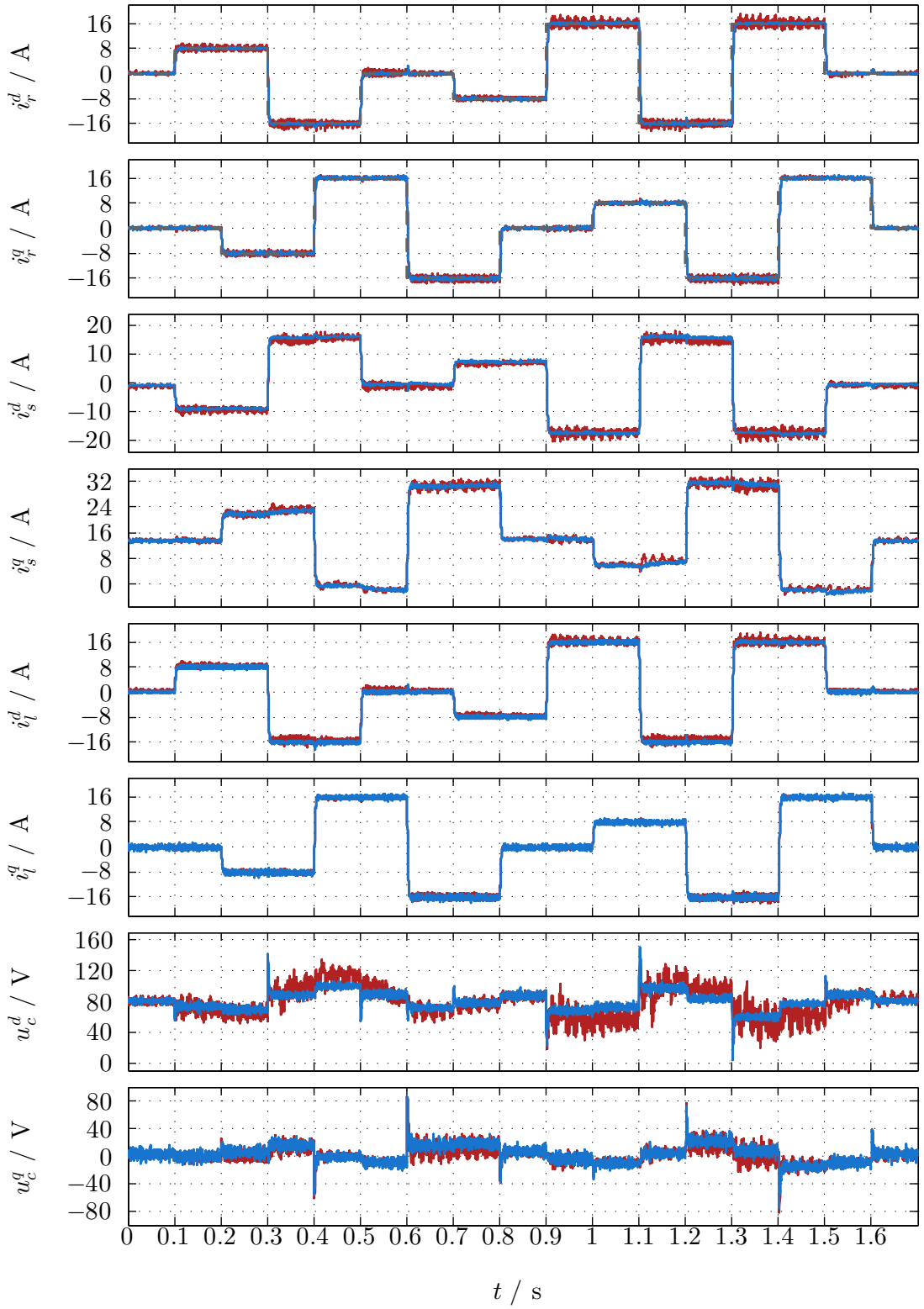

Figure 3.37: *Experiment (ζ.1):* — *measured quantities,* — *simulated quantities and* - - - *reference* $\boldsymbol{i}_{r,\mathrm{ref}}^{dq}$ *of the rotor current.*

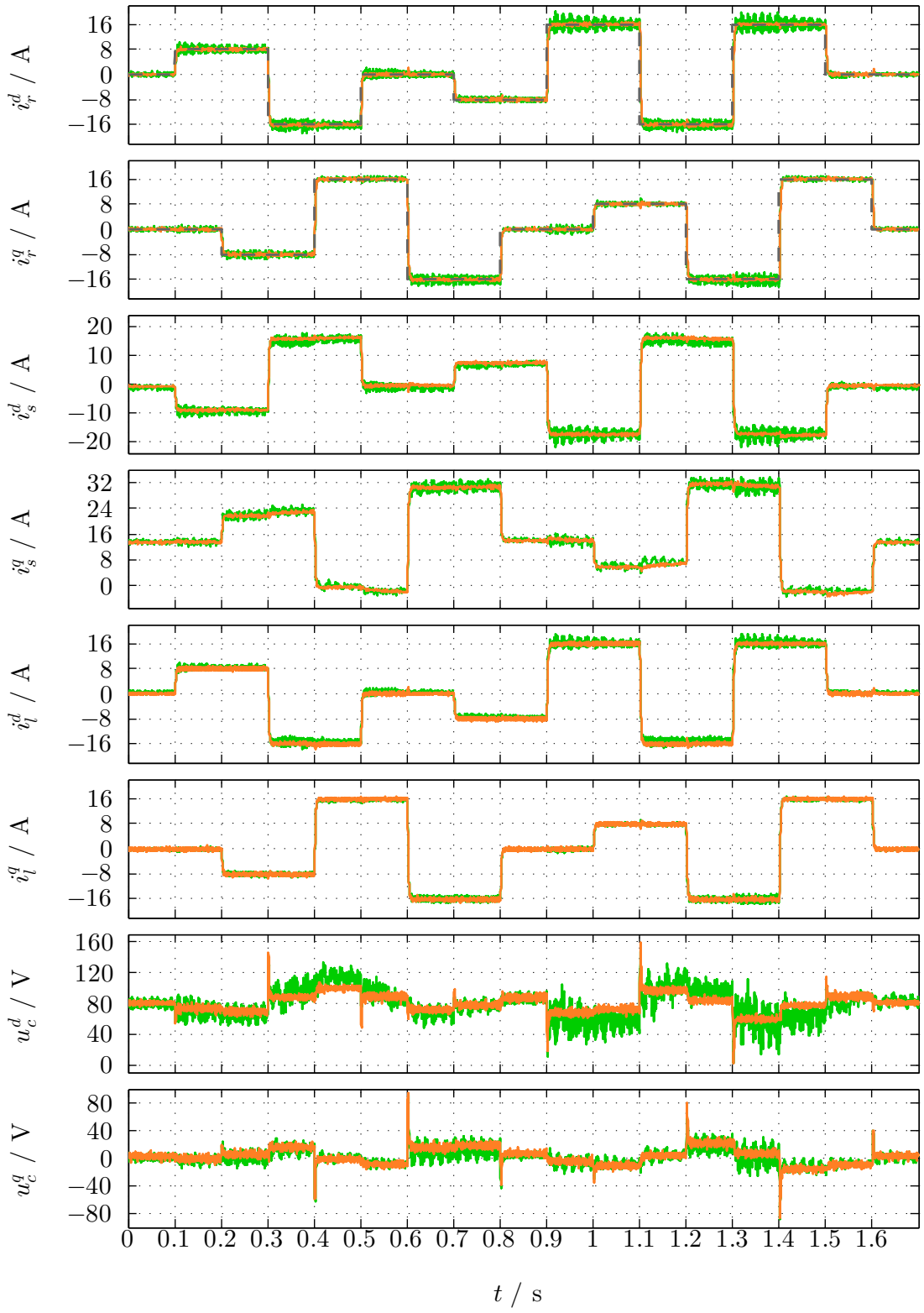

Figure 3.38: *Experiment (ζ.2):* — *measured quantities,* — *simulated quantities and* - - - *reference* $\boldsymbol{i}_{r,\mathrm{ref}}^{dq}$ *of the rotor current.*

the saturation function $h_{i,\zeta}$ limits the reference filter voltage $\boldsymbol{u}_{l,\mathrm{ref}}^{dq}$, which results in the saturated reference $\boldsymbol{u}_{l,\mathrm{ref,sat}}^{dq}$ (in V)[2] of the filter voltage:

$$\boldsymbol{u}_{l,\mathrm{ref,sat}}^{dq}[k] = h_{i,\zeta}(\boldsymbol{u}_{l,\mathrm{ref}}^{dq}, u_d)\boldsymbol{u}_{l,\mathrm{ref}}^{dq}[k] \quad \text{with} \quad h_{i,\zeta}(\boldsymbol{u}_{l,\mathrm{ref}}^{dq}, u_d) = \begin{cases} \dfrac{\sqrt{3}k_c u_d[k]}{2\left\|\boldsymbol{u}_{l,\mathrm{ref}}^{dq}[k]\right\|} & , \text{if } \left\|\boldsymbol{u}_{l,\mathrm{ref}}^{dq}[k]\right\| > \dfrac{\sqrt{3}k_c u_d[k]}{2} \\ 1 & , \text{if } \left\|\boldsymbol{u}_{l,\mathrm{ref}}^{dq}[k]\right\| \leq \dfrac{\sqrt{3}k_c u_d[k]}{2} \end{cases}. \tag{3.89}$$

The implementation of the overall strategy of the adaptive integral state-feedback controller for the rotor current $\boldsymbol{i}_r^{dq}$ is summarized in Fig. 3.36.

3.3.3.3 Reference tracking of the rotor currents with LC filter

To analyze the reference tracking of the adaptive integral state-feedback controller for the rotor current—unless stated otherwise—the parameters of the experimental setup in Tab. 3.6 and the parameters for the weighting matrices $\boldsymbol{Q}_{\zeta,k}$ and $\boldsymbol{R}_{\zeta,k}$ in Tab. 3.7 are used as well as the control strategy as shown in Fig. 3.36.
The two objectives of this section are: (i) to validate the implemented control strategy and (ii) to highlight the very good matching of the machine side model with the experimental setup at the test-bench. Therefor, the following experiments are conducted both in simulation and laboratory:

(ζ.1) the adaptive integral state-feedback controller for the rotor current $\boldsymbol{i}_r^{dq}$ (— measurement, — simulation) which is composed of: (a) the control law (3.73), where the overall feedback matrix $\boldsymbol{K}_{\zeta,k}^{\star}$ results from the DLQR theory (3.84) to (3.87), (b) the AWU strategy (3.88) and (c) the SAT as in (3.89). Moreover, the state-feedback controller is extended by the reference feed-forward controller, i.e. $\vartheta_i = 0$ in (3.74) and (3.75). The EESM is speed-controlled and adjusts the machine rotational speed ω_m to the constant value $120\,\frac{\mathrm{rad}}{\mathrm{s}} < \frac{\omega_g}{n_m}$ (sub-synchronous operation).

(ζ.2) Experiment (ζ.1) is repeated but with the following decisive variation (— measurement, — simulation): the filter current decoupling controller is utilized instead of the reference feed-forward controller, i.e. $\vartheta_i = 1$ in (3.74) and (3.75).

(ζ.3) to demonstrate that the control strategy works well independently from the machine rotational speed ω_m, the measurement of Experiment (ζ.1) is executed for the — machine rotational speed $\omega_m = 170\,\frac{\mathrm{rad}}{\mathrm{s}} > \frac{\omega_g}{n_m}$ (super-synchronous operation).

Fig. 3.37 presents the results of Experiment (ζ.1). The plots depict the machine side states from top to bottom: (a) the rotor current $\boldsymbol{i}_r^{dq}$ and its - - - reference $\boldsymbol{i}_{r,\mathrm{ref}}^{dq}$, (b) the stator current $\boldsymbol{i}_s^{dq}$, (c) the filter current $\boldsymbol{i}_l^{dq}$ and (d) the capacitance voltage $\boldsymbol{u}_c^{dq}$. In the two plots of the rotor current $\boldsymbol{i}_r^{dq}$ the good control performance can be seen. The rotor current $\boldsymbol{i}_r^{dq}$ tracks its corresponding reference $\boldsymbol{i}_{r,\mathrm{ref}}^{dq}$ very quickly and precisely. The augmented machine side dynamics by the integral state $\boldsymbol{x}_{i,\zeta}^{dq}$ guarantee steady-state accuracy. Also cross-couplings due to reference jumps in the orthogonal rotor current component hardly affect the reference tracking. Again, when the DC-link operates either in the *chopper resistance mode* or the *diode rectifier mode* (see Sec. 3.3.1), small oscillations in the machine side quantities occur. Moreover, the — measurements exhibit a very good matching with the — simulation results. Only the measured d-component u_c^d of the capacitance voltage is more noisy than the simulated one.

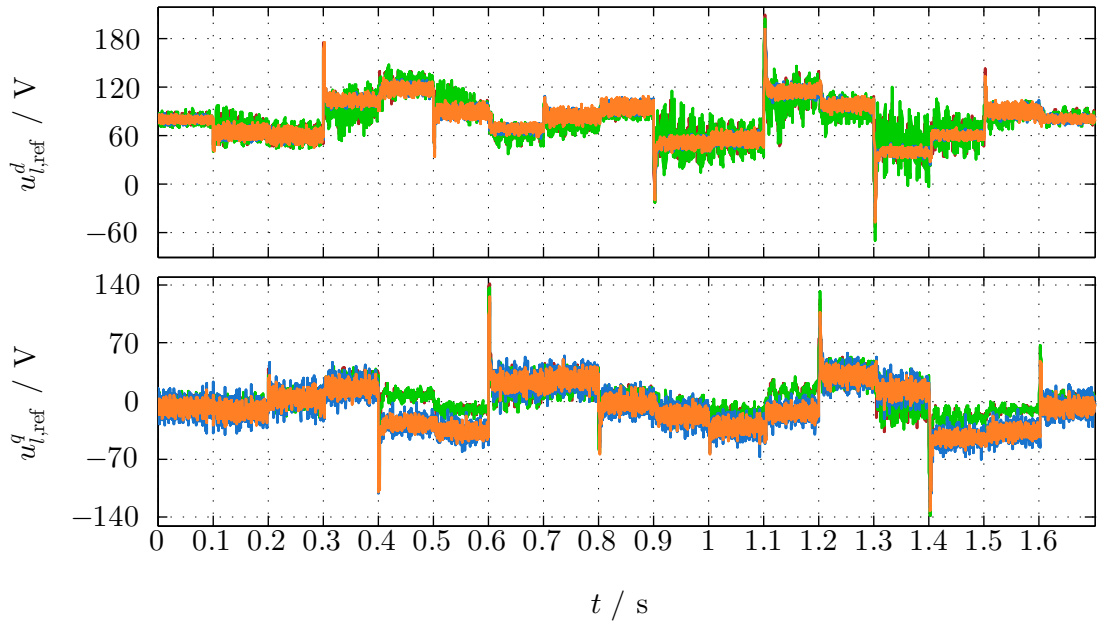

Figure 3.39: *Experiments (ζ.1) and (ζ.2) – Reference filter voltage* $\boldsymbol{u}^{dq}_{l,\mathrm{ref}}$*:* — *measured* $\boldsymbol{u}^{dq}_{l,\mathrm{ref}}$ *with reference feed-forward controller,* — *simulated* $\boldsymbol{u}^{dq}_{l,\mathrm{ref}}$ *with reference feed-forward controller,* — *measured* $\boldsymbol{u}^{dq}_{l,\mathrm{ref}}$ *with filter current decoupling controller,* — *simulated* $\boldsymbol{u}^{dq}_{l,\mathrm{ref}}$ *with filter current decoupling controller.*

In Fig. 3.38, the outcomes of Experiment (ζ.2) are shown, where the filter current decoupling controller is used instead of the reference feed-forward controller of Experiment (ζ.1). Again, the plots depict the machine side states from top to bottom: (a) the rotor current $\boldsymbol{i}^{dq}_r$ and its - - - reference $\boldsymbol{i}^{dq}_{r,\mathrm{ref}}$, (b) the stator current $\boldsymbol{i}^{dq}_s$, (c) the filter current $\boldsymbol{i}^{dq}_l$ and (d) the capacitance voltage $\boldsymbol{u}^{dq}_c$. The results both of the — measurements and the — simulations are very similar to the ones of Experiment (ζ.1). The rotor current reference $\boldsymbol{i}^{dq}_{r,\mathrm{ref}}$ is tracked quickly and accurately by the rotor current $\boldsymbol{i}^{dq}_r$ and cross-couplings in reaction to reference jumps in the orthogonal rotor current component do not influence the reference tracking significantly. Consequently, both variants are ideally suited for controlling the rotor current $\boldsymbol{i}^{dq}_r$.
Fig. 3.39 compares the reference filter voltage $\boldsymbol{u}^{dq}_{l,\mathrm{ref}}$ of the two Experiments (ζ.1) and (ζ.2). Both the measurements (— (ζ.1), — (ζ.2)) and the simulation results (— (ζ.1), — (ζ.2)) exhibit (almost) the same behavior for both experiments. Thereby, the d-component $u^d_{l,\mathrm{ref}}$ of the reference filter voltage of the measurements is noisier than the simulated one. Further, there are small deviations in the q-component $u^q_{l,\mathrm{ref}}$ between the measurements and the simulations. Apart from that the reference filter voltage $\boldsymbol{u}^{dq}_{l,\mathrm{ref}}$ shows a very similar behavior for all four cases.
To highlight the transient behaviors of the two control strategies, zooms of the two Experiments (ζ.1) and (ζ.2) are shown (i) in Fig. 3.40 for the d-components and (ii) in Fig. 3.41 for the q-components. Fig. 3.40 zooms in at the certain time instants $t = 0.3\,\mathrm{s}$, $t = 0.5\,\mathrm{s}$, $t = 0.9\,\mathrm{s}$ and $t = 1.1\,\mathrm{s}$ and depicts the d-components of (from top to bottom): (a) the rotor current i^d_r and its - - - reference $i^d_{r,\mathrm{ref}}$, (b) the stator current i^d_s, (c) the filter current i^d_l and (d) the capacitance voltage u^d_c. The transient behaviors of the measurements and the simulation results match brilliantly. Moreover, the two Experiments (ζ.1) and (ζ.2) exhibit (almost) the same dynamics. The rotor current i^d_r tracks its reference $i^d_{r,\mathrm{ref}}$ within about 7 ms in reaction to reference jumps of up to 32 A, which proves the very good performance of the two control strategies. The same outcomes can be seen for the q-components in Fig. 3.41, where zooms at the certain time

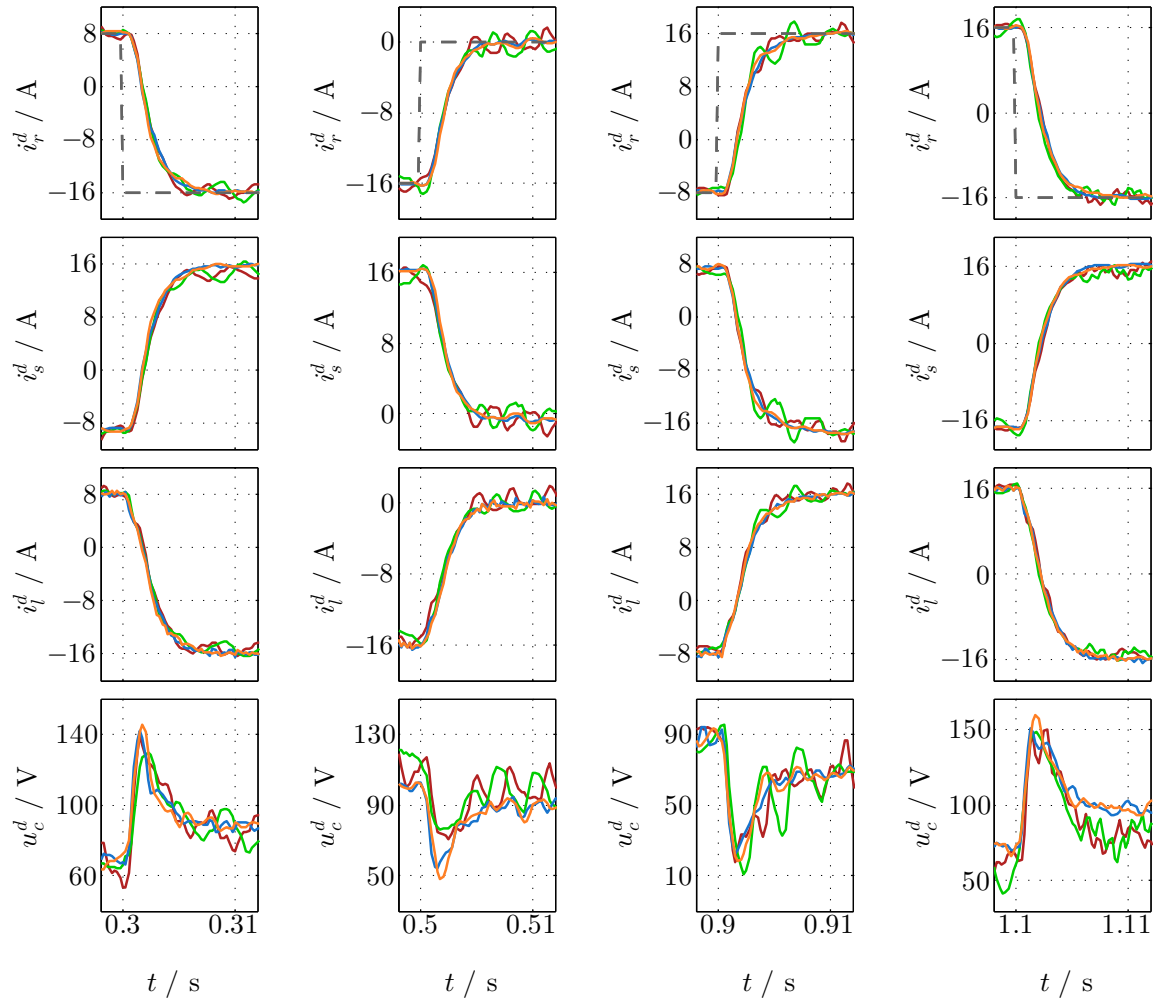

Figure 3.40: *Experiments (ζ.1) and (ζ.2) – Zoom of the d-component:* — *measured quantities with reference feed-forward controller,* — *simulated quantities with reference feed-forward controller,* — *measured quantities with filter current decoupling controller,* — *simulated quantities with filter current decoupling controller and* - - - *reference* $i_{r,\mathrm{ref}}^d$ *of the rotor current.*

instants $t=0.4\,\mathrm{s}$, $t=0.6\,\mathrm{s}$, $t=0.8\,\mathrm{s}$ and $t=1.2\,\mathrm{s}$ are shown for the following quantities (from top to bottom): (a) the rotor current i_r^q and its - - - reference $i_{r,\mathrm{ref}}^q$, (b) the stator current i_s^q, (c) the filter current i_l^q, and (d) the capacitance voltage u_c^q. Again, the rotor current i_r^q is adjusted to its reference $i_{r,\mathrm{ref}}^q$ within about 7 ms and the transient behaviors are (almost) the same for the two measurements and the two simulations.

Fig. 3.42 presents the — measurements of Experiment (ζ.3), where the machine rotational speed ω_m is increased to $170\,\frac{\mathrm{rad}}{\mathrm{s}} > \frac{\omega_g}{n_m}$. The results are compared to the — measurements of Experiment (ζ.1) with the slower machine rotational speed $120\,\frac{\mathrm{rad}}{\mathrm{s}} < \frac{\omega_g}{n_m}$. The plots depict the following quantities from top to bottom: (a) the rotor current $\boldsymbol{i}_r^{dq}$ and its - - - reference $\boldsymbol{i}_{r,\mathrm{ref}}^{dq}$, (b) the stator current $\boldsymbol{i}_s^{dq}$, (c) the filter current $\boldsymbol{i}_l^{dq}$, (d) the capacitance voltage $\boldsymbol{u}_c^{dq}$ and (e) the reference filter voltage $\boldsymbol{u}_{l,\mathrm{ref}}^{dq}$. The control performance in both cases is (almost) identical, so that the quality of the control does not depend on machine rotational speed ω_m. The currents of the rotor $\boldsymbol{i}_r^{dq}$, of the stator $\boldsymbol{i}_s^{dq}$ and of the filter $\boldsymbol{i}_l^{dq}$ match perfectly in both cases, while the capacitance voltage $\boldsymbol{u}_c^{dq}$ and the reference filter voltage $\boldsymbol{u}_{l,\mathrm{ref}}^{dq}$ show slight differences. In steady-state, the difference in the capacitance voltage $\boldsymbol{u}_c^{dq}$ is equal to $2\cdot 50\,\frac{\mathrm{rad}}{\mathrm{s}}\boldsymbol{J}\boldsymbol{\psi}_r^{dq\star}$, since the stationary rotor

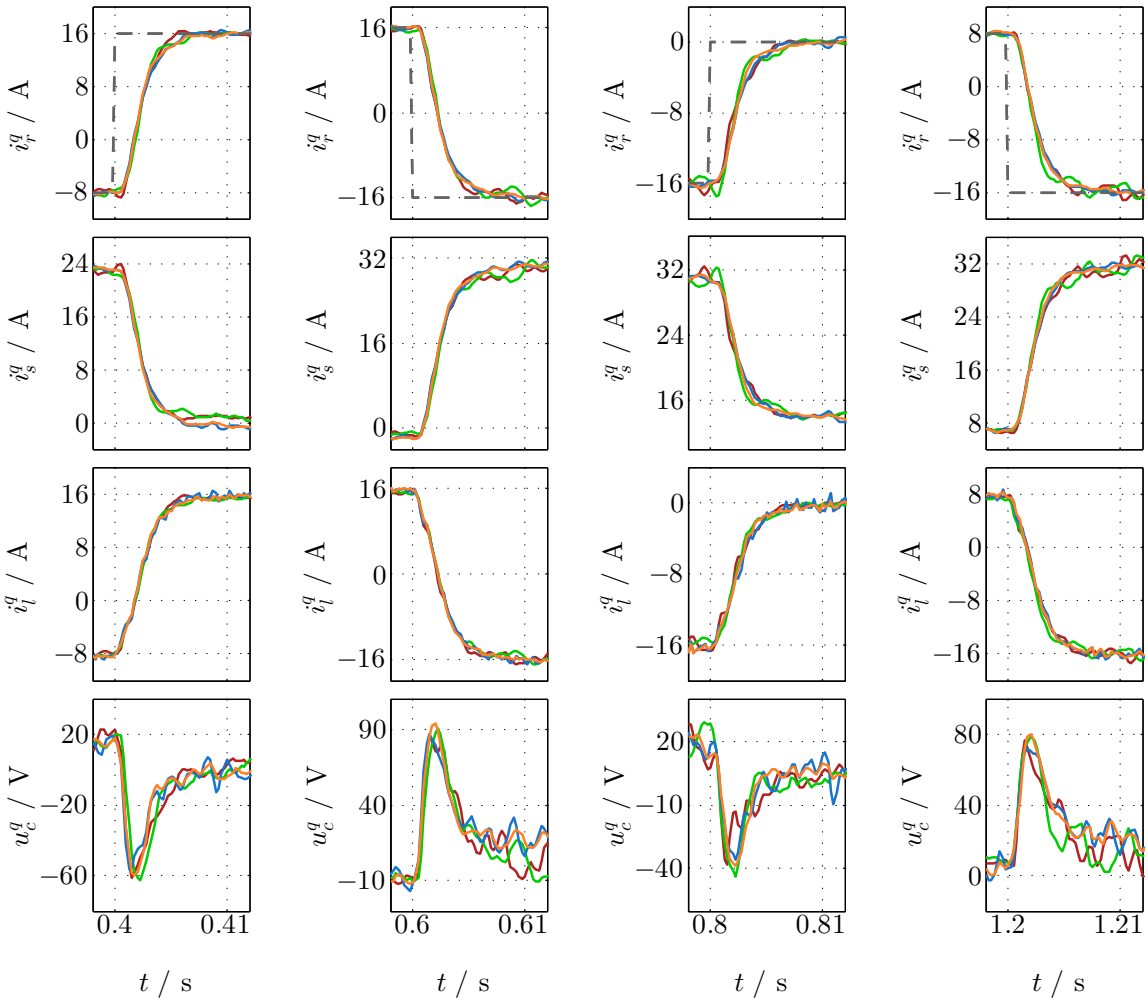

Figure 3.41: *Experiments (ζ.1) and (ζ.2) – Zoom of the q-component:* — *measured quantities with reference feed-forward controller,* — *simulated quantities with reference feed-forward controller,* — *measured quantities with filter current decoupling controller,* — *simulated quantities with filter current decoupling controller and* - - - *reference* $i_{r,\mathrm{ref}}^q$ *of the rotor current.*

equation of the machine side model (for $R_c = 0$) is given by: $\boldsymbol{u}_c^{dq\star} = -R_r \boldsymbol{i}_r^{dq\star} + (\omega_g - \omega_r^\star)\, \boldsymbol{J} \boldsymbol{\psi}_r^{dq\star}$ (see (3.66)).

3.3.4 Torque control and reactive power control

This sections presents the controller designs of the machine torque m_m and the stator reactive power q_s. The machine torque m_m is controlled to its reference $m_{m,\mathrm{ref}}$ via the d-component i_r^d of the rotor current, while the q-component i_r^q of the rotor current adjusts the stator reactive power q_s to its reference $q_{s,\mathrm{ref}}$.
Common wind turbine systems are not equipped with a torque sensor, so that a feed-forward controller is used to control the machine torque m_m. Fig. 2.9a shows that the (steady-state) machine torque m_m depends on the rotor current $\boldsymbol{i}_r^{dq}$. In Fig. 3.43a this dependency is reversed. Therein, the d-component i_r^d of the rotor current is uniquely determined by the machine torque m_m and the q-component i_r^q of the rotor current. This relationship is converted into a 2-D look-up table. The reference machine torque $m_{m,\mathrm{ref}}$ and the q-component $i_{r,\mathrm{ref}}^q$ of the reference rotor current result in the d-component $i_{r,\mathrm{ref}}^d$ of the reference rotor current as illustrated in Fig. 3.44.

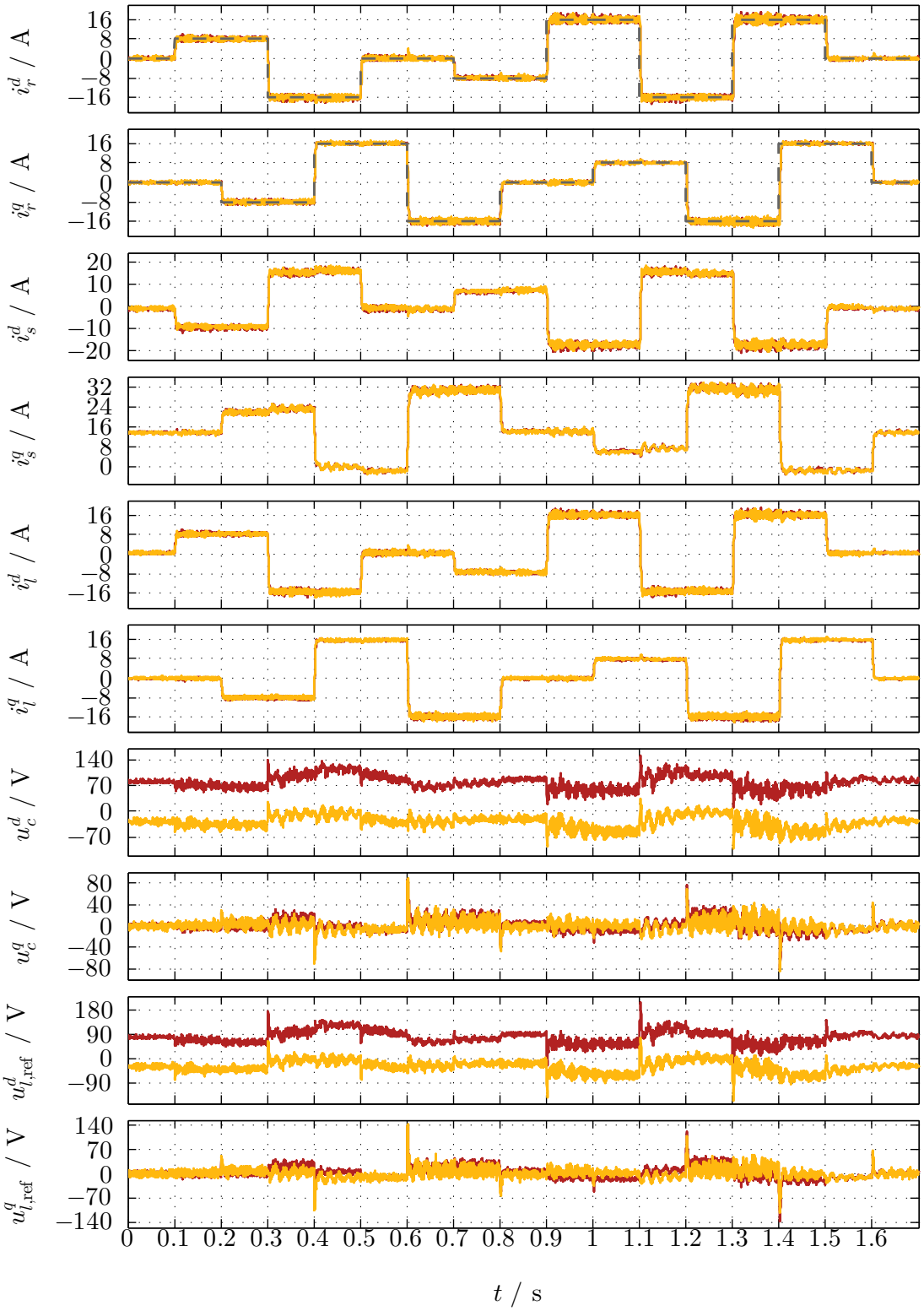

Figure 3.42: *Experiment (ζ.3):* — *measured quantities with machine rotational speed* $\omega_m = 120\,\frac{\mathrm{rad}}{\mathrm{s}}$, — *measured quantities with machine rotational speed* $\omega_m = 170\,\frac{\mathrm{rad}}{\mathrm{s}}$ *and* - - - *reference* $\boldsymbol{i}_{r,\mathrm{ref}}^{dq}$ *of the rotor current.*

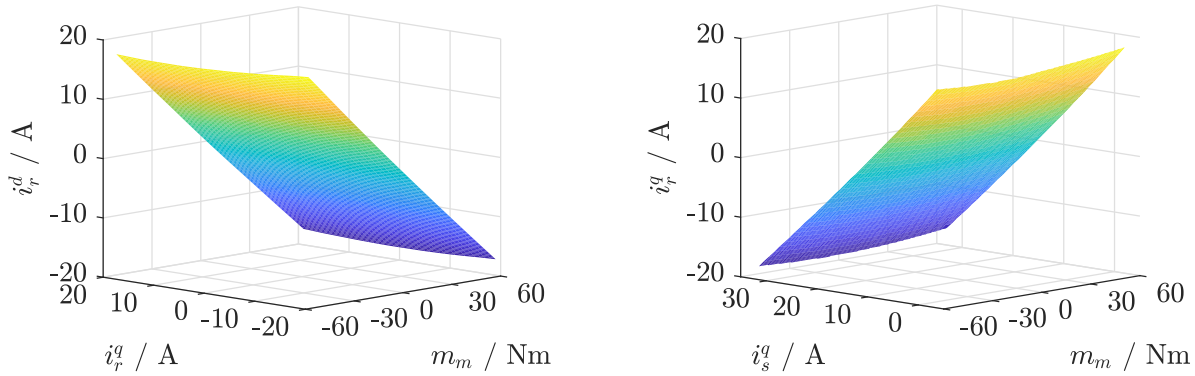

(a) *d-component* i_r^d *of the rotor current.* (b) *q-component* i_r^q *of the rotor current.*

Figure 3.43: *Rotor current maps for the feed-forward controllers of the machine torque and the stator reactive power (steady-state case***).*

Current sensors measure the stator current $\boldsymbol{i}_s^{abc}$ of the DFIM (cf. Fig. 3.1). By means of Clarke's and Park's transformation, the q-component i_s^q is available for feedback. Due to (A.3.2) and (2.33), the reference $q_{s,\mathrm{ref}}$ of the stator reactive power can be converted into the equivalent q-component $i_{s,\mathrm{ref}}^q$ of the reference stator current as follows:

$$q_s(t) \overset{(2.33),(A.3.2)}{=} -\frac{2}{3k_c^2}\hat{u}_g i_s^q(t) \quad \Rightarrow \quad i_{s,\mathrm{ref}}^q(t) = -\frac{3k_c^2}{2\hat{u}_g} q_{s,\mathrm{ref}}(t)\,. \tag{3.90}$$

To adjust the control error $i_{s,\mathrm{ref}}^q - i_s^q$ to zero, the stator reactive power PI controller with proportional gain $k_{p,q}$ (in 1), integral gain $k_{i,q}$ (in $\frac{1}{\mathrm{s}}$) and output current $i_{r,\mathrm{pi}}^q$ (in A)[2] is used. The integral (discrete) state $x_{i,q}$ (in As) is given by

$$x_{i,q}[k+1] = x_{i,q}[k] + t_{\mathrm{dis}}\left(i_{s,\mathrm{ref}}^q[k] - i_s^q[k]\right)\ ,\ x_{i,q,0} := x_{i,q}[0]\,. \tag{3.91}$$

Moreover, a feed-forward controller is additionally implemented to improve the control performance. Fig. 3.43b illustrates that a certain machine torque m_m and q-component i_s^q of the stator current uniquely determine the (steady-state) q-component i_r^q of the rotor current. By using a 2-D look-up table, this knowledge can be used to feed-forward the current $i_{r,\mathrm{ff}}^q$ (in A) as depicted in Fig. 3.44. The overall control law for the stator reactive power control is given by

$$i_{r,\mathrm{ref}}^q[k] = i_{r,\mathrm{ff}}^q[k] + i_{r,\mathrm{pi}}^q[k] \quad \text{with} \quad i_{r,\mathrm{pi}}^q[k] = k_{i,q}x_{i,q}[k] + k_{p,q}\left(i_{s,\mathrm{ref}}^q[k] - i_s^q[k]\right)\,. \tag{3.92}$$

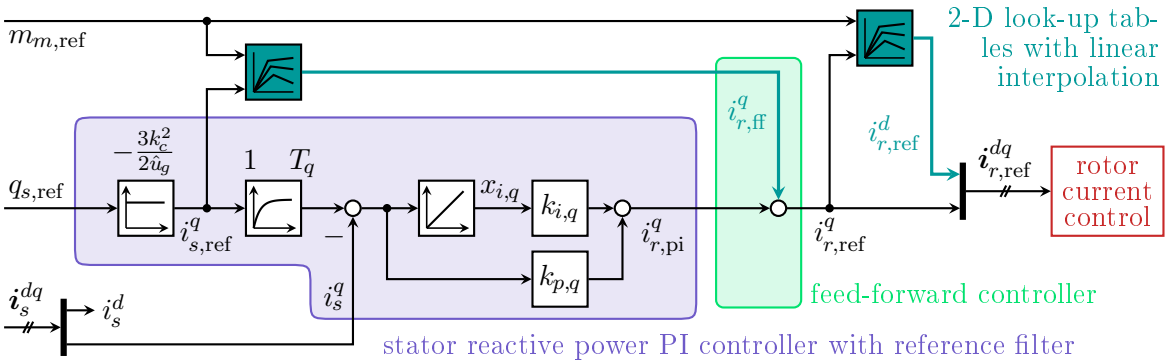

Figure 3.44: *Block diagram of the control strategies for the machine torque and the stator reactive power.*

description	symbols & values with unit
parameters of the PI controller	
proportional gain	$k_{p,q} = -2$
integral gain	$k_{i,q} = -\frac{0.05}{2t_{\mathrm{dis}}} = -100\,\frac{1}{\mathrm{s}}$
parameters of the reference filter	
time constant	$T_q = 2t_{\mathrm{dis}} = 0.5\,\mathrm{ms}$

Table 3.8: *Parameters of the stator reactive power control.*

Remark (R.3.13) *The measurements and simulation results will show that overshoots in the stator reactive power q_s can occur during reference tracking of $q_{s,\mathrm{ref}}$. To avoid these overshoots, a first order lag system*[69] *with the time constant $T_q = 2t_{\mathrm{dis}}$ (in s) is used as reference filter (see Fig. 3.44). Because of the tiny time constant $T_q = 2\,t_{\mathrm{dis}}$, the delaying reference filter does not affect the control performance negatively. Note that in* (3.91) *and* (3.92)*, the reference filter is neglected.*

The overall control strategy of the machine torque m_m and the stator reactive power q_s is presented in Fig. 3.44. Further, measurement and simulation results are presented to highlight the two objectives: (i) to validate the controller designs of the machine torque m_m and the stator reactive power q_s and (ii) to verify the matching of the simulation model and the experimental setup at the test-bench with the experimental setup parameters of Tab. 3.6 and Tab. 3.8. The following experiments are performed:

(q.1) the implemented control strategy (— measurement, — simulation) *without* the reference filter, which is composed of: (a) the 2-D look-up tables (with linear interpolation) to obtain the feed-forward current $i^q_{r,\mathrm{ff}}$ and the d-component $i^d_{r,\mathrm{ref}}$ of the reference rotor current, (b) the stator reactive power PI controller and (c) the control law (3.92). The (optional) LC filter is not in use. Moreover, the EESM is speed-controlled and adjusts the machine rotational speed ω_m to the constant value $120\,\frac{\mathrm{rad}}{\mathrm{s}} < \frac{\omega_g}{n_m}$ (sub-synchronous operation).

(q.2) the necessity of the reference filter is explained. Therefor, the implemented control strategy of Experiment (q.1) is repeated but *with* reference filter (— measurement, — simulation).

Fig. 3.45 shows the results for both Experiments (q.1) and (q.2). The plots depict the DFIM quantities from top to bottom: (a) the rotor current $\boldsymbol{i}_r^{dq}$, (b) the stator current $\boldsymbol{i}_s^{dq}$, (c) the machine torque m_m and its - - - reference $m_{m,\mathrm{ref}}$ and (d) the stator reactive power q_s and its - - - reference $q_{s,\mathrm{ref}}$. The last two plots validate the very good control performance of the overall control strategy of the machine torque m_m and the stator reactive power q_s. Both references $m_{m,\mathrm{ref}}$ and $q_{s,\mathrm{ref}}$ of the machine torque and the stator reactive power, respectively, are tracked quickly and precisely. Moreover, jumps in the reference machine torque $m_{m,\mathrm{ref}}$ do hardly affect the tracking of the reference $q_{s,\mathrm{ref}}$ of the stator reactive power and vice versa. Only huge reference jumps in the reference $q_{s,\mathrm{ref}}$ of about 15 kvar at $t = 0.6\,\mathrm{s}$ and $t = 1.4\,\mathrm{s}$ disturb the control of the machine torque noticeably. Further, the simulation results — *without* and — *with* reference filter correspond to their measurements — *without* and — *with* reference filter. Besides the small oscillations due to the *chopper resistance mode* or *diode rectifier mode*, the measurements and the simulation results match (almost) exactly. The big difference between the two Experiments (q.1) and (q.2) are the overshoots in the stator reactive power q_s, when the controller

[69] By considering the discretization time t_{dis}, a first-order lag system with time constant T_{fol} (in s) filters the input signal u_{fol} and gives the output signal x_{fol} as follows: $x_{\mathrm{fol}}[k+1] = \left(1 - \frac{t_{\mathrm{dis}}}{T_{\mathrm{fol}}}\right) x_{\mathrm{fol}}[k] + \frac{t_{\mathrm{dis}}}{T_{\mathrm{fol}}} u_{\mathrm{fol}}[k]$.

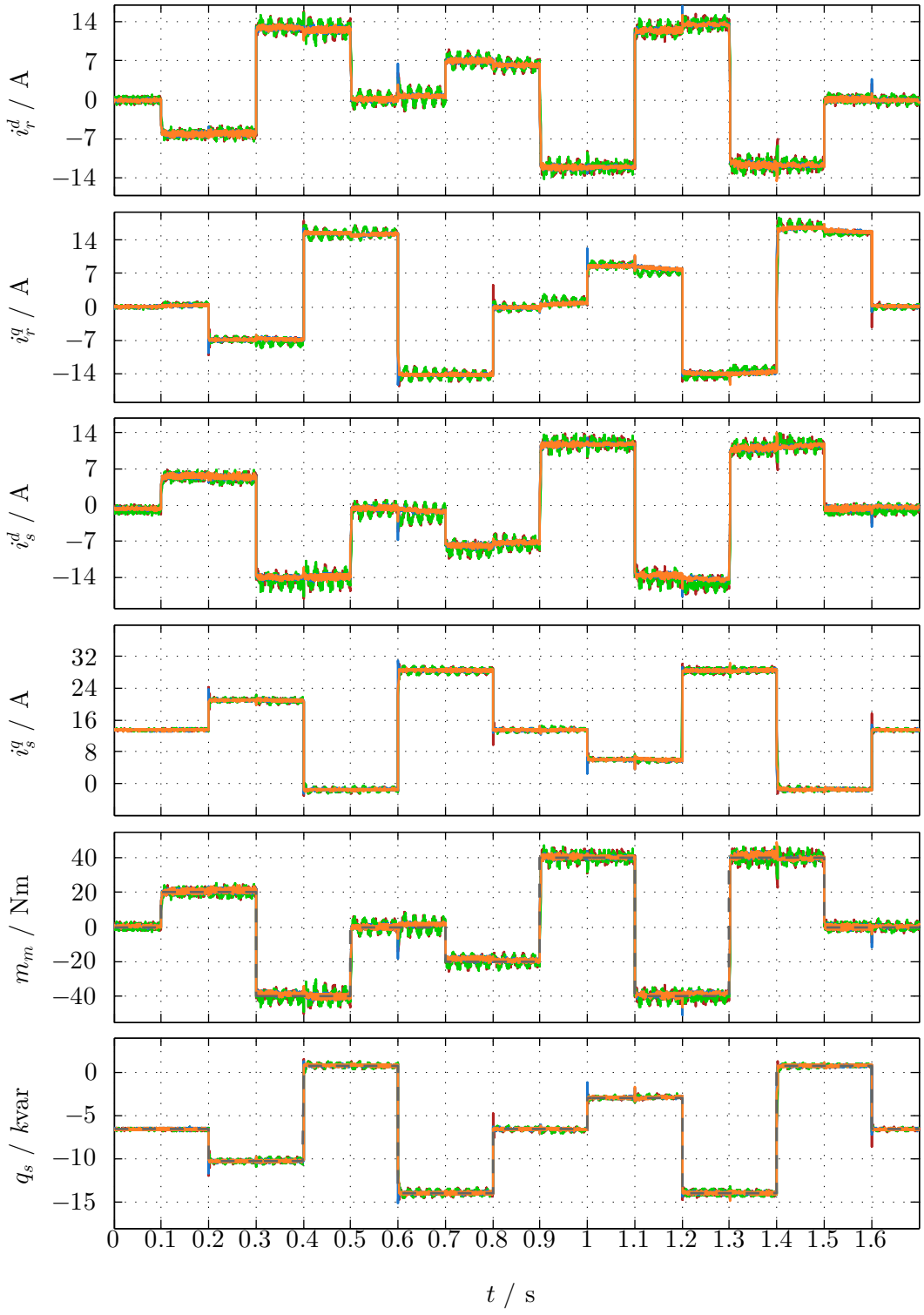

Figure 3.45: *Experiments (q.1) and (q.2):* — *measured quantities without reference filter,* — *simulated quantities without reference filter,* — *measured quantities with reference filter,* — *simulated quantities with reference filter and* - - - *references* $m_{m,\mathrm{ref}}$ *and* $q_{s,\mathrm{ref}}$ *of the machine torque and stator reactive power, respectively.*

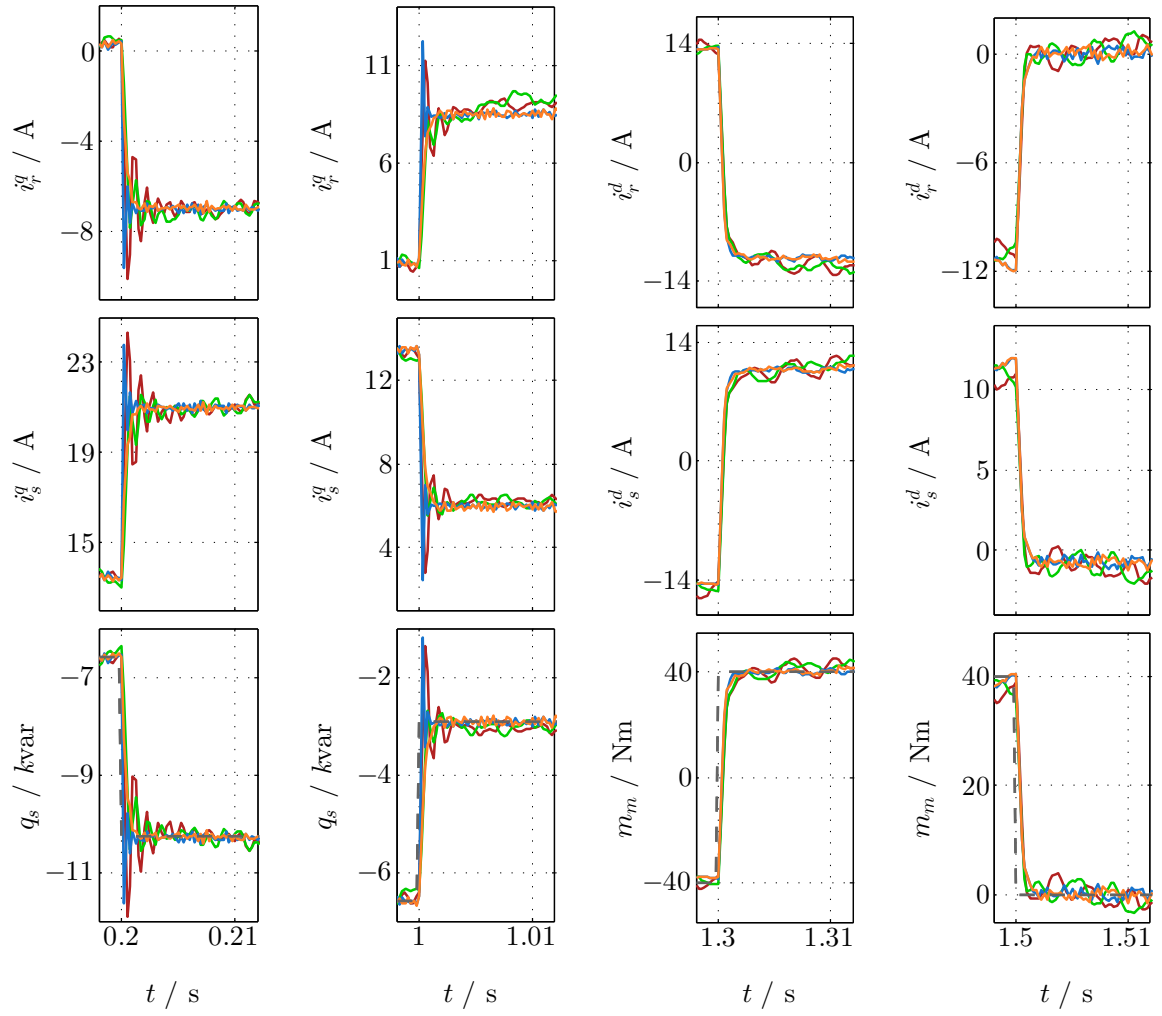

Figure 3.46: *Experiments (q.1) and (q.2) – Zoom:* — *measured quantities without reference filter,* — *simulated quantities without reference filter,* — *measured quantities with reference filter,* — *simulated quantities with reference filter and* - - - *references* $m_{m,\mathrm{ref}}$ *and* $q_{s,\mathrm{ref}}$ *of the machine torque and stator reactive power respectively.*

operates without the reference filter. E.g. the reference jump of about 3.75 kvar at $t=1$ s causes an overshoot of nearly 2 kvar in the stator reactive power q_s.
Fig. 3.46 highlights this difference between Experiments $(q.1)$ and $(q.2)$ by zooming in at the time instants $t=0.2$ s, $t=1$ s, $t=1.3$ s and $t=1.5$ s. The plots of the first two columns in Fig. 3.46 depict (a) the q-component i_r^q of the rotor current, (b) the q-component i_s^q of the stator current and (c) the stator reactive power q_s and its - - - reference $q_{s,\mathrm{ref}}$. Its last two columns show (d) the d-component i_r^d of the rotor current, (e) the d-component i_s^d of the stator current and (f) the machine torque m_m and its - - - reference $m_{m,\mathrm{ref}}$. Due to the two feed-forward controllers for both the stator reactive power (via $i_{r,\mathrm{ff}}^q$) and the machine torque (see Fig. 3.44), the controllers track their references $q_{s,\mathrm{ref}}$ and $m_{m,\mathrm{ref}}$ within about 2 ms, which equals the control performance of the inner rotor current control (cf. Sec. 3.3.2.2). While the machine torque control does not exhibit any differences between the Experiments $(q.1)$ and $(q.2)$, the use of the reference filter is necessary to avoid overshoots in stator reactive power q_s at $t=0.2$ s and $t=1$ s. Moreover, the plots demonstrate the accurate nonlinear DFIM model. All transients in the simulation results are (almost) identical to the corresponding measurements.

Chapter 4

Conclusion and Outlook

The thesis discussed modeling and control of wind turbine systems with DFIM. A holistic model approach was derived that considers both mechanical and electrical components of the wind turbine system. Based on this holistic model, the dynamic power flow was investigated. It summarizes system losses and power exchanges and allows for a detailed efficiency analysis. The focus of the thesis was put on the electrical system. Experimental measurements at the laboratory test-bench were compared to the simulation results of the implemented electrical models. The very precise match between simulation and measurement results verified the high quality of the developed models. Particularly, the nonlinear DFIM model based on nonlinear flux maps and differential inductances was able to emulate cross-couplings and saturation effects accurately, while a linear model approach for the DFIM led to significant deviations between model and real machine. To obtain flux, inductance and torque maps of the DFIM, an experimental setup was proposed, where both stator and rotor of the DFIM are connected to a converter.
Due to the nonlinear characteristics of the DFIM, new methods for the machine side control based on the nonlinear DFIM model had to be designed. In case of an operation without additional LC filter, the thesis presented an adaptive rotor current PI controller with disturbance and cross-coupling compensation for the inner current control. Measurements showed that the controller achieves a fast and precise reference tracking of the rotor currents. In addition, cross-couplings were well-compensated and disturbances did not negatively affect the control performance. In an outer cascade, the torque maps were integrated in the control strategies for machine torque and stator reactive power control. While the stator reactive power regulation includes a feed-forward term, a proportional-integral controller and a reference filter, the tracking of the machine torque reference depends on the quality of the torque maps. The torque maps were calculated on the basis of the rotor flux maps and showed high accuracy. Compared to measured values of the machine torque[70], the averaged deviation was 1.21 % and its maximal deviation was 3.45 %. Experiments regarding both machine torque and reactive power control verified the designed control strategies. Moreover, the rotor current control was investigated while using an additional LC filter between DFIM and back-to-back converter. Apart from regulating the rotor currents, the controller needs to damp the resonance frequency of the machine side. An adaptive discrete-time integral state-feedback controller with either filter current decoupling or reference feed-forward compensation was introduced. Therein, the feedback matrices depend on the operation point of the DFIM and the two weighting matrices for the DLQR design were defined on the basis of Bryson's rule. The proposed control strategy was validated by measurements at the laboratory test-bench. It showed a fast and accurate reference tracking of the rotor currents without steady-state errors. Also, cross-couplings in reaction to reference

[70] Torque sensors are expensive and thus rarely installed (in contrary to the used test bench). Hence, torque measurements are usually not available.

jumps in the orthogonal rotor current component do not significantly influence the reference tracking.

The employed grid connection of the wind turbine system came along with tough challenges for the control. A very small DC-link capacitance necessitates an extremely fast response of the DC-link voltage control to keep the DC-link voltage in the permitted range, especially when power flows from the grid into the back-to-back converter[71]. For this purpose, the proportional gain of the proportional-integral controller needs to be designed aggressively, while the integral gain determines the settling time of the DC-link voltage. However, it is not sufficient for the DC-link voltage control only to take its proportional-integral controller into account. Also the inner current control-loop must be designed properly and a detailed stability analysis based on the closed-loop dynamics of the overall grid side model is required to ensure a stable operation for all operation points. The analysis showed that four things strongly affect the system stability: (i) the d-component of the LCL filter's converter side current, (ii) the DC-link capacitance, (iii) the sampling frequency and (iv) the performance of the inner current control. For the current control, a state feedback controller in discrete-time domain was developed based on a DLQR optimization. Due to the low sampling frequency close to the resonance frequency of the implemented LCL filter, a continuous-time based controller design was not feasible. The following three features helped to improve the control performance of the current controller: (a) instead of using the d-component of the grid current, the d-component of the converter side current was selected as control variable; (b) the most stable standard discrete-time integrator of Matlab/Simulink[72] was employed for the integral state-feedback; (c) a weighting factor was introduced to prioritize the control error in the weighting matrices of the cost function. By means of this current controller design, both an active damping of the LCL filter's resonance frequency and a highly dynamic control performance—which is required for stabilizing the DC-link voltage—was achieved. Finally, measurements at the test-bench validated the implemented control strategy for the grid connection. The controllers showed a high robustness and fast reference tracking without steady-state errors. Moreover, disturbances were rejected quickly and the DC-link voltage stayed in its admissible range.

The experimental setups for the machine-side and the grid-side of the wind turbine system were built separately at the laboratory test-bench. For further research[73], it might be of interest to couple both sides, so all electrical components of wind turbine systems with DFIM are implemented in one integrated setup. Additionally, the scaling method in [142] can be used. It yields a physically reasonable emulation of the dynamical behavior of large wind turbine drive trains at a small-scale test-bench. By means of this method and the integrated setup, simulation results of the holistic model can be verified by measurements at the test-bench for DFIM-based wind turbine systems of any size and power rating.

[71] This is the case, when the DFIM operates in sub-synchronous operation mode.

[72] The integrator uses the integration method "trapezoidal" based on the bilinear transform.

[73] Topics for further research are e.g. operation strategies for unbalanced and distorted grids, integrating sensorless control approaches or optimizing the control objectives regarding loss minimization or cost efficiency.

Bibliography

[1] M. Durstewitz, V. Berkhout, S. Faulstich, P. Görg, L. Große, B. Hahn, M.-A. Lutz, J. Mayer, S. Pfaffel, F. Rehwald, and S. Spriestersbach, "Windenergiereport Deutschland 2018," *Fraunhofer-Institut für Windenergie und Energiesystemtechnik (IEE)*, 2018.

[2] I. Komusanac, G. Brindley, D. Fraile, and L. Ramirez, "Wind energy in europe 2020 statistics and the outlook for 2021-2025," *WindEurope: Brussels, Belgium*, 2020.

[3] T. André, D. Gibb, C. H. Kumar, H. E. Murdock *et al.*, "Renewables 2021 global status report," *REN21 Secretariat: Paris, France*, 2021.

[4] F. Blaabjerg and K. Ma, "Wind energy systems," *Proceedings of the IEEE*, vol. 105, no. 11, pp. 2116–2131, 2017.

[5] C. Dirscherl and C. M. Hackl, "Dynamic power flow in wind turbine systems with doubly-fed induction generator," *2016 IEEE International Energy Conference (ENERGYCON)*, pp. 1–6, 2016.

[6] R. Cardenas, R. Pena, S. Alepuz, and G. Asher, "Overview of control systems for the operation of dfigs in wind energy applications," *IEEE Transactions on Industrial Electronics*, vol. 60, no. 7, pp. 2776–2798, 2013.

[7] D. Zhou and F. Blaabjerg, "Optimized demagnetizing control of dfig power converter for reduced thermal stress during symmetrical grid fault," *IEEE Transactions on Power Electronics*, vol. 33, no. 12, pp. 10 326–10 340, 2018.

[8] P. S. J. van Heerden and H. J. Vermeulen, "Model-based condition monitoring of a doubly-fed induction generator slip ring component," *2013 48th International Universities' Power Engineering Conference (UPEC)*, pp. 1–6, 2013.

[9] S. Muller, M. Deicke, and R. W. De Doncker, "Doubly fed induction generator systems for wind turbines," *IEEE Industry applications magazine*, vol. 8, no. 3, pp. 26–33, 2002.

[10] R. Pena, J. Clare, and G. Asher, "A doubly fed induction generator using back-to-back pwm converters supplying an isolated load from a variable speed wind turbine," *IEE Proceedings-Electric Power Applications*, vol. 143, no. 5, pp. 380–387, 1996.

[11] M. Anu, "Introduction to modeling and simulation," *Proceedings of the 29th conference on Winter simulation*, pp. 7–13, 1997.

[12] T. Sauerbier and O. Mildenberger, "Vor- und Nachteile der Simulation," *Theorie und Praxis von Simulationssystemen: Eine Einführung für Ingenieure und Informatiker*, Vieweg+Teubner, pp. 5-6, 1999.

[13] J. F. Manwell, J. G. McGowan, and A. L. Rogers, *Wind energy explained: theory, design and application.* John Wiley & Sons, 2010.

[14] T. Burton, N. Jenkins, D. Sharpe, and E. Bossanyi, *Wind energy handbook.* John Wiley & Sons, 2011.

[15] E. Hau, *Windkraftanlagen: Grundlagen. Technik. Einsatz. Wirtschaftlichkeit.* Springer, 2017.

[16] T. Ackermann, *Wind power in power systems.* John Wiley & Sons, 2012.

[17] O. Kalmbach, C. Dirscherl, and C. M. Hackl, "Discrete-time dc-link voltage and current control of a grid-connected inverter with lcl-filter and very small dc-link capacitance," *Energies*, vol. 13, no. 21, 2020.

[18] C. Dirscherl, J. Fessler, C. M. Hackl, and H. Ipach, "State-feedback controller and observer design for grid-connected voltage source power converters with lcl-filter," *2015 IEEE Conference on Control Applications (CCA)*, pp. 215–222, 2015.

[19] C. Dirscherl, C. M. Hackl, and K. Schechner, "Explicit model predictive control with disturbance observer for grid-connected voltage source power converters," *2015 IEEE International Conference on Industrial Technology (ICIT)*, pp. 999–1006, 2015.

[20] B.-G. Gu and K. Nam, "A dc-link capacitor minimization method through direct capacitor current control," *IEEE Transactions on Industry Applications*, vol. 42, no. 2, pp. 573–581, 2006.

[21] W.-J. Lee and S. K. Sul, "Dc-link voltage stabilization for reduced dc-link capacitor inverter," *IEEE Transactions on Industry Applications*, vol. 50, no. 1, pp. 404–414, 2014.

[22] T. Friedli and J. W. Kolar, "Comprehensive comparison of three-phase ac-ac matrix converter and voltage dc-link back-to-back converter systems," *The 2010 International Power Electronics Conference - ECCE ASIA* -, pp. 2789–2798, 2010.

[23] J. W. G. Hwang, M. Winkelnkemper, and P. Lehn, "Control of ac-dc-ac converters with minimized dc link capacitance under grid distortion," *2006 IEEE International Symposium on Industrial Electronics*, vol. 2, pp. 1217–1222, 2006.

[24] R. Peña-Alzola and F. Blaabjerg, "Design and control of voltage source converters with lcl-filters," *Control of Power Electronic Converters and Systems*, pp. 207–242, 2018.

[25] X. Ruan, X. Wang, D. Pan, D. Yang, W. Li, and C. Bao, *Control techniques for LCL-type grid-connected inverters.* Springer, 2018.

[26] M. Lu, Z. Xin, X. Wang, R. N. Beres, and F. Blaabjerg, "Extended stable boundary of lcl-filtered grid-connected inverter based on an improved grid-voltage feedforward control," *2016 IEEE Energy Conversion Congress and Exposition (ECCE)*, pp. 1–7, 2016.

[27] J.-P. Corriou, *Process control.* Springer, 2018.

[28] Z. Yao, "Full feedforward of reference powers for the dpc-svm grid-connected inverter," *International Transactions on Electrical Energy Systems*, vol. 28, no. 9, p. e2588, 2018.

[29] C. Dirscherl, C. M. Hackl, and K. Schechner, "Pole-placement based nonlinear state-feedback control of the dc-link voltage in grid-connected voltage source power converters: A preliminary study," *2015 IEEE Conference on Control Applications (CCA)*, pp. 207–214, 2015.

[30] X. Dou, Y. Jiao, K. Yang, Z. Wu, W. Gu, H. Li, and X. Tang, "An optimal grid current control strategy with grid voltage observer (gvo) for lcl-filtered grid-connected inverters," *IEEJ Transactions on Electrical and Electronic Engineering*, vol. 13, no. 5, pp. 777–784, 2018.

[31] C. M. Hackl and M. Landerer, "Modified second-order generalized integrators with modified frequency locked loop for fast harmonics estimation of distorted single-phase signals," *IEEE Transactions on Power Electronics*, vol. 35, no. 3, pp. 3298–3309, 2020.

[32] C. M. Hackl and M. Landerer, "A unified method for generic signal parameter estimation of arbitrarily distorted single-phase grids with dc-offset," *IEEE Open Journal of the Industrial Electronics Society*, vol. 1, pp. 235–246, 2020.

[33] M. B. Saïd-Romdhane, M. W. Naouar, and I. Slama-Belkhodja, "Systematic design method for pi controller with virtual resistor-based active damping of lcl filter," *Global Energy Interconnection*, vol. 1, no. 3, pp. 319–329, 2018.

[34] S. Eren, M. Pahlevani, A. Bakhshai, and P. Jain, "An adaptive droop dc-bus voltage controller for a grid-connected voltage source inverter with lcl filter," *IEEE Transactions on Power Electronics*, vol. 30, no. 2, pp. 547–560, 2015.

[35] M. Merai, M. W. Naouar, and I. Slama-Belkhodja, "An improved dc-link voltage control strategy for grid connected converters," *IEEE Transactions on Power Electronics*, vol. 33, no. 4, pp. 3575–3582, 2018.

[36] I. Sefa, S. Ozdemir, H. Komurcugil, and N. Altin, "An enhanced lyapunov-function based control scheme for three-phase grid-tied vsi with lcl filter," *IEEE Transactions on Sustainable Energy*, vol. 10, no. 2, pp. 504–513, 2019.

[37] J. C. Mitchell, M. J. Kamper, and C. M. Hackl, "Small-scale reluctance synchronous generator variable speed wind turbine system with dc transmission linked inverters," *2016 IEEE Energy Conversion Congress and Exposition (ECCE)*, pp. 1–8, 2016.

[38] M. Rosyadi, S. M. Muyeen, R. Takahashi, and J. Tamura, "New controller design for pmsg based wind generator with lcl-filter considered," *2012 XXth International Conference on Electrical Machines*, pp. 2112–2118, 2012.

[39] X. Zheng, Y. Feng, F. Han, and X. Yu, "Integral-type terminal sliding-mode control for grid-side converter in wind energy conversion systems," *IEEE Transactions on Industrial Electronics*, vol. 66, no. 5, pp. 3702–3711, 2019.

[40] A. A. R. Al Tahir, "Semi-global output feedback nonlinear stabilization of variable speed grid connected direct drive wind turbine generator systems," *International Journal of Dynamics and Control*, vol. 6, pp. 233–261, 2018.

[41] Y. Boussairi, A. Abouloifa, A. Hamdoun, C. Aouadi, I. Lachkar, and F. Giri, "Nonlinear control of permanent magnet synchronous generator grid-connected applied to wind energy conversion system," *2017 IEEE International Conference on Industrial Technology (ICIT)*, pp. 452–457, 2017.

[42] Y. Boussairi, A. Abouloifa, I. Lachkar, C. Aouadi, and A. Hamdoun, "State feedback nonlinear control strategy for wind turbine system driven by permanent magnet synchronous generator for maximum power extraction and power factor correction," *Vibration Analysis and Control in Mechanical Structures and Wind Energy Conversion Systems*, pp. 75–94, 2018.

[43] M. Karimi-Ghartemani, S. Ali Khajehoddin, P. Jain, and A. Bakhshai, "Control of three-phase converters for grid-connected renewable energy systems using feedback linearization technique," *2010 IEEE International Symposium on Industrial Electronics*, pp. 179–183, 2010.

[44] E. Wu and P. Lehn, "Digital current control of a voltage source converter with active damping of lcl resonance," *Twentieth Annual IEEE Applied Power Electronics Conference and Exposition, 2005. APEC 2005.*, vol. 3, pp. 1642–1649, 2005.

[45] N.-B. Lai and K.-H. Kim, "Robust control scheme for three-phase grid-connected inverters with lcl-filter under unbalanced and distorted grid conditions," *IEEE Transactions on Energy Conversion*, vol. 33, no. 2, pp. 506–515, 2018.

[46] J. Kukkola and M. Hinkkanen, "Observer-based state-space current control for a three-phase grid-connected converter equipped with an lcl filter," *IEEE Transactions on Industry Applications*, vol. 50, no. 4, pp. 2700–2709, 2014.

[47] J. Kukkola, M. Hinkkanen, and K. Zenger, "Observer-based state-space current controller for a grid converter equipped with an lcl filter: Analytical method for direct discrete-time design in synchronous coordinates," *2014 IEEE Energy Conversion Congress and Exposition (ECCE)*, pp. 4458–4465, 2014.

[48] C. Ramos, A. Martins, and A. Carvalho, "Complex state-space current controller for grid-connected converters with an lcl filter," *2009 35th Annual Conference of IEEE Industrial Electronics*, pp. 296–301, 2009.

[49] A. Rodríguez-Cabero, F. H. Sánchez, and M. Prodanovic, "A unified control of back-to-back converter," *2016 IEEE Energy Conversion Congress and Exposition (ECCE)*, pp. 1–8, 2016.

[50] A. Rodríguez-Cabero, M. Prodanovic, and J. Roldán-Pérez, "Full-state feedback control of back-to-back converters based on differential and common power concepts," *IEEE Transactions on Industrial Electronics*, vol. 66, no. 11, pp. 9045–9055, 2019.

[51] L. A. Maccari, C. Luiz do Amarai Santini, R. C. de Leão Fontoura de Oliveira, and V. F. Montagner, "Robust discrete linear quadratic control applied to grid-connected converters with lcl filters," *2013 Brazilian Power Electronics Conference*, pp. 374–379, 2013.

[52] F. Huerta, D. Pizarro, S. Cobreces, F. J. Rodriguez, C. Giron, and A. Rodriguez, "Lqg servo controller for the current control of lcl grid-connected voltage-source converters," *IEEE Transactions on Industrial Electronics*, vol. 59, no. 11, pp. 4272–4284, 2012.

[53] S. Gupta, R. Garg, and A. Singh, "Grid integrated pmsg based wind energy system: Modelling, control and simulation," *2016 IEEE 1st International Conference on Power Electronics, Intelligent Control and Energy Systems (ICPEICES)*, pp. 1–6, 2016.

[54] M. G. Judewicz, S. A. González, J. R. Fischer, J. F. Martínez, and D. O. Carrica, "Inverter-side current control of grid-connected voltage source inverters with lcl filter based on generalized predictive control," *IEEE Journal of Emerging and Selected Topics in Power Electronics*, vol. 6, no. 4, pp. 1732–1743, 2018.

[55] C. M. Hackl, "Mpc with analytical solution and integral error feedback for lti mimo systems and its application to current control of grid-connected power converters with lcl-filter," *2015 IEEE International Symposium on Predictive Control of Electrical Drives and Power Electronics (PRECEDE)*, pp. 61–66, 2015.

[56] S. Ebrahimpanah, Q. Chen, and L. Zhang, "Model predictive current control with duty cycle optimization for two-level three-phase grid-tied inverter with output lcl filter based on forward euler approximation," *2017 International Conference on Industrial Informatics - Computing Technology, Intelligent Technology, Industrial Information Integration (ICIICII)*, pp. 155–158, 2017.

[57] P. Falkowski and A. Sikorski, "Finite control set model predictive control for grid-connected ac-dc converters with lcl filter," *IEEE Transactions on Industrial Electronics*, vol. 65, no. 4, pp. 2844–2852, 2018.

[58] T. Dragicevic, C. Zheng, J. Rodriguez, and F. Blaabjerg, "Robust quasi-predictive control of lcl-filtered grid converters," *IEEE Transactions on Power Electronics*, vol. 35, no. 2, pp. 1934–1946, 2020.

[59] X. Chen, W. Wu, N. Gao, H. S.-H. Chung, M. Liserre, and F. Blaabjerg, "Finite control set model predictive control for lcl-filtered grid-tied inverter with minimum sensors," *IEEE Transactions on Industrial Electronics*, vol. 67, no. 12, pp. 9980–9990, 2020.

[60] P. K. Gayen, "Stator flux producing current-based promoted rotor angle estimator of doubly-fed induction generator for encoderless operations," *IEEE Sensors Journal*, vol. 21, no. 13, pp. 15 133–15 141, 2021.

[61] L. M. Ying, X. Cui, Q. F. Liao, C. Tang, L. C. Le, and Z. Chen, "Stator flux observation and speed estimation of a doubly fed induction generator," *2006 International Conference on Power System Technology*, pp. 1–6, 2006.

[62] H. Wang, J. Zhang, C. Zhu, X. Cai, and M. Zhu, "Dc-link current optimal control of current source converter in dfig," *CPSS Transactions on Power Electronics and Applications*, vol. 6, no. 2, pp. 127–135, 2021.

[63] Y. Belkacem, S. Drid, A. Makouf, L. Chrifi-Alaoui, and M. Ouriagli, "Fuzzy controllers for a high performance of the doubly fed induction generator based on wind turbine in variable speed," *2019 International Conference on Intelligent Systems and Advanced Computing Sciences (ISACS)*, pp. 1–7, 2019.

[64] H. E. Azri, A. Essadki, and T. Nasser, "Lqr controller design for a nonlinear, doubly fed induction generator model," *2018 6th International Renewable and Sustainable Energy Conference (IRSEC)*, pp. 1–6, 2018.

[65] R. Akbari, A. Izadian, and R. S. Weissbach, "Quasi self-excited dfig-based wind energy conversion system," *IEEE Transactions on Industry Applications*, vol. 57, no. 3, pp. 2816–2824, 2021.

[66] X. Liu and X. Kong, "Nonlinear model predictive control for dfig-based wind power generation," *IEEE Transactions on Automation Science and Engineering*, vol. 11, no. 4, pp. 1046–1055, 2014.

[67] T. M. Chikouche, A. Mezouar, T. Terras, and S. Hadjeri, "Sensorless nonlinear control of a doubly fed induction motor using luenberger observer," *2015 4th International Conference on Electrical Engineering (ICEE)*, pp. 1–7, 2015.

[68] R.-J. Ye, H. Li, Z. Chen, and Q. Gao, "Comparison of transient behaviors of wind turbines with dfig considering the shaft flexible models," *2008 International Conference on Electrical Machines and Systems*, pp. 2585–2590, 2008.

[69] C. Dirscherl and C. M. Hackl, "Model predictive current control with analytical solution and integral error feedback of doubly-fed induction generators with lc filter," *2017 IEEE International Symposium on Predictive Control of Electrical Drives and Power Electronics (PRECEDE)*, pp. 25–30, 2017.

[70] N. Karakasis, E. Tsioumas, N. Jabbour, A. M. Bazzi, and C. Mademlis, "Optimal efficiency control in a wind system with doubly fed induction generator," *IEEE Transactions on Power Electronics*, vol. 34, no. 1, pp. 356–368, 2019.

[71] Y. Majdoub, A. Abbou, M. Akherraz, and R. E. Akhrif, "Modeling saturation of dfig wind turbine in presence of iron losses," *2017 International Conference on Electrical and Information Technologies (ICEIT)*, pp. 1–4, 2017.

[72] I. K. Amin and M. N. Uddin, "Nonlinear control operation of dfig-based wecs incorporated with machine loss reduction scheme," *IEEE Transactions on Power Electronics*, vol. 35, no. 7, pp. 7031–7044, 2020.

[73] C. M. Hackl, J. Kullick, and N. Monzen, "Generic loss minimization for nonlinear synchronous machines by analytical computation of optimal reference currents considering copper and iron losses," *2021 22nd IEEE International Conference on Industrial Technology (ICIT)*, vol. 1, pp. 1348–1355, 2021.

[74] C. M. Hackl, J. Kullick and N. Monzen, "Optimale Betriebsführung von nichtlinearen Synchronmaschinen," *Elektrische Antriebe — Regelung von Antriebssystemen*, Springer, pp. 1006-1068, 2020.

[75] G. Slemon, "Modelling of induction machines for electric drives," *IEEE Transactions on Industry Applications*, vol. 25, no. 6, pp. 1126–1131, 1989.

[76] J. Zhao, W. Zhang, Y. He, and J. Hu, "Modeling and control of a wind-turbine-driven dfig incorporating core saturation during grid voltage dips," *2008 International Conference on Electrical Machines and Systems*, pp. 2438–2442, 2008.

[77] V. Delli Colli, F. Marignetti, and C. Attaianese, "Analytical and multiphysics approach to the optimal design of a 10-mw dfig for direct-drive wind turbines," *IEEE Transactions on Industrial Electronics*, vol. 59, no. 7, pp. 2791–2799, 2012.

[78] S. D. Sudhoff, B. T. Kuhn, K. A. Corzine, and B. T. Branecky, "Magnetic equivalent circuit modeling of induction motors," *IEEE Transactions on Energy Conversion*, vol. 22, no. 2, pp. 259–270, 2007.

[79] H. Gorginpour, H. Oraee, and R. A. McMahon, "A novel modeling approach for design studies of brushless doubly fed induction generator based on magnetic equivalent circuit," *IEEE Transactions on Energy Conversion*, vol. 28, no. 4, pp. 902–912, 2013.

[80] Z. Zhang, C. L. Xia, Y. Yan, and H. M. Wang, "Analytical field calculation of doubly fed induction generator with core saturation considered," *8th IET International Conference on Power Electronics, Machines and Drives (PEMD 2016)*, pp. 1–6, 2016.

[81] M. Hacil, A. L. Nemmour, A. Khezzar, and M. Boucherma, "Improvement generating powers quality of a doubly-fed induction generator with a second-order lc filter in the rotor circuit," *2008 18th International Conference on Electrical Machines*, pp. 1–6, 2008.

[82] J. Adabi Firouzjaee and F. Zare, "Analysis, calculation and reduction of shaft voltage in induction generators," *Proceedings of the International Conference on Renewable Energies and Power Quality (ICREPQ'09)*, pp. 1–6, 2009.

[83] D. Krug, S. Bernet, S. S. Fazel, K. Jalili, and M. Malinowski, "Comparison of 2.3-kv medium-voltage multilevel converters for industrial medium-voltage drives," *IEEE Transactions on Industrial Electronics*, vol. 54, no. 6, pp. 2979–2992, 2007.

[84] J. Steinke, "Use of an lc filter to achieve a motor-friendly performance of the pwm voltage source inverter," *IEEE Transactions on Energy Conversion*, vol. 14, no. 3, pp. 649–654, 1999.

[85] T. Wang, L. Kong, H. Nian, and Z. Q. Zhu, "Coordinated elimination strategy of low order output current distortion for lc-filtered dfig system based on hybrid virtual impedance method," *IEEE Transactions on Power Electronics*, vol. 34, no. 8, pp. 7502–7520, 2019.

[86] R. Liu, J. Yao, X. Wang, P. Sun, J. Pei, and J. Hu, "Dynamic stability analysis and improved lvrt schemes of dfig-based wind turbines during a symmetrical fault in a weak grid," *IEEE Transactions on Power Electronics*, vol. 35, no. 1, pp. 303–318, 2020.

[87] A. Petersson, L. Harnefors, and T. Thiringer, "Comparison between stator-flux and grid-flux-oriented rotor current control of doubly-fed induction generators," *2004 IEEE 35th Annual Power Electronics Specialists Conference (IEEE Cat. No.04CH37551)*, vol. 1, pp. 482–486, 2004.

[88] A. Thommessen and C. M. Hackl, "Optimal feedforward torque control for nonlinear induction machines considering stator & rotor copper losses and current & voltage limits," *accepted for publication in Proceedings of IEEE International Symposium on Industrial Electronics (ISIE)*, 2021.

[89] R. Pena, J. C. Clare, and G. M. Asher, "Doubly fed induction generator using back-to-back pwm converters and its application to variable-speed wind-energy generation," *IEE Proceedings-Electric power applications*, vol. 143, no. 3, pp. 231–241, 1996.

[90] B. Hopfensperger, D. J. Atkinson, and R. A. Lakin, "Stator-flux-oriented control of a doubly-fed induction machine: with and without position encoder," *IEE Proceedings-Electric power applications*, vol. 147, no. 4, pp. 241–250, 2000.

[91] A. T. Nguyen and D.-C. Lee, "Sensorless control of dfig wind turbine systems based on sogi and rotor position correction," *IEEE Transactions on Power Electronics*, vol. 36, no. 5, pp. 5486–5495, 2021.

[92] R. Nair and G. Narayanan, "Stator flux based model reference adaptive observers for sensorless vector control and direct voltage control of doubly-fed induction generator," *IEEE Transactions on Industry Applications*, vol. 56, no. 4, pp. 3776–3789, 2020.

[93] M. Morawiec, K. Blecharz, and A. Lewicki, "Sensorless rotor position estimation of doubly fed induction generator based on backstepping technique," *IEEE Transactions on Industrial Electronics*, vol. 67, no. 7, pp. 5889–5899, 2020.

[94] M. Szypulski and G. Iwanski, "Sensorless state control of stand-alone doubly fed induction generator supplying nonlinear and unbalanced loads," *IEEE Transactions on Energy Conversion*, vol. 31, no. 4, pp. 1530–1538, 2016.

[95] M. Rostami, S. M. Madani, and S. Ademi, "Sensorless closed-loop voltage and frequency control of stand-alone dfigs introducing direct flux-vector control," *IEEE Transactions on Industrial Electronics*, vol. 67, no. 7, pp. 6078–6088, 2020.

[96] C. Karunanayake, J. Ravishankar, and Z. Y. Dong, "Nonlinear ssr damping controller for dfig based wind generators interfaced to series compensated transmission systems," *IEEE Transactions on Power Systems*, vol. 35, no. 2, pp. 1156–1165, 2020.

[97] C. A. Evangelista, A. Pisano, P. Puleston, and E. Usai, "Receding horizon adaptive second-order sliding mode control for doubly-fed induction generator based wind turbine," *IEEE Transactions on Control Systems Technology*, vol. 25, no. 1, pp. 73–84, 2017.

[98] A. Tohidi, H. Hajieghrary, and M. A. Hsieh, "Adaptive disturbance rejection control scheme for dfig-based wind turbine: Theory and experiments," *IEEE Transactions on Industry Applications*, vol. 52, no. 3, pp. 2006–2015, 2016.

[99] B. Qin, X. Zhang, J. Ma, S. Deng, S. Mei, and D. J. Hill, "Input-to-state stability based control of doubly fed wind generator," *IEEE Transactions on Power Systems*, vol. 33, no. 3, pp. 2949–2961, 2018.

[100] G. Rigatos, P. Siano, N. Zervos, and C. Cecati, "Control and disturbances compensation for doubly fed induction generators using the derivative-free nonlinear kalman filter," *IEEE Transactions on Power Electronics*, vol. 30, no. 10, pp. 5532–5547, 2015.

[101] M. A. Chowdhury and G. M. Shafiullah, "Ssr mitigation of series-compensated dfig wind farms by a nonlinear damping controller using partial feedback linearization," *IEEE Transactions on Power Systems*, vol. 33, no. 3, pp. 2528–2538, 2018.

[102] B. Qin, H. Sun, J. Ma, W. Li, T. Ding, Z. Wang, and A. Y. Zomaya, "Robust H_∞ control of doubly fed wind generator via state-dependent riccati equation technique," *IEEE Transactions on Power Systems*, vol. 34, no. 3, pp. 2390–2400, 2019.

[103] G. Rashid and M. H. Ali, "Nonlinear control-based modified bfcl for lvrt capacity enhancement of dfig-based wind farm," *IEEE Transactions on Energy Conversion*, vol. 32, no. 1, pp. 284–295, 2017.

[104] Y. M. Alsmadi, L. Xu, F. Blaabjerg, A. J. P. Ortega, A. Y. Abdelaziz, A. Wang, and Z. Albataineh, "Detailed investigation and performance improvement of the dynamic behavior of grid-connected dfig-based wind turbines under lvrt conditions," *IEEE Transactions on Industry Applications*, vol. 54, no. 5, pp. 4795–4812, 2018.

[105] P. Sun, J. Yao, R. Liu, J. Pei, H. Zhang, and Y. Liu, "Virtual capacitance control for improving dynamic stability of the dfig-based wind turbines during a symmetrical fault in a weak ac grid," *IEEE Transactions on Industrial Electronics*, vol. 68, no. 1, pp. 333–346, 2021.

[106] P. Kroplewski, M. Morawiec, A. Jąderko, and C. Odeh, "Simulation studies of control systems for doubly fed induction generator supplied by the current source converter," *Energies*, vol. 14, no. 5, 2021.

[107] K. Blecharz and M. Morawiec, "Nonlinear control of a doubly fed generator supplied by a current source inverter," *Energies*, vol. 12, no. 12, 2019.

[108] V. Quaschning, *Regenerative Energiesysteme.* Hanser, 2011.

[109] R. Gasch and J. Twetle, *Windkraftanlagen — Grundlagen, Entwurf, Planung und Betrieb*, 9th ed. Springer Vieweg, 2016.

[110] A. Betz, *Wind-Energie und ihre Ausnutzung durch Windmühlen.* Vandenhoeck & Ruprecht, 1926.

[111] C. Dirscherl, C. Hackl, and K. Schechner, "Modellierung und Regelung von modernen Windkraftanlagen: Eine Einführung," *Elektrische Antriebe — Regelung von Antriebssystemen*, Springer, pp. 1540-1614, 2015.

[112] J. Slootweg, S. de Haan, H. Polinder, and W. Kling, "General model for representing variable speed wind turbines in power system dynamics simulations," *IEEE Transactions on Power Systems*, vol. 18, no. 1, pp. 144–151, 2003.

[113] D. Schröder and M. Buss, "Einführung in mechatronische Systeme," *Intelligente Verfahren: Identifikation und Regelung nichtlinearer Systeme*, Springer Vieweg, pp. 9-34, 2017.

[114] D. Schröder, "Antriebsanordnungen: Grundlagen," *Elektrische Antriebe — Grundlagen*, Springer Vieweg, pp. 1-35, 2017.

[115] G. Pannell, D. J. Atkinson, and B. Zahawi, "Minimum-threshold crowbar for a fault-ride-through grid-code-compliant dfig wind turbine," *IEEE Transactions on Energy Conversion*, vol. 25, no. 3, pp. 750–759, 2010.

[116] L. Rade and B. Westergren, *Mathematics Handbook for Science and Engineering.* Springer, 2004.

[117] D. Schröder and J. Böcker, "Regelungstechnische Grundlagen," *Elektrische Antriebe — Regelung von Antriebssystemen*, Springer, pp. 1-315, 2021.

[118] G. Müller and B. Ponick, *Grundlagen elektrischer Maschinen.* John Wiley & Sons, 2014.

[119] Y. Zhang, J. Jiao, and D. Xu, "Direct power control of doubly fed induction generator using extended power theory under unbalanced network," *IEEE Transactions on Power Electronics*, vol. 34, no. 12, pp. 12 024–12 037, 2019.

[120] S. Walz and M. Liserre, "Hysteresis model predictive current control for pmsm with lc filter considering different error shapes," *IEEE Open Journal of Power Electronics*, vol. 1, pp. 190–197, 2020.

[121] R. Teodorescu, M. Liserre, and P. Rodríguez, "Grid converter structures for wind turbine systems," *Grid Converters for Photovoltaic and Wind Power Systems*, 2011.

[122] D. Schröder and R. Marquardt, "Selbstgeführte Wechselrichter mit eingeprägter Spannung," *Leistungselektronische Schaltungen*, Springer Vieweg, pp. 583-1040, 2019.

[123] R. Teodorescu, M. Liserre, and P. Rodríguez, "Grid converter control for wts," *Grid Converters for Photovoltaic and Wind Power Systems*, 2011.

[124] C. M. Hackl, "Current control of electric synchronous machines," *Non-identifier Based Adaptive Control in Mechatronics*, Springer, pp. 495-558, 2017.

[125] E. Rodriguez-Diaz, F. D. Freijedo, J. C. Vasquez, and J. M. Guerrero, "Analysis and comparison of notch filter and capacitor voltage feedforward active damping techniques for lcl grid-connected converters," *IEEE Transactions on Power Electronics*, vol. 34, no. 4, pp. 3958–3972, 2019.

[126] M. Fakharmanesh, C. M. Hackl, and R. Perini, "Instantaneous conduction and switching losses in two-level voltage source inverters," *2017 IEEE International Conference on Environment and Electrical Engineering and 2017 IEEE Industrial and Commercial Power Systems Europe (EEEIC / I CPS Europe)*, pp. 1–6, 2017.

[127] B. Rabelo and W. Hofmann, "Power flow optimisation and grid integration of wind turbines with the doubly-fed induction generator," *2005 IEEE 36th Power Electronics Specialists Conference*, pp. 2930–2936, 2005.

[128] P. A. Lynn, *Onshore and Offshore Wind Energy: An Introduction.* John Wiley & Sons, 2012.

[129] C. Dirscherl and C. M. Hackl, "Local stability analysis and controller design for speed-controlled wind turbine systems in regime II.5," *Energies*, vol. 11, no. 5, 2018.

[130] L. Hadjidemetriou, E. Kyriakides, and F. Blaabjerg, "A new hybrid pll for interconnecting renewable energy systems to the grid," *2012 IEEE Energy Conversion Congress and Exposition (ECCE)*, pp. 2075–2082, 2012.

[131] R. Teodorescu, M. Liserre, and P. Rodríguez, "Grid synchronization in single-phase power converters," *Grid Converters for Photovoltaic and Wind Power Systems*, 2011.

[132] dSPACE GmbH, *Catalog 2018.* p. 560, 2018.

[133] G. Ludyk, "Optimale zeitkontinuierliche Regelungssysteme," *Theoretische Regelungstechnik 2*, Springer, pp. 197-262, 1995.

[134] M. A. Johnson and M. J. Grimble, "Recent trends in linear optimal quadratic multivariable control system design," *IEE Proceedings D-Control Theory and Applications*, vol. 134, no. 1, pp. 53–71, 1987.

[135] J. Ackermann, "Kontinuierliche Systeme," *Abtastregelung*, Springer, pp. 95-172, 1988.

[136] H. Unbehauen, "Lineare zeitdiskrete Systeme (digitale Regelung)," *Regelungstechnik II*, Vieweg, pp. 101-172, 2007.

[137] G. Ludyk, "Optimale zeitdiskrete Regelungssysteme," *Theoretische Regelungstechnik 2*, Springer, pp. 145-196, 1995.

[138] C. M. Hackl, M. J. Kamper, J. Kullick, and J. Mitchell, "Nonlinear pi current control of reluctance synchronous machines," *arXiv preprint*, arXiv:1512.09301, 2015.

[139] G. Ludyk, "Mathematische Beschreibung dynamischer Systeme," *Theoretische Regelungstechnik 1*, Springer, pp. 8-111, 1995.

[140] J. Lunze, "Beschreibung und Analyse zeitdiskreter Systeme im Zeitbereich," *Regelungstechnik 2: Mehrgrößensysteme, Digitale Regelung*, Springer, pp. 441-500, 2020.

[141] G. Ludyk, "Zustandsrückführung und -beobachtung bei Mehrfachsystemen," *Theoretische Regelungstechnik 2*, Springer, pp. 67-144, 1995.

[142] K. Schechner and C. M. Hackl, "Scaling of the drive train dynamics of large-scale wind turbine systems for real-time emulation in small-scale laboratory setups," *IEEE Transactions on Industrial Electronics*, vol. 66, no. 9, pp. 6779–6788, 2019.

[143] J. Ackermann, "Steuerbarkeit, Steuerfolgen, Polvorgabe und Wahl der Tastperiode," *Abtastregelung*, Springer, pp. 173-198, 1988.

Appendix A

Mathematical preliminaries

This section covers mathematical preliminaries which are necessary to understand the thesis. In Sec. A.1, the space vector theory is introduced. It is shown, how to transform quantities between the used reference frames (see Fig. A.1) to describe electrical three-phase systems. Moreover, Sec. A.1 derives how the instantaneous power of electrical three-phase systems can be calculated for the different reference frames. In Sec. A.2, the relations between phase and line-to-line quantities of electrical three-phase systems are highlighted.

A.1 Space vector theory

A common way to model electrical three-phase systems is to use space vectors.[74]. Some advantages of using space vectors are the following:

- the electrical three-phase systems are characterized by sinusoidal quantities. A (clever) space vector description allows to model these systems by DC quantities. Clearly, the DC quantities (i) are independent of the system frequency and (ii) simplify the controller design, since standard linear controllers can be used.
- the models of the electrical three-phase system often feature side conditions, e.g. an isolated star connection constraints the sum of the phase currents to be zero. Commonly, the space vector models can easily consider these constraints during the implementation (e.g. in Matlab/Simulink).

Fig. A.1 shows the different reference frames which will be employed in the thesis to model the electrical three-phase systems:

(a) the three-phase reference frames $abc = (a, b, c)$ and $uvw = (u, v, w)$,

(b) the space vector reference frames $s = (\alpha, \beta, \gamma)$, $\alpha\beta = (\alpha, \beta)$, $r = (\alpha_r, \beta_r, \gamma)$, $\alpha_r\beta_r = (\alpha_r, \beta_r)$, $k = (d, q, \gamma)$ and $dq = (d, q)$.

By using Clarke's and Park's transformation, the quantities are transformed between the different reference frames. Sec. A.1.1 and Sec. A.1.2 introduce the Clarke and Park transformation respectively. In Sec. A.1.3, a direct transformation of quantities from the *abc*- into the *uvw*-reference frame (and vice versa) is covered. The formulas to calculate the instantaneous power in terms of the different reference frames are covered in Sec. A.1.4.

[74] An explanation of the space vector theory can e.g. also be found in [111].

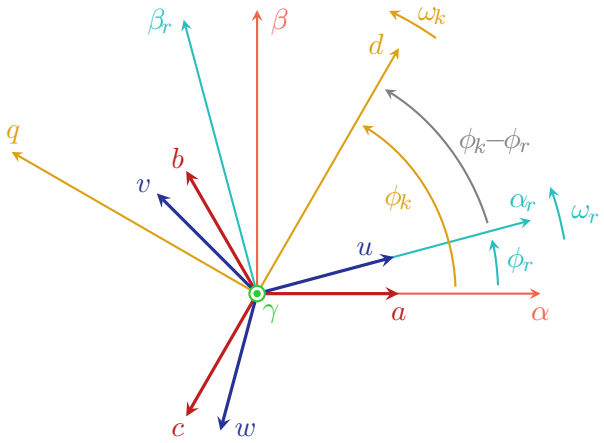

Figure A.1: *Different reference frames of the electrical three-phase systems and their geometrical relation:*
— *three-phase* $abc = (a, b, c)$*-reference frame,*
— *three-phase* $uvw = (u, v, w)$*-reference frame,*
— *stator fixed* $s = (\alpha, \beta, \gamma)$*-reference frame with* — γ*-component,*
— *stator fixed* $\alpha\beta = (\alpha, \beta)$*-reference frame without* γ*-component,*
— *rotor fixed* $r = (\alpha_r, \beta_r, \gamma)$*-reference frame with* — γ*-component,*
— *rotor fixed* $\alpha_r\beta_r = (\alpha_r, \beta_r)$*-reference frame without* γ*-component,*
— *arbitrarily* $k = (d, q, \gamma)$*-reference frame with* — γ*-component,*
— *arbitrarily* $dq = (d, q)$*-reference frame without* γ*-component.*

A.1.1 Clarke transformation

The Clarke transformation matrix $\boldsymbol{T}_C$ transforms the three-phase quantities $\boldsymbol{x}^{abc} := \left(x^a \; x^b \; x^c\right)^\top$ and $\boldsymbol{x}^{uvw} := \left(x^u \; x^v \; x^w\right)^\top$ into the stator-fixed s- and rotor-fixed r-reference frame, respectively. Its inverse $\boldsymbol{T}_C^{-1}$ transforms $\boldsymbol{x}^s := \left(x^\alpha \; x^\beta \; x^\gamma\right)^\top$ and $\boldsymbol{x}^r := \left(x^{\alpha_r} \; x^{\beta_r} \; x^\gamma\right)^\top$ back to the abc- and uvw-reference frame. The Clarke transformation matrix $\boldsymbol{T}_C$ and its inverse $\boldsymbol{T}_C^{-1}$ are defined by

$$\boldsymbol{T}_C := k_c \begin{bmatrix} 1 & -\frac{1}{2} & -\frac{1}{2} \\ 0 & \frac{\sqrt{3}}{2} & -\frac{\sqrt{3}}{2} \\ \kappa_c & \kappa_c & \kappa_c \end{bmatrix} \quad \text{and} \quad \boldsymbol{T}_C^{-1} := \frac{1}{k_c} \begin{bmatrix} \frac{2}{3} & 0 & \frac{1}{3\kappa_c} \\ -\frac{1}{3} & \frac{\sqrt{3}}{3} & \frac{1}{3\kappa_c} \\ -\frac{1}{3} & -\frac{\sqrt{3}}{3} & \frac{1}{3\kappa_c} \end{bmatrix} \quad \text{with} \quad k_c \,, \kappa_c > 0 \,, \tag{A.1}$$

such that the transformation rules are given by

$$\left.\begin{aligned} \boldsymbol{x}^s(t) &= \boldsymbol{T}_C \boldsymbol{x}^{abc}(t) \quad \text{and} \quad \boldsymbol{x}^{abc}(t) = \boldsymbol{T}_C^{-1} \boldsymbol{x}^s(t) \\ \boldsymbol{x}^r(t) &= \boldsymbol{T}_C \boldsymbol{x}^{uvw}(t) \quad \text{and} \quad \boldsymbol{x}^{uvw}(t) = \boldsymbol{T}_C^{-1} \boldsymbol{x}^r(t) \end{aligned}\right\} . \tag{A.2}$$

If $x^a(t) + x^b(t) + x^c(t) = 0$ pertains for all $t \geq 0$, then the γ-component x^γ is zero, i.e. $x^\gamma(t) = k_c\kappa_c(x^a(t) + x^b(t) + x^c(t)) = 0$. Accordingly, if $x^u(t) + x^v(t) + x^w(t) = 0$ holds for all $t \geq 0$, it follows that $x^\gamma(t) = k_c\kappa_c(x^u(t) + x^v(t) + x^w(t)) = 0$. Hence, in both cases the γ-component x^γ can be neglected which leads to the reduced Clarke transformation matrix (and its inverse)

$$\boldsymbol{T}_c := k_c \begin{bmatrix} 1 & -\frac{1}{2} & -\frac{1}{2} \\ 0 & \frac{\sqrt{3}}{2} & -\frac{\sqrt{3}}{2} \end{bmatrix} \quad \text{and} \quad \boldsymbol{T}_c^{-1} := \frac{1}{k_c} \begin{bmatrix} \frac{2}{3} & 0 \\ -\frac{1}{3} & \frac{\sqrt{3}}{3} \\ -\frac{1}{3} & -\frac{\sqrt{3}}{3} \end{bmatrix} . \tag{A.3}$$

The transformation rules for the quantities $\boldsymbol{x}^{\alpha\beta} := \left(x^\alpha \; x^\beta\right)^\top$ and $\boldsymbol{x}^{\alpha_r\beta_r} := \left(x^{\alpha_r} \; x^{\beta_r}\right)^\top$ in the

stator-fixed $\alpha\beta$- and the rotor-fixed $\alpha_r\beta_r$-reference frame (without γ-component) respectively, then, simplify to

$$\left.\begin{aligned} \boldsymbol{x}^{\alpha\beta}(t) &= \boldsymbol{T}_c \boldsymbol{x}^{abc}(t) \quad \text{and} \quad \boldsymbol{x}^{abc}(t) = \boldsymbol{T}_c^{-1} \boldsymbol{x}^{\alpha\beta}(t) \\ \boldsymbol{x}^{\alpha_r\beta_r}(t) &= \boldsymbol{T}_c \boldsymbol{x}^{uvw}(t) \quad \text{and} \quad \boldsymbol{x}^{uvw}(t) = \boldsymbol{T}_c^{-1} \boldsymbol{x}^{\alpha_r\beta_r}(t) \end{aligned}\right\} . \tag{A.4}$$

A.1.2 Park transformation

To transform $\boldsymbol{x}^{\alpha\beta}$ and $\boldsymbol{x}^{\alpha_r\beta_r}$ from the stator-fixed $\alpha\beta$- and rotor-fixed $\alpha_r\beta_r$-reference frame into $\boldsymbol{x}^{dq} := \begin{pmatrix} x^d & x^q \end{pmatrix}^\top$ of the arbitrarily (rotating) dq-reference frame and vice versa, the Park transformation matrix $\boldsymbol{T}_p$ and its inverse $\boldsymbol{T}_p^{-1}$ are used, which are given by

$$\boldsymbol{T}_p(\phi_x) := \begin{bmatrix} \cos(\phi_x) & -\sin(\phi_x) \\ \sin(\phi_x) & \cos(\phi_x) \end{bmatrix} \quad \text{and} \quad \boldsymbol{T}_p^{-1}(\phi_x) := \begin{bmatrix} \cos(\phi_x) & \sin(\phi_x) \\ -\sin(\phi_x) & \cos(\phi_x) \end{bmatrix} \tag{A.5}$$

with angle ϕ_x (in rad). Fig. A.1 depicts the geometrical relation between the different reference frames. The dq-reference frame features the transformation rotational speed ω_k (in $\frac{\text{rad}}{\text{s}}$) and is rotated by the (time-varying) transformation angle ϕ_k (in rad) with respect to the $\alpha\beta$-reference frame. The $\alpha_r\beta_r$-reference frame is rotated by the (time-varying) electrical machine angle ϕ_r (in rad) with respect to the $\alpha\beta$-reference frame and turns with electrical machine rotational speed ω_r (in $\frac{\text{rad}}{\text{s}}$), such that the following holds

$$\left.\begin{aligned} &\tfrac{\mathrm{d}}{\mathrm{d}t}\phi_k(t) = \omega_k(t) \ , \ \phi_{k,0} := \phi_k(0) \\ &\tfrac{\mathrm{d}}{\mathrm{d}t}\phi_r(t) = n_m \tfrac{\mathrm{d}}{\mathrm{d}t}\phi_m(t) = n_m\omega_m(t) = \omega_r(t) \ , \ \phi_{m,0} := \phi_m(0) \text{ and } \phi_{r,0} := \phi_r(0) = n_m\phi_{m,0} \end{aligned}\right\} . \tag{A.6}$$

The pole pair number n_m (in 1) relates the mechanical machine rotational speed ω_m (in $\frac{\text{rad}}{\text{s}}$) and angle ϕ_m (in rad) to their corresponding electrical quantities ω_r and ϕ_r. Then, by considering the geometrical relations between the reference frames, the transformation rules of Park's transformation result in

$$\left.\begin{aligned} \boldsymbol{x}^{dq}(t) &= \boldsymbol{T}_p^{-1}(\phi_k) \boldsymbol{x}^{\alpha\beta}(t) \quad \text{and} \quad \boldsymbol{x}^{\alpha\beta} = \boldsymbol{T}_p(\phi_k) \boldsymbol{x}^{dq}(t) \\ \boldsymbol{x}^{dq}(t) &= \boldsymbol{T}_p^{-1}(\phi_k - \phi_r) \boldsymbol{x}^{\alpha_r\beta_r}(t) \quad \text{and} \quad \boldsymbol{x}^{\alpha_r\beta_r}(t) = \boldsymbol{T}_p(\phi_k - \phi_r) \boldsymbol{x}^{dq}(t) \end{aligned}\right\} \tag{A.7}$$

If it is required to take the γ-component into account as well, the Park transformation matrices of (A.5) are extended to

$$\boldsymbol{T}_P(\phi_x) := \begin{bmatrix} \boldsymbol{T}_p(\phi_x) & \boldsymbol{0}_2 \\ \boldsymbol{0}_2^\top & 1 \end{bmatrix} \quad \text{and} \quad \boldsymbol{T}_P^{-1}(\phi_x) := \begin{bmatrix} \boldsymbol{T}_p^{-1}(\phi_x) & \boldsymbol{0}_2 \\ \boldsymbol{0}_2^\top & 1 \end{bmatrix} . \tag{A.8}$$

Accordingly, $\boldsymbol{T}_P$ and $\boldsymbol{T}_P^{-1}$ transform the quantities $\boldsymbol{x}^s$ and $\boldsymbol{x}^r$ from the stator fixed s- and the rotor-fixed r-reference frame into $\boldsymbol{x}^k := \begin{pmatrix} x^d & x^q & x^\gamma \end{pmatrix}^\top$ of the arbitrarily (rotating) k-reference frame (and vice versa) via

$$\left.\begin{aligned} \boldsymbol{x}^k(t) &= \boldsymbol{T}_P^{-1}(\phi_k) \boldsymbol{x}^s(t) \quad \text{and} \quad \boldsymbol{x}^s = \boldsymbol{T}_P(\phi_k) \boldsymbol{x}^k(t) \\ \boldsymbol{x}^k(t) &= \boldsymbol{T}_P^{-1}(\phi_k - \phi_r) \boldsymbol{x}^r(t) \quad \text{and} \quad \boldsymbol{x}^r(t) = \boldsymbol{T}_P(\phi_k - \phi_r) \boldsymbol{x}^k(t) \end{aligned}\right\} . \tag{A.9}$$

In the following, relevant properties of Park's transformation are highlighted.
An important Park transformation rotates the dq-reference frame by $\pm\frac{\pi}{2}$, that is why the follo-

wing three matrices $\boldsymbol{J}$, $\boldsymbol{J}^{-1}$ and $\boldsymbol{J}'$ are defined by

$$\boldsymbol{J} := \boldsymbol{T}_p(\tfrac{\pi}{2}) = \begin{bmatrix} 0 & -1 \\ 1 & 0 \end{bmatrix} \;,\; \boldsymbol{J}^{-1} := \boldsymbol{T}_p(-\tfrac{\pi}{2}) = \begin{bmatrix} 0 & 1 \\ -1 & 0 \end{bmatrix} \quad \text{and} \quad \boldsymbol{J}' := \begin{bmatrix} \boldsymbol{J} & \boldsymbol{0}_2 \\ \boldsymbol{0}_2^\top & 0 \end{bmatrix} . \tag{A.10}$$

Moreover, the inverse Park transformation matrices $\boldsymbol{T}_P^{-1}$ and $\boldsymbol{T}_p^{-1}$ fulfill the following identities

$$\boldsymbol{T}_P^{-1}(\phi_x) = \boldsymbol{T}_P(\phi_x)^\top = \boldsymbol{T}_P(-\phi_x) \quad \text{and} \quad \boldsymbol{T}_p^{-1}(\phi_x) = \boldsymbol{T}_p(\phi_x)^\top = \boldsymbol{T}_p(-\phi_x) . \tag{A.11}$$

A further property is that Park's transformation features an additive characteristic. Hence, defining the angles $\phi_{x,1}$ and $\phi_{x,2}$ (both in rad) leads to

$$\boldsymbol{T}_P(\phi_{x,1}+\phi_{x,2}) = \boldsymbol{T}_P(\phi_{x,1})\boldsymbol{T}_P(\phi_{x,2}) \quad \text{and} \quad \boldsymbol{T}_p(\phi_{x,1}+\phi_{x,2}) = \boldsymbol{T}_p(\phi_{x,1})\boldsymbol{T}_p(\phi_{x,2}) . \tag{A.12}$$

By defining the rotational speed by $\omega_x(t) = \frac{\mathrm{d}}{\mathrm{d}t}\phi_x(t)$ (in $\frac{\mathrm{rad}}{\mathrm{s}}$) with initial angle $\phi_{x,0} = \phi_x(0)$, the time derivatives of the Park transformation matrices $\boldsymbol{T}_P$ and $\boldsymbol{T}_p$ are given by

$$\left.\begin{aligned} \tfrac{\mathrm{d}}{\mathrm{d}t}\boldsymbol{T}_P(\phi_x) &= \omega_x(t)\boldsymbol{J}'\boldsymbol{T}_P(\phi_x) = \omega_x(t)\boldsymbol{T}_P(\phi_x)\boldsymbol{J}' \\ \text{and} \quad \tfrac{\mathrm{d}}{\mathrm{d}t}\boldsymbol{T}_p(\phi_x) &= \omega_x(t)\boldsymbol{J}\boldsymbol{T}_p(\phi_x) = \omega_x(t)\boldsymbol{T}_p(\phi_x)\boldsymbol{J} \end{aligned}\right\} . \tag{A.13}$$

Accordingly, the time derivatives of the inverse Park transformation matrices $\boldsymbol{T}_P^{-1}$ and $\boldsymbol{T}_p^{-1}$ result in

$$\left.\begin{aligned} \tfrac{\mathrm{d}}{\mathrm{d}t}\boldsymbol{T}_P^{-1}(\phi_x) &= -\omega_x(t)\boldsymbol{J}'\boldsymbol{T}_P^{-1}(\phi_x) = -\omega_x(t)\boldsymbol{T}_P^{-1}(\phi_x)\boldsymbol{J}' \\ \text{and} \quad \tfrac{\mathrm{d}}{\mathrm{d}t}\boldsymbol{T}_p^{-1}(\phi_x) &= -\omega_x(t)\boldsymbol{J}\boldsymbol{T}_p^{-1}(\phi_x) = -\omega_x(t)\boldsymbol{T}_p^{-1}(\phi_x)\boldsymbol{J} \end{aligned}\right\} . \tag{A.14}$$

A.1.3 Transformation of two three-phase systems

The relations between the different reference frames—covered in Sec. A.1.1 and Sec. A.1.2—yield the following:

$$\left.\begin{aligned} \boldsymbol{x}^{abc}(t) &= \boldsymbol{T}_C^{-1}\boldsymbol{x}^s(t) = \boldsymbol{T}_C^{-1}\boldsymbol{T}_P(\phi_r)\boldsymbol{x}^r(t) = \boldsymbol{T}_C^{-1}\boldsymbol{T}_P(\phi_r)\boldsymbol{T}_C\boldsymbol{x}^{uvw}(t) =: \boldsymbol{T}_{\circlearrowleft}(\phi_r)\boldsymbol{x}^{uvw}(t) \\ \boldsymbol{x}^{uvw}(t) &= \boldsymbol{T}_C^{-1}\boldsymbol{x}^r(t) = \boldsymbol{T}_C^{-1}\boldsymbol{T}_P^{-1}(\phi_r)\boldsymbol{x}^s(t) = \boldsymbol{T}_C^{-1}\boldsymbol{T}_P^{-1}(\phi_r)\boldsymbol{T}_C\boldsymbol{x}^{abc}(t) =: \boldsymbol{T}_{\circlearrowleft}^{-1}(\phi_r)\boldsymbol{x}^{abc}(t) \end{aligned}\right\} . \tag{A.15}$$

Consequently, with the help of the rotation matrix $\boldsymbol{T}_{\circlearrowleft}$ and its inverse $\boldsymbol{T}_{\circlearrowleft}^{-1}$, it is possible to transform the quantity $\boldsymbol{x}^{abc}$ from the *abc*-reference frame directly into $\boldsymbol{x}^{uvw}$ of the *uvw*-reference frame and vice versa (see (A.15)). The rotation matrix $\boldsymbol{T}_{\circlearrowleft}$ and its inverse $\boldsymbol{T}_{\circlearrowleft}^{-1}$ are given by

$$\left.\begin{aligned} \boldsymbol{T}_{\circlearrowleft}(\phi_x) &= \tfrac{1}{3}\cos(\phi_x(t)) \begin{bmatrix} 2 & -1 & -1 \\ -1 & 2 & -1 \\ -1 & -1 & 2 \end{bmatrix} + \tfrac{\sqrt{3}}{3}\sin(\phi_x(t)) \begin{bmatrix} 0 & -1 & 1 \\ 1 & 0 & -1 \\ -1 & 1 & 0 \end{bmatrix} + \tfrac{1}{3}\boldsymbol{1}_{3\times 3} \\ \boldsymbol{T}_{\circlearrowleft}^{-1}(\phi_x) &= \tfrac{1}{3}\cos(\phi_x(t)) \begin{bmatrix} 2 & -1 & -1 \\ -1 & 2 & -1 \\ -1 & -1 & 2 \end{bmatrix} - \tfrac{\sqrt{3}}{3}\sin(\phi_x(t)) \begin{bmatrix} 0 & -1 & 1 \\ 1 & 0 & -1 \\ -1 & 1 & 0 \end{bmatrix} + \tfrac{1}{3}\boldsymbol{1}_{3\times 3} \end{aligned}\right\} . \tag{A.16}$$

Two important properties of the rotation matrix $\boldsymbol{T}_{\circlearrowleft}$ and its inverse $\boldsymbol{T}_{\circlearrowleft}^{-1}$ are

$$\boldsymbol{T}_{\circlearrowleft}(\phi_{x,1}+\phi_{x,2}) = \boldsymbol{T}_{\circlearrowleft}(\phi_{x,1})\boldsymbol{T}_{\circlearrowleft}(\phi_{x,2}) \quad \text{and} \quad \boldsymbol{T}_{\circlearrowleft}^{-1}(\phi_x) = \boldsymbol{T}_{\circlearrowleft}(\phi_x)^\top = \boldsymbol{T}_{\circlearrowleft}(-\phi_x) . \tag{A.17}$$

A.1.4 Instantaneous power in space vector description

This section covers the instantaneous power p_x (in W) which is calculated for the different reference frames $n \in \{abc, uvw, s, k, dq\}$. Introducing the vectors $\boldsymbol{u}_x^n$ and $\boldsymbol{i}_x^n$ of voltage and current, respectively, and defining the power matrix

$$\boldsymbol{T}_\wp := (\boldsymbol{T}_C^{-1})^\top \boldsymbol{T}_C^{-1} = \frac{2}{3k_c^2} \operatorname{diag}\left(1\,,\,1\,,\,\frac{1}{2\kappa_c^2}\right) \tag{A.18}$$

yields the instantaneous power

$$\begin{aligned} p_x(t) &= \boldsymbol{u}_x^{uvw}(t)^\top \boldsymbol{i}_x^{uvw}(t) \overset{(A.15)}{=} \boldsymbol{u}_x^{abc}(t)^\top \boldsymbol{T}_{\circlearrowleft}^{-1}(\phi_r)^\top \boldsymbol{T}_{\circlearrowleft}^{-1}(\phi_r) \boldsymbol{i}_x^{abc}(t) \overset{(A.17)}{=} \boldsymbol{u}_x^{abc}(t)^\top \boldsymbol{i}_x^{abc}(t) \\ &\overset{(A.2)}{=} \boldsymbol{u}_x^{s}(t)^\top (\boldsymbol{T}_C^{-1})^\top \boldsymbol{T}_C^{-1} \boldsymbol{i}_x^{s}(t) \overset{(A.18)}{=} \boldsymbol{u}_x^{s}(t)^\top \boldsymbol{T}_\wp \boldsymbol{i}_x^{s}(t) \overset{(A.9)}{=} \boldsymbol{u}_x^{k}(t)^\top \underbrace{\boldsymbol{T}_P(\phi_k)^\top \boldsymbol{T}_\wp \boldsymbol{T}_P(\phi_k)}_{=\boldsymbol{T}_\wp} \boldsymbol{i}_x^{k}(t) \\ &= \boldsymbol{u}_x^{k}(t)^\top \boldsymbol{T}_\wp \boldsymbol{i}_x^{k}(t)\,. \end{aligned} \tag{A.19}$$

If either the γ-component of the voltage u_x^γ or the current i_x^γ is zero (i.e. $u_x^\gamma = 0 \vee i_x^\gamma = 0$), then the γ-component does not have any impact on the instantaneous power p_x and can be neglected. Hence, (A.19) simplifies to:

$$p_x(t) = \boldsymbol{u}_x^{k}(t)^\top \boldsymbol{T}_\wp \boldsymbol{i}_x^{k}(t) \quad \overset{u_x^\gamma = 0 \vee i_x^\gamma = 0}{\Longrightarrow} \quad p_x(t) = \frac{2}{3k_c^2} \boldsymbol{u}_x^{dq}(t)^\top \boldsymbol{i}_x^{dq}(t)\,. \tag{A.20}$$

A.2 Line-to-line transformation

Besides the quantities $\boldsymbol{x}^{abc}$ of the phases a, b, c and $\boldsymbol{x}^{uvw}$ of the phases u, v, w, often their corresponding line-to-line quantities $\boldsymbol{x}^{a\text{-}b\text{-}c}$ and $\boldsymbol{x}^{u\text{-}v\text{-}w}$ are relevant. To calculate the line-to-line quantities out of the phase quantities and vice versa, the following line-to-line matrices are defined:

$$\boldsymbol{T}_{LTL} := \begin{bmatrix} 1 & -1 & 0 \\ 0 & 1 & -1 \\ -1 & 0 & 1 \end{bmatrix} \quad , \quad \boldsymbol{T}_{ltl} := \begin{bmatrix} 1 & -1 & 0 \\ 0 & 1 & -1 \\ 0 & 1 & 2 \end{bmatrix} \quad \text{and} \quad \boldsymbol{T}_{ltl}^{-1} := \frac{1}{3} \begin{bmatrix} 3 & 2 & 1 \\ 0 & 2 & 1 \\ 0 & -1 & 1 \end{bmatrix}. \tag{A.21}$$

Then, by using the relations $x^\gamma(t) = k_c\kappa_c(x^a(t)+x^b(t)+x^c(t))$ and $x^\gamma(t) = k_c\kappa_c(x^u(t)+x^v(t)+x^w(t))$, the line-to-line quantities $\boldsymbol{x}^{a\text{-}b\text{-}c}$ and $\boldsymbol{x}^{u\text{-}v\text{-}w}$ result in

$$\left.\begin{aligned} \boldsymbol{x}^{a\text{-}b\text{-}c}(t) &:= \begin{pmatrix} x^a(t) - x^b(t) \\ x^b(t) - x^c(t) \\ x^c(t) - x^a(t) \end{pmatrix} = \boldsymbol{T}_{LTL} \boldsymbol{x}^{abc}(t) = \boldsymbol{T}_{ltl} \boldsymbol{x}^{abc}(t) - \begin{pmatrix} 0 \\ 0 \\ \frac{1}{k_c\kappa_c} x^\gamma(t) \end{pmatrix} \\ \boldsymbol{x}^{u\text{-}v\text{-}w}(t) &:= \begin{pmatrix} x^u(t) - x^v(t) \\ x^v(t) - x^w(t) \\ x^w(t) - x^u(t) \end{pmatrix} = \boldsymbol{T}_{LTL} \boldsymbol{x}^{uvw}(t) = \boldsymbol{T}_{ltl} \boldsymbol{x}^{uvw}(t) - \begin{pmatrix} 0 \\ 0 \\ \frac{1}{k_c\kappa_c} x^\gamma(t) \end{pmatrix} \end{aligned}\right\}. \tag{A.22}$$

Accordingly, with the help of the inverse line-to-line matrix $\boldsymbol{T}_{ltl}^{-1}$ and the line-to-line quantities $\boldsymbol{x}^{a\text{-}b\text{-}c}$ and $\boldsymbol{x}^{u\text{-}v\text{-}w}$, the phase quantities $\boldsymbol{x}^{abc}$ and $\boldsymbol{x}^{uvw}$ are calculated by

$$\boldsymbol{x}^{abc}(t) = \boldsymbol{T}_{ltl}^{-1} \boldsymbol{x}^{a\text{-}b\text{-}c}(t) + \frac{1}{3k_c\kappa_c} \boldsymbol{1}_3 x^\gamma(t) \quad \text{and} \quad \boldsymbol{x}^{uvw}(t) = \boldsymbol{T}_{ltl}^{-1} \boldsymbol{x}^{u\text{-}v\text{-}w}(t) + \frac{1}{3k_c\kappa_c} \boldsymbol{1}_3 x^\gamma(t)\,. \tag{A.23}$$

Remark (R.A.1) *The line-to-line quantities* $\boldsymbol{x}^{a\text{-}b\text{-}c}$ *and* $\boldsymbol{x}^{u\text{-}v\text{-}w}$ *can be determined directly from their corresponding phase quantities* $\boldsymbol{x}^{abc}$ *and* $\boldsymbol{x}^{uvw}$ *respectively (see* (A.22)*). Since the line-to-line matrix* $\boldsymbol{T}_{LTL}$ *does not have full rank, i.e.* $\det(\boldsymbol{T}_{LTL}) = 0$*, its inverse does not exist. Consequently, the workaround by using the special line-to-line matrix* $\boldsymbol{T}_{ltl}$ *with full rank is necessary which requires additional knowledge of the* γ*-component* x^{γ}*.*

Appendix B

Properties of the nonlinear DFIM model

Sec. 2.2.2 introduced the nonlinear DFIM model. Here, some additional relations and properties of this model are discussed. Sec. B.1 covers the DFIM resistances. Sec. B.2 highlights, how to transform the differential DFIM inductances between different reference frames. In Sec. B.3, the symmetry properties of the DFIM inductances are shown.

B.1 Properties of the DFIM resistances

In (A.2.8), the stator and rotor resistances are assumed to be symmetrical, i.e. $R_s := R_s^a = R_s^b = R_s^c$ and $R_r := R_r^u = R_r^v = R_r^w$, which leads to the resistance matrices $\boldsymbol{R}_s^k = R_s \boldsymbol{I}_3$ and $\boldsymbol{R}_r^k = R_r \boldsymbol{I}_3$ of stator and rotor, respectively. In the following, the case of unsymmetrical stator and rotor resistances is discussed, i.e. $R_s^a \neq R_s^b \neq R_s^c$ and $R_r^u \neq R_r^v \neq R_r^w$.

B.1.1 Stator resistances

In general, due to (2.13) and (2.17), the stator resistance matrix $\boldsymbol{R}_s^k$ in the arbitrarily k-reference frame is given by $\boldsymbol{R}_s^k(\phi_k) = \boldsymbol{T}_P^{-1}(\phi_k)\boldsymbol{T}_C \boldsymbol{R}_s^{abc} \boldsymbol{T}_C^{-1} \boldsymbol{T}_P(\phi_k)$ with $\boldsymbol{R}_s^{abc} := \mathrm{diag}(R_s^a, R_s^b, R_s^c)$. This results in

$$\begin{aligned}\boldsymbol{R}_s^k(\phi_k) =& \frac{1}{3}\left(R_s^a + R_s^b + R_s^c\right)\boldsymbol{I}_3 + \frac{\sqrt{3}}{6}\left(R_s^c - R_s^b\right)\begin{bmatrix} \sin(2\phi_k) & \cos(2\phi_k) & -\frac{\sin(\phi_k)}{\kappa_c} \\ \cos(2\phi_k) & -\sin(2\phi_k) & -\frac{\cos(\phi_k)}{\kappa_c} \\ -2\kappa_c \sin(\phi_k) & -2\kappa_c \cos(\phi_k) & 0 \end{bmatrix} \\ &+ \frac{1}{6}\left(2R_s^a - R_s^b - R_s^c\right)\begin{bmatrix} \cos(2\phi_k) & -\sin(2\phi_k) & \frac{\cos(\phi_k)}{\kappa_c} \\ -\sin(2\phi_k) & -\cos(2\phi_k) & -\frac{\sin(\phi_k)}{\kappa_c} \\ 2\kappa_c \cos(\phi_k) & -2\kappa_c \sin(\phi_k) & 0 \end{bmatrix}, \end{aligned} \tag{B.1}$$

such that the stator resistance matrix $\boldsymbol{R}_s^k$ exhibits the constant term $\frac{1}{3}\left(R_s^a + R_s^b + R_s^c\right)\boldsymbol{I}_3$ and an oscillating term. Thereby, the stator resistance matrix $\boldsymbol{R}_s^{dq}$ oscillates with frequency $\frac{\omega_k}{\pi}$, while the elements $R_s^{d\gamma}$, $R_s^{q\gamma}$, $R_s^{\gamma d}$ and $R_s^{\gamma q}$ oscillate with frequency $\frac{\omega_k}{2\pi}$. If the transformation angle ϕ_k is zero, i.e. $\phi_k = 0$, it gives the stator resistance matrix $\boldsymbol{R}_s^s$ in the stator-fixed s-reference frame as follows

$$\boldsymbol{R}_s^s = R_s^a \begin{bmatrix} \frac{2}{3} & 0 & \frac{1}{3\kappa_c} \\ 0 & 0 & 0 \\ \frac{2}{3}\kappa_c & 0 & \frac{1}{3} \end{bmatrix} + R_s^b \begin{bmatrix} \frac{1}{6} & -\frac{\sqrt{3}}{6} & -\frac{1}{6\kappa_c} \\ -\frac{\sqrt{3}}{6} & \frac{1}{2} & \frac{\sqrt{3}}{6\kappa_c} \\ -\frac{1}{3}\kappa_c & \frac{\sqrt{3}}{3}\kappa_c & \frac{1}{3} \end{bmatrix} + R_s^c \begin{bmatrix} \frac{1}{6} & \frac{\sqrt{3}}{6} & -\frac{1}{6\kappa_c} \\ \frac{\sqrt{3}}{6} & \frac{1}{2} & -\frac{\sqrt{3}}{6\kappa_c} \\ -\frac{1}{3}\kappa_c & -\frac{\sqrt{3}}{3}\kappa_c & \frac{1}{3} \end{bmatrix}. \tag{B.2}$$

B.1.2 Rotor resistances

Because of (2.14) and (2.18), the rotor resistance matrix $\boldsymbol{R}_r^k$ in the arbitrarily k-reference frame is given by $\boldsymbol{R}_r^k(\phi_k,\phi_r) = \boldsymbol{T}_P^{-1}(\phi_k-\phi_r)\boldsymbol{T}_C\boldsymbol{R}_r^{uvw}\boldsymbol{T}_C^{-1}\boldsymbol{T}_P(\phi_k-\phi_r)$ with $\boldsymbol{R}_r^{uvw} := \mathrm{diag}(R_r^u, R_r^v, R_r^w)$, which yields

$$\begin{aligned}\boldsymbol{R}_r^k(\phi_k-\phi_r) =& \frac{1}{3}\left(R_r^u+R_r^v+R_r^w\right)\boldsymbol{I}_3 + \frac{\sqrt{3}}{6}(R_r^w-R_r^v)\begin{bmatrix} \sin(2(\phi_k-\phi_r)) & \cos(2(\phi_k-\phi_r)) & -\frac{\sin(\phi_k-\phi_r)}{\kappa_c} \\ \cos(2(\phi_k-\phi_r)) & -\sin(2(\phi_k-\phi_r)) & -\frac{\cos(\phi_k-\phi_r)}{\kappa_c} \\ -2\kappa_c\sin(\phi_k-\phi_r) & -2\kappa_c\cos(\phi_k-\phi_r) & 0 \end{bmatrix} \\ &+ \frac{1}{6}\left(2R_r^u - R_r^v - R_r^w\right)\begin{bmatrix} \cos(2(\phi_k-\phi_r)) & -\sin(2(\phi_k-\phi_r)) & \frac{\cos(\phi_k-\phi_r)}{\kappa_c} \\ -\sin(2(\phi_k-\phi_r)) & -\cos(2(\phi_k-\phi_r)) & -\frac{\sin(\phi_k-\phi_r)}{\kappa_c} \\ 2\kappa_c\cos(\phi_k-\phi_r) & -2\kappa_c\sin(\phi_k-\phi_r) & 0 \end{bmatrix}. \end{aligned} \tag{B.3}$$

Thus, the rotor resistance matrix $\boldsymbol{R}_r^k$ exhibits the constant term $\frac{1}{3}\left(R_r^u+R_r^v+R_r^w\right)\boldsymbol{I}_3$ and an oscillating term. Thereby, the rotor resistance matrix $\boldsymbol{R}_r^{dq}$ oscillates with frequency $\frac{\omega_k-\omega_r}{\pi}$, while the elements $R_r^{d\gamma}$, $R_r^{q\gamma}$, $R_r^{\gamma d}$ and $R_r^{\gamma q}$ oscillate with frequency $\frac{\omega_k-\omega_r}{2\pi}$. If the transformation angle ϕ_k is equal to the electrical machine angle ϕ_r, i.e. $\phi_k = \phi_r$, it gives the rotor resistance matrix $\boldsymbol{R}_r^r$ in the rotor-fixed r-reference frame as follows

$$\boldsymbol{R}_r^r = R_r^u\begin{bmatrix} \frac{2}{3} & 0 & \frac{1}{3\kappa_c} \\ 0 & 0 & 0 \\ \frac{2}{3}\kappa_c & 0 & \frac{1}{3} \end{bmatrix} + R_r^v\begin{bmatrix} \frac{1}{6} & -\frac{\sqrt{3}}{6} & -\frac{1}{6\kappa_c} \\ -\frac{\sqrt{3}}{6} & \frac{1}{2} & \frac{\sqrt{3}}{6\kappa_c} \\ -\frac{1}{3}\kappa_c & \frac{\sqrt{3}}{3}\kappa_c & \frac{1}{3} \end{bmatrix} + R_r^w\begin{bmatrix} \frac{1}{6} & \frac{\sqrt{3}}{6} & -\frac{1}{6\kappa_c} \\ \frac{\sqrt{3}}{6} & \frac{1}{2} & -\frac{\sqrt{3}}{6\kappa_c} \\ -\frac{1}{3}\kappa_c & -\frac{\sqrt{3}}{3}\kappa_c & \frac{1}{3} \end{bmatrix}. \tag{B.4}$$

B.2 DFIM inductances in different reference frames

In Sec. 2.2.2, the nonlinear DFIM model is described (i) in the three-phase reference frames abc and uvw, (ii) in the stator-fixed and rotor-fixed reference frames s and r, respectively, and (iii) in the arbitrarily k-reference frame. Based on these descriptions, this section derives relations between

- the stator inductances $\boldsymbol{L}_s^{abc}$, $\boldsymbol{L}_s^s$ and $\boldsymbol{L}_s^k$
- the rotor inductances $\boldsymbol{L}_r^{uvw}$, $\boldsymbol{L}_r^r$ and $\boldsymbol{L}_r^k$
- the coupling inductances $\boldsymbol{L}_{sr}^{abc}$, $\boldsymbol{L}_{sr}^s$, $\boldsymbol{L}_{sr}^k$, $\boldsymbol{L}_{rs}^{uvw}$, $\boldsymbol{L}_{rs}^r$ and $\boldsymbol{L}_{rs}^k$
- the ϕ_m-derivatives $\boldsymbol{\varphi}_{sm}^{abc}$, $\boldsymbol{\varphi}_{sm}^s$ and $\boldsymbol{\varphi}_{sm}^k$ of the stator flux linkages $\boldsymbol{\psi}_s^{abc}$, $\boldsymbol{\psi}_s^s$ and $\boldsymbol{\psi}_s^k$, resp.
- the ϕ_m-derivatives $\boldsymbol{\varphi}_{rm}^{uvw}$, $\boldsymbol{\varphi}_{rm}^r$ and $\boldsymbol{\varphi}_{rm}^k$ of the rotor flux linkages $\boldsymbol{\psi}_r^{uvw}$, $\boldsymbol{\psi}_r^r$ and $\boldsymbol{\psi}_r^k$, resp.
- the ϕ_k-derivatives $\boldsymbol{\varphi}_{sk}^k$ and $\boldsymbol{\varphi}_{rk}^k$ of stator flux linkage $\boldsymbol{\psi}_s^k$ and rotor flux linkage $\boldsymbol{\psi}_r^k$, resp.

B.2.1 Stator side inductances in different reference frames

First, the stator side is investigated. Due to (2.11), (2.13) and (2.15), the time derivative of the stator flux $\boldsymbol{\psi}_s^s$ is calculated by

$$
\begin{aligned}
\frac{\mathrm{d}}{\mathrm{d}t}\boldsymbol{\psi}_s^s(\boldsymbol{i}_s^s,\boldsymbol{i}_r^r,\phi_m) &\overset{(2.13)}{=} \frac{\mathrm{d}}{\mathrm{d}t}\Big(\boldsymbol{T}_C\boldsymbol{\psi}_s^{abc}(\boldsymbol{T}_C^{-1}\boldsymbol{i}_s^s,\boldsymbol{T}_C^{-1}\boldsymbol{i}_r^r,\phi_m)\Big) = \boldsymbol{T}_C\frac{\mathrm{d}}{\mathrm{d}t}\boldsymbol{\psi}_s^{abc}(\boldsymbol{T}_C^{-1}\boldsymbol{i}_s^s,\boldsymbol{T}_C^{-1}\boldsymbol{i}_r^r,\phi_m)\\
&\overset{(2.11)}{=} -\boldsymbol{T}_C\boldsymbol{L}_s^{abc}(\boldsymbol{T}_C^{-1}\boldsymbol{i}_s^s,\boldsymbol{T}_C^{-1}\boldsymbol{i}_r^r,\phi_m)\frac{\mathrm{d}}{\mathrm{d}t}\Big(\boldsymbol{T}_C^{-1}\boldsymbol{i}_s^s(t)\Big) + \underbrace{\boldsymbol{T}_C\boldsymbol{\varphi}_{sm}^{abc}(\boldsymbol{T}_C^{-1}\boldsymbol{i}_s^s,\boldsymbol{T}_C^{-1}\boldsymbol{i}_r^r,\phi_m)}_{\overset{(2.15)}{=}\boldsymbol{\varphi}_{sm}^s(\boldsymbol{i}_s^s,\boldsymbol{i}_r^r,\phi_m)}\omega_m(t)\\
&\quad - \boldsymbol{T}_C\boldsymbol{L}_{sr}^{abc}(\boldsymbol{T}_C^{-1}\boldsymbol{i}_s^s,\boldsymbol{T}_C^{-1}\boldsymbol{i}_r^r,\phi_m)\frac{\mathrm{d}}{\mathrm{d}t}\Big(\boldsymbol{T}_C^{-1}\boldsymbol{i}_r^r(t)\Big)\\
&= -\overbrace{\boldsymbol{T}_C\boldsymbol{L}_s^{abc}(\boldsymbol{T}_C^{-1}\boldsymbol{i}_s^s,\boldsymbol{T}_C^{-1}\boldsymbol{i}_r^r,\phi_m)\boldsymbol{T}_C^{-1}}^{\overset{(2.15)}{=}\boldsymbol{L}_s^s(\boldsymbol{i}_s^s,\boldsymbol{i}_r^r,\phi_m)}\frac{\mathrm{d}}{\mathrm{d}t}\boldsymbol{i}_s^s(t) - \overbrace{\boldsymbol{T}_C\boldsymbol{L}_{sr}^{abc}(\boldsymbol{T}_C^{-1}\boldsymbol{i}_s^s,\boldsymbol{T}_C^{-1}\boldsymbol{i}_r^r,\phi_m)\boldsymbol{T}_C^{-1}}^{\overset{(2.15)}{=}\boldsymbol{L}_{sr}^s(\boldsymbol{i}_s^s,\boldsymbol{i}_r^r,\phi_m)}\frac{\mathrm{d}}{\mathrm{d}t}\boldsymbol{i}_r^r(t)\\
&\quad + \boldsymbol{\varphi}_{sm}^s(\boldsymbol{i}_s^s,\boldsymbol{i}_r^r,\phi_m)\omega_m(t)\,. \qquad \text{(B.5)}
\end{aligned}
$$

Accordingly, by considering (2.15), (2.17) and (B.5), the time derivative of the stator flux $\boldsymbol{\psi}_s^k$ is given by

$$
\begin{aligned}
\frac{\mathrm{d}}{\mathrm{d}t}\boldsymbol{\psi}_s^k(\boldsymbol{i}_s^k,\boldsymbol{i}_r^k,\phi_m,\phi_k) &\overset{(2.17)}{=} \frac{\mathrm{d}}{\mathrm{d}t}\Big(\boldsymbol{T}_P^{-1}(\phi_k)\boldsymbol{\psi}_s^s(\boldsymbol{T}_P(\phi_k)\boldsymbol{i}_s^k,\boldsymbol{T}_P(\phi_k{-}n_m\phi_m)\boldsymbol{i}_r^k,\phi_m)\Big)\\
&= \boldsymbol{T}_P^{-1}(\phi_k)\frac{\mathrm{d}}{\mathrm{d}t}\boldsymbol{\psi}_s^s(\boldsymbol{T}_P(\phi_k)\boldsymbol{i}_s^k,\boldsymbol{T}_P(\phi_k{-}n_m\phi_m)\boldsymbol{i}_r^k,\phi_m)\\
&\quad - \boldsymbol{T}_P^{-1}(\phi_k)\boldsymbol{J}'\boldsymbol{\psi}_s^s(\boldsymbol{T}_P(\phi_k)\boldsymbol{i}_s^k,\boldsymbol{T}_P(\phi_k{-}n_m\phi_m)\boldsymbol{i}_r^k,\phi_m)\omega_k(t)\\
&\overset{(2.15)}{=} -\boldsymbol{T}_P^{-1}(\phi_k)\boldsymbol{L}_s^s(\boldsymbol{T}_P(\phi_k)\boldsymbol{i}_s^k,\boldsymbol{T}_P(\phi_k{-}n_m\phi_m)\boldsymbol{i}_r^k,\phi_m)\frac{\mathrm{d}}{\mathrm{d}t}\Big(\boldsymbol{T}_P(\phi_k)\boldsymbol{i}_s^k(t)\Big)\\
&\quad - \boldsymbol{T}_P^{-1}(\phi_k)\boldsymbol{L}_{sr}^s(\boldsymbol{T}_P(\phi_k)\boldsymbol{i}_s^k,\boldsymbol{T}_P(\phi_k{-}n_m\phi_m)\boldsymbol{i}_r^k,\phi_m)\frac{\mathrm{d}}{\mathrm{d}t}\Big(\boldsymbol{T}_P(\phi_k{-}n_m\phi_m)\boldsymbol{i}_r^k(t)\Big)\\
&\quad + \boldsymbol{T}_P^{-1}(\phi_k)\boldsymbol{\varphi}_{sm}^s(\boldsymbol{T}_P(\phi_k)\boldsymbol{i}_s^k,\boldsymbol{T}_P(\phi_k{-}n_m\phi_m)\boldsymbol{i}_r^k,\phi_m)\omega_m(t)\\
&\quad - \boldsymbol{T}_P^{-1}(\phi_k)\boldsymbol{J}'\boldsymbol{\psi}_s^s(\boldsymbol{T}_P(\phi_k)\boldsymbol{i}_s^k,\boldsymbol{T}_P(\phi_k{-}n_m\phi_m)\boldsymbol{i}_r^k,\phi_m)\omega_k(t)\\
&= -\boldsymbol{T}_P^{-1}(\phi_k)\boldsymbol{L}_s^s(\boldsymbol{T}_P(\phi_k)\boldsymbol{i}_s^k,\boldsymbol{T}_P(\phi_k{-}n_m\phi_m)\boldsymbol{i}_r^k,\phi_m)\boldsymbol{T}_P(\phi_k)\frac{\mathrm{d}}{\mathrm{d}t}\boldsymbol{i}_s^k(t)\\
&\quad - \boldsymbol{T}_P^{-1}(\phi_k)\boldsymbol{L}_{sr}^s(\boldsymbol{T}_P(\phi_k)\boldsymbol{i}_s^k,\boldsymbol{T}_P(\phi_k{-}n_m\phi_m)\boldsymbol{i}_r^k,\phi_m)\boldsymbol{T}_P(\phi_k{-}n_m\phi_m)\frac{\mathrm{d}}{\mathrm{d}t}\boldsymbol{i}_r^k(t)\\
&\quad + n_m\boldsymbol{T}_P^{-1}(\phi_k)\boldsymbol{L}_{sr}^s(\boldsymbol{T}_P(\phi_k)\boldsymbol{i}_s^k,\boldsymbol{T}_P(\phi_k{-}n_m\phi_m)\boldsymbol{i}_r^k,\phi_m)\boldsymbol{T}_P(\phi_k{-}n_m\phi_m)\boldsymbol{J}'\boldsymbol{i}_r^k(t)\omega_m(t)\\
&\quad + \boldsymbol{T}_P^{-1}(\phi_k)\boldsymbol{\varphi}_{sm}^s(\boldsymbol{T}_P(\phi_k)\boldsymbol{i}_s^k,\boldsymbol{T}_P(\phi_k{-}n_m\phi_m)\boldsymbol{i}_r^k,\phi_m)\omega_m(t)\\
&\quad - \boldsymbol{T}_P^{-1}(\phi_k)\boldsymbol{L}_s^s(\boldsymbol{T}_P(\phi_k)\boldsymbol{i}_s^k,\boldsymbol{T}_P(\phi_k{-}n_m\phi_m)\boldsymbol{i}_r^k,\phi_m)\boldsymbol{T}_P(\phi_k)\boldsymbol{J}'\boldsymbol{i}_s^k(t)\omega_k(t)\\
&\quad - \boldsymbol{T}_P^{-1}(\phi_k)\boldsymbol{L}_{sr}^s(\boldsymbol{T}_P(\phi_k)\boldsymbol{i}_s^k,\boldsymbol{T}_P(\phi_k{-}n_m\phi_m)\boldsymbol{i}_r^k,\phi_m)\boldsymbol{T}_P(\phi_k{-}n_m\phi_m)\boldsymbol{J}'\boldsymbol{i}_r^k(t)\omega_k(t)\\
&\quad - \boldsymbol{T}_P^{-1}(\phi_k)\boldsymbol{J}'\boldsymbol{\psi}_s^s(\boldsymbol{T}_P(\phi_k)\boldsymbol{i}_s^k,\boldsymbol{T}_P(\phi_k{-}n_m\phi_m)\boldsymbol{i}_r^k,\phi_m)\omega_k(t)\\
&\overset{(B.5)}{=} -\boldsymbol{T}_P^{-1}(\phi_k)\boldsymbol{T}_C\boldsymbol{L}_s^{abc}(\boldsymbol{T}_C^{-1}\boldsymbol{T}_P(\phi_k)\boldsymbol{i}_s^k,\boldsymbol{T}_C^{-1}\boldsymbol{T}_P(\phi_k{-}n_m\phi_m)\boldsymbol{i}_r^k,\phi_m)\boldsymbol{T}_C^{-1}\boldsymbol{T}_P(\phi_k)\frac{\mathrm{d}}{\mathrm{d}t}\boldsymbol{i}_s^k(t)\\
&\quad - \boldsymbol{T}_P^{-1}(\phi_k)\boldsymbol{T}_C\boldsymbol{L}_{sr}^{abc}(\boldsymbol{T}_C^{-1}\boldsymbol{T}_P(\phi_k)\boldsymbol{i}_s^k,\boldsymbol{T}_C^{-1}\boldsymbol{T}_P(\phi_k{-}n_m\phi_m)\boldsymbol{i}_r^k,\phi_m)\boldsymbol{T}_C^{-1}\boldsymbol{T}_P(\phi_k{-}n_m\phi_m)\frac{\mathrm{d}}{\mathrm{d}t}\boldsymbol{i}_r^k(t)\\
&\quad + n_m\boldsymbol{T}_P^{-1}(\phi_k)\boldsymbol{T}_C\boldsymbol{L}_{sr}^{abc}(\boldsymbol{T}_C^{-1}\boldsymbol{T}_P(\phi_k)\boldsymbol{i}_s^k,\boldsymbol{T}_C^{-1}\boldsymbol{T}_P(\phi_k{-}n_m\phi_m)\boldsymbol{i}_r^k,\phi_m)\boldsymbol{T}_C^{-1}\boldsymbol{T}_P(\phi_k{-}n_m\phi_m)\boldsymbol{J}'\boldsymbol{i}_r^k(t)\omega_m(t)\\
&\quad + \boldsymbol{T}_P^{-1}(\phi_k)\boldsymbol{T}_C\boldsymbol{\varphi}_{sm}^{abc}(\boldsymbol{T}_C^{-1}\boldsymbol{T}_P(\phi_k)\boldsymbol{i}_s^k,\boldsymbol{T}_C^{-1}\boldsymbol{T}_P(\phi_k{-}n_m\phi_m)\boldsymbol{i}_r^k,\phi_m)\omega_m(t)\\
&\quad - \boldsymbol{T}_P^{-1}(\phi_k)\boldsymbol{T}_C\boldsymbol{L}_s^{abc}(\boldsymbol{T}_C^{-1}\boldsymbol{T}_P(\phi_k)\boldsymbol{i}_s^k,\boldsymbol{T}_C^{-1}\boldsymbol{T}_P(\phi_k{-}n_m\phi_m)\boldsymbol{i}_r^k,\phi_m)\boldsymbol{T}_C^{-1}\boldsymbol{T}_P(\phi_k)\boldsymbol{J}'\boldsymbol{i}_s^k(t)\omega_k(t)\\
&\quad - \boldsymbol{T}_P^{-1}(\phi_k)\boldsymbol{T}_C\boldsymbol{L}_{sr}^{abc}(\boldsymbol{T}_C^{-1}\boldsymbol{T}_P(\phi_k)\boldsymbol{i}_s^k,\boldsymbol{T}_C^{-1}\boldsymbol{T}_P(\phi_k{-}n_m\phi_m)\boldsymbol{i}_r^k,\phi_m)\boldsymbol{T}_C^{-1}\boldsymbol{T}_P(\phi_k{-}n_m\phi_m)\boldsymbol{J}'\boldsymbol{i}_r^k(t)\omega_k(t)\\
&\quad - \boldsymbol{T}_P^{-1}(\phi_k)\boldsymbol{J}'\boldsymbol{T}_C\boldsymbol{\psi}_s^{abc}(\boldsymbol{T}_C^{-1}\boldsymbol{T}_P(\phi_k)\boldsymbol{i}_s^k,\boldsymbol{T}_C^{-1}\boldsymbol{T}_P(\phi_k{-}n_m\phi_m)\boldsymbol{i}_r^k,\phi_m)\omega_k(t)\,. \qquad \text{(B.6)}
\end{aligned}
$$

Summarizing (B.5) yields the stator inductance $\boldsymbol{L}_s^s$, the coupling inductance $\boldsymbol{L}_{sr}^s$ and the ϕ_m-derivative $\boldsymbol{\varphi}_{sm}^s$ of the stator flux linkage $\boldsymbol{\psi}_s^s$ as follows

$$\left.\begin{aligned}
\boldsymbol{L}_s^s(\boldsymbol{i}_s^s,\boldsymbol{i}_r^r,\phi_m) &:= -\tfrac{\partial\boldsymbol{\psi}_s^s(\boldsymbol{i}_s^s,\boldsymbol{i}_r^r,\phi_m)}{\partial\boldsymbol{i}_s^s} &&= \boldsymbol{T}_C\boldsymbol{L}_s^{abc}(\boldsymbol{T}_C^{-1}\boldsymbol{i}_s^s,\boldsymbol{T}_C^{-1}\boldsymbol{i}_r^r,\phi_m)\boldsymbol{T}_C^{-1}\\
\boldsymbol{L}_{sr}^s(\boldsymbol{i}_s^s,\boldsymbol{i}_r^r,\phi_m) &:= -\tfrac{\partial\boldsymbol{\psi}_s^s(\boldsymbol{i}_s^s,\boldsymbol{i}_r^r,\phi_m)}{\partial\boldsymbol{i}_r^r} &&= \boldsymbol{T}_C\boldsymbol{L}_{sr}^{abc}(\boldsymbol{T}_C^{-1}\boldsymbol{i}_s^s,\boldsymbol{T}_C^{-1}\boldsymbol{i}_r^r,\phi_m)\boldsymbol{T}_C^{-1}\\
\boldsymbol{\varphi}_{sm}^s(\boldsymbol{i}_s^s,\boldsymbol{i}_r^r,\phi_m) &:= \tfrac{\partial\boldsymbol{\psi}_s^s(\boldsymbol{i}_s^s,\boldsymbol{i}_r^r,\phi_m)}{\partial\phi_m} &&= \boldsymbol{T}_C\boldsymbol{\varphi}_{sm}^{abc}(\boldsymbol{T}_C^{-1}\boldsymbol{i}_s^s,\boldsymbol{T}_C^{-1}\boldsymbol{i}_r^r,\phi_m)
\end{aligned}\right\}. \tag{B.7}$$

Because of (B.6), the stator inductance $\boldsymbol{L}_s^k$, the coupling inductance $\boldsymbol{L}_{sr}^k$, the ϕ_m-derivative $\boldsymbol{\varphi}_{sm}^k$ and the ϕ_k-derivative $\boldsymbol{\varphi}_{sk}^k$ of the stator flux linkage $\boldsymbol{\psi}_s^s$ result in

$$\left.\begin{aligned}
&\boldsymbol{L}_s^k(\boldsymbol{i}_s^k,\boldsymbol{i}_r^k,\phi_m,\phi_k) := -\tfrac{\partial\boldsymbol{\psi}_s^k(\boldsymbol{i}_s^k,\boldsymbol{i}_r^k,\phi_m,\phi_k)}{\partial\boldsymbol{i}_s^k}\\
&= \boldsymbol{T}_P^{-1}(\phi_k)\boldsymbol{T}_C\boldsymbol{L}_s^{abc}(\boldsymbol{T}_C^{-1}\boldsymbol{T}_P(\phi_k)\boldsymbol{i}_s^k,\boldsymbol{T}_C^{-1}\boldsymbol{T}_P(\phi_k{-}n_m\phi_m)\boldsymbol{i}_r^k,\phi_m)\boldsymbol{T}_C^{-1}\boldsymbol{T}_P(\phi_k)\\
&= \boldsymbol{T}_P^{-1}(\phi_k)\boldsymbol{L}_s^s(\boldsymbol{T}_P(\phi_k)\boldsymbol{i}_s^k,\boldsymbol{T}_P(\phi_k{-}n_m\phi_m)\boldsymbol{i}_r^k,\phi_m)\boldsymbol{T}_P(\phi_k)\\
&\\
&\boldsymbol{L}_{sr}^k(\boldsymbol{i}_s^k,\boldsymbol{i}_r^k,\phi_m,\phi_k) := -\tfrac{\partial\boldsymbol{\psi}_s^k(\boldsymbol{i}_s^k,\boldsymbol{i}_r^k,\phi_m,\phi_k)}{\partial\boldsymbol{i}_r^k}\\
&= \boldsymbol{T}_P^{-1}(\phi_k)\boldsymbol{T}_C\boldsymbol{L}_{sr}^{abc}(\boldsymbol{T}_C^{-1}\boldsymbol{T}_P(\phi_k)\boldsymbol{i}_s^k,\boldsymbol{T}_C^{-1}\boldsymbol{T}_P(\phi_k{-}n_m\phi_m)\boldsymbol{i}_r^k,\phi_m)\boldsymbol{T}_C^{-1}\boldsymbol{T}_P(\phi_k{-}n_m\phi_m)\\
&= \boldsymbol{T}_P^{-1}(\phi_k)\boldsymbol{L}_{sr}^s(\boldsymbol{T}_P(\phi_k)\boldsymbol{i}_s^k,\boldsymbol{T}_P(\phi_k{-}n_m\phi_m)\boldsymbol{i}_r^k,\phi_m)\boldsymbol{T}_P(\phi_k{-}n_m\phi_m)\\
&\\
&\boldsymbol{\varphi}_{sm}^k(\boldsymbol{i}_s^k,\boldsymbol{i}_r^k,\phi_m,\phi_k) := \tfrac{\partial\boldsymbol{\psi}_s^k(\boldsymbol{i}_s^k,\boldsymbol{i}_r^k,\phi_m,\phi_k)}{\partial\phi_m}\\
&= n_m\boldsymbol{T}_P^{-1}(\phi_k)\boldsymbol{T}_C\boldsymbol{L}_{sr}^{abc}(\boldsymbol{T}_C^{-1}\boldsymbol{T}_P(\phi_k)\boldsymbol{i}_s^k,\boldsymbol{T}_C^{-1}\boldsymbol{T}_P(\phi_k{-}n_m\phi_m)\boldsymbol{i}_r^k,\phi_m)\boldsymbol{T}_C^{-1}\boldsymbol{T}_P(\phi_k{-}n_m\phi_m)\boldsymbol{J}'\boldsymbol{i}_r^k(t)\\
&\quad+\boldsymbol{T}_P^{-1}(\phi_k)\boldsymbol{T}_C\boldsymbol{\varphi}_{sm}^{abc}(\boldsymbol{T}_C^{-1}\boldsymbol{T}_P(\phi_k)\boldsymbol{i}_s^k,\boldsymbol{T}_C^{-1}\boldsymbol{T}_P(\phi_k{-}n_m\phi_m)\boldsymbol{i}_r^k,\phi_m)\\
&= n_m\boldsymbol{T}_P^{-1}(\phi_k)\boldsymbol{L}_{sr}^s(\boldsymbol{T}_P(\phi_k)\boldsymbol{i}_s^k,\boldsymbol{T}_P(\phi_k{-}n_m\phi_m)\boldsymbol{i}_r^k,\phi_m)\boldsymbol{T}_P(\phi_k{-}n_m\phi_m)\boldsymbol{J}'\boldsymbol{i}_r^k(t)\\
&\quad+\boldsymbol{T}_P^{-1}(\phi_k)\boldsymbol{\varphi}_{sm}^s(\boldsymbol{T}_P(\phi_k)\boldsymbol{i}_s^k,\boldsymbol{T}_P(\phi_k{-}n_m\phi_m)\boldsymbol{i}_r^k,\phi_m)\\
&= n_m\boldsymbol{L}_{sr}^k(\boldsymbol{i}_s^k,\boldsymbol{i}_r^k,\phi_m,\phi_k)\boldsymbol{J}'\boldsymbol{i}_r^k(t)+\boldsymbol{T}_P^{-1}(\phi_k)\boldsymbol{\varphi}_{sm}^s(\boldsymbol{T}_P(\phi_k)\boldsymbol{i}_s^k,\boldsymbol{T}_P(\phi_k{-}n_m\phi_m)\boldsymbol{i}_r^k,\phi_m)\\
&\\
&\boldsymbol{\varphi}_{sk}^k(\boldsymbol{i}_s^k,\boldsymbol{i}_r^k,\phi_m,\phi_k) := \tfrac{\partial\boldsymbol{\psi}_s^k(\boldsymbol{i}_s^k,\boldsymbol{i}_r^k,\phi_m,\phi_k)}{\partial\phi_k}\\
&= -\boldsymbol{T}_P^{-1}(\phi_k)\boldsymbol{T}_C\boldsymbol{L}_s^{abc}(\boldsymbol{T}_C^{-1}\boldsymbol{T}_P(\phi_k)\boldsymbol{i}_s^k,\boldsymbol{T}_C^{-1}\boldsymbol{T}_P(\phi_k{-}n_m\phi_m)\boldsymbol{i}_r^k,\phi_m)\boldsymbol{T}_C^{-1}\boldsymbol{T}_P(\phi_k)\boldsymbol{J}'\boldsymbol{i}_s^k(t)\\
&\quad-\boldsymbol{T}_P^{-1}(\phi_k)\boldsymbol{T}_C\boldsymbol{L}_{sr}^{abc}(\boldsymbol{T}_C^{-1}\boldsymbol{T}_P(\phi_k)\boldsymbol{i}_s^k,\boldsymbol{T}_C^{-1}\boldsymbol{T}_P(\phi_k{-}n_m\phi_m)\boldsymbol{i}_r^k,\phi_m)\boldsymbol{T}_C^{-1}\boldsymbol{T}_P(\phi_k{-}n_m\phi_m)\boldsymbol{J}'\boldsymbol{i}_r^k(t)\\
&\quad-\boldsymbol{T}_P^{-1}(\phi_k)\boldsymbol{J}'\boldsymbol{T}_C\boldsymbol{\psi}_s^{abc}(\boldsymbol{T}_C^{-1}\boldsymbol{T}_P(\phi_k)\boldsymbol{i}_s^k,\boldsymbol{T}_C^{-1}\boldsymbol{T}_P(\phi_k{-}n_m\phi_m)\boldsymbol{i}_r^k,\phi_m)\\
&= -\boldsymbol{T}_P^{-1}(\phi_k)\boldsymbol{L}_s^s(\boldsymbol{T}_P(\phi_k)\boldsymbol{i}_s^k,\boldsymbol{T}_P(\phi_k{-}n_m\phi_m)\boldsymbol{i}_r^k,\phi_m)\boldsymbol{T}_P(\phi_k)\boldsymbol{J}'\boldsymbol{i}_s^k(t)\\
&\quad-\boldsymbol{T}_P^{-1}(\phi_k)\boldsymbol{L}_{sr}^s(\boldsymbol{T}_P(\phi_k)\boldsymbol{i}_s^k,\boldsymbol{T}_P(\phi_k{-}n_m\phi_m)\boldsymbol{i}_r^k,\phi_m)\boldsymbol{T}_P(\phi_k{-}n_m\phi_m)\boldsymbol{J}'\boldsymbol{i}_r^k(t)\\
&\quad-\boldsymbol{T}_P^{-1}(\phi_k)\boldsymbol{J}'\boldsymbol{\psi}_s^s(\boldsymbol{T}_P(\phi_k)\boldsymbol{i}_s^k,\boldsymbol{T}_P(\phi_k{-}n_m\phi_m)\boldsymbol{i}_r^k,\phi_m)\\
&= -\boldsymbol{L}_s^k(\boldsymbol{i}_s^k,\boldsymbol{i}_r^k,\phi_m,\phi_k)\boldsymbol{J}'\boldsymbol{i}_s^k(t)-\boldsymbol{L}_{sr}^k(\boldsymbol{i}_s^k,\boldsymbol{i}_r^k,\phi_m,\phi_k)\boldsymbol{J}'\boldsymbol{i}_r^k(t)-\boldsymbol{J}'\boldsymbol{\psi}_s^k(\boldsymbol{i}_s^k,\boldsymbol{i}_r^k,\phi_m,\phi_k)\ .
\end{aligned}\right\} \tag{B.8}$$

B.2.2 Rotor side inductances in different reference frames

Now, the procedure of Sec. B.2.1 is employed on the rotor side. Recalling (2.12), (2.14) and (2.16), leads to the time derivative of the rotor flux $\boldsymbol{\psi}_r^r$ as follows

$$\frac{\mathrm{d}}{\mathrm{d}t}\boldsymbol{\psi}_r^r(\boldsymbol{i}_s^s,\boldsymbol{i}_r^r,\phi_m)\overset{(2.14)}{=}\frac{\mathrm{d}}{\mathrm{d}t}\Big(\boldsymbol{T}_C\boldsymbol{\psi}_r^{uvw}(\boldsymbol{T}_C^{-1}\boldsymbol{i}_s^s,\boldsymbol{T}_C^{-1}\boldsymbol{i}_r^r,\phi_m)\Big)=\boldsymbol{T}_C\frac{\mathrm{d}}{\mathrm{d}t}\boldsymbol{\psi}_r^{uvw}(\boldsymbol{T}_C^{-1}\boldsymbol{i}_s^s,\boldsymbol{T}_C^{-1}\boldsymbol{i}_r^r,\phi_m)$$

$$
\begin{aligned}
&\overset{(2.12)}{=} -\boldsymbol{T}_C\boldsymbol{L}_{rs}^{uvw}(\boldsymbol{T}_C^{-1}\boldsymbol{i}_s^s,\boldsymbol{T}_C^{-1}\boldsymbol{i}_r^r,\phi_m)\frac{\mathrm{d}}{\mathrm{d}t}\Big(\boldsymbol{T}_C^{-1}\boldsymbol{i}_s^s(t)\Big) + \underbrace{\boldsymbol{T}_C\boldsymbol{\varphi}_{rm}^{uvw}(\boldsymbol{T}_C^{-1}\boldsymbol{i}_s^s,\boldsymbol{T}_C^{-1}\boldsymbol{i}_r^r,\phi_m)}_{\overset{(2.16)}{=}\boldsymbol{\varphi}_{rm}^r(\boldsymbol{i}_s^s,\boldsymbol{i}_r^r,\phi_m)}\omega_m(t)\\
&\quad -\boldsymbol{T}_C\boldsymbol{L}_r^{uvw}(\boldsymbol{T}_C^{-1}\boldsymbol{i}_s^s,\boldsymbol{T}_C^{-1}\boldsymbol{i}_r^r,\phi_m)\frac{\mathrm{d}}{\mathrm{d}t}\Big(\boldsymbol{T}_C^{-1}\boldsymbol{i}_r^r(t)\Big)\\
&= -\overbrace{\boldsymbol{T}_C\boldsymbol{L}_{rs}^{uvw}(\boldsymbol{T}_C^{-1}\boldsymbol{i}_s^s,\boldsymbol{T}_C^{-1}\boldsymbol{i}_r^r,\phi_m)\boldsymbol{T}_C^{-1}}^{\overset{(2.16)}{=}\boldsymbol{L}_{rs}^r(\boldsymbol{i}_s^s,\boldsymbol{i}_r^r,\phi_m)}\frac{\mathrm{d}}{\mathrm{d}t}\boldsymbol{i}_s^s(t) - \overbrace{\boldsymbol{T}_C\boldsymbol{L}_r^{uvw}(\boldsymbol{T}_C^{-1}\boldsymbol{i}_s^s,\boldsymbol{T}_C^{-1}\boldsymbol{i}_r^r,\phi_m)\boldsymbol{T}_C^{-1}}^{\overset{(2.16)}{=}\boldsymbol{L}_r^r(\boldsymbol{i}_s^s,\boldsymbol{i}_r^r,\phi_m)}\frac{\mathrm{d}}{\mathrm{d}t}\boldsymbol{i}_r^r(t)\\
&\quad +\boldsymbol{\varphi}_{rm}^r(\boldsymbol{i}_s^s,\boldsymbol{i}_r^r,\phi_m)\omega_m(t)\,. \qquad\qquad (\mathrm{B.9})
\end{aligned}
$$

Taking (2.15), (2.17) and (B.5) into account, accordingly, the time derivative of the rotor flux $\boldsymbol{\psi}_r^k$ is given by

$$
\begin{aligned}
&\frac{\mathrm{d}}{\mathrm{d}t}\boldsymbol{\psi}_r^k(\boldsymbol{i}_s^k,\boldsymbol{i}_r^k,\phi_m,\phi_k) \overset{(2.18)}{=} \frac{\mathrm{d}}{\mathrm{d}t}\Big(\boldsymbol{T}_P^{-1}(\phi_k{-}n_m\phi_m)\boldsymbol{\psi}_r^r(\boldsymbol{T}_P(\phi_k)\boldsymbol{i}_s^k,\boldsymbol{T}_P(\phi_k{-}n_m\phi_m)\boldsymbol{i}_r^k,\phi_m)\Big)\\
&= \boldsymbol{T}_P^{-1}(\phi_k{-}n_m\phi_m)\frac{\mathrm{d}}{\mathrm{d}t}\boldsymbol{\psi}_r^r(\boldsymbol{T}_P(\phi_k)\boldsymbol{i}_s^k,\boldsymbol{T}_P(\phi_k{-}n_m\phi_m)\boldsymbol{i}_r^k,\phi_m)\\
&\quad -\boldsymbol{T}_P^{-1}(\phi_k{-}n_m\phi_m)\boldsymbol{J}'\boldsymbol{\psi}_r^r(\boldsymbol{T}_P(\phi_k)\boldsymbol{i}_s^k,\boldsymbol{T}_P(\phi_k{-}n_m\phi_m)\boldsymbol{i}_r^k,\phi_m)\,(\omega_k(t)-n_m\omega_m(t))\\
&\overset{(2.16)}{=} -\boldsymbol{T}_P^{-1}(\phi_k{-}n_m\phi_m)\boldsymbol{L}_{rs}^r(\boldsymbol{T}_P(\phi_k)\boldsymbol{i}_s^k,\boldsymbol{T}_P(\phi_k{-}n_m\phi_m)\boldsymbol{i}_r^k,\phi_m)\frac{\mathrm{d}}{\mathrm{d}t}\Big(\boldsymbol{T}_P(\phi_k)\boldsymbol{i}_s^k(t)\Big)\\
&\quad -\boldsymbol{T}_P^{-1}(\phi_k{-}n_m\phi_m)\boldsymbol{L}_r^r(\boldsymbol{T}_P(\phi_k)\boldsymbol{i}_s^k,\boldsymbol{T}_P(\phi_k{-}n_m\phi_m)\boldsymbol{i}_r^k,\phi_m)\frac{\mathrm{d}}{\mathrm{d}t}\Big(\boldsymbol{T}_P(\phi_k{-}n_m\phi_m)\boldsymbol{i}_r^k(t)\Big)\\
&\quad +\boldsymbol{T}_P^{-1}(\phi_k{-}n_m\phi_m)\boldsymbol{\varphi}_{rm}^r(\boldsymbol{T}_P(\phi_k)\boldsymbol{i}_s^k,\boldsymbol{T}_P(\phi_k{-}n_m\phi_m)\boldsymbol{i}_r^k,\phi_m)\omega_m(t)\\
&\quad +n_m\boldsymbol{T}_P^{-1}(\phi_k{-}n_m\phi_m)\boldsymbol{J}'\boldsymbol{\psi}_r^r(\boldsymbol{T}_P(\phi_k)\boldsymbol{i}_s^k,\boldsymbol{T}_P(\phi_k{-}n_m\phi_m)\boldsymbol{i}_r^k,\phi_m)\omega_m(t)\\
&\quad -\boldsymbol{T}_P^{-1}(\phi_k{-}n_m\phi_m)\boldsymbol{J}'\boldsymbol{\psi}_r^r(\boldsymbol{T}_P(\phi_k)\boldsymbol{i}_s^k,\boldsymbol{T}_P(\phi_k{-}n_m\phi_m)\boldsymbol{i}_r^k,\phi_m)\omega_k(t)\\
&= -\boldsymbol{T}_P^{-1}(\phi_k{-}n_m\phi_m)\boldsymbol{L}_{rs}^r(\boldsymbol{T}_P(\phi_k)\boldsymbol{i}_s^k,\boldsymbol{T}_P(\phi_k{-}n_m\phi_m)\boldsymbol{i}_r^k,\phi_m)\boldsymbol{T}_P(\phi_k)\frac{\mathrm{d}}{\mathrm{d}t}\boldsymbol{i}_s^k(t)\\
&\quad -\boldsymbol{T}_P^{-1}(\phi_k{-}n_m\phi_m)\boldsymbol{L}_r^r(\boldsymbol{T}_P(\phi_k)\boldsymbol{i}_s^k,\boldsymbol{T}_P(\phi_k{-}n_m\phi_m)\boldsymbol{i}_r^k,\phi_m)\boldsymbol{T}_P(\phi_k{-}n_m\phi_m)\frac{\mathrm{d}}{\mathrm{d}t}\boldsymbol{i}_r^k(t)\\
&\quad +n_m\boldsymbol{T}_P^{-1}(\phi_k{-}n_m\phi_m)\boldsymbol{L}_r^r(\boldsymbol{T}_P(\phi_k)\boldsymbol{i}_s^k,\boldsymbol{T}_P(\phi_k{-}n_m\phi_m)\boldsymbol{i}_r^k,\phi_m)\boldsymbol{T}_P(\phi_k{-}n_m\phi_m)\boldsymbol{J}'\boldsymbol{i}_r^k(t)\omega_m(t)\\
&\quad +\boldsymbol{T}_P^{-1}(\phi_k{-}n_m\phi_m)\boldsymbol{\varphi}_{rm}^r(\boldsymbol{T}_P(\phi_k)\boldsymbol{i}_s^k,\boldsymbol{T}_P(\phi_k{-}n_m\phi_m)\boldsymbol{i}_r^k,\phi_m)\omega_m(t)\\
&\quad +n_m\boldsymbol{T}_P^{-1}(\phi_k{-}n_m\phi_m)\boldsymbol{J}'\boldsymbol{\psi}_r^r(\boldsymbol{T}_P(\phi_k)\boldsymbol{i}_s^k,\boldsymbol{T}_P(\phi_k{-}n_m\phi_m)\boldsymbol{i}_r^k,\phi_m)\omega_m(t)\\
&\quad -\boldsymbol{T}_P^{-1}(\phi_k{-}n_m\phi_m)\boldsymbol{L}_{rs}^r(\boldsymbol{T}_P(\phi_k)\boldsymbol{i}_s^k,\boldsymbol{T}_P(\phi_k{-}n_m\phi_m)\boldsymbol{i}_r^k,\phi_m)\boldsymbol{T}_P(\phi_k)\boldsymbol{J}'\boldsymbol{i}_s^k(t)\omega_k(t)\\
&\quad -\boldsymbol{T}_P^{-1}(\phi_k{-}n_m\phi_m)\boldsymbol{L}_r^r(\boldsymbol{T}_P(\phi_k)\boldsymbol{i}_s^k,\boldsymbol{T}_P(\phi_k{-}n_m\phi_m)\boldsymbol{i}_r^k,\phi_m)\boldsymbol{T}_P(\phi_k{-}n_m\phi_m)\boldsymbol{J}'\boldsymbol{i}_r^k(t)\omega_k(t)\\
&\quad -\boldsymbol{T}_P^{-1}(\phi_k{-}n_m\phi_m)\boldsymbol{J}'\boldsymbol{\psi}_r^r(\boldsymbol{T}_P(\phi_k)\boldsymbol{i}_s^k,\boldsymbol{T}_P(\phi_k{-}n_m\phi_m)\boldsymbol{i}_r^k,\phi_m)\omega_k(t)\\
&\overset{(\mathrm{B.9})}{=} -\boldsymbol{T}_P^{-1}(\phi_k{-}n_m\phi_m)\boldsymbol{T}_C\boldsymbol{L}_{rs}^{uvw}(\boldsymbol{T}_C^{-1}\boldsymbol{T}_P(\phi_k)\boldsymbol{i}_s^k,\boldsymbol{T}_C^{-1}\boldsymbol{T}_P(\phi_k{-}n_m\phi_m)\boldsymbol{i}_r^k,\phi_m)\boldsymbol{T}_C^{-1}\boldsymbol{T}_P(\phi_k)\frac{\mathrm{d}}{\mathrm{d}t}\boldsymbol{i}_s^k(t)\\
&\quad -\boldsymbol{T}_P^{-1}(\phi_k{-}n_m\phi_m)\boldsymbol{T}_C\boldsymbol{L}_r^{uvw}(\boldsymbol{T}_C^{-1}\boldsymbol{T}_P(\phi_k)\boldsymbol{i}_s^k,\boldsymbol{T}_C^{-1}\boldsymbol{T}_P(\phi_k{-}n_m\phi_m)\boldsymbol{i}_r^k,\phi_m)\boldsymbol{T}_C^{-1}\boldsymbol{T}_P(\phi_k{-}n_m\phi_m)\frac{\mathrm{d}}{\mathrm{d}t}\boldsymbol{i}_r^k(t)\\
&+n_m\boldsymbol{T}_P^{-1}(\phi_k{-}n_m\phi_m)\boldsymbol{T}_C\boldsymbol{L}_r^{uvw}(\boldsymbol{T}_C^{-1}\boldsymbol{T}_P(\phi_k)\boldsymbol{i}_s^k,\boldsymbol{T}_C^{-1}\boldsymbol{T}_P(\phi_k{-}n_m\phi_m)\boldsymbol{i}_r^k,\phi_m)\boldsymbol{T}_C^{-1}\boldsymbol{T}_P(\phi_k{-}n_m\phi_m)\boldsymbol{J}'\boldsymbol{i}_r^k(t)\omega_m(t)\\
&\quad +\boldsymbol{T}_P^{-1}(\phi_k{-}n_m\phi_m)\boldsymbol{T}_C\boldsymbol{\varphi}_{rm}^{uvw}(\boldsymbol{T}_C^{-1}\boldsymbol{T}_P(\phi_k)\boldsymbol{i}_s^k,\boldsymbol{T}_C^{-1}\boldsymbol{T}_P(\phi_k{-}n_m\phi_m)\boldsymbol{i}_r^k,\phi_m)\omega_m(t)\\
&\quad +n_m\boldsymbol{T}_P^{-1}(\phi_k{-}n_m\phi_m)\boldsymbol{J}'\boldsymbol{T}_C\boldsymbol{\psi}_r^{uvw}(\boldsymbol{T}_C^{-1}\boldsymbol{T}_P(\phi_k)\boldsymbol{i}_s^k,\boldsymbol{T}_C^{-1}\boldsymbol{T}_P(\phi_k{-}n_m\phi_m)\boldsymbol{i}_r^k,\phi_m)\omega_m(t)\\
&\quad -\boldsymbol{T}_P^{-1}(\phi_k{-}n_m\phi_m)\boldsymbol{T}_C\boldsymbol{L}_{rs}^{uvw}(\boldsymbol{T}_C^{-1}\boldsymbol{T}_P(\phi_k)\boldsymbol{i}_s^k,\boldsymbol{T}_C^{-1}\boldsymbol{T}_P(\phi_k{-}n_m\phi_m)\boldsymbol{i}_r^k,\phi_m)\boldsymbol{T}_C^{-1}\boldsymbol{T}_P(\phi_k)\boldsymbol{J}'\boldsymbol{i}_s^k(t)\omega_k(t)\\
&\quad -\boldsymbol{T}_P^{-1}(\phi_k{-}n_m\phi_m)\boldsymbol{T}_C\boldsymbol{L}_r^{uvw}(\boldsymbol{T}_C^{-1}\boldsymbol{T}_P(\phi_k)\boldsymbol{i}_s^k,\boldsymbol{T}_C^{-1}\boldsymbol{T}_P(\phi_k{-}n_m\phi_m)\boldsymbol{i}_r^k,\phi_m)\boldsymbol{T}_C^{-1}\boldsymbol{T}_P(\phi_k{-}n_m\phi_m)\boldsymbol{J}'\boldsymbol{i}_r^k(t)\omega_k(t)\\
&\quad -\boldsymbol{T}_P^{-1}(\phi_k{-}n_m\phi_m)\boldsymbol{J}'\boldsymbol{T}_C\boldsymbol{\psi}_r^{uvw}(\boldsymbol{T}_C^{-1}\boldsymbol{T}_P(\phi_k)\boldsymbol{i}_s^k,\boldsymbol{T}_C^{-1}\boldsymbol{T}_P(\phi_k{-}n_m\phi_m)\boldsymbol{i}_r^k,\phi_m)\omega_k(t)\,. \qquad (\mathrm{B.10})
\end{aligned}
$$

Summarizing (B.9) yields the rotor inductance $\boldsymbol{L}_r^r$, the coupling inductance $\boldsymbol{L}_{rs}^r$ and the ϕ_m-derivative $\boldsymbol{\varphi}_{rm}^r$ of the rotor flux linkage $\boldsymbol{\psi}_r^r$ as follows

$$\left.\begin{aligned}
\boldsymbol{L}_{rs}^r(\boldsymbol{i}_s^s,\boldsymbol{i}_r^r,\phi_m) &:= -\tfrac{\partial\boldsymbol{\psi}_r^r(\boldsymbol{i}_s^s,\boldsymbol{i}_r^r,\phi_m)}{\partial\boldsymbol{i}_s^s} &&= \boldsymbol{T}_C\boldsymbol{L}_{rs}^{uvw}(\boldsymbol{T}_C^{-1}\boldsymbol{i}_s^s,\boldsymbol{T}_C^{-1}\boldsymbol{i}_r^r,\phi_m)\boldsymbol{T}_C^{-1}\\
\boldsymbol{L}_r^r(\boldsymbol{i}_s^s,\boldsymbol{i}_r^r,\phi_m) &:= -\tfrac{\partial\boldsymbol{\psi}_r^r(\boldsymbol{i}_s^s,\boldsymbol{i}_r^r,\phi_m)}{\partial\boldsymbol{i}_r^r} &&= \boldsymbol{T}_C\boldsymbol{L}_r^{uvw}(\boldsymbol{T}_C^{-1}\boldsymbol{i}_s^s,\boldsymbol{T}_C^{-1}\boldsymbol{i}_r^r,\phi_m)\boldsymbol{T}_C^{-1}\\
\boldsymbol{\varphi}_{rm}^r(\boldsymbol{i}_s^s,\boldsymbol{i}_r^r,\phi_m) &:= \tfrac{\partial\boldsymbol{\psi}_r^r(\boldsymbol{i}_s^s,\boldsymbol{i}_r^r,\phi_m)}{\partial\phi_m} &&= \boldsymbol{T}_C\boldsymbol{\varphi}_{rm}^{uvw}(\boldsymbol{T}_C^{-1}\boldsymbol{i}_s^s,\boldsymbol{T}_C^{-1}\boldsymbol{i}_r^r,\phi_m)
\end{aligned}\right\}. \tag{B.11}$$

Due to (B.10), the rotor inductance $\boldsymbol{L}_r^k$, the coupling inductance $\boldsymbol{L}_{rs}^k$, the ϕ_m-derivative $\boldsymbol{\varphi}_{rm}^k$ and ϕ_k-derivative $\boldsymbol{\varphi}_{rk}^k$ of the rotor flux linkage $\boldsymbol{\psi}_r^r$ result in

$$\left.\begin{aligned}
&\boldsymbol{L}_{rs}^k(\boldsymbol{i}_s^k,\boldsymbol{i}_r^k,\phi_m,\phi_k) := -\tfrac{\partial\boldsymbol{\psi}_r^k(\boldsymbol{i}_s^k,\boldsymbol{i}_r^k,\phi_m,\phi_k)}{\partial\boldsymbol{i}_s^k}\\
&= \boldsymbol{T}_P^{-1}(\phi_k{-}n_m\phi_m)\boldsymbol{T}_C\boldsymbol{L}_{rs}^{uvw}(\boldsymbol{T}_C^{-1}\boldsymbol{T}_P(\phi_k)\boldsymbol{i}_s^k,\boldsymbol{T}_C^{-1}\boldsymbol{T}_P(\phi_k{-}n_m\phi_m)\boldsymbol{i}_r^k,\phi_m)\boldsymbol{T}_C^{-1}\boldsymbol{T}_P(\phi_k)\\
&= \boldsymbol{T}_P^{-1}(\phi_k{-}n_m\phi_m)\boldsymbol{L}_{rs}^r(\boldsymbol{T}_P(\phi_k)\boldsymbol{i}_s^k,\boldsymbol{T}_P(\phi_k{-}n_m\phi_m)\boldsymbol{i}_r^k,\phi_m)\boldsymbol{T}_P(\phi_k)\\
&\\
&\boldsymbol{L}_r^k(\boldsymbol{i}_s^k,\boldsymbol{i}_r^k,\phi_m,\phi_k) := -\tfrac{\partial\boldsymbol{\psi}_r^k(\boldsymbol{i}_s^k,\boldsymbol{i}_r^k,\phi_m,\phi_k)}{\partial\boldsymbol{i}_r^k}\\
&= \boldsymbol{T}_P^{-1}(\phi_k{-}n_m\phi_m)\boldsymbol{T}_C\boldsymbol{L}_r^{uvw}(\boldsymbol{T}_C^{-1}\boldsymbol{T}_P(\phi_k)\boldsymbol{i}_s^k,\boldsymbol{T}_C^{-1}\boldsymbol{T}_P(\phi_k{-}n_m\phi_m)\boldsymbol{i}_r^k,\phi_m)\boldsymbol{T}_C^{-1}\boldsymbol{T}_P(\phi_k{-}n_m\phi_m)\\
&= \boldsymbol{T}_P^{-1}(\phi_k{-}n_m\phi_m)\boldsymbol{L}_r^r(\boldsymbol{T}_P(\phi_k)\boldsymbol{i}_s^k,\boldsymbol{T}_P(\phi_k{-}n_m\phi_m)\boldsymbol{i}_r^k,\phi_m)\boldsymbol{T}_P(\phi_k{-}n_m\phi_m)\\
&\\
&\boldsymbol{\varphi}_{rm}^k(\boldsymbol{i}_s^k,\boldsymbol{i}_r^k,\phi_m,\phi_k) := \tfrac{\partial\boldsymbol{\psi}_r^k(\boldsymbol{i}_s^k,\boldsymbol{i}_r^k,\phi_m,\phi_k)}{\partial\phi_m}\\
&= n_m\boldsymbol{T}_P^{-1}(\phi_k{-}n_m\phi_m)\boldsymbol{T}_C\boldsymbol{L}_r^{uvw}(\boldsymbol{T}_C^{-1}\boldsymbol{T}_P(\phi_k)\boldsymbol{i}_s^k,\boldsymbol{T}_C^{-1}\boldsymbol{T}_P(\phi_k{-}n_m\phi_m)\boldsymbol{i}_r^k,\phi_m)\boldsymbol{T}_C^{-1}\boldsymbol{T}_P(\phi_k{-}n_m\phi_m)\boldsymbol{J}'\boldsymbol{i}_r^k(t)\\
&\quad+\boldsymbol{T}_P^{-1}(\phi_k{-}n_m\phi_m)\boldsymbol{T}_C\boldsymbol{\varphi}_{rm}^{uvw}(\boldsymbol{T}_C^{-1}\boldsymbol{T}_P(\phi_k)\boldsymbol{i}_s^k,\boldsymbol{T}_C^{-1}\boldsymbol{T}_P(\phi_k{-}n_m\phi_m)\boldsymbol{i}_r^k,\phi_m)\\
&\quad+n_m\boldsymbol{T}_P^{-1}(\phi_k{-}n_m\phi_m)\boldsymbol{J}'\boldsymbol{T}_C\boldsymbol{\psi}_r^{uvw}(\boldsymbol{T}_C^{-1}\boldsymbol{T}_P(\phi_k)\boldsymbol{i}_s^k,\boldsymbol{T}_C^{-1}\boldsymbol{T}_P(\phi_k{-}n_m\phi_m)\boldsymbol{i}_r^k,\phi_m)\\
&= n_m\boldsymbol{T}_P^{-1}(\phi_k{-}n_m\phi_m)\boldsymbol{L}_r^r(\boldsymbol{T}_P(\phi_k)\boldsymbol{i}_s^k,\boldsymbol{T}_P(\phi_k{-}n_m\phi_m)\boldsymbol{i}_r^k,\phi_m)\boldsymbol{T}_P(\phi_k{-}n_m\phi_m)\boldsymbol{J}'\boldsymbol{i}_r^k(t)\\
&\quad+\boldsymbol{T}_P^{-1}(\phi_k{-}n_m\phi_m)\boldsymbol{\varphi}_{rm}^r(\boldsymbol{T}_P(\phi_k)\boldsymbol{i}_s^k,\boldsymbol{T}_P(\phi_k{-}n_m\phi_m)\boldsymbol{i}_r^k,\phi_m)\\
&\quad+n_m\boldsymbol{T}_P^{-1}(\phi_k{-}n_m\phi_m)\boldsymbol{J}'\boldsymbol{\psi}_r^r(\boldsymbol{T}_P(\phi_k)\boldsymbol{i}_s^k,\boldsymbol{T}_P(\phi_k{-}n_m\phi_m)\boldsymbol{i}_r^k,\phi_m)\\
&= n_m\boldsymbol{L}_r^k(\boldsymbol{i}_s^k,\boldsymbol{i}_r^k,\phi_m,\phi_k)\boldsymbol{J}'\boldsymbol{i}_r^k(t)+\boldsymbol{T}_P^{-1}(\phi_k{-}n_m\phi_m)\boldsymbol{\varphi}_{rm}^r(\boldsymbol{T}_P(\phi_k)\boldsymbol{i}_s^k,\boldsymbol{T}_P(\phi_k{-}n_m\phi_m)\boldsymbol{i}_r^k,\phi_m)\\
&\quad+n_m\boldsymbol{J}'\boldsymbol{\psi}_r^k(\boldsymbol{i}_s^k,\boldsymbol{i}_r^k,\phi_m,\phi_k)\\
&\\
&\boldsymbol{\varphi}_{rk}^k(\boldsymbol{i}_s^k,\boldsymbol{i}_r^k,\phi_m,\phi_k) := \tfrac{\partial\boldsymbol{\psi}_r^k(\boldsymbol{i}_s^k,\boldsymbol{i}_r^k,\phi_m,\phi_k)}{\partial\phi_k}\\
&= -\boldsymbol{T}_P^{-1}(\phi_k{-}n_m\phi_m)\boldsymbol{T}_C\boldsymbol{L}_{rs}^{uvw}(\boldsymbol{T}_C^{-1}\boldsymbol{T}_P(\phi_k)\boldsymbol{i}_s^k,\boldsymbol{T}_C^{-1}\boldsymbol{T}_P(\phi_k{-}n_m\phi_m)\boldsymbol{i}_r^k,\phi_m)\boldsymbol{T}_C^{-1}\boldsymbol{T}_P(\phi_k)\boldsymbol{J}'\boldsymbol{i}_s^k(t)\\
&\quad-\boldsymbol{T}_P^{-1}(\phi_k{-}n_m\phi_m)\boldsymbol{T}_C\boldsymbol{L}_r^{uvw}(\boldsymbol{T}_C^{-1}\boldsymbol{T}_P(\phi_k)\boldsymbol{i}_s^k,\boldsymbol{T}_C^{-1}\boldsymbol{T}_P(\phi_k{-}n_m\phi_m)\boldsymbol{i}_r^k,\phi_m)\boldsymbol{T}_C^{-1}\boldsymbol{T}_P(\phi_k{-}n_m\phi_m)\boldsymbol{J}'\boldsymbol{i}_r^k(t)\\
&\quad-\boldsymbol{T}_P^{-1}(\phi_k{-}n_m\phi_m)\boldsymbol{J}'\boldsymbol{T}_C\boldsymbol{\psi}_r^{uvw}(\boldsymbol{T}_C^{-1}\boldsymbol{T}_P(\phi_k)\boldsymbol{i}_s^k,\boldsymbol{T}_C^{-1}\boldsymbol{T}_P(\phi_k{-}n_m\phi_m)\boldsymbol{i}_r^k,\phi_m)\\
&= -\boldsymbol{T}_P^{-1}(\phi_k{-}n_m\phi_m)\boldsymbol{L}_{rs}^r(\boldsymbol{T}_P(\phi_k)\boldsymbol{i}_s^k,\boldsymbol{T}_P(\phi_k{-}n_m\phi_m)\boldsymbol{i}_r^k,\phi_m)\boldsymbol{T}_P(\phi_k)\boldsymbol{J}'\boldsymbol{i}_s^k(t)\\
&\quad-\boldsymbol{T}_P^{-1}(\phi_k{-}n_m\phi_m)\boldsymbol{L}_r^r(\boldsymbol{T}_P(\phi_k)\boldsymbol{i}_s^k,\boldsymbol{T}_P(\phi_k{-}n_m\phi_m)\boldsymbol{i}_r^k,\phi_m)\boldsymbol{T}_P(\phi_k{-}n_m\phi_m)\boldsymbol{J}'\boldsymbol{i}_r^k(t)\\
&\quad-\boldsymbol{T}_P^{-1}(\phi_k{-}n_m\phi_m)\boldsymbol{J}'\boldsymbol{\psi}_r^r(\boldsymbol{T}_P(\phi_k)\boldsymbol{i}_s^k,\boldsymbol{T}_P(\phi_k{-}n_m\phi_m)\boldsymbol{i}_r^k,\phi_m)\\
&= -\boldsymbol{L}_{rs}^k(\boldsymbol{i}_s^k,\boldsymbol{i}_r^k,\phi_m,\phi_k)\boldsymbol{J}'\boldsymbol{i}_s^k(t)-\boldsymbol{L}_r^k(\boldsymbol{i}_s^k,\boldsymbol{i}_r^k,\phi_m,\phi_k)\boldsymbol{J}'\boldsymbol{i}_r^k(t)-\boldsymbol{J}'\boldsymbol{\psi}_r^k(\boldsymbol{i}_s^k,\boldsymbol{i}_r^k,\phi_m,\phi_k)\ .
\end{aligned}\right\} \tag{B.12}$$

B.3 Symmetry properties of the DFIM inductances

This section discusses the symmetry properties of the differential inductances of the stator $\boldsymbol{L}_s^k$, the rotor $\boldsymbol{L}_r^k$ and the couplings $\boldsymbol{L}_{sr}^k$ and $\boldsymbol{L}_{rs}^k$. To obtain these symmetry properties, the corresponding inductances in the three-phase reference frames *abc* and *uvw*, i.e. $\boldsymbol{L}_s^{abc}$, $\boldsymbol{L}_r^{uvw}$, $\boldsymbol{L}_{sr}^{abc}$ and $\boldsymbol{L}_{rs}^{uvw}$, are used. Because of (A.2.7), the following holds: $\boldsymbol{L}_s^{abc}=\left(\boldsymbol{L}_s^{abc}\right)^\top$, $\boldsymbol{L}_r^{uvw}=\left(\boldsymbol{L}_r^{uvw}\right)^\top$ and $\boldsymbol{L}_{sr}^{abc}=\left(\boldsymbol{L}_{rs}^{uvw}\right)^\top$.

Remark (R.B.1) *To simplify the readability of this section, the arguments of the upcoming derivations are restricted to the arguments of the Park transformation.*

B.3.1 Stator inductance

The symmetry property of the stator inductance $\boldsymbol{L}_s^k$ can be obtained by using (B.8), which contains the relation between the stator inductance $\boldsymbol{L}_s^k$ in the arbitrarily k-reference frame and the stator inductance $\boldsymbol{L}_s^{abc}=\left(\boldsymbol{L}_s^{abc}\right)^\top$ in the three-phase *abc*-reference frame. It follows

$$\begin{aligned}\boldsymbol{L}_s^k =& \boldsymbol{T}_P^{-1}(\phi_k)\boldsymbol{T}_C\boldsymbol{L}_s^{abc}\boldsymbol{T}_C^{-1}\boldsymbol{T}_P(\phi_k)\\ &\underset{\boldsymbol{L}_s^{abc}=\left(\boldsymbol{L}_s^{abc}\right)^\top}{\Longrightarrow} \quad \boldsymbol{L}_s^k-\left(\boldsymbol{L}_s^k\right)^\top=\begin{bmatrix}0 & 0 & (1-2\kappa_c^2)L_s^{d\gamma}\\ 0 & 0 & (1-2\kappa_c^2)L_s^{q\gamma}\\ (2\kappa_c^2-1)L_s^{d\gamma} & (2\kappa_c^2-1)L_s^{q\gamma} & 0\end{bmatrix}.\end{aligned} \tag{B.13}$$

Due to (A.2.3), the γ-component i_s^γ of the stator current is zero, i.e. $i_s^\gamma=0$. Hence, the stator flux linkage $\boldsymbol{\psi}_s^k$ is not a function of the γ-component i_s^γ of the stator current and, consequently, the third column $-\frac{\partial\boldsymbol{\psi}_s^k}{\partial i_s^\gamma}$ of the stator inductance $\boldsymbol{L}_s^k$ must be zero. Thus, it holds $L_s^{d\gamma}=L_s^{q\gamma}=L_s^{\gamma\gamma}=0$ and because of (B.13), the stator inductance $\boldsymbol{L}_s^k$ is symmetric, i.e. $\boldsymbol{L}_s^k=\left(\boldsymbol{L}_s^k\right)^\top$.

B.3.2 Rotor inductance

The relation between the rotor inductance $\boldsymbol{L}_r^k$ in the arbitrarily k-reference frame and the rotor inductance $\boldsymbol{L}_r^{uvw}=\left(\boldsymbol{L}_r^{uvw}\right)^\top$ in the three-phase *uvw*-reference frame is given in (B.12). This relation yields

$$\begin{aligned}\boldsymbol{L}_r^k =& \boldsymbol{T}_P^{-1}(\phi_k-n_m\phi_m)\boldsymbol{T}_C\boldsymbol{L}_r^{uvw}\boldsymbol{T}_C^{-1}\boldsymbol{T}_P(\phi_k-n_m\phi_m)\\ &\underset{\boldsymbol{L}_r^{uvw}=\left(\boldsymbol{L}_r^{uvw}\right)^\top}{\Longrightarrow} \quad \boldsymbol{L}_r^k-\left(\boldsymbol{L}_r^k\right)^\top=\begin{bmatrix}0 & 0 & (1-2\kappa_c^2)L_r^{d\gamma}\\ 0 & 0 & (1-2\kappa_c^2)L_r^{q\gamma}\\ (2\kappa_c^2-1)L_r^{d\gamma} & (2\kappa_c^2-1)L_r^{q\gamma} & 0\end{bmatrix}.\end{aligned} \tag{B.14}$$

Due to (A.2.3), the γ-component i_r^γ of the rotor current is zero, i.e. $i_r^\gamma=0$. Hence, the rotor flux linkage $\boldsymbol{\psi}_r^k$ is not a function of the γ-component i_r^γ of the rotor current and, accordingly, the third column $-\frac{\partial\boldsymbol{\psi}_r^k}{\partial i_r^\gamma}$ of the rotor inductance $\boldsymbol{L}_r^k$ must be zero. Thus, it holds $L_r^{d\gamma}=L_r^{q\gamma}=L_r^{\gamma\gamma}=0$ and because of (B.14), the rotor inductance $\boldsymbol{L}_r^k$ is symmetric, i.e. $\boldsymbol{L}_r^k=\left(\boldsymbol{L}_r^k\right)^\top$.

B.3.3 Coupling inductances

In (B.8) and (B.12), the relations between the coupling matrices $\boldsymbol{L}_{sr}^k$, $\boldsymbol{L}_{sr}^{abc}$, $\boldsymbol{L}_{rs}^k$ and $\boldsymbol{L}_{rs}^{uvw}$ are given by

$$\boldsymbol{L}_{sr}^k=\boldsymbol{T}_P^{-1}(\phi_k)\boldsymbol{T}_C\boldsymbol{L}_{sr}^{abc}\boldsymbol{T}_C^{-1}\boldsymbol{T}_P(\phi_k-n_m\phi_m) \quad\text{and}\quad \boldsymbol{L}_{rs}^k=\boldsymbol{T}_P^{-1}(\phi_k-n_m\phi_m)\boldsymbol{T}_C\boldsymbol{L}_{rs}^{uvw}\boldsymbol{T}_C^{-1}\boldsymbol{T}_P(\phi_k). \tag{B.15}$$

Considering the symmetry property $\boldsymbol{L}_{rs}^{uvw} = (\boldsymbol{L}_{sr}^{abc})^{\top}$, (B.15) leads to

$$\boldsymbol{L}_{rs}^{k} - (\boldsymbol{L}_{sr}^{k})^{\top} = \begin{bmatrix} 0 & 0 & L_{rs}^{d\gamma} - L_{sr}^{\gamma d} \\ 0 & 0 & L_{rs}^{q\gamma} - L_{sr}^{\gamma q} \\ L_{rs}^{\gamma d} - L_{sr}^{d\gamma} & L_{rs}^{\gamma q} - L_{sr}^{q\gamma} & 0 \end{bmatrix} = (1-2\kappa_c^2) \begin{bmatrix} 0 & 0 & L_{rs}^{d\gamma} \\ 0 & 0 & L_{rs}^{q\gamma} \\ -L_{sr}^{d\gamma} & -L_{sr}^{q\gamma} & 0 \end{bmatrix}. \tag{B.16}$$

Due to (A.2.3), the γ-components i_s^{γ} and i_r^{γ} of the stator and rotor current are zero, i.e. $i_s^{\gamma} = i_r^{\gamma} = 0$. Hence, the flux linkages $\boldsymbol{\psi}_s^k$ and $\boldsymbol{\psi}_r^k$ of stator and rotor, respectively, are not functions of the γ-components i_s^{γ} and i_r^{γ}. Accordingly, the third columns $-\frac{\partial \boldsymbol{\psi}_r^k}{\partial i_s^{\gamma}}$ and $-\frac{\partial \boldsymbol{\psi}_s^k}{\partial i_r^{\gamma}}$ of the coupling inductances $\boldsymbol{L}_{rs}^k$ and $\boldsymbol{L}_{sr}^k$ must be zero. Thus, it holds $L_{rs}^{d\gamma} = L_{rs}^{q\gamma} = L_{rs}^{\gamma\gamma} = L_{sr}^{d\gamma} = L_{sr}^{q\gamma} = L_{sr}^{\gamma\gamma} = 0$ and because of (B.16), for the coupling inductances $\boldsymbol{L}_{rs}^k$ and $\boldsymbol{L}_{sr}^k$, the following symmetry property holds: $\boldsymbol{L}_m^k := \boldsymbol{L}_{rs}^k = (\boldsymbol{L}_{sr}^k)^{\top}$.

Appendix C

Proofs of used mathematical correlations

This section covers two mathematical proofs. Sec. C.1 shows that the augmented LCL filter dynamics (3.3) are controllable, if and only if (C.3.1) is fulfilled. Sec. C.2 proves that the "stationary" system matrix $\boldsymbol{N}_{\mathrm{lcl}}$ is invertible, if and only if (3.40) holds.

C.1 Proof of controllability

To allow for controlling the augmented LCL filter dynamics (3.3), they must be controllable. Therefor, the corresponding controllability matrix $\boldsymbol{S}_\xi := \begin{bmatrix} \boldsymbol{B}_\xi & \boldsymbol{A}_\xi\boldsymbol{B}_\xi & \boldsymbol{A}_\xi^2\boldsymbol{B}_\xi & \boldsymbol{A}_\xi^3\boldsymbol{B}_\xi \end{bmatrix}$ with

$$\boldsymbol{A}_\xi = \begin{bmatrix} -\frac{R_f+R_h}{L_f}\boldsymbol{I}_2 - \omega_g\boldsymbol{J} & \frac{R_h}{L_f}\boldsymbol{I}_2 & -\frac{1}{L_f}\boldsymbol{I}_2 & \boldsymbol{O}_{2\times2} \\ \frac{R_h}{L_g}\boldsymbol{I}_2 & -\frac{R_g+R_h}{L_g}\boldsymbol{I}_2 - \omega_g\boldsymbol{J} & \frac{1}{L_g}\boldsymbol{I}_2 & \boldsymbol{O}_{2\times2} \\ \frac{1}{C_h}\boldsymbol{I}_2 & -\frac{1}{C_h}\boldsymbol{I}_2 & -\omega_g\boldsymbol{J} & \boldsymbol{O}_{2\times2} \\ -\begin{pmatrix}1 & 0\end{pmatrix}^\top & \boldsymbol{O}_{2\times2} & -\begin{pmatrix}0 & 1\end{pmatrix}^\top & \boldsymbol{O}_{2\times4} \end{bmatrix} \quad \text{and} \quad \boldsymbol{B}_\xi = \begin{bmatrix} \frac{1}{L_f}\boldsymbol{I}_2 \\ \boldsymbol{O}_{2\times2} \\ \boldsymbol{O}_{2\times2} \\ \boldsymbol{O}_{2\times2} \end{bmatrix} \tag{C.1}$$

needs to have full rank, i.e. $\operatorname{rank}(\boldsymbol{S}_\xi) = 8$ (see e.g. [143]). This leads to (C.3.1), which is obtained by carrying out the following five steps:

Step 1: $\boldsymbol{S}_{\xi,1}$ results from scaling the controllability matrix $\boldsymbol{S}_\xi$ by L_f. Adding the fifth and sixth row of $\boldsymbol{S}_{\xi,1}$, scaled by $-\frac{C_hR_h}{L_g}$, to the third and fourth row of $\boldsymbol{S}_{\xi,1}$, respectively, yields

$$\boldsymbol{S}_{\xi,1} = L_f\boldsymbol{S}_\xi \qquad \text{and} \qquad \boldsymbol{S}_{\xi,2} = \boldsymbol{S}_{\xi,1} - \frac{C_hR_h}{L_g}\begin{bmatrix} \boldsymbol{O}_{2\times4} & \boldsymbol{O}_{2\times2} & \boldsymbol{O}_{2\times2} \\ \boldsymbol{O}_{2\times4} & \boldsymbol{I}_2 & \boldsymbol{O}_{2\times2} \\ \boldsymbol{O}_{4\times4} & \boldsymbol{O}_{4\times2} & \boldsymbol{O}_{4\times2} \end{bmatrix}\boldsymbol{S}_{\xi,1}\,. \tag{C.2}$$

Step 2: Adding the fifth row of $\boldsymbol{S}_{\xi,2}$, scaled by C_h, to the seventh row of $\boldsymbol{S}_{\xi,2}$ gives $\boldsymbol{S}_{\xi,3}$. Commuting the fifth and sixth row of $\boldsymbol{S}_{\xi,3}$ with the third and fourth row of $\boldsymbol{S}_{\xi,3}$, respectively, results in

$$\boldsymbol{S}_{\xi,3} = \boldsymbol{S}_{\xi,2} + C_h\begin{bmatrix} \boldsymbol{O}_{6\times4} & \boldsymbol{0}_4 & \boldsymbol{O}_{3\times4} \\ \boldsymbol{0}_4^\top & 1 & \boldsymbol{0}_3^\top \\ \boldsymbol{0}_4^\top & 0 & \boldsymbol{0}_3^\top \end{bmatrix}\boldsymbol{S}_{\xi,2} \quad \text{and} \quad \boldsymbol{S}_{\xi,4} = \begin{bmatrix} \boldsymbol{I}_2 & \boldsymbol{O}_{2\times2} & \boldsymbol{O}_{2\times2} & \boldsymbol{O}_{2\times2} \\ \boldsymbol{O}_{2\times2} & \boldsymbol{O}_{2\times2} & \boldsymbol{I}_2 & \boldsymbol{O}_{2\times2} \\ \boldsymbol{O}_{2\times2} & \boldsymbol{I}_2 & \boldsymbol{O}_{2\times2} & \boldsymbol{O}_{2\times2} \\ \boldsymbol{O}_{2\times2} & \boldsymbol{O}_{2\times2} & \boldsymbol{O}_{2\times2} & \boldsymbol{I}_2 \end{bmatrix}\boldsymbol{S}_{\xi,3}\,. \tag{C.3}$$

Note that all entries of the fifth and sixth row of $\boldsymbol{S}_{\xi,4}$ are zero, i.e. $\begin{bmatrix}\boldsymbol{O}_{2\times4} & \boldsymbol{I}_2 & \boldsymbol{O}_{2\times2}\end{bmatrix}\boldsymbol{S}_{\xi,4}=\boldsymbol{O}_{2\times8}$, if $L_g-C_hR_gR_h=0$. Hence, $L_g-C_hR_gR_h\neq0$ must hold in order that $\boldsymbol{S}_\xi$ has full rank.

Step 3: Adding the fifth and sixth row of $\boldsymbol{S}_{\xi,4}$, scaled by $\frac{R_hC_hL_g}{L_g-C_hR_gR_h}$, to the seventh and eighth row of $\boldsymbol{S}_{\xi,4}$, respectively, yields

$$\boldsymbol{S}_{\xi,5}=\boldsymbol{S}_{\xi,4}+\frac{R_hC_hL_g}{L_g-C_hR_gR_h}\begin{bmatrix}\boldsymbol{O}_{6\times4} & \boldsymbol{O}_{6\times2} & \boldsymbol{O}_{6\times2}\\ \boldsymbol{O}_{2\times4} & \boldsymbol{I}_2 & \boldsymbol{O}_{2\times2}\end{bmatrix}\boldsymbol{S}_{\xi,4}\,. \tag{C.4}$$

Step 4: Adding the sixth row of $\boldsymbol{S}_{\xi,5}$, scaled by $-\frac{\omega_gC_hL_g^2}{L_g-C_hR_gR_h}$, to the seventh row of $\boldsymbol{S}_{\xi,5}$ gives

$$\boldsymbol{S}_{\xi,6}=\boldsymbol{S}_{\xi,5}-\frac{\omega_gC_hL_g^2}{L_g-C_hR_gR_h}\begin{bmatrix}\boldsymbol{O}_{6\times5} & \boldsymbol{0}_6 & \boldsymbol{O}_{6\times2}\\ \boldsymbol{0}_5^\top & 1 & \boldsymbol{0}_2^\top\\ \boldsymbol{0}_5^\top & 0 & \boldsymbol{0}_2^\top\end{bmatrix}\boldsymbol{S}_{\xi,5}\,. \tag{C.5}$$

Step 5: Adding the eighth column of $\boldsymbol{S}_{\xi,6}$, scaled by $-\omega_gC_hR_h$, to the seventh column of $\boldsymbol{S}_{\xi,6}$ results in

$$\boldsymbol{S}_{\xi,7}=\boldsymbol{S}_{\xi,6}-\omega_gC_hR_h\boldsymbol{S}_{\xi,6}\begin{bmatrix}\boldsymbol{O}_{7\times6} & \boldsymbol{0}_7 & \boldsymbol{0}_7\\ \boldsymbol{0}_6^\top & 1 & 0\end{bmatrix}. \tag{C.6}$$

$\boldsymbol{S}_{\xi,7}\in\mathbb{R}^{8\times8}$ is an upper triangular matrix and exhibits the following eight diagonal elements:

$$1,1,\frac{1}{C_h},\frac{1}{C_h},\frac{L_g-C_hR_gR_h}{C_hL_g^2},\frac{L_g-C_hR_gR_h}{C_hL_g^2},\frac{\omega_g^2C_hL_g-1-\omega_g^2C_h^2R_h\,(R_g+R_h)}{C_hL_g}\text{ and }-\frac{1}{C_hL_g}\,. \tag{C.7}$$

The controllability matrix $\boldsymbol{S}_\xi$ has full rank, i.e. $\operatorname{rank}(\boldsymbol{S}_\xi)=8$, if and only if all diagonal elements of $\boldsymbol{S}_{\xi,7}$ in (C.7) are not zero. This leads to the condition

$$L_g-R_gR_hC_h\neq0\;\text{ and }\;\frac{1}{\omega_g^2C_h}\neq L_g-R_hC_h\,(R_g+R_h)\quad\overset{R_h=0}{\Longrightarrow}\quad\omega_g\neq\frac{1}{\sqrt{L_gC_h}}\,.\quad\square \tag{C.8}$$

C.2 Proof of invertibility

The invertability of the "stationary" system matrix $\boldsymbol{N}_{\text{lcl}}$ is necessary to be able to calculate the "stationary" state vector $\boldsymbol{z}^\star_{\text{lcl}}$ as in (3.39). Accordingly, the "stationary" system matrix

$$\boldsymbol{N}_{\text{lcl}}=\begin{bmatrix}\frac{1}{L_f} & \omega_g & \frac{R_h}{L_f} & 0 & -\frac{1}{L_f} & 0\\ 0 & -\frac{R_f+R_h}{L_f} & 0 & \frac{1}{L_f} & 0 & -\frac{1}{L_f}\\ 0 & 0 & -\frac{R_g+R_h}{L_g} & 0 & \frac{1}{L_g} & 0\\ 0 & \frac{R_h}{L_g} & -\omega_g & 0 & 0 & \frac{1}{L_g}\\ 0 & 0 & -\frac{1}{C_h} & 0 & 0 & \omega_g\\ 0 & \frac{1}{C_h} & 0 & 0 & -\omega_g & 0\end{bmatrix} \tag{C.9}$$

needs to have full rank, i.e. $\operatorname{rank}(\boldsymbol{N}_{\text{lcl}})=6$. This leads to (3.40), which is obtained by carrying out the following three steps:

Step 1: The rows and columns of the "stationary" system matrix $\boldsymbol{N}_{\text{lcl}}$ are changed as follows

$$\boldsymbol{N}_{\text{lcl},1} = \boldsymbol{N}_{\text{lcl}} \begin{bmatrix} 1 & 0 & \boldsymbol{0}_2^\top & \boldsymbol{0}_2^\top \\ \boldsymbol{0}_2 & \boldsymbol{0}_2 & \boldsymbol{I}_2 & \boldsymbol{O}_{2\times 2} \\ 0 & 1 & \boldsymbol{0}_2^\top & \boldsymbol{0}_2^\top \\ \boldsymbol{0}_2 & \boldsymbol{0}_2 & \boldsymbol{O}_{2\times 2} & \boldsymbol{I}_2 \end{bmatrix} \quad \text{and} \quad \boldsymbol{N}_{\text{lcl},2} = \begin{bmatrix} \boldsymbol{I}_2 & \boldsymbol{O}_{2\times 2} & \boldsymbol{0}_2 & \boldsymbol{0}_2 \\ \boldsymbol{0}_2^\top & \boldsymbol{0}_2^\top & 0 & 1 \\ \boldsymbol{0}_2^\top & \boldsymbol{0}_2^\top & 1 & 0 \\ \boldsymbol{O}_{2\times 2} & \boldsymbol{I}_2 & \boldsymbol{0}_2 & \boldsymbol{0}_2 \end{bmatrix} \boldsymbol{N}_{\text{lcl},1}\,. \tag{C.10}$$

Step 2: Adding (i) the third row of $\boldsymbol{N}_{\text{lcl},2}$, scaled by $-\frac{C_h R_h}{L_g}$, to the sixth row of $\boldsymbol{N}_{\text{lcl},2}$, (ii) the fourth row of $\boldsymbol{N}_{\text{lcl},2}$, scaled by $-\omega_g C_h$, to the sixth row of $\boldsymbol{N}_{\text{lcl},2}$ and (iii) the fourth row of $\boldsymbol{N}_{\text{lcl},2}$, scaled by $-\frac{C_h(R_g+R_h)}{Lg}$, to the fifth row of $\boldsymbol{N}_{\text{lcl},2}$, gives

$$\boldsymbol{N}_{\text{lcl},3} = \boldsymbol{N}_{\text{lcl},2} - \begin{bmatrix} \boldsymbol{O}_{4\times 2} & \boldsymbol{0}_4 & \boldsymbol{0}_4 & \boldsymbol{O}_{4\times 2} \\ \boldsymbol{0}_2^\top & 0 & \frac{C_h(R_g+R_h)}{Lg} & \boldsymbol{0}_2^\top \\ \boldsymbol{0}_2^\top & \frac{C_h R_h}{L_g} & \omega_g C_h & \boldsymbol{0}_2^\top \end{bmatrix} \boldsymbol{N}_{\text{lcl},2}\,. \tag{C.11}$$

Step 3: Adding the fifth row of $\boldsymbol{N}_{\text{lcl},3}$, scaled by $-\omega_g C_h R_h$, to the sixth row of $\boldsymbol{N}_{\text{lcl},3}$ results in

$$\boldsymbol{N}_{\text{lcl},4} = \boldsymbol{N}_{\text{lcl},3} - \omega_g C_h R_h \begin{bmatrix} \boldsymbol{O}_{5\times 4} & \boldsymbol{0}_5 & \boldsymbol{0}_5 \\ \boldsymbol{0}_4^\top & 1 & 0 \end{bmatrix} \boldsymbol{N}_{\text{lcl},3}\,. \tag{C.12}$$

$\boldsymbol{N}_{\text{lcl},4} \in \mathbb{R}^{6\times 6}$ is an upper triangular matrix and exhibits the following six diagonal elements:

$$\frac{1}{L_f}\,,\ \frac{1}{L_f}\,,\ \frac{1}{C_h}\,,\ -\frac{1}{C_h}\,,\ \frac{1}{L_g} \quad \text{and} \quad \frac{1}{L_g} - \omega_g^2 C_h + \frac{\omega_g^2 C_h^2 R_h\,(R_g + R_h)}{L_g}\,. \tag{C.13}$$

The "stationary" system matrix $\boldsymbol{N}_{\text{lcl}}$ has full rank, i.e. $\operatorname{rank}(\boldsymbol{N}_{\text{lcl}}) = 6$, if and only if all diagonal elements of $\boldsymbol{N}_{\text{lcl},4}$ in (C.13) are not zero. This leads to the condition

$$\frac{1}{\omega_g^2 C_h} \neq L_g - R_h C_h\,(R_g + R_h) \quad \overset{R_h=0}{\Longrightarrow} \quad \omega_g \neq \frac{1}{\sqrt{L_g C_h}}\,. \qquad \square \tag{C.14}$$